Physics of the Solid State, Vol. 44, No. 3, 2002, pp. 399–404. From Fizika Tverdogo Tela, Vol. 44, No. 3, 2002, pp. 388–392.

PROCEEDINGS OF THE V INTERNATIONAL WORKSHOP "FULLERENES AND ATOMIC CLUSTERS"

(St. Petersburg, Russia, July 2–6, 2001)

Structural Transformations in Carbon Nanoparticles Induced by Electron Irradiation[1]

F. Banhart

Z.E. Elektronenmikroskopie, Universität Ulm, Ulm, 89069 Germany

Abstract—This paper reviews the electron-irradiation effects in graphitic nanoparticles. Irradiation-induced atomic displacements cause structural defects in graphite lattice forming the basis of carbon nanoparticles such as nanotubes or carbon onions. Defects of the type of non-six-membered rings induce topological alterations of graphene layers. The generation of curvature under electron irradiation leads to the formation of new structures, such as spherical carbon onions or coalescent nanotubes. At high temperatures, the self-compression of carbon onions can promote the nucleation of diamond cores or phase transformations of foreign materials that are encapsulated by onionlike graphitic shells. Under the nonequilibrium conditions of intense irradiation, the phase equilibrium between graphite and diamond can be reversed. It is shown that graphite can be transformed into diamond even if no external pressure is applied. All electron-irradiation and electron-microscopic studies described here were carried out using *in situ* transmission electron microscopy. *© 2002 MAIK "Nauka/Interperiodica".*

1. IRRADIATION OF GRAPHITIC STRUCTURES

Irradiation of solids with high-energetic particles can lead to structural alterations if atoms are persistently removed from their lattice positions. Graphite behaves under irradiation as most metals do; i.e., radiation damage is restricted to knock-on atom displacements, whereas excitations of the electron system do not lead to observable radiation effects [1]. Atoms can be displaced in a knock-on collision when the particle energy exceeds the displacement threshold energy. This energy is needed to displace an atom far enough from its position such that immediate recombination of the Frenkel pair does not occur. The minimum energy which has to be transferred to a carbon atom in graphite to induce its permanent displacement is approximately 15 eV [2]. The corresponding energy of the irradiating particles can be calculated from the laws of momentum conservation; for example, electrons with low mass need a threshold energy of 100 keV to induce structural changes in the graphite lattice. In the following, we will constrain our considerations to electrons as irradiating particles because of the importance of irradiation effects in the beams of electron microscopes.

The graphite lattice consists of flat graphene layers in which each carbon atom is bound covalently to three neighbor atoms such that a network of hexagonal rings is formed. When a carbon atom is knocked from its lattice site, a monovacancy is created, which is stable until recombination with a mobile interstitial atom can occur (Fig. 1a). The diffusivity of interstitials is an exponential function of temperature; therefore, the recombination dynamics in a graphitic structure under irradiation is governed by the temperature and also by the displacement rate, which is proportional to the irradiation intensity. At low temperatures, interstitials tend to form agglomerates between the basal layers. These agglomerates act as traps for further interstitials; as a result,

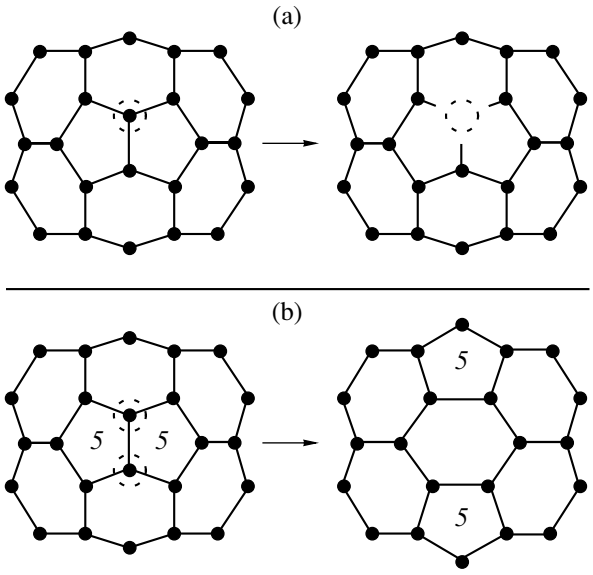

Fig. 1. Vacancy formation in the graphite lattice: (a) the removal of one carbon atom (encircled) from a curved graphene layer creates a stable monovacancy; (b) the removal of two adjacent atoms creates a divacancy that can close via Stone–Wales rearrangement. The number of hexagons is reduced by one, and the surface area is reduced.

[1] This article was submitted by the author in English.

1063-7834/02/4403-0399$22.00 © 2002 MAIK "Nauka/Interperiodica"

new basal layers are gradually generated [2]. This leads to a swelling of the graphite lattice in the *c* direction [3] and to a highly defective structure, as can be seen in high-resolution electron microscopy. At temperatures above approximately 600–700 K, the mobility of interstitials is high enough to promote annealing with vacancies. No more clustering of interstitials can take place, and the graphite lattice remains free of extended defects [4]. It is noteworthy that vacancies in graphite are immobile up to very high temperatures and do not play a considerable role in the defect dynamics and annealing behavior [5]. Since graphite has a layered crystal structure, the mobility of interstitials is highly anisotropic. Opposite to earlier expectations, the migration of interstitials is not restricted to the interplanar space [2]. When an interstitial is located between the planes, the local bonding character of the surrounding atoms can change from sp^2 towards sp^3. In such a way, the interstitial forms covalent bonds to the adjacent planes, which drastically reduces its mobility in the space parallel to the basal planes. Such an interstitial can rather migrate along the *c* direction by exchanging positions with atoms in the plane [6].

The defective graphite lattice has a peculiarity that distinguishes the behavior of graphite under irradiation from that of most other crystals. As soon as two adjacent atoms are displaced, i.e., a divacancy is created, the surrounding atoms within the plane can rearrange bonds in such a way that the open space is immediately closed, as shown schematically in Fig. 1b. These changes of bonding in a defective graphene layer are known as Stone–Wales rearrangements [7]. In such a process, hexagonal rings are converted to pentagons, heptagons, or other types of structural defects. Since the discovery of fullerenes, it has been known that non-six-membered rings introduce curvature into the otherwise flat graphene layer. Pentagons lead to positive (spherical) and heptagons to negative (saddlelike) curvature, whereas appropriate combinations of both pentagons and heptagons can be used to build up a variety of models of possible topologies [8, 9]. The irradiation-induced rearrangement of the atomic structure in graphitic networks is, therefore, a promising way to create new architectures in the world of carbon nanoparticles.

The first structural transformation was achieved when graphitic structures were transformed to spherical concentric shell particles (carbon onions) [10]. The introduction of pentagons and heptagons through irradiation induces curvature in the layers, which then close upon themselves by saturating all dangling bonds. However, it turned out that new structures that are created by irradiation can again be destroyed by atom displacements; as such, only those arrangements remain stable that are in a dynamic equilibrium under irradiation [2]. Since objects under intense irradiation are far from being in thermal equilibrium, the formation of ordered structures follows the principles of self-organization in dissipative systems. Apparently, the generation of carbon onions, as well as their transformations under further irradiation, can serve as examples of such self-organized nonequilibrium structure formation.

2. EXPERIMENTAL TECHNIQUES

The investigation of irradiation-induced structural transformations of carbon nanoparticles was undertaken using *in situ* transmission electron microscopy. Irradiation with high-energetic electrons and imaging on an atomic scale can be carried out at the same time. However, the electron energy has to exceed the displacement threshold, of approximately 100 keV, in graphitic structures. The studies presented in the following sections were carried out using a high-voltage electron microscope with an acceleration voltage of 1.25 MeV installed at the Max-Planck-Institut für Metallforschung in Stuttgart. A high-temperature specimen stage allowed the specimen temperature to be varied between room temperature and 1300 K. Specialized drift compensation systems were used to obtain a point resolution of 0.12 nm within the full temperature range. An imaging filter system was available to carry out electron energy-loss spectroscopy in order to obtain information on the bonding states and to distinguish between graphite and diamond-like modifications of carbon.

3. OBSERVATIONS AND DISCUSSION

3.1. Fullerenes

When fullerites, i.e., crystals that are built up of fullerene molecules, are exposed to an electron beam of more than 100 keV, the fullerene cages are rapidly damaged by a loss of atoms. In the microscope, this is seen as a collapse of the molecules, which then tend to coalesce so as to form larger irregular cages [11]. In the course of this process, the regular arrangement of molecules is completely lost. However, the picture can be different when individual fullerene molecules are irradiated. Under irradiation of graphite material, the formation of single fullerene-like cages of different size is often observed. These cages are located on the graphite surfaces and are surprisingly stable under the beam. Such a high radiation hardness was explained in terms of a mechanism where vacancies in the fullerene shell can recombine with free carbon atoms available on the graphite surface [11].

3.2. Carbon Nanotubes

Many-walled carbon nanotubes show the general behavior of graphite when irradiated with an electron beam. At low temperatures, radiation defects accumulate and the graphite planes curve and bend; this can eventually lead to the complete transformation of the tube to a carbon onion [10]. At temperatures above 600 K, the graphite lattice of the tubes remains free of extended defects and the tubes bend but do not transform to onionlike structures.

Single-walled carbon nanotubes are very sensitive to electron irradiation at low temperatures. Shrinkage and collapse of the tubes occur, leading to a necklace-like shape and eventually to complete disintegration [12]. As other graphite structures, single-walled nanotubes show a much improved stability when irradiated at higher temperatures. The irradiation of a bundle of single-walled nanotubes can lead to the coalescence of two adjacent tubes so as to form a tube of double diameter [13]. As shown in Fig. 2, such a coalescence can be monitored *in situ* in an electron microscope when curved bundles of tubes are locally aligned with their axes parallel to the viewing direction (along the optical axis of the microscope), such that they are imaged in cross section. Molecular-dynamics calculations show that the coalescence of adjacent tubes can only occur if the tubes have the same chirality [13].

3.3. Carbon Onions

The most spectacular irradiation effect of carbon nanoparticles is the transformation of graphite material to spherical concentric-shell carbon onions [10]. Almost all graphite precursors, such as soot particles, nanotubes, or any disordered graphite filaments, show this transformation when irradiated with an electron beam of sufficient intensity. The structure of carbon onions has been modeled by combining pentagons, hexagons, and heptagons in each shell (Fig. 3) [8, 14]. In such combinations, a uniform spherical curvature of the shells can be achieved without altering the bond length between two carbon atoms (0.14 nm). Complete spherical closure with saturation of all dangling bonds leaves a particularly stable structure, because further atom displacements just rearrange defects and do not change the curvature anymore.

The formation of carbon onions under irradiation at higher specimen temperatures leads to perfectly coherent graphite shells without extended defects. Such carbon onions show a spacing between the shells which is smaller than the equilibrium distance between basal planes in graphite (0.335 nm). Furthermore, the spacing decreases as one goes from the surface of the onion towards its center. This self-compression of carbon onions under irradiation has been explained in terms of the surface tension of the outer shells due to a sputtering-induced loss of atoms and successive closure of the shells around divacancies. The migration dynamics of interstitials through the onion, following the pressure gradient towards the surface, can explain why the pressure is not isostatic but increases towards the center [15]. The high mechanical strength of graphene layers makes the shells extremely rigid and allows the generation of enormous pressure inside the onion. The pressure can reach values that are high enough to promote the nucleation of a diamond crystal in the core of the onion [16]. The phase transformation into diamond is facilitated by the high curvature of the innermost shells, shifting the bonding character from sp^2 towards sp^3.

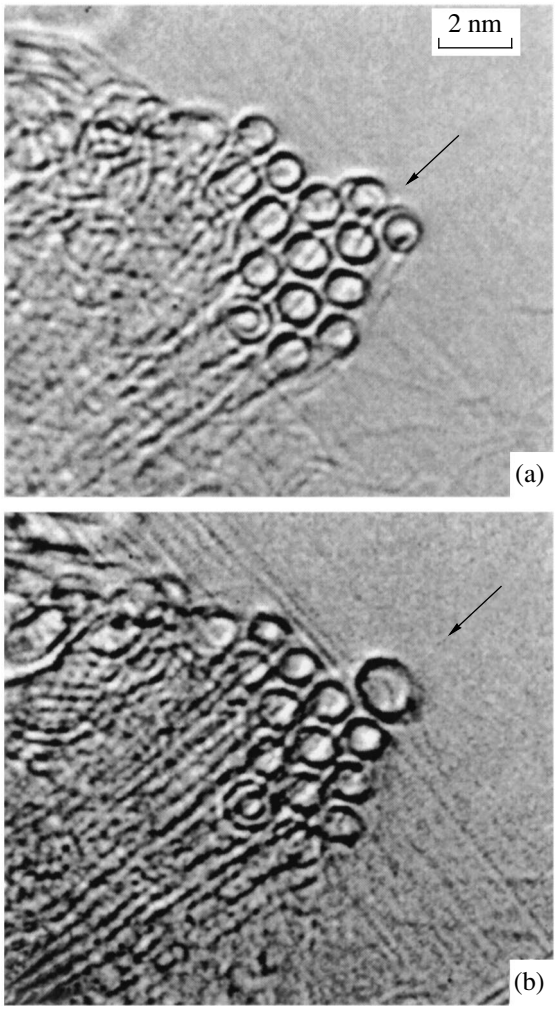

Fig. 2. Coalescence of two single-walled nanotubes under electron irradiation at 1000 K: (a) before and (b) after irradiation. The merging tubes are labeled with arrows.

3.4. Transformation of Graphite into Diamond under Irradiation

The phase equilibrium between graphite and diamond is determined by the difference in free enthalpy between the two phases. Close to thermal equilibrium, graphite is thermodynamically favored at low pressures and, thus, represents the stable phase of carbon. Diamond is the stable high-pressure phase but can exist in a metastable state at low pressures because the transformation into graphite is kinetically suppressed. The transformation of graphite into diamond requires the application of high pressure and high temperature and, to achieve a reasonable yield of diamond, the presence of metallic catalysts [17].

The function of carbon onions as pressure cells for diamond nucleation demonstrates a new way of transforming graphite into diamond. It has been observed that diamond cores in carbon onions, once nucleated, grow under sustained electron irradiation. Growth of

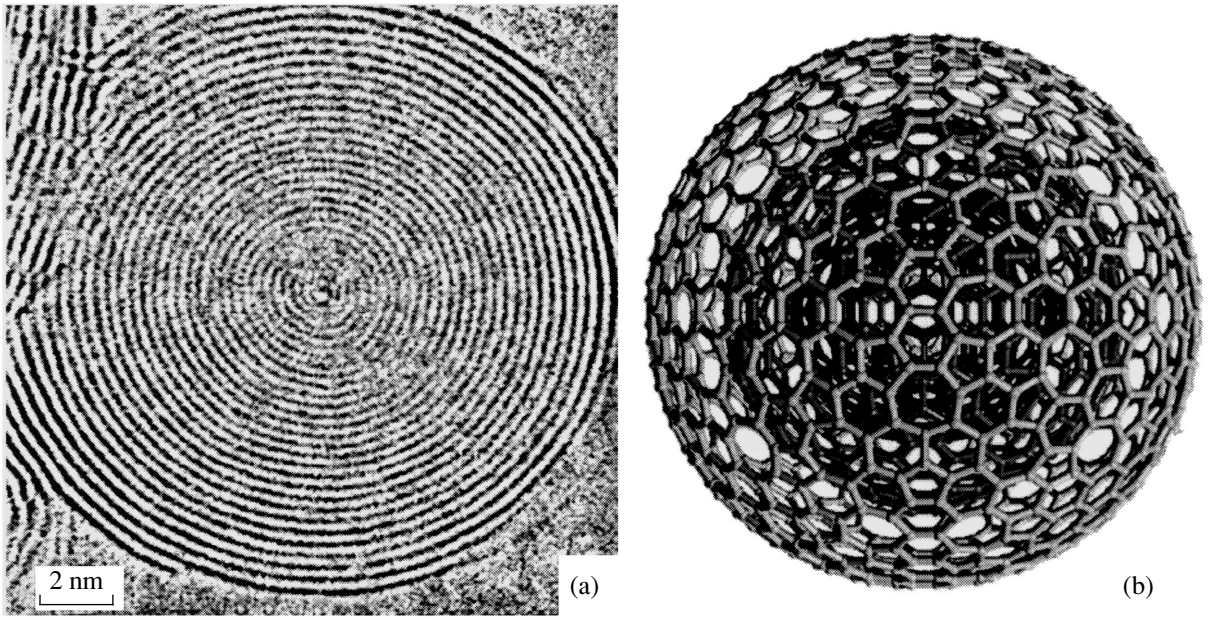

Fig. 3. The structure of carbon onions. (a) Electron microscopy image of a carbon onion formed under electron irradiation at 1000 K; the shells are coherent and show a decreasing spacing towards the center. (b) Model structure of a carbon onion with three shells (not on the same scale as in (a)); pentagons and heptagons ensure uniform curvature (courtesy of M. Terrones).

the diamond crystals at the expense of the surrounding graphite shells continues until the onions have wholly transformed into diamond, although no more pressure is applied to the system at the later stage of the process. This observation has motivated further studies, in which a flat interface between graphite and diamond was irradiated with an electron beam at different beam intensities and temperatures. Those experiments were carried out in the heating stage of an electron microscope; no external pressure was applied. It turned out that, within a limited temperature range, the phase equilibrium can be reversed such that diamond becomes the stable phase [18]. A theoretical treatment of the phase equilibrium between graphite and diamond under irradiation could explain the observations quantitatively [19]. The theory is based on the well-known fact that the radiation hardness of diamond exceeds that of graphite, i.e., that the atom displacement rate in graphite is higher than in diamond (under the same conditions of irradiation). When a carbon atom at the interface between the two phases is displaced, its survival time is longer if it aggregates to the diamond crystal. Thus, a net growth of diamond at the expense of graphite occurs, which depends on the displacement rate that is again proportional to the beam intensity. However, at high temperatures, thermal jumps of atoms across the interface prevail and restore thermal equilibrium, such that graphite becomes the stable phase again and grows at the expense of diamond. In such a way, a nonequilibrium phase diagram of carbon can be obtained such as that shown in Fig. 4. The only adjustable parameters in the model are the displacement threshold energies of graphite and diamond, which are not known with high accuracy from earlier studies. The adjustment of these parameters within a reasonable range has led to an excellent match of experimental and theoretical results [20]. These experiments have thus demonstrated for the first time that the transformation of graphite into diamond is feasible at zero pressure under the nonequilibrium conditions of intense particle irradiation.

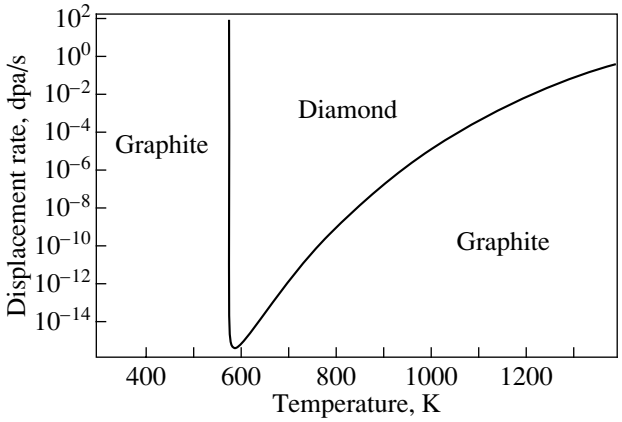

Fig. 4. Nonequilibrium phase diagram of carbon under high-energetic electron irradiation. The displacement rate (proportional to the beam intensity) is plotted as a function of temperature. The ratio of displacement cross sections in graphite and diamond of $\sigma_g/\sigma_d = 2.6$ was assumed.

3.5. Metal–Carbon Nanoparticles

The encapsulation of crystalline metals in graphite shells, either in nanotubes or in onions, is a subject of considerable interest [21]. Among techniques such as coevaporation of carbon together with metals at high temperature, irradiation of metal–carbon composites has been shown to produce metal crystals that are completely encapsulated in graphite shells [22]. This process occurs in a fashion similar to the formation of carbon onions under irradiation, with the difference that, here, graphite shells wrap around nanometer-sized metal crystals so as to form onionlike spherical graphitic particles with metal cores. Examples of the encapsulated transition metals Fe, Co, and Ni are shown in Fig. 5.

A peculiarity of these encapsulates is that the graphite shells self-compress under electron irradiation, such that considerable pressure is exerted on the metal crystal in the core. As a consequence, atoms at the metal–graphite interface can leave the metal crystal and migrate along the pressure gradient towards the surface of the graphite shell. This leads to a gradual shrinkage of the metal crystal inside the compressing shells until the crystal has completely vanished [22]. This phenomenon is of interest, because it allows one to study the migration of foreign atoms through graphite structures. Apparently, foreign atoms occupy irradiation-induced vacancies and migrate in the *c* direction via an exchange of position with carbon atoms. Most foreign atom species are unstable on lattice sites of graphite and tend to migrate rapidly; however, some elements form configurations with graphite that are at least temporarily stable. It has been observed that nickel atoms form metastable ordered arrangements during their migration through the graphite shells [23]. This can be seen on the right-hand side in Fig. 5, where the shells are modified due to the presence of Ni atoms.

The action of graphite shells as pressure cells for encapsulated foreign materials is highly useful for the study of pressure-induced phase transformations in small crystals. Very recent experiments show that the melting behavior of low-melting metals is completely altered when they are encapsulated in graphite shells [24].

A variety of new, unexpected phenomena resulted from the irradiation of graphite nanoparticles with high-energetic electrons. Although the atoms are displaced randomly by knock-on collisions with electrons, highly ordered structures can emerge from such nonequilibrium processes. The introduction of defects into graphene layers leads to curvature and to a change in topology of the structures. Perfectly spherical carbon onions have been shown to be the most stable arrangements of graphite carbon under irradiation. The self-compression of carbon onions can be made use of to nucleate diamond or to exert pressure on foreign materials that are encapsulated under irradiation in the cores. The study of carbon structures under irradiation has led to the discovery that the nonequilibrium conditions of irradiation can reverse the phase stability between graphite and diamond, which enabled us to transform graphite into diamond without applying pressure.

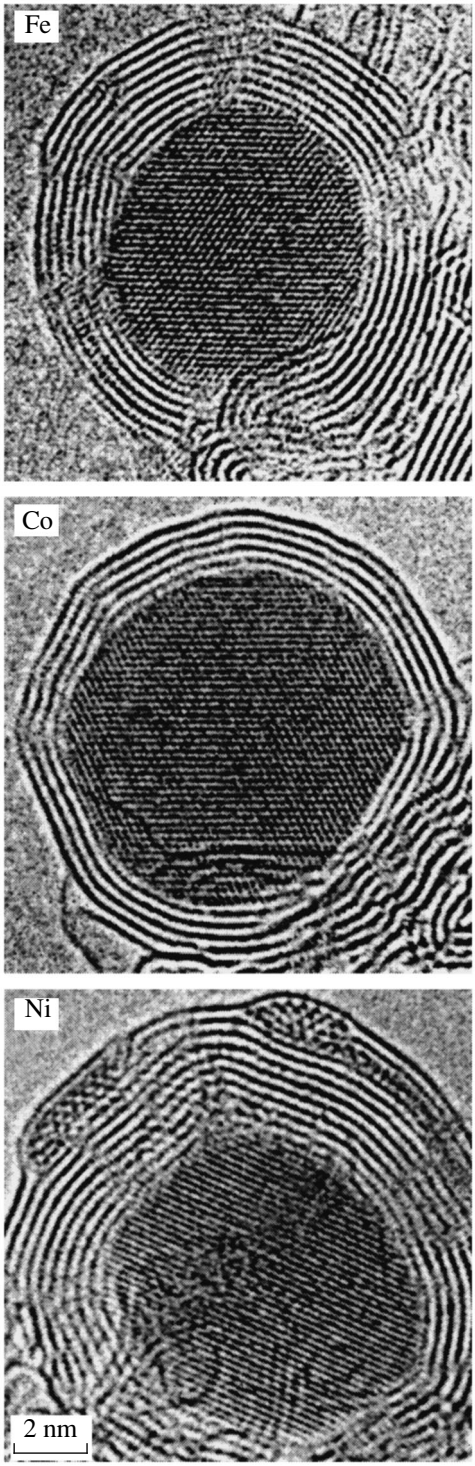

Fig. 5. Metal crystals that were encapsulated by graphite shells under electron irradiation. Examples for Fe, Co, and Ni crystals are shown.

ACKNOWLEDGMENTS

The author is grateful to Y. Lyutovich, M. Zaiser, M. Terrones, P.M. Ajayan, J.-C. Charlier, T. Füller, M. Zwanger, Ph. Kohler-Redlich, and A. Seeger, who contributed to the work presented in this review over years of excellent collaboration.

REFERENCES

1. B. T. Kelly, *Physics of Graphite* (Applied Science, London, 1981).
2. F. Banhart, Rep. Prog. Phys. **62**, 1181 (1999).
3. J. Koike and D. F. Pedraza, J. Mater. Res. **9**, 1899 (1994).
4. F. Banhart, T. Füller, Ph. Redlich, and P. M. Ajayan, Chem. Phys. Lett. **269**, 349 (1997).
5. P. A. Thrower and R. M. Mayer, Phys. Status Solidi A **47**, 11 (1978).
6. M. Heggie, B. R. Eggen, C. P. Ewels, P. Leary, S. Ali, G. Jungnickel, B. Jones, and P. R. Briddon, in *Fullerenes: Proceedings of the Symposium on Recent Advances in the Chemistry and Physics of Fullerenes and Related Materials*, Ed. by K. M. Kadish and R. S. Ruoff (The Electrochemical Society, Pennington, 1998), Vol. 6, p. 60.
7. A. J. Stone and D. J. Wales, Chem. Phys. Lett. **128**, 501 (1986).
8. H. Terrones, M. Terrones, and W. K. Hsu, Chem. Soc. Rev. **24**, 341 (1995).
9. M. Terrones and H. Terrones, Fullerene Sci. Technol. **4**, 517 (1996).
10. D. Ugarte, Nature **359**, 707 (1992).
11. T. Füller and F. Banhart, Chem. Phys. Lett. **254**, 372 (1996).
12. P. M. Ajayan, V. Ravikumar, and J.-C. Charlier, Phys. Rev. Lett. **81**, 1437 (1998).
13. M. Terrones, H. Terrones, F. Banhart, *et al.*, Science **288**, 1226 (2000).
14. K. R. Bates and G. E. Scuseria, Theor. Chem. Acc. **99**, 29 (1998).
15. M. Zaiser, Mater. Res. Soc. Symp. Proc. **540**, 243 (1999).
16. F. Banhart and P. M. Ajayan, Nature **382**, 433 (1996).
17. G. Davies, *Properties and Growth of Diamond* (INSPEC, London, 1994).
18. Y. Lyutovich and F. Banhart, Appl. Phys. Lett. **74**, 659 (1999).
19. M. Zaiser and F. Banhart, Phys. Rev. Lett. **79**, 3680 (1997).
20. M. Zaiser, Y. Lyutovich, and F. Banhart, Phys. Rev. B **62**, 3058 (2000).
21. M. Terrones, N. Grobert, W. K. Hsu, *et al.*, Mater. Res. Soc. Bull. **24**, 43 (1999).
22. F. Banhart, Ph. Redlich, and P. M. Ajayan, Chem. Phys. Lett. **292**, 554 (1998).
23. F. Banhart, J.-C. Charlier, and P. M. Ajayan, Phys. Rev. Lett. **84**, 686 (2000).
24. M. Terrones and F. Banhart, to be published.

Physics of the Solid State, Vol. 44, No. 3, 2002, pp. 405–409. Translated from Fizika Tverdogo Tela, Vol. 44, No. 3, 2002, pp. 393–397.

PROCEEDINGS OF THE V INTERNATIONAL WORKSHOP "FULLERENES AND ATOMIC CLUSTERS"

(St. Petersburg, Russia, July 2–6, 2001)

Correlations between the Physical Properties of the Carbon Phases Obtained at a High Pressure from C_{60} Fullerite

A. G. Lyapin and V. V. Brazhkin

Vereshchagin Institute of High-Pressure Physics, Russian Academy of Sciences, Troitsk, Moscow oblast, 142190 Russia
e-mail: alyapin@hppi.troitsk.ru

Abstract—Correlations between the density, elastic properties, and hardness of the carbon phases prepared from C_{60} at a high pressure are studied. By varying the high pressure and temperature properly, one can obtain from C_{60} a broad class of ordered polymerized and disordered phases, for which the fraction of the sp^2 and sp^3 states, the characteristic dimensionality of the structure, the degree of covalent bonding, etc. can be varied successfully. 3D-bonded carbon structures are shown to exhibit a clearly pronounced correlation between the hardness or bulk modulus and the density, with these correlations also apparently applying to the carbon phases in a general case. At the same time, the mechanical characteristics of structures with a lower dimension covalent bonding are worse than those of 3D-bonded phases with similar values of the density. © *2002 MAIK "Nauka/Interperiodica".*

1. INTRODUCTION

Investigation of correlations between the physical properties of various substances, in particular, between the density and mechanical characteristics, is of considerable interest. Considered from a physical standpoint, the relation between the density, elastic properties, and hardness may reflect the role played by the structure and atomic forces in the properties of the substance. Viewed practically, empirical relations may help in predicting the characteristics of new and hypothetical materials.

A variety of empirical relations connecting the density, elastic characteristics, hardness, and other physical properties have been thus far established for various groups of substances [1–10]. It is surprising that the elastic moduli of substances increase with decreasing molar volume [10]. However, the correlation between the elastic moduli and the electronic valence density is even stronger, which is clearly seen in the case of *s* and *p* solid elements (Fig. 1). Of particular interest are the empirical relations for the hardness, because, in contrast to elastic moduli, direct calculation of the macroscopic mechanical properties remains a problem of staggering complexity. It may be appropriate to mention, in this connection, the well-known correlation between the shear modulus and hardness [8–10], in particular, for superhard materials (Fig. 2).

Solid carbon offers a unique opportunity to study correlations between mechanical properties and density among numerous modifications of the same substance. The rich diversity of the real and hypothetical carbon phases derives from the fact that the carbon atom may reside in tetravalent sp^3, trivalent sp^2, or divalent *sp* states. The theoretical prediction of new carbon phases [13–19]; the discovery of new allotropic forms of carbon, such as fullerenes [20], nanotubes [21], and carbynes [22]; and the synthesis of various amorphous carbon sp^2–sp^3 phases [23–25] open new prospects for the physics of carbon materials.

In this paper, we analyze the elastic properties and hardness of a variety of carbon modifications prepared from the C_{60} fullerite at high pressures and temperatures. It is significant that the results obtained are compared with experimental and theoretical data available for other carbon phases. Section 2 considers general trends in the structural transformations of the C_{60} fullerite under pressure and briefly classifies the phases syn-

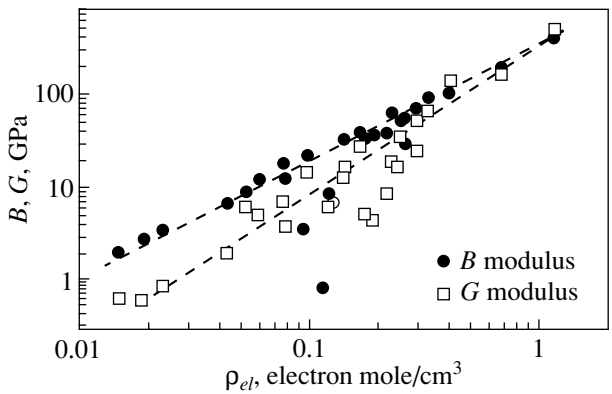

Fig. 1. Bulk modulus *B* and shear modulus for hard *s* and *p* elements vs. electronic valence density $\rho_{el} = n/V_m$, where V_m is the molar volume and *n* is the valence; for the *s* and *p* elements, the valence is equal to *N* for $N \le 4$ and to $(8 - N)$ for $N > 4$, where *N* is the number of outer-shell electrons. Numerical data taken from [2, 11, 12].

1063-7834/02/4403-0405$22.00 © 2002 MAIK "Nauka/Interperiodica"

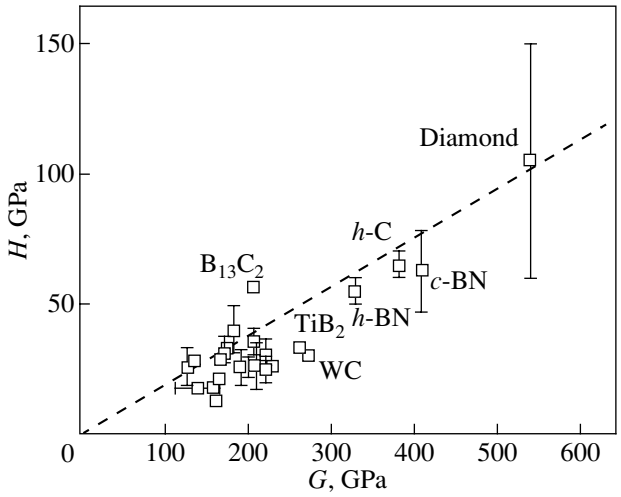

Fig. 2. Hardness plotted vs. density for a number of superhard substances [10].

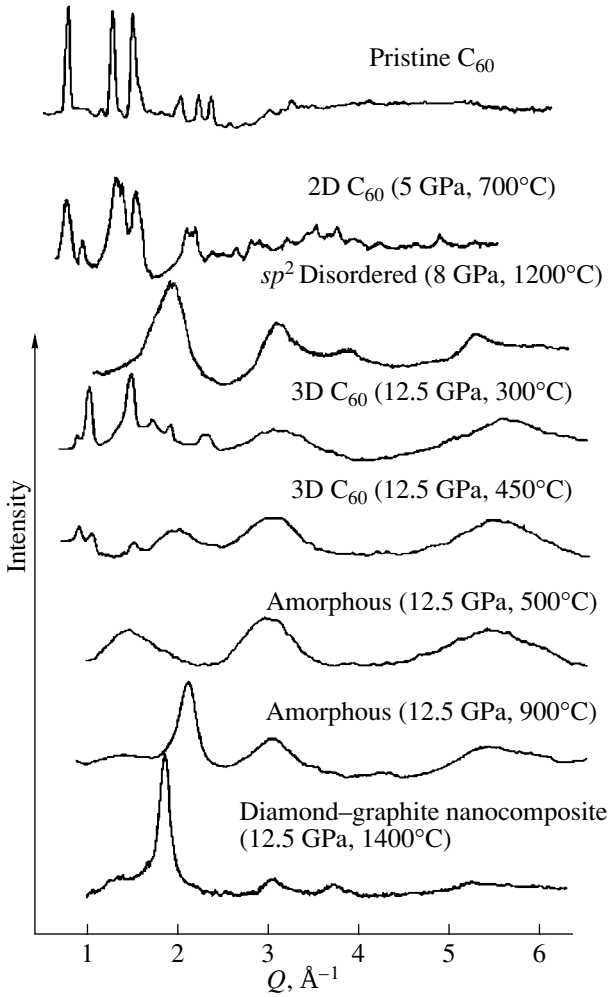

Fig. 3. Typical x-ray diffraction patterns for carbon phases prepared from C_{60} at a high pressure.

thesized from C_{60}. The main results of the work are summed up in Section 3.

2. STRUCTURAL TRANSFORMATIONS OF THE C_{60} FULLERITE AT HIGH PRESSURES AND TEMPERATURES

By subjecting the C_{60} fullerite, which is metastable with respect to transformation into graphite or diamond, to a high pressure or temperature, one can prepare a number of ordered or disordered carbon phases (Fig. 3). Among them are the one-dimensionally (1D) and two-dimensionally (2D) polymerized C_{60} phases [26–29], solid disordered phases with a graphite-like (sp^2) structure [28, 30, 31], three-dimensionally (3D) polymerized phases with a variable degree of polymerization [32–37], diamond-like (sp^3) amorphous phases [36–39], and nanocrystalline composites [36, 37, 40].

Analysis of the polymerized phases permits one to distinguish the region of low pressures, where low-dimensional polymers form from C_{60}, and the high-pressure region, which favors 3D polymerization. A crossover between the two regimes of polymerization is observed in the range between 8 and 9 GPa [41]. Within the 12- to 13-GPa interval, the regime of formation of graphite-like (sp^2) phases at high temperatures is replaced by the formation of predominantly sp^3 amorphous phases [28, 32, 33, 35, 36, 41].

One can single out the following main trends in the structural transformations of C_{60} at high pressures: (1) the C_{60} fullerite transforms at high pressures and temperatures to stabler graphite or diamond through intermediate molecularly polymerized and disordered phases; (2) increasing the temperature eventually brings about irreversible destruction of the C_{60} molecular structure; and (3) increasing the pressure when heating C_{60} increases the density and average coordination of carbon atoms (from three to four) in the synthesized phases and, in particular, initiates the 2D–3D transition in the polymerization regime or the sp^2–sp^3 transition in the disordering regime.

Thus, by subjecting C_{60} to high pressure and high temperature, one can vary the following structural characteristics of the carbon phases: (1) the type of covalent bonding (the ratio of the numbers of atoms in the sp^2 and sp^3 states), (2) the spatial dimension of the structure (1D, 2D, or 3D), (3) the degree of covalent bonding and the extent of disorder in molecular polymerized phases, (4) the type of short- and medium-range order structure in disordered phases, and (5) the extent of phase homogeneity in graphite–diamond nanocrystalline composites.

3. RELATIONS BETWEEN THE MECHANICAL PROPERTIES AND DENSITY OF THE CARBON PHASES

Prior to discussing the elastic properties and hardness of the carbon phases synthesized from C_{60}, a few comments on the experimental determination of these quantities are in order. Hardness is not a uniquely determined physical characteristic, because it depends on the method of measurement, the load on the indenter, and other factors [10]. We consider here the hardness measured using the Vickers method and reported in [31, 32, 37, 40]. The bulk modulus B of a substance is certainly a uniquely determined characteristic. However, the elastic properties of carbon phases obtained from C_{60} in quasi-hydrostatic conditions may exhibit considerable anisotropy [42]. This can naturally bring about errors in the determination of the elastic moduli from the ultrasonic technique made in the isotropic-medium approximation. For this reason, the velocities of ultrasound waves in the phases under study should be measured in different directions [42, 43].

Figure 4 plots the Vickers hardness H_V vs. density ρ for a variety of carbon phases prepared from C_{60} in comparison with the data obtained for amorphous sp^2–sp^3 carbon films [25]. Note the general trend in the behavior of the hardness, which increases with density, and also the fact that the results for the phases prepared

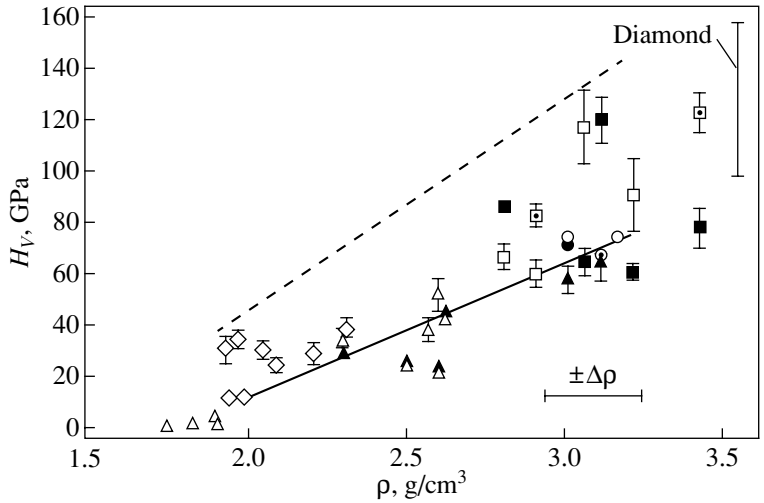

Fig. 4. Hardness vs. density dependence for carbon phases prepared from C_{60}: triangles are 3D polymers, rhombi are graphite-like amorphous phases, circles are diamond-like amorphous phases, and squares are sp^2–sp^3 nanocomposites. Open symbols relate to indenter loads ≈2 N; dotted symbols, to ≈3.5 N; and filled symbols, to ≈5 N. The data for diamond are taken for 2- to 5-N loads (see references in [40]). The solid line is the relation for amorphous films [25]. The dotted line apparently bounds the highest attainable hardness for carbon phases prepared from C_{60}.

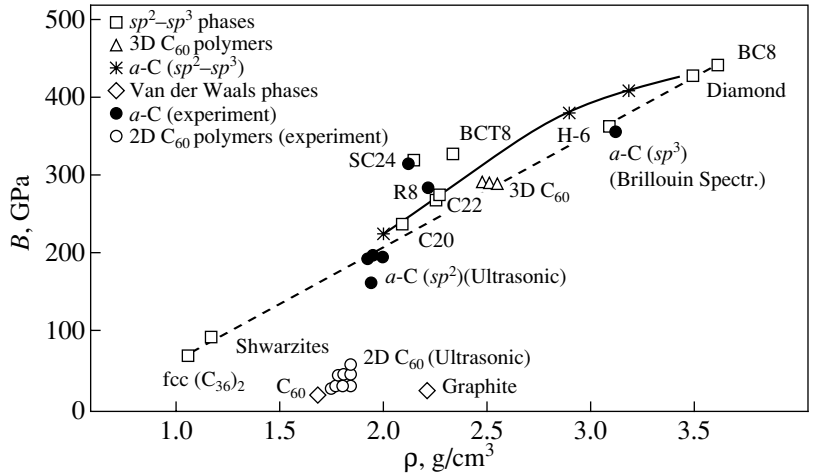

Fig. 5. Bulk modulus vs. density relation for allotropic forms of carbon [2] and for disordered phases prepared from C_{60} [31, 42, 43] (experiment), as well as theoretical data for various hypothetical phases (from [13–17, 25, 44–46]).

from C_{60} are in good agreement with the $H_V(\rho)$ data quoted for amorphous carbon films. Although the values of the hardness exhibit a scatter within a broad range, one clearly sees a correlation between the density and hardness, which is apparently of a general nature for various carbon phases.

Despite the existence of an $H_V(\rho)$ correlation, the phases with the same or similar densities in the region of densities typical of graphite (~1.8–2.2 g/cm^3) may have hardnesses differing by more than an order of magnitude (see [31] and Fig. 4). Graphite, as well as the starting C_{60} fullerite and the 1D and 2D polymerized phases, is a soft material [31], whereas disordered sp^2 phases with similar densities may have a hardness of up to 40 GPa (Fig. 4). Obviously enough, the soft phases are those which have a macroscopic two-dimensional ordering (or bonding) of the covalent structure (within a crystallite). At the same time, elastic recovery effects may play a significant part in hardness measurements on ordered phases made using the indenter technique.

A still better pronounced correlation is observed between the bulk modulus B and the density of the carbon phases with three-dimensional ordering of the covalent structure. In Fig. 5, the experimental data for the sp^2–sp^3 disordered phases prepared from C_{60} [31, 42, 43] and for real allotropic forms of carbon are compared with numerous calculations made for hypothetical phases, including amorphous structures [44] and 3D C_{60} polymers [45]. The observed $B(\rho)$ correlation is in accord with the general trend for hard elements (Fig. 1), and the experimental data for the carbon phases are in good agreement with theory. We note at the same time that phases with 1D or 2D covalent bonding (graphite and 1D or 2D C_{60} polymers), as well as the starting fullerite (a molecular van der Waals crystal with zero-dimensional covalent bonding), exhibit a much larger compressibility than the three-dimensionally bonded phases (Fig. 5).

Thus, the carbon phases, both synthesized from C_{60} and obtained otherwise, exhibit a direct correlation between the hardness or elastic properties and the density. However, phases with one- or two-dimensional macroscopic ordering of the covalent structure have lower values of the mechanical characteristics.

ACKNOWLEDGMENTS

The authors are indebted to E.L. Gromnitskaya, O.V. Stal'gorova, R.N. Voloshin, V.V. Mukhamad'yarov, A.G. Glazov, Yu.A. Klyuev, and A.M. Naletov for valuable discussions and assistance in the experiment.

This study was supported by the Russian Foundation for Basic Research, project nos. 99-02-17408, 00-15-99308, and 01-02-17543.

REFERENCES

1. I. N. Frantsevich, G. G. Gnesin, A. V. Kurdyumov, G. G. Karyuk, A. V. Bochko, and N. P. Semenenko, in *Superhard Materials*, Ed. by I. N. Frantsevich (Naukova Dumka, Kiev, 1980).
2. I. N. Frantsevich, F. F. Voronov, and S. A. Bokuta, *Elastic Constants and Elastic Moduli of Metals and Insulators: Handbook* (Naukova Dumka, Kiev, 1982).
3. P. S. Kislyĭ, in *Superhard and Refractory Materials*, Ed. by P. S. Kislyĭ (Inst. Sverkhtverdykh Materialov, Kiev, 1985), p. 86.
4. M. L. Cohen, Phys. Rev. B **32**, 7988 (1985).
5. J. M. Léger, J. Haines, and B. Blanzat, J. Mater. Sci. Lett. **13**, 1688 (1994).
6. J. J. Gilman, Mater. Sci. Eng. A **209**, 74 (1996).
7. J. M. Léger and J. Haines, Endeavour **21** (3), 121 (1997).
8. D. G. Clerc and H. M. Ledbetter, J. Phys. Chem. Solids **59** (6–7), 1071 (1998).
9. D. M. Teter, MRS Bull. **23**, 22 (1998).
10. V. V. Brazhkin, A. G. Lyapin, and R. J. Hemley, Philos. Mag. A **82**, 231 (2002).
11. D. A. Young, *Phase Diagrams of Elements* (Univ. of California Press, Berkley, 1991).
12. M. W. Guinan and D. J. Steinberg, J. Phys. Chem. Solids **35**, 1501 (1974).
13. A. Y. Liu, M. L. Cohen, K. C. Hass, and M. A. Tamor, Phys. Rev. B **43** (8), 6742 (1991).
14. G. Jungnickel, P. K. Sitch, Th. Frauenheim, *et al.*, Phys. Rev. B **57** (2), 661 (1998).
15. M. Côté, J. C. Grossman, M. L. Cohen, and S. G. Louie, Phys. Rev. B **58** (2), 664 (1998).
16. S. J. Townsend, T. J. Lenosky, D. A. Muller, *et al.*, Phys. Rev. Lett. **69** (6), 921 (1992).
17. V. Rosato, M. Celino, G. Benedek, and S. Gaito, Phys. Rev. B **60**, 16928 (1999).
18. F. Diederich, Nature **369**, 199 (1994).
19. R. H. Baughman, D. S. Galvão, C. Cui, and S. O. Dantas, Chem. Phys. Lett. **269**, 356 (1997).
20. H. W. Kroto, J. R. Heath, S. C. O'Brien, *et al.*, Nature **318**, 162 (1985).
21. S. Iijima, Nature **354**, 56 (1991); T. W. Ebbesen and P. M. Ajayan, Nature **358**, 220 (1992).
22. Yu. P. Kudryavtsev, R. B. Heimann, and S. E. Evsyukov, J. Mater. Sci. **31**, 557 (1996).
23. J. Robertson, Adv. Phys. **35**, 317 (1986).
24. D. R. McKenzie, D. Muller, and B. A. Pailthorpe, Phys. Rev. Lett. **67**, 773 (1991).
25. M. Weiler, S. Sattel, T. Giessen, *et al.*, Phys. Rev. B **53**, 1594 (1996).
26. Y. Iwasa, T. Arima, R. M. Fleming, *et al.*, Science **264**, 1570 (1994).
27. M. Núñez-Rogueiro, L. Marques, J.-L. Hodeau, *et al.*, Phys. Rev. Lett. **74** (2), 278 (1995).
28. L. Marques, J.-L. Hodeau, M. Núñez-Rogueiro, and M. Perroux, Phys. Rev. B **54** (18), R12633 (1996).
29. V. A. Davydov, L. S. Kashevarova, A. V. Rakhmanina, *et al.*, Phys. Rev. B **58** (22), 14786 (1998).
30. M. E. Kozlov, M. Hirabayashi, K. Nozaki, *et al.*, Appl. Phys. Lett. **66** (10), 1199 (1995).

31. A. G. Lyapin, V. V. Brazhkin, E. L. Gromnitskaya, *et al.*, Appl. Phys. Lett. **76** (6), 712 (2000).
32. V. V. Brazhkin, A. G. Lyapin, Yu. V. Antonov, *et al.*, Pis'ma Zh. Éksp. Teor. Fiz. **62** (4), 328 (1995) [JETP Lett. **62**, 350 (1995)].
33. V. D. Blank, S. G. Buga, N. R. Serebryanaya, *et al.*, Phys. Lett. A **205**, 208 (1995).
34. V. V. Brazhkin, A. G. Lyapin, and S. V. Popova, Pis'ma Zh. Éksp. Teor. Fiz. **64** (11), 755 (1996) [JETP Lett. **64**, 802 (1996)].
35. V. D. Blank, S. G. Buga, N. R. Serebryanaya, *et al.*, Phys. Lett. A **220**, 149 (1996).
36. V. V. Brazhkin, A. G. Lyapin, S. V. Popova, *et al.*, Phys. Rev. B **56** (18), 11465 (1997).
37. V. V. Brazhkin, A. G. Lyapin, S. V. Popova, *et al.*, J. Appl. Phys. **84** (1), 219 (1998).
38. H. Hirai, K. Kondo, N. Yoshizava, and M. Shiraishi, Appl. Phys. Lett. **64** (14), 1797 (1994).
39. H. Hirai, Y. Tabira, K. Kondo, *et al.*, Phys. Rev. B **52** (9), 6162 (1995).
40. V. V. Brazhkin, A. G. Lyapin, R. N. Voloshin, *et al.*, Pis'ma Zh. Éksp. Teor. Fiz. **69** (11), 822 (1999) [JETP Lett. **69**, 869 (1999)].
41. A. G. Lyapin, V. V. Brazhkin, S. G. Lyapin, *et al.*, Phys. Status Solidi B **211**, 401 (1999).
42. A. G. Glazov, V. V. Mukhamad'yarov, V. V. Brazhkin, *et al.*, Pis'ma Zh. Éksp. Teor. Fiz. **73** (10), 621 (2001) [JETP Lett. **73**, 552 (2001)].
43. M. H. Manghnani, S. Tkachev, P. V. Zinin, *et al.*, Phys. Rev. B **64**, 121403(R) (2001).
44. P. C. Kelires, Phys. Rev. Lett. **73**, 2460 (1994).
45. E. Burgos, E. Halac, R. Weht, *et al.*, Phys. Rev. Lett. **85**, 2328 (2000).
46. C. Mailhiot and A. K. McMahan, Phys. Rev. B **44** (21), 11578 (1991).

Translated by G. Skrebtsov

Physics of the Solid State, Vol. 44, No. 3, 2002, pp. 410–412. From Fizika Tverdogo Tela, Vol. 44, No. 3, 2002, pp. 398–400.

PROCEEDINGS OF THE V INTERNATIONAL WORKSHOP "FULLERENES AND ATOMIC CLUSTERS"

(St. Petersburg, Russia, July 2–6, 2001)

The Electronic State of Scandium Trimer Encapsulated in a C_{82} Cage[1]

T. Kato[1, 2], S. Okubo[1], M. Inakuma[3], and H. Shinohara[3]

[1] *The Graduate University for Advanced Studies, Okazaki, Myodaiji, 444-8585 Japan*

[2] *Institute for Molecular Science, Okazaki, Myodaiji, 444-8585 Japan*

[3] *Department of Chemistry, Nagoya University, Nagoya, 464-8602 Japan*

Abstract—The electron spin resonance spectrum of scandium trimer encapsulated in a C_{82} cage ($Sc_3@C_{82}$) was measured at low temperatures. The spectrum exhibited a specific pattern due to the strongly anisotropic hyperfine tensor of the scandium trimer. The electronic state of the $Sc_3@C_{82}$ was determined from an analysis of the hyperfine tensor. *© 2002 MAIK "Nauka/Interperiodica".*

Since the success of laboratory synthesis of C_{60} and other fullerenes [1], many papers on fullerenes and their chemical derivatives [2] have been published over the last decade. Especially metallofullerenes, i.e., fullerenes with metal(s) inside the hollow spherical carbon cage, have interested researchers (because of their possible use in free-tuning of "outside chemistry") and been prepared and characterized. In the beginning stage of the study, trace amounts of metallofullerenes were detected by an electron spin resonance (ESR) spectrometer. The recent progress made in the isolation and purification of endohedral metallofullerenes [3–5] expanded the investigation of the characterization of the physical [6–9] and chemical properties [10, 11].

Scandium trimer encapsulated in a C_{82} cage ($Sc_3@C_{82}$) has been produced by the Nagoya research group [3 (a)] and also by the IBM research group [3 (c)]. The Nagoya group succeeded in further separating and purifying $Sc_3@C_{82}$ of other metallofullerenes and empty fullerenes by the so-called two-stage high-performance liquid chromatography method. The ESR spectrum of $Sc_3@C_{82}$ in toluene and CS_2 solutions exhibits symmetric hyperfine splitting of 22 lines with a linewidth of 0.5 G at room temperature, which is consistent with the structure of $Sc_3@C_{82}$ with C_{3v} symmetry. The linewidths of the 22 lines were much broader than those for $Sc@C_{82}$. The broader linewidths of the scandium trimer in C_{82} could reflect the intramolecular dynamics, which causes averaging over the environments of the three Sc metal atoms in the Jahn–Teller distorted structure of the whole molecule [3 (d)]. The intramolecular dynamics is the inherent nature of the Sc trimer encapsulated in a C_{82} cage with C_{3v} symmetry.

Knight *et al.* [12] obtained matrix-isolated scandium trimer in solid neon and reported the ESR spectrum of Sc_3. The $^2A_1'$ electronic state and the D_{3h} molecular structure for the Sc_3 were drawn from an analysis of the ESR spectrum. The scandium trimer isolated in a solid neon matrix was a neutral radical; however, the scandium trimer encapsulated in C_{82} would be a radical cation. The intramolecular charge transfer from the central metal to the fullerene cage would give a stable electronic structure of an endo-metallofullerene. Professor Takata *et al.* [13] reported that there was no bonding electron between the cage and the trimer and that the charge state of Sc_3 was 3+, leading to the electronic structure of $(Sc_3)^{3+}@C_{82}^{3-}$.

1. EXPERIMENTAL

The scandium-containing fullerenes were produced by burning of a composite rod of graphite and Sc_2O_3 under 50–100 Torr He pressure. The soot was extracted with carbon disulfide (CS_2) over 12 hours. The $Sc_3@C_{82}$ fullerene was separated and isolated from various empty and other-type scandium fullerenes (such as $Sc@C_{82}$, $Sc_2@C_{84}$) by the two-stage high-performance liquid chromatography (HPLC) method. The two-stage HPLC method is described in detail elsewhere [14]. The $Sc_3@C_{82}$ fullerenes in CS_2, toluene, and liquid-paraffin solutions were degassed using a freeze-pump-thaw cycle and sealed in quartz tubes. The ESR spectra were obtained with Bruker ESR 300E and E500 spectrometers in combination with a temperature-control unit set for temperatures between 290 and 80 K.

2. RESULTS AND DISCUSSION

The temperature dependence of the ESR spectra of $Sc_3@C_{82}$ in liquid paraffin solution [3 (d)] was found to be strong in the temperature range below 200 K, as

[1] This article was submitted by the authors in English.

shown in Fig. 1. The linewidths of the hyperfine structure (HFS) components in both wings of the spectrum became broader, and this broadening effect was intensified with decreasing temperature. At temperatures below the freezing point of the solvent, the spectrum consisted of a single line with very broad wings. One of the origins of the line width of ESR spectra in a solution is an insufficient averaging of anisotropy of the HFS and g tensors due to hydrodynamic rotation in the solution. A linewidth of this type is proportional to the viscosity of the solvent and to the reciprocal of temperature. We have reported that the ESR spectrum of $Sc@C_{82}$ in toluene and CS_2 solutions showed a strong temperature dependence of the linewidths [15]. In the case of $Sc_3@C_{82}$, a strong temperature dependence of the linewidth was observed in a more viscous solvent of liquid paraffin. This type of line broadening is much enhanced in solvents with high viscosities, such as liquid paraffin. Once the solution was frozen, the ESR spectrum exhibited a so-called powder pattern, which was totally broadened and anisotropic. The line broadening of the HFS components in both wings of the spectrum preceded in the central part, and the central line persisted at 100 K. The features of the temperature dependence and the spectrum at 100 K were due to the highly anisotropic hyperfine tensor of the scandium trimer. This is especially true for the central single line observed at 100 K, which originated from the zero-valued perpendicular component of the anisotropic HFS tensor. The ESR spectrum of $Sc_3@C_{82}$ in a toluene solution observed at 80 K with a better signal-to-noise ratio is shown in Fig. 2. There were two prominent features in the spectrum of the frozen solution of $Sc_3@C_{82}$. One was the central line with broad spectra on each side of it. The other was the phase relationship, in which the high-field spectra were opposite in phase to those at low fields. The phase relationship for the broad spectra of both wings suggested that the observed spectra were due to parallel components of the HFS of an axial molecule with $A_\perp \ll A_\parallel$. The central line corresponded to the perpendicular component $A_\perp$. Considering that the central line remained strong at temperatures below the freezing point of the solvent, $A_\perp$ would be nearly evaluated as zero. In addition, an isotropic g value of 1.999 and an isotropic Sc hyperfine coupling constant of 6.25 G were obtained from an analysis of the solution spectrum at ambient temperature. Consequently, $A_{iso}(^{45}Sc) = 6.25$ G, $A_\parallel(^{45}Sc) = 18.8$ G, and $A_\perp(^{45}Sc) = 0$ were obtained. The value of the isotropic hyperfine coupling constant [$A_{iso}(^{45}Sc) = 6.25$ G] indicated that only 0.6% (in total, about 2% for the three Sc atoms) of the total unpaired-spin density was due to the 4s electron character. The magnetic dipole component A_{dip} of 6.25 G was found from the anisotropic HFS components, and 25% (in total, 75% for the three Sc atoms) of the total unpaired-spin density sat on the 3d orbital of Sc.

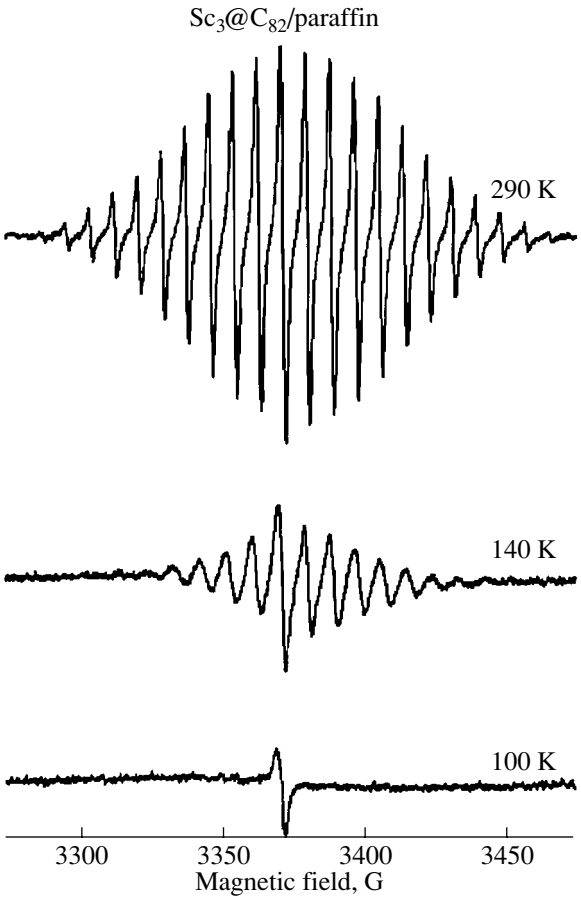

Fig. 1. ESR spectra of $Sc_3@C_{82}$ obtained at temperatures of 290, 140, and 100 K in liquid paraffin solution.

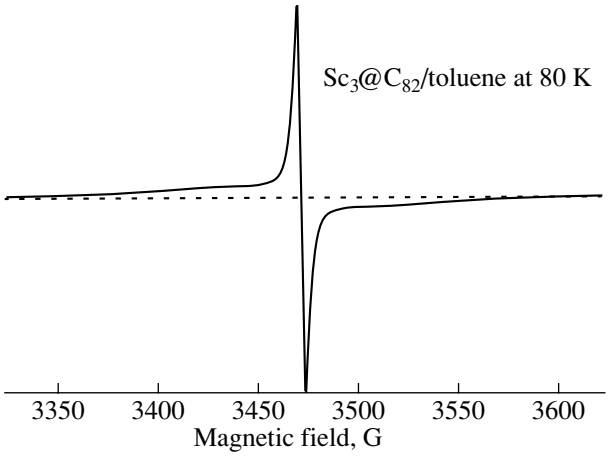

Fig. 2. ESR spectrum of $Sc_3@C_{82}$ in a toluene solution observed at 80 K.

The electronic structure of the Sc trimer consists of 18 (4s and 3p) molecular orbitals, into which nine valence electrons are placed. Assuming that the Sc tri-

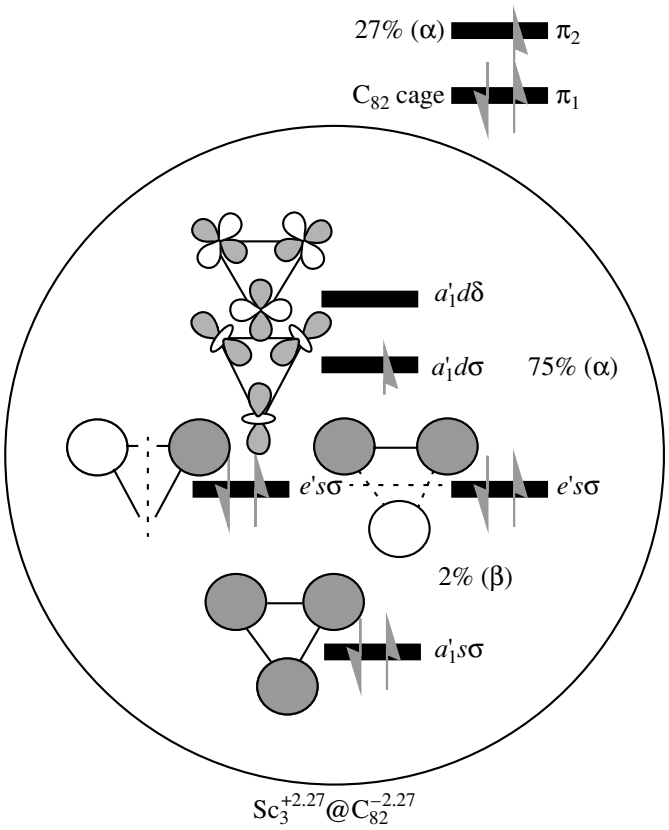

Fig. 3. Distribution of spin density on the $Sc_3@C_{82}$ molecule.

mer has D_{3h} symmetry with a threefold axis of symmetry perpendicular to the molecular plane, 5 orbitals out of 18 shown in Fig. 3 could be assigned as the 5 lowest energy orbitals. From the analysis of the Sc hyperfine coupling constant mentioned above, the distribution of the spin density on the $Sc_3@C_{82}$ molecule could be configured as in Fig. 3. The total spin density on the $Sc_3@C_{82}$ molecule equals unity because of the spin state of $S = 1/2$ (the spin doublet), so the density of an α spin and of a β spin is balanced to give the unity spin density. 75% density of an α spin is on the $a_1' d\sigma$ orbital of the Sc trimer, 2% density of a β spin is on the $e's\sigma$ orbital of the Sc trimer, and 27% density of an α spin is on the π_2 orbital of the fullerene cage. As a result, the charge state of Sc_3 is +2.27, describing the electronic state of $Sc_3^{+2.27}@C_{82}^{-2.27}$.

The ESR spectrum of an $Sc_3@C_{82}$ solution observed at low temperatures exhibited a specific pattern given by the strongly anisotropic HFS tensor of the scandium trimer. The electronic state of $Sc_3@C_{82}$ was deduced from the analysis of the HFS tensor. From this analysis, the spin density distribution on the $Sc_3@C_{82}$ molecule was estimated and the electronic state was identified as $Sc_3^{+2.27}@C_{82}^{-2.27}$.

REFERENCES

1. W. Kractschmer, L. D. Lamb, K. Fostiropoulos, and D. R. Huffman, Nature **347**, 354 (1990); W. Kractschmer, K. Fostiropoulos, and D. R. Huffman, Chem. Phys. Lett. **170**, 167 (1990).
2. J. M. Hawkins, T. A. Lewis, S. D. Loren, *et al.*, J. Org. Chem. **55**, 6250 (1990).
3. (a) H. Shinohara, H. Sato, M. Ohchochi, *et al.*, Nature **357**, 52 (1992); (b) H. Shinohara, H. Yamaguchi, N. Hayashi, *et al.*, Mater. Sci. Eng. B **B19**, 25 (1993); (c) C. S. Yannoni, M. Hoinkis, M. S. de Vries, *et al.*, Science **256**, 1191 (1992); (d) T. Kato, S. Bandou, M. Inakuma, and H. Shinohara, J. Phys. Chem. **99**, 856 (1995).
4. J. H. Weaver, Y. Chai, G. H. Kroll, *et al.*, Chem. Phys. Lett. **190**, 460 (1992); H. Shinohara, H. Sato, Y. Saito, *et al.*, J. Phys. Chem. **96**, 3571 (1992).
5. Y. Chai, T. Guo, C. Jin, *et al.*, J. Phys. Chem. **95**, 7564 (1991); M. M. Alvarez, E. G. Gillan, K. Holczer, *et al.*, J. Phys. Chem. **95**, 10561 (1991); R. D. Johnson, M. S. de Vries, J. Salem, *et al.*, Nature **355**, 239 (1992); K. Kikuchi, S. Suzuki, Y. Nakao, *et al.*, Chem. Phys. Lett. **216**, 67 (1993).
6. T. Kato, S. Suzuki, K. Kikuchi, and Y. Achiba, J. Phys. Chem. **97**, 13425 (1993).
7. E. Yamamoto, M. Tansho, T. Tomiyama, *et al.*, J. Am. Chem. Soc. **118**, 2293 (1996).
8. T. Akasaka, S. Nagase, K. Kobayashi, *et al.*, Angew. Chem. Int. Ed. Engl. **36**, 1643 (1997).
9. M. Takata, E. Nishibori, B. Umeda, *et al.*, Phys. Rev. Lett. **78**, 3330 (1997).
10. T. Akasaka, T. Kato, K. Kobayashi, *et al.*, Nature **374**, 600 (1995).
11. T. Akasaka, S. Nagase, K. Kobayashi, *et al.*, J. Chem. Soc., Chem. Commun., 1343 (1995); T. Akasaka, T. Kato, S. Nagase, *et al.*, Tetrahedron **52**, 5015 (1996).
12. L. B. Knight, Jr., R. W. Woodward, R. J. VanZee, and W. Weltner, Jr., J. Chem. Phys. **79**, 5820 (1983).
13. M. Takata, E. Nishibori, M. Sakata, *et al.*, Phys. Rev. Lett. **83**, 2214 (1999).
14. H. Shinohara, M. Inakuma, N. Hayashi, *et al.*, J. Phys. Chem. **98**, 8597 (1994).
15. T. Kato, S. Suzuki, K. Kikuchi, and Y. Achiba, J. Phys. Chem. **97**, 13425 (1993).

Physics of the Solid State, Vol. 44, No. 3, 2002, pp. 413–418. Translated from Fizika Tverdogo Tela, Vol. 44, No. 3, 2002, pp. 401–405.

PROCEEDINGS OF THE V INTERNATIONAL WORKSHOP "FULLERENES AND ATOMIC CLUSTERS"

(St. Petersburg, Russia, July 2–6, 2001)

Buckminsterfullerene, Higher Fullerenes, and Their Endohedral and Fluorine Derivatives

L. N. Sidorov

Moscow State University, Vorob'evy gory, Moscow, 119899 Russia
e-mail: sidorov@thermo.chem.msu.ru

Abstract—This paper presents an overview of recent works concerned with determination of the electron affinity (EA) and the ionization energy (IE) for higher fullerenes and their endohedral and fluorine derivatives. The numerical values of the electron affinity are analyzed for higher fullerenes up to C_{106} and lanthanum, gadolinium, and scandium endohedral fullerenes, including $Sc_3N@C_{80}$. Most attention is concentrated on two methods for producing fluorofullerenes, namely, direct fluorination of fullerenes with molecular fluorine in a manganese difluoride matrix and solid-phase reactions between fullerenes and fluorinating agents capable of donating fluorine to fullerene. The structures of three fluorofullerenes ($C_{60}F_{18}$, $C_{60}F_{20}$, and $C_{60}F_{48}$) characterized by a distortion of the carbon cage due to attachment of functional groups are discussed. © *2002 MAIK "Nauka/Interperiodica".*

1. INTRODUCTION

The electron affinity (EA) and the ionization energy (IE) are the fundamental characteristics of molecules. For the C_{60} fullerene, the electron affinity is equal to 2.667 ± 0.001 eV [1] and the ionization energy is 7.57 ± 0.01 eV [2]. It is worth noting that the electron affinity for the C_{60} fullerene is considerably higher than those for the majority of organic materials. This indicates that molecules of new fullerene compounds possess sufficiently strong electron-acceptor properties. Moreover, it turned out that fullerene molecules exhibit an unusual combination of relatively high electron affinity and low ionization energy. This is seldom the case in chemistry and suggests that fullerene molecules can serve as both donors and acceptors of electrons in chemical reactions.

The first results obtained for other representatives of the fullerene family—the so-called higher fullerenes C_{2n} ($n > 30$) that can also be prepared in macroamounts—have demonstrated that the properties of these compounds noticeably differ from those of the C_{60} fullerene. These differences should primarily manifest themselves in fundamental characteristics such as the ionization energy and electron affinity.

Among experimental parameters, the work function of a metal surface is of particular importance, because the surface properties of materials substantially affect the efficiency of thermal ionization responsible for ion formation. In the ion-molecular equilibrium (IME) method considered in the present work, we deal with the inner surface of a Knudsen effusion cell whose work function can vary over a wide range depending on the treatment conditions. For example, the work function for the inner surface of an effusion cell decreases upon introduction of alkali metals and their compounds into the cell and increases upon fluorination of the cell walls. Under actual conditions, the work function can be controlled in the range from 3 to 7 eV. It was found that the electron affinities and ionization energies for fullerenes correspond to the boundaries of this range. This has opened up strong and, in a sense, unique possibilities of generating negative and positive thermal ions of fullerenes. All this has lent impetus to a number of studies on the properties of gas-phase fullerene ions. The experimental technique, which is concisely named "the ion-molecular equilibrium method," is based on the classical effusion method with mass spectrometric detection of vaporization products or, in other words, on Knudsen cell mass spectrometry (KCMS). In addition to analysis of the relative content of neutral species ionized by electron impact in the KCMS method, the IME technique involves detection of charged species in saturated vapors of inorganic compounds. The use of $KAlF_4$-type salt additives characterized by a low energy of heterolytic dissociation into ions offered the key to attaining measurable concentrations of ions in vapors of inorganic compounds. In these vapors, the concentration of cations and anions even at 1000 K is so high that the Debye screening length becomes less than the effusion cell size and the electron-free plasma is formed. In this case, the pressure of neutral species is five or seven orders of magnitude higher than the pressure of ions [3]. The addition of these salts to other systems whose vapors contain no ions in measurable concentrations makes it possible to produce ion-molecular associates in large amounts.

In actual practice, the KCMS–IME technique often includes relative measurements, i.e., measurements of

1063-7834/02/4403-0413$22.00

equilibrium constants for isomolecular reactions involving the reference species *B* with standard thermochemical parameters:

$$A^- + B = A + B^-, \quad \Delta H_0^0 = EA(A) - EA(B), \quad (1)$$

$$AF^- + B = A + BF^-, \quad \Delta H_0^0 = FA(A) + FA(B). \quad (2)$$

2. ION-MOLECULAR EQUILIBRIA IN FULLERENE VAPORS

In the majority of works concerned with research into fullerene-containing systems, particular emphasis was placed on anions and, in many cases, additives of alkali metal compounds were used to decrease the work function. In order to examine fullerene cations, Boltalina *et al.* [4] added iron trifluoride to the reaction mixture for the purpose of increasing the work function of the inner surface of the nickel effusion cell.

Another problem associated with the attainment of measurable concentrations of ions in fullerene vapors is the difference between the sublimation and thermal ionization temperatures of the fullerenes. In most cases, the required degree of ionization can be achieved only with a superheated vapor. For this purpose, it was proposed to use double effusion cells of the "Russian matreshka" type. A volatile compound (fullerene) was placed in a small-sized cell. Then, the relative sizes of effusion orifices in exterior and interior cells were changed so as to decrease the degree of saturation of the fullerene vapor by a factor of seven or ten. This made it possible to increase the temperature without violating the conditions of molecular effusion from the effusion orifice of the exterior cell.

The experimental setup allowed successive measurements of the partial-pressure ratios for neutral and charged components of the vapor in the course of one experiment. The neutral species were detected by measuring the ionic currents generated under electron impact of the molecular beam evaporating from the effusion cell. The partial-pressure ratios were calculated from the equation relating the ionic currents to the partial pressures of neutral species, that is,

$$p_A/p_B = I_A/I_B\sigma_B/\sigma_A, \quad (3)$$

where σ is the total ionization cross section of the molecule and *I* is the intensity of the ionic current.

The charged species were detected by measuring the ionic currents induced through direct evacuation of thermal ions from the effusion cell. The pressure ratios of thermal anions were calculated from the equation

$$p_A/p_B = I_A/I_B M_A^{1/2}/M_B^{1/2}, \quad (4)$$

where *M* is the molecular mass. As a consequence, the equilibrium constants were obtained for ion-molecular reactions of the type

$$C_{60}^- + C_{2n} = C_{60} + C_{2n}^-. \quad (5)$$

The above technique provides a means for identifying species with a very low content in samples, because the dynamic range of measurable concentrations covers eight orders of magnitude. In this manner, reliable data were obtained for reactions involving the most abundant fullerenes (C_{70}, C_{76}, C_{78}, and C_{84}) and species (including the C_{106} fullerene) present in small amounts in the mixture but hitherto not isolated in pure form. It is these factors (the high sensitivity together with the mass spectrometric analysis of species) that constitute the advantage of the KCMS–IME method over conventional spectroscopic techniques widely used for determining the electron affinity and the ionization energy. For comparison, we note that the electron affinity of C_{60} fullerene was determined by the photodetachment method [1]. Reliable data on the electron affinity of the C_{70} fullerene were obtained in 1995 with the use of an experimental setup in which, prior to measuring the photodetachment threshold, excited anions of the C_{70} fullerene were cooled in storage in a 40-m ASTRID accelerator [2]. The electron affinities of higher fullerenes were experimentally determined only by the KCMS–IME method [5].

More recently, thermal cations were examined in vapors of higher fullerenes and the equilibrium constants were measured for reactions of the type

$$C_{60}^+ + C_{2n} = C_{2n}^+ + C_{60}. \quad (6)$$

The electron affinities, ionization energies, and electronegativities (the half-sum of the electron affinity and the ionization energy) determined for higher fullerenes are shown in Fig. 1.

A simple physical model, according to which the fullerene molecule is treated as a rigid conducting sphere, allows us to derive the following equations relating the electron affinity and the ionization energy to the sphere radius R_N:

$$EA = \varphi_\infty - \frac{1}{2}R_N^{-1} \quad (7)$$

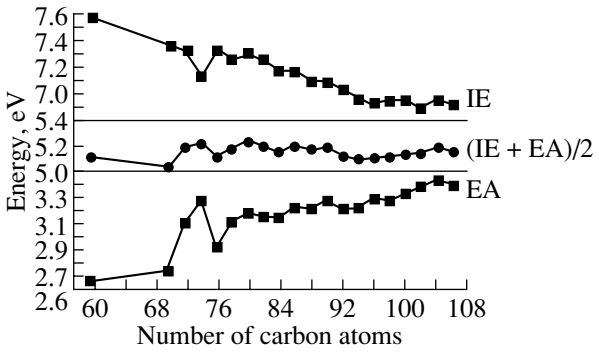

Fig. 1. Ionization energies (IE) and electron affinities (EA) of higher fullerenes.

and

$$\mathrm{IE} = \varphi_\infty + \frac{1}{2}R_N^{-1}. \quad (8)$$

Here, φ_∞ is the work function of a graphite monolayer, which corresponds to the limiting value of both the electron affinity and the ionization energy for the fullerene molecule in the case when the molecular size tends to infinity. The theoretical estimate of φ_∞ is equal to 5.37 eV. It should also be noted that the dependences of the electron affinity and the ionization energy exhibit a pronounced "mirror" behavior. This manifests itself in a sufficiently narrow energy range of electronegativities (EA + IE)/2 for all the fullerenes studied (Fig. 1). The aforementioned theoretical estimate made for the work function of the graphite monolayer also falls in this range.

The so-called exohedral and endohedral fullerenes form two main groups of fullerene derivatives. It is of interest to elucidate how these two types of functionalization affect the electron-acceptor properties of fullerenes. In the case of fluorofullerenes, an increase in the electron affinity, as compared to that for the initial C_{60} fullerene, can be assumed reasoning from the high electronegativity of fluorine. However, it is difficult to predict the effect of an encaged metal on the electron-acceptor properties of fullerenes without resorting to experimental data.

The constants of ion-molecular equilibria of the type

$$\mathrm{Gd@C}_{2n}^- + \mathrm{C}_{74} = \mathrm{Gd@C}_{2n} + \mathrm{C}_{74}^- \quad (9)$$

were measured in order to determine the electron affinity of endohedral metallofullerenes. According to the calculations, the electron affinities of $Gd@C_{2n}$ compounds fall in a narrow range (3.2–3.3 eV) (see table) and, on the average, exceed the electron affinities of the relevant empty fullerenes.

Thus, it was established that, compared to the empty fullerene molecule, the encapsulation of a gadolinium rare-earth metal atom within the fullerene cage leads to an increase (even if insignificant) in the electron affinity, except for $Gd@C_{74}$. We also succeeded in determining the electron affinities for a number of endohedral molecules with two scandium atoms within the cage and the electron affinity for a rather exotic compound, $Sc_3N@C_{80}$ (see table).

The electron affinity of fluorofullerenes was determined using the reactions

$$\mathrm{C}_{60}\mathrm{F}_2 + \mathrm{C}_{60}^- = \mathrm{C}_{60}\mathrm{F}_2^- + \mathrm{C}_{60}, \quad (10)$$

$$\mathrm{C}_{70}\mathrm{F}_2 + \mathrm{C}_{60}^- = \mathrm{C}_{70}\mathrm{F}_2^- + \mathrm{C}_{60}. \quad (11)$$

The electron affinities thus determined for C_{60} and C_{70} fullerene difluorides are equal to 2.73 and 2.82 eV, respectively. These data indicate that the electron affinity increases only slightly upon attachment of two fluorine atoms. It is reasonable to assume that molecules with a higher content of fluorine atoms possess a larger electron affinity. Hettich *et al.* [8] investigated electron exchange reactions between the $C_{60}F_{44–48}$ fluorofullerenes and different reference compounds by using the bracketing technique and revealed a substantial increase in the electron affinity (4.05 ± 0.5 eV).

Electron affinities of endohedral compounds

Compound	EA, eV	Compound	EA, eV
$La@C_{74}$	>2.9 [6]	$Gd@C_{80}$	3.37 ± 0.05 [6]
$La@C_{80}$	3.32	$Gd@C_{82}$	3.38 ± 0.06 [6]
$Gd@C_{60}$	2.85 [6]	$Sc_2@C_{80}$	3.20 ± 0.04 [7]
$Gd@C_{74}$	3.2 ± 0.1 [6]	$Sc_2@C_{82}$	3.21 ± 0.04 [7]
$Gd@C_{76}$	3.22 ± 0.02 [6]	$Sc_2@C_{84}$	3.10 ± 0.04 [7]
$Gd@C_{78}$	3.41 ± 0.09 [6]	$Sc_3N@C_{80}$	2.81 ± 0.05 [7]

3. FLUORINATION AND SELECTIVITY

The first experiments on fluorination of the C_{60} fullerene demonstrated that this reaction results in the formation of a mixture of products with the general formula $C_{60}F_{2n}$, where *n* varies in the range from 17 to 24. Subsequently, an active search for new methods of the selective synthesis of individual fluorofullerenes was performed *in situ* in a mass spectrometer with the aim of exercising mass spectrometric monitoring of gas-phase reaction products. The measurements were carried out concurrently on two virtually identical setups. The sole difference resided in the fact that one of these setups was equipped with a system of molecular fluorine inflow into an effusion cell. This setup was used to examine fluorination of the C_{60} fullerene with molecular fluorine. The solid-phase reactions between C_{60} and a number of fluorinating agents (such as MnF_3, CoF_3, CeF_4, TbF_4, K_2PtF_6, $KMnF_3$, $BaPbF_6$, and AgF_2) were investigated in the second setup. A reaction mixture composed of thoroughly mixed fullerene and fluorinating agent (taken in specified mass ratios) was placed in the effusion cell of the high-temperature evaporator of the ion source. The mixture was heated under high vacuum at temperatures varying over a wide range. The gas-phase products of fluorination in the form of positive ions (produced by electron impact) were detected using an output device of the mass spectrometer.

This approach involves the preliminary stage of the synthesis inside the mass spectrometer and offers obvious advantages over a conventional one-stage synthesis performed directly in a chemical reactor. First and foremost, this technique makes it possible, immediately in the course of synthesis, to obtain information on the time distribution of reaction products at different temperatures and, thus, to reduce substantially the number of experiments required for choosing the optimum con-

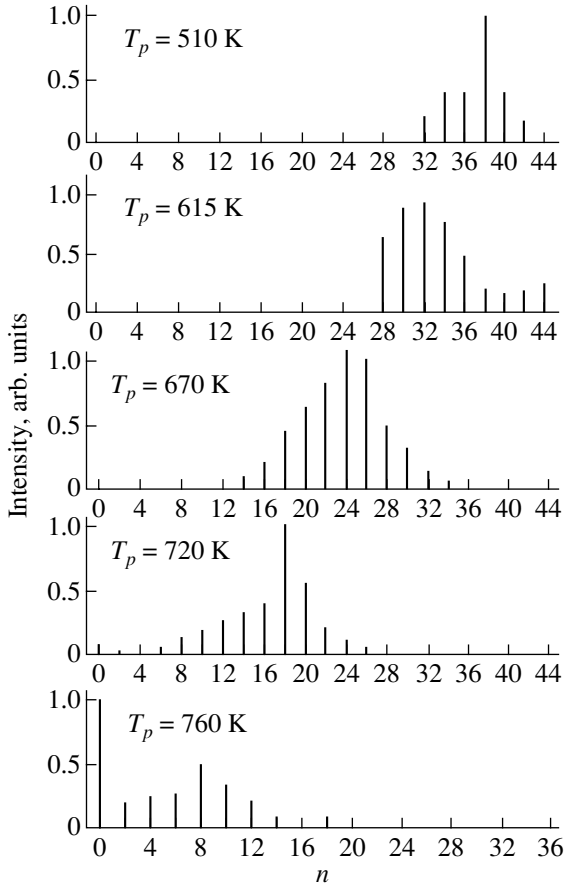

Fig. 2. Mass spectra of volatile fluorofullerenes prepared by direct fluorination of C_{60} with molecular fluorine.

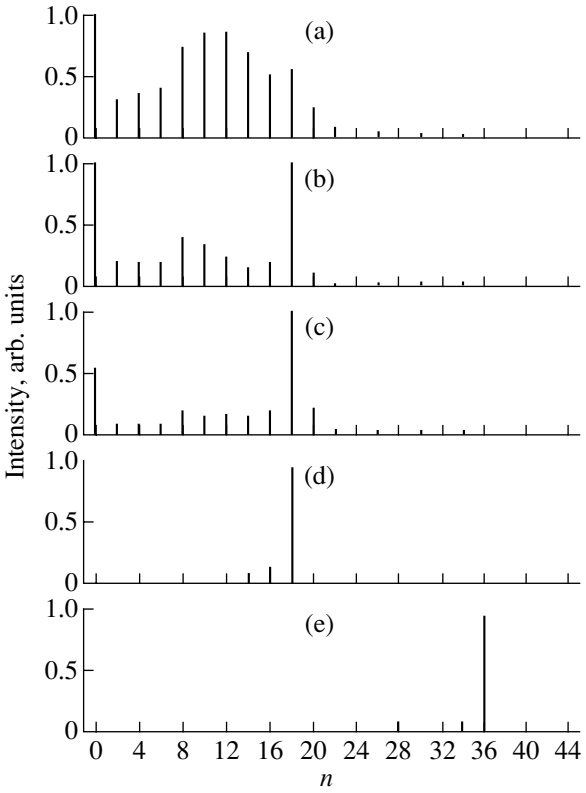

Fig. 3. Mass spectra of volatile fluorofullerenes prepared by direct fluorination of the C_{60}–MnF_2 mixture with molecular fluorine: (a) C_{60}, T = 720 K; (b) C_{60}–NiF_2 (97 mol %), T = 720 K; (c) C_{60}–MnF_2 (50 mol %), T = 720 K; (d) C_{60}–MnF_2 (97 mol %), T = 720 K; and (e) C_{60}–MnF_2 (97 mol %), T = 615 K.

ditions for the synthesis of compounds with a specific stoichiometric composition.

By using the above technique, Boltalina *et al.* [9] revealed that the reaction of the C_{60} fullerene with MnF_3 at a temperature of 615 K leads to the formation of only one compound, namely, $C_{60}F_{36}$, whereas the reaction with K_2PtF_6 at T = 730 K predominantly produces $C_{60}F_{18}$. In [10], the reaction of the C_{60} fullerene with $KMnF_3$ gave a fluorofullerene mixture enriched with $C_{60}F_{20}$: this compound was isolated in pure form (4 mg) through chromatographic separation of the mixture.

Experimental investigations into the direct fluorination of the C_{60} fullerene with molecular fluorine demonstrated that the composition of gas-phase products is characterized by a broad distribution over the number of fluorine atoms and includes virtually all molecules $C_{60}F_n$ with even numbers n up to 48. This distribution depends on the temperature, fluorination time, and the rate of fluorine flow arriving at the reaction zone. At constant flow rates and fluorination times, an increase in the temperature brings about a shift in the distribution maximum toward smaller values of n (Fig. 2).

It should be noted that no indications of fluorination selectivity are found; i.e., no predominant formation of a particular compound occurs. Specifically, at 615 K (the optimum temperature for selective solid-phase fluorination of the C_{60} fullerene with manganese trifluoride), the electron impact mass spectrum exhibits a series of peaks attributed to $C_{60}F_{28–44}$ with a weakly pronounced maximum in the range of n = 30. A different situation arises when the C_{60} fullerene is incorporated into a manganese difluoride matrix, i.e., when the fluorinated system consists of the C_{60} fullerene and 97 mol % MnF_2. In this case, the selective formation of $C_{60}F_{18}$ and $C_{60}F_{36}$ is observed at 720 and 615 K, respectively (Fig. 3).

Therefore, we can state that the direct fluorination of a mechanical mixture of C_{60} and 97 mol % MnF_2 with molecular fluorine makes it possible to synthesize both $C_{60}F_{18}$ and $C_{60}F_{36}$ fluorofullerenes. In the case when the fluorination is carried out at a temperature of 615 K, the $C_{60}F_{36}$ fluorofullerene is the main volatile product of the reaction. This result is in agreement with experimental data on the solid-phase fluorination of the C_{60} fullerene with manganese trifluoride, which also pre-

dominantly produces the $C_{60}F_{36}$ volatile compound. When the fluorination is performed at 720 K, the $C_{60}F_{18}$ fluorofullerene is the main volatile product of the reaction. This finding agrees with experimental data on the solid-phase fluorination of the C_{60} fullerene with potassium hexafluoroplatinate K_2PtF_6.

4. DISTORTION OF THE CARBON CAGE OF A C_{60} FULLERENE DUE TO ATTACHMENT OF FUNCTIONAL GROUPS

The most interesting feature of fullerenes is a combination of properties inherent in diene and aromatic compounds. This is clearly seen from a comparison of the carbon–carbon bond lengths in benzene (1.40 Å), butadiene –C=C–C=C– (1.35 and 1.47 Å), and C_{60} in which the interatomic distances in double and single bonds are equal to 1.40 and 1.46 Å, respectively. It is evident that the attachment of functional groups through double bonds transforms the π-electron system of the molecule. This is accompanied by the formation of isolated aromatic rings, diene chains, and isolated double bonds on the carbon cage and leads to a distortion of the initial icosahedron composed of carbon atoms.

The ^{19}F NMR spectrum (376.14 MHz) of the $C_{60}F_{18}$ fluorofullerene was recorded for the first time in 1996 by Boltalina *et al.* [9]. This spectrum consists of four lines with the intensity ratio 1 : 2 : 2 : 1. Among all the possible structures consistent with this spectrum, the fluorofullerene molecule of C_{3v} symmetry, in which all 18 fluorine atoms are attached to the same hemicage, has the most appropriate structure (Fig. 4).

In 2000, Boltalina *et al.* [11–13] succeeded in growing single crystals of the molecular complexes of $C_{60}F_{18}$ and $C_{60}F_{18}O$ with toluene and $C_{60}F_{18}$ with *m*-xylene and *p*-xylene. These authors performed complete x-ray diffraction analysis of these complexes and obtained the first crystallographic data for fluorinated fullerenes.

X-ray diffraction analysis of the $C_{60}F_{18}$ molecular complexes completely confirmed the NMR data on the arrangement of 18 fluorine atoms on the same half of the carbon cage. Moreover, it was shown that such a grouping of fluorine atoms around a hexagonal ring brings about a noticeable change in the C–C bond lengths or, more specifically, equalization of the bond lengths in this hexagonal fragment and its transformation into a purely aromatic (benzene-like) ring. The structure of the fluorinated hemicage also undergoes radical transformations. The radius of curvature of the hemicage increases considerably; in other words, the fluorinated hemicage becomes flattened, whereas the second fluorine-free hemicage retains its sizes and holds the shape of the initial fullerene molecule [11–13].

According to Avent *et al.* [14], the ^{19}F NMR spectrum of the $C_{60}F_{20}$ fluorofullerene contains only one line at 138.8 ppm. The structure proposed by these authors for the $C_{60}F_{20}$ compound is displayed in Fig. 4. The characteristic feature of this structure is that all 20 fluorine atoms are arranged along the equator, whereas the five-membered rings surrounded by five six-membered aromatic rings are located at the poles. This molecule received the name saturnene, and the distorted carbon cage was termed squashed.

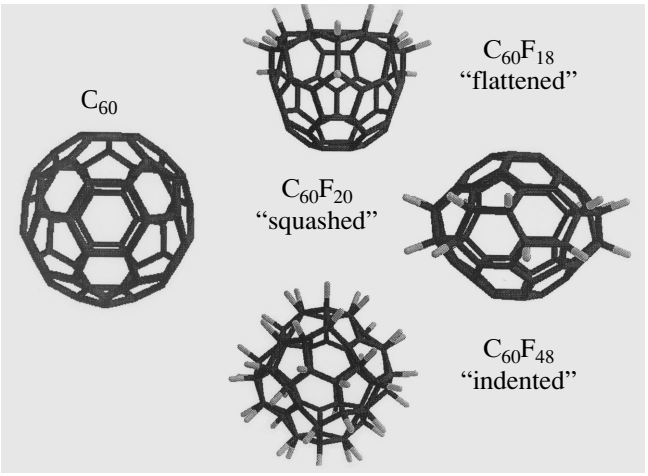

Fig. 4. Molecular structures of the initial C_{60} fullerene and distorted fluorofullerenes: $C_{60}F_{18}$ flattened, $C_{60}F_{20}$ squashed, and $C_{60}F_{48}$ indented fullerenes.

The $C_{60}F_{48}$ fullerene was investigated by x-ray diffraction in 2001, and this molecule was referred to as the indented fullerene (fullerene with indentations) [15]. All three fullerene structures, namely, the flattened, squashed, and indented fullerenes, and the initial undistorted buckminsterfullerene molecule are shown in Fig. 4.

ACKNOWLEDGMENTS

This work was supported by the State Scientific and Technical Program "Fullerenes and Atomic Clusters" and the Russian Foundation for Basic Research, project no. 00-03-32702.

REFERENCES

1. C. Brink, L. H. Andersen, P. Hvelplund, *et al.*, Chem. Phys. Lett. **233**, 52 (1995).
2. R. K. Yoo, B. Ruscic, and J. Berkowitz, J. Chem. Phys. **96**, 911 (1992).
3. L. N. Sidorov, L. V. Zhuravleva, and I. D. Sorokin, Mass Spectrom. Rev. **5**, 73 (1986).
4. O. V. Boltalina, I. N. Ioffe, L. N. Sidorov, *et al.*, J. Am. Chem. Soc. **122**, 9745 (2000).
5. O. V. Boltalina, E. V. Dashkova, and L. N. Sidorov, Chem. Phys. Lett. **256** (3), 253 (1996).
6. O. V. Boltalina, I. N. Ioffe, I. D. Sorokin, and L. N. Sidorov, J. Phys. Chem. **101** (50), 9561 (1997).

7. I. N. Ioffe, O. V. Boltalina, and L. N. Sidorov, in *Fullerenes 2000: Chemistry and Physics of Fullerenes and Carbon Nanomaterials*, Ed. by P. V. Kamat, D. M. Guldi, and K. M. Kadish (The Electrochemical Society, Pennington, 2000), Vol. 10, p. 166.
8. R. Hettich, C. Jin, and R. Compton, Int. J. Mass Spectrom. Ion Processes **138**, 263 (1994).
9. O. V. Boltalina, V. Yu. Markov, R. Taylor, and M. P. Waugh, Chem. Commun., 2549 (1996).
10. O. V. Boltalina, V. Yu. Markov, P. A. Troshin, *et al.*, Angew. Chem. Int. Ed. Engl. **40** (4), 787 (2001).
11. O. V. Boltalina, B. de La Vaissiere, P. W. Fowler, *et al.*, Chem. Commun., 1325 (2000).
12. I. S. Neretin, K. A. Lyssenko, M. Yu. Antipin, *et al.*, Angew. Chem. Int. Ed. Engl. **39** (18), 3273 (2000).
13. O. V. Boltalina, E. Kemnitz, I. V. Kuvichko, *et al.*, in *Proceedings of the 16th International Symposium on Fluorine Chemistry, Durham, 2000*, Abstract 2P-29.
14. A. G. Avent, R. Taylor, O. V. Boltalina, *et al.*, in *Fullerenes 2000: Functionalized Fullerenes*, Ed. by N. Martin, M. Maggini, and D. M. Guldi (The Electrochemical Society, Pennington, 2000), Vol. 9, p. 109.
15. S. I. Troyanov, P. A. Troshin, O. V. Boltalina, *et al.*, Angew. Chem. **40** (12), 2285 (2001).

Translated by O. Borovik-Romanova

Physics of the Solid State, Vol. 44, No. 3, 2002, pp. 419–423. From Fizika Tverdogo Tela, Vol. 44, No. 3, 2002, pp. 406–409.

PROCEEDINGS OF THE V INTERNATIONAL WORKSHOP "FULLERENES AND ATOMIC CLUSTERS"

(St. Petersburg, Russia, July 2–6, 2001)

Electron Density as the Main Parameter Influencing the Formation of Fullerenes in a Carbon Plasma[1]

G. N. Churilov*, P. V. Novikov, V. A. Lopatin**, N. G. Vnukova**, N. V. Bulina*, S. M. Bachilo***, D. Tsyboulski***, and R. B. Weisman*****

** Kirensky Institute of Physics, Siberian Division, Russian Academy of Sciences, Akademgorodok, Krasnoyarsk, 660036 Russia*

e-mail: churilov@iph.krasn.ru

*** Krasnoyarsk State Technical University, Krasnoyarsk, 660074 Russia*

**** Rice University, Houston, TX 77005 USA*

Abstract—Thermodynamic estimates are presented for the formation of spheroidal and flat carbon clusters from reactant species of different charges. Charge is shown to strongly influence the geometry and stability of flat clusters. Changes in the charge of flat clusters can promote both their folding to spheroidal structures and their dissociation. It is concluded that the fluctuations of electron concentration in carbon plasmas can result in the accumulation of fullerene clusters and the dissociation of flat clusters. *© 2002 MAIK "Nauka/Interperiodica".*

The carbon–helium plasma at a pressure of 100 Torr is the optimal environment for synthesizing fullerenes, as was first demonstrated using Krätschmer's method [1]. Different modifications of this method now exist [2]. Usually, at such pressures and, especially, in a rare-gas atmosphere, ionization waves can be observed [3].

The method used in our laboratory can be considered to be a modification of Krätschmer's method [2, 4, 5]. We designed and successfully used a plasma-chemical reactor based on thermal graphite evaporation with the formation of a carbon plasma jet combined with helium flow at atmospheric pressure in a water-cooled chamber. A transformer matched the amplifier impedance with that of the plasmatron. A distinctive feature of our setup is that the synthesis is conducted at atmospheric pressure in a stream of carbon–helium plasma. The arc was fed by an alternating current at a frequency of 66 or 44 kHz.

Carbon evaporated from the central electrode acted as a plasma-forming gas. The temperature of this carbon plasma jet was measured both by the relative intensity technique and by a pyrometer and was found to vary from 5000 K close to the outer electrode to 2000 K in the tail part.

Our latest measurements have shown that the fullerene mixture synthesized in our setup contains approximately 60% C_{60}, 25% C_{70}, and 15% higher fullerenes (Fig. 1). The total yield of fullerene from our setup is within the same range as obtained with other generally used methods. However, we are not aware of other reports of effective fullerene synthesis at atmospheric pressure; therefore, in this respect, our experimental setup is unique.

We carried out investigations of a discharge in an argon stream between a water-cooled coil of copper tubing and a water-cooled copper electrode containing an axial hole for introducing argon. The frequency of the current discharge was 44 kHz, and the current was 10 to 15 Å. It was found that the discharge at atmospheric pressure is stratified [6]. It has been known that such strata are the visual result of ionization waves (ionization instability). Until recently, however, strata

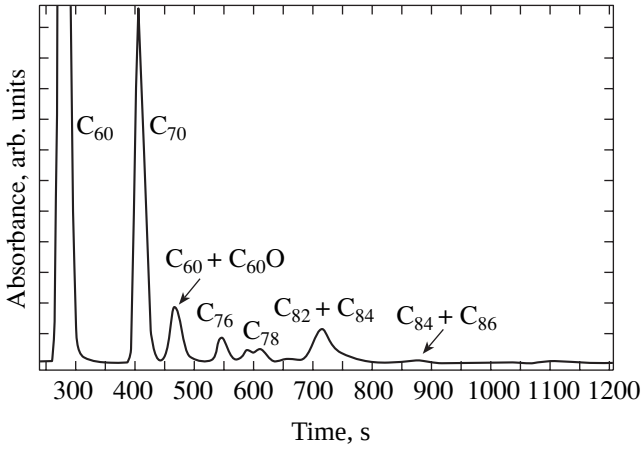

Fig. 1. Typical HPLC chromatogram obtained from the concentrated extract of a fullerene mixture by using toluene eluent and a Cosmosil Buckyprep column.

[1] This article was submitted by the authors in English.

1063-7834/02/4403-0419$22.00 © 2002 MAIK "Nauka/Interperiodica"

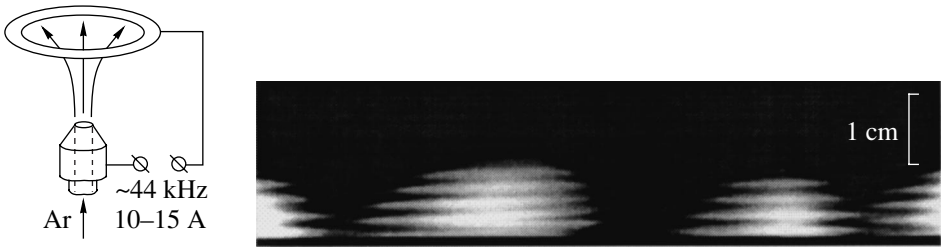

Fig. 2. The principal scheme of the discharge in an argon flow at atmospheric pressure, and a photoregistration of the irradiation intensity of the plasma discharge revealing forced running ionization waves. The current of the discharge arc is 7 Å, the frequency is 44 kHz, and the linear rate of argon flow is 42 m/s. The hole in the central electrode is about 2.0 mm in diameter.

were normally observed only at low pressures in regions restricted by glass tube walls.

Figure 2 shows a scheme of discharge in an argon stream and a high-speed photograph of this discharge. Here, the presence of running ionization waves is easily visible. Thus, we observe that the discharges at atmospheric pressure can also be stratified. Ionization waves arise when the discharge is driven by the alternating current.

In [7], the equilibrium states of rare gas plasmas were calculated using the method of level kinetics. According to those results, more than one value of the electron concentration can exist for definite values of the gas density and electron temperature. This effect of ionization instability is usually observed in experiments on the generation and study of ionization waves in rare gases at pressures ranging from fractions of one Torr to 200 Torr. In the well-known and popular experimental setup of Krätschmer, fullerene synthesis is usually carried out at pressures between 100 and 200 Torr. At these pressures, the local electron concentration in a carbon–helium plasma can vary over a wide range because of the presence of spontaneous ionization waves.

The above considerations suggest that electron concentration pulsations are also present in our atmospheric-pressure carbon–helium plasma arc. The common feature of effective fullerene synthesis in the experimental setups at low and atmospheric pressures is plasma instability related to electron concentration fluctuations. As a result, it is possible to deduce that the electron concentration (and, especially, variations in electron concentration) may be a major parameter that influences the production of carbon clusters in the form of fullerene molecules.

Many publications have now appeared concerning the local redistribution of electrons in plasmas caused by the injection of dust particles. As the electrons are condensed on the particles of dust [8], they will also be condensed on carbon clusters during their formation. Thus, in reviewing the formation of fullerene molecules from carbon clusters, it is necessary to take into account the charge of these clusters.

1. CALCULATIONS

We carried out computer simulations of the fullerene C_{60} formation from carbon clusters with different charges. The simulations were carried out using the HyperChem-5 program to calculate the optimal geometry of molecules and their molecular dynamics at different temperatures. All of the calculations were performed using the PM3 semiempirical quantum chemical method.

Estimations of the formation energies of different carbon clusters were made at a temperature of 1000 K, because the fullerene formation occurred at about 1000 to 2000 K. The influence of the charge of clusters on the process of their formation was investigated. We considered the formation of flat clusters consisting of hexagons alone, as well as of nonplanar clusters containing at least one pentagon. After calculating the total energy of different clusters, the energy of formation was estimated using the relation

$$C_n + C_m \longrightarrow C_{n+m},$$

$$\Delta E = E_t(C_{n+m}) - E_t(C_n) - E_t(C_m),$$

where ΔE is the energy of reaction and $E_t(C_i)$ is the calculated total energy of cluster C_i.

Our estimations showed that the spheroidal-cluster formation at 1000 K is more favorable than the formation of flat clusters with the same number of atoms (Figs. 3a, 3b, Table 1). This result can be explained by the increased number of carbon atoms with nonsaturated bonds in the flat clusters.

The energy of the reaction $C_n + C_m \longrightarrow C_{n+m}$ for the formation of a cluster C_{n+m} depends on the charges of the reacting clusters. Table 2 shows the calculated energies of formation of fullerene C_{60} from the clusters C_{20} and C_{40} with different charges, as well as the energies of formation of the flat cluster C_{60} from the flat clusters C_{20} and C_{40}.

The most favorable are the neutral–ion and the anion–cation reactions. The least favorable are reactions between ions with the same charge. Reactions between neutral clusters are intermediate in energy.

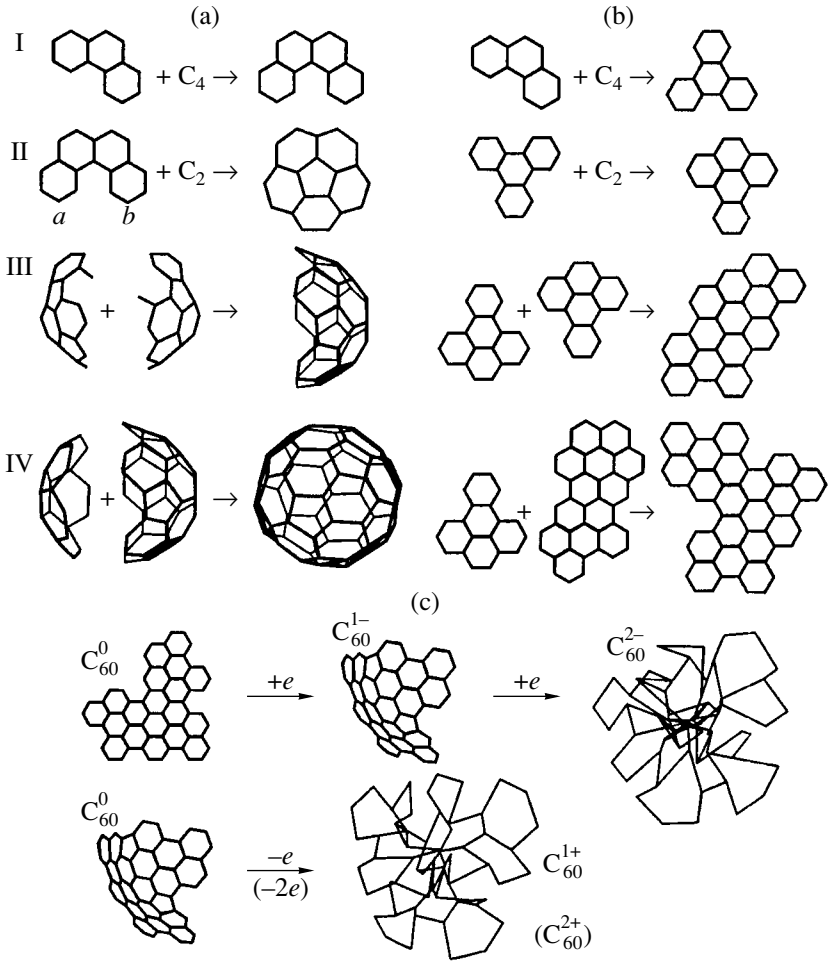

Fig. 3. Formation reactions of (a) spheroidal and (b) flat carbon clusters (the calculated reaction energies are presented in Table 1), and (c) energy minimization of a large flat cluster C_{60} with different charges.

Formation reactions for small-sized clusters follow the same pattern as that described above for fullerene C_{60}.

The most interesting results were obtained when analyzing the influence of charge on the geometry and stability of the clusters. In Table 2, missing data indicate that the final cluster does not exist. The charge of a cluster influences its geometry and stability significantly (Fig. 2c). Although the spherically symmetric fullerene molecule C_{60} keeps its structure regardless of its charge, the flat cluster C_{60} behaves differently, depending on charge. The neutral cluster C_{60} and singly charged anion C_{60}^- are folded into a portion of a spherical surface and remain stable at 1000 K. The folding happens in the places where two hexagons are divided by an incomplete hexagon having four bonds. In this place, the fifth bond appears and the cluster becomes curved due to the appearance of the pentagon. In our calculations, the flat singly charged cation C_{60}^+ and the doubly charged ions C_{60}^{2-} and C_{60}^{2+} dissociate in the process of geometry optimization.

The problem of pentagon formation in flat clusters is very important. Using the example of cluster C_{18} (Fig. 3a) with one incomplete pentagon, it is possible to observe that the changes in its geometry depend on its charge. A pentagon forms during the geometry optimi-

Table 1. Reaction energy for forming flat and spheroidal carbon clusters

Number in Fig. 3	Reaction	Spheroidal clusters, ΔE, kJ/mol	Flat clusters, ΔE, kJ/mol
I	$C_{14} + C_4 \longrightarrow C_{18}$	–1484	–886
II	$C_{18} + C_2 \longrightarrow C_{20}$	–1237	–853
III	$C_{20} + C_{20} \longrightarrow C_{40}$	–2337	–1379
IV	$C_{20} + C_{40} \longrightarrow C_{60}$	–3290	–1873

Table 2. Dependence of the reaction energy on the charges of reacting clusters

Type of reaction	Reaction $n = 40$, $m = 20$	Fullerene C_{60}, ΔE, kJ/mol	Flat cluster C_{60}, ΔE, kJ/mol
Neutral-ion	$C_n + C_m^+ \longrightarrow C_{n+m}^+$	–3440	*
	$C_n + C_m^- \longrightarrow C_{n+m}^-$	–3423	–2709
Anion–cation	$C_n^- + C_m^+ \longrightarrow C_{n+m}$	–3302	–949
Neutral–neutral	$C_n + C_m \longrightarrow C_{n+m}$	–3290	–1873
Anion–anion	$C_n^- + C_m^- \longrightarrow C_{n+m}^{2-}$	–2851	*
Cation–cation	$C_n^+ + C_m^+ \longrightarrow C_{n+m}^{2+}$	–2784	*

* Cluster is unstable.

zation of the singly charged ions C_{18}^- and C_{18}^+ and the doubly charged cation C_{18}^{2+}. The *ab* length (Fig. 3a) decreases to a typical C–C bond length of about 1.4 Å. With geometry optimization of the neutral cluster and doubly charged anion C_{18}^{2-}, the *ab* length between the outer hexagons increases. This example clearly suggests that a lower electron concentration in the plasma is necessary for the formation of spheroidal clusters containing pentagons.

2. CONCLUSIONS

In the phase of an ionization wave with a low electron concentration, the formation of clusters containing pentagons is favored. A further decrease in the electron concentration to a minimum reduces the efficiency of cluster formation because of the higher energy of cation–cation reactions.

As the electron concentration increases in the opposite phase to the ionization wave, the large flat clusters acquire negative charge and dissociate into smaller clusters or separate atoms. Because the time of elementary reactions is about 10^{-12} s, while the period of the electron concentration wave in the plasma is 10^{-3}–10^{-5} s, the cluster distributions can stay near equilibrium as the electron concentration varies. Therefore, small-sized clusters, including spheroidal ones, have time to be generated from separate atoms. With increasing electron concentration, the efficiency of the formation of these clusters decreases due to the higher energy of the anion–anion reactions. Because the electron concentration does not have such a strong effect on the stability of small spheroidal clusters and fullerene shells, the clusters and fullerene molecules already generated are not destroyed.

The large flat clusters tend to dissociate into smaller clusters during oscillations of the electron concentration. As the energies of formation of small clusters with and without pentagons are similar, there are always a number of clusters suitable for forming fullerenes in the plasma. These clusters remain stable once they have been formed.

Thus, the ionization wave executes two functions during the synthesis of fullerenes. At low electron concentrations, it favors the formation of clusters, especially spheroidal ones, whereas at high electron concentrations, it tends to preferentially destroy the flat clusters.

We note that the proposed mechanism does not consider statistical processes; it considers only the driving role of electron concentration variations. Recognition of the importance of electron concentration variations may provide an essential step to the controlled synthesis of fullerenes and, possibly, fullerene derivatives.

ACKNOWLEDGMENTS

The research described in this publication was made possible in part by award RE1-2231 of the US Civilian Research & Development Foundation for the Independent States of the Former Soviet Union (CRDF). Any opinions, findings, and conclusions or recommendations expressed in this material are those of the authors and do not necessarily reflect those of the CRDF. The work was also partially supported by the Russian State Program "Fullerenes and Atomic Clusters" (project no. 5-3-00) and the RF Education Ministry program "Scientific Research of Higher Schools in Important Directions of Science and Technology" (project no. 201.05.01.001).

REFERENCES

1. W. Krätschmer, K. Fostiropoulos, and D. R. Huffman, Chem. Phys. Lett. **170**, 167 (1990).
2. G. N. Churilov, Instrum. Exp. Tech. **43** (1), 1 (2000).

3. P. S. Landa, N. A. Miskinova, and Yu. V. Ponomarev, Usp. Fiz. Nauk **132** (4), 601 (1980) [Sov. Phys. Usp. **23**, 813 (1980)].

4. G. N. Churilov, in *Proceedings of International Winterschool on Electronic Properties of Novel Materials "Progress in Fullerene Research," Kirchberg, Tyrol, Austria, 1994* (World Scientific, Singapore, 1994), p. 135.

5. G. N. Churilov, L. A. Solovyov, Y. N. Churilova, *et al.*, Carbon **37** (3), 427 (1999).

6. G. N. Churilov, V. A. Lopatin, P. V. Novikov, and N. G. Vnukova, in *Proceedings of the 1st International Congress on Radiation Physics and Chemistry of Condensed Matter, High Current Electronics, and Modification of Materials with Particle Beams and Plasma Flows, Tomsk, 2000*, Vol. 2, p. 223.

7. A. Yu. Gavrilova, A. G. Kiselyov, E. P. Skorokhod, and M. E. Stanishevskaya, Mat. Modell. **8** (6), 103 (1996).

8. V. I. Molotkov, M. Yu. Nefedov, M. Yu. Pustyl'nik, *et al.*, Pis'ma Zh. Éksp. Teor. Fiz. **71**, 152 (2000) [JETP Lett. **71** (3), 102 (2000)].

Physics of the Solid State, Vol. 44, No. 3, 2002, pp. 424–426. From Fizika Tverdogo Tela, Vol. 44, No. 3, 2002, pp. 410–412.

PROCEEDINGS OF THE V INTERNATIONAL WORKSHOP "FULLERENES AND ATOMIC CLUSTERS"

(St. Petersburg, Russia, July 2–6, 2001)

The Oxidation of Fullerenes (C_{60}, C_{70}) with Various Oxidants under Ultrasonication[1]

Weon-Bae Ko and Kyung-Nam Baek

Department of Chemistry, Sahmyook University, 139-742 Seoul, Korea
e-mail: kowb@syu.ac.kr

Abstract—The reaction of C_{60}, under ultrasonication, with various oxidants, such as 3-chloroperoxy benzoic acid (Fluka 99%), 4-methyl morpholine N-oxide (Aldrich 97%), chromium (VI) oxide (Aldrich 99.9%), and the oxone® monopersulfate compound, causes the oxidation of fullerenes at room temperature. The FAB-MS spectra and HPLC profile confirmed that the products of fullerene oxidation were $[C_{60}(O)_n]$ ($n = 1 \sim 3$ or $n = 1$). C_{70} also reacted, under ultrasonication, with various oxidants, but the reaction rate of C_{70} was lower than that of C_{60}. © *2002 MAIK "Nauka/Interperiodica".*

The $[C_{60}(O)_n]$ ($n = 1 \sim 3$) has been obtained by a number of oxidation processes in solution. These include the photooxygenation of C_{60} [1, 2], the electrochemical oxidation of C_{60}, the addition of dimethyldioxirane to C_{60} [3], the ozonolysis of C_{60} [4, 5], and the ultrasound-induced oxidation of C_{60} [9]. The fullerene monooxide $C_{60}O$ has been shown to have an epoxide structure in which the oxygen atom is positioned over a 6 : 6 ring junction [2, 6, 7].

Ultrasonic waves in liquids are known to cause chemical reactions either in homogeneous or in heterogeneous systems [7, 8]. The chemical reactions are promoted by cavitation of liquids caused by ultrasonic waves traveling in the liquid.

Here, cavitation implies the formation of microbubbles in a liquid subjected to sonication, which implode and generate high pressures and temperatures in their surroundings [8, 9]. We report that the reactions of C_{60} and C_{70} under ultrasonication with various oxidants, such as 3-chloroperoxy benzoic acid, 4-methyl morpholine N-oxide, chromium (VI) oxide, and the oxone® monopersulfate compound, give rise to the oxidation of fullerenes at room temperature with the formation of $[C_{60}(O)_n]$ ($n = 1 \sim 3$ or $n = 1$) and $[C_{70}(O)_n]$ ($n = 1 \sim 2$ or $n = 1$).

1. EXPERIMENTAL

The fullerenes (C_{60}, C_{70}) used in this work were of Golden grade from Hoechest and the Southern Chemical Group Inc. All solvents and chemical reagents were from Aldrich and Fluka.

[1] This article was submitted by the authors in English.

1.1. The Reaction of Fullerenes (C_{60}, C_{70}) under Ultrasonication with 3-Chloroperoxy Benzoic Acid

Solutions of C_{60} (20 mg, 0.028 mmol) and C_{70} (20 mg, 0.024 mmol) dissolved in 60 ml of benzene reacted under ultrasonication with 3-chloroperoxy benzoic acid (96 mg, 0.56 mmol in the case of C_{60} and 82.8 mg, 0.48 mmol in the case of C_{70}) in air at room temperature for 5 h. Each resulting solution was evaporated; then, the remaining solid material was washed with methanol to remove excess 3-chloroperoxy benzoic acid and dried in a vacuum oven.

1.2. The Reaction of Fullerenes (C_{60}, C_{70}) under Ultrasonication with 4-Methyl Morpholine N-Oxide

Solutions of C_{60} (20 mg, 0.028 mmol) and C_{70} (20 mg, 0.024 mmol) dissolved in 50 ml of benzene reacted under ultrasonication with 4-methyl morpholine N-oxide (32.5 mg, 0.280 mmol in the case of C_{60} and 28.1 mg, 0.240 mmol in the case of C_{70}) dissolved in 10 ml of benzene in air at room temperature for 5 h. Each resulting solution was evaporated, so that the remaining solid material was a mixture of fullerene oxidation products.

1.3. The Reaction of Fullerenes (C_{60}, C_{70}) under Ultrasonication with Chromium (VI) Oxide

Solutions of C_{60} (20 mg, 0.028 mmol) and C_{70} (20 mg, 0.023 mmol) dissolved in 60 ml of carbon disulfide reacted under ultrasonication with chromium (VI) oxide (28.0 mg, 0.280 mmol in the case of C_{60} and 23.0 mg, 0.230 mmol in the case of C_{70}) dissolved in 10 ml of acetone in air at room temperature for 5 h.

1063-7834/02/4403-0424$22.00 © 2002 MAIK "Nauka/Interperiodica"

The FAB-MS and HPLC analysis of $C_{60}(O)_n$ ($n = 1 \sim 3$ or $n = 1$) and $[C_{70}(O)_n]$ ($n = 1 \sim 2$ or $n = 1$) produced in the reaction with various oxidants under ultrasonication for 5 h

Oxidants	Fullerenes	Formation of $C_{60}(O)_n$ ($n = 1 \sim 3$ or $n = 1$) and $C_{70}(O)_n$ ($n = 1 \sim 2$ or $n = 1$)	Molecular mass (m/z)	Retention times, min
3-Chloroperoxy benzoic acid	C_{60}	$C_{60}O_3$	769	6.67
	C_{60}	$C_{60}O_2$	753	9.00
	C_{60}	$C_{60}O_1$	737	12.72
	C_{60}	C_{60}	721	17.11
	C_{70}	$C_{70}O_2$	873	14.23
	C_{70}	$C_{70}O_1$	857	20.57
	C_{70}	C_{70}	841	28.07
4-Methyl morpholine N-oxide	C_{60}	$C_{60}O_3$	769	6.68
	C_{60}	$C_{60}O_2$	753	9.01
	C_{60}	$C_{60}O_1$	737	12.73
	C_{60}	C_{60}	721	17.14
	C_{70}	$C_{70}O_2$	873	14.18
	C_{70}	$C_{70}O_1$	857	20.06
	C_{70}	C_{70}	841	28.14
Chromium (VI) oxide	C_{60}	$C_{60}O_1$	737	12.70
	C_{60}	C_{60}	721	17.17
	C_{70}	$C_{70}O_1$	857	20.09
	C_{70}	C_{70}	841	28.14
Oxone® monopersulfate	C_{60}	$C_{60}O_1$	737	12.67
	C_{60}	C_{60}	721	17.08
	C_{70}	$C_{70}O_1$	857	20.57
	C_{70}	C_{70}	841	28.07

Note: FAB-MS analysis conditions: the acceleration voltage was 10 kV, FAB source was CSI ionized in 20 kV, and the matrix was nitrobenzyl alcohol. HPLC analysis conditions: model number: Hewlett packard 1100; column: ZorbaxSB C_{18}; detector: 340 nm; flow rate: 1.0 ml/min; mobile phase: acetonitrile/toluene 50 : 50 (v/v); injection volume: 10.00 ml; pump pressure: 1.000 psi.

Each resulting solution was evaporated, so that the remaining solid material was a mixture of fullerene oxidation products.

1.4. The Reaction of Fullerenes (C_{60}, C_{70}) under Ultrasonication with Oxone® Monopersulfate Compound

Solutions of C_{60} (20 mg, 0.028 mmol) and C_{70} (20 mg, 0.023 mmol) dissolved in 60 ml of benzene reacted under ultrasonication with the oxone® monopersulfate compound (170.7 mg, 0.280 mmol in the case of C_{60} and 146.0 mg, 0.238 mmol in the case of C_{70}) dissolved in 1 ml of H_2O and 10 ml of methanol (99%). Then 18-crown-6 (5 mg, 0.019 mmol) was added and reacted in air with the solution at room temperature for 5 h. Each resulting solution was evaporated, so that the remaining solid material was a mixture of fullerene oxidation products.

2. RESULTS AND DISCUSSION

The FAB-MS spectra and HPLC profile revealed that the oxidation of fullerenes (C_{60}, C_{70}) subjected to ultrasonication in the presence of various oxidants, such as 3-chloroperoxy benzoic acid, 4-methyl morpholine N-oxide, chromium (VI) oxide, and the oxone® monopersulfate compound, resulted in the formation of $[C_{60}(O)_n]$ ($n = 1 \sim 3$ or $n = 1$) and $[C_{70}(O)_n]$ ($n = 1 \sim 2$ or $n = 1$). 4-Methyl morpholine N-oxide is not as well known as other powerful oxidants for their reactivity under mild conditions. The differences between various oxidation with and without ultrasonication are as follows. First, the reaction time is shortened due to the high pressure and temperature produced by ultrasonication. Second, in the reactions of C_{60} and C_{70} with 4-methyl morpholine N-oxide, $[C_{60}(O)_n]$ ($n = 1 \sim 3$) and $[C_{70}(O)_n]$ ($n = 1 \sim 2$) are produced by ultrasonication rather than through a thermal reaction.

Epoxidation with various oxidants mediated by ultrasonication is efficient for both electron-rich olefins

and fullerenes. The results of FAB-MS and HPLC analysis presented in the table show the formation of $[C_{60}(O)_n]$ ($n = 1 \sim 3$ or $n = 1$) and $[C_{70}(O)_n]$ ($n = 1 \sim 2$ or $n = 1$).

The reactivity of C_{70} with various oxidants under ultrasonication is lower than that of C_{60} under the same conditions. This reactivity difference probably results from the difference in the symmetry of their structures. The oxidation of fullerenes (C_{60}, C_{70}) by ultrasonication may proceed through a nucleophilic attack of oxidants to a 6–6 bond, followed by heterolytic breakage of the O–O bond. The common mechanism for fullerene oxidation by ultrasonication with various oxidants involves oxygen atom transfer to fullerenes (C_{60}, C_{70}).

It is suggested that the fullerene epoxides $[C_{60}(O)_n]$ ($n = 1 \sim 3$ or $n = 1$) and $[C_{70}(O)_n]$ ($n = 1 \sim 2$ or $n = 1$) may be used as oxygen-transferring materials. Furthermore, the fullerene epoxides $[C_{60}(O)_n]$ ($n = 1 \sim 3$ or $n = 1$) and $[C_{70}(O)_n]$ ($n = 1 \sim 2$ or $n = 1$) are interesting starting materials for the formation of other fullerene-based entities.

In conclusion, using the HPLC profile and FAB-MS spectra, we identified the $[C_{60}(O)_n]$ ($n = 1 \sim 3$ or $n = 1$) and $[C_{70}(O)_n]$ ($n = 1 \sim 2$ or $n = 1$) formed in the reaction of C_{60} and C_{70} under ultrasonication with 3-chloroperoxy benzoic acid, 4-methyl morpholine N-oxide, chromium (VI) oxide, and the oxone® monopersulfate compound at room temperature. We observed that the reaction rate of C_{70} was slower than that of C_{60}, which may be due to the lower symmetry of the C_{70} structure. The epoxidation of olefin by the multiepoxide of fullerene, $[C_{60}(O)_n]$ ($n = 1 \sim 3$ or $n = 1$) and $[C_{70}(O)_n]$ ($n = 1 \sim 2$ or $n = 1$), is presently under investigation.

ACKNOWLEDGMENTS

We thank Dr. J.J. Seo of the Korea Basic Sciences Institute (Seoul) for measuring the FAB-MS spectra.

This work was supported by the Sahmyook University, Korea.

REFERENCES

1. J. M. Wood, B. Kahr, S. H. Hake, II, *et al.*, J. Am. Chem. Soc. **113**, 5907 (1991).
2. K. M. Creegan, W. K. Robbins, J. M. Millar, *et al.*, J. Am. Chem. Soc. **114**, 1103 (1992); J. M. Millar, K. M. Creegan, J. L. Robbins, *et al.*, Synth. Met. **59**, 317 (1993).
3. W. A. Kalsbeck and H. H. Thorp, J. Electroanal. Chem. **314**, 363 (1991).
4. Y. Elemes, S. K. Silverman, C. Sheu, *et al.*, Angew. Chem. Int. Ed. Engl. **31**, 351 (1992).
5. D. Heymann and L. P. F. Chibante, Chem. Phys. Lett. **207**, 339 (1993).
6. A. L. Balch, D. A. Costa, J. W. Lee, *et al.*, Inorg. Chem. **32**, 2071 (1994).
7. T. J. Mason and J. P. Lorimer, *Sonochemistry: Theory, Applications, and Uses of Ultrasound in Chemistry* (Ellis Horwood, Chichester, 1988).
8. K. S. Suslick, *Ultrasound. Its Chemical, Physical and Biological Effects* (VCH, Weinheim, 1989).
9. F. Cataldo and D. Heymann, Fullerene Sci. Technol. **7**, 752 (1999).

Physics of the Solid State, Vol. 44, No. 3, 2002, pp. 427–428. From Fizika Tverdogo Tela, Vol. 44, No. 3, 2002, pp. 413–414.

PROCEEDINGS OF THE V INTERNATIONAL WORKSHOP "FULLERENES AND ATOMIC CLUSTERS"

(St. Petersburg, Russia, July 2–6, 2001)

Cluster Approach to the Synthesis of Ternary Metal Sulfides: Molybdenum Disulfide Single Layers as a Precursor[1]

A. S. Golub*, N. D. Lenenko*, Ya. V. Zubavichus*, Yu. L. Slovokhotov*, A. M. Marie, M. Danot**, and Yu. N. Novikov***

** Institute of Organoelement Compounds, Russian Academy of Sciences, Moscow, 117813 Russia*

e-mail: golub@ineos.ac.ru

*** Institut des Matériaux Jean Rouxel, UMR 6502, CNRS-Univ. Nantes, BP 32229, 44322 Nantes-Cedex 3, France*

Abstract—The reactivity of negatively charged $(MoS_2)^{x-}$ layers in aqueous single-layer dispersions resembles that of molecular Mo–S cluster compounds. These layers form covalent bonds with metal (M) cations (M = Cu, Ag, Pb, Cd, Hg, Pd), giving rise to ternary metal sulfides M_zMoS_2 whose Mo network contains direct Mo–Mo bonds. © *2002 MAIK "Nauka/Interperiodica".*

Lithiation of MoS_2 is known to result in a solid ionic compound $Li^+(MoS_2)^-$ containing negatively charged $(MoS_2)^-$ layers [1]. These layers can be considered to be extended quasi-two-dimensional anionic $[S–Mo–S]^{n-}$ clusters whose electronic and chemical nature (valence-electron concentration per Mo atom and the presence of outer-shell sulfur atoms) allow one to expect a behavior resembling that of molecular Mo–S clusters (Mo_6S_8, for instance). The characteristic structural feature of the latter clusters (associated with their electronic structure) is the existence of Mo–Mo bonds in the cluster framework. Regarding chemical reactivity, their sulfur ligands easily coordinate with extra-metal cations [2].

The exfoliaton of solid $LiMoS_2$ in an aqueous medium has already been shown to produce a dispersed system containing negatively charged extended $(MoS_2)^{x-}$ cluster species separated by water molecules, with their sulfur atoms being accessible for coordination [3, 4]:

$$LiMoS_2 \xrightarrow{H_2O} [Li^+ + (MoS_2)^{x-} + (1-x)OH^-]_{aq} + \frac{1-x}{2}H_2.$$

The approach presented here consists in the use of these clusterlike species as precursors to the chemical reactions.

RESULTS AND DISCUSSION

We found recently [5] that the restacking of exfoliated MoS_2 layers in the presence of some M cations yields powdered ternary metal sulfides of the general composition M_zMoS_2 (M = Cu, Ag, Cd, Pb, Hg, Pd):

$$(MoS_2)^{x-} + M^{n+} \longrightarrow M_zMoS_2.$$

As follows from EXAFS data obtained at the M K (M = Cu, Ag, Pd, Cd) and M L_{III} (M = Hg, Pb) absorption edges, the closest atomic environment of the M atoms in M_zMoS_2 is composed exclusively of S atoms. This confirms the incorporation, between neighboring S–Mo–S sandwiches, of metal cations forming covalent bonds with S atoms of the matrix and agrees with XRD results on the lattice expansion observed for M_zMoS_2 (see table). There are two types of vacant sites, octahedral and tetrahedral, in the MoS_2 interlayer space. Analysis of the guest-metal coordination environment indicates that this environment is strongly disordered (particularly, for Ag and Hg; see their reduced coordination numbers) and that incorporated metal cations tend to approach a coordination typical of the given metal in the sulfur surrounding (see table).

The formation of the ternary compounds is evidently accompanied by electron transfer from the negatively charged $(MoS_2)^{x-}$ layers to some metal cations involved [Ag(I), Pd(II), Hg(II), Cu(II)]. This results in reduction of part of these cations in the course of the reaction and, in the case of Pd, Ag, and Hg, leads to the formation of additional phases (metalic Pd, Ag, or Hg(I) compounds) along with the phase of ternary sulfide, as indicated by XRD and EXAFS data. It is interesting that, in the case of Cu(II) involved in the reaction, the resulting Cu(I) cations occupy guest positions in the structure of ternary sulfide, so that all the intercalated Cu ions are Cu(I), as follows from XPS data [6].

Despite the decrease in the negative charge on S–Mo–S layers due to the redox process, a part of the charge does remain on these layers in ternary com-

[1] This article was submitted by the authors in English.

Interlayer spacing expansions with respect to parent MoS_2(Δc) and parameters of the closest environment around guest *M* atoms in M_zMoS_2

M_zMoS_2	Δc, Å	N_{M-S}	R_{M-S}, Å	Presumable coordination
$Pb_{0.18}MoS_2$	1.0	5.7	2.87	Octahedral
$Cd_{0.20}MoS_2$	0.4	4.0	2.55	Tetrahedral
$Cu_{0.35}MoS_2$	0.1	3.1	2.29	Tetrahedral
$Ag_{0.86}MoS_2^*$	0.8	1.0 (+0.5 Ag–Ag at 2.87 Å)	2.40	Strongly distorted tetrahedral
$Pd_{0.45}MoS_2^{**}$	0.05	1.5 (+5.1 Pd–Pd at 2.73 Å)	2.33	Tetrahedral
$Hg_{0.20}MoS_2$	0.2	1.1	2.37	Strongly distorted octahedral

* (95% $Ag_{0.82}MoS_2$ + 5% Ag), ** (60% $Pd_{0.25}MoS_2$ + 40% Pd).

pounds, being balanced by covalently bonded guest *M* cations. This means that part of the electrons transferred to MoS_2 layers upon lithiation should remain on *d* orbitals of the Mo atoms and can stabilize the distortions of the Mo network in the compounds obtained. Indeed, EXAFS measurements at the Mo *K* edge indicated that there are drastic changes in the host structure in M_zMoS_2 compared to the parent 2*H*-MoS_2. Instead of a unique Mo…Mo contact at 3.16 Å in the parent MoS_2, three Mo–Mo distances appear in the ternary compounds (see figure). The shorter distance (approximately 2.75 Å) corresponds to direct Mo–Mo bonds in the layers.

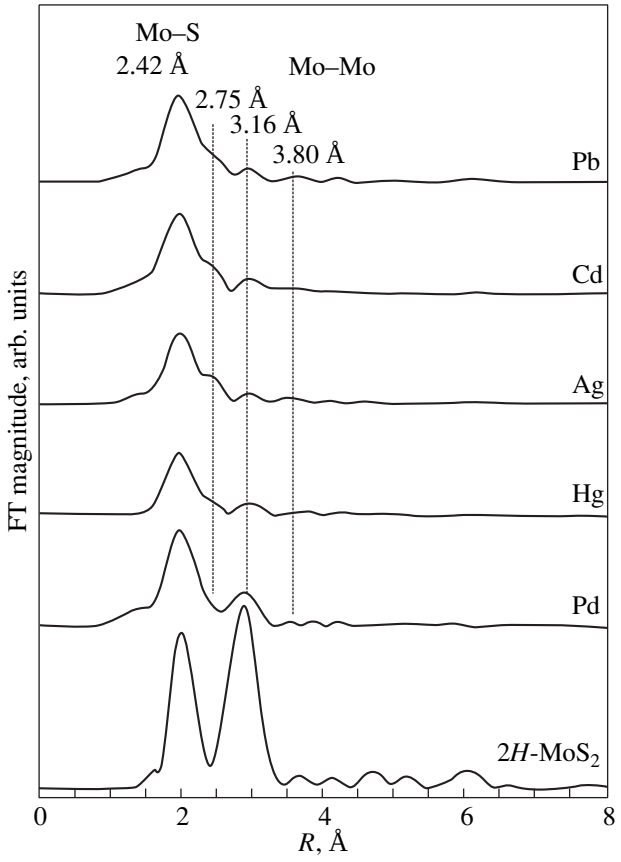

Fourier transforms (FTs) of Mo *K*-edge spectra for M_zMoS_2 and 2*H*-MoS_2.

It appears from the present study that $(MoS_2)^{x-}$ layers in single-layer dispersions are effectively capable of coordinating with metal cations by sulfur atoms and of producing ternary metal sulfides. The host structure of these ternary compounds exhibits strong distortions due to periodic in-layer displacements of the Mo atoms forming direct Mo–Mo bonds.

ACKNOWLEDGMENTS

This work was supported by the Russian Foundation for Basic Research (project nos. 00-03-32544, 99-03-32810) and the Russian Academy of Sciences (program "Nanomaterials and Supramolecular Structures").

REFERENCES

1. M. A. Py and R. R. Haering, Can. J. Phys. **61** (1), 76 (1983).
2. R. Chevrel, P. Gougeon, M. Potel, and M. Segent, J. Solid State Chem. **57** (1), 25 (1985).
3. P. Joensen, R. F. Frindt, and S. R. Morrison, Mater. Res. Bull. **21** (4), 457 (1986).
4. M. Danot, J. L. Mansot, A. S. Golub, *et al.*, Mater. Res. Bull. **29** (8), 833 (1994).
5. A. S. Golub, N. D. Lenenko, Ya. V. Zubavichus, *et al.*, Izv. Akad. Nauk, Ser. Khim. (in press).
6. A. S. Golub, I. B. Shumilova, Ya. V. Zubavichus, *et al.*, Solid State Ionics **122** (1–4), 137 (1999).

Physics of the Solid State, Vol. 44, No. 3, 2002, pp. 429–431. Translated from Fizika Tverdogo Tela, Vol. 44, No. 3, 2002, pp. 415–416.

PROCEEDINGS OF THE V INTERNATIONAL WORKSHOP "FULLERENES AND ATOMIC CLUSTERS"

(St. Petersburg, Russia, July 2–6, 2001)

The Temperature Dependences of the Elastic Moduli of Solid C_{60}

N. P. Kobelev, R. K. Nikolaev, N. S. Sidorov, and Ya. M. So ĭfer

Institute of Solid-State Physics, Russian Academy of Sciences, Chernogolovka, Moscow oblast, 142432 Russia
e-mail: kobelev@issp.ac.ru

Abstract—This paper reports on the determination of the temperature dependences of the complete set of the elastic moduli of solid C_{60} from sound-velocity measurements made along different crystallographic directions in single-crystal samples within the 100- to 300-K range. Substantial differences in their behavior were revealed, which are accounted for by different relative contributions from relaxation processes to various elastic moduli. © *2002 MAIK "Nauka/Interperiodica".*

1. INTRODUCTION

Elastic constants are among the fundamental characteristics of solids. While the elastic constants of solid C_{60} at room temperature may be considered to be established [1, 2], information on their temperature dependence is incomplete and partially contradictory [3–8]. These observations, as well as the reasons for the above discrepancies, call for reliable determination of the temperature dependences for the complete set of the elastic constants of solid C_{60}.

2. EXPERIMENTAL TECHNIQUE AND RESULTS

The studies were performed on single-crystal samples of solid C_{60} measuring typically $6 \times 8 \times (1–3)$ mm. The growth technique used to obtain single crystals and the procedure employed in sample preparation were similar to those described earlier in [1, 2]. The elastic moduli were determined using the acoustic method. The measurements were carried out at a frequency of ~4 MHz in the 100- to 300-K temperature range using the high-frequency resonance technique [9]. We measured the damping and velocities of longitudinal sound waves in the ⟨100⟩ and ⟨111⟩ crystallographic directions and those of transverse sound waves along the ⟨111⟩ direction [10]. The temperature dependences of damping exhibited two internal-friction peaks, at $T \approx$ 212 K and in the region of T_c = 260 K [phase transition from the fcc to sc (simple cubic) structure]. The former peak could be identified with the steps in the temperature dependence of the velocity (which were less pronounced for transverse waves). The phase transition was signaled by various types of anomalies (a decrease or an upward jump) in the behavior of the velocity for different sonic modes.

Using the well-known relations between the elastic moduli and sound velocity in cubic crystals, the experimental data obtained were converted into temperature dependences of the elastic moduli C_{11}, C_{12}, and C_{44} (see figure). The temperature dependences of these moduli are seen to differ noticeably. This relates both to the

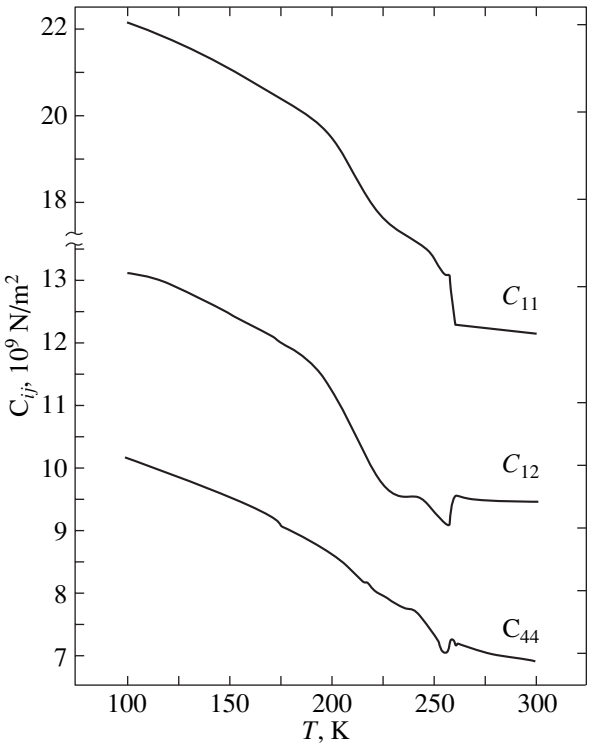

Temperature dependences of the effective elastic moduli of solid C_{60} derived from experimental temperature dependences of sound velocity obtained in different crystallographic directions at a frequency of ≈4 MHz.

1063-7834/02/4403-0429$22.00 © 2002 MAIK "Nauka/Interperiodica"

magnitude of the step in the region of 212 K and to the behavior of the moduli at T_c (an upward jump for C_{11} and a dip for C_{12} and C_{44}).

3. DISCUSSION

The features in the behavior of the effective elastic moduli of solid C_{60} can be understood if we consider all the processes contributing to their temperature dependence within the temperature range under study. One of these processes is the linear growth of the moduli with decreasing temperature, which results from the change in the lattice parameter connected with the crystal anharmonicity. According to [11], $d(\ln C)/dT$ is $\sim 7 \times 10^{-4}$ K^{-1} for this process. Superposed on this process in the sc phase is the variation of the moduli due to the concentration of excited orientational states decreasing with decreasing temperature. As follows from rough estimates, for temperatures above 120–130 K, the temperature dependence of the elastic modulus in the sc phase should remain very close to linear.

Another process is the fcc–sc phase transition and the associated jump in the elastic moduli at T_c [5, 12].

The temperature dependence of the elastic moduli is also affected by the relaxation processes, which result in a decrease in their effective values by $R/(1 + \omega^2\tau^2)$, where the temperature-dependent values R and τ are the amount of relaxation and the effective relaxation time, respectively, and ω is the circular frequency. The best known of these processes is the orientational relaxation of C_{60} molecules in the strain field of a sound wave; this process is due to the molecules partially retaining their orientational mobility in the sc phase. An analysis of this process within a phenomenological model of two-level orientational states [13] yields the following expressions for τ and R [10, 14, 15]:

$$\tau = \tau_0[n_0(1-n_0)]^{1/2}\exp(E_0/kT),$$
$$R = n_0(1-n_0)(V_\Delta)^2/(v_0 kT),$$

where τ_0 is a characteristic time ($\sim 10^{-13}$–10^{-14} s), E_0 is the activation energy ($\approx$0.3 eV), n_0 is the relative excited-state density at the given temperature, v_0 is the effective volume per excited state ($\sim 10^{-27}$ m^3), and V_Δ is the difference between the deformation potentials of the ground and excited orientational states. Accepting these values of the activation parameters τ_0 and E_0, the step in the temperature dependence of the moduli at a frequency of $\approx$4 MHz is found to lie in the 200- to 230-K interval. It was assumed earlier [14] that V_Δ is nonzero only for elastic waves of the longitudinal type accompanied by crystal dilatation; however, if the specific features of the fullerite sc-phase structure (four molecules per unit cell with different rotation-axis directions) are taken into account, the expression for R_{ijkl} (the relaxation of the elastic modulus C_{ijkl}) assumes the form [15]

$$R_{ijkl} = [n_0(1-n_0)/(v_0 kT)][(V_{\Delta,1} + V_{\Delta,2})^2\delta_{ij}\delta_{kl} + (V_{\Delta,2})^2(\delta_{ik}\delta_{jl} + \delta_{il}\delta_{jk})(1-\delta_{ij})], \quad (1)$$

which shows that a relaxation term of this type also exists for the shear moduli.

Near T_c, the moduli in the sc phase are also affected by one more process [5, 10] associated with relaxation of the order parameter η, because the free energy has a contribution proportional to $\eta^2\varepsilon$ [12] (ε is the elastic strain). We believe that, because the states of molecules with differently directed rotation vectors S^α (α = 1–4) become inequivalent in the presence of an external shear strain, the free energy should contain not only the term $\sim\eta^2\varepsilon_{ii}$ but also terms of the type $\sim(\eta_\alpha)^2 S_i^\alpha S_j^\alpha \varepsilon_{ij}$, which are also dependent on the shear strain. The order-parameter relaxation should bring about a softening of the elastic moduli near the fcc–sc transition temperature T_c [5, 10].

One more contribution to the free energy ($\sim\eta^2\varepsilon^2$) [5, 12] originates from the above-mentioned jump of the moduli at the phase transition. This contribution should contain the term $\sim\eta^2\varepsilon_{ii}\varepsilon_{jj}$ and, in addition, terms of the type $\sim\eta^2 S_i^\alpha S_j^\alpha \varepsilon_{ik}\varepsilon_{jk}$; in other words, all elastic moduli should undergo jumps, but of different magnitude.

Thus, our consideration shows that the character of the temperature dependence of an effective elastic modulus of solid C_{60} should be governed, including the region near T_c, by the relation between the modulus and the contributions due to the two relaxation processes discussed above and to the jump of the modulus occurring at the phase transition. Because these relations may differ noticeably for different elastic moduli, this factor is capable of accounting for the broad spectrum of the temperature dependences of the elastic moduli obtained in experiments on solid C_{60}.

ACKNOWLEDGMENTS

This study was supported by the State R & D program "Topical Problems of Physics of Condensed Media: Fullerenes and Atomic Clusters," project no. 2.

REFERENCES

1. N. P. Kobelev, R. K. Nikolaev, Ya. M. Soĭfer, and S. S. Khasanov, Fiz. Tverd. Tela (St. Petersburg) **40**, 173 (1998) [Phys. Solid State **40**, 154 (1998)].
2. N. P. Kobelev, Ya. M. Soifer, R. K. Nikolaev, and V. M. Levin, Phys. Status Solidi B **214**, 303 (1999).
3. X. D. Shi, A. R. Kortan, J. M. Williams, *et al.*, Phys. Rev. Lett. **68**, 827 (1992).
4. S. Hoen, N. G. Chopra, R. Mostovoy, *et al.*, Phys. Rev. B **46**, 12737 (1992).

5. W. Schranz, A. Fuith, P. Dolinar, *et al.*, Phys. Rev. Lett. **71**, 1561 (1993).
6. N. P. Kobelev, A. P. Moravskiĭ, Ya. M. Soĭfer, *et al.*, Fiz. Tverd. Tela (St. Petersburg) **36**, 2732 (1994) [Phys. Solid State **36**, 1491 (1994)].
7. Ya. M. Soifer and N. P. Kobelev, Mol. Mater. **7**, 267 (1996).
8. F. Yan, M. Gu, and Y. N. Wang, J. Phys. IV **6**, C8-819 (1996).
9. N. P. Kobelev and Ya. M. Soĭfer, Fiz. Tverd. Tela (Leningrad) **21**, 1362 (1979) [Sov. Phys. Solid State **21**, 787 (1979)].
10. N. P. Kobelev, R. K. Nikolaev, N. S. Sidorov, and Ya. M. Soĭfer, Fiz. Tverd. Tela (St. Petersburg) **43**, 2262 (2001) [Phys. Solid State **43**, 2344 (2001)].
11. E. Burgos, E. Halas, and H. Bonadeo, Phys. Rev. B **49**, 15544 (1994).
12. D. Lamoen and K. H. Mishel, Phys. Rev. B **48**, 807 (1993).
13. W. I. F. David, R. M. Ibberson, T. J. S. Dennis, *et al.*, Europhys. Lett. **18**, 219 (1992); **18**, 735 (1992).
14. V. D. Natsik and A. V. Podol'skiĭ, Fiz. Nizk. Temp. **24**, 689 (1998) [Low Temp. Phys. **24**, 523 (1998)].
15. N. P. Kobelev, Fiz. Tverd. Tela (St. Petersburg) **44**, 188 (2002) [Phys. Solid State **44**, 195 (2002)].

Translated by G. Skrebtsov

Physics of the Solid State, Vol. 44, No. 3, 2002, pp. 432–433. From Fizika Tverdogo Tela, Vol. 44, No. 3, 2002, pp. 417–418.

PROCEEDINGS OF THE V INTERNATIONAL WORKSHOP "FULLERENES AND ATOMIC CLUSTERS"

(St. Petersburg, Russia, July 2–6, 2001)

The Illumination-Time and Wavelength Dependences of Photoinduced Hardening of C_{60} Crystals[1]

I. Manika*, J. Maniks*, R. Pokulis, and J. Kalnacs*****

**Institute of Solid State Physics, University of Latvia, Riga, LV-1063 Latvia*

*** Daugavpils Pedagogical University, Daugavpils, LV-5400 Latvia*

**** Institute of Physical Energetics, Latvian Academy of Sciences, Riga, LV-1006 Latvia*

Abstract—The fullerite photopolymerization in air in the wavelength range 350–900 nm was investigated using microhardness and dislocation mobility methods. The photoinduced effects of the hardening and reduction of a dislocation mobility were found to increase linearly with increasing photon energy. The existence of two phototransformed states is supposed from the kinetics data on photoinduced hardening. © *2002 MAIK "Nauka/Interperiodica".*

In recent years, the polymeric phases of fullerite C_{60} have attracted much attention. The photoinduced polymerization of C_{60} is of special interest, suggesting possible photolithographic and other applications of fullerite. Because C_{60} absorbs light very strongly, the photopolymerization occurs in a thin surface layer; thus, the limited sample volumes available make full characterization of phototransformed C_{60} rather difficult. According to light absorption data, the thickness of a phototransformed layer depends on the wavelength. The formation of covalently bonded fullerene dimers or chains in the molecular lattice through a photochemical 2 + 2 cycloaddition reaction is considered to be the main mechanism of photopolymerization [1]. Generally, an increase in the efficiency of photopolymerization with decreasing wavelength can be expected. However, investigations have shown contradictory results. In [2], the photoinduced effect was found to appear under green-light irradiation, but little or no effect was observed with red light, while in [3], the effect was observed to be maximum with red light. In the present study, the wavelength dependence and kinetics of fullerite photopolymerization in air was investigated using microhardness and dislocation mobility methods.

1. EXPERIMENTAL

C_{60} single-crystals were grown from the vapor phase in a temperature gradient through sublimation of a twice sublimed C_{60} powder (99.9% C_{60}). The density of grown-in dislocations was 10^3–10^4 cm^{-2}. The typical size of the samples selected for the experiments was approximately $0.5 \times 2 \times 7$ mm. Investigations were performed on the (111) face of as-grown crystals in the wavelength range 350–900 nm at a power density from 2 to 140 mW/cm^2 and illumination time of 1 to 5×10^3 s. The Vickers microhardness was measured at loads of 3.2–5.5 mN small enough for the indentation depth to be lower or comparable with the thickness of the phototransformed surface layer. A microhardness tester with a vibration-insensitive loading system was used [4]. The scatter of the hardness measurements was typically about 12%, but it increased up to 22% for the smallest impressions. The dislocation structure around indents was detected by selectively etching the crystals in toluene. The parameters l/d or $\Delta l/l_0$ (l_0 and l are the dislocation arm lengths before and after illumination, respectively; Δl is the difference between them) were mainly used as the characteristics of phototransformation.

2. RESULTS AND DISCUSSION

An increase in microhardness and decrease in the dislocation arm length in fullerite crystals under illumination was observed, thus confirming the results obtained earlier [3, 5–8]. The effects increased with decreasing wavelength. A two-stage wavelength dependence of the photoinduced change in the dislocation mobility was observed. For each stage, the magnitude of the effect increased linearly with increasing photon energy. A steeper slope was observed for photon energies of 1.55 to 1.8 eV, which are lower than the band gap and correspond to energies of exciton photogeneration in fullerite. Obviously, for incident photon energies above the bandgap (about 1.8–2 eV), the efficiency of exciton generation is lowered due to photogeneration of distant electron–hole pairs and their trapping at different lattice sites. The rate of phototransformation depends on the incident power density and the duration of illumination. The figure shows the kinetics of the photoinduced change in the hardness and dislocation

[1] This article was submitted by the authors in English.

mobility. The dislocation mobility gradually decreases with increasing duration of light exposure. It is supposed that the photoinduced formation of fullerene dimers or chains is the main reason for the reduction of the dislocation mobility. Some contribution is also observed from physically absorbed oxygen. A measurable change in hardness was detected when the thickness of the phototransformed surface layer exceeded approximately 0.1–0.2 μm. The illumination-time dependence of photoinduced hardening showed a stepwise behavior. The saturation stage of hardening is ascribed to the formation of the well-known fullerite photopolymer phase with a definite concentration and spatial distribution of the dimers and chains. This phase possesses a constant hardness (450–470 MPa) and reverts to the pristine fullerite on heating above 470 K in air [5, 6]. No photoinduced hardening was observed above 400 K [3]. An additional mechanism of hardening was found to be involved at the saturation stage of phototransformation, during which the hardness of a surface layer ~0.5 μm thick increased up to 0.6–1 GPa (figure). This phototransformed state was thermally less stable. A photochemical transformation with the participation of absorbed oxygen and creation of C–O–C bonds [2] or a higher extent of photopolymerization with the formation of branched polymeric chains [9] could be responsible for the additional hardening. Moreover, the photopolymerization at the saturation stage could be affected by stresses due to the difference in the lattice constants of the pristine and photopolymerized fullerite. In addition we observed the relaxation of stresses through the generation of dislocations, stacking faults, displacement domains, and cracks, which leads to the formation of a substructure and hardening.

In conclusion, our results confirm that there is an increase in the efficiency of photopolymerization with decreasing wavelength. The existence of two phototransformed states is suggested by the kinetics of photoinduced hardening. The results show that the dislocation mobility method is useful for characterization of the initial stage, while the microindentation technique is applicable for investigation of the developed stage of phototransformation.

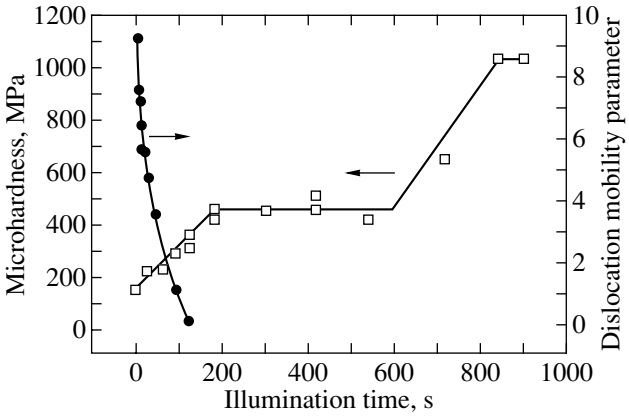

Dependence of the microhardness and dislocation mobility parameter (l/d) on the illumination time. Illumination was performed at a wavelength of 632.8 nm at 147 mW/cm^2.

REFERENCES

1. P. C. Eklund, A. M. Rao, P. Zhou, *et al.*, Thin Solid Films **257**, 185 (1995).
2. M. Haluska, M. Zehetbauer, M. Hulman, and H. Kuzmany, Mater. Sci. Forum **210–213**, 267 (1996).
3. M. Tachibana, K. Kojima, H. Sakuma, *et al.*, J. Appl. Phys. **84**, 1944 (1998).
4. G. P. Upit and S. A. Varchenya, in *Scientific Instruments*, Ed. by G. Matis (Zinatne, Riga, 1986), p. 12.
5. I. Manika, J. Maniks, and J. Kalnacs, Latv. J. Phys. Tech. Sci. **3**, 12 (1997).
6. I. Manika, J. Maniks, and J. Kalnacs, Philos. Mag. Lett. **77**, 321 (1998).
7. I. Manika, J. Maniks, and J. Kalnacs, Fullerene Sci. Technol. **7**, 825 (1999).
8. M. Tachibana, H. Sakuma, and K. Kojima, J. Appl. Phys. **82**, 4253 (1997).
9. T. Wagberg, P. Jacobsson, and B. Sundqvist, Phys. Rev. B **60**, 4535 (1999).

Physics of the Solid State, Vol. 44, No. 3, 2002, pp. 434–436. Translated from Fizika Tverdogo Tela, Vol. 44, No. 3, 2002, pp. 419–421.

PROCEEDINGS OF THE V INTERNATIONAL WORKSHOP "FULLERENES AND ATOMIC CLUSTERS"

(St. Petersburg, Russia, July 2–6, 2001)

Thermodynamic Properties of C_{60} Polyfullerites

B. V. Lebedev and A. V. Markin

Chemical Research Institute, Nizhni Novgorod State University, pr. Gagarina 23, Nizhni Novgorod, 603950 Russia
e-mail: lebedevb@ichem.unn.runnet.ru

Abstract—This paper discusses the results of calorimetric studies of the 1D C_{60} (orthorhombic) and 2D C_{60} (tetragonal and rhombohedral) fullerites, as well as of the graphite-like polyfullerite, which are produced from a starting C_{60} fullerite subjected to a pressure of 1–8 GPa at temperatures ranging from 300 to 1270 K. The analysis is made primarily of the C_p^0 heat capacity measurements performed in adiabatic calorimeters in the 5- to 350-K range. © *2002 MAIK "Nauka/Interperiodica".*

The purpose of this paper is to discuss the results of calorimetric studies of the C_{60} polyfullerites available in the literature (Table 1).

The temperature dependences of the heat capacity of 1D C_{60} and 2D C_{60} (irrespective of their crystal structure) do not exhibit any features, and their heat capacities increase smoothly with temperature. The dependence of the heat capacity of graphite-like C_{60} fullerite C_p^0 on T has a small anomaly in the 49- to 66-K interval consisting in a positive deviation of the heat capacity from its normal course (see figure, curve *4*). This anomaly was suggested as being caused by a relaxation transition of the order–disorder type [4]. For $T > 100$ K, the heat capacities of the 1D and 2D polymers are almost equal, the difference between their numerical values not exceeding 0.7%. The values of C_p^0 for the graphite-like fullerite in the 70- to 180-K interval are larger, and

Table 1. Main information on the C_{60} polyfullerites studied, including the results of calorimetric measurements

Polyfullerites			Temperature interval of heat capacity study, K	δ, %	Representation of measurements and calculations of C_p^0–T*, TTF**	References
notation	conditions of preparation and treatment of starting C_{60}: p, GPa; T, K	structure				
1D C_{60}	5; 550	Orthorhombic	5–340	0.2	C_p^0–T, TTF	[1]
	1.1; 500	"	4–350	1	C_p^0–T, $\{S^0(T) - S^0(0)\}$–T	[2]
	1–1.2; 550–585	"	200–650	–	C_p^0–T	[3]
2D C_{60}	3.5; 960	Tetragonal	5–340	0.2	C_p^0–T, TTF	[1]
	8; 920	Rhombohedral	5–320	0.2	C_p^0–T, TTF	[4]
	2; 830	Rhombohedral and tetragonal	4–350	1	C_p^0–T, $\{S^0(T) - S^0(0)\}$–T	[2]
	2; 800	"	7–340 250–600	1–1.5 –	C_p^0–T	[5]
Graphite-like C_{60}	8; 1270	Layered structure composed of fragments of broken C_{60} molecules	5–320	0.2	C_p^0–T, TTF	[4]

* C_p^0–T is a plot of the temperature dependence of heat capacity, and $\{S^0(T) - S^0(0)\}$–T is a plot of the temperature dependence of entropy.

** TTF is a table of thermodynamic functions.

1063-7834/02/4403-0434$22.00 © 2002 MAIK "Nauka/Interperiodica"

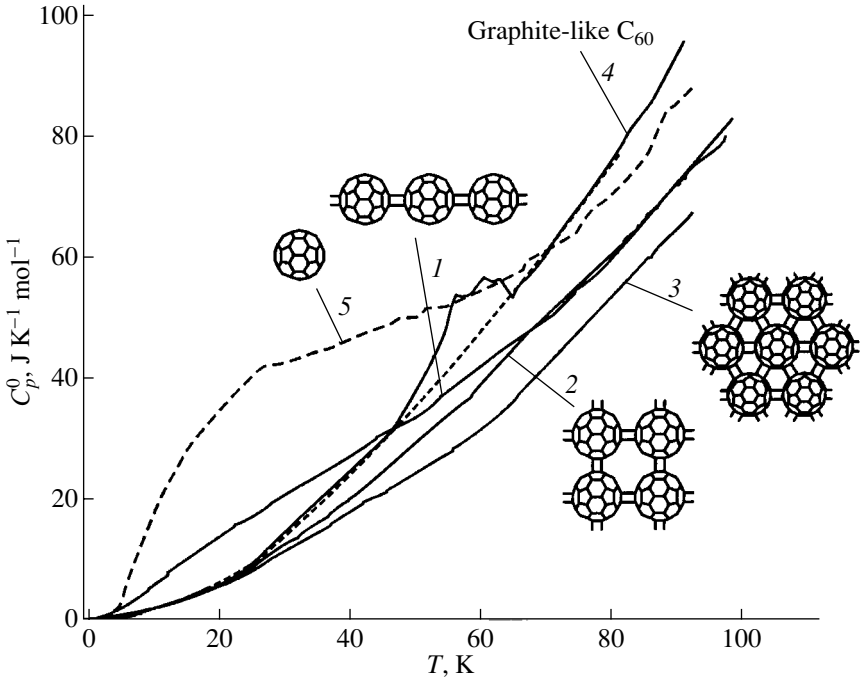

Low-temperature heat capacity of polyfullerites: (*1*) orthorhombic 1D C_{60}, (*2*) tetragonal 2D C_{60}, (*3*) rhombohedral 2D C_{60}, (*4*) graphite-like C_{60}, and (*5*) C_{60} fullerite.

for $T > 180$ K, smaller, than those of the 1D C_{60} and 2D C_{60} fullerites. However, the differences between these heat capacities are small and at 300 K, for instance, do not exceed 1%. The pattern observed in the low-temperature domain is different (see figure). The polyfullerites studied differ not only in the magnitude of C_p^0 but also in the character of its temperature dependence. This is clearly associated with the difference in heterodynamics among the polymers studied. According to Tarasov's theory of heat capacity of solids [6], which, similar to that of Debye, is a particular case of the fractal theory of heat capacity, the $C_p^0(T)$ at low temperatures is proportional to T for chain-structure solids, to T^2 for a layered structure, and to T^3 for a three-dimensional structure. In the fractal theory of heat capacity, the exponent of T in the heat-capacity function, denoted by D, is called the fractal dimension. According to [7, 8], D can be estimated from experimental data on the temperature dependence of the heat capacity plotted as $\ln C_v$ vs. $\ln T$, on making the reasonable assumption that, for $T < 50$–60 K, $C_p^0 = C_v$. The values of D derived from experimental data on C_p^0 in the 20- to 55-K interval are 1 for the 1D C_{60} (orthorhombic), 1.5 for the 2D C_{60} (rhombohedral), 2 for the 2D C_{60} (tetragonal), and 2.2 for the graphite-like fullerite. It turns out that the fractal dimensions thus found are indicative of the

Table 2. Thermodynamic functions of the polyfullerites studied and of the starting C_{60} fullerite per 1 mole of C_{60} (M = 720.66 mol^{-1}) calculated for 298.15 K and standard pressure

Polyfullerites	$C_p^0(T)$, J K^{-1} mol^{-1}	$H^0(T) - H^0(0)$, kJ mol^{-1}	$S^0(T)$, J K^{-1} mol^{-1}	$-[G^0(T) - H^0(0)]$, kJ mol^{-1}	References
Starting C_{60} fullerite (fcc)	524.8	72.44	426.5	54.72	[9]
1D C_{60} (orthorhombic)	517.2	60.63	334.6	39.12	[1]
1D C_{60}	–	–	365.7	–	[2]
2D C_{60} (tetragonal)	514.5	60.11	321.5	35.74	[1]
2D C_{60} (rhombohedral)	514.8	57.51	304.7	33.30	[4]
2D C_{60} (tetragonal + rhombohedral)	–	–	334.1	–	[2]
Graphite-like C_{60} fullerite	495.5	62.49	382.0	51.40	[4]

chain structure of the 1D C_{60} fullerite and the layered structure of the tetragonal 2D C_{60}; as for the rhombohedral 2D C_{60} fullerite, it appears that it has a chain-layered structure, and the graphite-like fullerite has an intermediate structure between layered and three-dimensional. At low temperatures, the dependence of C_p^0 on T is practically linear for 1D C_{60}, parabolic for 2D C_{60}, and close-to-cubic for the graphite-like fullerite (see figure). For comparison, the figure shows the temperature dependence of the heat capacity of the starting C_{60} fullerite (curve *5*). For $T < 70$ K, the heat capacities of the C_{60} fullerite and of the polyfullerites obtained from it are seen to differ strongly. As the temperature is lowered to 5–6 K, the heat capacities of all the subjects considered here become similar and the fractal dimensions grow, so that, for $T < 10$ K, the variations of C_p^0 of the 1D and 2D C_{60} fullerite are well fitted by the Debye heat capacity function, which corresponds to the limiting T^3 law. For the graphite-like polyfullerite, the temperature dependence of C_p^0 becomes cubic at still lower temperatures.

The data on $C_p^0(T)$ were used to calculate the thermodynamic functions; their values for 298.15 K are given in Table 2. The values of these functions, including the absolute values of the Gibbs functions, are seen to decrease as one goes from C_{60} to 1D C_{60} and 2D C_{60} (tetragonal and rhombohedral). The values of the functions for the graphite-like fullerite are smaller than those for the starting fullerite but are larger than those for the polyfullerites studied (except C_p^0 at 298.15 K). The entropies of the compounds were calculated without inclusion of the zero-temperature entropies $S^0(0)$, which apparently have small nonzero values for all the subjects discussed.

As expected, the decrease in the entropy associated with the transformation of the C_{60} fullerite to the polyfullerites considered can be arranged in the following series: ΔS^0 ($C_{60} \longrightarrow$ graphite-like C_{60}) < ΔS^0 ($C_{60} \longrightarrow$ 1D C_{60}) < ΔS^0 ($C_{60} \longrightarrow$ 2D $C_{60,\,\mathrm{tetra}}$) < ΔS^0 ($C_{60} \longrightarrow$ 2D $C_{60,\,\mathrm{rhomb}}$).

ACKNOWLEDGMENTS

This study was supported by the Russian Foundation for Basic Research (project nos. 01-03-32061, 00-03-40136), the Ministry of Science and Technologies of the RF, and INTAS (grant no. 00-807).

REFERENCES

1. B. V. Lebedev, K. B. Zhogova, N. N. Smirnova, *et al.*, Thermochim. Acta **364**, 23 (2000).
2. A. Inaba, T. Matsuo, A. Fransson, and B. Sundqvist, J. Chem. Phys. **110** (24), 12226 (1999).
3. B. Sundqvist, O. Andersson, U. Edlund, *et al.*, in *Fullerenes: Proceedings of the Symposium on Recent Advances in the Chemistry and Physics of Fullerenes and Related Materials*, Ed. by K. M. Kadish and R. S. Ruoff (The Electrochemical Society, Pennington, 1996), Vol. 3, p. 1014.
4. B. V. Lebedev, K. B. Zhogova, V. D. Blank, and R. Kh. Bagramov, Izv. Ross. Akad. Nauk, Ser. Khim., No. 2, 277 (2000).
5. B. Sundqvist, A. Fransson, A. Inaba, *et al.*, in *Fullerenes: Proceedings of the Symposium on Recent Advances in the Chemistry and Physics of Fullerenes and Related Materials*, Ed. by K. M. Kadish and R. S. Ruoff (The Electrochemical Society, Pennington, 1998), Vol. 6, p. 705.
6. V. V. Tarasov, Zh. Fiz. Khim. **24**, 111 (1950).
7. T. S. Yakubov, Dokl. Akad. Nauk SSSR **310**, 145 (1990).
8. A. D. Izotov, O. V. Shebershneva, and K. S. Gavrichev, in *Proceedings of All-Russia Conference on Thermodynamic Analysis and Calorimetry, Kazan, 1996*, p. 200.
9. B. V. Lebedev, K. B. Zhogova, T. A. Bykova, *et al.*, Izv. Akad. Nauk, Ser. Khim., No. 9, 2229 (1996).

Translated by G. Skrebtsov

Physics of the Solid State, Vol. 44, No. 3, 2002, pp. 437–440. From Fizika Tverdogo Tela, Vol. 44, No. 3, 2002, pp. 422–424.

PROCEEDINGS OF THE V INTERNATIONAL WORKSHOP "FULLERENES AND ATOMIC CLUSTERS"

(St. Petersburg, Russia, July 2–6, 2001)

C_{60} Molecular Configurations Leading to Ferromagnetic Exchange Interactions in TDAE*C_{60}[1]

B. Narymbetov[1], A. Omerzu[2], V. Kabanov[2], M. Tokumoto[1, 3], H. Kobayashi[1], and D. Mihailovic[2]

[1] *Institute for Molecular Science, Okazaki 444, Japan*

[2] *Josef Stefan Institute, Ljubljana, 1000 Slovenia*

[3] *Electrotechnical Laboratory, Umezono, Tsukuba, Japan*

Abstract—The charge-transfer salt tetrabis(dimethylamino)ethylene-fullerene (C_{60}), or TDAE*C_{60}, is a rare exception among pure organic crystalline systems, because it shows a transition to a ferromagnetic (FM) state with fully saturated $s = 1/2$ molecular spins at a respectable $T_c = 16$ K. In spite of extensive experimental and theoretical work over the past ten years, the origin of the ferromagnetism in TDAE*C_{60} has remained a mystery. To resolve this problem, we performed a comparative structural study of two different magnetic forms of TDAE*C_{60} crystals, one of which is magnetic and the other is nonmagnetic at low temperatures, and fully correlated their structural properties (particularly, the intermolecular orientations) with their magnetic properties. We identified the relative orientation of C_{60} molecules along the *c* axis as the primary variable that controls the ferromagnetic order parameter and showed that both FM and low-temperature spin-glass-like ordering are possible in this material, depending on the orientational state of the C_{60} molecules. Thus, we resolved the apparent contradictions intrinsic to different macroscopic measurements and opened a path to a microscopic understanding of *p*-electron FM exchange interactions. © *2002 MAIK "Nauka/Interperiodica".*

Much effort has been made by many research groups to investigate the low-temperature state of crystals of the purely organic molecular ferromagnet TDAE*C_{60}. However, until recently, despite numerous studies having been made on its physical properties, the structural features of the TDAE*C_{60} compound have not been characterized by single-crystal diffraction methods at low temperatures. The room-temperature structure of TDAE*C_{60} has been determined from single-crystal x-ray diffraction data. It was shown that the space group of symmetry is $C2/c$ with the *c* parameter 19.992 Å and with four formula units per unit cell [1]. The low lattice symmetry suggests anisotropic interactions between the constituent molecules, which might be subject to a variety of instabilities leading to solid-state phase transitions. On the other hand, ^{13}C NMR studies have shown that, in TDAE*C_{60} crystals, the C_{60} molecules rotate rapidly at room temperature [2]. As the temperature is lowered, rotation of the C_{60} molecules gradually slows down, but, although NMR data suggest that the rotational motion freezes out below approximately 150 K [2], the onset of the ferromagnetic (FM) state occurs at a significantly lower temperature, suggesting that stationary C_{60} molecules may be a necessary but not sufficient condition for the realization of an FM state.

[1] This article was submitted by the authors in English.

It has been well established that TDAE*C_{60} exists in two modifications, one being ferromagnetic and the other paramagnetic (PM). Fresh single crystals show no FM behavior and are PM down to 2 K. On annealing at a high temperature, they transform into the FM phase [3]. We performed comparative diffraction and structural studies of the two different forms of TDAE*C_{60} crystals and showed that both FM and low-temperature spin-glass-like ordering are possible in this material, depending on the orientational state of the C_{60} molecules.

1. EXPERIMENTAL

The diffusion method was used to grow crystals. The measurements were performed on a selected sample in the PM phase without annealing, and the results were compared with data obtained on the same sample after its transformation to the FM phase by annealing at 70°C for 6 h.

Single-crystal x-ray diffraction studies were carried out using an Imaging Plate (IP) system (DIP 320S, MAC Science Co., Inc., monochromatized MoK_α radiation, $\lambda = 0.7107$ Å) equipped with a liquid-helium cooling device. The standard oscillation and Weissenberg-type diffraction patterns were used to control the crystal structures of both samples (unannealed PM and annealed FM) at different temperatures. The crystal structure of TDAE*C_{60} was determined by the direct

1063-7834/02/4403-0437$22.00 © 2002 MAIK "Nauka/Interperiodica"

method from the data obtained on the unannealed crystal at 7 K and refined by the least-squares method using the *C*2/*c* space group. The averaged structure of the annealed sample at 7 K was first refined by using the model structure of the unannealed crystal and was then refined further by taking into account the presence of two orientations in which the C_{60} molecules are found with equal probability.

2. RESULTS AND DISCUSSION

All diffraction spots observed on x-ray oscillation patterns are indexed in the *C*2/*c* space group. The diffraction patterns did not reveal any essential changes in the structure in the temperature range 250–70 K, except that some redistribution of reflection intensities occurred and the total number of reflections on the diffraction images decreased with decreasing temperature. Remarkable changes in the diffraction patterns are observed for both samples below 50 K. Figure 1 presents the temperature dependences of the lattice constants, which testify to the presence of noticeable changes in the *b* and *c* parameters of both crystals around 50 K. At this temperature, the reflection intensities become higher, which results in an essential increase in the total number of observed reflections. Characteristic for both crystals are the appearance of additional diffuse scatterings on the x-ray oscillation patterns located between structural reflections and their transformation over a period of a few hours. Diffuse scatterings from the unannealed sample disappear as the sample is kept at a low temperature for 3–4 h. A distinctive feature of the annealed sample is that the diffuse lines on the diffraction patterns are transformed into additional diffraction spots whose positions coincide with those for a primitive lattice, which indicates a violation of the C centricity of the lattice. These observations testify to the existence of some structural changes in both unannealed and annealed TDAE*C_{60} crystals around 50 K and of the crystal-lattice tendency to transform from a C-centered lattice to a primitive one in the case of annealed samples. It should be noted that these changes are reversible; i.e., on heating the samples from a low temperature, the diffraction patterns of the high-temperature state are restored above 50 K.

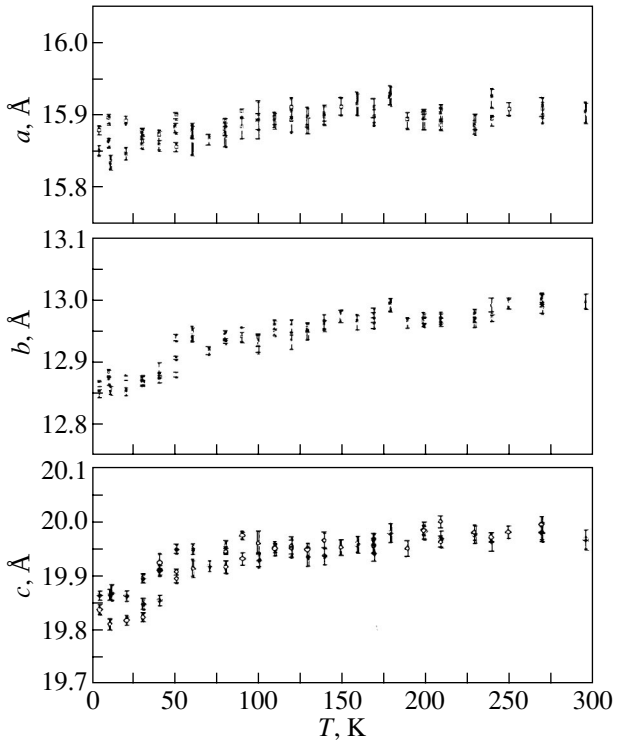

Fig. 1. Temperature dependence of the lattice constants for an unannealed TDAE*C_{60} crystal (open symbols) and after the first cycle of its annealing (filled symbols).

The x-ray structure analysis of the PM sample revealed the presence of some degree of molecular orientational disorder of the C_{60} molecules (due to their rotations) along the threefold molecular axis. In the FM phase, the positions of the additional diffraction spots coincide with those of a primitive unit cell, which suggests that the crystal transforms from the C-centered structure to a primitive one. Our attempts to determine the structure in terms of a primitive unit cell failed and resulted in high values of the R factor (~0.16) and in a large divergence of the temperature factors of individual atoms. Refinement of the structure with a C-centered unit cell also resulted in high R factors (~0.20) but gave reasonable thermal-displacement ellipsoids of individual atoms of C_{60}, which testifies to the presence of a high degree of orientational disorder of the C_{60} molecules. Further analysis of the obtained C_{60} molecular structure showed that, in the FM sample, the molecules are statistically distributed in two orientations related to each other by a 60° rotation about their threefold axis. The model in which two differently oriented molecules occupy the same positions with equal probability allowed us to essentially improve the R factor in the refinement procedure, and its final value was found to be 0.066. Thus, in the FM phase, in addition to the conventional 120° rotations found in other C_{60}-based crystal structures, we find evidence of additional positions in which C_{60} molecules are rotated by ±60° about their threefold molecular axes. Figure 2 shows the mechanism of crystal transformation from a C-centered (PM) lattice to a primitive-type (FM) lattice. This leads to a set of new inter-fullerene contact configurations, which are shown in Fig. 3. In the PM sample, the relative C_{60} orientations are similar to those encountered in other C_{60} solids, namely, the 6–6 double bond is nearly in the center of the hexagon of the neighboring molecule (Fig. 3a), thereby minimizing the electronic overlap [4]. In the FM samples, on the other hand, a new orientation (II) appears, which leads to three different possible relative orientations of the C_{60} molecules, as shown in Figs. 3b–3d. In the first configuration, two C_{60}

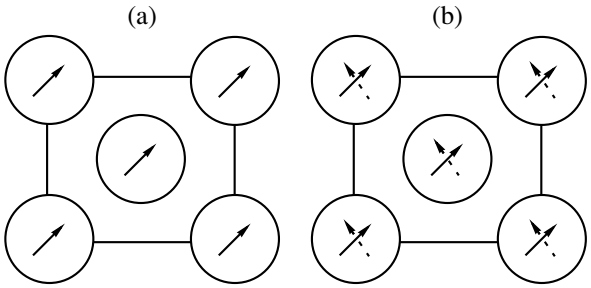

Fig. 2. Schematic diagram of the C_{60} molecular orientations in the *ab* plane for (a) the unannealed sample (PM phase) and (b) the annealed sample (FM phase). Corresponding C-centered and primitive unit cells are shown.

molecules of orientation I face each other, with the molecules slightly rotated about the *c* axis, as shown in Fig. 3b. In the second possible configuration, two C_{60} molecules with type II orientations are in contact, as shown in Fig. 3c. This orientation corresponds essentially to a slightly displaced PM configuration (Fig. 3a), with the double bond displaced to one side. The third configuration involves two C_{60} with orientations I and II. In this case, the double bond on one molecule approximately faces the center of the pentagon of the neighboring molecule (Fig. 3d). The II–II configuration can be eliminated from further consideration of the possible low-temperature equilibrium positions, since the occurrence of two 6–6 double bonds in close proximity to each other is, clearly, energetically very unfavorable. Therefore, we can conclude with reasonable confidence that only one of these configurations is compatible with the near 50% occupancy of configurations I and II and with the primitive unit cell determined in the structural refinement (Fig. 3d).

We note that the observed arrangement associated with the FM state is in excellent agreement with calculations of the angular dependence of the effective FM exchange coupling strength J_{eff} [5], which also shows a minimum corresponding to the I–II configuration (Fig. 3d) for which the *c*-axis Euler angle is $\gamma \approx 30°$. Our consideration of the magnetic behavior of the system in terms of the Hamiltonian for a noninteracting two-level system in which there is a coupling between the configurational and magnetic degrees of freedom

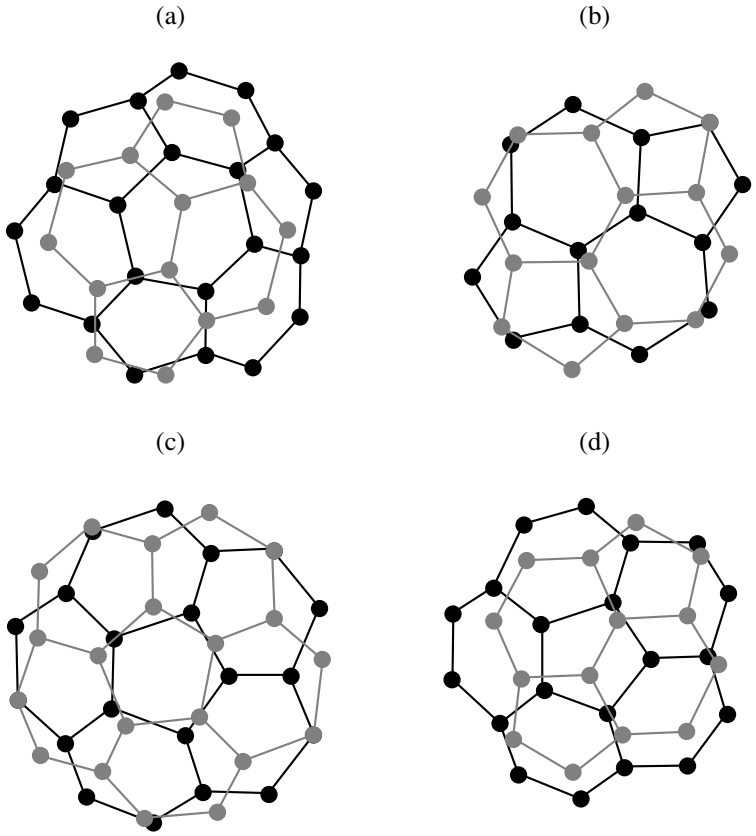

Fig. 3. Projections of two neighboring C_{60} molecules of TDAE*C_{60} along the [001] direction for (a) the unannealed crystal (PM phase), (b) the I–I configuration of C_{60} molecules (annealed sample, FM phase), (c) the II–II configuration in the FM phase, and (d) the mixed I–II configuration in the FM phase.

shows [6] that both ferromagnetism and spin-glass-like ordering are possible in TDAE*C_{60} crystals, depending on the orientational state of the C_{60} molecules.

In summary, low-temperature x-ray diffraction studies of TDAE*C_{60} single crystals show that some molecular reorientations and ordering take place in the structure below 50 K. We determined low-temperature crystal structures for both unannealed and annealed samples and identified the relative orientation of C_{60} molecules in these structures along the c axis of the crystals as the primary variable that controls the ferromagnetic order parameter. Analysis of the relative orientations shows that both FM and low-temperature spin-glass-like ordering are possible in the TDAE*C_{60} compound, depending on the orientational state of the C_{60} molecules.

REFERENCES

1. L. Golic, R. Blinc, P. Cevc, D. Arcon, D. Mihailovic, A. Omerzu, and P. Venturini, in *Fullerenes and Fullerene Nanostructures*, Ed. by H. Kuzmany, J. Fink, M. Mehring, and S. Roth (World Scientific, Singapore, 1996), pp. 531–534.
2. D. Arcon, J. Dolinsek, and R. Blinc, Phys. Rev. B **53**, 9137 (1996).
3. A. Mrzel, P. Cevc, A. Omerzu, and D. Mihailovic, Phys. Rev. B **53**, R2922 (1996).
4. B. Sundqvist, Adv. Phys. **48**, 1 (1999).
5. T. Sato, T. Saito, T. Yamabe, *et al.*, Phys. Rev. B **55**, 11052 (1997).
6. B. Narymbetov, A. Omerzu, V. V. Kabanov, *et al.*, Nature **407**, 883 (2000).

Physics of the Solid State, Vol. 44, No. 3, 2002, pp. 441–443. From Fizika Tverdogo Tela, Vol. 44, No. 3, 2002, pp. 425–427.

PROCEEDINGS OF THE V INTERNATIONAL WORKSHOP "FULLERENES AND ATOMIC CLUSTERS"

(St. Petersburg, Russia, July 2–6, 2001)

Magnetism of C_{60}-Based Molecular Complexes: High-Field-Magnetization and Magnetooptical Study[1]

S. V. Demishev[1, 4], N. E. Sluchanko[1], L. Weckhuysen[2], V. V. Moshchalkov[2], H. Ohta[3, 4], S. Okubo[3], Y. Oshima[5], and N. G. Spitsina[6]

[1] *Low Temperatures Laboratory, Institute of General Physics, Russian Academy of Sciences, Moscow, 117942 Russia*
e-mail: demis@lt.gpi.ru

[2] *Laboratorium voor Vaste-Stoffysica en Magnetisme, Katholieke Universiteit Leuven, Heverlee, B-3001 Belgium*

[3] *Molecular Photoscience Research Center and Department of Physics, Kobe University, Rokkodai, Nada, Kobe, 657-8501 Japan*

[4] *Venture Business Laboratory, Kobe University, Rokkodai, Nada, Kobe, 657-8501 Japan*

[5] *Graduate School of Science and Technology, Kobe University, Rokkodai, Nada, Kobe, 657-8501 Japan*

[6] *Institute of Problems of Chemical Physics, Russian Academy of Sciences, Chernogolovka, Moscow oblast, 142432 Russia*

Abstract—Magnetization study of the $C_{60} \cdot TMTSF \cdot 2CS_2$ molecular complex in magnetic fields up to 47 T for the temperature range 1.8–300 K and ESR spectroscopy of the molecular complex $(ET)_2C_{60}$ at $T = 1.8$ K for the frequency range 60–90 GHz in magnetic fields up to 32 T provide experimental evidence that paramagnetic centers with reduced g-factor values $g < 1$ control the magnetic properties of these solids. A model is suggested in which the renormalization of the g factor is due to the dynamic Jahn–Teller effect involving negative C_{60} ions that appear as defects in the crystalline structure with a weak charge transfer. © *2002 MAIK "Nauka/Interperiodica".*

1. Since the discovery of fullerenes, it was believed that for weakly magnetic C_{60}-based compounds with a small charge transfer, the magnetization can be represented as the sum of two terms [1, 2]:

$$M(B, T) = M_{para}(B, T) + M_{dia}(B) = [3\chi_{para}(T)k_BT/(J + 1)g\mu_B]B_J(g\mu_BJB/k_BT) + \chi_{dia}B, \quad (1)$$

where the negative diamagnetic term χ_{dia} is connected with the completely filled electron orbitals of C_{60} and other molecules in the complex, while $\chi_{para}(T) \sim 1/T$ is a Curie term originating from oxygen impurity.

Unfortunately, Eq. (1) fails to provide a description of the field dependence of the low-temperature magnetization $M(B)$ for the complex $(ET)_2C_{60}$, where ET = bis(ethylenedithio)tetrathiafulvalene, as well as for pure C_{60} [3, 4], and the observed discrepancy rules out any model of magnetic impurity with a g factor $g \approx 2$ [3, 4]. Experimental data suggest that Eq. (1) may be used assuming a renormalized value $|g| \sim 0.14$ [3, 4], which may be characteristic for the negative ion C_{60}^-, where a strong reduction of the g factor may originate from the dynamic Jahn–Teller effect [5].

It is of interest to check the possible presence of these exotic centers in other fullerene-based molecular complexes. The aim of the present work was to investigate the magnetic properties of the molecular complex $C_{60} \cdot TMTSF \cdot 2CS_2$ and to look for unusual paramagnetic centers in $(ET)_2C_{60}$ by means of magnetooptical spectroscopy.

2. The synthesis and structure of the $C_{60} \cdot TMTSF \cdot 2CS_2$ (where TMTSF = tetramethyl-tetra-selenefulvalene) molecular complex are described in [6, 7]. Similar to $(ET)_2C_{60}$, the charge transfer in $C_{60} \cdot TMTSF \cdot 2CS_2$ is small. However, application of an external pressure of about 5 GPa moves one electron from TMTSF to the C_{60} molecule, thus forming a complex based on the C_{60}-ion [8]. Therefore, $C_{60} \cdot TMTSF \cdot 2CS_2$ seems to be a good candidate for checking the models suggested in [3, 4].

The temperature dependence of magnetization for the field B = 8 T is shown in Fig. 1a. The $M(T)$ curve demonstrates the onset of a "paramagnetic" contribution below 40 K superimposed on the diamagnetic background M_{dia}. However, the use of Eq. (1) for $C_{60} \cdot TMTSF \cdot 2CS_2$ gives a poor description of $M(T)$ [compare the experimental data (curve *1* in Fig. 1a) with the best fit (curve *2* in Fig. 1a) obtained using Eq. (1)].

The field dependence of $M(B)$ at $T = 4.2$ K for $C_{60} \cdot TMTSF \cdot 2CS_2$ deviates from that reported previously [3, 4]. The linear section of the $M(B)$ lasts up to a value of 20 T, which is about 10 T less than that for $(ET)_2C_{60}$ [3, 4]. Above 20 T, the experimental curve first deviates

[1] This article was submitted by the authors in English.

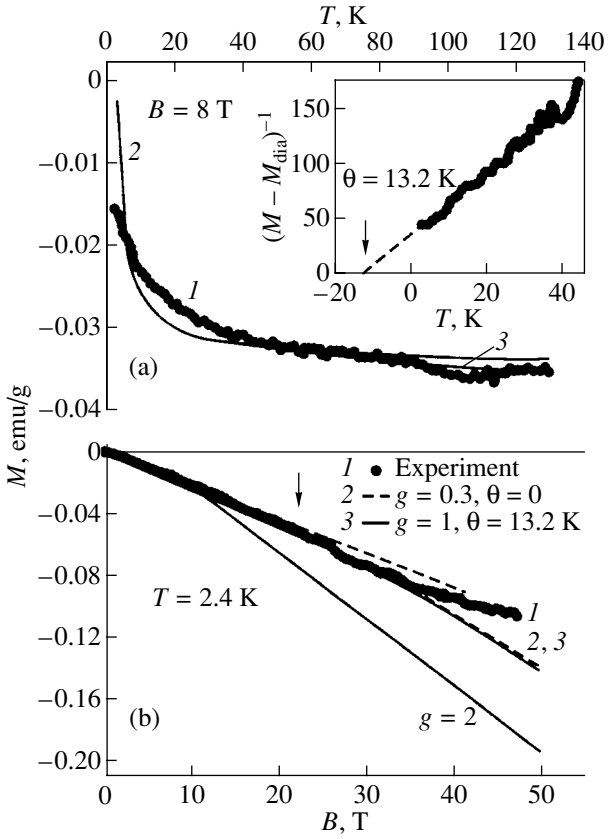

Fig. 1. (a) Temperature and (b) field dependences of magnetization for $C_{60} \cdot TMTSF \cdot 2CS_2$. Curves 1 are experimental data for $M(T)$ and $M(B)$, curves 2 are $M(T)$ and $M(B)$ calculated from Eq. (1), and curves *3* are $M(T)$ and $M(B)$ calculated from Eq. (2). Inset in (a) shows the temperature dependence of the quantity $(M - M_{dia})^{-1} = f(T)$.

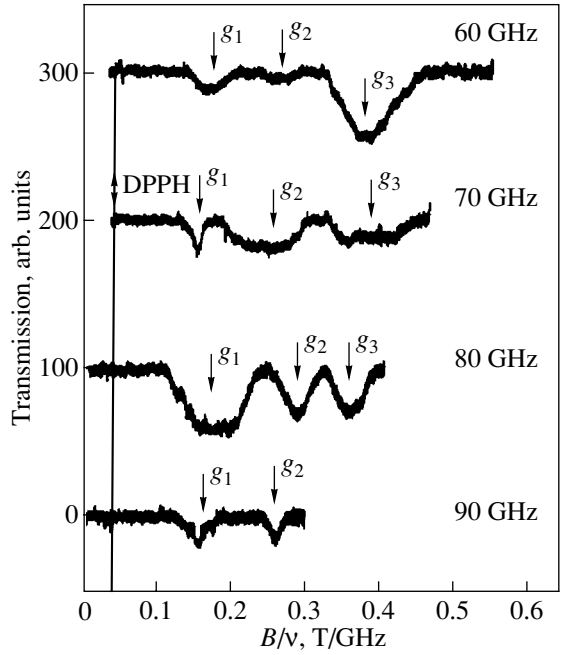

Fig. 2. ESR absorption lines in the $(ET)_2C_{60}$ molecular complex at $T = 1.8$ K.

downwards from a straight line (Fig. 1b), which indicates the possible presence of paramagnetic centers with a reduced value of the g factor [3]. Taking Eq. (1) as a first approximation and following [3], we calculated the field dependence of the magnetization from Fig. 1 assuming that $g = 2$ and $J = 1/2$. The result is presented in Fig. 1b, and it is obvious that a straightforward model of the "oxygen-like" impurity is inconsistent with the $M(B)$ data. Assuming that a reduction of the g factor plays a key role [3] and restricting further analysis to the interval $B < 35$ T, we find a renormalized (reduced) g-factor value $g \sim 0.3$ (curve *2* in Fig. 1b).

Nevertheless, the small g factor (which makes the $M(B)$ data for $B < 8$ T "linear") does not improve the calculated temperature dependence of magnetization (curve *2* in Fig. 1a). A good approximation to $M(T)$ can be provided by the empirical expression

$$M(B, T) = M_{para}(B, T) + M_{dia}(B) = \chi_{dia}B + M_0 \tanh[g\mu_B B/2k_B(T + \theta)], \quad (2)$$

which corresponds to the Curie–Weiss law in weak magnetic fields and describes the saturation of the magnetic moment in strong magnetic fields. Approximating both $M(T)$ and $M(B)$ data in Fig. 1 by Eq. (2), we find $g = 1$, $M_{dia}(B = 8\text{ T}) = -0.0373$ emu/g, and $\theta = 13.2$ K (see also the inset to Fig. 1a). The calculated $M(T)$ and $M(B)$ are represented by curves *3* in Figs. 1a and 1b, respectively. It is clear that Eq. (2) provides an adequate and consistent description of the field and temperature dependences of magnetization for $B < 35$ T; however, the g-factor value found is considerably higher than that in the model given by Eq. (1).

The analysis of the $M(B, T)$ data for $C_{60} \cdot TMTSF \cdot 2CS_2$ and $(ET)_2C_{60}$ leads to the following conclusions. First, the validity of Eq. (2) suggests the presence of interaction between magnetic moments in $C_{60} \cdot TMTSF \cdot 2CS_2$. At the present time, the possible interaction mechanism is entirely unknown and further theoretical investigation is required to reveal the origin of the unexpected $M(T)$ dependence (Fig. 1a).

Second, the analysis of the magnetization data in fullerene-based complexes gives a very rough estimate of the effective g factor, which depends on the type of the solid and on the model used and may vary in a wide range of $g \sim 0.14$–1. In this situation, determination of this parameter by direct spectroscopic methods is required.

3. A magnetooptical study of a mosaic sample prepared from $(ET)_2C_{60}$ single crystals was carried out in pulsed magnetic fields up to 32 T in the frequency range $\nu = 60$–90 GHz at $T = 1.8$ K. The obtained transmission curves show three broad absorption lines corresponding to $g_1 = 0.43 \pm 0.03$, $g_2 = 0.27 \pm 0.02$, and $g_3 = 0.19 \pm 0.01$ (see Fig. 2, where the experimental data are pre-

sented as a function of reduced field B/ν). At the same time, no ESR absorption in the sample was found around $g = 2$ (see Fig. 2, where the narrow vertical line for $g = 2$ corresponds to the reference DPPH powder).

The obtained result qualitatively confirms the predictions of [3, 4], as well as the results of the previous section. Moreover, the model of the *g*-factor renormalization caused by the dynamic Jahn–Teller effect [5] can explain the presence of several ESR absorption lines. If the origin of the *g*-factor reduction is the coupling to a phonon mode [5], the existence of different strong modes in the vibronic spectrum of a weakly magnetic complex can give rise to several different *g*-factor values being experimentally observed (Fig. 2).

4. To summarize, we provide experimental evidence that the paramagnetic centers with renormalized *g*-factor values $g < 1$ are (i) characteristic for weakly magnetic C_{60}-based molecular solids and (ii) responsible for the magnetism of these compounds. These centers may be identified with the negative C_{60} ions which appear as defects in the crystalline structure with a weak charge transfer. In this model, the reduction of the *g*-factor value is due to the dynamic Jahn–Teller effect [3] and the presence of several ESR absorption lines may be due to the coupling to several phonon modes.

ACKNOWLEDGMENTS

This work was supported by the Programs of the Russian Ministry of Science and Technology "Fullerenes and Atomic Clusters," "Physics of Microwaves," and "Fundamental Spectroscopy" and by INTAS, grant no. 00-807.

REFERENCES

1. M. S. Dresselhaus, G. Dresselhaus, and P. C. Eklund, *Science of Fullerenes and Carbon Nanotubes* (Academic, San Diego, 1996), p. 739.
2. V. Buntar, H. W. Weber, and M. Ricco, Solid State Commun. **98**, 175 (1995).
3. S. V. Demishev, A. A. Pronin, N. E. Sluchanko, *et al.*, Pis'ma Zh. Éksp. Teor. Fiz. **69**, 733 (1999) [JETP Lett. **69**, 785 (1999)].
4. S. V. Demishev, L. Weckhuysen, J. Vanacken, and N. G. Spitsina, Physica B (Amsterdam) **294–295**, 324 (2001).
5. E. Tosatti, N. Manini, and O. Gunnarson, Phys. Rev. B **54**, 17184 (1996).
6. Yu. M. Shul'ga, V. I. Ribtsov, and N. G. Spitsina, Zh. Fiz. Khim. **70**, 564 (1996).
7. S. V. Konovalikhin, O. A. D'yachenko, G. V. Shilov, *et al.*, Izv. Ross. Akad. Nauk, Ser. Khim., No. 8, 1480 (1997).
8. G. A. Kourouklis, K. P. Meletov, J. Arvanitides, *et al.*, Rev. High Pressure Sci. Technol. **7**, 733 (1998).

Physics of the Solid State, Vol. 44, No. 3, 2002, pp. 444–446. Translated from Fizika Tverdogo Tela, Vol. 44, No. 3, 2002, pp. 428–430.

PROCEEDINGS OF THE V INTERNATIONAL WORKSHOP "FULLERENES AND ATOMIC CLUSTERS"

(St. Petersburg, Russia, July 2–6, 2001)

Investigation of the Extent, Rate, and Mechanisms of Electron-Stimulated Modification of the C_{60} Fullerite by EELS

V. V. Shnitov, V. M. Mikushkin, V. V. Bryzgalov, and Yu. S. Gordeev

Ioffe Physicotechnical Institute, Russian Academy of Sciences, ul. Politekhnicheskaya 26, St. Petersburg, 194021 Russia

Abstract—A parameter representing the intensity ratio of the two features in the characteristic electron energy loss spectrum that are most sensitive to electron irradiation is proposed for use in characterizing the extent of electron-stimulated modification of fullerite. By normalizing this parameter, we succeeded in obtaining a universal scale for the extent of modification that can be unambiguously related to the π-electron density. The dose dependence of this parameter is shown to be described by one exponential, thus permitting one to conclude that both the polymerization and amorphization of the fullerite are dominated by one mechanism, namely, the formation of intermolecular chemical bonds, which is stimulated by valence-electron excitation. The rate of the electron-stimulated modification, or the dose susceptibility of the material, is defined through the derivative of this parameter. The dependence of this rate on the incident electron energy is obtained. It is shown that structural changes are mainly due to a swarm of numerous secondary and decelerated electrons rather than to the primary electron. © *2002 MAIK "Nauka/Interperiodica".*

Photo- and electron-stimulated polymerization of fullerites has become a subject of intense study in recent years [1–5]. The polymer phases produced by UV and electron irradiation turned out to be, in contrast to the starting fullerite, weakly soluble in organic solvents. Regardless of the incompleteness of the polymerization studies, this property permits one, even at the present time, to use the fullerite as a resist in photo- and electron lithography [5–8]. The irradiation dose is chosen experimentally for each concrete set of such parameters of the process as the energy of photons or electrons and their incidence angle and flux density. The choice is made from the rich variety of such sets. To optimize the lithographic processes and prepare more sensitive fulleride resists, one has to develop universal criteria for quantitative evaluation of the extent and rate of polymerization. Quantitative characterization of the extent and rate of the fullerite and fulleride modification is also needed to establish the mechanisms governing these processes. In addition to the above-mentioned polymerization, one should place among these processes the recently revealed electron-stimulated amorphization of fullerite [9], which can follow polymerization as a result of the formation of additional intermolecular bonds or proceed simultaneously with the polymerization due to fullerene fragmentation. The present paper proposes a method for quantitative determination of the degree and rate of electron-stimulated fullerite modification, which is based on characteristic electron energy loss spectroscopy (EELS). This method is made attractive by the possibility of employing an electron probe for this purpose, making this technique a controllable technology. The method was used to study the mechanisms underlying electron-stimulated fullerite modification.

The proposed approach is based on a study of numerous EELS spectra obtained on *in situ* grown C_{60} fullerite films subjected to irradiation by electrons of various energies (E_0 = 150–1500 eV) with increasing doses Q. Figure 1 displays such a spectrum. The energy losses of inelastically scattered electrons ΔE are reckoned from the center of the electron elastic-scattering peak ($\Delta E = 0$). The peak at $\Delta E \sim 6.2$ eV corresponds to the excitation of collective π-electron vibrations of the fullerite (π plasmons). As established earlier, the intensity of this peak I_1 decreases with increasing electron irradiation dose because of the π electrons being involved in the formation of intermolecular chemical bonds [9–11]. Conversely, the intensity I_2 of the low-energy part of the spectrum ($\Delta E \sim 1$–2 eV) grows under electron irradiation as a result of the increasing density of occupied and empty states near the Fermi level, which is accompanied by an increase in the conductivity of the material. Therefore, the ratio $P = I_2/I_1$ of the intensities of these parts of the spectrum, which vary in opposite directions, turns out to be very sensitive to irradiation. It is this parameter that is proposed for use in characterizing the extent of fullerite transformation, as a result of which the density of the π electrons decreases and the density of states near the Fermi level increases.

1063-7834/02/4403-0444$22.00 © 2002 MAIK "Nauka/Interperiodica"

Figure 2 plots the normalized parameter $P(Q)/P_{max}$ as a function of electron irradiation dose for a number of incident electron energies E_0. The normalization was made against the maximum value of the parameter P reached under irradiation to an infinite dose. This permits one to reduce the experimental data obtained under different technological conditions (energy, angle of incidence) to a common scale of the state of the material structure. This scale can be related unambiguously to the π-electron concentration or the degree of sp^2–sp^3 valence-electron hybridization [9]. Each curve in Fig. 2 reflects a monotonically rising function tending to saturation. In the low-dose domain, the curves characterize the polymerization process, while the high-dose region corresponds to the fullerite transforming to amorphous carbon. It appears significant that each dependence can be fitted by one exponential, $P(Q) \sim P_{max}[1 - \exp(-\alpha Q)]$. Given the function describing the state of the modified material, one can readily determine the rate of its modification (the dose susceptibility to irradiation) from the derivative of this function: $P'(Q) \sim \alpha P^*_{max} \exp(-\alpha Q)$. This is a monotonically falling-off function, which implies a high rate of structural changes in the initial polymerization stage, slowing down of this process, and slow changes in the material in the stage close to the amorphous carbon phase.

The $P(Q)$ and $P'(Q)$ dependences thus obtained permit a certain conclusion to be made as to the part played by the hypothetical mechanism of fullerene fragmentation, which is associated with the formation of a core hole and its Auger decay. The Auger decay leaves positively charged carbon atoms close to one another in the molecule (1.44–7.3 Å). The energy of their Coulomb interaction may be comparable to the energy required to detach a C_2 fragment. In any case, Coulomb repulsion should enhance the efficiency of all other fragmentation mechanisms associated, for instance, with excitation of the electronic system or local heating of the molecule. However, the fact that the dependences discussed above have no feature close to and beyond the formation threshold of a carbon 1*s* hole (E_i = 287 eV) shows that the mechanism of Coulomb explosion of the fullerene in the fullerene condensate plays an insignificant role. The possibility of approximating both the $P(Q)$ and $P'(Q)$ relations by one exponential and the absence of breaks, peaks, and other features attest to there being one dominant mechanism of fullerite modification in all its stages. This mechanism, similar to the decrease in charge on the plates of a discharging capacitor, is characterized by an exponential decrease in the density of the π electrons (the decrease in intensity of the π-plasmon peak), which are involved in chemical bond formation between molecules or their fragments, up to complete destruction of the fullerite [9]. It should be pointed out that this result is at odds with the conclusion (reached in a study of photostimulated polymerization of fullerite) that structural changes come to an end after the formation of six pairs of chemical bonds per molecule (in accordance with the number of nearest neighbors) [8].

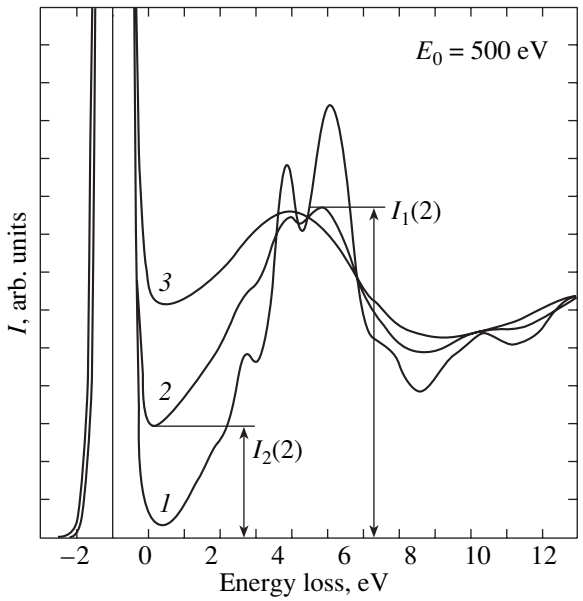

Fig. 1. Characteristic electron-energy loss spectra of the C_{60} fullerite. Curves *1–3* correspond to respectively increasing electron irradiation dose.

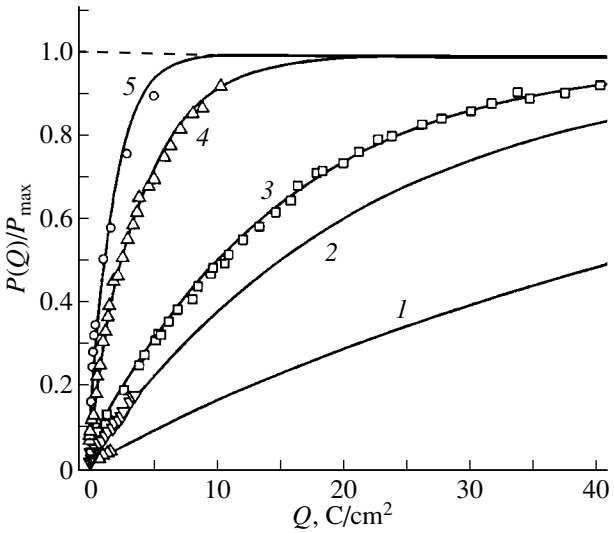

Fig. 2. Normalized fullerite modification parameter plotted vs. incident electron dose. Incident electron energy E_0 equal to (*1*) 150, (*2*) 250, (*3*) 500, (*4*) 1000, and (*5*) 1500 eV.

The data displayed in Fig. 2 contain information on the effect of incident electron energy E_0 on the rate of fullerite transformation, which is important for understanding the mechanism of the modification. The characteristic modification rate (the exponent α), which is

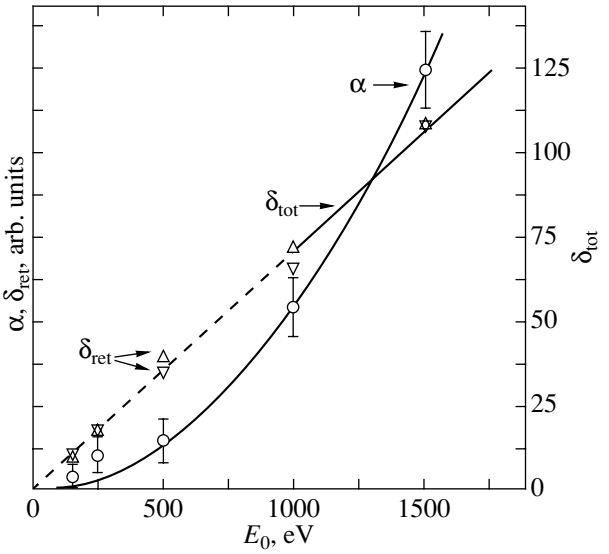

Fig. 3. Characteristic rate of electron-stimulated modification of the C_{60} fullerite plotted vs. incident electron energy.

the polymerization rate in the earliest stage [$P'(Q \longrightarrow 0)$], is plotted in an explicit form in Fig. 3. This is a monotonically rising power-law function $\alpha(E_0)$, whose value increases by more than an order of magnitude within the incident-electron energy range studied. These results come, at first glance, as a surprise. The fact is that the low electron-beam densities used by us exclude the operation of thermally induced polymerization mechanisms. Obviously enough, intermolecular chemical bonds form after the valence-electron excitation, whose threshold is typically a few electronvolts. Therefore, one would expect the polymerization rate to reach a maximum in the region of maximum electron-excitation cross section (3–5 threshold energies), i.e., at a few tens of electronvolts. Thus, the polymerization rate should be a decreasing rather than a rising function throughout the energy range studied. This discrepancy between the experimental and the expected relations is removed if we assume that the valence electrons are excited primarily by a swarm of truly secondary electrons and of electrons slowed down in multiple scattering, rather than by the primary particles. Indeed, the calculated energy dependence of the number of secondary electrons (δ_{tot}) created by one primary electron in beryllium, an element close in atomic number to carbon, which is reproduced from [12] and presented in Fig. 3, agrees qualitatively with the experimental $\alpha(E_0)$ relation. The flux density of the retarded electrons (δ_{ret}) escaping from the sample also increases with energy. This flux density was derived as the ratio of the area under the spectral curve in the region adjoining the peak of elastically scattered electrons ($0.9E_0 < E_e < E_0$) to the area of this peak. The cross sections of elastic backscattering are similar for both groups of electrons; therefore, the normalization to the peak of elastically scattered electrons permits one to exclude the dependence of these cross sections on the energy E_0 from consideration. The flux density of retarded electrons increases with energy E_0 because of the increasing number of inelastic collisions with the electron system of the material, each of which is accompanied by a change in the momentum and in the direction of motion of the retarding electron. As seen from Fig. 3, a broadening of the range within which the retarded electrons are integrated ($0.7E_0 < E_e < E_0$) does not affect this dependence substantially, despite the noticeable difference between the elastic scattering cross sections at the limits of the range. Thus, our analysis supports the assumption that fullerite modification is due to a swarm of secondary electrons rather than to primary ones.

ACKNOWLEDGMENTS

This study was supported by the Interdisciplinary Scientific and Technological Program “Fullerenes and Atomic Clusters” (project no. 98090) and the Presidium of the Russian Academy of Sciences (program “Low-Dimensional Quantum Structures”). The study of the fullerene fragmentation mechanisms was also supported by NWO (Netherlands).

REFERENCES

1. A. Ito, T. Morikawa, and T. Takahashi, Chem. Phys. Lett. **211**, 333 (1993).
2. Y. B. Zhao, D. M. Poirier, R. J. Pechman, and J. H. Weaver, Appl. Phys. Lett. **64** (5), 577 (1994).
3. G. B. Adams, J. B. Page, O. F. Sankey, and M. O’Keefe, Phys. Rev. B **50** (22), 17471 (1994).
4. Y. Wang, J. M. Holden, A. M. Rao, *et al.*, Phys. Rev. B **51** (7), 4547 (1995).
5. G. P. Lopinski, J. R. Fox, and J. S. Lannin, Chem. Phys. Lett. **239**, 107 (1995).
6. T. Tada and T. Kanayana, Jpn. J. Appl. Phys. **35** (1A), L63 (1996).
7. A. Hoffman, P. J. K. Paterson, S. T. Johnston, and S. Prawer, Phys. Rev. B **53** (3), 1573 (1996).
8. J. Onoe and K. Takeuchi, Phys. Rev. Lett. **79** (16), 2987 (1997).
9. Yu. S. Gordeev, V. M. Mikushkin, and V. V. Shnitov, Fiz. Tverd. Tela (St. Petersburg) **42** (2), 371 (2000) [Phys. Solid State **42**, 381 (2000)].
10. V. M. Mikushkin and V. V. Shnitov, Fiz. Tverd. Tela (St. Petersburg) **39** (1), 187 (1997) [Phys. Solid State **39**, 164 (1997)].
11. Yu. S. Gordeev, V. M. Mikoushkin, and V. V. Shnitov, Mol. Mater. **13**, 1 (2000).
12. H. J. Fitting, H. Glaefeke, W. Wild, and G. Nuemann, J. Phys. D **9**, 2499 (1976).

Translated by G. Skrebtsov

Physics of the Solid State, Vol. 44, No. 3, 2002, pp. 447–449. Translated from Fizika Tverdogo Tela, Vol. 44, No. 3, 2002, pp. 431–432.

PROCEEDINGS OF THE V INTERNATIONAL WORKSHOP "FULLERENES AND ATOMIC CLUSTERS"

(St. Petersburg, Russia, July 2–6, 2001)

The Influence of Dimerization on the Orientational Phase Transition in the C_{60} Fullerite

M. V. Kondrin, A. G. Lyapin, S. V. Popova, and V. V. Brazhkin

Vereshchagin Institute of High-Pressure Physics, Russian Academy of Sciences, Troitsk, Moscow oblast, 142190 Russia

Abstract—The influence of dimerization of a C_{60} fullerite subjected to thermobaric treatment on the change in linear dimensions upon the orientational phase transition is investigated. It is demonstrated that the effects associated with the dimerization of fullerites substantially affect the thermal expansion coefficient only for samples synthesized under the conditions $P_{syn} \geq 8$ GPa and $T_{syn} \geq 70$°C (where P_{syn} and T_{syn} are the pressure and temperature of the synthesis, respectively). These effects bring about a smearing of the phase transition, a shift of the transition toward low temperatures, and a decrease in the volume jump. *© 2002 MAIK "Nauka/Interperiodica".*

1. INTRODUCTION

Fullerite C_{60} is an allotropic carbon modification that consists of C_{60} fullerene molecules bound through van der Waals forces. Under a standard pressure, the C_{60} fullerite can crystallize in two types of crystal lattices, namely, in a face-centered cubic lattice at high temperatures and in a simple cubic lattice at low temperatures with the phase transition temperature in the range 230–260 K [1]. The structural change is due to orientational ordering of fullerite molecules at low temperatures. However, thermobaric treatment makes it possible to obtain polymerized phases of C_{60}, specifically, $(C_{60})_2$ dimers, which are metastable under standard conditions [2]. The degree of polymerization can be controlled through appropriate choice of the synthesis conditions (temperature and pressure). In the present work, we analyze the behavior of thermal expansion of weakly polymerized fullerite samples in the vicinity of the orientational phase transition. This investigation is aimed at gaining information on the influence of the synthesis conditions on the degree of polymerization of the fullerite samples and, thus, pro-

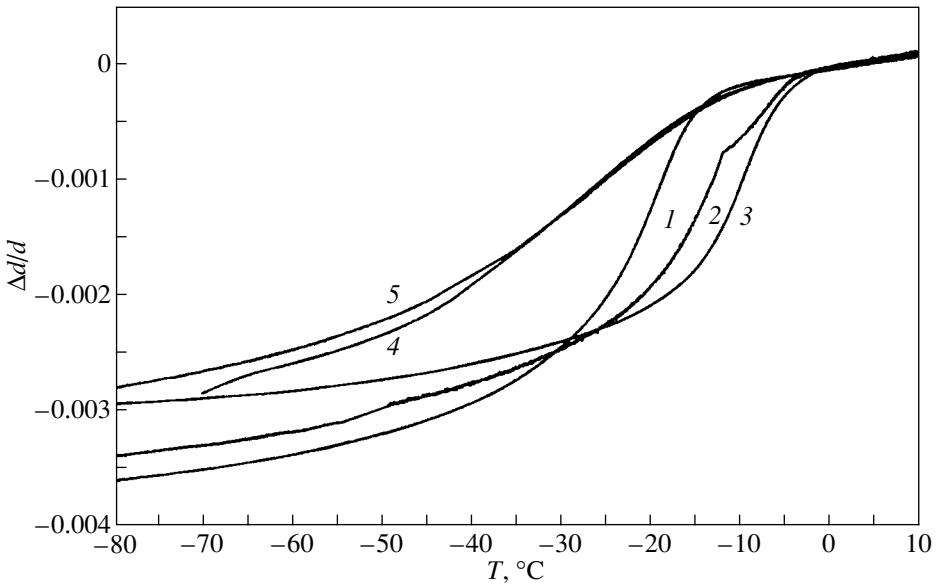

Thermal expansion of the fullerite samples synthesized at room temperature under different pressures *P*: (*1*) 3, (*2*) 5, (*3*) 7, and (*4*) 8 GPa. (*5*) The sample is synthesized at a temperature of 70°C and a pressure of 5 GPa.

1063-7834/02/4403-0447$22.00 © 2002 MAIK "Nauka/Interperiodica"

Synthesis pressure and temperature, phase transition parameters [$\delta(\Delta d/d)$ is the change in the elongation per unit length upon the phase transition], and lattice constants for the fullerite samples under investigation

Sample no.	Synthesis pressure, GPa	Synthesis temperature, °C	T_c, °C	$\delta(\Delta d/d)$	Lattice parameter, Å
1	3	20	–21	0.0029	14.2
2	5	20	–14	0.0026	14.2
3	7	20	–10	0.0025	–
4	8	20	–30	0.0018	13.6
5	5	70	–30	0.0018	13.5

Note: Numbering in the first column corresponds to the numbers of the curves shown in the figure.

vides a way of synthesizing fullerite samples with specified physical properties.

2. SAMPLES AND EXPERIMENTAL TECHNIQUE

A fullerite powder prepared at the Russian Research Center Kurchatov Institute was used as the initial material. Polymerized samples were synthesized at pressures of 3–8 GPa in a Toroid-type chamber. X-ray diffraction analysis of the samples synthesized was carried out on a DRON-4 diffractometer (CuK_α radiation). The thermal expansion was measured using a capacitance dilatometer. The basic design of this dilatometer is similar to that described in [3]. The elongation per unit length of the sample was calculated from the temperature dependence of the measuring capacitance $C(T)$ according to the formula

$$\frac{\Delta d}{d} = \frac{\pi\varepsilon_0 r^2(1+\alpha_{\mathrm{Cu}}(T))^2}{d} \times\left(\frac{1}{C(T)} - \frac{1}{C(T_0 = 273\ \mathrm{K})} + d\alpha_{\mathrm{Cu}}(T)\right).$$

Here, $\alpha_{\mathrm{Cu}}(T)$ is the thermal expansion coefficient of the material of the measuring cell (in our case, copper), d is the length of the sample, Δd is the elongation of the sample, and r is the radius of the measuring capacitor plates. Test measurements for the aluminum (99.999) sample demonstrated that the result of the calculation performed with this formula using the $\alpha_{\mathrm{Cu}}(T)$ parameter taken from [4] coincides with the data available in the literature [4] to a reasonable accuracy (5%). The temperature variation was accomplished by cooling the measuring cell in liquid-nitrogen vapors, followed by controlled heating at a rate of 0.007 K/s.

3. RESULTS AND DISCUSSION

The results of measurements of the relative expansion of fullerites are shown in the figure. It can be seen that monotonic dependences of the volume jump and the phase transition temperature on the synthesis pressure are observed for the samples synthesized under a pressure in the range 3–7 GPa without heating (curves *1*–*3*). Note that the change in linear dimensions upon the phase transition coincides with that obtained earlier [1] using x-ray diffraction methods. The shift of the phase transition onset toward higher temperatures with an increase in the synthesis pressure can be associated with residual strains in the crystal lattice and the influence of dimerization on the orientational phase transition. This tendency (an increase in the critical temperature with an increase in the pressure) was revealed by Lundin and Sundquist [5]. A substantial variation in the behavior of the volume jump due to the phase transition is observed for the samples synthesized at a pressure of 8 GPa (curve *4*) and a temperature of 70°C (curve *5*). Specifically, the volume jump decreases, the phase transition becomes smeared, and the midpoint of the transition range shifts to lower temperatures. It seems likely that the fullerite samples synthesized at these temperatures and pressures contain a considerable amount of dimerized molecules $(C_{60})_2$ and, possibly, other coupled clusters, such as $(C_{60})_3$, $(C_{60})_4$, etc. These clusters can bring about a disordering of the crystal lattice, which causes a smoothing of the phase transition. This assumption is confirmed by the results of x-ray diffraction. In particular, Davydov *et al.* [2, 6] proved that the formation of additional covalent bonds in polymerized fullerites leads to a decrease in the lattice constant. We also observed this effect for samples *4* and *5* (see table), unlike the samples synthesized at lower temperatures and pressures, for which the lattice parameter remains virtually constant.

4. CONCLUSION

The results obtained in this work demonstrated that changes in the synthesis pressure for fullerites in the range 3–7 GPa lead to a shift in the temperature of the orientational phase transition. Moreover, the effects associated with the dimerization of fullerites considerably affect the behavior of the thermal expansion coefficient for the samples synthesized under the conditions $P_{\mathrm{syn}} \geq 8$ GPa and $T_{\mathrm{syn}} \geq 70$°C.

ACKNOWLEDGMENTS

We would like to thank V.G. Velikanov and R.S. Sadykov for x-ray diffraction analysis of the samples used in our measurements.

This work was supported by the Russian Foundation for Basic Research, project nos. 99-02-17408 and 01-02-17543.

REFERENCES

1. P. A. Heinley, G. B. M. Vaughan, J. E. Fischer, *et al.*, Phys. Rev. B **45** (8), 4544 (1992).
2. V. A. Davydov, L. S. Kashevarova, A. V. Rakhmanina, *et al.*, Pis'ma Zh. Éksp. Teor. Fiz. **68** (12), 881 (1998) [JETP Lett. **68**, 928 (1998)].
3. R. Pott and R. Schefzyk, J. Phys. E **16**, 444 (1983).
4. F. R. Kroeger and C. A. Swenson, J. Appl. Phys. **48** (3), 853 (1977).
5. A. Lundin and B. Sundquist, Phys. Rev. B **53** (11), 8329 (1996).
6. V. A. Davydov, L. S. Kashevarova, A. V. Rakhmanina, *et al.*, Chem. Phys. Lett. **333**, 224 (2001).

Translated by N. Korovin

Physics of the Solid State, Vol. 44, No. 3, 2002, pp. 450–453. From Fizika Tverdogo Tela, Vol. 44, No. 3, 2002, pp. 433–436.

PROCEEDINGS OF THE V INTERNATIONAL WORKSHOP "FULLERENES AND ATOMIC CLUSTERS"

(St. Petersburg, Russia, July 2–6, 2001)

Ultraviolet–Visible Absorption Spectroscopy of Carbon Onions[1]

S. Tomita[1], S. Hayashi[1, 2], Y. Tsukuda[1], and M. Fujii[2]

[1] *Graduate School of Science and Technology, Kobe University, Rokkodai, Nada, Kobe, 657-8501 Japan*

[2] *Department of Electrical and Electronics Engineering, Faculty of Engineering, Kobe University, Rokkodai, Nada, Kobe, 657-8501 Japan*

e-mail: hayashi@eedept.kobe-u.ac.jp

Abstract—The optical properties of spherical and polyhedral carbon onions were studied in relation to the strong hump centered at 217.5 nm (4.6 μm^{-1}) in the interstellar-dust extinction curve. The ultraviolet–visible absorption spectra of onions prepared by thermal annealing of diamond nanoparticles were measured. Theoretical calculations for the spherical and polyhedral carbon onions were also carried out to explain the experimental spectra. © *2002 MAIK "Nauka/Interperiodica".*

The carbon onion is a novel carbon nanoparticle consisting of concentric curved graphene sheets. The physical properties of this new member of fullerene-related materials are very attractive. In particular, the optical properties of carbon onions are of great interest, because they are possible components of interstellar dust: they could contribute to a strong extinction maximum centered at 217.5 nm (4.6 μm^{-1}) in the ultraviolet–visible (UV–Vis.) region.

Several theoretical analyses have been reported [1, 2] regarding the UV–Vis. absorption properties of the onions. Nevertheless, owing mainly to the small quantity of material available for macroscopic experiments, absorption properties derived from laboratory experiments remain poorly understood [3].

In 1994, Kuznetsov *et al.* [4] succeeded in preparing carbon onions in large quantities by annealing diamond nanoparticles about 5 nm in diameter. Such diamond nanoparticles would also be synthesized in the external atmosphere of a star by chemical vapor deposition of light hydrocarbon molecules; carbon onions are very likely generated in interstellar space by the transformation of diamond nanoparticles under an appropriate heating process [5]. As related to this astrophysical context, laboratory data on the UV–Vis. absorption for carbon onions prepared from diamond nanoparticles is highly desired.

Recently, we prepared spherical and polyhedral carbon onions by annealing diamond nanoparticles in vacuum and studied them using transmission electron microscopy (TEM), electron energy-loss spectroscopy, Raman spectroscopy, and electron spin resonance (ESR) [6, 7]. In the present communication, we report the UV–Vis. absorption spectra of these onions. Theoretical calculations for spherical and polyhedral carbon onions are also carried out to explain the experimental spectra.

1. EXPERIMENTAL RESULTS

A detailed description of the sample preparation procedure can be found in [7]. In brief, we prepared carbon onions by annealing diamond nanoparticles 5 nm in diameter in vacuum. As the annealing temperature increases, the transformation of a diamond nanoparticle into a spherical carbon onion proceeds from the surface to the center [4]. Our previous TEM examination [6] revealed that spherical onions 5 nm in diameter are formed at about 1700°C. At temperatures above 1900°C, further graphitization leads to the formation of polyhedral carbon onions with facets [7]. In the present study, diamond nanoparticles were annealed at temperatures ranging from 900 to 2100°C. The samples were ultrasonically dispersed in distilled water (about 0.2 mg/cc) and then put into a synthesized-quartz cell. UV–Vis. transmission spectra in the wavelength (λ) range from 0.5 to 0.2 μm were recorded with a double-beam spectrometer. The transmittance (T) was converted into the extinction (E) using the equation $E = -\log T$.

Figure 1 shows UV–Vis. extinction spectra for all samples. The abscissa is the wavenumber $1/\lambda$. The extinction is normalized using the expression $(E_{(\lambda)} - E_{(\lambda = 0.55\,\mu m)})/(E_{(\lambda = 0.44\,\mu m)} - E_{(\lambda = 0.55\,\mu m)})$, where $E_{(\lambda)}$ is the extinction at the wavelength λ. The extinction for diamond nanoparticles denoted by "nc-D" increases monotonically as we go to the ultraviolet region. The increasing magnitude of the extinction continuum cannot be due to the intrinsic absorption of isolated diamond nanoparticles but is likely caused by the aggregation of diamond nanoparticles. Further discussion on the spectrum for initial diamonds is beyond the scope of

[1] This article was submitted by the authors in English.

this communication and will be published in a later paper.

As the annealing temperature increases, the extinction at higher wavenumbers decreases. In addition, the sample annealed at 1100°C shows a broad peak at about 3.7 μm^{-1}. At 1700°C, the broad peak is more pronounced and slightly shifted to a higher wavenumber. Note here that spherical onions were observed by TEM at this temperature. With a further increase in the annealing temperature, an additional peak at about 4.6 μm^{-1} emerges; the spectrum at 2100°C shows two peaks. The appearance of double peaks is believed to be due to the formation of polyhedral onions.

2. THEORETICAL CONSIDERATIONS

2.1. Spherical Onions

The broad extinction maximum at 3.8 μm^{-1} observed for the spectra in the annealing-temperature range from 1100 to 1700°C is due to spherical carbon onions with a diamond or hollow core. The absorption spectra for such onions have already been calculated by Henrard *et al.* [2]. In their model, the dielectric tensor of the graphitic multishell (in a spherical coordinate system with unit vectors $\bar{\theta}$, $\bar{\phi}$, and $\bar{\rho}$) can be expressed as

$$\bar{\bar{\varepsilon}}(\omega) = \varepsilon_{pp}(\omega)(\bar{\theta}\bar{\theta} + \bar{\phi}\bar{\phi}) + \varepsilon_{pl}(\omega)\bar{\rho}\bar{\rho}, \quad (1)$$

where $\varepsilon_{pp}(\omega)$ and $\varepsilon_{pl}(\omega)$ are the in-plane and out-of-plane dielectric functions of graphite, respectively. The radii of the external graphitic shell and inner core are denoted by R and r, respectively (see inset to Fig. 2). The diamond or vacuum core is described by an isotropic dielectric function ε_1. For an onion immersed in a homogeneous medium with a dielectric function ε_m, the multipolar polarizability of order l is expressed as

$$\alpha(\omega) = 4\pi\varepsilon_0 R^{2l+1}\frac{\varepsilon_m[(\varepsilon_{pl}u_- - \varepsilon_1 l)(\varepsilon_{pl}u_+ - \varepsilon_m l) - \rho_l(\varepsilon_{pl}u_+ - \varepsilon_1 l)(\varepsilon_{pl}u_- - \varepsilon_m l)]}{(l\varepsilon_1 - \varepsilon_{pl}u_+)[\varepsilon_{pl}u_- + \varepsilon_m(l+1)]\rho_l - (l\varepsilon_1 - \varepsilon_{pl}u_-)[\varepsilon_{pl}u_+ + \varepsilon_m(l+1)]}, \quad (2)$$

where $\rho_l = (r/R)^{u_+ - u_-}$ and $u_\pm = -0.5 \pm \sqrt{0.25 + l(l+1)\varepsilon_{pp}/\varepsilon_{pl}}$. In the non-retarded limit, the electric field of an electromagnetic plane wave with frequency ω only induces an electric dipole ($l = 1$), which absorbs energy from the wave with the cross section

$$\sigma(\omega) = \frac{4\pi\omega}{c}\mathrm{Im}[\alpha_1(\omega)]. \quad (3)$$

Our previous ESR studies for spherical onions [7] revealed that graphite shells contain a number of defects, such as dangling bonds. The dielectric function of such defective graphite shells should be different from that of bulk graphite. In order to take the effects of defects into consideration, the dielectric function of defective graphite shells was assumed to be a combination of those of bulk graphite (ε_{pp} or ε_{pl}) and amorphous carbon (ε_{ac}). The in-plane (ε'_{pp}) and out-of-plane (ε'_{pl}) dielectric functions of a defective graphite shell are assumed to be

$$\varepsilon'_{pp} = c\varepsilon_{pp} + (1-c)\varepsilon_{ac}, \quad \varepsilon'_{pl} = c\varepsilon_{pl} + (1-c)\varepsilon_{ac}, \quad (4)$$

where c is the concentration of the graphite component in the shell. We can calculate the absorption cross section of a defective spherical onion from Eq. (2), in which ε_{pp} and ε_{pl} are replaced by ε'_{pp} and ε'_{pl}, respectively. In our calculations, we used the dielectric data tabulated by Draine and Lee [8] for graphite, by Philipp and Taft [9] for diamond, and by Michel *et al.* [10] for amorphous carbon.

Figure 2 shows the absorption cross section per particle volume (R^3) for several isolated onions. The outer radius R is 2.5 nm and the inner radius r is 2 (curve *a*), 1 (*b*), 0.5 (*c*), and 0.35 nm (*d*). The inner core is of diamond for curves *a*–*c* and vacuum for curve d. The surrounding medium was assumed to be water (ε_m = 1.777). The absorption peak due to surface plasmons in the spherical onion can be seen at about 3.7 μm^{-1}. With

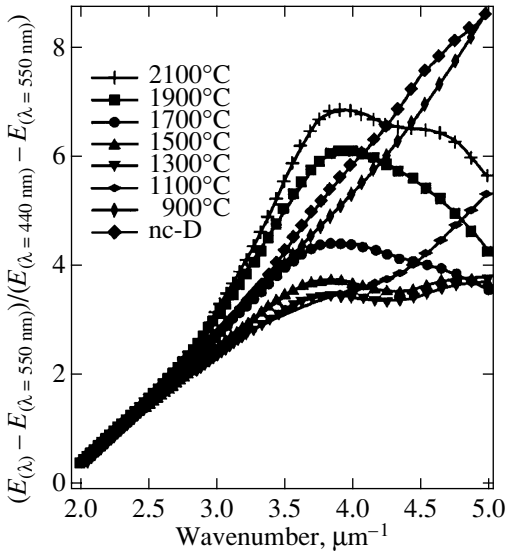

Fig. 1. Annealing-temperature dependence of normalized experimental UV–Vis. extinction spectra for carbon onions.

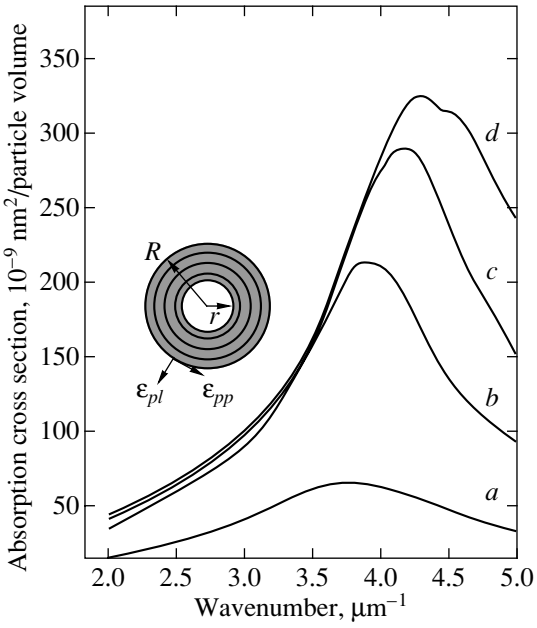

Fig. 2. Calculated spectra for defective spherical onions with external radius R = 2.5 nm in water. The inner core radius r is 2 (curve *a*), 1 (*b*), 0.5 (*c*), and 0.35 nm (*d*). The cores are of diamond for curves *a*–*c* and of vacuum for curve *d*. The graphite concentration in the shell *c* is equal to (*a*) 0.2, (*b*) 0.4, (*c*) 0.6, and (*d*) 0.8.

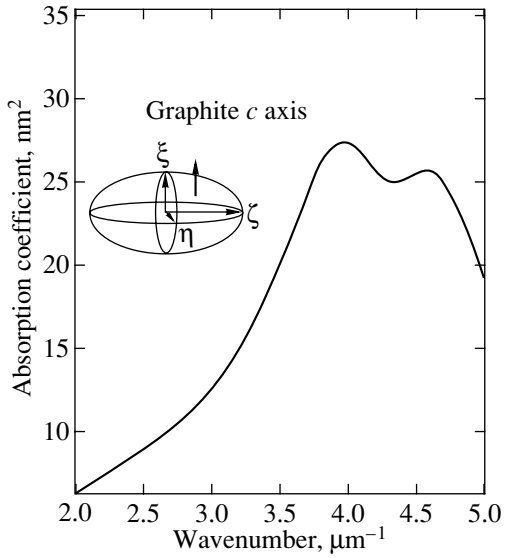

Fig. 3. Calculated spectrum for graphite ellipsoids of revolution randomly dispersed in water. The depolarization factors are $L_\xi = L_\eta = 0.45$ and $L_\zeta = 0.1$, and the filling factor is $f = 0.3$.

increasing *c* and decreasing *r*, i.e., as the transformation from a diamond nanoparticle into a defective spherical onion proceeds, the peak shifts to higher wavenumbers. This shift qualitatively agrees with the experimental results. However, the peak of the calculated spectra is located at a higher wavenumber than that of the experimental spectrum. A defective spherical onion without a diamond core (curve *d*) shows a peak at 4.3 μm^{-1}, while the corresponding peak in the experimental spectrum (1700°C) is at 3.9 μm^{-1}. The wavenumber misfit between the calculated and experimental spectra is thought to be caused by the aggregation effect [1]. The aggregation of onions by van der Waals forces is likely to subsist in a water suspension, because the applied ultrasonic dispersion seems to be insufficient to break the adhesion between the particles. A detailed theoretical consideration of aggregated onions is presently being undertaken by our group.

We also simulated the absorption spectrum of a defective spherical onion in vacuum ($\varepsilon_m = 1$). The calculated spectrum (not shown here) shows a peak at about 4.6 μm^{-1} and just fits the interstellar-dust extinction spectrum. This strongly suggests that defective spherical onions are likely a component of interstellar dust, which shows an extinction maximum centered at 4.6 μm^{-1}.

2.2. Polyhedral Onions

The appearance of two absorption peaks above 1900°C is apparently attributed to the formation of polyhedral carbon onions with facets. We assume that a polyhedral onion is composed of planar graphite nanocrystals and that a nanocrystal can be treated as an anisotropic graphite ellipsoid. Polyhedral onions dispersed in water are thus modeled as a system consisting of anisotropic graphite ellipsoids randomly oriented in water. We discuss the optical properties of the system in the framework of the average dielectric function of anisotropic ellipsoids calculated by Hayashi *et al.* [11]. For an ellipsoidal particle, the ξ, η, and ζ axes are set as shown in the inset to Fig. 3. The dielectric functions along these axes are denoted by ε_ξ, ε_η, and ε_ζ, respectively. By introducing the depolarization factor L_j (j = ξ, η, ζ) along the j axis and the filling factor f, the average dielectric function can be written as

$$\varepsilon_{av} = 1 + \frac{3(1-f)(\varepsilon_m - 1) + f(\tilde{\varepsilon}_\xi + \tilde{\varepsilon}_\eta + \tilde{\varepsilon}_\zeta)}{3(1-f) + f(\hat{\varepsilon}_\xi + \hat{\varepsilon}_\eta + \hat{\varepsilon}_\zeta)}, \quad (5)$$

where

$$\hat{\varepsilon}_j = \left[1 + L_j\left(\frac{\varepsilon_j}{\varepsilon_m} - 1\right)\right]^{-1}, \quad j = \xi, \eta, \zeta, \quad (6)$$

$$\sum_j L_j = 1, \quad (7)$$

$$\tilde{\varepsilon}_j = (\varepsilon_j - 1)\hat{\varepsilon}_j, \quad j = \xi, \eta, \zeta. \quad (8)$$

Here, the absorption coefficient is directly given by

$$\alpha = \frac{2\omega}{c}\mathrm{Im}\sqrt{\varepsilon_{av}}. \quad (9)$$

In the present study, the ξ axis of the ellipsoid is set parallel to the graphite *c* axis. Therefore, ε_ξ corresponds to ε_{pl}, while ε_η and ε_ζ correspond to ε_{pp}. For the depolarization factors of an ellipsoid of revolution, we have $L_\xi = L_\eta$ and $2L_\xi + L_\zeta = 1$. Figure 3 shows the calculated absorption coefficient for a graphite ellipsoid in water. L_ζ is 0.1, L_η and L_ξ are 0.45, and f is 0.3. The graphite ellipsoids that we consider here successfully reproduce an absorption spectrum with two peaks. These two absorption peaks at approximately 4.0 and 4.6 μm^{-1} are associated with surface plasmons along the η and ζ axes of the ellipsoid.

We have studied the optical properties of spherical and polyhedral carbon onions in relation to interstellar dust particles. The laboratory absorption spectroscopy indicated that spherical onions in water show a broad extinction peak at approximately 3.8 μm^{-1}. The theoretical calculation suggested that the peak is due to surface plasmons in defective spherical onions. Furthermore, the calculated spectrum for the defective onion in vacuum can reproduce the interstellar-dust extinction spectrum. This suggests that the defective spherical onion is a strong candidate for interstellar dust, which shows an extinction maximum centered at 4.6 μm^{-1}. Experimental spectra for polyhedral onions showed two extinction peaks at 3.9 and 4.6 μm^{-1}. By approximating a facet of the polyhedral onion as a graphite ellipsoid and using the average dielectric function, we succeeded in reproducing the absorption spectrum with double peaks. Both peaks originate from surface plasmons in the facet part of the polyhedral onion.

ACKNOWLEDGMENTS

One of the authors (S.T.) is grateful for financial support from a Research Fellowship of the Japan Society for the Promotion of Science (JSPS) for Young Scientists. This work was funded by a grant-in-aid for scientific research from the Ministry of Education, Science, Sports, and Culture, Japan, and a grant for the Future Program from the JSPS (JSPS-RETF-98P-01203).

REFERENCES

1. A. A. Lucas, L. Henrard, and Ph. Lambin, Phys. Rev. B **49**, 2888 (1994).
2. L. Henrard, Ph. Lambin, and A. A. Lucas, Astrophys. J. **487**, 719 (1997).
3. W. A. de Heer and D. Ugarte, Chem. Phys. Lett. **207**, 480 (1993).
4. V. L. Kuznetsov, A. L. Chuvilin, Y. V. Butenko, *et al.*, Chem. Phys. Lett. **222**, 343 (1994).
5. D. Ugarte, Astrophys. J. **443**, L85 (1995).
6. S. Tomita, M. Fujii, S. Hayashi, and K. Yamamoto, Chem. Phys. Lett. **305**, 225 (1999).
7. S. Tomita, T. Sakurai, H. Ohta, *et al.*, J. Chem. Phys. **114**, 7477 (2001).
8. B. T. Drain and H. M. Lee, Astrophys. J. **285**, 89 (1984).
9. H. R. Phillip and E. A. Taft, Phys. Rev. **136**, A1445 (1964).
10. B. Michel, Th. Henning, C. Jäger, and U. Kreibig, Carbon **37**, 391 (1999).
11. S. Hayashi, N. Nakamori, and H. Kanamori, J. Phys. Soc. Jpn. **46**, 176 (1979).

Physics of the Solid State, Vol. 44, No. 3, 2002, pp. 454–458. From Fizika Tverdogo Tela, Vol. 44, No. 3, 2002, pp. 437–440.

PROCEEDINGS OF THE V INTERNATIONAL WORKSHOP "FULLERENES AND ATOMIC CLUSTERS"

(St. Petersburg, Russia, July 2–6, 2001)

Nonadiabatic Superconductivity in Fullerene-Based Materials[1]

C. Grimaldi*, E. Cappelluti, L. Pietronero**, and S. Strässler***

** Département de Microtechnique—IPM, École Polytecnique Féderale Lausanne, Lausanne, Switzerland*

*** Department of Physics, University "La Sapienza" and INFM, Rome 1, Italy*

Abstract—Fullerene compounds have phonon frequencies up to $\omega_{max} = 0.2$ eV and a Fermi energy of the order $E_F = 0.3$ eV. It is, therefore, expected that the adiabatic parameter $\lambda\omega_{ph}/E_F$ (where λ is the electron–phonon coupling constant and ω_{ph} is a typical phonon frequency) is not *a priori* negligible and the conventional theory of phonon-mediated superconductivity is inapplicable in this case. Here, we discuss how the conventional theory is inconsistent with a number of experimental data and provide a generalization of the theory in order to include nonadiabatic electron–phonon effects. We show that the inclusion of nonadiabatic channels in the electron–phonon interaction is a key element for the high values of T_c in these materials. We make several predictions regarding the superconducting and normal-state properties of fullerene compounds that can be tested experimentally. © *2002 MAIK "Nauka/Interperiodica".*

It is certainly due to their apparently ordinary phenomenology that the superconductivity in C_{60} materials has often been assumed to be consistently described by the conventional Migdal–Eliashberg (ME) theory of phonon-mediated superconductivity [1, 2]. In favor of this point of view, we can enlist several features, such as the Fermi liquidlike normal-state properties, order parameter of *s*-wave symmetry, sizeable carbon isotope effect, etc. [3]. However, despite these reassuring properties, fullerene-based superconductors also display less ordinary features, making the ME picture problematic. In fact, like the high-T_c copper oxides, C_{60} compounds have extremely low charge carrier density [4], have a significant electron correlation, and are close to a metal–insulator transition, showing a strong dependence of T_c upon doping and disorder [3, 5]. Within the framework of the ordinary ME theory, all these features tend to degrade superconductivity.

The recent discovery of superconductivity at $T_c = 52$ K in hole-doped C_{60} [6] raises even more doubts as to the validity of the ME picture. In fact, $T_c = 52$ K is the highest critical temperature among non-cuprate superconductors (it also exceeds $T_c = 39$ K of the recently discovered MgB_2 superconductivity [7]) and it is difficult to understand why C_{60} should represent the best optimized ME material and, at the same time, display properties which degrade ME superconductivity.

In addition to the above conceptual difficulties, there are actually several hints opposing the ME scenario; this is disseminated in both experimental and theoretical published works on fullerides. Let us consider, for example, what is known on the relevant energy scales involved in the electron–phonon interaction. The C_{60} molecule has a rather wide range of phonon modes of energy extending from $\omega_{min} = 400$ K to $\omega_{max} = 2300$ K. The relevant bandwidth for both electron- and hole-doped materials is $W = 0.5$ eV = 5800 K; therefore, for the A_3C_{60} half-filled compounds, the Fermi energy is $E_F = 0.25$ eV = 2900 K [3]. The value of E_F for the optimum hole doping ($T_c = 52$ K) is even lower. Note that these are very small values compared to those of conventional superconductors, for which E_F is of several electronvolts. A great effort has been devoted in the past to the calculation of the electron–phonon interaction in C_{60} materials. In Fig. 1, we summarize several published results on A_3C_{60} compounds obtained using different calculation schemes [8]. In the figure, $V = \sum_i V_i$ is the total interaction arising from the coupling of the eight H_g C_{60} phonons to the t_{1u} electrons and $\omega_{ph} = \sum_i V_i\omega_i/V$, where ω_i is the frequency associated with the *i*th phonon mode. Figure 1 is quite illuminating since, although the discrepancies in the value of V among the different calculations are rather important, all these calculations agree in estimating the ratio ω_{ph}/E_F to be larger than 0.4. This result is in contradiction with the adiabatic hypothesis on which the entire ME framework rests. The ME equations of superconductivity are, in fact, defined only in the adiabatic limit $\omega_{ph}/E_F \longrightarrow 0$, in which all the additional nonadiabatic vertex corrections can be neglected in virtue of Migdal's theorem [1].

The analysis of the energy scales and the data of Fig. 1 represent the first evidence of the inadequacy of the ME theory of superconductivity in fullerides. Another important indication stems from an analysis of the experimental data of Rb_3C_{60} ($T_c = 30$ K), for which

[1] This article was submitted by the authors in English.

1063-7834/02/4403-0454$22.00 © 2002 MAIK "Nauka/Interperiodica"

a very accurate measurement of the carbon isotope coefficient $\alpha_C = -d\ln(T_c)/d\ln(M)$, where M is the isotopic carbon mass, became available only recently [9]. In fact, the measured value $\alpha_C = 0.21 \pm 0.012$ is sufficiently accurate to permit one to test the consistency of the ME theory by estimating the values of the electron–phonon coupling λ, of the phonon frequency ω_{ph}, and of the Coulomb pseudopotential μ^* that correspond to the experimental values of T_c and α_C for Rb_3C_{60}. To this end, we considered different models for the electron–phonon spectral function $\alpha^2F(\omega)$ and numerically solved the ME equations by inserting the values of λ, ω_{ph}, and μ^* that reproduce the experimental data T_c = 30 K and $\alpha_C = 0.21$. In Fig. 2, we show the results (filled squares) obtained by employing an Einstein phonon spectrum $\alpha^2F(\omega) = (\lambda\omega_{ph}/2)\delta(\omega - \omega_{ph})$. The main point of Fig. 2 is that the calculated ω_{ph} (lower panel) depends strongly on the electron–phonon coupling constant λ. Large values of λ, T_c = 30 K, and $\alpha_C = 0.21$ are reproduced only for quite small phonon frequencies, while decreasing λ quickly enhances ω_{ph}. The C_{60} phonon spectrum is, however, limited by a maximum phonon frequency of ~2300 K [3, 8], so that λ cannot be less than about 1.25. By using different shapes of the function $\alpha^2F(\omega)$ and of the frequency cutoff in μ^*, we can lower the minimum allowed value of λ to about $\lambda_{min} \approx 1.0$. Note that the obtained values of the Coulomb pseudopotential μ^* (Fig. 2, upper panel, filled squares) are always quite large compared to the standard value $\mu^* \approx 0.1$ [10].

According to the ME analysis, Rb_3C_{60} is, therefore, an intermediate- or strong-coupling superconductor. Let us now address the question of whether this conclusion is consistent or not with the ME framework [1, 2, 10]. As pointed out before, the assumption at the basis of the ME framework is Migdal's theorem, which states that, as long as the phonons have a much slower dynamics than that of the electrons, the nonadiabatic interference effects (vertex corrections) can be neglected [1]. We can test whether the data of Fig. 2 are consistent with Migdal's theorem by making an order-of-magnitude estimate of the first nonadiabatic electron–phonon vertex correction P. According to Migdal [1], P is given by

$$P = \lambda\frac{\omega_{ph}}{E_F}. \qquad (1)$$

Conventional superconductors, such as Pb and Al, have Fermi energies of the order of $E_F \sim 5$ to 10 eV, phonon frequencies usually not exceeding ~50 meV, and λ less than about 1–1.5 [10]. Hence, for conventional materials, $P \ll 1$, the vertex corrections are negligibly small and the ME framework is well founded. To estimate the value of P in Rb_3C_{60}, we insert the value of λ and ω_{ph} resulting from our solution of the ME equations into Eq. (1). We obtain that, for any couple of values of λ and ω_{ph} from Fig. 2 (lower panel, filled squares), the Migdal parameter P is always larger than ~0.4. This result is remarkably robust, and different shapes of the function $\alpha^2F(\omega)$ that eventually include contributions from the lowest intermolecular phonon modes always lead to $P >$ ~0.4. We conclude, therefore, that the conventional phonon-mediated superconductivity is not a self-consistent picture of Rb_3C_{60} since the

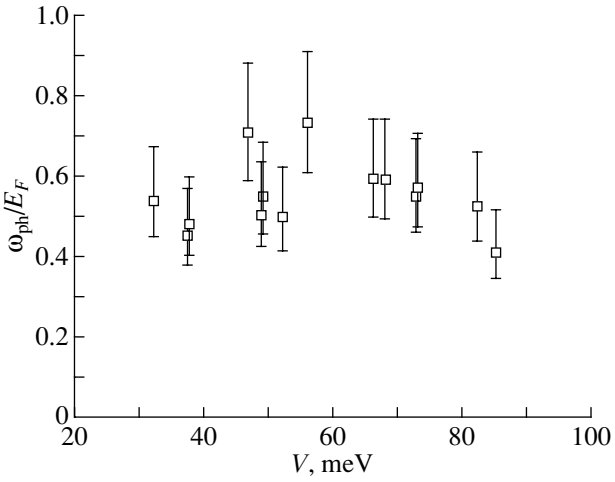

Fig. 1. Adiabatic parameter ω_{ph}/E_F versus electron–phonon pairing interaction V as extracted from various calculations of the intramolecular electron–phonon pairing in fullerides [8]. V is related to the electron–phonon coupling constant λ via $V = \lambda/N_0$, where N_0 is the density of states at the Fermi level. The Fermi energy is set equal to $E_F = 0.25 \pm 0.05$ eV [13].

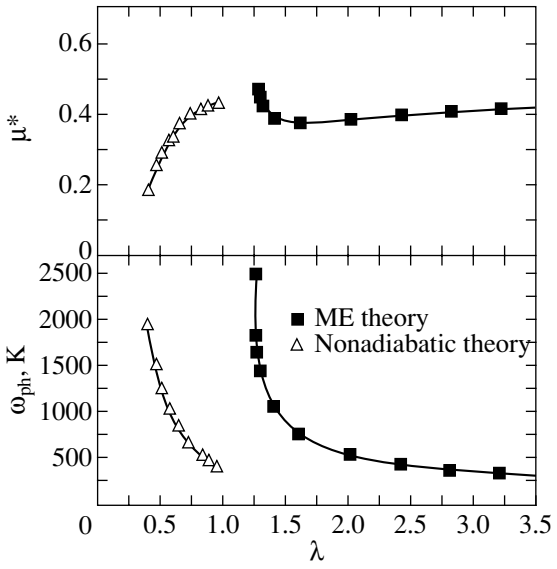

Fig. 2. Coulomb pseudopotential μ^* (upper panel) and phonon frequency ω_{ph} (lower panel) as a function of the electron–phonon coupling λ. Both the ME (filled squares) and nonadiabatic (open triangles) equations are solved in order to fit the experimental data T_c = 30 K and $\alpha_C = 0.21$.

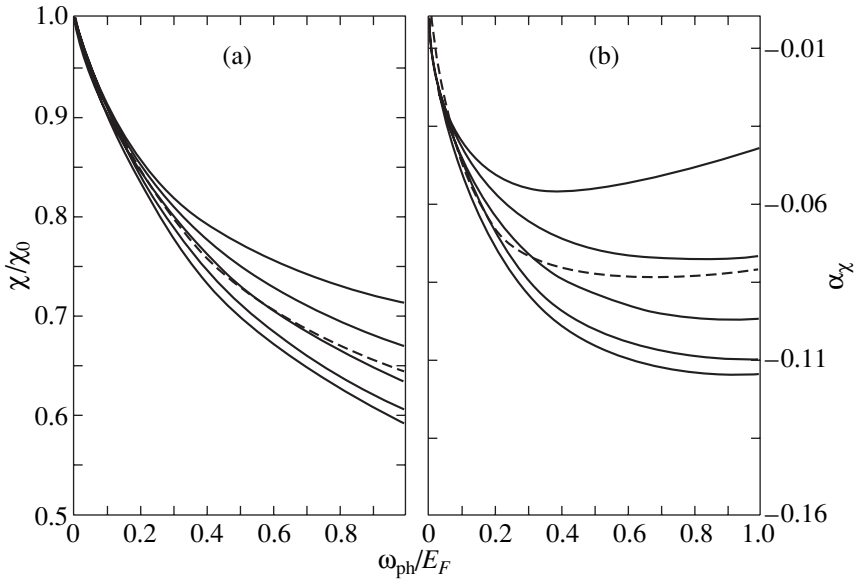

Fig. 3. (a) Nonadiabatic Pauli susceptibility and (b) its isotope coefficient as a function of the adiabatic parameter ω_{ph}/E_F for $\lambda = 0.7$. Dashed (solid) lines refer to the first- (second-) order nonadiabatic approximation (see text). From lower to upper solid lines: $Q_c = 0.1$, 0.3, 0.5, 0.7, and 1.0, respectively.

values of λ and ω_{ph} needed to fit $T_c = 30$ K and $\alpha_C = 0.21$ strongly violate Migdal's theorem [11].

The results of Figs. 1 and 2 imply that the description of superconductivity in C_{60} materials should be formulated beyond the ME theory. In particular, the low value of E_F suggests that the adiabatic hypothesis and Migdal's theorem should be abandoned from the start and that a consistent theory should be formulated by allowing ω_{ph}/E_F to have large values. In this perspective, in the past years, we constructed a theory of nonadiabatic superconductivity by explicitly including the vertex and other diagrammatic terms arising in the nonadiabatic regime [12, 13]. A primary role is played by the vertex diagrams, which have been shown to strongly depend on the exchanged phonon momentum and frequency **q** and ω, respectively [13]. The momentum and frequency dependences of the vertex diagrams are quite complex, and it is hard, in principle, to determine in which way these nonadiabatic terms affect the superconducting properties, in particular, if they favor or disfavor the onset of superconductivity. In this regard, the microscopic characteristics of real materials are important. In particular, the strong degree of electronic correlation in fullerenes has been shown to have an important and positive effect in the nonadiabatic regime by favoring small **q** scattering [14], the case where vertex corrections mainly enhance the superconducting pairing [12, 13]. In this context, the electron–phonon coupling λ no longer characterizes the strength of superconducting pairing, whereas the opening of new nonadiabatic channels of pairing appears to be the driving element of large critical temperatures. In simple words, this means that a moderate coupling λ, which, in the context of the conventional adiabatic ME theory, is expected to yield no or low-temperature superconductivity, can actually account for large values of T_c in the new framework based on the nonadiabatic theory of superconductivity.

To illustrate this point, let us reconsider Rb_3C_{60} in the broader framework of nonadiabatic superconductivity. The open triangles in Fig. 2 are λ and μ^* values generated by numerical solutions of the nonadiabatic equations constrained to fit the experimental values $T_c = 30$ K and $\alpha_C = 0.21$ [11]. In order to model the strong correlation, we used an upper cutoff $q_c = 0.2k_F$ for the momentum transfer of the electron–phonon scattering (k_F is the Fermi momentum). The first remarkable difference between the ME theory (filled squares) and the nonadiabatic solutions (open triangles) is that much lower (and more realistic) values of λ are now needed to reproduce the experimental data. In nonadiabatic superconductivity, high values of the critical temperature arise from conventional values of λ ($\lambda < 1$) embedded in the new theory, rather than from extremely large values of λ ($\lambda > 1$) predicted by the conventional theory. It is also certainly worth stressing that the nonadiabatic solutions of Fig. 2 lead to values of P that are always less than ~0.25 [11]. This is perfectly compatible with the perturbative approach used, which disregards all nonadiabatic irreducible vertex diagrams of order P^2 and higher order terms.

At this point, it is significant to make a comparison between fullerides and intercalated graphite compounds (GICs), for which quite low values of T_c are observed (for example, $T_c = 0.2$ K for K_8C). Supercon-

ductivity in GICs is explained by the weak-to-moderate (~0.3) coupling to carbon-phonon modes of energies close to those in C_{60}. Within the ME framework, some current theories claim that the enhancement of T_c as one goes from GICs to fullerides arises from an amplification of λ (from ~0.3 to ~1 or more) due to the finite curvature of the C_{60} molecule [15]. In the nonadiabatic model, instead, the most important difference between GICs and fullerides is the value of E_F. In the former compounds, in fact, E_F is of several electronvolts and Migdal's theorem holds true. Hence, in these terms, the increase in T_c as one goes from GICs to fullerides stems mainly from the opening of electron–phonon nonadiabatic channels rather than from a ~300% enhancement of λ.

The interpretation of superconductivity in C_{60}-based materials in terms of the nonadiabatic scenario can be sustained by the observation of clear additional fingerprints of such a nonadiabatic regime. In order to gain robustness, such fingerprints should be sought among those physical quantities for which some well-established properties in the ME regime are qualitatively modified in the nonadiabatic one. Let us consider, for example, the charge carrier mass m^* renormalized by electron–phonon interaction. In the ME regime, we have $m^* = (1 + \lambda)m$, where m is the bare mass. A strong prediction of the ME theory is that, since λ is independent of the ion mass M, no isotope effect is expected for m^*. Within the nonadiabatic model, the situation is completely different. Now, the electron self-energy is modified by the nonadiabatic vertex correction, so that m^* acquires an additional $\omega_{ph}/E_F \propto 1/M^{1/2}$ dependence, leading to a nonzero isotope effect on m^*. We found that, in general, the m^* isotope coefficient, $\alpha_{m^*} = -d\ln(m^*)/d\ln(M)$, is negative and that, for example, $\alpha_{m^*} \sim -0.2$ for $\omega_{ph}/E_F = 0.4$ and $\lambda = 1$ [16]. The experimental observation of nonzero values of α_{m^*} in fullerides would certainly imply a breakdown of the ME theory and strongly support the nonadiabatic picture.

Another measurable quantity which could unveil signatures of nonadiabaticity is the normal-state Pauli susceptibility χ. As pointed out by Fay and Appel [17], the lowest order electron–phonon correction to χ is a vertex diagram; thereby, the renormalization of the Pauli susceptibility is of the order $P = \lambda\omega_{ph}/E_F$. In the adiabatic regime, therefore, χ is expected to be unaffected by the electron–phonon interaction. Conversely, when P is no longer negligible, χ becomes dependent on λ and ω_{ph}, which can be detected using suitable experiments. We calculated the nonadiabatic effects on the Pauli susceptibility for different stages of perturbation theory in P; the results are shown in Fig. 3 [18]. In the figure, the dashed lines refer to a simple ladder vertex correction, while the solid lines are results obtained including the second-order nonadiabatic terms for different values of the momentum cutoff $Q_c = q_c/2k_F$. For $P \longrightarrow 0$, both approximation schemes lead to the ME result $\chi = \chi_0 = 2\mu_B^2 N_0$, where μ_B is the Bohr magneton and N_0 is the density of states at the Fermi level. The first main result (Fig. 3a) is that, in the nonadiabatic regime ($P \neq 0$), χ is significantly reduced with respect to the adiabatic limit χ_0. Hence, χ is no longer simply proportional to N_0. This means that disregarding the electron–phonon coupling would lead to a substantial underestimation of the bare density of states as determined from spin susceptibility measurements as long as the system is in the nonadiabatic regime. A more striking consequence of the nonadiabatic effects on χ is that the Pauli susceptibility now becomes ion-mass dependent, which is reflected in its nonzero (negative) isotope coefficient $\alpha_\chi = -d\ln(\chi)/d\ln(M)$ (Fig. 3b). The observation of such an isotope effect, absent in the ME regime, represents a stringent test of the nonadiabatic hypothesis.

A further interesting qualitative difference between the ME and the nonadiabatic regimes is in the response of the superconducting state to disorder and nonmagnetic impurities. Within the adiabatic regime, isotropic *s*-wave superconductors are stable to the presence of weak disorder. In particular, T_c is nearly independent of the extent of disorder. This situation changes when we consider nonadiabatic superconductors [19]. In fact, the vertex corrections are quite sensitive to the extent of disorder, with the consequence that the effective nonadiabatic pairing is reduced. Therefore, for an *s*-wave superconductor in the nonadiabatic regime, disorder would reduce T_c, contrary to the expectations of the ME theory [19]. It is remarkable that a T_c reduction under ion irradiation has been recently reported for K_3C_{60} [5].

In summary, we have shown how the breakdown of Migdal's theorem and the opening of nonadiabatic channels identify the fulleride superconductors as nonconventional materials. The physics of such systems is largely governed by nonadiabatic interference effects, which are reflected in the anomalous behavior of observable quantities such as m^*, χ, and T_c. We believe that experiments in this direction are of great importance.

As a concluding remark, we think it interesting to add some considerations of the newly discovered superconductivity at $T_c = 39$ K in MgB_2 [7]. This material has a structure similar to that of GICs, with the boron atoms forming layers of two-dimensional honeycomb lattices. However, contrary to the GICs, the Fermi level crosses the in-plane σ bands, leading to a markedly two-dimensional character of the electronic properties. Moreover, the charge transfer of the intercalated Mg atoms is such that the σ bands are slightly doped with holes and the distance of the Fermi level crossing from the top of the band is only about 0.5 eV [20]. This feature, together with the high phonon frequency ω_{ph} of the boron atoms (up to 0.1 eV), indicates that MgB_2 could be in the nonadiabatic regime of the electron–phonon interaction. An additional interesting

point is that MgB_2 is far away from half-filling; in this case, it has been shown that the vertex corrections are, for the most part, positive, leading to enhanced pairing even in the absence of strong electron correlations [21]. Further analysis of the relevance of this hypothesis is currently under development.

REFERENCES

1. A. B. Migdal, Zh. Éksp. Teor. Fiz. **34**, 1438 (1958) [Sov. Phys. JETP **7**, 996 (1958)].
2. G. M. Eliashberg, Zh. Éksp. Teor. Fiz. **38**, 966 (1960) [Sov. Phys. JETP **11**, 696 (1960)].
3. O. Gunnarsson, Rev. Mod. Phys. **69**, 575 (1997).
4. Y. J. Uemura *et al.*, Nature (London) **352**, 605 (1991).
5. S. K. Watson *et al.*, Phys. Rev. B **55**, 3866 (1997).
6. J. H. Schön, Ch. Kloc, and B. Batlogg, Nature (London) **408**, 549 (2000).
7. J. Nagamatsu, N. Nakagawa, T. Muranaka, *et al.*, Nature (London) **410**, 63 (2001).
8. M. Schluter *et al.*, Phys. Rev. Lett. **68**, 526 (1992); M. Schluter *et al.*, J. Phys. Chem. Solids **53**, 1473 (1992); J. C. R. Faulhaber *et al.*, Phys. Rev. B **48**, 661 (1993); C. M. Varma *et al.*, Science **254**, 989 (1991); V. P. Antropov *et al.*, Phys. Rev. B **48**, 7651 (1993); N. Breda *et al.*, Chem. Phys. Lett. **286**, 350 (1998).
9. M. S. Fuhrer, K. Cherrey, A. Zettl, *et al.*, Phys. Rev. Lett. **83**, 404 (1999).
10. J. P. Carbotte, Rev. Mod. Phys. **62**, 1027 (1990).
11. E. Cappelluti, C. Grimaldi, L. Pietronero, and S. Strässler, Phys. Rev. Lett. **85**, 4771 (2000).
12. C. Grimaldi, L. Pietronero, and S. Strässler, Phys. Rev. Lett. **75**, 1158 (1995).
13. L. Pietronero, S. Strässler, and C. Grimaldi, Phys. Rev. B **52**, 10516 (1995); **52**, 10530 (1995).
14. M. L. Kulic, Phys. Rep. **338**, 1 (2000) and references therein.
15. P. J. Benning *et al.*, Science **252**, 1417 (1991).
16. C. Grimaldi, E. Cappelluti, and L. Pietronero, Europhys. Lett. **42**, 667 (1998).
17. D. Fay and J. Appel, Phys. Rev. B **20**, 3705 (1979); **22**, 1461 (1980).
18. E. Cappelluti, C. Grimaldi, and L. Pietronero, Phys. Rev. B (in press).
19. M. Scattoni, C. Grimaldi, and L. Pietronero, Europhys. Lett. **47**, 588 (1999).
20. J. M. An and W. E. Pickett, Phys. Rev. Lett. **86**, 4366 (2001).
21. A. Perali, C. Grimaldi, and L. Pietronero, Phys. Rev. B **58**, 5736 (1998).

Physics of the Solid State, Vol. 44, No. 3, 2002, pp. 459–460. From Fizika Tverdogo Tela, Vol. 44, No. 3, 2002, pp. 441–442.

PROCEEDINGS OF THE V INTERNATIONAL WORKSHOP "FULLERENES AND ATOMIC CLUSTERS"

(St. Petersburg, Russia, July 2–6, 2001)

A Two-Band Electron–Phonon Model for Superconductivity in Graphite Intercalation Compounds[1]

P. Konsin and B. Sorkin

Institute of Physics, University of Tartu, Tartu, 51014 Estonia

Abstract—A two-band electron–phonon model for superconductivity in graphite intercalation compounds is developed. A new mechanism for the relaxation times due to interband scattering of intraband pairs is proposed for a superconductor with a two-component order parameter. Two distinct relaxation times τ_1 and τ_2 of the order parameters are predicted for C_6K and C_8K. © *2002 MAIK "Nauka/Interperiodica".*

Intercalation under high pressure, up to 50 kbar, has been used to synthesize alkali-metal graphite intercalation compounds (GICs), such as C_6K, C_3K, C_4Na, C_3Na, C_2Na, and C_2Li, with a relatively high metal concentration. It has been established that T_c increases with the metal concentration and reaches 5 K for C_2Na. In order to explain the superconductivity in alkali-metal GICs, it is important to take into account the nature of the electronic bands in these compounds. An alkali metal in GICs acts as a donor; hence there is a charge transfer from the intercalate layer to the host carbon layers, resulting in partially filled overlapping intercalate *s* band and graphite π bands. The fractional part of this electron transfer per intercalant atom, *f*, plays an important role in the electronic properties of GICs.

A few years ago, Jishi [1] proposed a two-band model for superconductivity in C_8K to explain the experimental data available at that time. It was shown that superconductivity is caused by electron–phonon interaction between the *s* band and π band. In this report, we further develop the interband electron–phonon model of superconductivity [2, 3]. The superconducting transition temperature is

$$k_B T_c = 1.14\hbar\omega_D \exp\left\{\frac{-1}{|W|\sqrt{\rho_s\rho_\pi}}\right\}, \qquad (1)$$

where ρ_s and ρ_π are the densities of states at the Fermi surface for the *s* band and π band, respectively, ω_D is the Debye frequency, and *W* is the effective interband electron–phonon interaction. In the case where the values of *f* for C_4Na, C_3Na, and C_2Na are equal to 0.615, 0.60, and 0.54, respectively (in C_8K, $f \approx 0.6$), $\rho = \sqrt{\rho_\sigma\rho_\pi}$ will have the values 1.067G and 1.16G for C_3Na and C_2Na, respectively (G is the effective density of states at E_F for C_4Na). Choosing the Debye temperature $\Theta_D \approx 300$ K and using the experimental value of $T_c = 2.8$ K for C_4Na, we obtain $|W|G \approx 0.208$. Supposing that the values of $|W|$ are the same for C_xNa ($x = 2, 3, 4$), the transition temperature T_c is found to be 5.4 K for C_2Na and 3.7 K for C_3Na, which is in good agreement with the experimental values of 5, 3.5, and 2.8 K found for C_2Na, C_3Na, and C_4Na.

We also derived time-dependent Ginzburg–Landau (GL) equations and calculated the relaxation times τ_1 and τ_2 for the order parameters (gaps):

$$\frac{1}{\tau_{1,2}(\mathbf{k})} = \frac{1}{2}\left(\frac{r_s + \gamma_s'^2 k^2}{\gamma_s} + \frac{r_\pi + \gamma_\pi'^2 k^2}{\gamma_\pi}\right)$$
$$\mp \left[\frac{1}{4}\left(\frac{r_s + \gamma_s'^2 k^2}{\gamma_s} - \frac{r_\pi + \gamma_\pi'^2 k^2}{\gamma_\pi}\right) + \frac{R_s R_\pi}{\gamma_s\gamma_\pi}\right]^{1/2}, \qquad (2)$$

$$\gamma_s'^2 = \frac{\hbar\beta_1}{4m_s\eta_s(0, T)}, \quad \gamma_\pi'^2 = \frac{\hbar\beta_3}{4m_\pi\eta_\pi(0, T)},$$

$$\gamma_{s,\pi} = 4m_{s,\pi}\gamma_{s,\pi}'^2, \qquad (3)$$

$$\eta_{s,\pi}(0, T) = \sum_{\mathbf{k}} \frac{\tanh(\tilde{\varepsilon}_{s,\pi}(\mathbf{k})/2k_BT)}{\tilde{\varepsilon}_{s,\pi}(\mathbf{k})}, \qquad (4)$$

where $\tilde{\varepsilon}_{s,\pi}$ are the electronic energy spectra,

$$\beta_1 = \frac{7\zeta(3)\rho_s p_{sF}^2}{12m_s\pi^2 k_B^2 T_c^2}\chi_{s0}, \quad \beta_3 = \frac{7\zeta(3)\rho_\pi p_{\pi F}^2}{12m_\pi\pi^2 k_B^2 T_c^2}\chi_{\pi 0},$$

$$\chi_{\sigma 0} = \frac{8}{7\zeta(3)}\sum_{n=0}^{\infty}(2n+1)^{-2}\left(2n + 1 + \frac{\xi_{\sigma 0}}{l_\sigma}\right)^{-1},$$

$$\xi_{\sigma 0} = \frac{v_{\sigma F}\hbar}{2\pi k_B T_c},$$

[1] This article was submitted by the authors in English.

1063-7834/02/4403-0459$22.00 © 2002 MAIK "Nauka/Interperiodica"

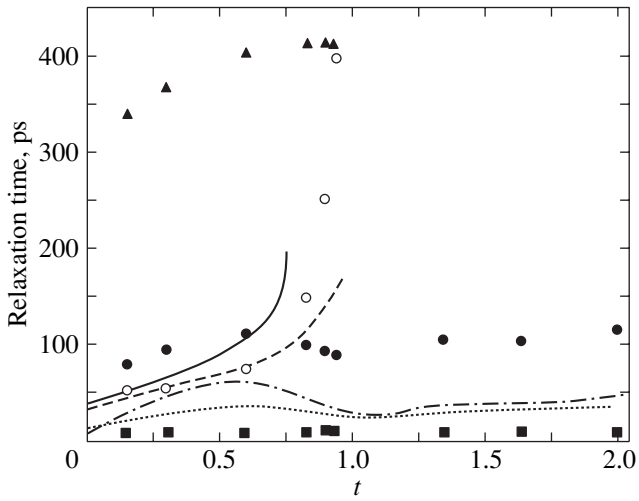

Temperature dependences of the relaxation times: τ_1, C_8K, $k = 0$ (solid line); τ_1, C_8K, $k = 1 \times 10^{-10}$ m^{-1} (dashed line); τ_2, C_8K, $k = 0$ (dashed–dotted line); τ_2, C_8K, $k = 1 \times 10^{-10}$ m^{-1} (dotted line); $\tau_1 \times 10^{-2}$, C_6K, $k = 0$ (open circles); τ_1, C_6K, $k = 1 \times 10^{-10}$ m^{-1} (solid triangles); τ_2, C_6K, $k = 0$ (solid squares); and $\tau_2 \times 10^{-1}$, C_6K, $k = 1 \times 10^{-10}$ m^{-1} (solid circles).

$r_{s,\pi}$ and $R_{s,\pi}$ are the linearization coefficients of the GL equations in the two-band model [2], the quantities l_σ ($\sigma = s, \pi$) are the electron mean free paths, $v_{\sigma F}$ and $p_{\sigma F}$ are the Fermi velocities and momenta, k is the wave vector in the spatially inhomogeneous case (involved in the gradient term of the GL equation), and $\zeta(3) = 1.202$. The quantity $\chi_{\sigma 0}$ takes into account the intraband impurity s-wave scattering of electrons. We obtain the following values of parameters for C_8K: $T_c = 0.134$ K, $l_s = 400$ Å, $l_\pi = 5030$ Å, $\xi_{s0} = 4.6 \times 10^4$ Å, $\xi_{\pi 0} = 8 \times 10^4$ Å, $m_s = 1.615 m_0$, and $m_\pi = 0.25 m_0$. For C_6K, we obtain $T_c = 1.5$ K, $l_s = 340$ Å, $l_\pi = 560$ Å, $\xi_{s0} = 4000$ Å, $\xi_{\pi 0} = 7000$ Å, $m_s = m_0$, and $m_\pi = 0.25 m_0$. The calculated relaxation times τ_1 and τ_2 for C_8K and C_6K are given in the figure. As can be seen from the figure, the relaxation time τ_2 as a function of the temperature $t = T/T_c$ does not show a critical behavior, just as is the case for cuprates (for K_3C_{60} and Rb_3C_{60}, see [4]).

ACKNOWLEDGMENTS

This work was supported by ESF, grant no. 3874.

REFERENCES

1. R. Al-Jishi, Phys. Rev. B **28** (1), 112 (1983).
2. P. Konsin, Phys. Status Solidi B **189** (1), 185 (1995).
3. P. Konsin and B. Sorkin, Phys. Rev. B **58** (9), 5795 (1998).
4. S. B. Fleisher, B. Pevzner, D. J. Dougherty, *et al.*, Phys. Rev. B **62** (2), 1366 (2000).

Physics of the Solid State, Vol. 44, No. 3, 2002, pp. 461–462. Translated from Fizika Tverdogo Tela, Vol. 44, No. 3, 2002, pp. 443–444.

PROCEEDINGS OF THE V INTERNATIONAL WORKSHOP "FULLERENES AND ATOMIC CLUSTERS"

(St. Petersburg, Russia, July 2–6, 2001)

Interaction of Polymers with Fullerene C_{60}

E. V. Anufrieva, M. G. Krakovyak, T. D. Anan'eva, T. N. Nekrasova, and R. Yu. Smyslov

Institute of Macromolecular Compounds, Russian Academy of Sciences, Bol'shoĭ pr. 31, St. Petersburg, 199004 Russia
e-mail: polar@mail.macro.ru

Abstract—The fundamentals of the method for estimating the fullerene-binding power of polymer macromolecules and supramolecular formations are developed for fullerene C_{60}. Polymers with covalently attached anthracene groups (one group per macromolecule) whose luminescence decreases in the presence of fullerene in solution in direct proportion to the stability of the fullerene–polymer complex are used. The effect of the anthracene mark on the fullerene-binding power of a luminescent-marked polymer is taken into account or discarded on the basis of an analysis of the interaction between fullerene and low-molecular models of luminescent marks. © *2002 MAIK "Nauka/Interperiodica".*

1. The interaction of fullerene with a polymer and the duration of fullerene–polymer intermolecular contacts may play a significant role in the modification of properties of polymer systems through the addition of fullerene C_{60}. The conditions determining the duration of fullerene–polymer contacts were studied using polymers with covalently attached emitting oscillators that can transfer electron excitation energy to the fullerene. The electron excitation energy transfer takes place for a certain mutual arrangement of interacting molecules, which is achieved when the duration of contact between molecules is sufficient for matching. For an oscillator covalently attached to a polymer, the duration of its contact with fullerene is determined by the interaction of the carrier polymer with fullerene. For example, information on the interaction between fullerene and the carrier polymer can be obtained from the change in the luminescence intensity of an emitting covalently attached oscillator in the presence of fullerene.

The solution of the problem formulated above required the development of methods for synthesizing polymers and polymer systems with a covalently attached emitting oscillator of the same chemical structure. For this purpose, oscillators of anthracene groups in anthracene-containing polymers (one mark per 700–1000 links) and in low-molecular anthracene-containing models of luminescent marks were used as emitting oscillators [1].

2. We studied the ability of fullerene to quench the luminescence of anthracene-containing molecules (low-molecular models or marked polymers) in solution. The luminescence intensity of the solution under investigation was measured on an LS-100 luminescence spectrophotometer (PTI, Canada) at a wavelength of 440 nm with an excitation wavelength of 365 nm. The fullerene concentration c_{ful} was varied from 0 to 0.02 mg/ml and the concentration of the marked polymer was 1 mg/ml. As the fullerene concentration in the solution increased, the intensity of exciting light (365 nm) decreased due to its absorption by fullerene, which was determined from the change in the optical density of the solution.

We analyzed the dependence of I^{red}/I_0 on the fullerene concentration c_{ful} in the solution (I_0 is the luminescence intensity of the solution in the absence of fullerene and I^{red} is the luminescence intensity of the solution in the presence of fullerene, which was determined taking into account the effect of fullerene on the optical density of the solution) for all the studied solutions of low-molecular luminescent models of marks and marked polymers. We determined the luminescence quenching parameters $\chi^{lm} = (1 - I^{red}/I_0)^{lm} \times 100$ for low-molecular models of marks and $\chi^{pol} = (1 -$

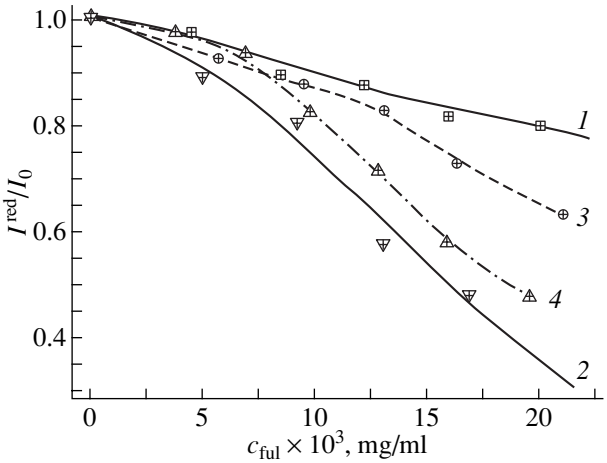

Dependence of I^{red}/I_0 on c_{ful} in a DMFA solution containing the following polymers: (*1*) PMMA, (*2*) PMMA in a stereopolycomplex, (*3*) poly(*N*-vinylpyrrolidone), and (*4*) poly(*N*-vinyl caprolactam).

1063-7834/02/4403-0461$22.00 © 2002 MAIK "Nauka/Interperiodica"

Parameter $\Delta\chi^{pol}$ characterizing the interaction of C_{60} with PMMA in various solvents and with polymers having a varying chemical structure in DMFA for c_{ful} = 0.02 mg/ml

Polymer	$\Delta\chi^{pol}$	Solvent
Poly(methyl methacrylate)	4	Toluene
	37	Toluene–octane (17%)
	4	DMFA
Poly(methyl methacrylate) (78% syndiotriad)	8	DMFA
Poly(methyl methacrylate) (97% isotriad)	2	DMFA
Poly(styrene)	20	DMFA
Poly(*N*-methacryloyl-orthoaminobenzoic acid)	19	DMFA
Poly(*n*-phenoxyphenyl methacrylamide)	49	DMFA
Poly(*N*-vinylpyrrolidone)	15	DMFA
Poly(*N*-vinyl caprolactam)	33	DMFA

$I^{red}/I_0)^{pol} \times 100$ for marked polymers with c_{ful} = 0.02 mg/ml, as well as the polymer contribution $\Delta\chi^{pol} = \chi^{pol} - \chi^{lm}$. The value of $\Delta\chi^{pol}$ characterizes the increase in quenching efficiency associated with the interaction of the fullerene and the anthracene group of the polymer carrier chain.

We used solvents such as toluene, dimethylformamide (DMFA), and toluene–octane and toluene–methanol mixtures.

3. The dependences of I^{red}/I_0 on the fullerene concentration c_{ful} in a solution for luminescent-marked polymers (curves *1*, *3*, *4*) and a stereopolycomplex (curve *2*) are presented in the figure. These curves are used for determining the parameter $\Delta\chi^{pol}$ characterizing the interaction of C_{60} with the polymer carrier chain of the anthracene group for all polymers and polymer systems under investigation.

An analysis of the values of $\Delta\chi^{pol}$ presented in the table for poly(methyl methacrylate) (PMMA) shows an increase in the value of $\Delta\chi^{pol}$ upon a transition from toluene (thermodynamically good solvent) to a mixture of toluene with 17% octane (thermodynamically poor solvent).

It follows from the data contained in the table that polymers with aromatic rings [such as poly(*n*-phenoxyphenyl methacrylamide), poly(styrene), and poly(*N*-methacryloyl-aminobenzoic acid)] bind C_{60} better than polymers without aromatic groups (PMMA). The results obtained for poly(*N*-vinyl amide) in DMFA indicate a higher fullerene-binding power for poly(*N*-vinyl caprolactam) as compared to poly(*N*-vinylpyrrolidone).

The results obtained for the fullerene-binding power of polymer chains in interpolymer complexes and stereopolycomplexes proved interesting. It turned out that, for all polymers included in a supramolecular compound, the values of $\Delta\chi^{pol}$ increase for every component constituting a polycomplex. The component of the polycomplex under investigation was singled out by a luminescent mark. For example, the value of $\Delta\chi^{pol}$ for poly(methacrylic acid) included in the interpolymer complex in DMFA increases from 14 to 24, while the value of $\Delta\chi^{pol}$ for isotactic PMMA included into the stereopolycomplex with syndiotactic PMMA changes from 4 to 42. The increase in the value of $\Delta\chi^{pol}$ in polycomplexes indicates the role played by double-stranded formations in the increase in the number of contacts between polymer chains and fullerene.

Thus, new data indicating methods and ways of increasing the fullerene-binding power of polymers have been obtained on the basis of the method proposed in this communication.

REFERENCE

1. E. V. Anufrieva and Yu. Ya. Gotlib, Adv. Polym. Sci. **40**, 1 (1981).

Translated by N. Wadhwa

Physics of the Solid State, Vol. 44, No. 3, 2002, pp. 463–466. From Fizika Tverdogo Tela, Vol. 44, No. 3, 2002, pp. 445–448.

PROCEEDINGS OF THE V INTERNATIONAL WORKSHOP "FULLERENES AND ATOMIC CLUSTERS"

(St. Petersburg, Russia, July 2–6, 2001)

Complete Characterization of an $(Sb_2O_3)_n$/SWNT Inclusion Composite[1]

S. Friedrichs*, R. R. Meyer, J. Sloan*, A. I. Kirkland**, J. L. Hutchison***, and M. L. H. Green***

** Wolfson Catalysis Centre (Carbon Nanotechnology Group), Inorganic Chemistry Laboratory, Oxford OX1 3QR, UK*
*** Department of Materials Science, Cambridge CB2 3QZ, UK*
**** Department of Materials, Oxford OX1 3PH, UK*

Abstract—The detailed inclusion crystallography of a one-dimensional valentinite Sb_2O_3 crystal incorporated within a helical (21, –8) single-walled carbon nanotube (SWNT) was identified from a phase image that was recovered via a modified object wave restoration scheme. A detailed analysis of asymmetric fringe contrast in the tube walls provided strong evidence for the chiral sense of the tube itself. Due to the good agreement of the observed wall periodicity with the determined absolute focus values and power spectra obtained from single-pixel line traces along both tube walls, we were able to determine the chiral sense of the SWNT and the tilt angle of the Sb_2O_3/SWNT composite relative to the electron beam. The angle between the optimum $\langle 10\bar{1} \rangle$ viewing direction of the crystal fraction and the tube axis, which is aligned with the $\langle 4\bar{1}2 \rangle$ direction of the Sb_2O_3 crystal, is 78.3°. Since small deviations from this viewing direction make an insignificant difference to the observed contrast, a tube inclination of 15° is plausible for both the Sb_2O_3 crystal and the assigned (21, –8) SWNT, which is the mirror image of a (13, 8) SWNT. © *2002 MAIK "Nauka/Interperiodica".*

A modified object wave restoration scheme was used to recover the phase image of an Sb_2O_3 valentinite nanocrystal encapsulated within a single-walled carbon nanotube (SWNT) [1]. Within the nanocrystal, the atomic thickness in the projection of individual antimony columns was determined and a substantial lattice contraction of the crystal along the tube axis was observed. For the first time, a detailed analysis of asymmetric fringe contrast in tube walls has provided strong evidence for the chiral conformation of the nanotube itself.

SWNTs were produced using a metal catalyzed arc synthesis similar to the method previously reported in [2] and filled using Puratonic Sb_2O_3 (ALFA, 99.999%) according to the capillary technique described in [3]. The product mixture was ground, dispersed in Analar pentane, placed onto a holey carbon support film, and examined at 300 kV in a JEOL JEM-300F field emission gun transmission electron microscope (FEGTEM). The chemical identity of the filling material was confirmed using an energy dispersive x-ray microanalysis system (LINK "ISIS"). High-resolution transition electron microscopy simulations, giving the complex wave function of the previously modeled objects, were performed using a standard multislice algorithm [4, 5] utilizing a code provided by Kirkland [6]. Atomic coordinates for (n, m) nanotubes were generated by mapping the strip $\{\mathbf{r}|0 \le \mathbf{r} \cdot \mathbf{C}_h < |\mathbf{C}_h|^2\}$ of a planar hexagonal graphene lattice (with a carbon–carbon distance d_{C-C} = 1.44 nm and lattice vectors $\mathbf{a}_1$, $\mathbf{a}_2$) onto a cylinder surface (Fig. 1). The integers (n, m) with $n > 0$ and $-n/2 < m \le n$ [7] uniquely define the structure of the nanotube via the chiral vector $\mathbf{C}_h = n\mathbf{a}_1 + m\mathbf{a}_2$ [8]. The special cases $(n, 0)$ and (n, m) represent the nonchiral zigzag and armchair configurations, respectively, while all other (n, m) nanotubes are chiral, with $(n + m, -m)$ being the mirror image of (n, m).

The coordinates for the encapsulated Sb_2O_3 crystal were initially determined from a crystal fragment generated from the published valentinite structure of Sb_2O_3 [9].

Figure 1 illustrates the relationship between the observed wall periodicity, nanotube conformation, and tilt angle β for structure models and corresponding simulations of SWNTs with diameters close to that of the imaged SWNT 1.45 nm in diameter, i.e., for a (10, 10) armchair SWNT (Fig. 1a), an (18, 0) zigzag SWNT (Fig. 1b), and a chiral (21, –8) SWNT (Fig. 1c).

The illustration shows that the center-to-center spacings will not be resolvable in the armchair case, as the carbon separation is only 0.125 nm in projection and this distance will be reduced further as the tubule is tilted with respect to the image plane, causing the carbon atoms to stagger in projection. In the case of an untilted zigzag tubule (Fig. 1b), both carbon walls are

[1] This article was submitted by the authors in English.

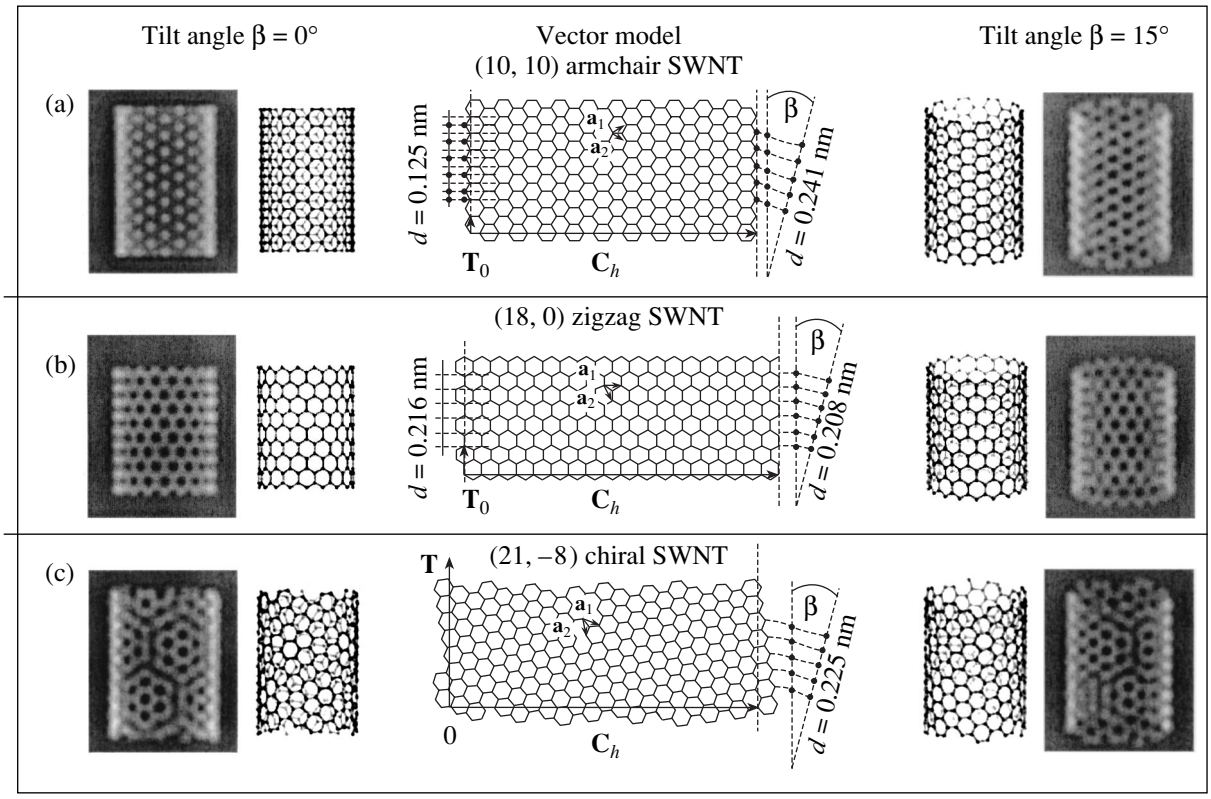

Fig. 1. Schematic illustration of the observable resolution of SWNT walls, depending on the their classification and the tilt angle β. The visible appearance of carbon–carbon spacings in the walls of a (10, 10) armchair, an (18, 0) zigzag, and a (21, –8) chiral tube are explained, respectively. The middle column shows the unrolled honeycomb lattice of a nanotube, illustrating the chiral vector $\mathbf{C}_h$ and the translation vector $\mathbf{T}$, which define the rolling of the graphene sheet to give a nanotube of a specific classification and diameter ($\mathbf{T}[(10, 10)] = (1, -1)$, $\mathbf{T}[(18, 0)] = (1, -2)$, $\mathbf{T}[(21, -8)] = (5, -34)$). $\mathbf{a}_1$ and $\mathbf{a}_2$ are the unit vectors. The rectangle bounded by the thin dashed lines and the chiral vector marks the unit cell (note: the unit cell of the (21, –8) SWNT is only partially displayed). The columns adjacent to the illustrated graphene sheet display modeled fractions of the SWNTs parallel to the image plane (i.e., tilt angle β = 0°; left column) and tilted by β = 15° out of the image plane (right column). The two outer columns show simulated phase images of the displayed models.

clearly visible as they have a separation of 0.216 nm in projection (Fig. 1b, left panel). As the tubule is tilted, the simulated wall spacings smear as the carbon zigzags start to stagger in projection. For both nonchiral tubules, the contrast will still be equal on both walls as the tube is tilted. A chiral tube (e.g., Fig. 1c), however, will display a resolvable contrast on one tube wall if the difference $\delta = |\alpha \pm \beta|$ is small, where $\alpha = \angle(\mathbf{C}_h, \mathbf{a}_1) = \arctan(\sqrt{3}\,m/(2n + m))$ is the chiral angle and the angle β is the tilt angle between the tube axis and the image plane. β is defined as positive if the top end of the tube is above the plane, as for this specimen.

Figure 2a shows the restored phase image of a 1.45-nm-diameter SWNT containing an encapsulated single crystal of Sb_2O_3, for each of which an individual absolute defocus level was determined independently. Recombination of the absolute defocus levels along the tube revealed that the imaged composite is inclined by a tilt angle of $\beta = 17° \pm 5°$ with respect to the image plane, with the top end of the tube being higher in the beam path.

The phase image in Fig. 2a displays a periodic lattice spacing of 0.224 ± 0.04 nm along the right wall of the SWNT, whereas the contrast variations on the left wall are effectively random. The observed periodic spacing on the right wall corresponds to the center-to-center spacing ($1.5d_{C-C} = 0.216$ nm) between neighboring zigzag rows of carbon atoms in the SWNT wall lattice when viewed in projection. This indicates that the imaged tube is chiral with a negative chiral angle α and, hence, a negative integer m. As the number of atoms in projection on the tube wall is small, a strong contrast will be visible for values of δ of up to 10° and the observed spacing will be given by $1.5d_{C-C}\cos\beta/\cos\alpha$, as we can see for the modeled (21, –8) SWNT in Fig. 1c.

The phase image and corresponding line profiles in Fig. 2a can best be matched to an approximate $\langle 10\bar{1} \rangle$ projection through a fragment of Sb_2O_3 derived from the orthorhombic polymorph valentinite form, which consists of infinite double chains of SbO_3 units, as

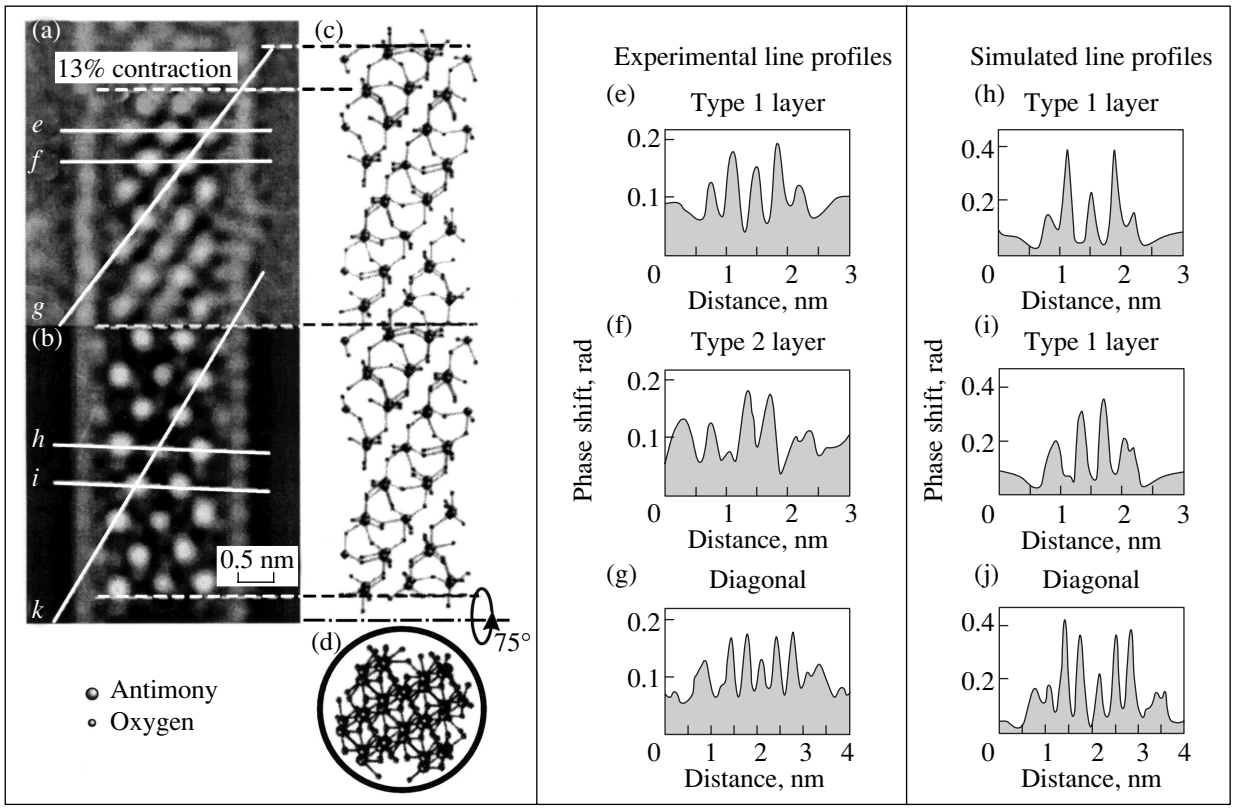

Fig. 2. Composite diagram showing (a) the experimental restored phase image, (b) the simulated phase image, and the structural model (c) in the observed orientation and (d) in end-on view. The white lines mark single-pixel line profiles through the experimental phase image (e–g) and through the simulated phase image (h–j).

opposed to the cubic senarmontite form consisting of molecular units of Sb_4O_6 [10]. The proposed structure model is shown in Fig. 2c, and an end-on view of the Sb_2O_3/SWNT composite is shown in Fig. 2d. A corresponding simulated phase image is given in Fig. 2b.

The white spots in the reconstructed phase correspond to projection through atomic columns of antimony only. The oxygen sublattice could not be resolved due to the weak scattering properties of oxygen atoms, their staggered positions in projection, and the limited resolution (*ca*. 0.16 nm) present in the restoration. Comparison of multislice simulations of the restored phase of Sb_2O_3 lattice fractions of appropriate thickness with equivalent simulated antimony sublattice fractions confirmed that the phase contrast due to the oxygen sublattice is negligible compared to that due to the antimony sublattice.

In the bulk valentinite structure, the Sb_2O_3 double chains run parallel to $\langle 0\,0\,1\rangle$, with each antimony atom being coordinated by three oxygen atoms and each Sb of the infinite SbO_3 chains being bridged by a shared oxygen [9]. In the case of the encapsulated crystal, the $\langle 4\bar{1}2\rangle$ direction of the Sb_2O_3 crystal is aligned along the tube axis, which has a tilt angle of 78.3° with respect to the optimum $\langle 10\bar{1}\rangle$ viewing direction. Small deviations from this viewing direction make an insignificant difference to the observed contrast; as a result, a tube inclination of 15° was used for the simulated object (Fig. 2b) in order to account for the observed contrast within the tube wall. The same inclination angle was applied to the model shown in Fig. 2c.

The repeating structural motif of the imaged encapsulated Sb_2O_3 crystal can be described as a repeating sequence of a layer (type 1 layer) containing three columns of antimony atoms followed by a layer (type 2 layer) containing two columns of antimony atoms arranged perpendicular to the tube axis. In the structure model, we assume the coordination appropriate for the bulk valentinite structure. Within each type 1 or type 2 layer, the intensities of the peaks corresponding to individual Sb columns vary in a complex fashion. The line profile across a type 1 layer shows a stacking pattern of 3–2–3 Sb atoms in projection (Fig. 2e). By contrast, the line profile across a type 2 layer gives two peaks of equal intensity (Fig. 2f), approximately equivalent to the higher peak within the type 1 layer, indicating Sb columns three atoms in thickness. These observations lead to a modeled Sb_2O_3 crystal fragment that has

sequences of 3–2–3 and 3–3 layers with a fourfold repeat period along the $\langle 4\bar{1}2\rangle$ direction (Fig. 2c).

Comparison with the equivalent line profiles through the simulated image supports the interpretation of the observed Sb_2O_3/SWNT composite.

Since the oxygen sublattice could not be resolved, the oxygen coordination is predicted from the bulk valentinite structure. In order to fit the modeled Sb_2O_3 crystal into the 1.45-nm-diameter SWNT, some oxygen atoms on the surface of the crystal were omitted. This can be justified in terms of the reduction in coordination expected at the Sb_2O_3/SWNT interface (cf. 2×2 and 3×3 KI crystals formed within SWNT [11, 12]).

The multislice simulation in Fig. 2b also shows a weak contrast close to the tube walls, indicating the presence of single-atom columns at the edge of the encapsulated valentinite crystal fragment, as is visible in Fig. 2c. The corresponding experimental phase image also shows evidence for there being additional weak peaks at some of these sites, possibly caused by individual Sb atoms. However, the intensities of these peaks are sufficiently close to the background noise levels; as a result, it is impossible to definitely assign these contrasts to such single atoms without a more accurate analysis of the phase shift.

Significant lattice distortions were observed in the Sb_2O_3 crystal encapsulated within the (21, –8) SWNT. In comparison with the bulk structure of valentinite, the encapsulated crystal shows a longitudinal contraction of 13% along the $\langle 4\bar{1}2\rangle$ axis. This contraction occurs in a similar fashion but is relatively larger than that which we reported for the SWNT-encapsulated Kl 3×3 crystal [11]. Direct lattice measurements from line traces show an average spacing of ~0.552 nm between two type 1 layers or two type 2 layers, respectively, whereas in the simulated phase image (based on the Sb positions in bulk valentinite), equivalent layers are spaced at average intervals of ~0.638 nm. The observed lattice contraction may be caused by an interaction between the Sb_2O_3 crystal and the SWNT walls and may be partially caused by the reduction in coordination at the Sb_2O_3/SWNT interface.

ACKNOWLEDGMENTS

We acknowledge the Petroleum Research Fund, administered by the American Chemical Society (grant no. 33765-AC5), the EPSRC (grant nos. GR/L59238, GR/L22324), and Colebrand Ltd. for financial support. S.F. is indebted to BMBF and Fonds der Chemischen Industric for additional financial support. J.S. is indebted to the Royal Society.

We thank the Department of Materials Science and Metallurgy, Cambridge, for the provision of computational facilities.

REFERENCES

1. S. Friedrichs, R. R. Meyer, J. Sloan, *et al.*, Phys. Rev. B (in press).
2. C. Journet, W. K. Maser, P. Bernier, *et al.*, Nature (London) **388**, 756 (1997).
3. J. Sloan, D. M. Wright, H.-G. Woo, *et al.*, Chem. Commun., 699 (1999).
4. J. M. Cowley and A. F. Moodie, Acta Crystallogr. **10**, 609 (1957).
5. P. Goodman and A. F. Moodie, Acta Crystallogr. A **30**, 280 (1974).
6. E. J. Kirkland, in *Advanced Computing in Electron Microscopy* (Plenum, New York, 1998).
7. The lower limit for *m* used here differs from the definition given in [8], to ensure that the chiral angle α lies in the range $-30° < \alpha \leq 30°$.
8. R. Saito, C. Dresselhaus, and M. S. Dresselhaus, *Physical Properties of Carbon Nanotubes* (Imperial College Press, London, 1998).
9. C. Svensson, Acta Crystallogr. B **30**, 458 (1974).
10. C. Svensson, Acta Crystallogr. B **31**, 2016 (1975).
11. R. R. Meyer, J. Sloan, R. E. Dunin-Borowski, *et al.*, Science **289**, 1324 (2000).
12. If the K and I atoms are superposed in projection as in the case of a crystal viewed along $\langle 100\rangle$, for example, then the resulting image contrast from both columns is summed in projection as we reported for a 2×2 KI crystal formed inside a SWNT; J. Sloan *et al.*, Chem. Phys. Lett. **329**, 61 (2000).

Physics of the Solid State, Vol. 44, No. 3, 2002, pp. 467–469. Translated from Fizika Tverdogo Tela, Vol. 44, No. 3, 2002, pp. 449–451.

PROCEEDINGS OF THE V INTERNATIONAL WORKSHOP "FULLERENES AND ATOMIC CLUSTERS"

(St. Petersburg, Russia, July 2–6, 2001)

The Density of States for Carbon Nanotubes in a Uniform Magnetic Field

V. A. Geyler, O. G. Kostrov, and V. A. Margulis

Mordovian State University, ul. Bol'shevistskaya 68, Saransk, 430000 Russia
e-mail: geyler@mrsu.ru
e-mail: kostrovog@mrsu.ru
e-mail: margulis@mrsu.ru

Abstract—Dispersion laws for carbon nanotubes in a uniform magnetic field are obtained in an explicit form in a zero-range-potential model. The band structure of the spectrum is studied, and the density of states is calculated numerically. *© 2002 MAIK "Nauka/Interperiodica".*

The band structure of the energy spectrum of a carbon nanotube in a magnetic field was studied in [1, 2] in the tight-binding approximation. On the other hand, the theory of condensed matter also makes use of a zero-range-potential model [3]; in particular, this model is successfully employed in studies of the transport properties of quasi-one-dimensional systems [4]. The present paper uses this model to study the one-electron energy spectrum of carbon nanotubes in a uniform magnetic field **B** and investigates their density of states numerically. We consider the same field range as in [1, 2].

The Hamiltonian of the system can be written as

$$H = \frac{1}{2m_e}\left(\mathbf{p} - \frac{e}{c}\mathbf{A}\right)^2 + \alpha \sum_{\gamma \in \Gamma} V_\gamma, \qquad (1)$$

where $\mathbf{A} = \mathbf{B} \times \mathbf{r}/2$ is the vector potential of the field $\mathbf{B} = B\mathbf{e}_z$, Γ is the atomic chain of the nanotube, V_γ is the atom confinement potential, and α is the coupling constant determined by the scattering length l_s, namely, $\alpha = 2\pi\hbar^2 m_e^{-1} l_s$. In the gauge chosen, we have

$$V_\gamma = \delta(\mathbf{r}_\gamma)\left[r_\gamma \frac{\partial}{\partial r_\gamma} + 1 - \pi i \Phi^{-1} \mathbf{B}(\mathbf{r} \times \boldsymbol{\gamma})\right],$$

where $\Phi = 2\pi\hbar c/|e|$ is the magnetic flux quantum and $\mathbf{r}_\gamma = \mathbf{r} - \boldsymbol{\gamma}$. The Green's function for H can be found explicitly [5]:

$$G(\mathbf{r}, \mathbf{r}'; E) = G_0(\mathbf{r}, \mathbf{r}', E) - \sum_{\gamma, \gamma' \in \Gamma} [Q(E) + \alpha^{-1}]^{-1}_{\gamma\gamma'} G_0(\mathbf{r}, \gamma; E) G_0(\gamma', \mathbf{r}', E). \qquad (2)$$

Here, $G_0(\mathbf{r}, \mathbf{r}'; E)$ is the Green's function for a free electron in the magnetic field (see [5]) and $Q(E)$ is an infinite matrix, whose elements are defined as

$$Q_{\gamma, \gamma'}(E) = \begin{cases} G_0(\gamma, \gamma'; E), & \gamma \neq \gamma' \\ \dfrac{m_e}{2\sqrt{2}\pi\hbar^2 l_B} \zeta\left(\dfrac{1}{2}; \dfrac{1}{2} - \dfrac{E}{\hbar\omega_c}\right), & \gamma = \gamma'. \end{cases} \qquad (3)$$

Here, $\zeta(x; s)$ is the generalized Riemann ζ function, l_B is the magnetic length, and ω_c is the cyclotron frequency. Let Λ and Ω denote the Bravais lattice and the unit cell for Γ respectively; obviously enough, Λ consists of sites of the type $m\mathbf{a}$, with $m \in Z$.

The state of a free electron in a uniform magnetic field is fully described by three quantum numbers, namely, n (the Landau level number), y_0 (the ordinate of the cyclotron orbit center), and p_z (the momentum projection on the field direction); in the gauge chosen here, we have $y_0 = -cP_x/eB$, where $\hat{P}_x = \hat{p}_x + eBy/2m_e$ is the gauge-invariant generalized momentum. To describe the electron states in the nanotube, one has to impose Bloch magnetic constraints on the wave function while taking into account, that in the free-electron case, a translation by a vector parallel to **a** leaves only the linear combination $a_x P_x + a_z p_z$ unchanged. One may now conveniently introduce a dimensionless parameter $p = (2\pi\hbar)^{-1}(a_x P_x + a_z p_z)$ and denote $s = (2\pi\hbar)^{-1}|\mathbf{e}_x|P_x$ for $\mathbf{B} \parallel \mathbf{a}$ and $s = (2\pi\hbar)^{-1}|\mathbf{e}_z|P_x$ otherwise. Clearly enough, in describing a free electron, one may use p and s in place of the pair of numbers y_0 and p_z. In the nanotube potential, a translation by a vector $m\mathbf{a}$ characterizing the Bravais lattice Λ preserves p to within an integer. For this reason, we define the magnetic Brillouin zone Z_B as a closed interval $[-1/2, 1/2]$. In this case, in describing the electron state in a nanotube, we shall

1063-7834/02/4403-0467$22.00 © 2002 MAIK "Nauka/Interperiodica"

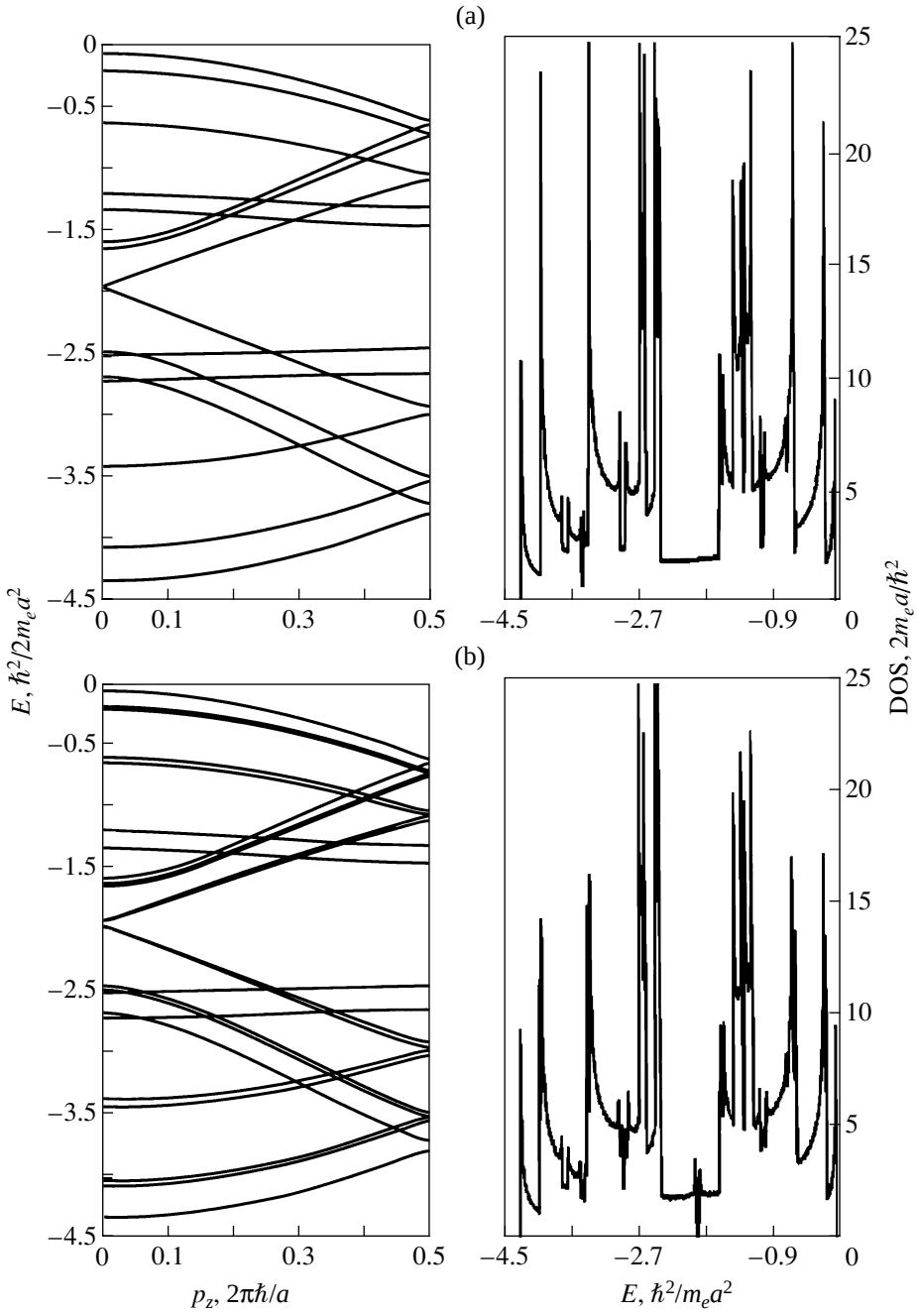

Fig. 1. Dispersion relations and the density-of-states function of the (6, 0) zigzag structure constructed for the cases of (a) zero and (b) nonzero external magnetic fields (for the same field range as in [1]).

have to use, in place of p, the quasi-momentum q from Z_B and an integer j, which is the number of the magnetic Bloch band.

The electronic spectrum in a nanotube for a fixed quasi-momentum depends essentially on the direction of field **B**. Indeed, if the field is parallel to the tube, the field completely quantizes the electron motion in the plane perpendicular to the tube, so that the free-electron spectrum for a fixed quasi-momentum q is purely point-like and consists of infinity-fold degenerate levels $E_{nj}(q) = \hbar\omega_c(n + 1/2) + 2\pi\hbar^2(q + j)^2/m_e a^2$ (s plays here the part of the degeneracy parameter). If the field and the tube are not parallel to each other, the projection of the free-motion momentum along the z axis on the plane perpendicular to the tube axis is nonzero. Therefore, the free-electron spectrum for a fixed q is continuous, $E_n(s) = \hbar\omega_c(n + 1/2) + 2\pi\hbar^2 s^2/m_e \mathbf{e}_z^2$, does not depend on q, and is degenerate in j. In the presence of the nanotube potential, the levels are broadened into

magnetic Bloch bands, which can be determined from the dispersion relation

$$\det[\tilde{Q}(q; E) + \alpha^{-1}] = 0, \quad (4)$$

where $\tilde{Q}(q; E)$ is a finite matrix whose elements are indexed by sites κ and κ' of Ω:

$$\tilde{Q}_{\kappa\kappa'}(q; E) = \sum_{m=-\infty}^{\infty} \exp[\pi i e m \mathbf{B}(\kappa \times \mathbf{a})/\hbar c] \times Q_{m\mathbf{a}+\kappa, \kappa'}(E) e^{-imq}. \quad (5)$$

As follows from Eq. (4), the number of bands which can split off from each level (in the **B** || **a** case) or, otherwise, from the continuum cannot be more than N, where N is the number of sites in Ω. Because the free-electron spectrum for a fixed quasi-momentum is infinity-fold degenerate, the spectrum of the perturbed operator H consists of a ray $[\hbar\omega_c/2, \infty]$ and of a finite number of bands lying below $\hbar\omega_c/2$; these bands can overlap with one another and with the above-mentioned ray. Thus, the number of gaps in the spectrum does not exceed N.

For the (6, 0) zigzag structure, Fig. 1 shows the lower branches of the dispersion relations, which were constructed by numerically solving Eq. (4), as well as the density of states for the same energy range. A comparison with the zero-field case reveals branch splitting, which accounts for the formation of magnetic subbands. This gives rise to additional van Hove-type singularities arising in the density-of-states function. Note that the density-of-states functions and the dispersion relations are in good agreement with the results [1, 2] obtained in the tight-binding approximation.

ACKNOWLEDGMENTS

This work was supported by the Russian Foundation for Basic Research (project no. 01-02-16564), the "Universities of Russia" Program (project no. 015.01.01.049), DFG (project no. 436 RUS 113/572), and INTAS (project no. 00-257).

REFERENCES

1. S. Roche, G. Dresselhaus, M. S. Dresselhaus, and R. Saito, Phys. Rev. B **62**, 16092 (2000).
2. R. Saito, C. Dresselhaus, and M. S. Dresselhaus, *Physical Properties of Carbon Nanotubes* (Imperial College Press, London, 1998).
3. Yu. N. Demkov and V. N. Ostrovskiĭ, *Zero-Range Potentials and Their Applications in Atomic Physics* (Leningr. Gos. Univ., Leningrad, 1975; Plenum, New York, 1988).
4. V. A. Geyler, V. A. Margulis, and L. I. Filina, Zh. Éksp. Teor. Fiz. **113**, 1376 (1998) [JETP **86**, 751 (1998)].
5. S. Albeverio, V. A. Geyler, and O. G. Kostrov, Rep. Math. Phys. **44** (1), 13 (1999).

Translated by G. Skrebtsov

Physics of the Solid State, Vol. 44, No. 3, 2002, pp. 470–472. From Fizika Tverdogo Tela, Vol. 44, No. 3, 2002, pp. 452–454.

PROCEEDINGS OF THE V INTERNATIONAL WORKSHOP "FULLERENES AND ATOMIC CLUSTERS"

(St. Petersburg, Russia, July 2–6, 2001)

Signatures of Irradiation-Induced Defects in Scanning-Tunneling Microscopy Images of Carbon Nanotubes[1]

A. V. Krasheninnikov [1, 2] and K. Nordlund [2]

[1] *Moscow State Engineering Physics Institute (Technical University), Kashirskoe sh. 31, Moscow, 115409 Russia*
[2] *Accelerator Laboratory, University of Helsinki, Helsinki, FIN-00014 Finland*

Abstract—Using empirical-potential and tight-binding models, we study the structure and stability of irradiation-induced atomic-scale defects in the walls of carbon nanotubes. We model the temporal evolution of such defects and calculate their lifetimes at various temperatures. We also simulate scanning-tunneling microscopy (STM) images of irradiated nanotubes with such defects. Our simulations indicate that, at low temperatures, the defects live long enough to be detected by STM and that different defects manifest themselves in STM images in different ways, which allows one to distinguish the defects experimentally. *© 2002 MAIK "Nauka/Interperiodica".*

Recently, numerous experimental and theoretical studies on carbon nanotubes (NTs) have demonstrated the possibilities of developing carbon-based electronics [1, 2]. However, implementation of even the simplest electronic devices demands a thorough understanding of the structural and electronic properties not only of perfect NTs but also of NTs with various defects. Moreover, recent experiments [3] indicate that defects in NTs can be used to fabricate an intratube quantum-dot device. Thus, the methodological development of such electronic NT-based devices requires that one knows what defects are involved and how they can be produced.

Inasmuch as irradiation of NTs potentially makes it possible to create defects in a controllable way, the effects of electron [4, 5] and ion [6–8] irradiation on the structural and electronic properties of NTs are of particular interest. However, the behavior of irradiation-induced defects, as well as their experimental detection, is still an open question.

In this paper, we study the stability and temporal evolution of irradiation-induced defects in single-walled NTs and simulate scanning-tunneling microscopy (STM) images of irradiated NTs with such defects.

1. THE SIMULATION METHOD

The method used in this study has been described in detail in other publications [7, 9–11]; therefore, only a brief description is given here.

We considered individual (10, 10) armchair NTs. Using molecular dynamics [12], we simulated impact events of Ar ions with energies of 50 to 3000 eV on NTs. The Brenner potential [13] without bond-conjugation terms was used for modeling the carbon atom interaction. To examine the stability of the irradiation-induced defects, we simulated the time evolution of a 100-Å-long NT with defects over time scales of up to ten nanoseconds at temperatures of 1000 to 3000 K. For every temperature considered, we carried out at least 40 independent runs and averaged the results.

Having calculated the geometry of the defects within the framework of the classical model by minimizing the total energy of the carbon network after defect creation, we computed the STM images of the irradiated NTs near the defects within the framework of the tight-binding approximation [14].

2. RESULTS AND DISCUSSION

As follows from our simulations, the most common defects produced under ion irradiation are vacancies, which are metastable long-lived defects at low temperatures. At high temperatures, the vacancies (which have three dangling bonds, see Fig. 1b) can transform into two other defects. These are a single-pentagon and one dangling-bond atomic configuration and a fourfold coordinated atom shared by two pentagons and two hexagons (cf. Figs. 1c, 1d). For brevity, we label the former defect "5–1 db" and the latter "5–6." Observations of such defects forming under high-dose electron irradiation have also been reported [5].

The 5–1-db defect has the lowest energy [5, 7]. Therefore, although defects of all three types can appear as a result of ion impact, the long quenching of the NT should eventually lead to the transformation of single vacancies and defects 5–6 into 5–1 db defects. However, since single vacancies and 5–6 defects are metastable (i.e., there is an energy barrier separating

[1] This article was submitted by the authors in English.

1063-7834/02/4403-0470$22.00 © 2002 MAIK "Nauka/Interperiodica"

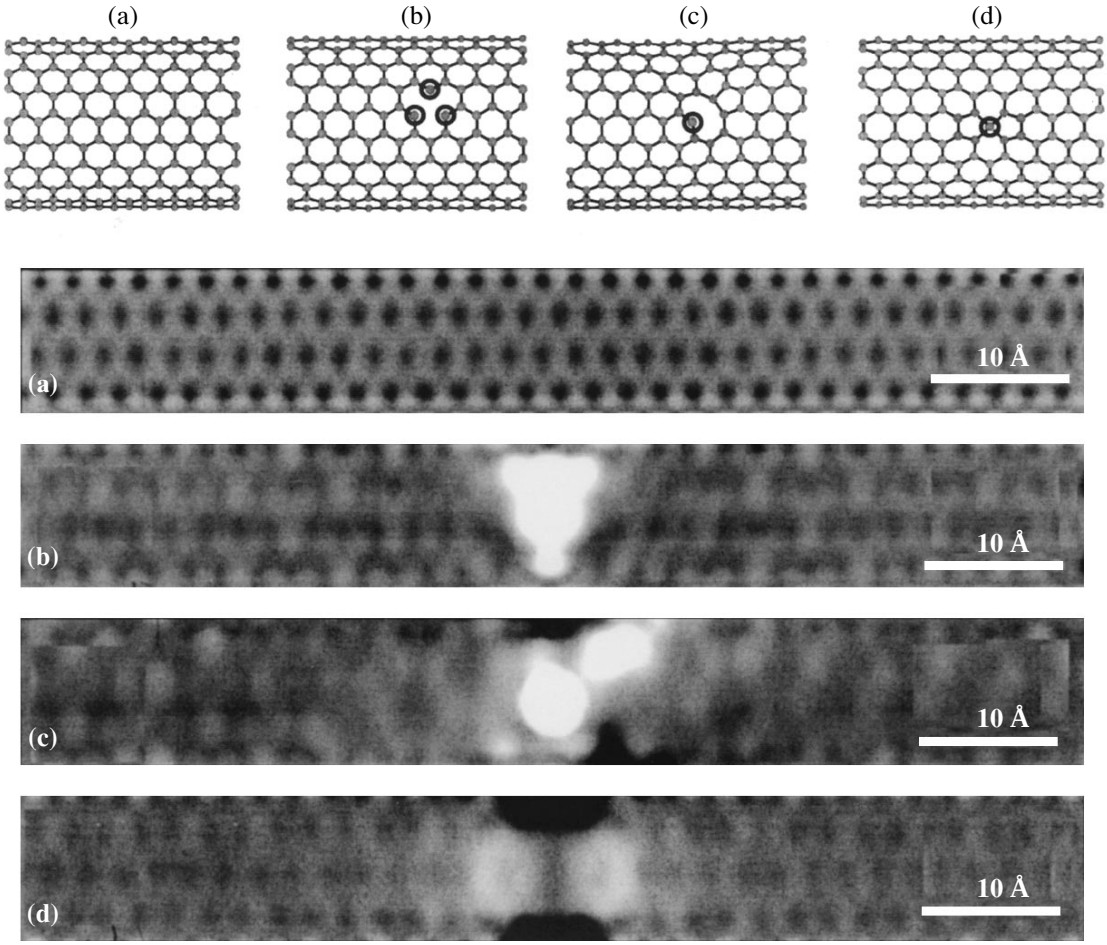

Fig. 1. Ball-and-stick representation of the carbon network of a pristine (10, 10) single-walled nanotube and of a nanotube with defects and their STM images. (a) Pristine nanotube and the nanotube with an irradiation-induced (b) vacancy, (c) 5–1-db defect, and (d) 5–6 defect. Only the front walls of the nanotubes are sketched. Atoms with unusual numbers of bonds are encircled. The defects are at the centers of the STM images.

these two configurations from the configuration with a minimum energy), such defects may survive at low temperatures for finite times, which may be long enough to detect the defects experimentally.

We estimated the lifetimes of the metastable defects as described in the previous section. For single vacancies, simulations were carried out in the temperature range 1500–2200 K and it was found that the average vacancy lifetime can be well described in terms of a single activation energy, i.e., by the formula $\tau_{vac} = a\exp(b/k_BT)$, where τ_{vac} is the time required for a vacancy to transform into a 5–1 db defect, k_B is Boltzmann's constant, T is the temperature, and a and b are fitting constants. With the constants determined at high temperatures, we estimated the lifetime at room temperature, which proved to be as long as at least a hundred hours. Thus, the vacancies could be experimentally detected by, e.g., STM.

We also carried out similar simulations for defects 5–6 in the temperature range 1200–1800 K. The lifetime of defects 5–6 was found to be about five hours at room temperature. Thus, defects 5–6 can also survive long enough to be detected.

To facilitate experimental identification of defects, Fig. 1 presents gray-scale STM images of NTs with defects calculated for positive $V_{bias} = 0.2$ V. Defects are always at the origin. To establish a correspondence with the already published results, a gray-scale STM image of a perfect NT is also shown.

The main feature of the STM image with a vacancy is a dramatic protrusion above the defect. Depending on the sign of V_{bias}, the height of the hillock is ≈0.7–0.8 Å, while its linear size is independent of V_{bias} and equal to ≈5 Å. The enhancement in the tunneling current is due to vacancy-induced states near the Fermi energy, which may be interpreted as "dangling bonds;" these states are spatially localized on the atoms surrounding the vacancies. Since it is specifically these states that STM probes at small bias voltages, a vacancy is imaged as a protrusion.

Figure 1c shows an STM image of the NT with a 5–1-db defect. Again, similar to the case of a vacancy, a hillocklike feature above the defect is evident, which is also of electronic origin. However, the shape of the feature is quite different from that in the case of the single vacancy.

The 5–6 defect, if it exists long enough to be measured by STM, also gives rise to a small bump in the STM image of the NT (see Fig. 1d). The shape of the hillock reflects the symmetry of the underlying atomic structure of the defect (cf. Fig. 1d, top panel). Additional information may also be obtained from the current–voltage characteristics, which are different for defects of different types.

Thus, it is possible to experimentally detect and distinguish irradiation-induced defects in NTs. It is also noteworthy that experiments on irradiating NTs with inert-gas ions and subsequent STM probing may enable one to observe the temporal evolution of irradiation-induced defects at various temperatures and to compare experimental lifetimes to those predicted theoretically. Such experiments may not only contribute to the understanding of the mechanisms of defect formation but also serve as a test for the validity of tight-binding and empirical-potential molecular-dynamics models.

In summary, the behavior of atomic-scale defects produced by low-dose irradiation of nanotubes with Ar ions was studied and their lifetimes at various temperatures were computed. We demonstrated that, at low temperatures, the defects are likely to be stable on macroscopically long time scales and appear as hillocklike features in STM images due to the growth in the local electron density of states on atoms surrounding the defects. Since the hillocks are different in shape for different defects, the defects could be experimentally distinguished using STM.

ACKNOWLEDGMENTS

We thank E. Salonen for valuable discussions.

Grants of computer time from the Center for Scientific Computing in Espoo, Finland, are gratefully acknowledged.

This research was supported by the Academy of Finland, project nos. 44215 and 73722.

REFERENCES

1. P. L. McEuen, Nature **393**, 15 (1998).
2. C. Dekker, Phys. Today **52** (5), 22 (1999).
3. M. Bockrath, W. Liang, D. Bozovic, *et al.*, Science **291**, 283 (2001).
4. C.-H. Kiang, W. A. Goddard, R. Beyers, and D. S. Bethune, J. Phys. Chem. **100**, 3749 (1996).
5. P. M. Ajayan, V. Ravikumar, and J.-C. Charlier, Phys. Rev. Lett. **81**, 1437 (1998).
6. H. Stahl, J. Appenzeller, R. Martel, *et al.*, Phys. Rev. Lett. **85**, 5186 (2000).
7. A. V. Krasheninnikov, K. Nordlund, M. Sirviö, *et al.*, Phys. Rev. B **63**, 245405 (2001).
8. Y. Zhu, T. Yi, B. Zheng, and L. Cao, Appl. Surf. Sci. **137**, 83 (1999).
9. A. V. Krasheninnikov, Solid State Commun. **118**, 361 (2001).
10. A. V. Krasheninnikov, Phys. Low-Dimens. Struct. **11/12**, 1 (2000).
11. K. Nordlund, J. Keinonen, and T. Mattila, Phys. Rev. Lett. **77**, 699 (1996).
12. M. P. Allen and D. J. Tildesley, *Computer Simulation of Liquids* (Oxford Univ. Press, Oxford, 1989).
13. D. W. Brenner, Phys. Rev. B **42**, 9458 (1990).
14. C. H. Xu, C. Z. Wang, C. T. Chan, and K. M. Ho, J. Phys.: Condens. Matter **4**, 6047 (1992).

Physics of the Solid State, Vol. 44, No. 3, 2002, pp. 473–474. Translated from Fizika Tverdogo Tela, Vol. 44, No. 3, 2002, pp. 455–456.

PROCEEDINGS OF THE V INTERNATIONAL WORKSHOP "FULLERENES AND ATOMIC CLUSTERS"

(St. Petersburg, Russia, July 2–6, 2001)

Electron Diffraction Investigation of Catalytic Particles at the Tips of Carbon Nanotubes

O. M. Gur'yanova, E. F. Kukovitsky, S. G. L'vov, N. A. Sainov, and V. A. Shustov

Zavoĭskiĭ Physicotechnical Institute, Russian Academy of Sciences, Sibirskiĭ trakt 10/7, Kazan 29, 420029 Tatarstan, Russia
e-mail: kuk@kfti.knc.ru

Abstract—Catalytic nickel particles at the tips of carbon nanotubes grown under different physicochemical conditions are experimentally studied by high-energy electron diffraction. The spacings of the crystal lattice are determined. It is demonstrated that the nanoparticles consist of a supersaturated solid solution of carbon in nickel with an abnormally high carbon content. *© 2002 MAIK "Nauka/Interperiodica".*

This paper reports on the results of an electron diffraction investigation of finely dispersed nickel–carbon phases formed during the catalytic growth of carbon nanotubes.

In order to elucidate how the experimental conditions affect the catalytic growth of carbon nanotubes, the nanotubes under investigation were prepared using two methods, namely, pyrolysis of poly(ethylene) and synthesis in a carbon vapor atmosphere [1, 2]. Supported nickel catalysts were produced according to two procedures. In the first case, the procedure involved vacuum deposition of nickel onto silica substrates and subsequent heat treatment for the purpose of producing nanoparticles. In the second case, the catalysts were prepared by chemical vapor deposition with the use of nickel dimethylglyoximate as an initial organometallic compound. It was assumed that the deposition of nickel in the presence of carbon-containing compounds should favor the formation of nickel–carbon phases and materials typical of the catalytic growth of nanotubes. We examined a large number of electron diffraction patterns and measured the interplanar distances in the prepared films. It was found that the films under investigation contain the following phases: (1) amorphous carbon at different degrees of graphitization, (2) disperse metallic nickel, (3) nickel oxide NiO, and (4) nickel carbide Ni_3C in minor amounts. The results of measurements of the interplanar distances and the corresponding lattice parameters are presented in the table. The lattice spacings were also determined for catalytic particles at the tips of carbon nanotubes of two types. Nanotubes of the first type were synthesized from poly(ethylene) with a vacuum-deposited catalyst at a temperature of 700°C. An examination of the nanotubes through an electron microscope revealed that the catalytic particles had a faceted form. This is characteristic of solid particles during the growth of nanotubes. Nanotubes of the second type were synthesized on chemically deposited films in a carbon vapor atmosphere at a temperature of 950°C. In this case, the catalytic particles had a prolate form and resembled drops of a liquid that poorly wets the inner walls of nanotubes. In our recent work [2], we demonstrated that catalytic particles are in the liquid state during the growth of nanotubes from carbon vapor. The interplanar distances and lattice parameters determined for catalytic nanoparticles at the tips of carbon nanotubes are also given in the table. As can be seen, the lattice spacings for particles in chemically deposited films and carbon nanotubes prepared from poly(ethylene) are considerably larger than those for pure nickel.

It should be noted that the increase in the lattice spacing is observed independently of the presence of other phases in the sample. Therefore, we can conclude that the above increase is caused by the high content of carbon dissolved in the nickel nanoparticles. According to Ruhl and Cohen [3], the concentration dependence of the lattice parameter for nickel in nickel–carbon alloys is described by the relationship $a = 3.524 + 0.008x$ (Å/at. %). Under the assumption that this relationship is valid over a sufficiently wide concentration range, we found that the content of carbon dissolved in nickel nanoparticles involved in chemically deposited films is equal to 9–13 at. %. The lattice spacing obtained for catalytic particles at the tips of nanotubes produced from poly(ethylene) (700°C) corresponds to a carbon content of ~15 at. %. The carbon content in liquid particles during the growth of nanotubes from the carbon vapor (950°C) does not exceed 6 at. %. At first glance, this result seems unexpected, because the growth of nanotubes from the carbon vapor occurs at the higher temperature and the solubility of carbon in liquid nickel is substantially larger. However, the content of carbon dissolved in catalytic particles at the tips of carbon nanotubes can be adequately estimated only by using sufficiently justified models of catalytic growth of carbon nanotubes. For example, the surface carbide model proposed by Alstrup [4] does not stipu-

1063-7834/02/4403-0473$22.00 © 2002 MAIK "Nauka/Interperiodica"

Interplanar distances for the studied phases in chemically deposited films and nanoparticles at the tips of carbon nanotubes

Phases in chemically deposited films						Nanoparticles at the tips of carbon nanotubes			
Ni_3C		NiO		Ni		tubes from poly(ethylene)		tubes from carbon vapor	
1		2		3		4		5	
d	*hkl*	*d*	*hkl*	*d*	*hkl*	*d*	*hkl*	*d*	*hkl*
2.15	0006	2.410	111	2.080 ± 0.01	111	2.100 ± 0.02	111	2.033 ± 0.02	111
2.08	$11\bar{2}3$	2.085	200	1.808 ± 0.008	200	1.820 ± 0.016	200	1.774 ± 0.016	200
1.336	$03\bar{3}0$			1.271 ± 0.004	220				
1.221	$11\bar{2}9$			1.089 ± 0.003	311	1.092 ± 0.006	311	1.070 ± 0.006	311
1.131	$03\bar{3}6$								
						0.825 ± 0.004	331	0.811 ± 0.004	331
								0.797 ± 0.004	420
								0.716 ± 0.004	422
						0.694 ± 0.004	333	0.682 ± 0.004	333
				$a = 3.61 \pm 0.01$		$a = 3.64 \pm 0.035$		$a = 3.54 \pm 0.03$	

late the chemical composition for this carbide. Under the assumption that the carbide composition is closely similar to Ni_3C and that the carbon content in a particle at the boundary with a nanotube corresponds to an equilibrium with graphite (~0.4 at. %), the mean content of dissolved carbon can be as high as 10–12 at. %. This value is close to the experimentally found content of dissolved carbon (15 at. %). However, it should be remembered that the estimates thus obtained depend on the concentration distribution of carbon over the particle length. The diffusion rate of carbon in liquid catalytic particles should be considerably higher than the rate of solid-phase diffusion. Hence, it is unreasonable to assume that the growth rate of carbon nanotubes is controlled by the diffusion stage. The stationary growth of nanotubes can occur at lower concentrations of carbon and at smaller concentration gradients. The mere fact that the nanotube growth is provided by liquid catalytic particles indicates the following: the basic principles of the surface carbide model are not universal and have failed to explain the growth of carbon nanotubes over a wide range of experimental conditions. Undeniably, the crystallographic features of the deposition, dissolution, and precipitation of carbon in solid catalytic particles play a certain role. However, not only these factors are responsible for the structural and chemical states of the catalytic particles and their shape. The thermodynamic aspects of carbon deposition are of crucial importance in processes of nanotube growth. A growth model formulated in terms of the thermodynamic activity of carbon was proposed by Safvi *et al.* [5]. Within this model, the considerable difference in the contents of dissolved carbon in catalytic particles at the tips of carbon nanotubes can be qualitatively explained by the different carbon activities in the gas phases used in the two different syntheses of carbon nanotubes and by the different diffusion rates of carbon in the particle bulk. Unfortunately, we cannot make quantitative estimates, because existing models are not sufficiently developed and important parameters of the process under investigation (such as the carbon activity in the gas phase and the diffusion rate of carbon in liquid nickel) are unavailable.

ACKNOWLEDGMENTS

This work was supported by the Russian Foundation for Basic Research (project no. 01-03-32272) and the State Scientific and Technical Program "Fullerenes and Atomic Clusters," the Ministry of Science of the Russian Federation (project no. 5-2-98).

REFERENCES

1. E. F. Kukovitsky, L. A. Chernozatonskii, S. G. L'vov, and N. N. Mel'nik, Chem. Phys. Lett. **266**, 323 (1997).
2. E. F. Kukovitsky, S. G. L'vov, and N. A. Sainov, Chem. Phys. Lett. **317**, 65 (2000).
3. R. C. Ruhl and A. Cohen, Scr. Metall. **1**, 73 (1967).
4. J. Alstrup, J. Catal. **109**, 241 (1988).
5. S. A. Safvi, E. C. Bianchini, and C. R. F. Lund, Carbon **29**, 1245 (1991).

Translated by O. Borovik-Romanova

Physics of the Solid State, Vol. 44, No. 3, 2002, pp. 475–477. Translated from Fizika Tverdogo Tela, Vol. 44, No. 3, 2002, pp. 457–459.

PROCEEDINGS OF THE V INTERNATIONAL WORKSHOP "FULLERENES AND ATOMIC CLUSTERS"

(St. Petersburg, Russia, July 2–6, 2001)

Comparative Analysis of Various Methods of Purification of Single-Walled Carbon Nanotubes

A. S. Lobach*, N. G. Spitsina*, S. V. Terekhov, and E. D. Obraztsova****

** Institute of Problems of Chemical Physics, Russian Academy of Sciences, Chernogolovka, Noginskiĭ raĭon, Moscow oblast, 142432 Russia*

*** Research Center for Natural Sciences, Institute of General Physics, Russian Academy of Sciences, ul. Vavilova 38, Moscow, 117942 Russia*

e-mail: lobach@cat.icp.ac.ru

e-mail: elorb@kapella.gpi.ru

Abstract—A comparative analysis of the purification methods for single-walled carbon nanotubes (SWNTs) obtained by electric-arc-discharge synthesis is carried out. The purification methods include air oxidation of the initial material at various temperatures, treatment and/or oxidation in solutions of inorganic acids, microfiltration of the suspension of the initial and/or oxidized materials, and various combinations of these methods. The purity of the SWNTs obtained is determined with the help of Raman spectroscopy. It is shown that the best results can be obtained using a purification method including the following consecutive stages: treatment and oxidation of the initial material in nitric acid, microfiltration of the suspension of the oxidized material in aqueous solutions of surface-active substances through track membranes, drying, air oxidation, and vacuum annealing at various temperatures. The purity of the SWNTs obtained attains 70–80%. © *2002 MAIK "Nauka/Interperiodica".*

Modern methods developed for obtaining single-walled carbon nanotubes (SWNTs) are based on the evaporation of graphite through thermal sputtering in an electric arc or laser evaporation, etc. [1–3]. The initial material obtained as a result of these processes contains, in addition to SWNTs, amorphous carbon impurities and nanoparticles of graphite and a metallic catalyst. For this reason, an important stage in the SWNT synthesis is the development of methods of SWNT purification for obtaining nanotubes with a maximum degree of purity. In addition to this, a simple and reliable express method for monitoring the purity of the obtained SWNTs in the course of purification is required. Raman spectroscopy, which is the basic method for characterizing nanotubes, was used for developing the quantitative express analysis of SWNTs [4, 5].

In this paper, we present the results of a comparative analysis of various methods for the purification of SWNTs obtained by electric-arc-discharge synthesis. The identification of SWNTs and the quantitative control of their purity were carried out using the Raman technique.

The initial material (sample *1*) containing SWNTs was obtained through the thermal evaporation of metal–graphite electrodes ($C : Ni : Y_2O_3 = 2 : 1 : 1$, in weight proportion) in an electric arc according to the procedure described earlier in [6]. The results of transmission electron microscopy showed that the SWNT content in the initial material is 15–20 wt %. The characteristics of the purification methods of the SWNT samples under investigation are given in the table.

Raman spectra were recorded on a Jobin Yvon S-3000 device with spectrum excitation by an Ar^+ laser (the pumping radiation wavelength was 514.5 nm). The Raman spectra of SWNTs display characteristic peaks in the low-frequency range 150–200 cm^{-1} (breathing mode) and in the high-frequency range at 1567 and 1592 cm^{-1} (tangential mode). The absolute intensity of the Raman peaks cannot serve as a measure of the SWNT purity since it is difficult to create identical experimental conditions for spectrum recording. Recently, Terekhov and Obraztsova [4] developed a quantitative method of SWNT identification on the basis of the dependence of the shift of the 1592-cm^{-1} peak on the power density of the laser beam. This dependence is linear, and the slope characterizes the SWNT content in the sample [5]. Figure 1 shows the dependences of the shift of the tangential mode peak in the Raman spectra of SWNTs on the power density of the laser beam for various samples. The straight line *1* corresponds to the initial material with 15 wt % of nanotubes in the sample, whereas the straight line *S* corresponds to the highest degree of the SWNT purity (95 wt %).

All methods of the SWNT purification are based on the removal of nanoparticles of carbon, amorphous carbon, and metallic catalyst particles. The purification

1063-7834/02/4403-0475$22.00 © 2002 MAIK "Nauka/Interperiodica"

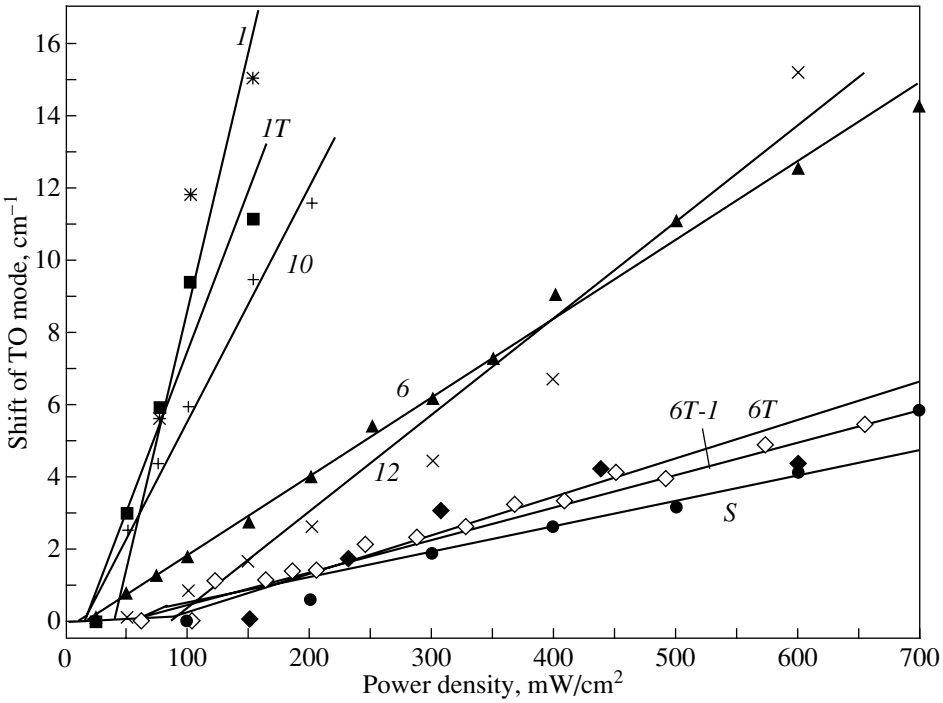

Fig. 1. Dependences of the shift of the tangential mode peak in the Raman spectrum of SWNTs on the laser beam power density for samples with different SWNT contents.

method based on simple heating of the initial material in air at $T = 350$°C over 1 h (sample *1T*) leads to a partial (15–20%) loss in the weight of the initial sample due to graphite burning and to an increase in the SWNT content from 15 wt % for the initial material to 25 wt % for sample *1T* (straight lines *1* and *1T* in Fig. 1, respectively). The treatment of oxidized samples with hydrochloric acid leads to further purification of SWNTs. The degree of purity increases with the time of treatment (straight lines *10* and *12*). The SWNT purity is equal to 30% for sample *10* and 35% for sample *12*.

Figure 2 shows the Raman spectra for the SWNT samples obtained by the treatment of the initial material with nitric acid followed by air oxidation and high-temperature vacuum annealing (samples *6–6T-1*). The Raman spectrum of sample *6* measured for a low-power laser beam is the spectrum of disordered carbon (curve *1*), with two bands *D* (1360 cm^{-1}) and *G* (1602 cm^{-1})

Characteristics of SWNT purification methods

Sample	Purification methods
1	Initial material was not subjected to any treatment and was kept in air
1T	Oxidation of the initial material in air for 1 h at $T = 350$°C
6	Oxidation of the initial material in an HNO_3 solution (2.5 M) at $T = 103$°C for 35 h. Filtration of the suspension of an oxidized material in an aqueous solution of the surface-active material (SAM) Triton X-100 through a track membrane (pore diameter $d = 0.4$ μm), washing with water and methanol, and 5.5-h vacuum drying at $T = 110$–120°C
6T	Oxidation of sample *6* in air for 30 min at $T = 550$°C
6T-1	Vacuum annealing of sample *6T* in a quartz ampule for 1 h at $T = 1200$°C
10	Oxidation of the initial material in air for 15 min at $T = 350$°C. The treatment of the same material in 36% HCl during boiling ($T = 102$–109°C) for 35 min. The filtration of the obtained material suspended in an aqueous solution of the SAM sodium dodecyl sulfate (the SAM concentration was 1.2 of the critical concentration of the micelle formation) through a track membrane ($d = 1$ μm), washing with water and methanol, and 3-h vacuum drying at $T = 160$°C
12	Oxidation of the initial material in air for 2 h at $T = 350$°C. The treatment of the oxidized material in 36% HCl during boiling ($T = 110$°C) for 3 h. The filtration of the obtained material suspended in an aqueous solution of Triton X-100 through a track membrane ($d = 1$ μm), washing with water and methanol, and 4-h vacuum drying at $T = 140$°C
S	SWNT sample obtained in [1]

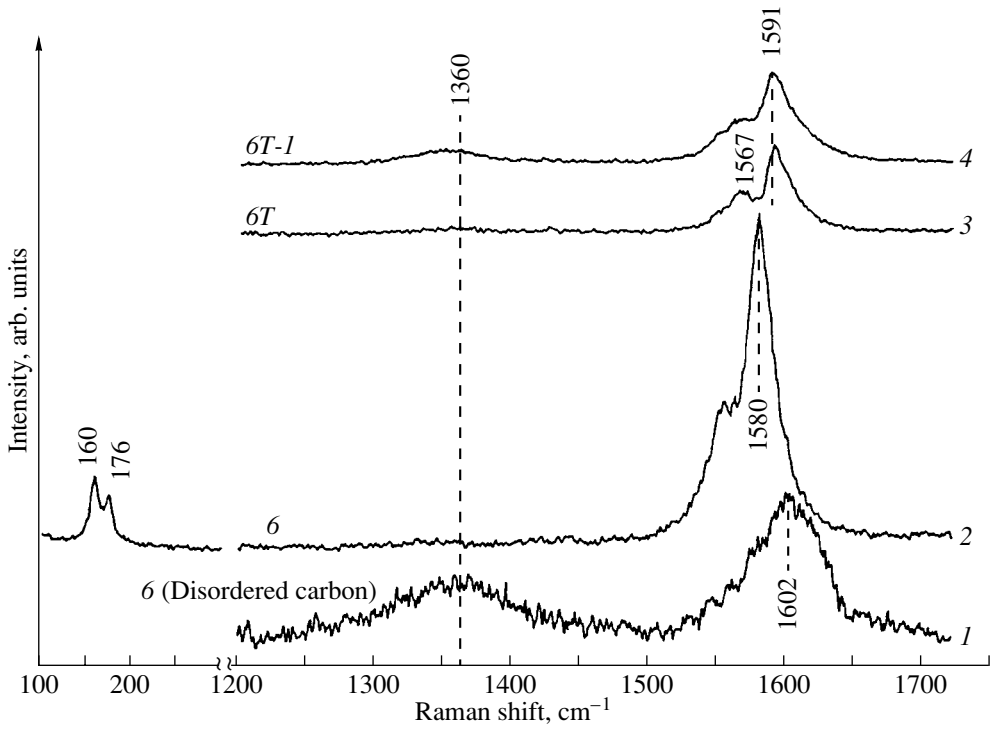

Fig. 2. Raman spectra of SWNTs in samples *6* (surface disordered carbon), *6*, *6T*, and *6T-1*.

indicating the presence of a disordered carbon layer on the SWNT surface. A twofold increase in the laser beam power results in a spectrum (curve *2*) typical of SWNTs. This can be explained by the burning out of surface disordered carbon whose burning temperature is lower than that for nanotubes. For this reason, the sample was subjected to air oxidation to remove the surface disordered carbon layer. The spectrum of the sample obtained in this way (sample *6T*) has a shape typical of SWNTs (curve *3*) with clearly resolved peaks at 1567 and 1591 cm^{-1}. Vacuum annealing of SWNT (sample *6T-1*) leads to an insignificant increase in the purity of nanotubes, their partial destruction (which is manifested in the emergence of a band at 1360 cm^{-1} characterizing the presence of disordered carbon), and a decrease in the resolution of the peaks at 1567 and 1591 cm^{-1} (curve *4*). It can be seen from Fig. 1 (straight lines *6*, *6T*, *6T-1*) that the SWNT purity increases in the course of the treatment of the initial material in accordance with this method and amounts to 40% (sample *6*), 75% (sample *6T*), and 80% (sample *6T-1*) depending on the purification stage.

ACKNOWLEDGMENTS

This work was supported by the Russian Foundation for Basic Research (project nos. 00-03-32086 and 01-02-17358), MNTTs-1400, the State Scientific and Technical Program “Fullerenes and Atomic Clusters,” and INTAS.

REFERENCES

1. A. Thess, R. Lee, P. Nikolaev, *et al.*, Science **273**, 483 (1996).
2. A. G. Rinzler, J. Liu, H. Dai, *et al.*, Appl. Phys. A **67**, 29 (1998).
3. A. C. Dillon, T. Gennett, K. M. Jones, *et al.*, Adv. Mater. **11** (16), 1354 (1999).
4. S. V. Terekhov and E. D. Obraztsova, in *Abstracts of EUROCARBON 2000: 1st World Conference on Carbon, Berlin, 2000*, Vol. 1, p. 465.
5. S. V. Terekhov, E. D. Obraztsova, A. S. Pozharov, *et al.*, in *Abstracts of the 11th International Symposium on Intercalation Compounds, Moscow, 2001*, p. 220.
6. E. D. Obraztsova, J.-M. Bonard, and V. L. Kuznetsov, Nanostruct. Mater. **12**, 567 (1999).

Translated by N. Wadhwa

Physics of the Solid State, Vol. 44, No. 3, 2002, pp. 478–479. Translated from Fizika Tverdogo Tela, Vol. 44, No. 3, 2002, pp. 460–461.

PROCEEDINGS OF THE V INTERNATIONAL WORKSHOP "FULLERENES AND ATOMIC CLUSTERS"

(St. Petersburg, Russia, July 2–6, 2001)

Electron Magnetotransport in Carbon Nanotubes and Negative Magnetoresistance: The Density Matrix Method

V. É. Kaminskiĭ

Institute of Radio Engineering and Electronics, Russian Academy of Sciences, ul. Mokhovaya 11, Moscow, 101999 Russia
e-mail: kamin@mail.cplire.ru

Abstract—A solution (stationary and linear in electric field) to the kinetic equation for a one-electron density matrix in an arbitrary magnetic field is found for deformation-potential scattering in the approximation of a small deviation of the electron gas from equilibrium. An expression for the nanotube conductivity is obtained in the form of a sum over magnetic-quantization states. In the absence of a magnetic field, this expression coincides with the corresponding classical relations. In weak magnetic fields, the magnetoresistance of a multilayer nanotube is positive for high electron mobilities and negative for low mobilities. In intermediate fields, it reverses sign with increasing field strength. The magnetoresistance of a one-layer nanotube is always positive.

Negative magnetoresistance (NMR) cannot be interpreted either in classical terms or within the approach proposed in [1]. The explanation of NMR in quantum wires [2] and nanotubes [3–6] rests on a weak localization theory and interference corrections to the conductivity [7–9]. This paper puts forward a kinetic description of NMR. The kinetic equation for the one-electron density matrix in a magnetic field is solved assuming there to be a small deviation from equilibrium for the case of deformation-potential scattering, and an expression for the nanotube conductivity is derived.

Because of the limited space allotted for the report, we consider electron transport only in a nanotube with a large band gap and a parabolic dispersion law. We assume the magnetic field B to be directed along the z axis, perpendicular to the nanotube axis. The current through a nanotube can be calculated from the expression

$$j = \mathrm{Tr}(RJ), \tag{1}$$

where Tr(…) denotes the trace of the operator, R is the statistical operator, and J is the current-density operator in a magnetic field. The properties of our system in the one-electron approximation are described by the Hamiltonian operator

$$H = H_0 + W + U = H_e + H_p + W + U, \tag{2}$$

where H_e is the Hamiltonian of an electron in a magnetic field, H_p is the phonon Hamiltonian in the second-quantization representation, W is the electron–phonon coupling operator, and $U = -qE_x x$ is the potential-energy operator in an electric field. In the Schrödinger representation, the statistical operator is described by a Liouville equation,

$$i\hbar\frac{\partial R}{\partial t} = [HR]. \tag{3}$$

To solve this equation, we consider the sum $W + U$ to be a perturbation. We choose the vector potential of the magnetic field in the gauge $A = (-By, 0, 0)$. In the case where the nanotube radius is $a \ll \lambda$, the approximate wave functions of the operator H_0 can be written as

$$\Psi_{nl} = \exp(ikx)\frac{1}{a}\sin(k_0 lz) f_n \chi_s |N\rangle, \tag{4}$$

where

$$\lambda^2 = \frac{\hbar}{qB}, \quad g_{nr} = \frac{4nr}{\pi k_0 (n^2 - r^2)^2}[1 - (-1)^{n-r}],$$

$$k_0 = \frac{\pi}{2a},$$

$$f_n = \sin(k_0 n(y + a))$$

$$+ \frac{2k}{k_0^2 \lambda^2}\sum_{r \neq n}\frac{g_{nr}}{n^2 - r^2}\sin(k_0 r(y + a)),$$

k is the electron wave vector along the nanotube axis (the x axis), χ_s is the spin wave function, and $|N\rangle$ is the phonon wave function in the occupation number representation. For the sake of simplicity, the tube is replaced by a parallelepiped of the same dimensions. In this case, the electron energy is

$$E_1 = \frac{\hbar^2 k_1^2}{2m} + \frac{\hbar^2 k_0^2}{2m_1}(n_1^2 + l_1^2) + \mu_B g_s B, \tag{5}$$

where μ_B is the Bohr magneton, g is the Landé factor, and $s = \pm\frac{1}{2}$. Because the current and perturbation operators do not contain spin operators, their matrix elements are diagonal in the spin variables. We assume the phonon system to be equilibrium and not quantized. For a steady state, Eq. (3) yields, in the second order of perturbation theory,

$$(E_1 - E_2)R_{12} + U_{13}R_{32} - R_{13}U_{32} + i\pi S_{12} = 0, \quad (6)$$

where S_{12} is the collision integral, which depends on the density matrix elements. The substantiation of the method and the procedure used to obtain the approximate equation (6) are discussed in detail in [10]. We present the density matrix in the form

$$R_{12} = F_1\delta_{12} + G_{12}\delta(k_1 - k_2), \quad (7)$$

where $G_{12} = G_{n_1 l_1, n_2 l_2}(k_1)$. If the electric field does not break the spatial uniformity of the electron system, then $F_1 = F(E_1)$ is usually assumed to be the Fermi–Dirac distribution function, which depends on energy (5) and the Fermi quasi-level. At high temperatures and/or in a weak magnetic field, this approximation is quite satisfactory. In the case of deformation-potential scattering, assuming G_{12} to be a small correction, the solution to Eqs. (6) and (7) is found to be

$$G_{12} = \frac{U_{12}(F_1 - F_2)}{E_1 - E_2 + i\hbar\nu_{12}}. \quad (8)$$

The matrix elements of the current and potential energy are calculated in a straightforward way in terms of the wave functions given by Eq. (4). Substituting these matrix elements and Eq. (8) into Eq. (1), the conductivity is found to be

$$\sigma = \frac{q^2}{2\pi m}\int dk\left[\sum_{s,n,l}\frac{k}{\nu_{11}}\left(-\frac{\partial F}{\partial k}\right) + \frac{2\hbar}{k_0^2\lambda^4}\right.$$
$$\left.\times \sum_{s,n_1,n_2,l_1=l_2}\frac{\hbar\nu_{12}(F_1 - F_2)}{(E_2 - E_1)^2 + (\hbar\nu_{12})^2}\frac{g_{n_1 n_2}^2}{n_2^2 - n_1^2}\right], \quad (9)$$

where

$$\nu_{12} = \frac{\sqrt{kT}}{2\tau_{DA}}\sum_{n_3 l_3}\left[\frac{\Theta(z_{13})}{\sqrt{z_{13}}} + \frac{\Theta(z_{23})}{\sqrt{z_{23}}}\right],$$

$$z_{13} = E_1 - \frac{\hbar^2 k_0^2}{2m_1}(l_3^2 + n_3^2), \quad \tau_{DA} = \frac{2\sqrt{2}\hbar^2\rho s^2}{mkTE_A^2}.$$

The first term in Eq. (9) describes the conductivity in a zero magnetic field. We readily see that an additional positive term proportional to B^2 appears in the presence of a magnetic field. The dependence on a strong magnetic field will be different. For nanotubes with a narrow band gap, spin–orbit coupling should be taken into account, which results in a linear dispersion relation. In this case, calculations are performed in a similar manner, but they will be considerably more complex. The magnetoresistance depends linearly on the field, and its sign is determined by the parameters of the spin–orbit coupling. Modern concepts associate NMR with weak localization, which requires a disordered distribution of the scattering centers. The results obtained in this work show that transverse NMR can be observed in an electron gas without a random potential. This is a consequence of taking magnetic quantization into account in a self-consistent way.

REFERENCES

1. E. Adams and T. Holstein, J. Phys. Chem. **10** (4), 254 (1959); E. Adams and T. Holstein, in *Problems of Quantum Theory of Irreversible Processes* (Inostrannaya Literatura, Moscow, 1961).
2. A. D. Visser, V. I. Kadushkin, V. A. Kul'bachinskiĭ, *et al.*, Pis'ma Zh. Éksp. Teor. Fiz. **59** (5), 340 (1994) [JETP Lett. **59**, 363 (1994)].
3. A. V. Eletskiĭ, Usp. Fiz. Nauk **167**, 945 (1997) [Phys. Usp. **40**, 899 (1997)].
4. L. Langer, K. Bayot, E. Grivei, *et al.*, Phys. Rev. Lett. **76** (3), 479 (1996).
5. S. N. Song, X. K. Wang, R. P. H. Chang, and J. B. Ketterson, Phys. Rev. Lett. **72** (5), 697 (1994).
6. G. Baumgartner, M. Carrard, L. Zuppiroli, *et al.*, Phys. Rev. B **55** (11), 6704 (1997).
7. S. Nikami, A. Larkin, and Y. Nagaoka, Prog. Theor. Phys. **63** (2), 707 (1980).
8. B. Altshuler, D. Khmel'nitskii, A. Larkin, and P. Lee, Phys. Rev. B **22** (19), 5142 (1980).
9. B. L. Al'tshuler, A. G. Aronov, D. E. Khmel'nitskiĭ, and A. I. Larkin, Zh. Éksp. Teor. Fiz. **81** (9), 768 (1981) [Sov. Phys. JETP **54**, 411 (1981)].
10. A. I. Akhiezer and S. V. Peletminskii, *Methods of Statistical Physics* (Nauka, Moscow, 1977; Pergamon, Oxford, 1981), Chaps. 3–5.

Translated by G. Skrebtsov

Physics of the Solid State, Vol. 44, No. 3, 2002, pp. 480–481. Translated from Fizika Tverdogo Tela, Vol. 44, No. 3, 2002, pp. 462–463.

PROCEEDINGS OF THE V INTERNATIONAL WORKSHOP "FULLERENES AND ATOMIC CLUSTERS"

(St. Petersburg, Russia, July 2–6, 2001)

Emission Properties of Carbon Nanocrystallites

V. M. Lobanov*, Yu. M. Yumaguzin, and R. Z. Bakhtizin****

** Bashkortostan State Agricultural University, Ufa, 450001 Bashkortostan, Russia*
e-mail: bgau@soros.bashedu.ru
*** Bashkortostan State University, ul. Frunze 32, Ufa, 450074 Bashkortostan, Russia*
e-mail: rector@bsu.bashedu.ru

Abstract—The crystalline phase of a graphitized carbon emitter is identified using the Zener effect as a criterion for the occurrence of a crystallite on the emitting surface of the autocathode. The observed phenomena are interpreted as a spontaneous and thermal-field-induced transformation of the emitting carbon nanocrystallite.

1. INTRODUCTION

Investigations of graphitized carbon materials by field-emission microscopy and spectroscopy are substantially complicated by the heterogeneous composition, because an emitter containing crystalline and amorphous phases does not provide a regular image in a field-emission microscope. For this reason, it is impossible to evaluate the state of the emitting surface, to determine the crystallographic orientation, and to compare the obtained data with the phase composition of the region being probed.

The updated program-driven instrumental complex devised in our earlier work [1] permitted monitoring of the emitting surface of the graphitized carbon emitter within the probed region against the autoelectron energy distribution and the current–voltage characteristic of the probe current.

2. EXPERIMENTAL TECHNIQUE

The investigation of carbon crystallites was carried out using a Rovilon carbon fiber with an annealing temperature of 1173 K, which contains crystallites with basal planes oriented along the fiber axis. The field emitter was prepared from a fiber segment (~1 mm long) attached to a tungsten bow through aquadag. After drying in air, the sample was heated at a temperature of 1023 K under vacuum.

The precipitation of crystallites on the emitting surface of the emitter was accomplished through cathode sputtering of amorphous carbon by ions of residual gases under rough vacuum according to the procedure described in [2]. The sample was purified by annealing at a temperature of 1023 K under ultrahigh vacuum. The autoelectron energy distribution was measured using the procedure described in [1]. The current–voltage characteristics of the emission current of the crystallite were constructed with the use of the anode potential U_a and the electron current passing through the energy analyzer.

3. RESULTS

Scanning of the dependence of the autoelectron energy distribution on the anode potential revealed that it shifts to the low-energy range with respect to the Fermi level with a step proportional to the step of increase in the anode potential; i.e., the Zener effect takes place. This shift was taken as a criterion for the occurrence of a crystallite on the emitting surface of the autocathode.

For a series of samples, a further increase in the anode potential to a limiting value leads to a sharp decrease in the emission current of the crystallite by almost one order of magnitude. In this case, the autoelectron energy distribution exhibits an additional low-energy maximum located at 0.45–0.5 eV below the principal maximum. Upon annealing of the cathodes at 1023 K, the crystallite regains its initial state. The figure displays the current–voltage characteristics of the probe current, which correspond to the states of the emitting crystallite prior to (the current–voltage characteristic *I*) and after (the current–voltage characteristic *II*) a spontaneous decrease in the emission current.

The observed phenomenon of variations in the state of the emitting carbon nanocrystallite was interpreted by analogy with the behavior of current–voltage characteristics during the transformation of metal and semiconductor autocathodes. This phenomenon is accompanied by changes in the position and slope of the current–voltage characteristic of the emission current and can be treated as a spontaneous transformation of the carbon crystallite due to Joule heating in a penetrating electric field. Experimental verification of this assumption was performed using the dependence of the auto-

1063-7834/02/4403-0480$22.00

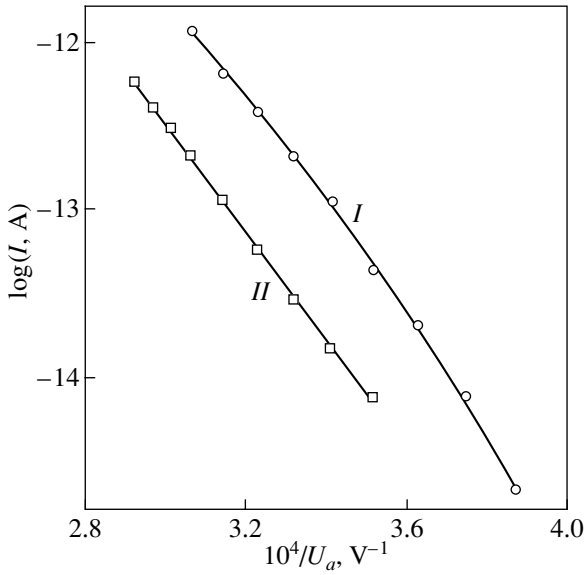

Current–voltage characteristics of the emission current of the carbon crystallite prior to (*I*) and after (*I*) spontaneous transformation for the normal autoelectron energy distribution (curve *I*) and the autoelectron energy distribution with an additional low-energy maximum (curve *II*).

electron energy distribution on the thermal annealing of the carbon crystallite in an electric field.

After annealing of the emitter at a temperature of 1023 K under ultrahigh vacuum, the autoelectron energy distribution has a normal shape and the current–voltage characteristic of the probe emission current of the crystallite corresponds to curve *I*. Annealing of the emitter at the same temperature in an electric field brings about a decrease in the probe current by one order of magnitude. Scanning of the dependence of the autoelectron energy distribution on the anode potential revealed an additional low-energy maximum located at 0.45–0.5 eV below the principal maximum. In this case, the current–voltage characteristic of the probe current corresponds to curve *II*. An increase in the anode potential leads to a shift in the autoelectron energy distribution toward the low-energy range with a step proportional to the step of change in the anode potential. This confirms the crystalline structure of the region under investigation. When the anode potential reaches a limiting value, the emission current and the autoelectron energy distribution abruptly regain their initial values; i.e., the autoelectron energy distribution and the current–voltage characteristic of the crystallite change in the direction $II \longrightarrow I$.

4. CONCLUSIONS

Thus, the emission current of the carbon crystallites of the graphitized carbon material annealed at 1173 K has an upper limit determined by Joule heating of the crystallite. Joule heating of the emitting carbon crystallite causes its spontaneous transformation. This transformation can be accompanied either by a decrease in the emission current by one order of magnitude and the appearance of an additional low-energy maximum in the autoelectron energy distribution or, conversely, by an increase in the emission current by one order of magnitude and the restoration of the autoelectron energy distribution to its normal shape. Annealing of the carbon crystallite in an electric field leads to its thermal-field-induced transformation. This is attended by a decrease in the emission current of the crystallite by one order of magnitude and the appearance of an additional low-energy maximum in the autoelectron energy distribution.

REFERENCES

1. R. Z. Bakhtizin, V. M. Lobanov, and Yu. M. Yumaguzin, Prib. Tekh. Éksp., No. 4, 247 (1987).
2. B. V. Bondarenko, A. Yu. Cherepanov, E. P. Sheshin, *et al.*, Radiotekh. Élektron. (Moscow) **30** (11), 2234 (1985).

Translated by N. Korovin

Physics of the Solid State, Vol. 44, No. 3, 2002, pp. 482–484. Translated from Fizika Tverdogo Tela, Vol. 44, No. 3, 2002, pp. 464–465.

PROCEEDINGS OF THE V INTERNATIONAL WORKSHOP "FULLERENES AND ATOMIC CLUSTERS"

(St. Petersburg, Russia, July 2–6, 2001)

A Study of the Oxidation and Fluorination of Single-Walled Carbon Nanotubes by the MNDO Method

I. V. Zaporotskova, N. G. Lebedev, and L. A. Chernozatonski ĭ

Volgograd State University, Vtoraya Prodol'naya ul. 30, Volgograd, 400062 Russia
e-mail: gnisr@online.ru

Abstract—This paper reports on the results of MNDO calculations of the atomic adsorption of oxygen and fluorine on the surface of armchair and zigzag single-walled carbon nanotubes with a cylindrical symmetry. The calculations are carried out within the molecular cluster and ion-incorporated covalent-periodic cluster models at the modern quantum-mechanical semiempirical MNDO level. The electronic and energy characteristics of the oxidation and fluorination processes are analyzed, and the most energetically favorable oxide structure of the (6, 6) nanotube is determined. It is found that narrow-gap tubulenes show a tendency to metallic behavior as their surface is saturated with oxygen atoms. © *2002 MAIK "Nauka/Interperiodica".*

1. INTRODUCTION

In recent years, considerable attention has been focused on investigating the electronic band structure of single-walled carbon nanotubes modified by different methods. In particular, it was revealed that the properties of tubulenes can change depending on the particular modifying or doping technique, the choice of incorporated or adsorbed elements, and treatment conditions. In this work, we studied the dynamic and energy characteristics of the processes of oxidation and fluorination of achiral carbon nanotubulenes that are small in diameter. For this purpose, we performed the MNDO simulation of the atomic adsorption of oxygen and fluorine on the outer surface of carbon nanotubes. The adsorption processes were investigated using successive quantum-mechanical calculations within the framework of the MNDO method [1] modified to the cases of a periodic cluster (the so-called ion-incorporated covalent-periodic cluster model [2]) and a molecular cluster.

2. OXYGEN ADSORPTION

A single-walled nanotube of the (6, 6) type was chosen as the object of investigation. One or several oxygen atoms were adsorbed on the outer surface of the nanotube. The calculations were performed within the ion-incorporated covalent-periodic cluster approach, which was successfully used earlier to investigate the electronic band structure of extended solid-state systems, including tubulenes. The position of an oxygen adatom was chosen according to the results obtained in our earlier work [3]. More specifically, this atom was located above a carbon atom of a hexagon located on the nanotube surface.

The potential energy surface of the nanotube–oxygen atom system was constructed by step-by-step placement of the oxygen adatom closer to the tubulene surface. It was found that the energy minimum is located at the distance $r_{C–O}$ = 1.3 Å. This minimum corresponds to the formation of a chemical bond between the oxygen adatom and the carbon atom on the tubulene surface.

Analysis of the results obtained in optimizing the geometry of the system revealed that the oxygen adsorption on the nanotube surface leads to an increase in the length of three C–C bonds (to 1.47 Å) involved in the carbon hexagon adsorbing the oxygen atom. Therefore, we can make the inference that the oxygen adsorption brings about the distortion of the nanotube surface, because the carbon atom adsorbing the oxygen atom rises above the tubulene surface, whereas the neighboring carbon atom sinks below the surface, thus forming an active center inside the nanotube.

Table 1. Band gaps and adsorption energies of oxygen atoms on the (6, 6) carbon tubulene

Number of O atoms	ΔE_g, eV	E_{ad} per atom, eV
0	3.76	–
1	3.67	10.76
2	3.50	7.96
3	3.47	8.27
6	2.31	7.54
24 (layer 1)	0.87	–3.81
24 (layer 2)	0.04	28.70

1063-7834/02/4403-0482$22.00

In addition, we carried out the MNDO calculations for two variants of the attachment of oxygen atoms to the nanotube surface. In the first variant, the oxygen atoms are arranged above the carbon atoms of three adjacent sheets of hexagons in such a way that rings of the superlattice formed by adatoms are not shifted relative to each other. In the second variant, even rings consisting of adatoms are displaced with respect to odd rings by the C–C bond length. Analysis of the results (Table 1) demonstrated that the second variant of the oxide structure of the nanotube is more energetically favorable.

Recently, there appeared a number of experimental works concerned with the investigation of the electronic properties of semiconducting carbon nanotubulenes treated with gaseous oxygen [4]. It was revealed that, after interaction with oxygen, the narrow-gap semiconducting tubulenes exhibit metallic behavior. We investigated the electronic and energy properties of tubulenes whose surface was saturated with oxygen atoms. In particular, we analyzed how the saturation of the nanotube surface with adsorbed oxygen atoms affects the band gap ΔE_g (Table 1). As can be seen from Table 1, the band gap decreases with an increase in the number of oxygen atoms adsorbed on the nanotube surface. This suggests a crossover of the conductivity from one type to another in the material formed upon adsorption. It should be noted that, for the oxidized nanotube, the O 2*p* atomic orbitals are located within the valence band rather than at the valence band edge.

Thus, our theoretical results completely confirm the experimental data on changes in the conducting properties of carbon nanotubes upon their oxidation.

3. FLUORINE ADSORPTION

The adsorption energies and the activation energies for adsorption of atomic fluorine on the outer surface of the (6, 6) carbon nanotube were calculated within the MNDO formalism for a simple molecular cluster. The attack of the carbon nanotube surface by fluorine was simulated through step-by-step placement of a fluorine atom closer to the carbon atom located on the surface.

As follows from the results of quantum-chemical calculations (Table 2 and figure), the energy of interaction between the nanotube and fluorine has two minima at the distances $R_W = 2.5$ Å and $R_{ch} = 1.8$ Å. The former minimum at the R_W distance corresponds to the van der Waals interaction between fluorine and the nanotube, i.e., to the so-called physical adsorption. The latter minimum is associated with the chemical adsorption. In order to occur at a point corresponding to the R_W distance, the fluorine atom must overcome the potential barrier $E_W \approx 2.1$ eV (activation energy). The energy gain for this adsorption can be estimated as $E_{ad} \approx 1.8$ eV. In this case, the energy is reckoned from the energy of the system at $R_{C–F} = \infty$.

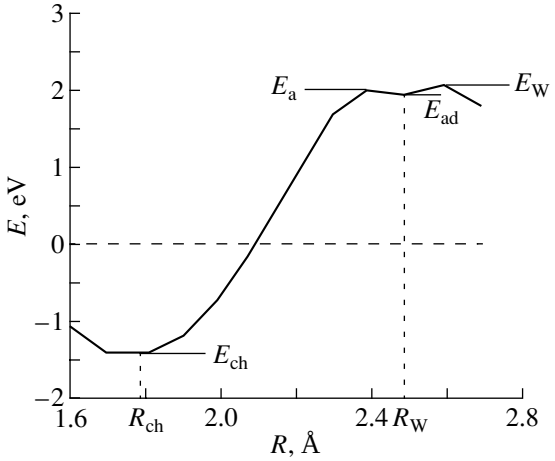

Dependence of the energy *E* on the reaction coordinate *R*.

The positive value of E_{ad} implies that the physical minimum at the R_W coordinate corresponds to a metastable state. By overcoming the potential barrier of the height $E_a - E_{ad} = 0.2$ eV, the fluorine atom can transfer from the metastable state to a more stable state at the R_{ch} coordinate. The energy gain E_{ch} for chemisorption is equal to –1.4 eV. The negative value of the E_{ch} energy means that the system under investigation is in a stable state. The C–F bond length R_{ch} is approximately equal to 1.7 Å. Apparently, the formation of fluorinated carbon nanotubes can occur through classical and tunneling mechanisms. In the quasi-classical approximation, the number of atoms attached to the surface in a unit time can be estimated from the standard formulas. The reaction rate V_s is found to be equal in order of magnitude to $\sim 6 \times 10^{-5}$ ns^{-1}. In the case when the barrier is overcome through the tunneling mechanism, the process proceeds only provided the energy α of particles attacking the nanotube surface is higher than the E_{ad} energy. The probability of a particle tunneling through this barrier is determined as $w\alpha \sim 10^{-3}$ s^{-1}.

The fluorine adatom interacting with the surface of the carbon nanotube attracts the surface carbon atom, as is the case in the atomic oxygen adsorption described

Table 2. Calculated physical and chemical adsorption energies, activation energies, and the relevant distances

Nanotube type	E_W, eV	R_W, Å	E_{ch}, eV	R_{ch}, Å	E_a, eV	E_{ad}, eV
(6, 6)	–2.1	2.5	–5.2	1.8	1.9	1.8
(6, 6)–F	1.8	–	–2.4	1.8	–	–

above. This atom deviates from the nanotube surface so that the bond length increases, on the average, by 4%.

Moreover, we investigated the adsorption of a fluorine atom on the (6, 0) nanotube surface. It was revealed that the attack of the (6, 0) nanotube surface by a fluorine atom leads to barrier-free adsorption; i.e., each collision of atoms results in the formation of an F–C chemical bond. The surface of the (6, 0) carbon nanotube is characterized by considerable dihedral angles between the hexagon planes. The surface carbon atoms change their electronic configuration and become $s^{\delta}p^{2+\delta}$-hybridized. One of the $s^{\delta}p^{2+\delta}$-hybridized orbitals of the carbon atom is unsaturated. Therefore, the nanotube under investigation possesses a high reactivity and efficiently adsorbs fluorine atoms.

4. CONCLUSION

Thus, the successive MNDO calculations of the processes of oxidation and fluorination of carbon nanotubes demonstrated the possibility of forming oxide and fluoride materials based on carbon nanotubes. The attachment of oxygen or fluorine atoms brings about a substantial distortion of the tubulene surface, thus changing the physicochemical and adsorption properties of the tubulenes. The saturation of the nanotube surface with oxygen atoms leads to changes in the semiconducting properties of the tubulenes, which exhibit a tendency to metallic behavior. The estimate of the chemical reaction rate showed that its value depends on the concentration of atomic fluorine over the nanotube surface; i.e., the reaction rate is determined by the gas pressure in the experimental setup.

REFERENCES

1. M. J. S. Dewar and W. Thiel, J. Am. Chem. Soc. **99**, 4899 (1977).
2. A. O. Litinskiĭ, N. G. Lebedev, and I. V. Zaporotskova, Zh. Fiz. Khim. **69** (1), 189 (1995).
3. I. V. Zaporotskova, A. O. Litinskiĭ, and L. A. Chernozatonskiĭ, Pis'ma Zh. Éksp. Teor. Fiz. **66** (12), 799 (1997) [JETP Lett. **66**, 841 (1997)].
4. P. G. Collins, K. Bradley, M. Ishigami, and A. Zettl, Science **287**, 1801 (2000).

Translated by O. Borovik-Romanova

Physics of the Solid State, Vol. 44, No. 3, 2002, pp. 485–486. Translated from Fizika Tverdogo Tela, Vol. 44, No. 3, 2002, pp. 466–467.

PROCEEDINGS OF THE V INTERNATIONAL WORKSHOP "FULLERENES AND ATOMIC CLUSTERS"

(St. Petersburg, Russia, July 2–6, 2001)

Electrodynamic Response of a Quantum Nanotube in a Parallel Magnetic Field

N. G. Galkin, V. A. Margulis, and A. V. Shorokhov

Mordovian State University, ul. Bol'shevistskaya 68, Saransk, 430000 Russia
e-mail: theorphysics@mrsu.ru

Abstract—This paper reports on a theoretical study of intraband resonances arising in the absorption of electromagnetic radiation by a quantum nanotube both with and without involvement of optical phonons. Explicit relations are derived for the absorption coefficients. The relative intensities of the resonance peaks are analyzed.

Nanostructures support two main types of intraband resonances associated with absorption of high-frequency electromagnetic radiation. The first type is due to electron transitions between two energy levels caused by photon absorption. The second type is associated with transitions between two electron states accompanied by simultaneous absorption or emission of a phonon. Note that the investigation of intraband resonances is presently attracting considerable interest [1–3], because it offers an efficient method for determining the parameters of electron and phonon energy spectra.

It is well known that a carbon nanotube is geometrically close to a cylinder. Note that the electronic properties of nonplanar nanostructures are governed primarily not by the actual form of the crystal lattice but rather by the geometry of the system. Therefore, a number of the physical properties of a carbon nanotube can apparently be described satisfactorily in terms of the electron gas model in the effective-mass approximation. In particular, the results obtained for the magnetic response of a 2D electron-gas layer rolled into a cylinder [4] were found to be in very good agreement with those derived [5] for a carbon nanotube in the tight-binding approximation. With this in mind, we model the carbon nanotube using a quasi-2D electron-gas layer rolled into a cylinder, as described in [6]. The spectrum of such a system placed in a magnetic field B parallel to the cylinder axis can be written as

$$E_{nmp} = \hbar\Omega\left(n + \frac{1}{2}\right) + \lambda m^2 + \frac{p^2}{2m^*}, \qquad (1)$$

where $\Omega = \sqrt{\omega_c^2 + \omega_1^2}$, $\omega_c = |e|B/m^*c$ is the cyclotron frequency, ω_1 is the characteristic frequency of the parabolic confinement potential constraining the radial motion of electrons, $\lambda = \hbar^2\omega_1^2/2\pi m^* R^2\Omega^2$ is the size quantization energy, R is the average nanotube radius, p is the electron momentum along the nanotube axis, $m = 0, \pm1, \pm2, \ldots$, and $n = 0, 1, 2, \ldots$.

We calculate the absorption coefficient for electromagnetic radiation using the perturbation-theory formalism [7] in order to study the interactions of electrons with a high-frequency field and lattice (characterized by the interaction Hamiltonians H_R and H_L) that are simultaneously switched on in the case of transitions involving phonons.

The absorption coefficient can be written as a sum of partial absorption coefficients (the direction of the electromagnetic wave polarization is chosen perpendicular to the nanotube symmetry axis),

$$\Gamma^{(\pm)}(\omega) = \sum_{n', m', n, m} \Gamma^{(\pm)}(n', m', n, m), \qquad (2)$$

where the plus and minus signs relate to the phonon emission and absorption processes, respectively; ω is the photon frequency; and n', m' and n, m are discrete quantum numbers of the initial and final states, respectively.

Note that, in the case of a nondegenerate gas, transitions from the ground state will provide the major contribution to the absorption coefficient. Therefore, we shall subsequently consider the case with $n' = 0$ and $m' = 0$.

In the case of scattering from DO phonons, the partial absorption coefficients are

$$\frac{\Gamma^{(\pm)}(0, 0, n, m)}{\Gamma_0} = (-1)^n\frac{\sqrt{\pi}}{m!}\sqrt{\frac{\hbar\omega_0}{T}}\frac{\omega}{\Omega(1-\omega^2/\Omega^2)^2}$$
$$\times\frac{\sinh(\hbar\Omega/T)}{\Theta_3(\exp(-\lambda/T))}\left(N_0 + \frac{1}{2} \pm \frac{1}{2}\right)\exp(-b^2m^2)$$
$$\times\exp(-\hbar\Omega/2T)\exp(\hbar\Delta\omega/2T)K_0\left(\frac{\hbar|\Delta\omega|}{2T}\right) \qquad (3)$$

1063-7834/02/4403-0485$22.00 © 2002 MAIK "Nauka/Interperiodica"

$$\times\left[b^2m^2\left(\frac{\Omega^2}{\omega^2}-1\right)L_n^{-n-1/2}(b^2m^2)-L_{n+1}^{-n-3/2}(b^2m^2)\right],$$

where $K_0(x)$ is a Bessel function, $L_n^m(x)$ are the associated Laguerre polynomials, $\Theta_3(x)$ is the Jacobian function, $\Delta\omega = \omega - \Omega n - \frac{\lambda}{\hbar}m^2 \mp \omega_0$ is the resonance detuning, ω_0 is the phonon frequency, $b^2 = \omega_c^2 l^2/2\Omega^2R^2$, $N_0 = [\exp(\hbar\omega_0/T) - 1]^{-1}$ is the Planckian distribution function, $\Gamma_0 = 32\sqrt{2\pi}e^2N\hbar^2\alpha_L/c\sqrt{\varepsilon}L_zm^{*3}l^3\Omega^3$, α_L is the electron–phonon coupling constant, L_z is the nanotube length, $l = \sqrt{\hbar/m^*\Omega}$, N is the number of electrons per unit volume, and ε is the real part of the dielectric permittivity.

As seen from Eq. (3), if one neglects phonon dispersion, the absorption coefficient has a logarithmic singularity originating from the behavior of the Bessel function at the points where $\Delta\omega$ vanishes. Note that the same singularity exists in the case of scattering from PO phonons as well. This singularity broadens if one takes into account the level width due to collisions or includes the dispersion of optical phonons.

Let us estimate the intensity of the resonance peaks. We note first of all that, because of the factor $\exp(-\hbar\omega_0/T)$, the intensity of the absorption peaks for $\hbar\omega_0 \gg T$ is much weaker than that of the emission peaks. Furthermore, the peak intensity falls off rapidly with increasing m as $\exp(-b^2m^2)$. Therefore, the $m = 0$ transitions dominate (except in the case where the transitions occur without a change in the magnetic quantum number, $m' = m$). The relative intensity of the resonance peaks with different n for such transitions is given by

$$\frac{\Gamma^{(\pm)}(0,0,n,0)}{\Gamma^{(+)}(0,0,0,0)} = \frac{1}{n!}\frac{(\Omega n\pm\omega_0)(\Omega^2-\omega_0^2)^2}{\omega_0[\Omega^2-(\Omega n\pm\omega_0)^2]^2} \times\left[\exp(-\hbar\omega_0/t)+\frac{1}{2}\pm\frac{1}{2}\right]\left(\frac{1}{2}+1\right)\ldots\left(\frac{1}{2}+n\right). \quad (4)$$

Note that if the absorption process does not involve optical phonons, only the transitions between the adjacent levels, with $n = n' \pm 1$, will be allowed (and the transitions involving a change in the magnetic quantum number m will be forbidden) [8]. The participation of optical phonons in absorption makes resonance transitions between levels with different m and n allowed. The existence of resonance does not depend on the actual kind of electron statistics; therefore, the relation for the absorption coefficient in the degenerate case will have the same resonance frequencies as in the nondegenerate case. However, in the degenerate-gas case, one may expect there to be features associated with the gas degeneracy, namely, breaks appearing in the $\Gamma(\omega)$ graph.

ACKNOWLEDGMENTS

This study was supported by the Russian Foundation for Basic Research (project no. 01-02-16564), DFG (grant no. 436 RUS 113/572), and the "Universities of Russia" Program (project no. 0.15.01.01.049).

REFERENCES

1. M. F. Lin, F. L. Shyu, and R. B. Chem, Phys. Rev. B **61**, 14114 (2000).
2. V. D. Krevchik and R. V. Zaĭtsev, Fiz. Tverd. Tela (St. Petersburg) **43**, 504 (2001) [Phys. Solid State **43**, 522 (2001)].
3. D. V. Zav'yalov and S. V. Kryuchkov, Fiz. Tekh. Poluprovodn. (St. Petersburg) **33**, 1355 (1999) [Semiconductors **33**, 1225 (1999)].
4. V. A. Geĭler, V. A. Margulis, and A. V. Shorokhov, Zh. Éksp. Teor. Fiz. **115**, 1450 (1999) [JETP **88**, 800 (1999)].
5. M. F. Lin and K. W.-K. Shung, Phys. Rev. B **52**, 8423 (1995).
6. V. A. Margulis, A. V. Shorokhov, and M. P. Trushin, Phys. Lett. A **276**, 180 (2000).
7. F. G. Bass and I. B. Levinson, Zh. Éksp. Teor. Fiz. **49**, 914 (1965) [Sov. Phys. JETP **22**, 635 (1966)].
8. N. G. Galkin, V. A. Margulis, and A. V. Shorokhov, Fiz. Tverd. Tela (St. Petersburg) **43**, 511 (2001) [Phys. Solid State **43**, 530 (2001)].

Translated by G. Skrebtsov

Physics of the Solid State, Vol. 44, No. 3, 2002, pp. 487–489. Translated from Fizika Tverdogo Tela, Vol. 44, No. 3, 2002, pp. 468–470.

PROCEEDINGS OF THE V INTERNATIONAL WORKSHOP "FULLERENES AND ATOMIC CLUSTERS"

(St. Petersburg, Russia, July 2–6, 2001)

The Temperature Dependence of the Electrical Resistivity and the Negative Magnetoresistance of Carbon Nanoparticles

A. I. Romanenko [1, 2], O. B. Anikeeva [1, 3], A. V. Okotrub [1], L. G. Bulusheva [1], V. L. Kuznetsov [4], Yu. V. Butenko [4], A. L. Chuvilin [4], C. Dong [5], and Y. Ni [5]

[1] *Institute of Inorganic Chemistry, Siberian Division, Russian Academy of Sciences, pr. Akademika Lavrent'eva 3, Novosibirsk, 630090 Russia*

e-mail: romanenk@casper.che.nsk.su

[2] *Novosibirsk State University, ul. Pirogova 2, Novosibirsk, 630090 Russia*

[3] *Novosibirsk State Technical University, Novosibirsk, 630092 Russia*

[4] *Boreskov Institute of Catalysis, Siberian Division, Russian Academy of Sciences, pr. Akademika Lavrent'eva 5, Novosibirsk, 630090 Russia*

[5] *National Laboratory for Superconductivity, Institute of Physics, Chinese Academy of Sciences, Beijing, 100080 China*

Abstract—Temperature dependences of the electrical resistivity of samples of carbon nanoparticles obtained from nanodiamonds by annealing at 1800, 1900, and 2140 K were studied. The magnetoresistance of these samples was measured at 4.5 K. Data on the positive magnetoresistance obtained in fields above 3 T were used to estimate the mean free path l of carriers at liquid-helium temperature, $l \sim 12$ Å for a sample annealed at 1800 K, $l \sim 80$ Å for a sample annealed at 1900 K, and $l \sim 18$ Å for the case of annealing at 2140 K. The samples annealed at 1800 and 2140 K exhibit a negative magnetoresistance in fields below 2 T. The carrier concentrations n in the samples annealed at 1800 and 2140 K were estimated as $n \sim 8 \times 10^{21}$ and 3×10^{21} cm^{-3}, respectively. © *2002 MAIK "Nauka/Interperiodica".*

Investigation of the electron transport properties of carbon materials is attracting considerable interest, because it provides information on their structural imperfection and electronic structure. Structural defects in carbon materials directly affect their electron-transport and magnetic properties. For instance, the extrinsic-carrier concentration in quasi-two-dimensional graphites is determined by the concentration and structure of defects [1], and their electrical and magnetic properties are governed by this concentration [2, 3]. A number of experimental [4–6] and theoretical [7] studies indicate that defects play the same part in multilayer carbon nanotubes. The present paper reports on experimental evidence of defects playing a similar role in carbon nanoparticles prepared by graphitization of nanodiamonds.

Bulk samples of carbon nanoparticles were prepared by annealing nanodiamonds at 1800 K (sample *1*), 1900 K (sample *2*), and 2140 K (sample *3*). The samples thus obtained (Fig. 1) consisted mainly of multilayer spheres with an interlayer distance of ~3.5 Å in a sphere, which is close to that in quasi-two-dimensional graphites. These spheres merge to form agglomerates measuring 500–5000 Å. Powder bulk samples consisted of these agglomerates. Powders to be measured were packed into a cylindrical ampule with four silver contacts. The electrical resistance of the samples thus prepared was measured using the four-probe technique.

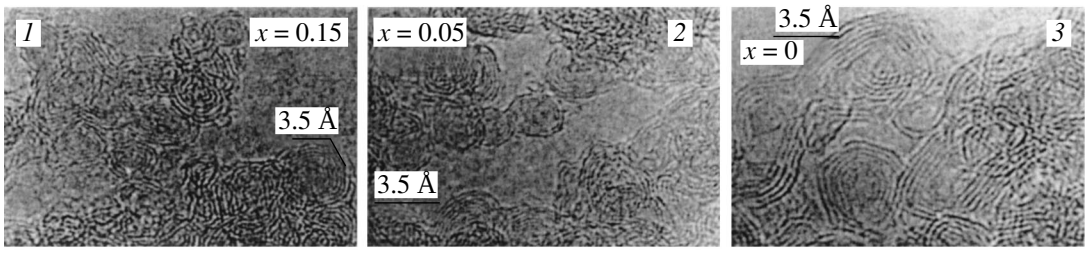

Fig. 1. Electron microscope images of carbon nanoparticle samples prepared from nanodiamonds by annealing at (*1*) 1800, (*2*) 1900, and (*3*) 2140 K. The parameter x shown in the photographs specifies the number of the remaining amount of nanodiamonds determined by weighing the sample.

1063-7834/02/4403-0487$22.00 © 2002 MAIK "Nauka/Interperiodica"

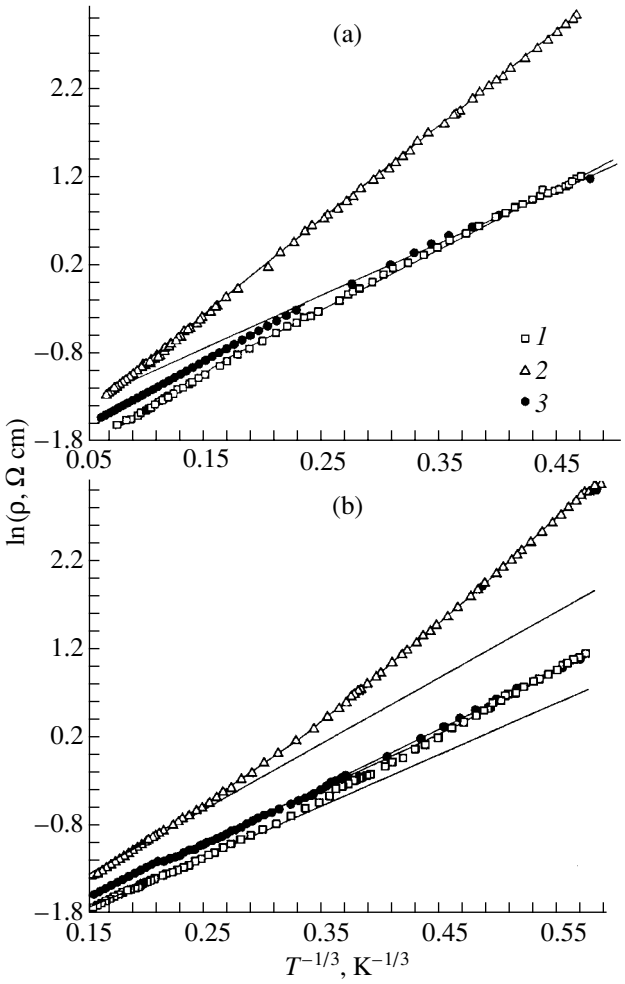

Fig. 2. Temperature dependence of the electrical resistivity of carbon nanoparticle samples prepared from nanodiamonds by annealing at (*1*) 1800, (*2*) 1900, and (*3*) 2140 K. The continuous lines are fits with Eq. (1) made with the following fitting parameters: (a) $n = 2$ for all curves, $C = 47$ K and $\rho_0 = 140$ mΩ cm for curve *1*, $C = 121$ K and $\rho_0 = 141$ mΩ cm for curve *2*, and $C = 38$ K and $\rho_0 = 189$ mΩ cm for curve *3*; (b) $n = 3$ for all curves, $C = 174$ K and $\rho_0 = 75$ mΩ cm for curve *1*, $C = 355$ K and $\rho_0 = 91$ mΩ cm for curve *2*, and $C = 180$ K and $\rho_0 = 87$ mΩ cm for curve *3*.

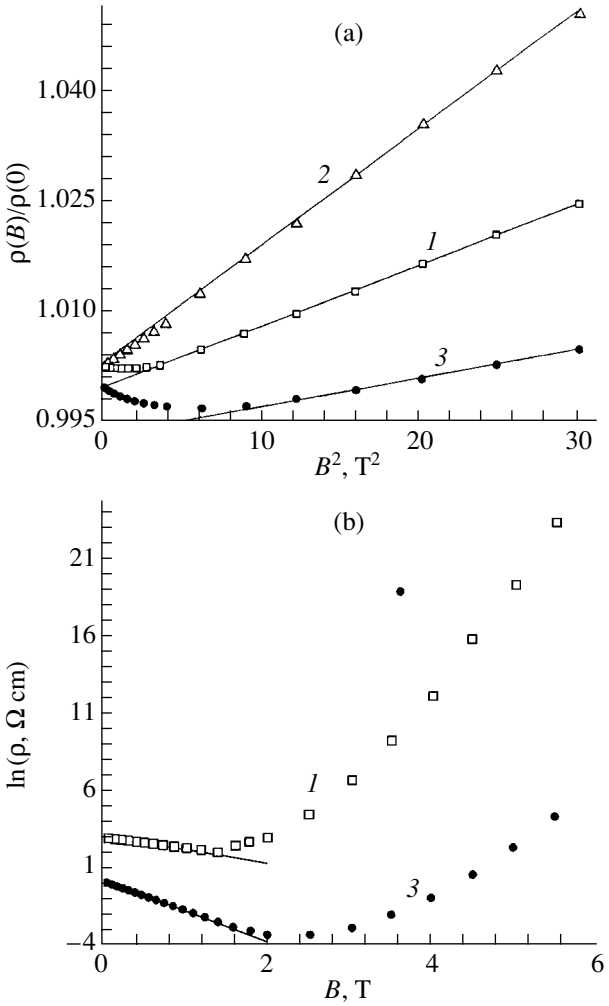

Fig. 3. Relative electrical resistivity vs. magnetic field B for carbon nanoparticle samples prepared from finely dispersed diamonds by annealing at (*1*) 1800, (*2*) 1900, and (*3*) 2140 K. The continuous lines are plots of Eq. (2) in (a) and of Eq. (3) in (b).

Figure 2 plots the temperature dependences of the electrical resistivity $\rho(T)$ of samples of the three types mentioned above. The continuous lines are fits of the experimental data to the relation

$$\rho(T) = \rho_0 \exp(C/k_B T)^{1/n}, \qquad (1)$$

where ρ_0 and C are constants specified in the caption to Fig. 2. The experimental data are best fitted by Eq. (1), with the parameter $n = 2$ at low temperatures (Fig. 2a) and $n = 3$ for high temperatures (Fig. 2b). Relation (1) is characteristic of variable-range hopping conduction (the so-called strong-localization case [8]) in systems with a semiconducting character of electrical conduction in the presence of local disorder. The coefficient n in Eq. (1) may vary from 1/2 to 1/4, depending on the dimensionality of carrier motion [8] and on whether the Coulomb gap is significant or not [9]. The value $n = 2$ observed in all samples at low temperatures (for $T <$ 100 K in sample *2*, and for $T < 20$ K for samples *1* and *3*) implies a dominant role of the Coulomb gap. For $T > 20$ K for samples *1* and *3* and for $T > 100$ K for sample *2*, Eq. (1) is observed to hold with $n = 3$ (two-dimensional localization), which indicates a weakening of the part played by the Coulomb gap in the temperature dependence of the electrical resistivity of these samples at high temperatures.

We also measured the magnetic-field dependence of the electrical resistivity of the same samples at liquid-helium temperature (4.5 K) with an MPMS-5 SQUID (Quantum Design, USA) magnetometer. The data obtained are displayed in Fig. 3. The experimental relations obtained on both samples in magnetic fields B

above 3 T are described by Eq. (2), which is typical of classical positive magnetoresistance (continuous lines in Fig. 3a) [10]:

$$\Delta\rho(B)/\rho(0) \cong (l/r_L)^2, \quad (2)$$

where l is the mean free path of carriers, $r_L = veB/mc$ is the electron Larmor precession radius in a magnetic field, and v, e, and m are the velocity, charge, and effective mass of an electron, respectively. An estimation of the mean free path l from data on the positive magnetoresistance yields $l \sim 12$ Å for sample *1*, ~80 Å for sample *2*, and ~18 Å for sample *3*. Thus, sample *1* has more defects than sample *3*. The most ordered is sample *2*. Electron microscope images of sample *2* (Fig. 1) show well-pronounced, multilayer nanospheres with characteristic diameters $D \sim 30$–50 Å. In samples subjected to the lowest or highest annealing temperatures, these spheres merged into agglomerates with common surface layers. These layers have more defects than those of the almost isolated nanoparticles in the sample annealed at the intermediate temperature. Carrier motion with such small mean free paths as those in samples *1* and *3* occurs through diffusion and should bring about negative magnetoresistance in weak magnetic fields [11]. As seen from Fig. 3, samples *1* and *3* exhibit negative magnetoresistance in fields up to 2 T. The continuous lines in Fig. 3b plot the equation [11]

$$\ln[\rho(T, H)/\rho(T, 0)] = A\{(eB/\hbar c)n_c^{-2/3}\}\ln[\rho(T)/\rho_0], \quad (3)$$

where A is a constant of order unity, n_c is the critical carrier concentration near the mobility edge, and ρ_0 is the residual resistivity. The experimental data obtained were used to estimate the carrier concentration in the samples (assuming $n \sim n_c$): $n \sim 8 \times 10^{21}$ cm^{-3} for sample *1*, and ~3×10^{21} cm^{-3} for sample *3*.

As seen from the above estimates, the carrier concentration in the sample annealed at the maximum temperature of 2140 K is lower than that in the sample annealed at 1800 K. This result correlates with the fact that extrinsic carriers associated with defects in graphite layers provide a substantial contribution to the carrier concentration in graphite-like systems [1–7]. Sample *1*, annealed at the lowest temperature, has more of such defects; this is what brings about the increase in the carrier concentration in this sample compared to sample *3*. This conclusion conforms well with the mean-free-path estimate made from the positive magnetoresistance data ($l \sim 12$ Å for sample *1*, and ~18 Å for sample *3*). The magnitude of l for samples *1* and *3* is less than the characteristic diameter of the spheres, and, hence, the defects are contained within these spheres. Sample *2*, annealed at the intermediate temperature (1900 K), turned out to consist of practically defect-free multilayer spheres (Fig. 1, panel *2*); this accounts for the much larger mean free path ($l \sim 80$ Å) and the absence of negative magnetoresistance.

Thus, our data on the temperature dependence of the electrical resistivity and on magnetoresistance permit one to conclude that carbon nanoparticle samples obtained from nanodiamonds by annealing at 1800 and 2140 K contain defects inside the graphite-like layers they are composed of. These defects bring about a decrease in the mean free path of the carriers and an increase in their concentration, as is the case in quasi-two-dimensional graphites and multilayer carbon nanotubes. The mean free path in the sample annealed at 1800 K is smaller and the carrier concentration is higher than their respective values in the sample annealed at 2140 K. The sample annealed at the intermediate temperature (1900 K) is made up predominantly of practically defect-free multilayer spherical nanoparticles (Fig. 1, panel *2*).

ACKNOWLEDGMENTS

This study was supported by the Russian Research and Development Program "Fullerenes and Atomic Clusters" (project no. 5-1-98), the federal program "Integration" (project no. K0042), the Russian Foundation for Basic Research (project nos. 00-02-17987, 01-02-06500), the Ministry of Education of Russia (project no. E00-3.4-506), the Interdisciplinary Integration Program of the Siberian Division, Russian Academy of Sciences (project no. 061), and INTAS (grant nos. 97-170, 00-237).

REFERENCES

1. A. S. Kotosonov, Pis'ma Zh. Éksp. Teor. Fiz. **43** (1), 30 (1986) [JETP Lett. **43**, 37 (1986)].
2. A. S. Kotosonov, Zh. Éksp. Teor. Fiz. **93** (5), 1870 (1987) [Sov. Phys. JETP **66**, 1068 (1987)].
3. A. S. Kotosonov, Fiz. Tverd. Tela (Leningrad) **33** (9), 2616 (1991) [Sov. Phys. Solid State **33**, 1477 (1991)].
4. A. S. Kotosonov and S. V. Kuvshinnikov, Phys. Lett. A **230**, 377 (1997).
5. A. S. Kotosonov and D. V. Shilo, Carbon **36**, 1649 (1998).
6. A. S. Kotosonov, Pis'ma Zh. Éksp. Teor. Fiz. **70**, 468 (1999) [JETP Lett. **70**, 476 (1999)].
7. A. S. Kotosonov and V. V. Atrazhev, Pis'ma Zh. Éksp. Teor. Fiz. **72** (2), 76 (2000) [JETP Lett. **72**, 53 (2000)].
8. N. F. Mott and E. A. Davis, *Electronic Processes in Non-Crystalline Materials* (Clarendon, Oxford, 1979; Mir, Moscow, 1982).
9. B. I. Shklovskiĭ and A. L. Efros, *Electronic Properties of Doped Semiconductors* (Nauka, Moscow, 1979; Springer, New York, 1984).
10. A. A. Abrikosov, *Fundamentals of the Theory of Metals* (Nauka, Moscow, 1987; North-Holland, Amsterdam, 1988).
11. B. L. Al'tshuler, A. G. Aronov, and D. E. Khmel'nitskiĭ, Pis'ma Zh. Éksp. Teor. Fiz. **36** (5), 157 (1982) [JETP Lett. **36**, 195 (1982)].

Translated by G. Skrebtsov

Physics of the Solid State, Vol. 44, No. 3, 2002, pp. 490–492. Translated from Fizika Tverdogo Tela, Vol. 44, No. 3, 2002, pp. 471–472.

PROCEEDINGS OF THE V INTERNATIONAL WORKSHOP "FULLERENES AND ATOMIC CLUSTERS"

(St. Petersburg, Russia, July 2–6, 2001)

Electrodynamic Response of a Nanosphere

D. V. Bulaev, V. A. Geyler, and V. A. Margulis

Mordovian State University, ul. Bol'shevistskaya 68, Saransk, 430000 Russia

e-mail: theorphysics@mrsu.ru

Abstract—The electrodynamic response of electron gas on the surface of a nanosphere in a weak magnetic field is studied. The case of the photon polarization vector oriented parallel to the magnetic field (the Faraday geometry) is considered. An analytic expression for the coefficient of electromagnetic-radiation absorption by the nanosphere is derived. It is shown that, at low temperatures, the absorption curve has, in the general case, two resonance peaks. The curve also exhibits breaks. © *2002 MAIK "Nauka/Interperiodica".*

New technologies permit one to produce nanospheres with diameters from a few to hundreds of nanometers [1], and, quite recently, it has become possible to deposit metal or semiconductor coatings on them [2]. The progress made in this technology has stimulated an explosive growth in the number of publications on nanospheres. The spectral [3] and transport properties of spherical particles [4, 5] and the effect of system nonsphericity on the spectral and magnetic characteristics [6] and optical properties [7] are attracting considerable interest. Investigation of intraband optical transitions in nanostructures offers important information on the parameters of the energy spectrum and of the electronic Fermi surface [8, 9].

In this work, we investigate the electrodynamic response of a nanosphere placed in a weak magnetic field. The model of the sphere can be used to study dielectric spherical particles coated by a thin metal or semiconductor shell with a thickness considerably less than the particle diameter.

We consider a gas of noninteracting electrons moving over the nanosphere surface in a weak uniform magnetic field. In this case, the term quadratic in the field in the Hamiltonian can be dropped. Then, the energy spectrum and the wave function of an electron can be written as

$$E_{l,m} = \frac{\hbar\Omega}{2} l(l+1) + \frac{\hbar\omega_c}{2} m,$$

$$\psi_{l,m}(\vartheta, \varphi) = Y_{l,m}(\vartheta, \varphi),$$

where l and m are the orbital and magnetic quantum numbers, respectively; $\Omega = \hbar/m^*R^2$; m^* is the effective electron mass; R is the radius of the nanosphere; ω_c is the cyclotron frequency; and $Y_{l,m}$ are the spherical harmonics. These relations are applicable if the inequality $\omega_c \ll 4\Omega$ holds.

We calculate absorption for the Faraday configuration, namely, for the photon polarization vector parallel to the uniform magnetic field.

The method developed in [10] permits one to derive the absorption coefficient by treating the electron interaction with a high-frequency electromagnetic field in terms of perturbation theory. By assuming there to be a degenerate electron gas, neglecting spontaneous photon emission, and dropping exponentially small terms, we obtain the following estimate for the absorption coefficient in the dipole approximation:

$$\frac{\Gamma}{\Gamma_0} \approx \frac{\Omega}{\omega} \sum_{l=0}^{\infty} \sum_{m=-l}^{l} \frac{l^2[(l+1)^2 - m^2]}{4(l+1)^2 - 1} \times \frac{f_0(E_{l,m})[1 - f_0(E_{l,m} + \hbar\omega)]}{1 + \tau^2(\omega - \Omega(l+1))^2}, \quad (1)$$

where $\Gamma_0 = 4\pi e^2\tau/cm^*S\sqrt{\varepsilon(\omega)}$, τ is the phenomenological relaxation time, S is the area of the sphere's surface that intercepts the electromagnetic radiation, $\varepsilon(\omega)$ is the real part of the dielectric permittivity (assuming no dispersion in the frequency range considered here), and $f_0(E_{l,m})$ is the Fermi function.

At low temperatures, the major contribution to the absorption coefficient is due solely to transitions from the levels lying below the chemical potential. Let l_0 be the orbital quantum number such that $E_{l_0,-l_0} \le \mu < E_{l_0+1,-l_0-1}$. Then, resonance will occur only in transitions between the levels of the l_0 and $l_0 + 1$ shells, as well as between those of the $l_0 - 1$ and l_0 shells (the latter is possible only if the l_0 shell is not closed); in other words, resonances in the absorption appear at frequencies $\omega = \Omega l_0$ and $\Omega(l_0 + 1)$.

1063-7834/02/4403-0490$22.00 © 2002 MAIK "Nauka/Interperiodica"

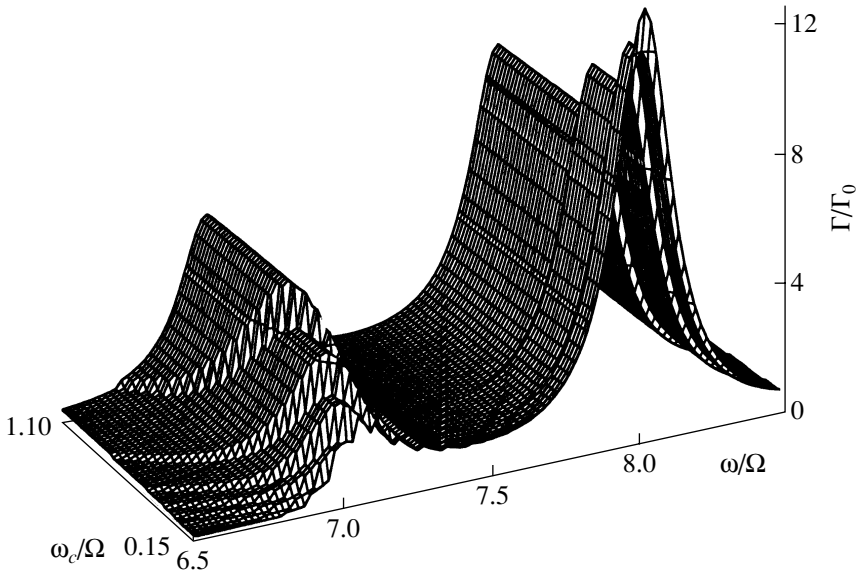

Absorption coefficient of a nanosphere vs. electromagnetic radiation frequency and magnetic field strength; $R = 10^{-5}$ cm, $T = 0.00001$ K, $\tau = 5 \times 10^{-11}$ s, and $\mu = 5.165 \times 10^{-15}$ erg.

Considering the contribution of only these resonance transitions, we obtain the following estimate for the absorption coefficient in the case of a strongly degenerate gas ($\mu \gg T$):

$$\frac{\Gamma}{\Gamma_0} \approx \frac{\Omega}{\omega} \times \left\{ \frac{l_0^2(l_0+m_0)(4l_0^2-2m_0^2+2l_0m_0+9l_0+3m_0+5)}{6(2l_0+1)(2l_0+3)[1+\tau^2(\omega-\Omega(l_0+1))^2]} + \frac{l_0^2[(l_0+1)^2-m_0^2]f_0(E_{l_0,m_0})}{(2l_0+1)(2l_0+3)[1+\tau^2(\omega-\Omega(l_0+1))^2]} + \sum_{m=-l_0+1}^{l_0-1} \frac{(l_0-1)^2(l_0^2-m^2)}{(2l_0-1)(2l_0+1)} \frac{1-f_0(E_{l_0-1,m}+\hbar\omega)}{1+\tau^2(\omega-\Omega l_0)^2} \right\}. \quad (2)$$

In the case of $E_{l_0,l_0} \le \mu < E_{l_0+1,-l_0-1}$, the magnetic quantum number is $m_0 = l_0$; otherwise, m_0 is found from the double inequality $E_{l_0,m_0} \le \mu < E_{l_0,m_0+1}$. As shown by a numerical analysis, the plots of Eqs. (1) and (2) almost coincide in the vicinity of the resonance frequencies.

As already pointed out, variation of the field B can cause the electronic levels to cross the chemical potential. In this case, the quantum numbers l_0 and m_0 may change. As a result, the peak height will change in a jump, and, as seen from the figure, this will increase the height of the first peak and reduce that of the second.

As follows from Eq. (1), at low enough temperatures, only those electrons whose energy lies in the $[\mu - \hbar\omega, \mu]$ interval take part in absorption. When the frequency of the electromagnetic radiation varies, the electron energy level may cross the $\mu - \hbar\omega$ level. As a result, the number of electrons involved in absorption will change and, as seen from the figure, a break will form in the dependence of Γ on ω.

In weak fields, breaks form in series. Each series of breaks corresponds to a crossing of levels of the same shell with $\mu - \hbar\omega$. The number of breaks in a series is equal to the number of levels in the corresponding shell. For instance, the number of breaks for the l shell is $2l + 1$. As seen from the condition of the break formation $\mu - \hbar\omega = E_{l,m}$, breaks appear at the frequencies $\omega = \mu/\hbar - \Omega l(l+1)/2 - \omega_c m/2$. Whence it follows that the distance between neighboring breaks in a series is $\Delta\omega = \omega_c/2$. The magnitude of the jump at a break is very small compared to the peak height.

Note that an increase in temperature smoothens the breaks substantially and, in addition, results in a decrease in the height of the large peak and an increase in the amplitude of the small one.

ACKNOWLEDGMENTS

This study was supported by the Russian Foundation for Basic Research (project no. 01-02-16564), DFG (project no. 436 RUS 113/572), and the "Universities of Russia" Program (project no. 015.01.01.049).

REFERENCES

1. Yu. A. Vlasov, V. N. Astratov, O. Z. Karimov, *et al.*, Phys. Rev. B **55** (20), R13357 (1997).
2. L. Fu and L. Resca, Phys. Rev. B **56** (17), 10963 (1997).
3. D. N. Aristov, Pis'ma Zh. Éksp. Teor. Fiz. **70** (6), 405 (1999) [JETP Lett. **70**, 410 (1999)].
4. C. L. Foden, M. L. Leadbeater, and M. Peper, Phys. Rev. B **52** (12), 8646 (1995).
5. J. Brüning, V. A. Geyler, V. A. Margulis, and M. A. Pyataev, in *Proceedings of the 9th International Symposium "Nanostructures: Physics and Technology", St. Petersburg, Russia, 2001*, p. 367.
6. D. V. Bulaev, V. A. Geyler, and V. A. Margulis, Phys. Rev. B **62** (17), 11517 (2000).
7. R. Ruppin, Phys. Rev. B **45**, 11209 (1992).
8. N. G. Galkin, V. A. Margulis, and A. V. Shorokhov, Fiz. Tverd. Tela (St. Petersburg) **43** (3), 511 (2001) [Phys. Solid State **43**, 530 (2001)].
9. V. A. Geyler, V. A. Margulis, and A. V. Shorokhov, Phys. Rev. B **63**, 245316 (2001).
10. F. G. Bass and I. B. Levinson, Zh. Éksp. Teor. Fiz. **49** (3), 914 (1965) [Sov. Phys. JETP **22**, 635 (1965)].

Translated by G. Skrebtsov

Physics of the Solid State, Vol. 44, No. 3, 2002, pp. 493–496. From Fizika Tverdogo Tela, Vol. 44, No. 3, 2002, pp. 473–475.

PROCEEDINGS OF THE V INTERNATIONAL WORKSHOP "FULLERENES AND ATOMIC CLUSTERS"

(St. Petersburg, Russia, July 2–6, 2001)

Electrodiffusion Phenomena in C_{60} Thin Films[1]

E. A. Katz[1], D. Faiman[1, 2], S. M. Tuladhar[1], S. Shtutina[2], N. Froumin[3], and M. Polak[3]

[1] *Department of Solar Energy and Environmental Physics, J. Blaustein Institute for Desert Research, Ben-Gurion University of the Negev, Sede Boqer, 84990 Israel*

e-mail: keugene@bgumail.bgu.ac.il

[2] *Department of Physics, Ben-Gurion University of the Negev, Beersheba, 84105 Israel*

[3] *Department of Materials, Ben-Gurion University of the Negev, Beersheba, 84105 Israel*

Abstract—As part of our ongoing research program to produce semiconductor devices based on C_{60} thin films, we report here on our first attempts at the intercalative doping of C_{60} thin films through the diffusion of metals. Two techniques were employed: (a) chemically induced counter electrodiffusion of Cu and I_2 into a C_{60} matrix and (b) Au diffusion under the action of an external electric field. © *2002 MAIK "Nauka/Interperiodica".*

The most commonly practiced kind of doping of a C_{60} solid is intercalation whereby dopants are located between the C_{60} molecules in the interstitial positions of the host crystal structure [1]. Intercalated fullerides can be produced by the simultaneous vacuum evaporation of C_{60} molecules and dopant atoms or by diffusion of dopant atoms into a pristine C_{60} crystal. Such diffusion can occur as a spontaneous process or it can be induced by an external stimulus, like vapor pressure or an electric field applied to the sample. The study of impurity diffusion in C_{60} crystals and thin films has recently become an important subject in fullerene research [2].

This paper presents the results of an experimental study of two diffusion phenomena in C_{60} thin films (with emphasis on the possible semiconductor doping of the material): (a) chemically induced counter electro-diffusion (CICED) of Cu and I_2 into a C_{60} matrix and (b) diffusion of Au under the action of an external electric field. The resulting samples were characterized by x-ray diffraction, Auger electron spectroscopy (AES), and conductivity measurements.

1. EXPERIMENTAL

C_{60} films 100 nm thick were grown, using a vacuum deposition technique, on glass and mica substrates, as well as on glass substrates, predeposited with a Cu sublayer [3, 4].

The crystalline structure of these C_{60} films was studied by x-ray diffraction (XRD). The morphology of the front surface of the films (in particular, the grain size at the front surface) was studied by atomic-force microscopy.

[1] This article was submitted by the authors in English.

The elemental composition at the surface and in-depth concentration distributions ("sputter depth profiling") for C_{60} films were studied by AES combined with controlled Ar ion bombardment. The details of the AES measurements are presented elsewhere [5].

The conductivity of C_{60} films was measured in two- and four-probe configurations of electrodes (Fig. 1) using a Hewlett Packard 4140B picometer dc voltage source.

The other experimental details are given below.

2. RESULTS AND DISCUSSION

2.1. Chemically Induced Counter Electrodiffusion of Cu and I_2 into the C_{60} Matrix

Recently [5], we developed a new technique for doping (intercalation) C_{60} thin films, the so-called

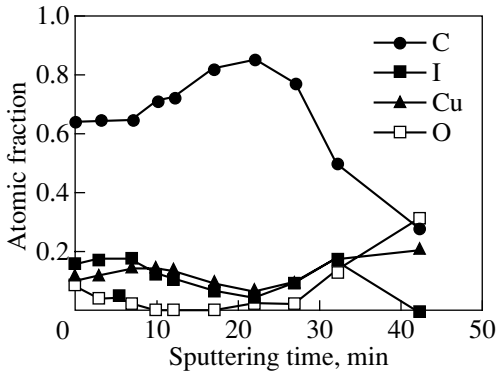

Fig. 1. Depth distribution of Cu, I, O, and C atomic fractions (in units corresponding to the time of sputtering by Ar ions) measured by AES after ten minutes of exposure to an I_2 atmosphere of a Cu-supported C_{60} film.

1063-7834/02/4403-0493$22.00 © 2002 MAIK "Nauka/Interperiodica"

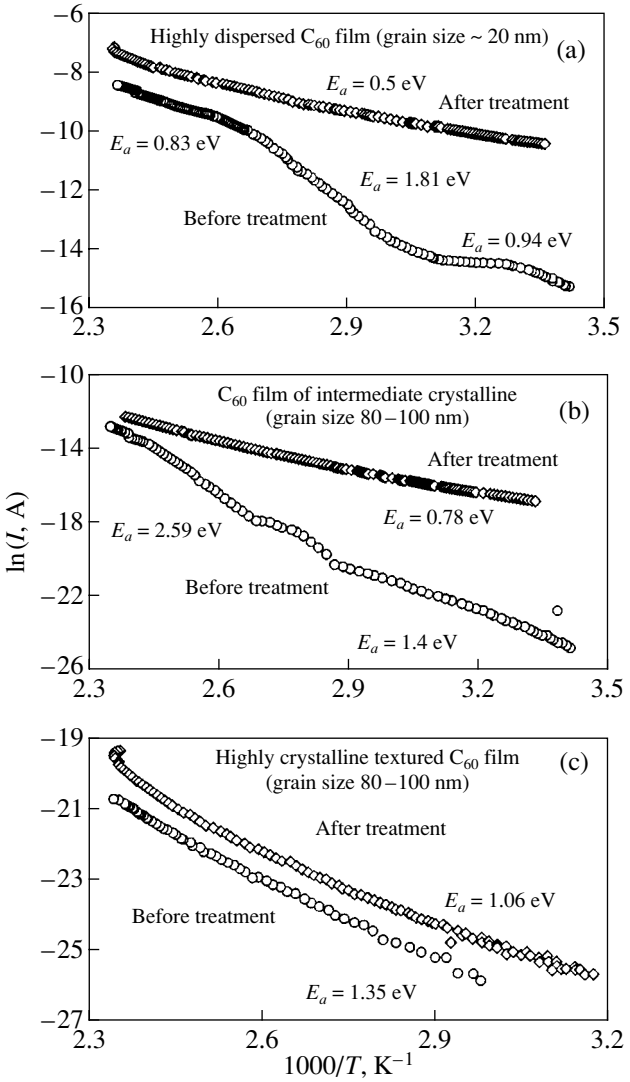

Fig. 2. Temperature dependences of two-probe coplanar conductivity before and after treatment of the C_{60} films for an hour under an electric field of 500 V/cm at 150°C: (a) a highly dispersed film, (b) a film of intermediate crystallinity, and (c) a highly crystalline film.

CICED. The technique involves vacuum deposition of a highly crystalline C_{60} thin film onto a metal (Cu, Au, Ag) sublayer [3] and subsequent exposure of the samples to a reactive gas atmosphere.

If oxygen is employed as the reactive gas atmosphere, diffusion of oxygen atoms through the front surface of the fullerene film is observed and a corresponding slow counter diffusion of metal from the sublayer occurs (with a characteristic time measured in months). Analysis of the resulting doped material, after ten months of exposure to air of the Cu-supported C_{60} films at room temperature, revealed the presence of Cu and O atoms at all depths in the samples and the formation of a complex which we refer to as $Cu_xO_yC_{60}$. We have published [5] detailed results of an oxygen-induced-doping experiment, together with a suggestion that the following CICED multistep process takes place under the experimental conditions: (1) well-known diffusion of molecular oxygen (O_2) from air into the C_{60} film, (2) emission of free electrons from the Cu sublayer to oxygen molecules in the C_{60} matrix, (3) generation of an internal electric field between $(O_2–C_{60})^-$ complexes and the Cu^+ sublayer, (4) drift of Cu^+ from the sublayer to the $(O_2–C_{60})^-$ complexes, and (5) formation of the $Cu_xO_yC_{60}$ complex.

In the case of an iodine atmosphere, the metal diffusion was observed to occur on a time scale that is several orders of magnitude faster. Indeed, even ten minutes of exposure of the Cu-supported C_{60} films to an I_2 atmosphere at room-temperature led to a complete disappearance of the Cu sublayer due to Cu diffusion into the C_{60} film. X-ray diffraction revealed an absence of Cu peaks. At the same time, together with the {111} reflections from the C_{60} lattice, four intense CuI peaks appeared after exposure. AES depth profiling measurements of this sample (Fig. 1) revealed the presence of Cu and I_2 at all depths in the C_{60} film (the most surprising result being that Cu is present even at the front surface of the film!). A clear correlation between the Cu and I atomic fractions is also in evidence. This indicates the existence of CuI over the entire thickness of the C_{60} film. In other words, we may conclude that the exposure of a Cu-supported C_{60} film to an I_2 atmosphere leads to counter diffusion of Cu and I_2 into the C_{60} matrix, resulting in the formation of a C_{60}–CuI composite material.

Using a two-probe measuring technique, a substantial increase in the dark conductivity [from 10^{-9}–10^{-12} to 10^{-3}–10^{-4} $(\Omega\ \mathrm{cm})^{-1}$] was observed after CuI doping. Unfortunately, no semiconductor behavior or photoconductivity of the doped samples were observed. These results suggest that electronic transport occurs mainly by percolation through the CuI phase of the composite material, which has low dark resistivity but is not photosensitive.

We believe, however, that by using this counter diffusion approach and optimizing the process conditions, it is possible to produce C_{60}-based materials doped with various compounds in the form of both phase-separated composites and solid solutions (intercalated fullerides). Intercalation of C_{60} with compounds is now becoming a research direction of vital importance because of the following recently published findings. Schon *et al.* [6] discovered superconductivity with a transition temperature T_c = 52 K in a single crystal of C_{60} doped by holes by using the technique of gate-induced doping in a field-effect transistor. This value of T_c is the highest ever observed in a C_{60}-based material. Furthermore, the authors believe that values of T_c up to 100 K will be achievable in a suitably expanded, acceptor-intercalated C_{60} lattice. On the other hand, to the best of our knowledge, the only successful examples of the doping

of C_{60} by acceptors is intercalation by compounds such as $InCl_3$, AsF_5, SbF_5, and $SbCl_5$ [7–9].

Furthermore, one of the most important CICED results presented—extremely fast metal diffusion into the C_{60} film under the action of an internal electric field—suggested that one should attempt the diffusion of metals into C_{60} films under the action of an external electric bias.

2.2. Diffusion of Au into C_{60} Films under the Action of an External Electric Bias

Three types of C_{60} films grown on an insulator substrate were used in these experiments: (a) highly dispersed films (grain size of ~20 nm, no texture), (b) films of intermediate crystallinity (grain size of 80–100 nm, no texture), and (c) highly crystalline films (grain size of 500–1500 nm, ⟨111⟩ texture).

The conductivity measurements were performed *in situ* while pumping the quartz tube with the sample to a dynamic vacuum of 10^{-6} Torr and heating the samples to elevated temperatures. After the sample temperature had reached a value of 150°C, we applied a series of external electric fields, with strengths of 150, 300, and 500 V/cm, between the Au electrodes. We observed an increase in the measured value of current (i.e., in the film conductivity) with time related to the length of time the field was applied. The rate of increase was observed to be intensified as the electric field strength was increased. These results are in agreement with those of a similar experiment performed by Firlej *et al.* [2, 10]. However, in addition, we revealed a strong correlation between the rate of the conductivity increase and the crystalline structure of the films: for increased film grain sizes, the rate of conductivity increase was observed to diminish.

Figure 2 shows the temperature dependences of the two-probe coplanar conductivity of C_{60} films with various degrees of crystallinity before and after treatment by a 500 V/cm electric field at a temperature of 150°C for an hour. All temperature-dependent results show a semiconductor-like activated behavior. Furthermore, we can certainly conclude that the values of activation energy decrease as a result of treatment in all three cases. This is direct evidence that semiconductor doping occurred during the treatment.

Another interesting feature of these results is the observed relationship between the decrease in activation energy and the crystalline structure of the samples (table). Specifically, the minimum value of activation energy (or, in the other words, the maximum doping effect) after treatment was observed for those samples with the smallest grains. In this case, the room-temperature conductivity was found to increase by more than 50 times (Fig. 2a). Conversely, the maximum activation energy (i.e., the minimum doping effect) was observed for a highly crystalline sample (Fig. 2c). Both a decrease in activation energy and an increase in the conductivity values (after treatment) with decreasing grain size were observed.

Correlation between the grain sizes in C_{60} films and their value of activation energy of conductivity after treatment under an electric field of 500 V/cm at 150°C for an hour

C_{60} film structure	Grain size, nm	Activation energy, eV
Highly dispersed	~20	0.5
Intermediate crystalline	80–100	0.78
Highly crystalline, textured	500–1500	1.06

The electrodiffusion experiment using a four-probe configuration of electrodes demonstrated similar results. AES and x-ray photoelectron spectroscopy (XPS) characterization of the doped samples, as well as photoconductivity measurements, are in progress.

In general, the diffusion rate of an impurity atom is known to be higher along grain boundaries than within a crystal grain [11]. We interpret the observed doping behavior as the electrodiffusion of Au from an electrode dominantly along grain boundaries and the subsequent intercalation of the C_{60} lattice by Au atoms.

3. CONCLUSIONS

(1) Structural and chemical changes in Cu-supported C_{60} thin films during their room-temperature-exposure to an I_2 atmosphere were studied by XRD, AES, XPS, and conductivity measurements. A C_{60}–CuI composite material was found to be produced during the exposure of a Cu-supported C_{60} film to an I_2 atmosphere. Even ten minutes of exposure resulted in complete disappearance of the Cu sublayer and the formation of a CuI phase over the whole thickness of the C_{60} film. The room-temperature dark conductivity of the CuI-doped samples was observed to increase by several orders of magnitude, but semiconductor behavior was not observed.

(2) We reported the effect of an external electric field on the *in situ* measured conductivity of C_{60} films with different degrees of crystallinity. Semiconductor behavior with increased conductivity values and decreased conductivity activation energy has been demonstrated for the doped samples. The results are explained by the electrodiffusion of Au from an electrode dominantly along grain boundaries and by the subsequent intercalation of the C_{60} lattice by Au atoms.

ACKNOWLEDGMENTS

This work was partly supported by the Israel Ministry of National Infrastructures. E.A.K. also thanks the financial support of the Israel Ministry of Immigrant Absorption. S.M.T. thanks the Albert Katz School (for Desert Studies) and the Bonna Terra Foundation.

REFERENCES

1. M. S. Dresselahaus, G. Dresselahaus, and P. C. Eklund, *Science of Fullerenes and Carbon Nanotubes* (Academic, San Diego, 1996).
2. L. Firlej, Condens. Matter News **8**, 22 (2000).
3. E. A. Katz, U.S. Patent No. 5876790 (1999).
4. E. A. Katz, D. Faiman, S. Shtutina, and A. Isakina, Thin Solid Films **368**, 49 (2000).
5. E. A. Katz, D. Faiman, S. Shtutina, *et al.*, Physica B (Amsterdam) **304**, 348 (2001).
6. J. H. Schön, C. H. Kloc, and B. Batlogg, Nature **408**, 549 (2000).
7. W. Maser, S. Roth, J. Anders, *et al.*, Synth. Met. **51**, 103 (1992).
8. W. R. Datars, T. R. Chien, R. K. Nkum, and P. K. Ummat, Phys. Rev. B **50**, 4937 (1994).
9. M. Barati, P. K. Ummat, and W. R. Datars, Solid State Commun. **106**, 91 (1998).
10. L. Firlej, N. Kirova, and A. Zahab, Phys. Rev. B **59**, 16028 (1999).
11. J. C. Fisher, J. Appl. Phys. **22**, 74 (1951).

Physics of the Solid State, Vol. 44, No. 3, 2002, pp. 497–499. Translated from Fizika Tverdogo Tela, Vol. 44, No. 3, 2002, pp. 476–477.

PROCEEDINGS OF THE V INTERNATIONAL WORKSHOP "FULLERENES AND ATOMIC CLUSTERS"

(St. Petersburg, Russia, July 2–6, 2001)

Low-Frequency Raman Scattering in a Polycrystalline C_{60} Film: The Role of Orientational Disorder

A. E. Batalov*, V. K. Malinovsky*, A. M. Pugachev*, N. V. Surovtsev*, and A. P. Shebanin**

** Institute of Automatics and Electrometry, Siberian Division, Russian Academy of Sciences, Universitetskiĭ pr. 1, Novosibirsk, 630090 Russia*

*** Institute of Geology and Geophysics, Siberian Division, Russian Academy of Sciences, pr. Nauki 3, Novosibirsk, 630090 Russia*

e-mail: malinovsky@iae.nsk.su

Abstract—Low-frequency Raman scattering in the orientationally disordered phase of a polycrystalline C_{60} film is investigated. By analogy with disordered media (glasses), the low-frequency Raman spectra are interpreted in terms of light scattering by localized vibrational states. *© 2002 MAIK "Nauka/Interperiodica".*

1. INTRODUCTION

In recent years, terahertz (THz) dynamics in disordered media has attracted the particular attention of researchers in the field of solid-state physics. The data obtained in this frequency range contain information on elementary relaxation processes occurring in different media and on vibrational states at wavelengths of the order of 1–10 nm. Investigations into the THz dynamics in the orientationally disordered phase of fullerite crystals make it possible to elucidate the nature of fullerene relaxation and the specific features of ordering on a nanometer scale. Moreover, analysis of the THz dynamics in fullerenes provides a better insight into elementary relaxation processes and the kinetic features of chemical reactions and transfer in fullerene materials.

Although low-frequency (<100 cm^{-1}) Raman scattering is one of the most widely used experimental techniques of investigating THz dynamics, the available data on low-frequency Raman scattering in the orientationally disordered phase of fullerites are very scarce. In particular, Horoyski and Thewalt [1] observed the central peak in the low-frequency Raman spectrum of the C_{60} fullerene compound. This peak was attributed to light scattering by isotropically rotating fullerene molecules. However, as was shown later in [2], this interpretation is inconsistent with the experimental data obtained for polycrystalline C_{60} films. The results of the present work complemented the data reported in [2]: we estimated the rotational broadening from the high-frequency Raman spectrum, made the assumption that the low-frequency Raman spectra can be associated with light scattering by vibrational excitations localized in orientational clusters, and compared the Raman spectra of the C_{60} film and C_{60} single crystals.

2. EXPERIMENTAL TECHNIQUE

The Raman scattering spectra of the polycrystalline C_{60} film were recorded on a U1000 spectrometer using the 514-nm exciting line. A grazing incidence of a low-power (<1 W/cm^2) laser beam was used to exclude photopolymerization. The absence of photopolymerization in the course of measurements was checked against the Raman line at ~1470 cm^{-1}.

3. RESULTS AND DISCUSSION

Earlier [2], it was demonstrated that the low-frequency spectrum of a polycrystalline C_{60} film cannot be described by a Lorentzian contour, as would be expected for light scattering due to isotropic rotation of fullerene molecules. Recall that the low-frequency Raman spectrum of fullerite single crystals differs in shape from the Lorentzian contour [1, 3]. In [2], it was also noted that the relaxation time estimated from the low-frequency Raman spectrum is 30 times shorter than the characteristic rotation time determined from the experimental NMR data by Tycko *et al.* [4]. It is of interest to verify the estimate of the characteristic time of rotation of C_{60} molecules by using Raman spectroscopy. The estimation technique is based on the fact that the broadening of the anisotropic Raman modes involves the vibrational broadening [5]. According to the experimental data obtained in the present work, the width of the anisotropic mode at a frequency of 1120 cm^{-1} does not exceed 1.5 cm^{-1}. Consequently, the

1063-7834/02/4403-0497$22.00 © 2002 MAIK "Nauka/Interperiodica"

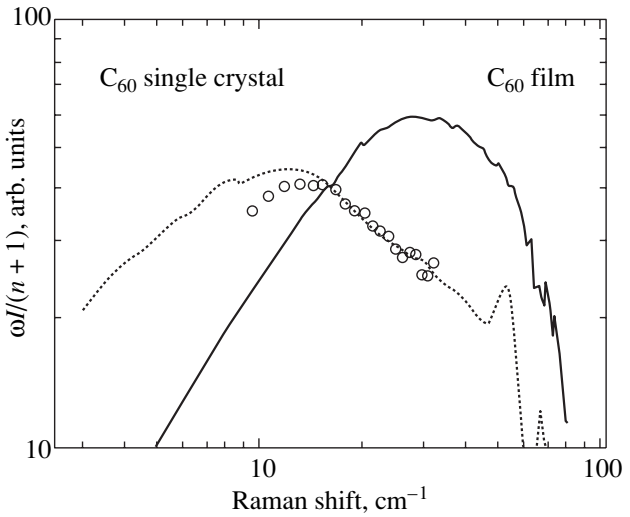

Low-frequency Raman spectra of the C_{60} fullerite film (solid line) and C_{60} single crystals according to the data taken from [1] (circles) and [3] (dashed line).

contribution from the vibrational broadening cannot be greater than 1.5 cm^{-1} (the corresponding rotation time is longer than 3.5 ps). The maximum of the spectral susceptibility $I/(n + 1)$ for the C_{60} film is observed at 17 cm^{-1}. This value considerably exceeds both the estimate obtained from the NMR data (0.44 cm^{-1}) and the upper boundary determined from the high-frequency Raman spectrum (<1.5 cm^{-1}). Thus, the spectral shape of the low-frequency Raman spectrum of the C_{60} film and the disagreement between the location of the Raman susceptibility maximum and the estimated characteristic time of rotation of C_{60} molecules are in contradiction with the interpretation of low-frequency Raman scattering in the C_{60} fullerite as light scattering due to rotations of fullerene molecules.

Alternatively, the low-frequency Raman spectrum can be interpreted in terms of light scattering by acoustic vibrational states localized through orientational disorder [2]. This interpretation makes allowance for the fact that the characteristic time of rotation of C_{60} molecules is substantially longer than the period of acoustic vibrations in the frequency range covered. In this case, on the time scale of vibrational excitations, the fullerite structure can be considered to be formed by C_{60} molecules with frozen random mutual orientations, which leads to fluctuations in the effective elastic constants. These fluctuations bring about the localization of vibrations. Therefore, the Stokes component of the Raman spectrum can be described by the formula [6]

$$I(\omega) = C(\omega)g(\omega)\frac{n+1}{\omega}. \quad (1)$$

Here, $g(\omega)$ is the density of vibrational states and $C(\omega)$ is the photon–photon coupling coefficient. As was shown in [2], the low-frequency (<40 cm^{-1}) component of the spectrum is characterized by the photon–photon coupling coefficient $C(\omega) \approx$ const. Within this approximation, the $g(\omega)$ density can be written as

$$g(\omega) \propto \omega\frac{I}{n+1}. \quad (2)$$

The Raman spectrum of the C_{60} film in representation (1) is displayed in the figure. For comparison, this figure depicts the Raman spectra of C_{60} single crystals according to the data taken from [1, 3]. It can be seen that the Raman spectrum of the C_{60} film is considerably shifted with respect to the spectra of single-crystal samples. In the framework of the proposed model, the above shift can be explained by the different sizes of orientational clusters in these samples. In our case, the orientational cluster represents a set of C_{60} molecules whose mutual orientation and orientational motion are correlated at a certain instant of time. A vibrational excitation at a wavelength of the order of the cluster size undergoes strong scattering and becomes localized. Within the spherical cluster shape approximation, the frequency of the fundamental vibrational mode and the cluster size L are related by the expression [7]

$$\omega_{max} \approx 0.85 v_t/cL. \quad (3)$$

Here, v_t is the transverse acoustic velocity and c is the velocity of light. Expression (3) gives the following estimate of the cluster size for single crystals: $L \approx$ 4.0 nm (v_t = 1.7 km/s and ω_{max} = 12 cm^{-1}). The evaluated cluster size agrees with the correlation length of the orientation of C_{60} molecules, which was estimated by Pintschovius *et al.* [8] from x-ray and neutron scattering data. This agreement counts in favor of the model proposed above for low-frequency Raman scattering in C_{60} fullerites. According to the Raman spectra of the polycrystalline C_{60} film, the size of orientational clusters is estimated as $L \approx 1.7$ nm. The difference between the correlation lengths of the orientational order in the C_{60} single crystal and polycrystalline film can be associated with the high concentration of defects in the film as compared to that in the single crystal.

4. CONCLUSION

Thus, the low-frequency Raman scattering in the C_{60} fullerite can be explained in terms of light scattering by vibrational excitations localized through the orientational disorder. The correlation lengths estimated from the Raman spectra and structural data are in good agreement. It was found that the length of orientational ordering in the C_{60} film is considerably smaller than that in single crystals.

ACKNOWLEDGMENTS

This work was supported by the State Scientific and Technical Program "Fullerenes and Atomic Clusters," the Ministry of Science of the Russian Federation (project no. 5-4-99).

REFERENCES

1. P. J. Horoyski and M. L. W. Thewalt, Phys. Rev. B **48** (15), 11446 (1993).
2. V. K. Malinovsky, N. V. Surovtsev, and A. P. Shebanin, Pis'ma Zh. Éksp. Teor. Fiz. **72** (2), 88 (2000) [JETP Lett. **72**, 62 (2000)].
3. A. E. Batalov *et al.* (in press).
4. R. Tycko *et al.*, Phys. Rev. Lett. **67** (14), 1886 (1991).
5. F. J. Bartoli and T. A. Litovitz, J. Chem. Phys. **56** (1), 404 (1972).
6. R. Shuker and R. W. Gammon, Phys. Rev. Lett. **25** (4), 222 (1970).
7. E. Duval, A. Boukenter, and B. Champagnon, Phys. Rev. Lett. **56** (19), 2052 (1986).
8. L. Pintschovius *et al.*, Phys. Rev. Lett. **75** (15), 2843 (1995).

Translated by O. Borovik-Romanova

Physics of the Solid State, Vol. 44, No. 3, 2002, pp. 500–502. Translated from Fizika Tverdogo Tela, Vol. 44, No. 3, 2002, pp. 478–480.

PROCEEDINGS OF THE V INTERNATIONAL WORKSHOP "FULLERENES AND ATOMIC CLUSTERS"

(St. Petersburg, Russia, July 2–6, 2001)

Analysis of Spectral Features of the Optical Constants of Fullerene and Halogen-Fullerene Films near the Absorption Edge

T. L. Makarova* and I. B. Zakharova**

** Ioffe Physicotechnical Institute, Russian Academy of Sciences, ul. Politekhnicheskaya 26, St. Petersburg, 194021 Russia*
e-mail: tatiana.makarova@physics.umu.se
*** St. Petersburg State Technical University, ul. Politekhnicheskaya 29, St. Petersburg, 195251 Russia*

Abstract—This paper reports on measurements of IR spectra and of the extinction coefficient in the 1.2- to 4.2-eV range made on $C_{60}Br_x$ films and compared with those for pure C_{60} films. The modification of the electronic spectrum near the absorption edge is connected with differences in the film structure and with suppression of charge-transfer excitons. The $C_{60}Br_x$ films exhibit additional absorption below the fundamental absorption edge of C_{60}. © *2002 MAIK "Nauka/Interperiodica".*

Several stable chemical fullerene compounds are known presently, namely, $C_{60}Br_6$, $C_{60}Br_8$, and $C_{60}Br_{24}$, whose molecules have covalent C–Br bonds that form from double bonds in the C_{60} molecule [1, 2]. The best studied of them, $C_{60}Br_{24}$, has a spherically symmetric structure, with the halogen atoms attached to the reactive double bond of the C_{60} cluster. Experimental studies of the physical properties and electronic structure of the material are hampered by the thermal instability of $C_{60}Br_{24}$, which renders preparation of thin $C_{60}Br_x$ films and of crystals of a sufficiently large size difficult [3]. Special measures have to be taken to prevent decomposition of the material during thin film deposition or crystal growth.

Our films were prepared using quasi-equilibrium methods of vacuum deposition, more specifically, by fast evaporation in a quasi-closed volume [4] and by the hot-wall technique. The starting material for film preparation was a yellow-brown microcrystalline $C_{60}Br_{24}$ powder with grains 5–10 μm in diameter. The elemental composition of the pristine material was determined by pyrohydrolysis. The reference films were obtained from a 99.98%-pure C_{60} powder. KBr (100) and KDB-10 silicon (111) were used as substrates. The C_{60} films were deposited at a substrate temperature of 250–300°C, providing a perfect crystalline structure, while the halofullerene films were deposited at substrate temperatures no higher than 100–120°C and at a high rate (100–200 nm/min) in order to preclude thermal decomposition. Evaporation of $C_{60}Br_{24}$ can be considered to be that of a two-component mixture in which one component (Br) is volatile and the other (C_{60}) is not. $C_{60}Br_{24}$ is known to decompose at a temperature of about 170°C into C_{60} and Br_2 [3], while the saturated vapor pressure of C_{60} is such that effective evaporation occurs only at 400–500°C. We showed earlier [4] that condensation performed in such conditions produces variable-composition films with a high bromine content near the interface and that the deposition of multicomponent vapor on a substrate may give rise to chemical bonding of the fullerene and bromine molecules in accordance with the saturated vapor pressure of each component.

The crystal structure and surface morphology of the films thus obtained were studied with scanning electron microscopy. The C_{60} films on silicon are polycrystalline, with grain size closes to the film thickness (300–500 nm). The halofullerene films are either amorphous or fine-grained crystalline, because the material was deposited on colder substrates in this case.

We measured the IR spectrum of the starting $C_{60}Br_{24}$ powder and of the $C_{60}Br_x$ films. The table compares literature data on the absorption lines of known stable bromofullerene compounds with experimental data. The film spectra exhibit absorption lines characteristic of the $C_{60}Br_{24}$, $C_{60}Br_8$, and $C_{60}Br_6$ compounds, which suggests the formation of a C–Br chemical bond in the films.

We used spectral ellipsometry in the 1.2- to 4.2-eV photon energy range to determine the energies of the main optical transitions in C_{60} and $C_{60}Br_x$ in the solid state. An analysis of the optical absorption edge in C_{60} requires that both intra- and intermolecular electronic processes be taken into account. The former processes give rise to the formation of Frenkel excitons; the latter, to the formation of charge-transfer excitons, in which the two charges are located on adjacent molecules.

The figure compares the absorption spectra (extinction coefficients) of the C_{60} reference sample and

1063-7834/02/4403-0500$22.00 © 2002 MAIK "Nauka/Interperiodica"

Comparison of the absorption lines observed in $C_{60}Br_{24}$, $C_{60}Br_8$, and $C_{60}Br_6$ molecules and $C_{60}Br_x$ films

IR mode energy, cm^{-1}					
data of [1–3]			our measurements		main IR C_{60} modes
$C_{60}Br_{24}$	$C_{60}Br_8$	$C_{60}Br_6$	$C_{60}Br_{24}$, powder	$C_{60}Br_x$ film	
	526	529		526	526
		538			
546	546	551		546	
	563	562			
		575		576	576
606	610	606	*	604	
		661			
		679			
	706	708			
720	718		720		
		742			
751	750	751	750	752	
	766				
776			776	776	
		801			
		812			
	820	829			
849	845	850	850		
912			914	914	
946	947	945			
	963		970	970	
1050	1047				
		1065			
	1086	1085			
1117					
	1142	1152	1146		
	1182	1198			1183
1244	1250	1265			
		1291	1270		
1400	1422	1421		1420	1429
			1440	1435	
				1455	
		1473			
*	*	*	1600	1604	
			1650		

$C_{60}Br_x$. Deconvolution of the spectra into constituent Lorentzians permits one to isolate three optical transitions for C_{60}, namely, 3.52 eV (the $h_g \longrightarrow t_{1u}$ transition), 2.64 eV ($h_u \longrightarrow t_{1g}$), and 2.94 eV. The 2.94-eV band corresponds to none of the transitions in the C_{60} molecule and can be apparently assigned to the charge-transfer exciton, because its energy is higher than that of the lowest Frenkel exciton. A common feature is the presence of an absorption band at 3.52 eV, which even has the same intensity in all the three spectra, and of the 2.64-eV band. However, the oscillator strength of the corresponding $h_u \longrightarrow t_{1g}$ transition in the spectra of bromine-containing films is considerably lower than that in the starting fullerene. An important difference

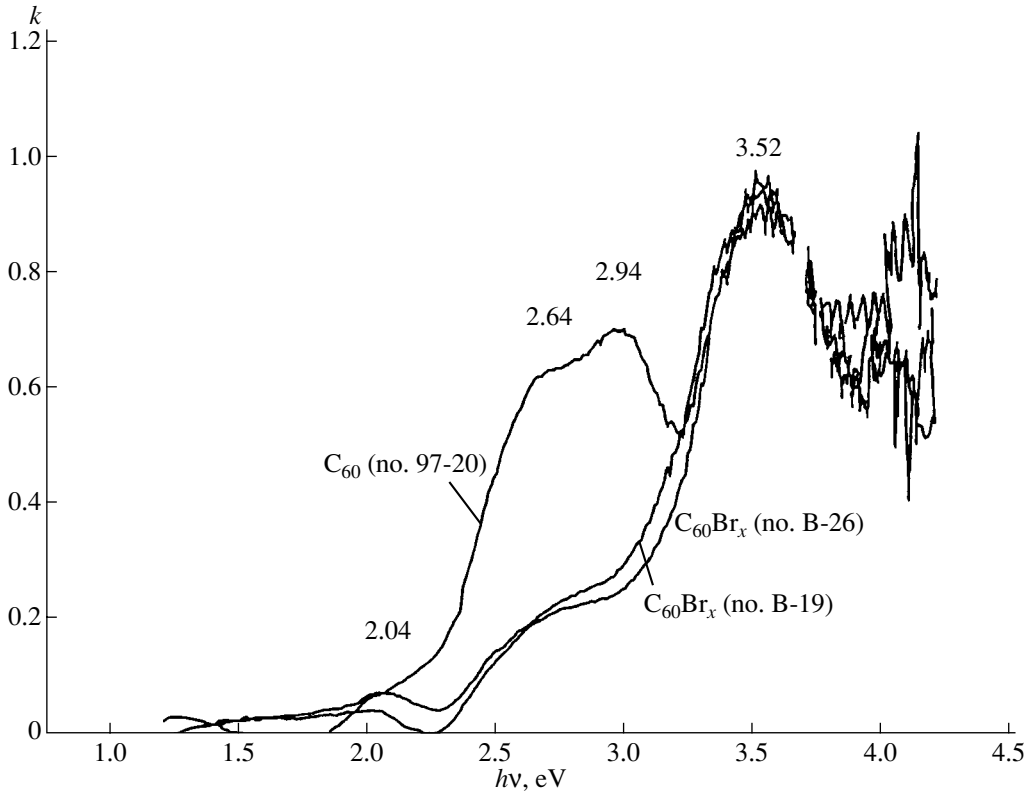

Comparative spectra of the extinction coefficient k of pure C_{60} films (no. 97-20) and of $C_{60}Br_x$ (nos. B-19 and B-26).

between the spectra is that the transition at 2.94 eV, associated with the charge-transfer exciton, is practically suppressed in the $C_{60}Br_x$ films. Additional studies showed, however, that the amplitude of this peak is also connected with the film structure in pure C_{60} films and that it depends strongly on the film deposition temperature, so that the disappearance of this peak in the halogen-containing films is associated, most likely, with their being amorphous. The presence of bromine in the $C_{60}Br_x$ films gives rise to an additional absorption band below 2 eV, which is not seen in the C_{60} spectrum. The absorption remains nonzero down to ~1.3 eV, which agrees with the theoretical estimates of the HOMO–LUMO energy gap (1.5 eV).

Thus, we have shown that structural degradation of thin fullerene films brings about noticeable modification of the electronic energy spectrum, which is associated with suppression of charge-transfer excitons. In $C_{60}Br_x$ films, we observed additional electronic transitions at energies below the fundamental absorption edge in C_{60}.

ACKNOWLEDGMENTS

This study was supported by the Russian Foundation for Basic Research, project no. 99-02-18170.

REFERENCES

1. P. L. Birkett, P. B. Hitchcock, H. W. Kroto, *et al.*, Nature **357**, 479 (1992).
2. F. N. Tebbe, R. L. Harlow, D. B. Chase, *et al.*, Science **256**, 822 (1922).
3. A. Djordjevic, M. Vojinovic-Miloradov, N. Petranovic, *et al.*, Fullerene Sci. Technol. **6**, 6899 (1998).
4. T. L. Makarova, L. B. Zakharova, I. T. Serenkov, and V. I. Sakharov, Mol. Mater. **13**, 105 (2000).

Translated by G. Skrebtsov

Physics of the Solid State, Vol. 44, No. 3, 2002, pp. 503–505. Translated from Fizika Tverdogo Tela, Vol. 44, No. 3, 2002, pp. 481–482.

PROCEEDINGS OF THE V INTERNATIONAL WORKSHOP "FULLERENES AND ATOMIC CLUSTERS"

(St. Petersburg, Russia, July 2–6, 2001)

Study of Intercalated Fullerene Films by Medium-Energy Ion Scattering

V. V. Afrosimov*, I. B. Zakharova, R. N. Il'in*, T. L. Makarova*, V. I. Sakharov*, and I. T. Serenkov***

** Ioffe Physicotechnical Institute, Russian Academy of Sciences, ul. Politekhnicheskaya 26, St. Petersburg, 194021 Russia*
e-mail: r.ilin@pop.ioffe.rssi.ru
*** St. Petersburg State Technical University, ul. Politekhnicheskaya 29, St. Petersburg, 195251 Russia*

Abstract—This paper reports on a study of films of fullerenes and their halogen compounds, deposited on mica and silicon, by medium-energy ion scattering (MEIS). The film thickness nonuniformity was determined. A considerable increase in the halogen concentration was found at the interface, which is associated with the specific film deposition conditions. It was demonstrated that the composition of individual layers of a film can be determined using MEIS. © *2002 MAIK "Nauka/Interperiodica".*

The medium-energy ion scattering (MEIS) method permits one to probe nanometer-scale thin films of various compositions and, in particular, to determine the thickness of a film and its nonuniformity, the elemental composition, and its depth profile in a nondestructive way [1]. The method includes measurement of the energy spectra of backscattered ions (BSI) and determination of the film parameters by comparing measured spectra with calculated ones or with reference spectra obtained by investigating films of a known composition.

The present work was aimed at studying films of pure and halogen-intercalated C_{60} fullerenes prepared by thermal evaporation in a quasi-closed volume [2]. Films of the pure fullerene were deposited on mica and silicon substrates; films of intercalated fullerenes, on (111) silicon. Intercalated fullerenes were obtained by evaporating $C_{60}Br_{24}$ and $C_{60}Cl_{12}$. The temperature of the evaporator was 500–520°C, and that of substrates was 200–250°C.

The films were probed with 190- to 230-keV H^+ and He^+ ions. The backscattered ions were detected by a

Characteristics of fullerene films

Item no.	Composition, substrate	Thickness, nm	Thickness spread		Coverage, %	Depth interval, nm	Composition variation with depth
			nm	%			
1	C_{60}/mica	390	35	9	100		
2	C_{60}/mica	290	35	12	100		
3	C_{60}/mica	270	12	5	100		
4	C_{60}/mica	130	30	23	90		
5	C_{60}/Si	400	18	5	100		
6	$C_{60}Cl_x$/Si	270	12	5	100	0–175	C_{60}
						175–213	$C_{60}Cl_3$
						213–270	$C_{60}Cl_6$
7	$C_{60}Br_x$/Si	145	12	8	100	0–58	$C_{60}Br_{0.1}$
						58–138	$C_{60}Br_{0.3}$
						138–145	$C_{60}Br_{10}$
8	$C_{60}Br_x$/Si	55	18	33	100	0–45	C_{60}
						45–55	$C_{60}Br_{20}$

1063-7834/02/4403-0503$22.00 © 2002 MAIK "Nauka/Interperiodica"

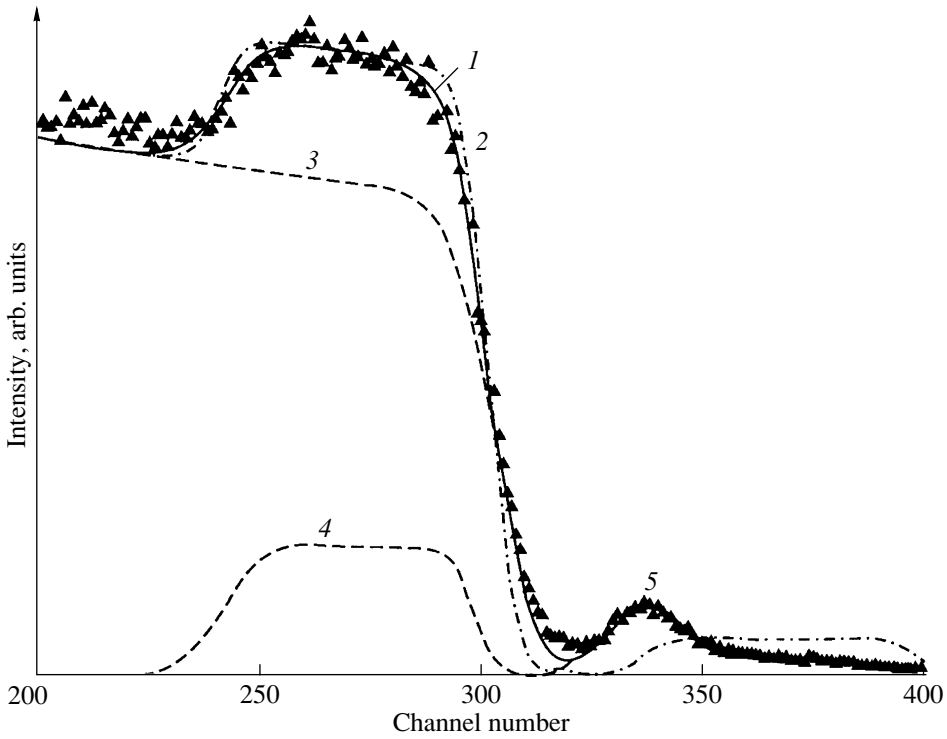

Energy spectrum of protons with an initial energy of 230 keV scattered in a 145-nm-thick $C_{60}Br_x$ film. Points are the experimental spectrum; (*1*) total spectrum calculated taking into account the thickness and compositional nonuniformities, (*2*) same assuming uniform film thickness and composition, and (*3–5*) partial spectra of Si, C, and Br, respectively.

spectrometric semiconductor detector and an electrostatic analyzer, with the depth resolution in the near-surface region being 5–10 nm in the first case and 0.5–1 nm in the second. The film thickness was determined as the number of atoms per cm^2 and reduced to the linear thickness by using the target density, which was taken equal to 1.7 g/cm^3 for C_{60}.

To develop the technique of fullerene film preparation, we studied four C_{60} films deposited on mica and four films on silicon, including three films (containing halogen impurities) of $C_{60}Br_x$ and $C_{60}Cl_x$. The parameters of the films are listed in the table. For all films, the thicknesses and their spread were determined, and the halogen distribution in depth was found for the halogen-containing films. As seen from the table, the relative spread in film thickness, both on mica and on silicon, decreases with increasing thickness. The films on mica, which were shown by x-ray analysis to be preferentially $\langle 111 \rangle$ oriented, have a less imperfect structure while, at the same time, exhibiting a large spread in thickness, which is connected with the pyramidal character of growth on mica substrates [3]. Films grown on silicon substrates are polycrystalline [4]; this accounts for the practically constant spread in thickness (12–18 nm).

The figure illustrates a BSI energy spectrum obtained experimentally from a $C_{60}Br_x$ film on silicon (no. 7 in table). This spectrum is compared with calculated total spectra obtained by summing partial spectra of the elements. The spectra were obtained under two alternative assumptions. One is that a film has a uniform thickness and a uniform distribution of bromine in depth. The other assumption is that a film is nonuniform in thickness and consists of layers differing in bromine content. As seen from the figure, the model of a nonuniform film provides better agreement with the experiment.

The halogen-containing films revealed a strong compositional nonuniformity in depth. The halogen concentration is the highest near the interface. As one goes away from the interface toward the surface, the concentration falls off rapidly to zero. This is also seen in the spectrum of sample 7 in the figure, wherein the partial spectrum of bromine is substantially narrower than that of carbon. The reason for the nonuniformity in the impurity distribution lies in the different evaporation rates of C_{60} and of the halogens in the course of film deposition. The variations in the rate may be caused by charge decomposition under heating [5], which takes place already at 170°C, a temperature substantially lower than the operating temperature of C_{60} evaporation. The deposition of fullerene compounds with halogens should apparently be accomplished through explosive evaporation or by using special devices to control the fluxes of the components to be deposited.

We may note in conclusion that studies of films of fullerenes and of their halogen compounds by MEIS have permitted us to determine the film thickness and its nonuniformity nondestructively, to detect an increase in the halogen concentration near the interface, and to establish the average stoichiometry of various film layers, which is necessary for improving the technology of their preparation.

ACKNOWLEDGMENTS

This study was supported by the Russian Foundation for Basic Research (project no. 99-02-18170) and the State Research and Development program "Fullerenes and Atomic Clusters" (project "Plenka").

REFERENCES

1. V. V. Afrosimov, R. N. Il'in, S. F. Karmanenko, *et al.*, Fiz. Tverd. Tela (St. Petersburg) **41** (4), 28 (1999) [Phys. Solid State **41**, 527 (1999)].
2. T. L. Makarova, N. V. Seleznev, I. B. Zakharova, and T. I. Zubkova, Mol. Mater. **10**, 105 (1998).
3. D. Stifter and H. Sitter, Thin Solid Films **280** (1), 83 (1996).
4. G. Gensterblum, L.-M. Yu, J.-J. Pireaux, *et al.*, Appl. Phys. A **A56**, 175 (1993).
5. D. Heymann, F. Cateldo, R. F. K. Kens, and N. M. M. Nibbering, Fullerene Sci. Technol. **7** (2), 159 (1999).

Translated by G. Skrebtsov

Physics of the Solid State, Vol. 44, No. 3, 2002, pp. 506–508. From Fizika Tverdogo Tela, Vol. 44, No. 3, 2002, pp. 483–485.

PROCEEDINGS OF THE V INTERNATIONAL WORKSHOP "FULLERENES AND ATOMIC CLUSTERS"

(St. Petersburg, Russia, July 2–6, 2001)

Comparative Raman Study of the Ti Complex $Cp_2Ti(\eta^2\text{-}C_{60}) \cdot C_6H_5CH_3$ and Ti_xC_{60} Films[1]

A. V. Talyzin*, U. Jansson*, A. V. Usatov, V. V. Burlakov**, V. B. Shur**, and Y. N. Novikov****

**Department of Inorganic Chemistry, Ångström Laboratory, Uppsala, SE-751 21 Sweden*

*** A.N. Nesmeyanov Institute of Organoelement Compounds, Russian Academy of Sciences, Moscow, 117813 Russia*

Abstract—Raman spectra from the first Ti fullerene complex $Cp_2Ti(\eta^2\text{-}C_{60}) \cdot C_6H_5CH_3$ are presented. Compared to spectra of pure C_{60}, the spectra of the Ti complex exhibit a number of new peaks due to the symmetry lowering for C_{60}. The $A_g(2)$ mode is downshifted by 12 cm^{-1} compared to C_{60}, which corresponds to a charge transfer of one electron per Ti–C_{60} bond. This value (6 cm^{-1} for one transferred electron) is identical to the downshift of the $A_g(2)$ mode in alkali metal fullerides with ionic bonding. The spectra of $Cp_2Ti(\eta^2\text{-}C_{60}) \cdot C_6H_5CH_3$ were compared to the spectra of evaporated Ti_xC_{60} films. The $A_g(2)$ mode in Ti_4C_{60} showed a downshift of about 25 cm^{-1} compared to pure C_{60}, which corresponds to a charge transfer of one electron per Ti atom; this is similar to the ionic alkali metal fullerides and different from η^2-C_{60}-type bonding. © *2002 MAIK "Nauka/Interperiodica".*

Raman spectroscopy is widely used for characterization of different C_{60} compounds. The effect of different kinds of bonding on the Raman spectra has been established for many C_{60}-based materials; stronger bonding gives new peaks, some silent modes can appear, and a number of C_{60} modes become split due to lowering of the molecular symmetry [1–4]. In many cases, the shift of the $A_g(2)$ mode is very sensitive to the structural modifications of the C_{60}. For example, softening of the $A_g(2)$ mode was widely used for characterization of the stoichionetry in M_xC_{60} alkali metal fullerides, since it had been found that the dowshift is linearly dependent on the number of intercalating metal atoms with a typical value of the downshift of ~6 cm^{-1} per transferred electron [1]. Other compounds with strong covalent bonding also exhibit a similar downshift of 5–6 cm^{-1} [2–4]. In contrast, weaker donor-acceptor bonding with partial charge transfer from the ligand to C_{60} leads to a much smaller downshift and, for van der Waals bonding, the position of the $A_g(2)$ mode of C_{60} remains unchanged [5, 6].

Valuable information can be obtained using Raman spectroscopy for new amorphous materials, such as Ti_xC_{60}, which was recently deposited as thin films by coevaporation of Ti and C_{60} [7]. The nature of bonding in this compound is still unclear, although it has been suggested that Ti is covalently bonded to C_{60}. The recent discovery and structural characterization of the first fullerene Ti complex $Cp_2Ti(\eta^2\text{-}C_{60})$ makes it possible to study the effects of covalent Ti–C_{60} bonding on Raman spectra [8]. In the present contribution, we report the first Raman study of this complex and compare it with the spectra of Ti_4C_{60} films.

1. EXPERIMENTAL

The details of the preparation and structural characterization of the $Cp_2Ti(\eta^2\text{-}C_{60}) \cdot C_6H_5CH_3$ were reported elsewhere [6]. In this compound, toluene molecules form weak van der Waals bonds similar to known solvates of pure C_{60}. Thin films of Ti_xC_{60} were deposited by coevaporation of C_{60} and Ti under UHV conditions. Details of the experimental setup were published elsewhere [5]. A film with composition Ti_4C_{60}, as determined by XPS, was deposited on the glass substrate and capped with Ti to protect the sample from oxidation. Raman spectra of Ti_4C_{60} were recorded through the glass substrate using a Renishaw Raman 2000 spectrometer with 514 nm excitation wavelengths and a resolution of 2 cm^{-1}. If the Ti capping layer had microholes, it was possible to observe, using an optical microscope, how the color of the film changes due to oxidation around such holes. The process was sufficiently slow for the spectra from the same spot before and after oxidation to be recorded. Raman spectra of the $Cp_2Ti(\eta^2\text{-}C_{60}) \cdot C_6H_5CH_3$ were recorded in a sealed ampule filled with argon through glass using a 785-nm laser.

[1] This article was submitted by the authors in English.

1063-7834/02/4403-0506$22.00 © 2002 MAIK "Nauka/Interperiodica"

2. RESULTS AND DISCUSSION

2.1. Raman Spectrum of the $Cp_2Ti(\eta^2\text{-}C_{60}) \cdot C_6H_5CH_3$

Let us first analyze the Raman spectrum of $Cp_2Ti(\eta^2\text{-}C_{60}) \cdot C_6H_5CH_3$. As can be seen in the figure, this spectrum exhibits a number of new peaks compared to pure C_{60}. Raman spectra of C_{60} solvates are almost identical to pure C_{60}, and the presence of toluene in the structure should not affect Raman modes of C_{60} significantly [6]. The lines of toluene are very weak, and only the strongest line at 1008 cm^{-1} can be identified in our spectra. The other lines are a combination of C_{60}-derived modes and vibrations of the Cp_2Ti-group. Some of the vibrational modes of the Cp_2Ti-group can be identified by comparison with the Raman spectrum of Cp_2TiCl_2. The assignment of the vibrational modes for Cp_2TiCl_2 was made according to the data by Holubova *et al.* [9]. From the similarity of the compounds, we can expect some of the modes in the Cp_2TiCl_2 spectrum to be similar to those of the Ti–C_{60} complex. Indeed, the C–H modes of Cp_2TiCl_2 are situated at 843, 864, and 1074 cm^{-1}; the peaks, at 881, 894, and 1095 cm^{-1}. The peak of *Cp* vibrations at 394 cm^{-1} for Cp_2TiCl_2 can probably be identified with the peak at 400 cm^{-1} for the Ti–C_{60} complex. The peaks of Ti–*Cp* vibrations of niobocene dichloride are at 412 and 301 cm^{-1}, and the corresponding peaks in the $Cp_2Ti(\eta^2\text{-}C_{60})$ are most probably located first at 430 cm^{-1} and second at 280 or 337 cm^{-1}. It is very interesting that $Cp_2Ti(\eta^2\text{-}C_{60})$ spectra exhibit a sharp peak at 134 cm^{-1}, which can probably be associated with vibrations due to Ti bonded to C_{60}. C–C vibrations of titanocene dichloride are more difficult to identify with $Cp_2Ti(\eta^2\text{-}C_{60})$ because, in the same spectral region, there are several peaks, some of them from C_{60} vibrations.

All other peaks in the spectra of $Cp_2Ti(\eta^2\text{-}C_{60})$ originate from C_{60}. The $A_g(2)$ mode is downshifted compared to pure C_{60} by 12 cm^{-1}. Taking into account that Ti forms two bonds with two carbon atoms from the C_{60} molecule, we calculated the shift of 6 cm^{-1} per bond. This is very similar to the alkali metal fullerides, which exhibit a downshift of the $A_g(2)$ mode by 6 cm^{-1} per transferred electron. The $H_g(7)$ and $H_g(8)$ modes of C_{60} are split in $Cp_2Ti(\eta^2\text{-}C_{60})$ and can be found at 1407, 1417 cm^{-1} and 1546, 1563 cm^{-1}. The $H_g(5)$ and $H_g(6)$ modes are also split into several weak peaks. Four strong peaks and several weak peaks can be found also around 600–800 cm^{-1}, which are typically ascribed to $H_g(3)$ and $H_g(4)$ derived for different kinds of C_{60} complexes and polymers. The strongest peaks in the spectrum of $Cp_2Ti(\eta^2\text{-}C_{60})$ are those at 484 and 526 cm^{-1}. The first peak can be assigned to the downshifted $A_g(1)$ mode; the second peak, to the typically silent infrared-active mode $F_{1u}(1)$ of C_{60}. The $H_g(1)$ mode is split into several components represented as weak peaks around 240–290 cm^{-1}. The $H_g(2)$ mode is split into two sharp peaks at 430 and 436 cm^{-1}. Some other weak peaks can also be assigned to different silent and infrared-active modes. The main conclusion that can be drawn from the above discussion is that lowering of the C_{60} symmetry leads to splittings and shifts of most modes and the activation of silent and infrared modes. The shift of the $A_g(2)$ mode allows us to draw the conclusion that η^2 bonding between Ti and C_{60} leads to a charge transfer of two electrons, one electron per Ti–C bond.

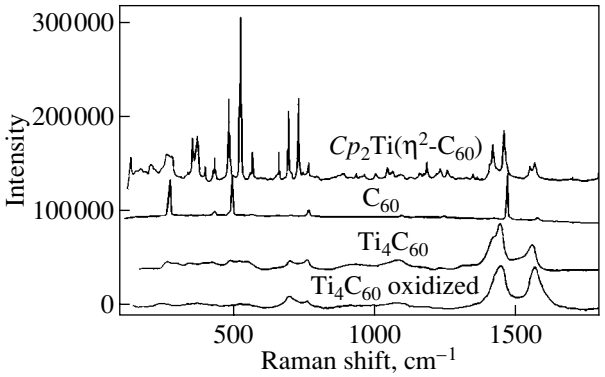

Raman spectrum of $Cp_2Ti(\eta^2\text{-}C_{60})$ compared to the spectra of pure C_{60}, Ti_4C_{60}, and oxidized Ti_4C_{60}.

2.2. Ramam Spectra of the Ti_4C_{60} Films

The spectra of the unoxidized Ti_4C_{60} is clearly different from those of pure C_{60}. The main signature of the chemical bonding in this material is a shift of the $A_g(2)$ mode to 1443 cm^{-1}, which is 26 cm^{-1} lower than that in pure C_{60}. The other modes of C_{60} are also shifted or split. $H_g(7)$ and $H_g(8)$ modes can be found at 1416 and 1554 cm^{-1}, which corresponds to a downshift compared to pure C_{60} by 10 and 22 cm^{-1}, respectively. The $H_g(1)$ mode is clearly split into three components at 257, 265, and 293 cm^{-1}. A group of new peaks is observed at 330–400 cm^{-1}. The peak at 425 cm^{-1} can be assigned to the $H_g(1)$ mode; the peak at 490 cm^{-1}, to the $A_g(1)$ mode. The peaks at 522 and 553 cm^{-1} belong, most likely, to the activated infrared modes $F_{1u}(1)$ and $F_{1u}(2)$. The peaks at 707 and 766 cm^{-1} can be assigned to the $H_g(3)$ and $H_g(4)$ modes, respectively. Very typical features of Ti_4C_{60} are two broad peaks around 939 and 1089 cm^{-1}. The nature of these peaks is unknown, but it can be clearly seen that they strongly decrease in intensity after oxidation. It is known that Ti_xC_{60} is extremely sensitive to oxidation. This observation is confirmed by the comparison of the Ti_4C_{60} Raman spectra with the spectrum of the same film after oxidation, which is measured through a microhole in the capping layer. The oxidation can be observed as a change in color using an

optical microscope. Other remarkable changes due to oxidation are a strong decrease in the $A_g(2)$ intensity with a simultaneous upshift by 6 cm^{-1}; an upshift of the $H_g(7)$ and $H_g(8)$ modes by 12 and 10 cm^{-1}, respectively; and a strong change in relative intensity for other peaks, e.g., the peaks at 707 and 766 cm^{-1}. It shall be noted that the spectra of oxidized Ti_4C_{60} shown in the figure were recorded within one hour of exposure to air. Longer exposure leads to complete degradation of the sample. It is interesting to note that the peaks in the spectra of Ti_4C_{60} are much broader compared to those in the spectrum of the Ti complex. Most probably, this can be explained by stronger disorder in the amorphous Ti_4C_{60}.

Several different structural models can be proposed for Ti_xC_{60}. Donor-acceptor η^6-C_{60} bonding has been theoretically studied by Saito *et al.* [10]. This kind of bonding suggests a charge transfer of 0.25 electrons from Ti to C_{60}, which would result in a much smaller shift of the $A_g(2)$ mode compared to the observed value of 6 cm^{-1} per metal atom. Therefore, this possibility must be ruled out for our samples. Ionic bonding similar to alkali metal fullerides and covalent bonding have been discussed by Norin *et al.* [7]. Different structural models can be proposed for covalent bonding of Ti and C_{60}. A probable model is η^2-C_{60} bonding when Ti has two bonds with neighboring carbon atoms of the C_{60}. Another kind of bonding was reported for Pd_xC_{60} where Pd served as a bridge between two neighboring C_{60} molecules. A similar polymeric structure can also be suggested for Ti_xC_{60}. Using the Raman spectra of $Cp_2Ti(\eta^2\text{-}C_{60})$, we can rule out η^6-C_{60} bonding for Ti_xC_{60}, because it is clear that each Ti–C_{60} bond results in a charge transfer of one electron in $Cp_2Ti(\eta^2\text{-}C_{60})$. Since each Ti atom forms two bonds with C_{60} in $Cp_2Ti(\eta^2\text{-}C_{60})$, the resulting shift value is 12 cm^{-1} per metal atom, which is different from 6 cm^{-1} per Ti atom observed for Ti_4C_{60}. It is, therefore, possible to suggest that Ti forms an intercalation compound similar to alkali metal fullerides or that Ti is bonded to C_{60} with single bonds, e.g., in dimers with Ti serving as a bridge.

REFERENCES

1. K. A. Wang, Y. Wang, P. Zhou, *et al.*, Phys. Rev. B **45**, 1955 (1992).
2. B. Chase and P. J. Fagan, J. Am. Chem. Soc. **114**, 2252 (1992).
3. Y. Zhang, Y. Du, J. R. Shapley, and M. J. Weaver, Chem. Phys. Lett. **205**, 508 (1993).
4. K. Pokhodnia, J. Demsar, A. Omerzu, and D. Mihailovich, Phys. Rev. B **55**, 3757 (1997).
5. M. F. Limonov, Yu. Kitaev, A. V. Chugreev, *et al.*, Phys. Rev. B **57**, 7586 (1998).
6. A. Talyzin and U. Jansson, J. Phys. Chem. B **104**, 5064 (2000).
7. L. Norin, U. Jansson, C. Dyer, *et al.*, Chem. Mater. **10**, 1184 (1998).
8. V. V. Burlakov, A. V. Usatov, K. A. Lyssenko, *et al.*, Eur. J. Inorg. Chem., 1855 (1999).
9. J. Holubova, Z. Cernosek, and I. Pavlik, Vib. Spectrosc. **14**, 147 (1997).
10. T. Saito, Y. Akita, H. Kobayashi, and K. Tanaka, Synth. Met. **108**, 67 (2000).

Physics of the Solid State, Vol. 44, No. 3, 2002, pp. 509–510. Translated from Fizika Tverdogo Tela, Vol. 44, No. 3, 2002, pp. 486–487.

PROCEEDINGS OF THE V INTERNATIONAL WORKSHOP "FULLERENES AND ATOMIC CLUSTERS"

(St. Petersburg, Russia, July 2–6, 2001)

Ionization and Fragmentation of Fullerenes in Ion Collisions with Them at Various Impact Parameters

V. V. Afrosimov, A. A. Basalaev, K. V. Kashnikov, and M. N. Panov

Ioffe Physicotechnical Institute, Russian Academy of Sciences, ul. Politekhnicheskaya 26, St. Petersburg, 194021 Russia
e-mail: a.basalaev@pop.ioffe.rssi.ru

Abstract—This paper reports on the first measurements of the differential cross sections (with respect to scattering angle) of various elementary processes accompanying electron capture by keV-range H^+ and He^{2+} ions from a fullerene molecule. Estimation of the impact parameter from the ion scattering angle in the polarization interaction with a fullerene molecule shows that the processes of capture and capture with fullerene ionization and fragmentation occur primarily at impact parameters far exceeding the fullerene radius. © *2002 MAIK "Nauka/Interperiodica".*

It was experimentally established (see, e.g., [1]) that collisions of ions with fullerenes can give rise to the formation of multiply charged, nonfragmented C_{60}^{q+} ions in charge states of up to $q = 7$ and that the processes involved in fragmentation of the fullerene ion proceed over two channels. One of these channels is detachment of light neutral fragments with a mass equal to a multiple of the mass of two carbon atoms C_{2k} ($k = 1, 2, \ldots$), and the other channel is complete breakup of the fullerene into several light fragments comparable in mass [1–3].

Collisions of a fullerene with slow ions (in the keV energy range), similar to ion collisions with atoms, are dominated in the cross section by processes accompanied by electron capture by the projectile ion (charge exchange). The model of classical over-barrier transitions [4, 5] is the most advanced theoretical approach employed to describe the electron-capture processes that occur at high values of the impact parameter ρ, in excess of the fullerene radius R_f, and are accompanied by neither excitation of the fullerene that has lost electrons nor its fragmentation. On the other hand, the processes taking place at impact parameters $\rho < R_f$, which correspond to penetration of the projectile particle into the molecule and entail multiple ionization and fragmentation, are considered in terms of the electronic stopping-power model [6, 7].

The most straightforward way to experimentally check the dependence of the various processes on the impact parameter is to measure the differential cross sections of the projectile scattering. As shown earlier [3, 8], the capture of one electron by various keV-range ions virtually does not result in fullerene fragmentation, whereas if an He^{2+} ion captures two electrons, fragmentation into several light fragments is most probable. Therefore, for the study of the impact parameter dependence, we chose the elementary processes taking place in the capture of one electron by an H^+ ion and of two electrons by an He^{2+} ion. The experimental setup described in [9] had an angular resolution $\Delta\theta \approx 0.08°$ and made it possible to investigate the scattering of fast atoms produced in electron-capture events within an angular interval $\theta = \pm 3°$. The mass and charge states of the recoil ions created in the breakup of the fullerene molecule were analyzed using the time-of-flight technique. The elementary process of interest was selected by detecting coincidences between the fast projectile particle scattered at a certain angle and the recoil ions formed in the same collision.

The capture of one electron by an H^+ ion initiates four elementary processes (Fig. 1a). The differential cross section of one-electron capture (the process with the largest total cross section [9]) falls off rapidly with increasing scattering angle of the fast particle, which is in good agreement with the results of [10]. Capture of two electrons by an He^{2+} ion gives rise to seven elementary processes (Fig. 1b), molecule fragmentation into several charged fragments being dominant in the magnitude of the total cross section.

In the region of small scattering angles, the corresponding impact parameters were determined with due account of the fact that interaction of the projectile ion with the fullerene at internuclear distances in excess of the fullerene radius is governed by polarization attraction, which decreases substantially after electron capture, because the polarizability of the atom thus formed becomes small compared to that of the fullerene. The capture is determined by the Landau–Zener transitions in the term-crossing region of the quasi-molecular system formed. The term-crossing points were determined taking into account the possible capture of the fullerene electrons with binding energies of 7.44, 9.3, 12, and 12.33 eV.

1063-7834/02/4403-0509$22.00 © 2002 MAIK "Nauka/Interperiodica"

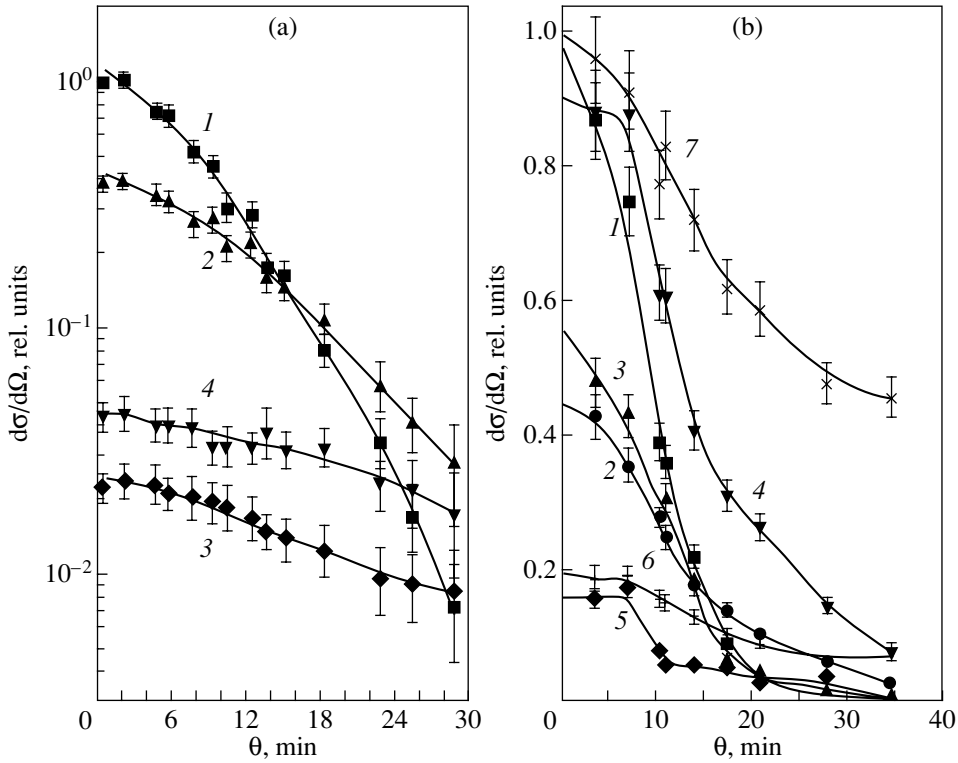

Fig. 1. Differential cross sections (with respect to the scattering angle) of elementary processes: (a) $H^+ + C_{60} \longrightarrow H^0 + \{C_{60}\}^+$, collision energy E = 4.4 keV: (*1*) capture of one electron (C_{60}^+), (*2*) electron capture with ionization (C_{60}^{2+}), (*3*) electron capture with double ionization (C_{60}^{3+}), and (*4*) electron capture with ionization and detachment of k C_2 fragments (C_{60-2k}^{2+}); (b) $He^{2+} + C_{60} \longrightarrow He^0 + \{C_{60}\}^{2+}$, collision energy E = 8.8 keV: (*1*) capture of two electrons (C_{60}^{2+}), (*2*) capture of two electrons with detachment of k C_2 fragments (C_{60-2k}^{2+}), (*3*) capture of two electrons with ionization (C_{60}^{3+}), (*4*) capture of two electrons with ionization and detachment of k C_2 fragments (C_{60-2k}^{3+}), (*5*) capture of two electrons with double ionization (C_{60}^{4+}), (*6*) capture of two electrons with double ionization and detachment of k C_2 fragments (C_{60-2k}^{4+}), and (*7*) capture of two electrons with fragmentation of the fullerene ion into several light fragments (ΣC_n^{m+}, n/m = 3–11).

An analysis shows that multiple ionization and fragmentation in ion collisions with fullerenes occur primarily at impact parameters $\rho > R_f$. The processes of fullerene ionization and fragmentation accompanying the electron capture by the projectile ions are dominated not by the kinetic-energy transfer but rather by the structure of the electronic levels populated in the collision and by the electron excitation energy of the fullerene ion formed.

ACKNOWLEDGMENTS

This study was supported by the Russian Research Program “Fullerenes and Atomic Clusters.”

REFERENCES

1. S. Martin, L. Chen, A. Denis, and J. Desesquelles, Phys. Rev. A **59**, R1734 (1999).
2. B. Walch, C. L. Cocke, R. Voelpel, and E. Salzborn, Phys. Rev. Lett. **72**, 1439 (1994).
3. V. V. Afrosimov, A. A. Basalaev, V. P. Belik, *et al.*, Zh. Tekh. Fiz. **68** (4), 12 (1998) [Tech. Phys. **43**, 358 (1998)].
4. U. Thumm, J. Phys. B **27**, 3515 (1994).
5. A. Barany and C. J. Setterling, Nucl. Instrum. Methods Phys. Res. B **98**, 184 (1995).
6. T. Bergen, A. Brenac, F. Chandezon, *et al.*, Eur. Phys. J. D **14**, 317 (2001).
7. H. Tsuchida, A. Itoh, K. Miyabe, *et al.*, J. Phys. B **32**, 5289 (1999).
8. V. V. Afrosimov, A. A. Basalaev, V. P. Belik, *et al.*, Mol. Mater. **11**, 125 (1998).
9. V. V. Afrosimov, A. A. Basalaev, V. P. Belik, *et al.*, Fullerene Sci. Technol. **6** (3), 393 (1998).
10. B. Walch, U. Thumm, M. Stockli, *et al.*, Phys. Rev. A **58**, 1261 (1998).

Translated by G. Skrebtsov

Physics of the Solid State, Vol. 44, No. 3, 2002, pp. 511–514. From Fizika Tverdogo Tela, Vol. 44, No. 3, 2002, pp. 488–491.

PROCEEDINGS OF THE V INTERNATIONAL WORKSHOP "FULLERENES AND ATOMIC CLUSTERS"

(St. Petersburg, Russia, July 2–6, 2001)

Recent Results on Multiple Ionization and Fragmentation of Negatively Charged Fullerene Ions by Electron Impact[1]

D. Hathiramani*, P. Scheier, and E. Salzborn***

** Institut für Kernphysik, University of Giessen, Giessen, D-35392 Germany*

*** Institut für Ionenphysik, University of Innsbruck, Innsbruck, A-6020 Austria*

Abstract—Employing the dynamic crossed-beams technique, the absolute cross sections of the electron-impact multiple ionization and fragmentation of mass-selected negatively charged fullerene ions $C_m^- \longrightarrow C_{m-n}^{2+}$ (m = 60, 70, 84; q = 1, 2, 3; n = 0, 2, 4) were measured. The electron energy varied from the respective threshold up to 1 keV. A scaling law was observed for the cross-section magnitude as a function of the fullerene size m and the charge state q of product ions. The data indicate that different mechanisms account for the detachment of an extra electron from the negatively charged fullerene and the formation of a positively charged ion, respectively. Moreover, the multiple ionization of a fullerene anion is found to be a sequential process. A novel ionization mechanism is proposed which might be expected to be valid for all negatively charged molecular or cluster ions able to shield the attached electron from the incident electron. © *2002 MAIK "Nauka/Interperiodica".*

Over the last decade, the formation of positively charged ions out of neutral fullerenes has been studied extensively [1]. Although the threshold energy for different ionization processes has been determined repeatedly [2–5], only a few reports contain information on the absolute magnitude of these cross sections [6–9]. Parallel to experimental work, several papers have been published on calculations of the ionization energies [10–13] and the ionization cross sections of fullerenes [14, 15].

Völpel *et al.* [16] measured cross sections of the electron-impact ionization of positively charged fullerene ions. Since the cross section for the attachment of free electrons to a neutral molecule [17] is large, intense beams of negatively charged fullerene ions can also be easily produced. Furthermore, electron attachment to fullerenes does not lead to the production of negatively charged fragments.

The properties of C_{84} have been investigated less extensively in comparison to C_{60} and C_{70} due to the relatively small amount of larger fullerenes present in the soot. Moreover, the separation with chemical methods is complicated and, thus, pure C_{84} soot is very expensive. Mass separation is a possible method for separating fullerenes of different sizes. In the case of positively charged ions, problems arise, because fragmentation of larger fullerenes may contribute to the ion signal of smaller carbon clusters. The presently used technique allows one to separate these different fullerenes free of fragmentation processes.

[1] This article was submitted by the authors in English.

1. EXPERIMENTAL

The measurements were performed employing the electron–ion crossed-beams setup described in detail by Tinschert *et al.* [18]. A commercially available mixture of fullerenes mainly containing C_{60} and C_{70}, and also trace amounts of larger fullerenes, was used. A sample of fullerene soot (with a purity higher than 96%) was heated in a tailor-made oven to a temperature of about 800 K. The neutral vapor was introduced into a 10 HGz Electron Cyclotron Resonance (ECR) ion source [19]. The ion source was operated at a low microwave power. A high ion yield of negatively charged fullerenes and stable conditions of the ECR plasma were maintained after argon was introduced into the ion source at a pressure of about 10^{-4} Pa. The electron-impact ionization of Ar produces slow electrons which can attach to fullerenes. After mass and energy analysis, the separated ion beam was collimated to 2×2 mm and crossed with an intense electron beam providing a current up to 450 mA [20]. The energy of electrons can be varied between 10 and 1000 eV. In order to avoid unwanted effects on the ionizing electrons caused by the strong stray field of the analyzing magnet, the acceleration voltage was reduced from its nominal value 10 to 4 kV for measurements of the cross section of transformation of C_{84}^- into singly charged positive ions. After the electron–ion interaction, the product ions were separated from the incident ion beam by a 90° magnet and detected by a single-particle detector located approximately 1 m behind the interaction region. The current of the parent ion beam was measured simultaneously on a Faraday cup.

1063-7834/02/4403-0511$22.00 © 2002 MAIK "Nauka/Interperiodica"

The absolute cross sections were measured using a dynamic crossed-beams technique [21] where the electron beam is moved up and down through the ion beam with simultaneous registration of both actual beam currents and the signal of the observed fragment ions. The total experimental uncertainties were typically ±10% at the maximum of the cross sections, calculated as a quadrature sum of nonstatistical errors of about 8.9% and a statistical error at a 95% confidence level.

2. RESULTS

The measured absolute cross sections for double, triple, and quadruple ionization of C_{60}^-, C_{70}^-, and C_{84}^- are shown in Fig. 1. The error bars indicate the total experimental uncertainties. The expected thresholds of the ionization processes are indicated by arrows. In the case of quadruple ionization of C_{60}^-, product ions C_{60}^{3+} were mixed with fragment ions C_{20}^+. The contribution from the latter was subtracted from the cross-section data by extrapolating the C_{20}^+ production cross section.

The shape of the cross section versus electron energy plots for a given ionization process is the same for the three different fullerene sizes. The measured cross sections for the three different fullerenes C_m (m = 60, 70, 84) increase with m. This effect becomes larger for higher charge states of the product cations. This behavior can be described by a scaling law, which allows one to predict an electron-impact ionization

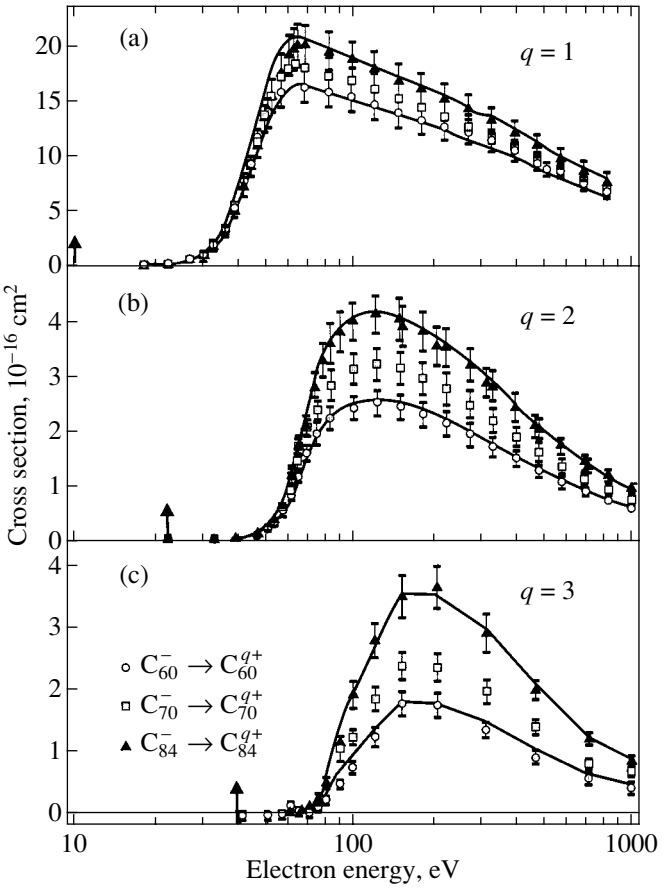

Fig. 1. Absolute cross sections of electron-impact (a) double, (b) triple, and (c) quadruple ionization of C_{60}^- (circles), C_{70}^- (squares), and C_{84}^- (triangles) ions, respectively. Solid lines are calculated cross sections using a new scaling law. For more details, see the text. The error bars represent the total experimental uncertainties, including the statistical error at a 95% confidence level. The expected thresholds of the ionization processes are indicated by arrows.

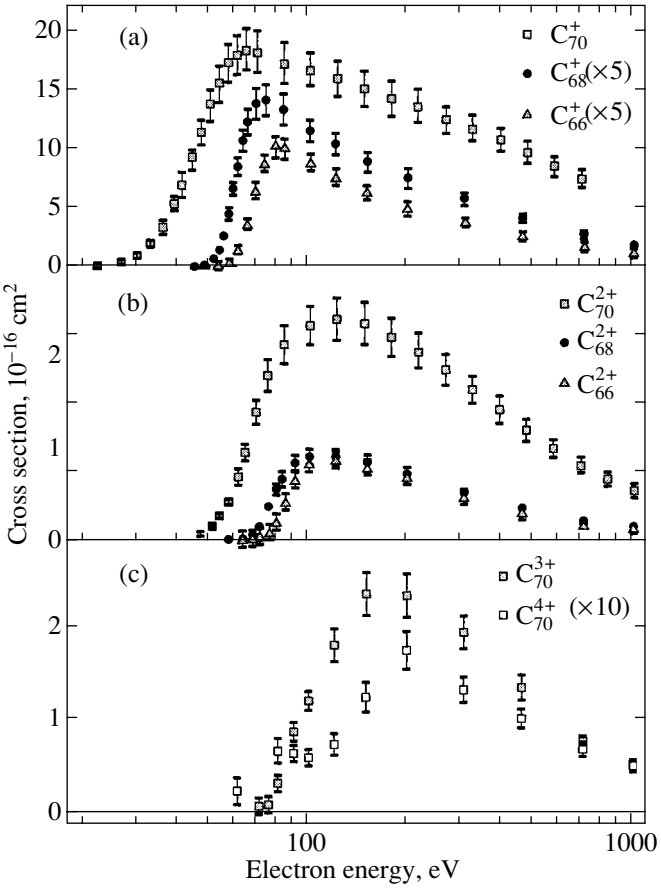

Fig. 2. Absolute cross sections of the electron-impact (a) double, (b) triple, and (c) quadruple and quintuple ionization of C_{70}^- ions into various product ions. The squares represent the cross-section data for pure ionization. The circles and triangles correspond to the fragment ions C_{68}^{q+} and C_{66}^{q+}, respectively (q = 1, 2). The error bars represent the total experimental uncertainties, including the statistical error at a 95% confidence level.

cross section $\sigma(m, q)$ of negatively charged fullerene ions C_m^- as a function of the fullerene size m and the charge state q of the product ion C_m^{q+} [22]. To calculate the cross section $\sigma(m, q)$, knowledge of the ratio of the geometrical cross sections of C_m and C_n and the electron-impact ionization cross section $\sigma(n, q)$ for any one value of n is necessary. Since the data on the cross section $\sigma(60, 3)$ were corrected for the contribution of C_{20}^+ ions, the scaling law was applied to the measured C_{70}^- ($n = 70$) cross sections. The results for $m = 60$ and 84 are shown as lines in Fig. 1 and agree well with the respective measurements.

The threshold energies for the measured cross sections are approximately 10 eV higher than expected for a direct ionization process. It is conceivable that, in order to create a positively charged ion from a negatively charged fullerene, the kinetic energy of the impacting electron has to be enlarged by the electron affinity in comparison to the case of a neutral fullerene.

In addition to pure ionization, the cross sections for double and triple ionization, including the evaporation of either a C_2 or two C_2 molecules, were measured for all three fullerene sizes. Figure 2 shows, as an example, the cross-section energy dependences measured for the product ions of the C_{70} primary ion. From a comparison of all electron-impact cross-section data for negatively charged fullerene ions with the cross sections for the respective neutral fullerenes [5, 7, 23, 24], further conclusions can be drawn: (i) only a small difference between the threshold energies of the fragment ions for neutral and negatively charged primary ions is observed, (ii) the relative quantity of fragment ions in the case of negatively charged primary fullerenes is approximately 3.5 times larger than in the case of neutral fullerenes, and (iii) ion-yield curves for neutral fullerenes can be matched perfectly with the cross-section data of the same product ions. In contrast, the removal of the same number of electrons from a negatively charged or a neutral fullerene does not lead to similar cross-section energy dependences.

The following simple model (Fig. 3) agrees well with all relevant experimental findings [25]:

(1) As the projectile electron approaches, the attached electron is pushed to the back side of the fullerene by Coulomb repulsion. Therefore, the attached electron is shielded by the fullerene itself and does not interact with the impacting electron strongly enough to be detached. The energy needed to surmount the potential barrier due to repulsion between the fullerene anion and the projectile electron is about 2 eV (the Coulomb energy of two charges spaced 7 Å apart) and is taken from the kinetic energy of the projectile. An intermediate highly excited dianion is formed. The electron affinities of some fullerene dianions have been determined to be very small [10, 26].

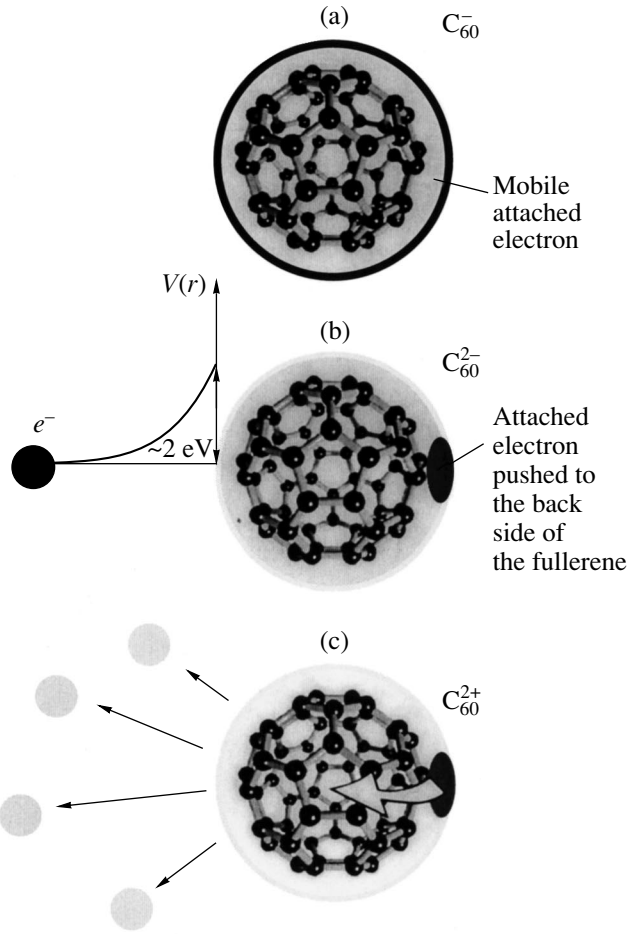

Fig. 3. Proposed model for collision between an electron and a negatively charged fullerene ion with the example of (a) a C_{60}^- ion. (b) The approaching electron pushes the attached electron to the back and, after surmounting the barrier, ejects electrons. (c) The attached electron recombines with the fullerene ion, which leads to an excitation energy of almost 8 eV.

(2) The incident electron collides with the fullerene and ejects several electrons from the fully occupied π orbital of the fullerene with the lowest energy. The kinetic energy of the ejected electrons is supplied by the approaching projectile with allowance for the potential barrier due to the Coulomb repulsion, the interaction with the image charge the electron forms at close distances [27], and the attraction between the emitted electrons and the charged fullerene ion.

(3) The attached electron drops into the vacancies of the HOMO. The energy difference is transferred to vibrational degrees of freedom.

The described model for the electron-impact ionization of negatively charged fullerenes can also be expected to apply to other large molecular and cluster anions. The only necessity is that the attached electron be mobile enough to avoid a direct collision with the projectile electron.

ACKNOWLEDGMENTS

One of the authors (P.S.) thanks the Austrian Academy of Sciences for his APART fellowship.

This study was supported by Deutsche Forschungsgemcinschaft (DFG).

REFERENCES

1. C. Lifshitz, Mass Spectrom. Rev. **12**, 261 (1994).
2. C. Lifshitz, M. Iraqi, T. Peres, and I. E. Fisher, Rapid Commun. Mass Spectrom. **5**, 238 (1991).
3. G. Javahery, H. Wincel, S. Petrie, and D. K. Böhme, Chem. Phys. Lett. **204**, 467 (1993).
4. H. Steger, J. Holzapfel, A. Hielscher, *et al.*, Chem. Phys. Lett. **234**, 455 (1995).
5. S. Matt, O. Echt, R. Wörgötter, *et al.*, Chem. Phys. Lett. **264**, 149 (1997).
6. A. Itoh, H. Tsuchida, K. Miyabe, *et al.*, J. Phys. B **32**, 277 (1999).
7. S. Matt, B. Dünser, M. Lezius, *et al.*, J. Chem. Phys. **105**, 1880 (1996).
8. M. S. Baba, T. S. L. Narashiman, K. Balasubramanian, and C. K. Mathews, Int. J. Mass Spectrom. Ion Processes **114**, R1 (1992).
9. V. Tarnovsky, P. Kurunczi, S. Matt, *et al.*, J. Phys. B **31**, 3403 (1998).
10. C. Yannouleas and U. Landman, Chem. Phys. Lett. **217**, 175 (1994).
11. M. C. Böhm, J. Schulte, and S. Philipp, Chem. Phys. Lett. **226**, 381 (1994).
12. U. Thumm, T. Bastug, and B. Fricke, Phys. Rev. A **52**, 2955 (1995).
13. G. Seifert, K. Vietze, and R. Schmidt, J. Phys. B **29**, 5183 (1995).
14. S. Keller and E. Engel, Chem. Phys. Lett. **299**, 165 (1999).
15. H. Deutsch, K. Becker, J. Pittner, *et al.*, J. Phys. B **29**, 5175 (1996).
16. R. Völpel, G. Hotmann, M. Steidl, *et al.*, Phys. Rev. Lett. **71**, 3439 (1993).
17. S. Matejcik, T. D. Märk, P. Spanel, *et al.*, J. Chem. Phys. **102**, 2516 (1995).
18. K. Tinschert, A. Müller, G. Hofmann, *et al.*, J. Phys. B **22**, 531 (1989).
19. M. Liehr, M. Schlapp, R. Trassl, *et al.*, Nucl. Instrum. Methods Phys. Res. B **79**, 697 (1993).
20. R. Becker, A. Müller, C. Achenbach, *et al.*, Nucl. Instrum. Methods Phys. Res. B **9**, 385 (1985).
21. A. Müller, K. Tinschert, C. Achenbach, and E. Salzborn, Nucl. Instrum. Methods Phys. Res. B **10/11**, 204 (1985).
22. D. Hathiramani, P. Scheier, K. Aichele, *et al.*, Chem. Phys. Lett. **319**, 13 (2000).
23. P. Scheier, B. Dünser, R. Wörgötter, *et al.*, Int. Rev. Phys. Chem. **15**, 93 (1996).
24. G. Siefert, R. Gutiérrez, and R. Schmidt, Phys. Lett. A **211**, 357 (1996).
25. P. Scheier, D. Hathiramani, W. Arnold, *et al.*, Phys. Rev. Lett. **84**, 55 (2000).
26. R. N. Compton, A. A. Tuinman, C. E. Klots, *et al.*, Phys. Rev. Lett. **78**, 4367 (1997).
27. G. Senn, T. D. Märk, and P. Scheier, J. Chem. Phys. **108**, 990 (1998).

Physics of the Solid State, Vol. 44, No. 3, 2002, pp. 515–517. Translated from Fizika Tverdogo Tela, Vol. 44, No. 3, 2002, pp. 492–494.

PROCEEDINGS OF THE V INTERNATIONAL WORKSHOP "FULLERENES AND ATOMIC CLUSTERS"

(St. Petersburg, Russia, July 2–6, 2001)

Ion-Cluster Reactions Initiated by an Electron Beam in Mixtures of Argon with Methane and Monosilane

V. Zh. Madirbaev*, A. E. Zarvin*, N. G. Korobeĭshchikov*, and R. G. Sharafutdinov**

** Institute of Thermal Physics, Siberian Division, Russian Academy of Sciences, pr. Akademika Lavrent'eva 1, Novosibirsk, 630090 Russia*

*** Novosibirsk State University, ul. Pirogova 2, Novosibirsk, 630090 Russia*

e-mail: madirbaev@phys.nsu.ru

Abstract—The excitation of argon radiation in condensing supersonic jets of argon mixtures with methane, monosilane, and carbon dioxide upon electron-beam activation of the flow is investigated experimentally. It is found that, at certain condensation stages, the radiation intensity at some atomic argon lines increases anomalously. It is shown that the effect appears at the initial stages of condensation and is damped upon the formation of large mixed clusters. © *2002 MAIK "Nauka/Interperiodica".*

We studied experimentally the energy transfer in the course of electron-beam activation in pulsed supersonic jets of argon with impurities. For this purpose, we used argon mixtures with 5% CH_4, SiH_4, CO_2, and He, as well as pure argon. It turned out that the addition of methane, monosilane, or carbon dioxide impurity leads to a relative increase in the radiation intensity for individual lines of atomic argon. The range of stagnation parameters for which the effect is observed was determined for each mixture. It was shown that neither pure argon nor its mixture with noncondensing helium displays selective excitation of the energy levels of atomic argon in the entire range of flow quantities.

The experiments were made on the LÉMPUS gasdynamic installation complex at the Novosibirsk State University [1]. Radiation was excited with an electron beam [2] emitted by an electron gun with an energy of 6 keV. The electron current i = 10 mA was maintained at a constant level. The spectra of radiation excited in pulsed jets of Ar and mixtures were studied at the stagnation pressure P_0 = 0–1500 kPa and stagnation temperature T_0 = 300 K. A jet was formed behind a sonic nozzle with the edge diameter d = 0.55 mm with the help of a pulsed electromagnetic valve. Measurements were made at a distance x/d = 30 downstream from the nozzle edge. We compared the dependences of the intensities of lines corresponding to the argon atom (λ = 549.6 nm) and argon ion (λ = 461.0 nm), which are used as reference lines, on the stagnation pressure.

An anomalous increase in the radiation intensity at individual lines of an argon atom in an electron-activated mixture with monosilane was observed for the first time in [3]. The authors attributed the discovered effect to flow condensation. However, the level of density attainable in the jet was limited to a considerable extent by the use of a continuous gas jet flowing from a stationary source. The application of the pulsed method of the formation of jets in the present work enabled us to extend the range of stagnation pressures by an order of magnitude.

For all the mixtures studied, the intensity of emission lines of the argon ion (λ = 461.0 nm) increases linearly with pressure P_0 at the initial stage and then the intensity increase is slightly decelerated as a result of collision-induced quenching [4]. In contrast to this, the behavior of the radiation intensity of the Ar atom (λ = 549.6 nm) depends on the type of impurity involved. No features in the behavior of Ar atom radiation intensity are observed in a jet of pure argon, nor in argon diluted with helium, in the entire range of parameters under investigation. In the flows of argon mixtures with methane, monosilane, and carbon dioxide, the radiation intensity first increases linearly over a short segment, then sharply increases, and, upon a further increase in pressure, returns to a linear dependence similar to that on the initial segment of the curve. This anomaly is observed in the mixtures under investigation for various stagnation pressures.

The boundaries of the nonlinear increase in the intensity can be seen in Fig. 1a, where the symbols correspond to the line intensities of the argon atom in different mixtures. The intensities are normalized to the stagnation pressure and the coefficient equating the normalized intensity for small P_0 to unity. Apart from determining the boundaries of the effect, such a normalization makes it possible to compare the contributions to the excitation of the argon atom from a secondary process leading to an anomalous increase in the intensity and from the excitation by a direct electron impact. Since a manifold increase in the intensity of radiation emitted by the atom is observed (by a factor

1063-7834/02/4403-0515$22.00 © 2002 MAIK "Nauka/Interperiodica"

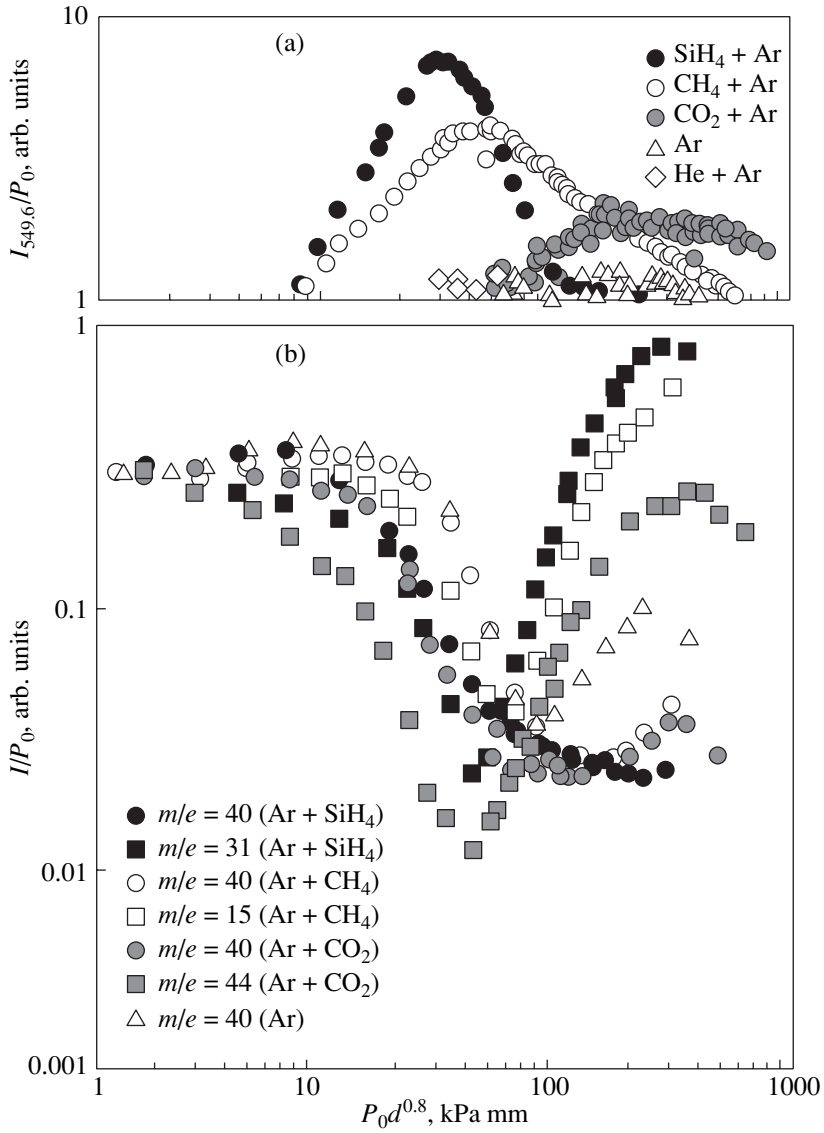

Fig. 1. (a) Intensity of radiation emitted by Ar atoms in jets of their mixtures with other gases and (b) the results of mass-spectrometer measurements in the same mixtures as a function of the similarity parameter $P_0d^{0.8}$.

of 8 at the peak for the Ar + SiH_4 mixture), a high-efficiency excitation channel associated with an abnormally large collision cross section is activated in the process.

The radiation intensity curves are compared with the results of mass-spectrometer measurements [5] in the same mixtures (Fig. 1b). The intensity of the mass-spectrometer signal for monomers of argon and impurities were also normalized to the stagnation pressure. The onset of the anomalous excitation process correlates with the initial stage of flow condensation, while the completion of the process correlates with the stage of formation of large (including mixed) clusters [6]. For convenience of comparison, the results of spectral measurements and mass-spectrometric data are presented as functions of the similarity parameter $P_0d^{0.8}$, which is widely used in analyzing condensation.

Since the anomalous excitation of the argon atom is observed, first, in a mixture with a condensing impurity and, second, under the conditions of condensation, we can assume that the effect of impurity on the magnitude and boundaries of the effect must correlate with the properties of a cluster and, hence, with the behavior of the monomer curves for the carrier gas and for the impurity, which were measured with the help of molecular-beam mass spectrometry. It should be noted that, in the pressure range $P_0d^{0.8} > 100$ kPa mm, the main contribution to the signal of monomers comes from the fragmentation of large clusters in the ionizer of the mass spectrometer [5]. Consequently, in the range of high stagnation pressures, the relative variations in the

intensities of the mass-spectrometer signal for monomers of the carrier gas and of the impurity demonstrate a change in the composition of the clusters formed and characterize the efficiency of their defragmentation by an electron impact. An analysis of the mass spectrometric data shows that the anomalous effect is manifested the more clearly, the larger the number of impurity monomers running out of a cluster under electron impact and the later the cluster starts being enriched with argon atoms.

The observed features of the excitation process (correlations with the mass spectrometric data, the linear dependence on the beam current [3], the large energy transfer cross section, and the long lifetime of intermediate excited states) suggest that the pumping of atomic argon is due to the ion-cluster interaction induced by the electron-beam plasma in the flow. As a result, long-lived excited complexes, including both carrier-gas atoms and impurity particles, are formed. After the excitation is transferred to the radiative states of the argon atom, argon is apparently ejected from the cluster, followed by the emission of radiation.

Thus, we have demonstrated that mixtures of argon with methane, monosilane, and carbon dioxide display anomalous excitation of the argon atom. The large magnitude of the effect being detected indicates the significant role played by ionized particles. The effect is localized in the range of stagnation quantities, which is limited by the initial stage of condensation (from below) and by the formation of large mixed clusters and, apparently, by the rearrangement of their structure facilitating the knocking out of an impurity particle by an electron (from above).

ACKNOWLEDGMENTS

This work was supported by the Russian Foundation for Basic Research (project no. 00-03-33021) and by grants for fundamental natural science from the Ministry of Education (project no. E00-3.2-150) and the Ministry of Industry, Science, and Technology of the Russian Federation (project no. 06-05).

REFERENCES

1. A. E. Zarvin, N. G. Korobeĭshchikov, V. Zh. Madirbaev, *et al.*, Prib. Tekh. Éksp., No. 5, 64 (2000) [Instrum. Exp. Tech. **43** (5), 640 (2000)].
2. G. G. Gartvich, A. E. Zarvin, V. V. Kalyada, and V. Zh. Madirbaev, Prikl. Mekh. Tekh. Fiz. **34** (5), 150 (1993).
3. S. Ya. Khmel and R. G. Sharafutdinov, in *Abstracts of Invited Lectures and Contributed Papers of 15th ESCAMPIC, Hungary, 2000*, Vol. 24A, p. 384.
4. V. Zh. Madirbaev and A. E. Zarvin, Prikl. Mekh. Tekh. Fiz. **39** (6), 16 (1998) [J. Appl. Mech. Tech. Phys. **39** (6), 832 (1998)].
5. A. E. Zarvin, N. G. Korobeĭshchikov, V. Zh. Madirbaev, and R. G. Sharafutdinov, Pis'ma Zh. Tekh. Fiz. **26** (22), 21 (2000) [Tech. Phys. Lett. **26**, 989 (2000)].
6. R. G. Sharafutdinov, A. E. Zarvin, N. G. Korobeĭshchikov, *et al.*, Pis'ma Zh. Tekh. Fiz. **25** (21), 47 (1999) [Tech. Phys. Lett. **25**, 865 (1999)].

Translated by N. Wadhwa

Physics of the Solid State, Vol. 44, No. 3, 2002, pp. 518–520. Translated from Fizika Tverdogo Tela, Vol. 44, No. 3, 2002, pp. 495–497.

PROCEEDINGS OF THE V INTERNATIONAL WORKSHOP "FULLERENES AND ATOMIC CLUSTERS"

(St. Petersburg, Russia, July 2–6, 2001)

Interaction of Fullerenes with Metallic Lithium in the Condensed State

G. A. Domrachev, Yu. A. Shevelev, V. K. Cherkasov, E. G. Domracheva, and G. V. Markin

Razuvaev Institute of Organometallic Chemistry, Russian Academy of Sciences, ul. Tropinina 49, Nizhni Novgorod, 603600 Russia

e-mail: domrachev@imoc.sinn.ru

Abstract—The relative stability of exo- and endohedral lithium complexes with the C_{60} fullerene was estimated using quantum chemistry and molecular-dynamics methods. Endohedral compounds were shown to have a higher stability. The possible maximum filling of the C_{60} inner sphere by lithium was estimated theoretically. The interaction of metallic lithium with the C_{60} fullerene and a $C_{60} + C_{70}$ mixture was studied using DTA and EPR and established to proceed in several stages. © *2002 MAIK "Nauka/Interperiodica".*

Exohedral compounds of lithium with C_{60} are obtained in fullerene interaction both with atomic lithium (in the gas state) [1] and with various lithium reagents (metallic lithium [2], lithium azide [3], etc.), whereas endohedral compounds form only in collisions of atomic or ionic lithium beams with the fullerene [1]. There are reports of the formation of saltlike exoderivatives $C_{60}@Li_n$ (n = 1–6 and up to 25) and endoderivatives $Li_n@C_{60}$ (n = 1–3) and $Li_n@C_{70}$ (n = 1).

We theoretically estimated the possibility of existence, stability, and directions of synthesis of polymetallic endo- and exohedral fullerene compounds with lithium. The ground state and geometric parameters of systems in the $Li_n@C_{60}$ series with n = 1, 6, 8, 10, 12, 14, 15, 18, 20, 21, 22, 27, and 41 (η^m-C_{60}, m = 1, 2, 5) were found using the method of molecular mechanics (MM+) and self-consistent Hartree–Fock formalism with intermediate neglect of differential overlap (INDO). The stability of the compounds under increasing temperature was estimated using the molecular dynamics (MD) method. The enthalpies of formation, the electron density distribution, spin density, and the HOMO and LUMO energies of the systems in the ground state were calculated using the modified INDO method. In all cases, except the case of n = 1, the lithium atoms were inside the fullerene in an unbound state. By optimizing the geometry, we succeeded in determining and excluding the extra-unstable compounds. The maximum number of lithium atoms n that can reside inside the fullerene is 27. Several compounds (n = 1, 10, 20) were calculated using the INDO method complemented by ground-state geometry optimization.

As follows from the calculations, in the $C_{60}@Li$ exohedral compound, the lithium atom location opposite the center of a five- or six-member ring is prefera-

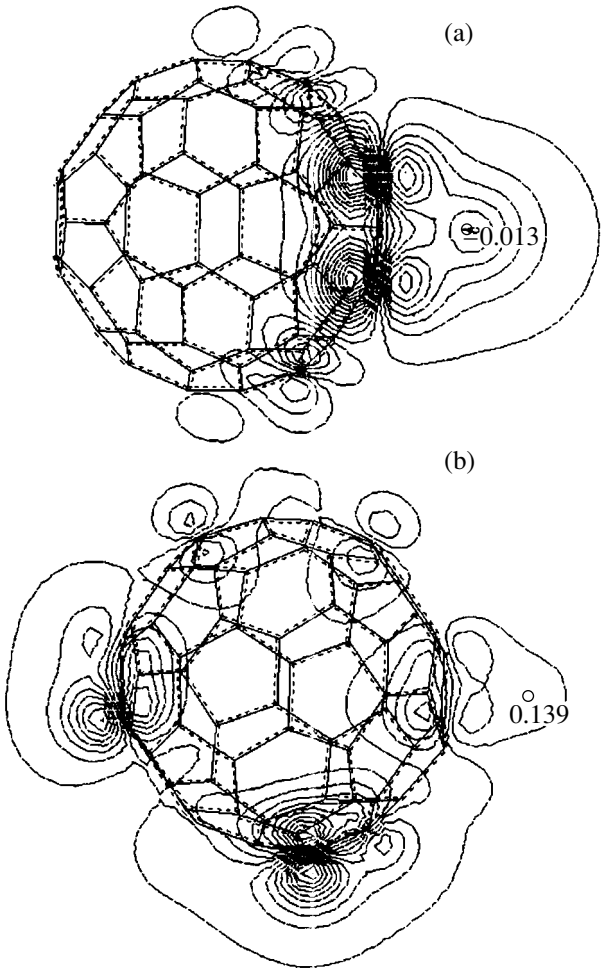

Fig. 1. (a) The highest occupied molecular orbital (HOMO) of $C_{60}@Li$ and (b) the 119th molecular orbital of the $C_{60}@Li^+$ cation.

1063-7834/02/4403-0518$22.00 © 2002 MAIK "Nauka/Interperiodica"

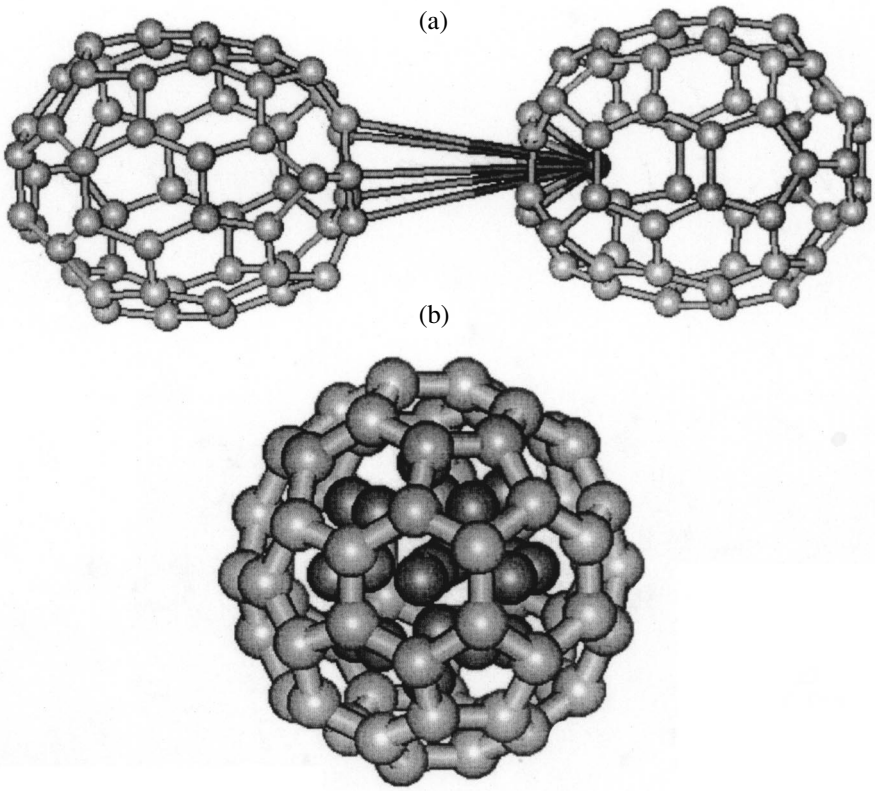

Fig. 2. (a) Lithium atom incorporation from an exo- to an endohedral position (MD calculation) and (b) optimized molecular structure of $Li_{20}@C_{60}$.

ble to that above carbon atoms (Fig. 1); the effective charge on the metal atom is close to zero, and the occupation of its 2*s* and 2*p* atomic orbitals (AOs) approaches 0.25. Hence, the effective charge distribution in a molecule is determined not only by the donation of a lithium 2*s* electron to the fullerene as an acceptor but also by the reverse electron density transfer from the $2p_\pi$ AO of the C_{60} carbon to the vacant 2*p* metal AOs. As a result, the lithium–fullerene bond should have a substantial covalent component, which is characteristic of lithium-organic compounds, in contrast to the organic complexes of other alkali metals.

An MD calculation of the behavior of the bis-η^5-lithium fullerene with increasing temperature suggests possible lithium incorporation into the fullerene void at the moment when asymmetric metal vibrations coincide in phase with stretching bond vibrations of carbon atoms in the five-member ring (Fig. 2).

Now, we turn to endohedral $Li_n@C_{60}$ compounds (n = 1–22). For n = 20 (Fig. 2), one observes an extremum in the enthalpy of formation, which corresponds to maximum stability of the complex in the whole series of polymetallic compounds (see table). As seen from the table, endohedral derivatives with one lithium atom are stabler than the corresponding exohedral complexes. As n increases, the C–C distances in $Li_n@C_{60}$ increase, while the Li–Li and Li–C bonds become shorter. MD calculations permitted us, however, to establish the range of stability of the $Li_n@C_{60}$ molecule as a function of the number of lithium atoms. For instance, compounds with n = 18–20 are unstable above

Calculated enthalpies of formation (from atoms) of lithium derivatives of the fullerene and their dipole moments

Compound	ΔH_f, kcal/mol	μ, D
$C_{60}@Li$	–10151.7	4.25
$C_{60}@Li^+$	–10070.0	8.12
$Li@C_{60}$-η^5	–10313.9	3.70
$(Li@C_{60}$-$\eta^5)^+$	–10223.0	2.06
Central-$Li@C_{60}$	–10297.9	3.76
$Li@C_{60}$-η^1	–10305.1	5.14
$Li@C_{60}$-η^2	–10303.3	2.45
$Li_{10}@C_{60}$	–29400.4	0.47
$Li_{15}@C_{60}$	–31134.4	2.89
$Li_{18}@C_{60}$	–32183.7	2.13
$Li_{20}@C_{60}$	–32465.9	0.82
$Li_{21}@C_{60}$	–32286.3	–
$Li_{22}@C_{60}$	–31663.5	–

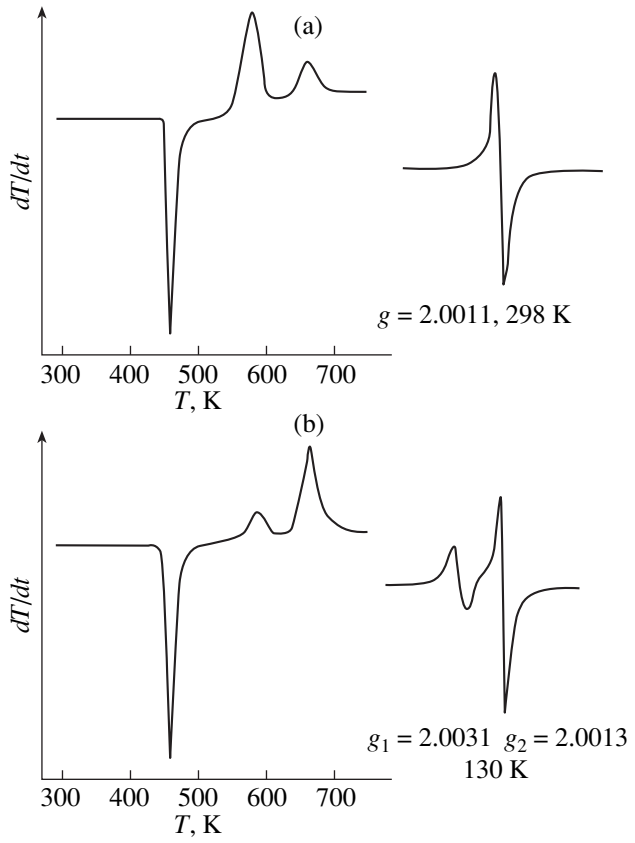

Fig. 3. DTA curves of the systems (a) C_{60} + *m*Li (*m* = 19, 40) and (b) C_{60} + C_{70} + 28Li, as well as EPR spectra of the products formed during the DTA analysis.

950 K and should break up. Despite the HOMO being delocalized considerably over the molecule, its energy is low in all cases (3 eV) and the electron density is higher on the outer side of the fullerene. The ionization potential of C_{60}@Li estimated as the difference in the enthalpy of formation between the C_{60}@Li and C_{60}@Li^+ complexes (see table) is relatively low, and, therefore, such derivatives may possess metallic properties in the condensed state. The same applies to Li@C_{60}-η^5.

The coupling in the systems $(C_{60} + mLi)_{solid}$ [*A*], $(C_{60}/C_{70} + nLi)_{solid}$ [*B*], $(Li)_{solid}$ [*C*] (test), and $(fullerenes)_{solid}$ [*D*] (test), with *m* = 19 and 40 and *n* = 28, was subjected to a comparative DTA study in the following manner. A mixture of Li with C_{60} or C_{60}/C_{70} was placed in a container evacuated to $P = 10^{-2}$ Torr. The temperature rise rate was 8–10°C/min. The thermograms of system [*D*] do not exhibit any peaks, system [*C*] reveals the Li melting endothermic peak only, and the [*A*] and [*B*] DTA curves exhibit the Li melting endothermic peak and two exothermic peaks (different in magnitude for [*A*] and [*B*]) at 583 and 663 K (Fig. 3), which apparently indicates a stepwise character of interaction in the [*A*] and [*B*] systems.

After the DTA study, we measured the EPR spectra in the solid reaction products at 298 K; for the [*A*] system, one observes a strong symmetric singlet with g = 2.0011, which may indicate the formation of particles of the $C_{60}^{\bullet-}$ type; system [*B*] shows an EPR line, which splits at 130 K into two singlets with g_1 = 2.0031 and g_2 = 2.0013 and an intensity ratio N = 2.8. These singlets can be assigned to $C_{70}^{\bullet-}$ and $C_{60}^{\bullet-}$ particles. In view of the first reduction potentials of C_{60} and C_{70} being equal [4], the probability ratio of formation of $C_{60}^{\bullet-}$ and $C_{70}^{\bullet-}$ particles in system [*B*] should be proportional to the molar fraction ratio chosen, K = 2.7, of C_{60} and C_{70} in [*B*], which is in accordance with the value of N.

ACKNOWLEDGMENTS

This study was supported by the Russian Foundation for Basic Research (project nos. 00-15-97439, 00-03-42004), the RF Ministry of Science program "Fullerenes and Atomic Clusters" (project "Metall-2"), and the RAS program "Nanomaterials and Supramolecular Systems" (project "Preparation and Structure of Nanomaterials").

REFERENCES

1. N. Krawez, R. Tellgmann, I. V. Hertel, *et al.*, Mol. Mater. **10**, 19 (1998).
2. L. Cristofolini, M. Riccö, and R. De Renzi, Phys. Rev. B **59**, 8343 (1999).
3. M. Yasukawa and S. Yamanaka, in *Abstrcats of the 18th Fullerene General Symposium, Okazaki, 2000*, p. 134.
4. R. M. Allemand, A. Koch, F. Wudl, *et al.*, J. Am. Chem. Soc. **113**, 1050 (1991).

Translated by G. Skrebtsov

Physics of the Solid State, Vol. 44, No. 3, 2002, pp. 521–524. From Fizika Tverdogo Tela, Vol. 44, No. 3, 2002, pp. 498–501.

PROCEEDINGS OF THE V INTERNATIONAL WORKSHOP "FULLERENES AND ATOMIC CLUSTERS"

(St. Petersburg, Russia, July 2–6, 2001)

Clustering and Polymerization of $Li_{15}C_{60}$[1]

T. Shiroka*, M. Riccò*, F. Barbieri*, E. Zannoni*, M. Tomaselli**

** Department of Physics, University of Parma & INFM, Parma, I-43100 Italy*

e-mail: toni.shiroka@fis.unipr.it

*** Laboratory of Physical Chemistry-ETH, Zurich, CH-8092 Switzerland*

Abstract—The structural and electronic properties of lithium intercalated fullerides (of which $Li_{15}C_{60}$ is the most representative) are still puzzling and unclear. Above 520 K, x-ray/neutron diffraction shows an fcc phase in which the 15 Li atoms clusterize in the octahedral interstices. However, at lower temperatures, a change in the crystalline symmetry and also in the electronic properties takes place as observed from ^{13}C, $^{7}Li/^{6}Li$ NMR and x-ray diffraction measurements. X-ray diffraction data suggest the presence of two different stable structures: a tetragonal monomeric and an orthorhombic polymerised phase. Detailed ^{13}C magic angle spinning NMR experiments in the latter phase indicate sp^3 bondings among the carbon atoms, whereas the relative (sp^2/sp^3) intensities, together with x-ray data, suggest the C_{60} polymerization to be a [2 + 2] cycloaddition. Multiple quantum NMR experiments on ^{7}Li confirm the presence of lithium clusters, as observed by x-ray diffraction in the high temperature phase, also at lower temperatures. However, the inferred cluster size is significantly smaller than that suggested by the stoichiometry. The distortion in the low-T structure of $L_{15}C_{60}$ is supposed to induce the migration of Li atoms from octahedral to tetrahedral voids, thus accounting for the lower number of Li atoms in the clusters. Further evidence of this scenario is obtained also from preliminary measurements of line shapes and T_1 relaxation times, which exhibit a multiexponential recovery with very different constants that are hardly compatible with a single family of Li atom sites. © *2002 MAIK "Nauka/Interperiodica".*

Unlike other alkali doped fullerenes, Li_xC_{60} has been somewhat overlooked in recent works on fullerene doped systems. Probably, this is due to difficulties in its preparation and perhaps to its lack of superconducting properties. However, the small radius of the intercalant gives Li_xC_{60} some peculiar properties, which are different from the case of the better known A_xC_{60} (where A = K, Rb, Cs and $1 \le x \le 6$). Namely, fullerenes show a considerable degree of Li atom acceptance, yielding systems with x as high as ~30. Being the less studied of the alkali doped fullerenes, very little is known about its properties, especially in the low-T lattice distorted phase, which occurs for temperatures below 520 K. Apart from some basic structural features determined by x-ray and quasielastic and inelastic neutron scattering [1], there exist many questions regarding both the behavior of Li atoms and that of the fullerene host lattice.

These include the existence in the low-T phase of Li clustering, the C_{60} packing and polymerization, the possible charge transfer and interaction between Li and C_{60}, etc., which are decisive in the construction of a model that would explain the electronic properties of the Li_xC_{60} systems.

In this work, we report on investigations performed on $Li_{15}C_{60}$, a typical representative of the whole class of compounds, by using local techniques such as NMR and x-ray diffraction to elucidate its structural characteristics.

1. EXPERIMENTAL

The samples were prepared by thermal decomposition in a dynamic vacuum of high purity, isotopically enriched $^{7}LiN_3$ mixed with stoichiometric amounts of C_{60}. Heating the mixture at ~450 K yielded $Li_{15}C_{60}$ with a 5% accuracy in lithium content. Annealing for several hours at 520 K gave powder pellets of improved crystallinity and homogeneity. Depending on the preparation conditions, some of the samples turned out to be a mixture of polymerized and nonpolymerized phases, whereas most of them resulted in a single nonpolymerized phase. Here, we are concerned only with the former type of samples.

X-ray measurements were performed with a GADDS (Bruker AXS) diffractometer. For the NMR lineshape measurements, we used a Spinmaster (Stelar) spectrometer, whereas for those involving more complex multiple quantum NMR, a home-built instrument was employed.

2. FULLERENE POLYMERIZATION IN $Li_{15}C_{60}$

The presence of a polymerized structure in a crystalline lattice is reflected not only in the modified electron density distribution; it can also alter the lattice symme-

[1] This article was submitted by the authors in English.

Lattice symmetries and parameters for the orthorhombic and tetragonal phase of $Li_{15}C_{60}$ as obtained from x-ray diffraction measurements

Symmetry	Angles	Lattice parameters, Å
Orthorhombic	$\alpha = \beta = \gamma = 90°$	$\alpha = 9.06$, $b = 9.32$, $c = 15.10$
Tetragonal	$\alpha = \beta = \gamma = 90°$	$a = b = 9.87$, $c = 14.30$

try group and/or the lattice parameters. Therefore, the joint use of experimental techniques, such as NMR and x-ray diffraction, capable of detecting these changes could provide useful information on polymerization.

We measure the CuK_α x-ray diffraction intensity as a function of sample temperature from 300 up to ~550 K. From a comparison with well-known powder diffraction patterns for $Li_{12}C_{60}$ [1] and pristine C_{60} [2], we deduce the presence of two distinct phases at room temperature. Successive indexing procedures identify one tetragonal and one orthorhombic phase; the respective lattice parameters and symmetries are shown in the table. Preliminary results from structure refinement performed on the orthorhombic phase suggest a 1D carbon polymerization of C_{60}.

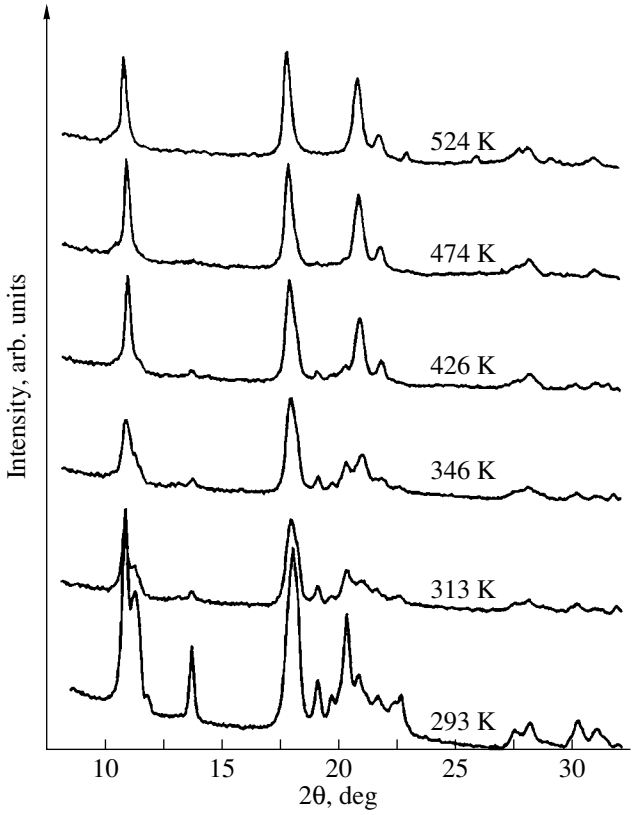

Fig. 1. X-ray diffraction patterns for a $Li_{15}C_{60}$ sample as a function of temperature. The room temperature spectrum shows the coexistence of an orthorhombic and a tetragonal phase, which transform into a single cubic phase upon heating. The spectra were recorded using laboratory CuK_α radiation.

As the temperature is increased (Fig. 1), the intensities relative to the two distinct phases begin to merge, such that, for $T > 550$ K, only one pattern, compatible with a single cubic phase, is present. The occurrence of an orthorhombic-to-cubic transition (in addition to the already known tetragonal-to-cubic transition [1]) implies, therefore, the disappearance of C_{60} polymerization upon sample heating.

Further evidence on fullerene polymerization in $Li_{15}C_{60}$ was obtained by static and magic angle spinning (MAS) ^{13}C NMR. At room temperature, the static lineshapes display an inhomogeneously broadened shift-anisotropy powder pattern typical of static sp^2 fullerene carbons. Moreover, two additional sharp peaks are found at 155 and at 59 ppm, which could be assigned, respectively, to a motion-averaged C_{60}^{n-} sp^2 line and to sp^3 hybridized carbons. These findings suggest both a blocked rotation for a considerable amount of C_{60} molecules due to covalent bonding in a polymer configuration and also the presence of a phase inhomogeneity as found from x-ray diffraction.

Additional evidence supporting these result comes from MAS experiments, which allow more precise quantitative assignments for the individual peaks. From an accurate fit of the lineshapes, one can evaluate the intensity ratio $f = I_{sp^3}/I_{sp^2}$ from which (once the C_{60}^{n-} contribution is subtracted) the average number of four sp^3 atoms per C_{60} molecule can be inferred.

This result is compatible with several bonding configurations among C_{60} molecules, which may include two [2 + 2] cycloadditions, regular 2D single-bond polymerization, or even random 2D polymerization. However, the symmetry requirements from the x-ray diffraction data restrict the possible structures to those where C_{60} polymerization takes place in rows of [2 + 2] cycloadditions, giving rise to an 1D polymerized structure (Fig. 2). This is supposed to induce a local structure disorder which, apart from x-ray measurements, is also supported by the presence of two slightly shifted sp^3 lines in the NMR spectra [3].

Finally, one should note that, although there is an important C_{60}–C_{60} interaction which brings fullerenes to polymerization, the Li–C_{60} interaction is only secondary. Several NMR measurements support this conclusion: (a) the absence of J couplings among ^7Li and ^{13}C, (b) the absence of cross-polarization transfer between these atoms (for contact times as long as 20 ms at room temperature), and (c) the presence of a considerable ^7Li motional narrowing due to lithium diffusion processes.

3. LITHIUM CLUSTERING STUDIED BY SINGLE AND MULTIPLE-QUANTUM NMR

Both conventional and more advanced multiple-quantum (MQ) NMR provide a wealth of information on lithium behavior in $Li_{15}C_{60}$, including its dynamics, diffusion, clustering, etc. We use standard NMR to measure the temperature dependence of the ^{7}Li line width and shape, as well as the spin-lattice relaxation time; MQ NMR, in contrast, is a more suitable method to investigate potential cluster formation. Indeed, the monitoring of time evolution of MQ coherences in coupled spin systems provides an excellent tool to study their clustering properties.

The ^{7}Li (spin 3/2) lineshapes, measured by a magic echo sequence, display symmetric features at all temperatures. At 50 K, the line consists of two distinct peaks: a narrow peak attributed to the (1/2, –1/2) transition and a broad peak ascribed to the satellite transitions (±1/2, ±3/2). As the temperature increases, both of them merge into a single central peak, 1.8(1) kHz. The rather narrow single line observed at room temperature as compared to that measured at 50 K (4.3(2) kHz FWHM) suggests motional narrowing due to rotational lithium diffusion inside the clusters (cfr. infra). The diffusion, however, is believed to stop at temperatures below 50 K, since no significant change in lineshape and width are observed for $T < 50$ K.

The absence of any distinguishable quadrupole powder pattern in the whole temperature range could be due to an averaging of the anisotropic part of the quadrupole and dipole interactions. Since no indication of a ^{7}Li Knight shift was found, we believe the clusters not to show metallic properties.

A simple rough estimate of the aggregation of lithium atoms in clusters can be made from dipolar line width calculations, where we consider the interactions among N identical 3/2 spins.

They yield a theoretical line width of 4.6 kHz FWHM, which is slightly in excess of the measured value at 50 K, suggesting either an underestimated internuclear distance or a reduced average number of lithium nuclei per cluster.

More direct evidence of Li clustering is obtained by multiple quantum NMR experiments. In the case of N nuclei with spin 3/2, the set of possible quantum coherences ΔM goes from 0 to $3N$. They can be detected by a radio frequency coil only after exciting and successively converting them into single quantum coherences (which correspond to the familiar transverse magnetization).

With the use of an appropriate multiple quantum excitation-detection sequence, essentially based on the magic-echo scheme [4], one can obtain a dipolar and a quadrupolar echo provided the condition $\tau_2 = \tau_1/2$ is satisfied (here, τ_1 is the rotating-frame defocusing time and τ_2 is the laboratory-frame refocusing time). A systematic increment of the dynamical evolution time τ_1 leads to an ever increasing signal intensity for all orders of coherence. This confirms the presence of strongly dipolar-coupled ^{7}Li spins whose network grows wider the longer τ_1. However, beyond a certain threshold time ($\tau_1 = 2.5$ ms in our case), the intensity will no longer rise, indicating that the limit of a finite size cluster has been reached.

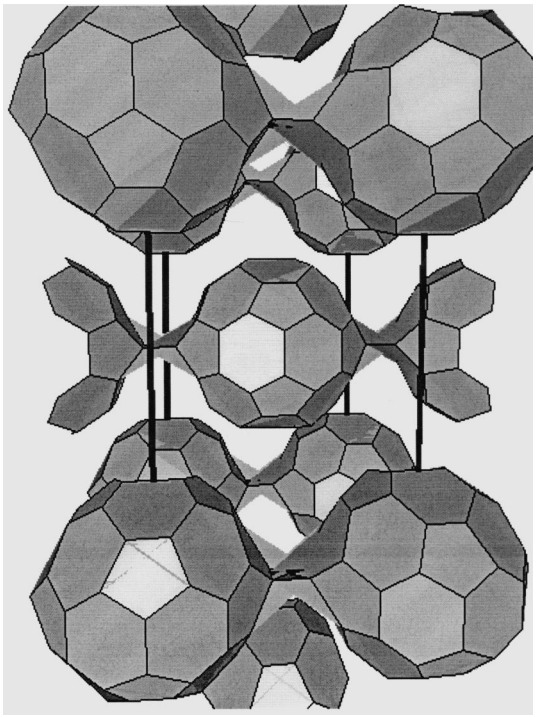

Fig. 2. Pictorial view of the polymerized $Li_{15}C_{60}$ structure as obtained from x-ray diffraction data. The horizontal planes contain fullerenes with a 1D polymeric structure; [2 + 2] cycloaddition along the a direction. The sp^2/sp^3 intensity ratio is consistent with the NMR results.

In the presence of the saturation regime, the intensities of various MQ transitions follow an approximate Gaussian distribution function. In the particular case of nuclei with spin 3/2, the intensity profile $I_{\Delta M}$ as a function of $(\Delta M)^2$ follows the curve $I_{\Delta M} \propto \exp[-(\Delta M)^2/5N]$ [5].

Therefore, from a logarithmic plot of the ratio $I_{\Delta M}/I_2$ as a function of $(\Delta M)^2$, where I_2 is the intensity of double-quantum coherence (i.e., $I_{\Delta M}$ when $\Delta M = 2$), one can easily evaluate the number of interacting spins which make up a cluster. Such a plot and the relative fit for the case of $Li_{15}C_{60}$ are shown in Fig. 3. The fitted value $N = 9(1)$ is significantly lower than the expected stoichiometric value of 15. Apart from the very improbable underestimate from the statistical analysis (whose correctness was also tested by simulations), we believe that a more realistic reason for the inferred cluster size could be found in the presence of structural disorder.

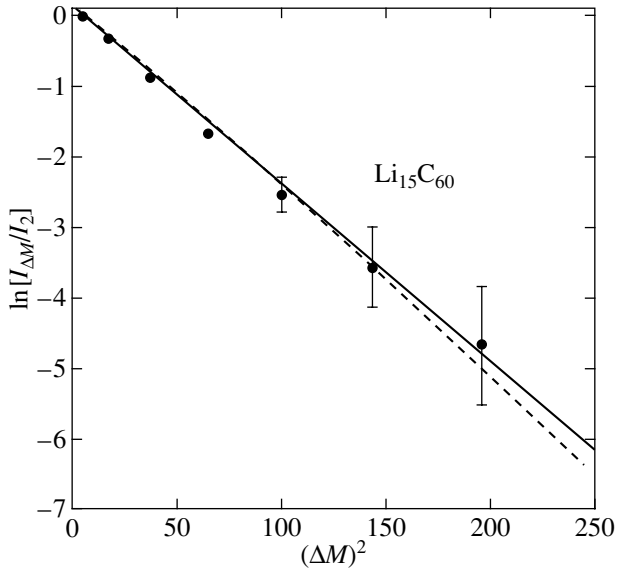

Fig. 3. Logarithm of the intensity profile $I_{\Delta M}/I_2$ as a function of $(\Delta M)^2$ for $Li_{15}C_{60}$. The solid and the doted lines are fits according to slightly different models, both yielding $N = 9(1)$ for the number of lithium atoms in a cluster.

Indeed, one can assume that the previously empty tetrahedral sites, under lattice deformation, will be partially filled, therefore accounting for the lower number of atoms in the octahedral clusters.

4. SUMMARY

The intercalation compound $Li_{15}C_{60}$ was studied with ^{13}C, ^{7}Li NMR, and x-ray diffraction in its low-temperature phase ($T < 530$ K).

^{13}C MAS experiments showed evidence of sp^3 bonding among carbon atoms, whereas the relative intensities sp^2/sp^3 suggest C_{60} polymerization.

MQ NMR experiments on ^{7}Li confirm the presence of lithium clusters, previously shown by x-ray diffraction in the high temperature phase, also at lower temperatures. The inferred cluster size, significantly smaller than that suggested by the stoichiometry, can be explained as a consequence of C_{60} lattice distortion. In this case, the overall number of atoms in octahedral sites would be reduced by a partial occupation of tetrahedral sites also.

REFERENCES

1. L. Cristofolini, M. Riccò, and R. De Renzi, Phys. Rev. B **59**, 8343 (1999).
2. M. Núñez-Regueiro, L. Marques, J.-L. Hodeau, *et al.*, Phys. Rev. Lett. **74**, 278 (1995).
3. M. Tomaselli, B.-H. Meier, M. Riccò, *et al.*, Phys. Rev. B **63**, 113405 (2001).
4. W. K. Rhim, A. Pines, and J. S. Waugh, Phys. Rev. Lett. **25**, 218 (1970).
5. M. Tomaselli, B. H. Meier, M. Riccò, *et al.*, submitted to J. Chem. Phys.

Physics of the Solid State, Vol. 44, No. 3, 2002, pp. 525–526. Translated from Fizika Tverdogo Tela, Vol. 44, No. 3, 2002, pp. 502–503.

PROCEEDINGS OF THE V INTERNATIONAL WORKSHOP "FULLERENES AND ATOMIC CLUSTERS"

(St. Petersburg, Russia, July 2–6, 2001)

Investigation of Metal-Containing Carbon Nanostructures Prepared from Functional Polymers

O. A. Nikolaeva*, V. I. Kodolov*, L. G. Makarova*, A. Yu. Volkov, and E. G. Volkova****

** Scientific and Educational Center of Chemical Physics and Mesoscopy, Ural Division, Russian Academy of Sciences, Izhevsk, 426069 Russia*

*** Institute of Metal Physics, Ural Division, Russian Academy of Sciences, ul. S. Kovalevskoĭ 18, Yekaterinburg, 620219 Russia*

e-mail: nik@istu.udm.ru

Abstract—Metal-containing carbon nanostructures are prepared by heating poly(vinyl alcohol) in mineral media with a lamellar structure at a temperature below 300°C. It is demonstrated that three possible types of nanostructures can be formed, namely, multilayer carbon nanotubes, spherical carbon nanoparticles, and finely crystalline carbon structures. According to the data of transmission electron microscopy, the nanotube size falls in the range from 50 to 300 nm and the nanotubes themselves have a stranded structure. © *2002 MAIK "Nauka/Interperiodica".*

1. INTRODUCTION

The existing methods of preparing carbon nanotubes require large energy consumption and complex apparati. Recent studies [1, 2] revealed that dehydropolycondensation of aromatic amines in interlayer spaces of vanadium–oxide systems occurs with the formation of tubulenes. In this respect, we analyzed the possibility of producing metal-containing carbon tubulenes from functional polymers in inorganic media with a lamellar structure.

2. SAMPLE PREPARATION AND EXPERIMENTAL TECHNIQUE

We studied the products of the heat treatment of poly(vinyl alcohol) in lamellar inorganic media. In the case when metal chlorides or poly(phosphoric acid) were used as media favorable to carbonation of the polymer, the mixture of finely dispersed powders of the polymer and the mineral phase was heated in the temperature range from 250 to 300°C for 4–8 h. When poly(vanadic acid) and its derivatives containing Cr and Mo served as the favorable medium, the reaction was performed in an aqueous solution. After mixing of poly(vinyl alcohol) and acid, the resultant mixture was subjected to an electric field with a voltage of 12 V. Then, the reaction mixture was heated to a temperature of 90°C. The treatment of the reaction mixture was carried out according to the procedure described in [3].

3. RESULTS AND DISCUSSION

Analysis of the x-ray photoelectron spectra (magnetic x-ray photoelectron spectrometer, AlK_α radiation) of the samples under investigation revealed the following structural features. The overall spectra contain intense peaks associated with carbon and oxygen. The x-ray photoelectron spectra of the samples prepared in the inorganic media containing metal ions exhibit weak peaks of the relevant metals. The C 1*s* spectrum consists of three components corresponding to the C–C (284 eV), C–H (285 eV), and C–O (287–288 eV) bonds. Their ratio varies according to the synthesis conditions and the medium composition. The maximum content of graphitic carbon (81–87%) is observed in the samples prepared in the 3*d* metal chloride medium. For the samples prepared in poly(vanadic acid) and its derivatives, the content of C–C bonds is equal to 75–78%. The content of the carbonyl and carbonate groups in all samples does not exceed 5%.

According to electron microscopy, the studied samples are in amorphous and finely crystalline states. The samples prepared from poly(vinyl alcohol) in the manganese chloride medium are predominantly in a finely crystalline state. The microdiffraction pattern consists of bright and diffuse spots, which, as a whole, form pictures of the six-pointed star type. Such complex reflections are usually observed for quasicrystals, for example, manganese alloys. According to transmission electron microscopy, the structure of the samples prepared in the manganese chloride medium is characterized by extended tubular formations approximately 50 nm in diameter. Carbon nanostructures of polyhedral and spherical forms (from 50 to 200 nm in size) were obtained in the poly(phosphoric acid) medium. The diffraction pattern taken from these nanostructures contains diffuse fringes.

1063-7834/02/4403-0525$22.00 © 2002 MAIK "Nauka/Interperiodica"

Micrograph of a carbon nanotube prepared from poly(vinyl alcohol) in the $H_2V_{10}Mo_{02}O_{31}$ medium.

The electron microscopic investigation of the samples prepared from poly(vinyl alcohol) in the poly(vanadic acid) solution containing molybdenum revealed cylindrical, rather extended, structures 100–300 nm in diameter. We examined the structure of a 154-nm-long multilayer tube with an interlayer distance of approximately 11 nm (see figure). This is approximately 30 times larger than the interplanar distance in graphite (0.34 nm). It is known that, when nanotubes involve defects (or when one of the layers is partially absent), the interlayer distance in multilayer tubes can increase to 0.68 or even to 0.95 nm upon intercalation [4]. In our case, the interlayer distance is one order of magnitude greater than that cited in the literature. This can be associated with the influence of the low-energy synthesis procedure on the growth mechanism of carbon nanotubes.

The microdiffraction pattern exhibits distinct reflections with strands directed perpendicular to the tube axis. The $10\bar{1}0$ reflections are split into two reflections each and located on either side of the tube axis, which is typical of tubulenes [5]. The total chirality angle of the tube is 15°–16°. Upon prolonged exposure of the tube to an electron beam, the microstructure of the tube is destroyed and diffraction becomes amorphous in character.

4. CONCLUSION

Our investigation demonstrated that metal-containing carbon nanostructures can be produced by the low-energy method from polymers with functional groups in interlayer spaces of inorganic media.

ACKNOWLEDGMENTS

This work was supported by the International Association of Assistance for the promotion of cooperation with scientists from the New Independent States of the former Soviet Union (INTAS), project no. 97-30810.

REFERENCES

1. H. J. Muhr, F. Krumeich, U. P. Schonholzer, *et al.*, Adv. Mater. **12** (3), 231 (2000).
2. F. Krumeich, H. J. Muhr, M. Niederberger, *et al.*, J. Am. Chem. Soc. **121** (36), 8324 (1999).
3. V. I. Kodolov, O. A. Nikolaeva, L. G. Makarova, *et al.*, Khim. Fiz. Mezoskop. **2**, 164 (2000).
4. A. V. Eletskiĭ, Usp. Fiz. Nauk **167** (9), 945 (1997) [Phys. Usp. **40**, 899 (1997)].
5. D. Bernaerts, M. Op de Beeck, and S. Amelinckx, Philos. Mag. A **74** (3), 723 (1996).

Translated by O. Moskalev

Physics of the Solid State, Vol. 44, No. 3, 2002, pp. 527–528. Translated from Fizika Tverdogo Tela, Vol. 44, No. 3, 2002, pp. 504–505.

PROCEEDINGS OF THE V INTERNATIONAL WORKSHOP "FULLERENES AND ATOMIC CLUSTERS"

(St. Petersburg, Russia, July 2–6, 2001)

Electric Conduction Properties of $M@C_{2n}$ Endohedral Metallofullerenes (M = La, Y)

V. P. Bubnov*, I. E. Kareev*, **, E. É. Laukhina*, L. I. Buravov*, V. K. Koltover*, and É. B. Yagubskiĭ*

** Institute of Problems of Chemical Physics, Russian Academy of Sciences, Chernogolovka, Moscow oblast, 142432 Russia*
e-mail: bubnov@icp.ac.ru
*** Moscow State University, Vorob'evy gory, Moscow, 119899 Russia*

Abstract—The electrical conduction properties of powder samples of $M@C_{2n}$ endohedral metallofullerenes (M = La, Y) isolated from soot by extraction with *N*,*N*-dimethylformamide and by sublimation were studied. It was established that the conductivity of sublimated samples exceeded that of the extracted ones by four orders of magnitude and was as high as 0.2–0.5 Ω^{-1} cm^{-1} at room temperature. © *2002 MAIK "Nauka/Interperiodica".*

1. INTRODUCTION

Endohedral metallofullerenes (EMFs) $M@C_{2n}$ represent a novel type of carbon clusters, which differ substantially from empty fullerenes in their properties [1–3]. They contain one or several metal atoms encapsulated in the fullerene molecule. The formation of such compounds is most characteristic of the C_{82} molecule with Group III metals (Sc, Y, La) and lanthanides. A metal atom encapsulated into the fullerene molecule changes its electronic properties considerably. In the case of $La@C_{82}$ and $Y@C_{82}$ EMFs, three electrons are donated by the metal to the fullerene to form the $M^{3+}@C_{82}^{3-}$ complex. Depending on the nature of the metal and the number of its encapsulated atoms, EMFs can be paramagnetic or diamagnetic. The unique structure of the EMFs and the diversity of their properties, which vary with the encapsulated metal and the fullerene, have stimulated a great scientific interest. The EMFs can be expected to form a basis for the development of new materials, such as molecular conductors and ferromagnets, laser and ferroelectric materials, and pharmaceuticals [3]. However, the chemical and physical properties of EMFs remain poorly studied; in particular, their electrical conduction characteristics have thus far not been investigated. This is primarily caused by the limited availability of EMFs, which is associated with problems that hinder their synthesis and isolation in sizable amounts [2, 3]. Recently, we developed a method for selective EMF extraction of up to grams of EMFs [4, 5] that removes the problem of EMF availability to a considerable extent.

This paper reports on the first study of the electrical conduction properties of $M@C_{2n}$ powder samples (M = La, Y) isolated from soot by extraction and sublimation.

2. EXPERIMENTAL

Soot containing $La@C_{82}$ and $Y@C_{82}$ EMFs was prepared by evaporating composite graphite electrodes with metallic La or Y in an arc-discharge reactor [4, 5]. The electrodes were evaporated in arc discharge at a helium pressure of 120 Torr, arc current of 90 A, voltage of 28–30 V, arc length of 5 mm, a distance between the arc and the cooled reactor wall of 50 mm, and an evaporation rate of 1 mm/min.

EMFs were isolated from soot using two methods: (a) extraction with *N*,*N*-dimethylformamide[1] (DMFA) in an argon atmosphere at the solvent boiling temperature [4, 5] and (b) gradient sublimation in vacuum at 800°C. In both cases, the soot was preliminarily extracted with *o*-xylene to remove empty fullerenes from it to the maximum possible extent.

The products thus prepared were characterized using mass spectrometry, elemental analysis, and optical, IR, and EPR spectroscopy.

The EMF conductivity was measured by the dc four-probe technique on pressed pellets in a helium atmosphere at temperatures ranging from 4.2 to 300 K. The pellets of the DMFA extraction and sublimation products, 7.5 × 1.5 × 1 mm in size, were pressed at 3800 kg/cm^2. To exclude errors associated with the thermopower, the sample electrical resistivity was measured for two opposite current directions.

3. RESULTS AND DISCUSSION

The data obtained using mass spectrometry and electron and EPR spectroscopy show the main compo-

[1] Polar solvent for selective extraction of endohedral metallofullerenes from soot.

1063-7834/02/4403-0527$22.00 © 2002 MAIK "Nauka/Interperiodica"

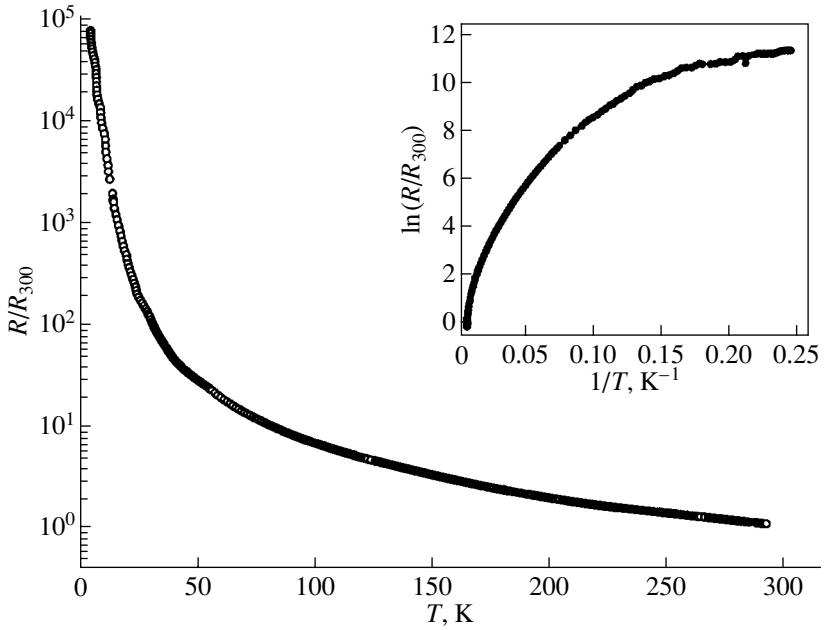

Temperature dependence of the electrical resistance of an $Y@C_{82}$ sample isolated by sublimation.

nents of the DMFA extracts to be $La@C_{82}$ and $Y@C_{82}$ [4, 5]. The EPR spectra of the *o*-dichlorobenzene solutions revealed lines with a hyperfine structure corresponding to two isomers of $La@C_{82}$ and $Y@C_{82}$ [3]. Other $M@C_{2n}$ EMFs (n = 40, 42–46) were present in the extracts in insignificant amounts, and empty fullerenes were virtually absent. Elemental analysis and IR spectroscopy also showed the extracts to contain solvent (DMFA, ~20 wt %).

In contrast to the extracts, the $Y@C_{82}$ EMF obtained by sublimation contained, as revealed by electron spectroscopy, empty fullerenes (C_{60}) in addition to $Y@C_{82}$. The EPR spectrum of the sublimate in *o*-dichlorobenzene showed doublet lines corresponding to two $Y@C_{82}$ isomers.

Conductivity measurements showed the EMF extracts to have a low electrical conductivity ($\sigma_{300} \sim 10^{-5}$ Ω^{-1} cm^{-1}). Thermal treatment of the extracts in vacuum increased the conductivity due to a partial solvent loss. The conductivity of a solvent-free $Y@C_{82}$ sample obtained by sublimation is four orders of magnitude higher (~0.2–0.5 Ω^{-1} cm^{-1}) than that of the extracted $Y@C_{82}$. The electrical resistivity grows slowly with decreasing temperature down to ~80 K, after which it starts to increase rapidly (see figure). Within the range 300–160 K, the resistivity exhibits an activated behavior, with an activation energy of 0.029 eV (inset to figure). In the low-temperature range, the nonactivated process is dominant. Note the low activation energy, which is possibly associated with the polycrystalline nature of the sample rather than reflects the intrinsic properties of $Y@C_{82}$. The relatively high conductivity of the pellets and the low activation energy allow one to assume that $Y@C_{82}$ behaves as a molecular metal down to ~80 K. At lower temperatures, a transition to the dielectric state probably occurs. This assumption is borne out by the behavior of the spin paramagnetic susceptibility of the solvent-free $La@C_{82}$ sample obtained by sublimation [3, 6]. The susceptibility was virtually temperature-independent within the range 300–80 K (Pauli paramagnetism); this feature is characteristic of metals.

ACKNOWLEDGMENTS

This study was supported by the Russian Foundation for Basic Research (project no. 02-03-33352) and the Russian programs “Fullerenes and Atomic Clusters” (project no. 107-14(00)-П) and “Chemistry and Prospects of Fullerene Applications” (project no. 402-22.2(00)-П).

REFERENCES

1. D. S. Bethune, R. D. Johnson, J. R. Salem, *et al.*, Nature **336**, 123 (1993).
2. K. Sueki, K. Kikuchi, K. Akiyama, *et al.*, Chem. Phys. Lett. **300**, 140 (1999).
3. H. Shinohara, Rep. Prog. Phys. **63**, 843 (2000).
4. E. E. Laukhina, V. P. Bubnov, Ya. I. Estrin, *et al.*, J. Mater. Chem. **8**, 893 (1998).
5. V. P. Bubnov, E. E. Laukhina, I. E. Kareev, *et al.*, Chem. Mater. (in press).
6. T. Waranuki, H. Suematsu, Y. Nakao, *et al.*, in *Abstracts of the 13th Fullerene Symposium, 1997*, p. 83.

Translated by G. Skrebtsov

Physics of the Solid State, Vol. 44, No. 3, 2002, pp. 529–530. Translated from Fizika Tverdogo Tela, Vol. 44, No. 3, 2002, pp. 506–507.

PROCEEDINGS OF THE V INTERNATIONAL WORKSHOP "FULLERENES AND ATOMIC CLUSTERS"

(St. Petersburg, Russia, July 2–6, 2001)

Stability and Mobility of the Endohedral Metallofullerene of La@C_{82} in Polycarbonate Polymer Films

V. K. Koltover*, T. A. Parnyuk, V. P. Bubnov*, E. É. Laukhina*, Ya. I. Éstrin*, and É. B. Yagubskiĭ***

** Institute of Problems in Chemical Physics, Russian Academy of Sciences, Chernogolovka, Moscow oblast, 142432 Russia*
e-mail: koltover@icp.ac.ru
*** Taras Shevchenko Kiev National University, pr. Glushkova 6, Kiev, 03022 Ukraine*

Abstract—An La@C_{82}-doped polymer (bisphenol-A polycarbonate) was prepared. EPR spectra of La@C_{82} in a solid polymer film and in a polycarbonate solution in *o*-dichlorobenzene were studied. The EPR spectrum shape of La@C_{82} was shown to be sensitive to the phase state of the polymer. La@C_{82} in the film was found to have a high chemical stability below the glass formation temperature, thus permitting one to use the polymer for the storage and study of endohedral metallofullerenes. © *2002 MAIK "Nauka/Interperiodica"*.

1. INTRODUCTION

Endohedral metallofullerenes (M@C_{2n}) are carbon compounds containing one (sometimes, two or three) metal atoms inside the C_{2n} fullerene cage [1]. M@C_{2n} compounds have an application potential as a basis for the development of new materials, including polymer composites, as well as in NMR tomography and nuclear medicine [2–5]. Until recently, however, M@C_{2n} compounds had limited availability. Moreover, studies of M@C_{2n} are made difficult by their instability in the presence of oxygen, which requires they be stored in vacuum or argon [2–7]. Earlier, we developed a method of step extraction of M@C_{2n} that permitted us to increase the yield of these compounds up to 5% of the original soot mass [3].

This paper reports on an EPR study of the chemical stability and rotational mobility of La@C_{82} in solid films and solutions of polycarbonate (PC).

2. EXPERIMENTAL

The synthesis of La@C_{82}-containing soot in an electric arc-discharge reactor and extraction of La@C_{82} from it are described in [3]. Analysis of La@C_{82} samples using mass spectrometry and liquid chromatography did not reveal the presence of C_{60} or C_{70} [3]. To prepare an La@C_{82}-doped polymer, 1 g of bisphenol-A PC (Aldrich) was dissolved in 50 ml of *o*-dichlorobenzene (DCB), then 20 mg La@C_{82} was added to the solution, and the mixture was heated in an argon environment at 120°C until a homogeneous solution formed. Next, the solution was placed on a plane glass and the solvent was removed in an argon flow until a solid film formed.

EPR spectra were obtained on an E-104A EPR spectrometer under conditions ensuring an undistorted line shape. The oxygen was removed from the solutions by evacuation at a pressure of ~10^{-3} mm Hg.

3. DISCUSSION

The room-temperature spectrum of La@C_{82} in a PC solution in DCB exhibits two octet signals with partially overlapping lines (spectrum *1* in figure). The octet hyperfine structure (HFS) appears due to the interaction of the unpaired 5*d* electron of lanthanum with a magnetic moment of ^{139}La (I = 7/2). The higher intensity octet has an HFS constant a_{La} = 0.115 mT, and the weaker octet has a_{La} = 0.081 mT. Both octets are similar to the signals of the La@C_{82} isomers in pure DCB (without polymer addition) [2–7]. Despite the polymer solution being a gel at room temperature, the HFS linewidth measured in it was found to be practically the same as in pure DCB. Hence, the viscosity of the polymer solution affects the rotational mobility of La@C_{82} only weakly [8], which implies its localization in the volume phase of the solvent. When La@C_{82}, both in the gel and in pure solvent, was subjected to air, the EPR signal disappeared irreversibly within several days.

The spectra of La@C_{82} in a PC film (spectra *2*, *3* in figure) differ substantially from its spectra in the liquid solution, which is caused by the low rotational mobility of La@C_{82} in the solid polymer. The octet HFS appears above the PC vitrification temperature (~400 K), when segment motions in the polymer unfreeze to a considerable extent. The PC transition from the glassy to a high-elasticity state and back was clearly manifested in the temperature dependences of the spectral parameters of La@C_{82}.

1063-7834/02/4403-0529$22.00

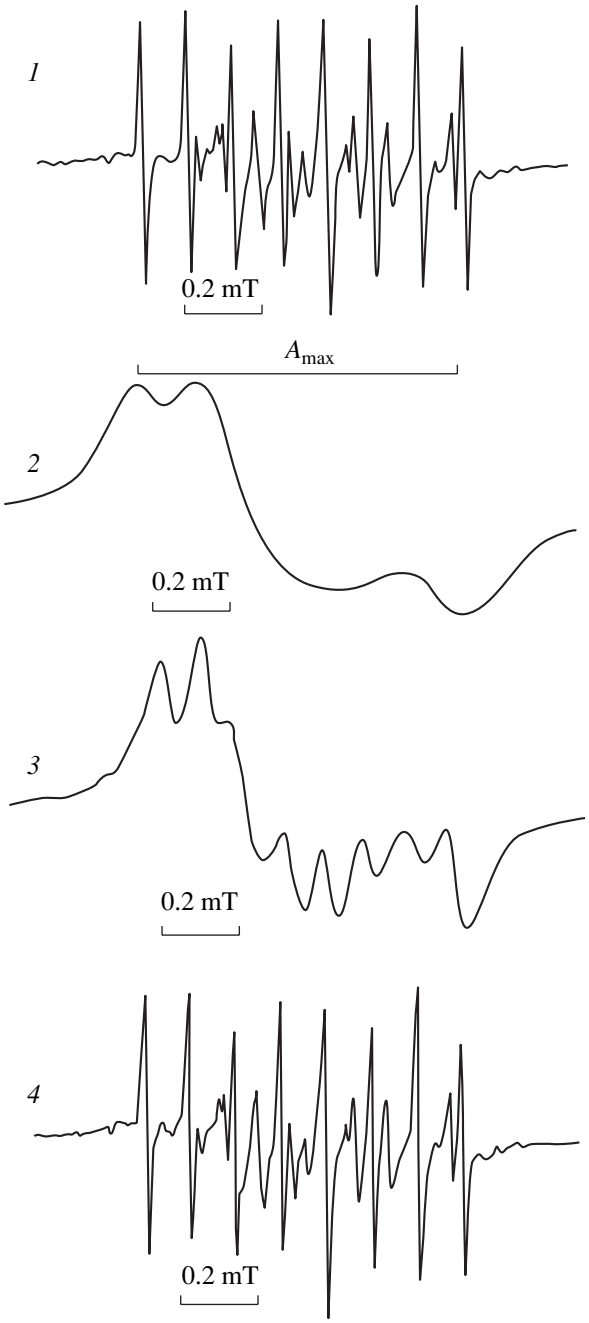

EPR spectra of PC-La@C_{82} samples. (*1*) Starting polymer solution (gel) in DCB, 293 K; (*2*, *3*) polymer film, 293 and 425 K, respectively; and (*4*) solution in DCB after one year of storage in air, 293 K. The spectra were measured in the absence of oxygen at a microwave power P = 0.5 mW and high-frequency modulation amplitude H_m = 0.01 mT.

The La@C_{82}-doped PC film was stored for a year in laboratory conditions in air. After this, it was dissolved in DCB. The EPR spectrum of the gel thus formed (spectrum *4* in figure) was found to be practically identical to the spectrum of the gel of the starting sample, dissolved in DCB immediately after its preparation (spectrum *1*).

The M@C_{2n} compounds are known to become oxidized irreversibly when subjected to air for a few days; therefore, as already mentioned, powders and solutions of these compounds have to be stored in vacuum or in an argon atmosphere [2]. The remarkable stability of La@C_{82} in PC films should be apparently attributed to the fact that oxygen diffusion in this polymer is very slow below the vitrification temperature.

Thus, we found La@C_{82} to be very stable in PC films, which permits one to use these films to store M@C_{2n} compounds for further use. The sensitivity of the La@C_{82} EPR spectrum to the phase state of the polymer makes it possible to use this compound, in addition to nitroxyl radicals [8], as a spin probe in studies of conventional polymers and biopolymers.

ACKNOWLEDGMENTS

This study was supported by the Russian Foundation for Basic Research (project nos. 01-03-32945, 00-03-33200) and the Russian program “Fullerenes and Atomic Clusters” (project no. 4-1-98).

REFERENCES

1. Y. Chai, T. Guo, C. Jin, *et al.*, J. Phys. Chem. **95**, 7564 (1991).
2. H. Shinohara, Rep. Prog. Phys. **63**, 843 (2000).
3. E. E. Laukhina, V. P. Bubnov, Ya. I. Estrin, *et al.*, J. Mater. Chem. **8**, 893 (1998).
4. V. K. Koltover, Ya. I. Estrin, L. T. Kasumova, *et al.*, J. Biosci. Suppl. **1**, 188 (1999).
5. D. W. Cagle, S. J. Kennel, S. Mirzadeh, *et al.*, Proc. Natl. Acad. Sci. USA **96**, 5182 (1999).
6. V. K. Koltover, V. P. Bubnov, E. E. Laukhina, and Ya. I. Estrin, Mol. Mater. **13**, 239 (2000).
7. V. K. Koltover, Ya. I. Estrin, V. P. Bubnov, and E. E. Laukhina, Izv. Ross. Akad. Nauk, Ser. Khim., No. 10, 1765 (2000).
8. J. A. Freed, in *Spin Labeling. Theory and Applications*, Ed. by L. J. Berliner (Academic, New York, 1976), p. 53.

Translated by G. Skrebtsov

Physics of the Solid State, Vol. 44, No. 3, 2002, pp. 531–533. Translated from Fizika Tverdogo Tela, Vol. 44, No. 3, 2002, pp. 508–510.

PROCEEDINGS OF THE V INTERNATIONAL WORKSHOP "FULLERENES AND ATOMIC CLUSTERS"

(St. Petersburg, Russia, July 2–6, 2001)

A New Molecular C_{60} Complex with Bis(methylenedithio)tetrathiafulvalene (*BMDT–TTF*): Synthesis, Crystal Structure, and Properties

N. G. Spitsina, V. V. Gritsenko, O. A. D'yachenko, and É. B. Yagubskiĭ

Institute of Problems of Chemical Physics, Russian Academy of Sciences, Chernogolovka, Moscow oblast, 142432 Russia

e-mail: spitsina@icp.ac.ru

Abstract—A new molecular C_{60} complex of the composition (*BMDT–TTF*) · C_{60} · $2CS_2$ (**I**) with the bis(methylenedithio)tetrathiafulvalene (*BMDT–TTF*) organic donor is synthesized. The molecular and crystal structures of this complex are determined by x-ray diffraction. The (*BMDT–TTF*) · C_{60} · $2CS_2$ (**I**) compound crystallizes in a monoclinic crystal system. The main crystal data are as follows: a = 13.550(5) Å, b = 9.964(7) Å, c = 17.125(8) Å, β = 99.52(4)°, V = 2280(2) Å^3, M = 1229.45, and space group $P2_1/m$. Crystals of **I** have a layered structure: layers consisting of C_{60} molecules alternate with layers composed of *BMDT–TTF* and CS_2 molecules. It is found that, in complex **I**, the donor and C_{60} molecules are linked through the shortest contacts, which leads to a change in the molecular geometry of *BMDT–TTF*. The donor molecules in a crystal layer are characterized by the shortest S…S contacts. The IR data indicate the electroneutrality of the fullerene molecule. The electrical conductivity of (*BMDT–TTF*) · C_{60} · $2CS_2$ single crystals is measured using the four-point probe method at room temperature: $\sigma_{RT} = 2 \times 10^{-5}$ Ω^{-1} cm^{-1}. © *2002 MAIK "Nauka/Interperiodica".*

1. INTRODUCTION

The great interest expressed by researchers in fullerene-based compounds stems from the recent discoveries of superconductivity and ferromagnetic phenomena in fullerides [1–4]. Fullerene C_{60} exhibits the properties of an acceptor and can form molecular donor–acceptor charge-transfer complexes with organic electron donors based on tetrachalcogenfulvalenes. The majority of these electron-donor compounds are capable of forming radical cation salts with metallic and superconducting properties [4]. In our earlier works [5–8], we synthesized and investigated C_{60} molecular complexes with symmetric and nonsymmetric tetrachalcogenfulvalenes. The purpose of the present work was to synthesize a C_{60} complex with an organic donor, namely, bis(methylenedithio)tetrathiafulvalene, and to investigate the crystal structure, IR spectra, and the electrical conductivity of the complex synthesized.

2. SAMPLE PREPARATION AND EXPERIMENTAL TECHNIQUE

Single crystals of (*BMDT–TTF*) · C_{60} · $2CS_2$ (**I**) were prepared from a carbon disulfide (CS_2) solution containing *BMDT–TTF* and C_{60} in the 3 : 1 ratio. The solution was allowed to evaporate slowly at room temperature for 5 days to a volume of 2 to 3 ml. The evaporation was accompanied by precipitation of black lustrous crystals in the form of oblong prisms. The crystals precipitated were filtered off, washed with alcohol, and dried under vacuum. The composition of the (*BMDT–TTF*) · C_{60} · $2CS_2$ complex was determined from the elemental analysis data.

For $C_{70}H_4S_{12}$, anal. calcd. (wt %): C, 68.40; H, 0.30; S, 31.30.

Found (wt %): C, 69.12; H, 0.30; S, 30.83.

The elemental composition is in close agreement with the x-ray diffraction data.

X-ray structure investigation was performed on a KM-4 KUMA DIFFRACTION automated four-circle diffractometer (CuK_α radiation, graphite monochromator, ω/2Θ scan mode). The x-ray diffraction experiments were carried out at room temperature. The main crystal data for **I** are as follows: $C_{70}H_4S_{12}$, M = 1229.45, monoclinic crystal system, a = 13.550(5) Å, b = 9.964(7) Å, c = 17.125(8) Å, β = 99.52(4)°, V = 2280(2) Å^3, space group $P2_1/m$, Z = 2, and calculated density d_{calcd} = 1.791 mg/m^3.

3. RESULTS AND DISCUSSION

Crystals of complex **I** have a layered structure (Fig. 1): layers consisting of fullerene molecules alternate with layers composed of *BMDT–TTF* donor molecules. Molecules of the CS_2 solvent are sandwiched

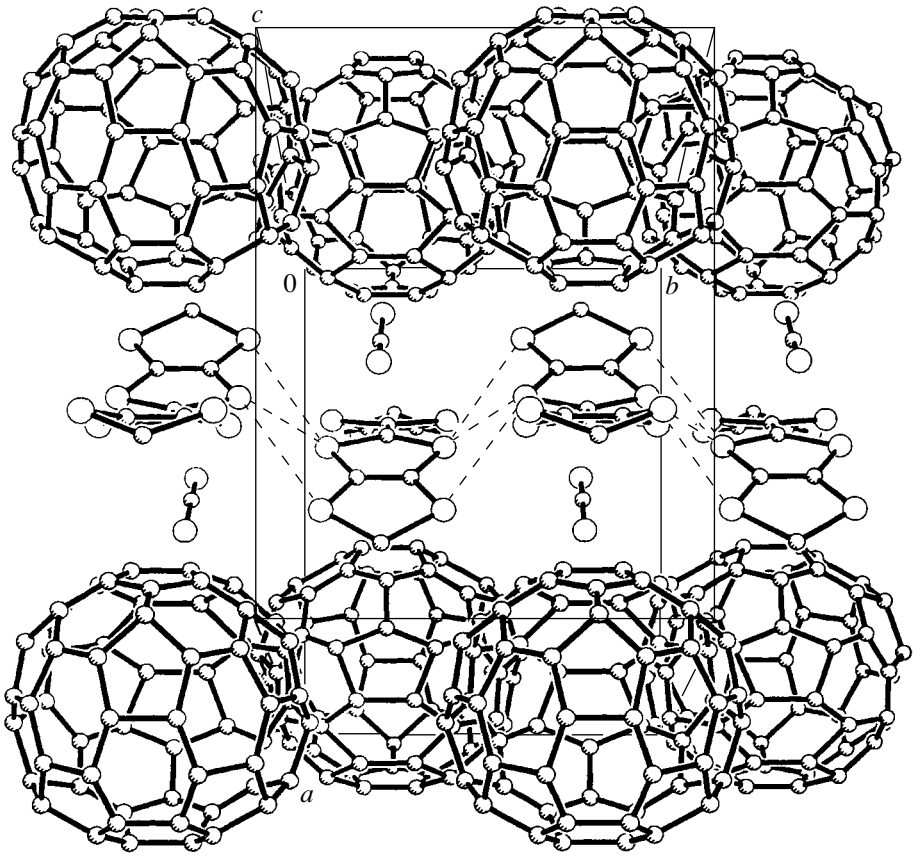

Fig. 1. A fragment of the crystal structure of the (*BMDT–TTF*) · C_{60} · $2CS_2$ complex.

between the donor molecules. In the structure of complex **I**, the mirror plane *m* passes through the centers of the fullerene molecules and along the central C=C bonds involved in the *BMDT–TTF* molecules. Two independent molecules CS_2 are located in the *m* plane. The *BMDT–TTF* donor molecules arranged in layers are linked through the shortest S…S contacts in a side-by-side manner [3.283(3) and 3.519(3) Å]. The standard van der Waals distances for sulfur atoms are equal to 3.68 Å [9]. Similar contacts are usually observed in crystal structures of quasi-two-dimensional molecular conductors based on radical cation salts of organosulfur donors [1]. In C_{60} fullerene complexes, the polarization van der Waals forces play a significant role (the polarizability of the C_{60} fullerene is equal to 85 $Å^3$). The energy of electrostatic interaction depends on the distance between the donor and acceptor molecules, and the electrostatic interaction itself is primarily determined by the dispersion component. In order to provide the strongest interaction, the donor molecule should approach the fullerene molecule as closely as possible, thus matching its own shape with the spherical shape of the fullerene molecule. This can be achieved only through geometric distortions of the donor molecule, as is the case in complex **I**. Unlike the neutral *BMDT–TTF* molecule, which is characterized by a planar geometry, the donor molecule exhibits a nonplanar conformation in the structure of complex **I** due to the interaction between C_{60} and *BMDT–TTF*. In the structure of the (*BMDT–TTF*) · C_{60} · $2CS_2$ complex, the C_{60} and *BMDT–TTF* molecules are linked by the shortest intermolecular contacts S…C [3.47(2) Å] and C…C [3.34(2) and 3.35(2) Å]. Consequently, upon complex formation, the donor molecule adopts a new conformation in which the donor and fullerene molecules are spaced as closely as possible.

Earlier [7, 10], it was shown that the force coupling constants depend on the electron density of the molecule and that the degree of charge transfer to the C_{60} molecule can be determined from the IR spectra: the charge transfer correlates with the linear shift of the C_{60} fundamental vibrational mode (1429 cm^{-1}). The IR spectra of the (*BMDT–TTF*) · C_{60} · $2CS_2$ complex, the *BMDT–TTF* molecule, and pure C_{60} fullerene are displayed in Figs. 2a–2c, respectively. The IR spectrum of the studied compound contains all the absorption bands associated with atomic vibrations of C_{60}, *BMDT–TTF*, and CS_2. Some absorption bands in the IR spectrum of complex **I** are shifted with respect to their location in

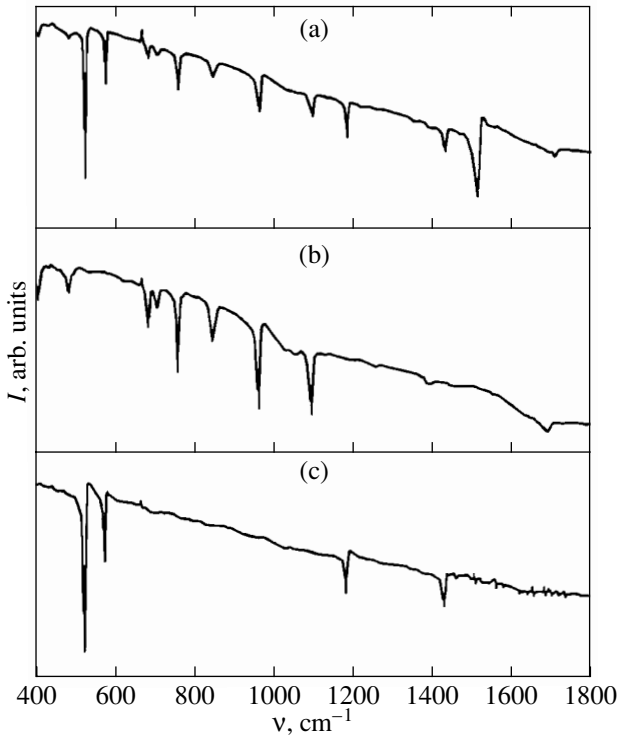

Fig. 2. IR spectra of the (a) (*BMDT–TTF*) · C_{60} · $2CS_2$ complex, (b) *BMDT–TTF* molecule, and (c) C_{60} fullerene at room temperature (Specord IR-75 spectrophotometer, KBr tablets).

the spectra of the initial donor and acceptor molecules by 1 to 2 cm^{-1}. Analysis of the IR spectra of complex **I** revealed that the *BMDT–TTF* molecules form a weak complex with the C_{60} fullerene in which the charge transfer between the donor and acceptor molecules is absent (or is insignificant). The molecular nature of the (*BMDT–TTF*) · C_{60} · $2CS_2$ complex is confirmed by the electrical conductivity measurements with single-crystal samples of (*BMDT–TTF*) · C_{60} · $2CS_2$. The low electrical conductivity ($\sigma_{RT} = 2 \times 10^{-5}\ \Omega^{-1}\ cm^{-1}$) indicates a weak charge transfer in the studied compound.

ACKNOWLEDGMENTS

This work was supported by the Russian Foundation for Basic Research, project no. 02-03-33218.

REFERENCES

1. J. M. Williams, J. R. Ferraro, R. J. Thorn, K. D. Carlson, U. Geiser, H. H. Wang, A. M. Kini, and M.-H. Whangbo, *Organic Superconductors (Including Fullerenes): Synthesis. Structure. Properties, and Theory* (Prentice-Hall, Englewood Cliffs, 1992).
2. A. Izuoka, T. Tachikawa, T. Sugawara, *et al.*, J. Chem. Soc., Chem. Commun., 1472 (1992).
3. N. G. Spitsina, V. N. Semkin, and A. Graja, Acta. Phys. Pol. **84**, 869 (1995).
4. Yu. M. Shul'ga, V. I. Rubtsov, and N. G. Spitsina, Zh. Fiz. Khim. **70**, 564 (1996).
5. S. V. Konovalikhin, O. A. D'yachenko, G. V. Shilov, *et al.*, Izv. Akad. Nauk, Ser. Khim., No. 8, 1480 (1997).
6. S. V. Konovalikhin, O. A. Dyachenko, G. V. Shilov, *et al.*, Fullerene Sci. Technol. **6**, 563 (1998).
7. K. P. Meletov, V. K. Dolganov, N. G. Spitsina, *et al.*, Chem. Phys. Lett. **281**, 360 (1997).
8. N. G. Spitsyna, S. V. Konovalikhin, A. S. Lobach, *et al.*, Izv. Akad. Nauk, Ser. Khim., 2298 (1999).
9. Yu. V. Zefirov, Kristallografiya **42** (5), 936 (1997) [Crystallogr. Rep. **42**, 865 (1997)].
10. V. N. Semkin, N. G. Spitsina, S. Krol, and A. Graja, Chem. Phys. Lett. **256**, 616 (1996).

Translated by O. Borovik-Romanova

Physics of the Solid State, Vol. 44, No. 3, 2002, pp. 534–535. From Fizika Tverdogo Tela, Vol. 44, No. 3, 2002, pp. 511–512.

PROCEEDINGS OF THE V INTERNATIONAL WORKSHOP "FULLERENES AND ATOMIC CLUSTERS"

(St. Petersburg, Russia, July 2–6, 2001)

Isomeric $C_{60}F_{36}$(g) Species: Computed Structures and Heats of Formation[1]

Z. Slanina*, F. Uhlík, O. V. Boltalina***, and V. P. Kolesov*****

** Institute of Chemistry, Academia Sinica, Nankang, Taipei, 11529 Taiwan-R.O.C.*
e-mail: zdenek@chem.sinica.edu.tw
*** Department of Physical and Macromolecular Chemistry, Charles University, Prague, 12843 Czech Republic*
**** Chemistry Department, Moscow State University, Vorob'evy gory, Moscow, 119899 Russia*

Abstract—The recently measured heat of formation ΔH_f^o of $C_{60}F_{36}$(g) is submitted for extensive computational treatment. The computations are performed at the AM1, PM3 and SAM1 semiempirical quantum-chemical levels on a set of selected isomers, especially those of *T*, C_3, and D_{3d} symmetries. The SAM1 method produces somewhat lower values than PM3 and, in particular, AM1 (as is the case for pristine fullerenes). For example, the SAM1 computed value for the *T* isomer is –1293 kcal/mol; i.e., it is within the experimental error. However, the issue of isomerism should also be taken into consideration accordingly and related kinetic aspects should be checked using computations. Even without these two additional steps being carried out, the agreement between the observed and computed values is encouraging. *© 2002 MAIK "Nauka/Interperiodica".*

At the present time, there are only four neutral fullerenic species with measured [1–6] heats of formation ΔH_f^o: C_{60}, C_{70}, $C_{60}F_{48}$, and, most recently [7], $C_{60}F_{36}$. The thermochemical data for fullerenes are relatively meager owing to an usually small quantity of available samples. Some thermochemical information can also be derived for charged gas-phase species [8] using the Knudsen cell mass spectrometry method. $C_{60}F_{36}$ has been rather well characterized experimentally, as ^{19}F NMR spectra of its two isomers, *T* and C_3, are available [9] (the *T* to C_3 isomeric ratio is about 1 : 3). Clearly enough, the thermochemical measurements [7] on $C_{60}F_{36}$ represent an important addition to the data on fullerenes (in the gaseous state at room temperature, the experimental value reads $\Delta H_{f,298}^o = -1248 \pm 48$ kcal/mol). In order to verify the reliability of the computational tools, the heat of formation $\Delta H_{f,298}^o$ is computed in this paper by means of semiempirical methods of quantum chemistry for several selected isomers of $C_{60}F_{36}$(g).

1. COMPUTATIONS

The full geometry optimizations were performed using three key semiempirical methods that generally produce quantitative values of heats of formation: AM1 [10], PM3 [11], and SAM1 [12]. The SAM1 (semi-*ab initio* model 1) method is the newest semiempirical quantum-chemical procedure; it was constructed [12] in order to fix some deficiencies of previous approximations. The computations were carried out primarily with the SPARTAN [13] and AMPAC [14] program packages. The geometry optimizations were performed with no symmetry constraints on the Cartesian coordinates and with an analytically constructed energy gradient.

The full geometry optimizations were followed by a harmonic vibrational analysis in each of the three methods. The harmonic vibrational analysis was carried out by numerical differentiation of the analytical energy gradient. The computed vibrational eigenvalues were analyzed for the presence of an imaginary frequency so that local minima and possible saddle points could be distinguished. Special attention was paid to evaluating the symmetries of the relaxed structures. The symmetry of the optimized structures was determined not only following the AMPAC built-in procedure [14] but primarily using a new flexible technique [15].

2. RESULTS AND DISCUSSION

We computed a set of isomers of $C_{60}F_{36}$ with higher symmetries [16], such as *T*, D_{3d}, T_h, C_3, and C_{2v}. However, in this report, we present results only for four isomers found as the lowest energy structures in a preliminary search using the PM3 method: *T*, D_{3d}, T_h, and C_3.

The *T* isomer is the lowest energy structure in all the three semiempirical methods applied (see table). In fact, the order of isomers is the same in the AM1 and PM3 methods but differs in the SAM1 method. It is known [17–19] that the AM1 method overestimates the heats of formation for the pristine species more greatly

[1] This article was submitted by the authors in English.

The AM1, PM3, and SAM1 heats of formation $\Delta H^o_{f,298}$ for selected $C_{60}F_{36}$ isomers

Species	$\Delta H^o_{f,298}$, kcal/mol		
	AM1	PM3	SAM1
C_3	–889.68	–1079.52	–1228.94
T_h	–898.03	–1086.39	–1175.95
D_{3d}	–924.32	–1112.69	–1226.79
T	–952.76	–1134.27	–1292.97

Note: Gas phase species throughout; the standard state is an ideal gas phase at 1 atm = 101325 Pa.

than the PM3 method does. The data presented in the table suggest that this is also likely to remain true for fullerene fluoro-derivatives. On the other hand, the $\Delta H^o_{f,298}$ terms given by the SAM1 method are actually closer [18, 19] to the observed values for the pristine fullerenes than those given by the PM3 treatment. It is also seen from the table for $C_{60}F_{36}$ that the SAM1 $\Delta H^o_{f,298}$ values basically coincide with the observed value [7] of –1248 kcal/mol (if considered within its error bars of ±48 kcal/mol). It should be noted that it is difficult to compute the total heats of formation *ab initio* unless some empirical terms are introduced. On the other hand, the separation energies between isomers can be computed by both semiempirical and nonempirical methods. The separation energies given by both treatments usually agree well.

There is, however, a substantial qualitative difference. It is seen from the table that the SAM1 order of structures is not exactly the same as those found from the AM1 and PM3 methods. Once again, SAM1 more adequately describes the observed facts [7, 9], as the structures seen in the experiment are of C_3 and T symmetries. In fact, two C_3 species are considered in [9] because there is no direct way to distinguish between these two C_3 isomers with the presently available data. According to the SAM1 calculations, the C_3 species selected in [9] is the next-lowest energy structure.

However, there is one problem with the SAM1 results: the ratio of the C_3 and T isomers is observed [9] to be about 3 : 1. Hence, it is important to perform a numerical evaluation of the entropy effects according to statistical-mechanical treatment [20] based on quantum-chemical computations. It is known for isomeric higher fullerenes [21] that the most abundant species is not necessarily the lowest energy structure. This interesting fact is a consequence of the entropy effects at higher temperatures. $C_{60}F_{36}$ is indeed prepared [9] at temperatures around 350°C.

Overall, the reported quantum-chemical semiempirical computations point to the SAM1 method as the best applicable treatment able to reproduce the experimental thermochemical data [7]. The final conclusion should be further supported by entropy evaluations and also by some *ab initio* calculations or even by kinetic evaluations, these being topics of advanced research currently in progress.

ACKNOWLEDGMENTS

The authors thank the National Center for High-Performance Computing in Hsinchu, Taiwan, Republic of China, for computer time.

This study was supported by the National Science Council, Taiwan, Republic of China.

REFERENCES

1. H. D. Beckhaus, C. Ruchardt, M. Kao, *et al.*, Angew. Chem. Int. Ed. Eng. **31**, 63 (1992).
2. W. V. Steele, R. D. Chirico, N. K. Smith, *et al.*, J. Phys. Chem. **96**, 4731 (1992).
3. T. Kiyobayashi and M. Sakiyama, Fullerene Sci. Technol. **1**, 269 (1993).
4. H. P. Diogo, M. E. Minas da Pielade, T. J. S. Dennis, *et al.*, J. Chem. Soc., Faraday Trans. **89**, 3541 (1993).
5. H.-D. Beckhaus, S. Verevkin, C. Rüchardt, *et al.*, Angew. Chem. Int. Ed. Engl. **33**, 996 (1994).
6. T. S. Papina, V. P. Kolesov, V. A. Lukyanova, *et al.*, J. Chem. Thermodyn. **31**, 1321 (1999).
7. T. S. Papina, V. P. Kolesov, V. P. Lukyanova, *et al.*, J. Phys. Chem. B **104**, 5403 (2000).
8. O. V. Boltalina, E. V. Dashkova, and L. N. Sidorov, Chem. Phys. Lett. **256**, 253 (1996).
9. O. V. Boltalina, J. M. Street, and R. Taylor, J. Chem. Soc., Perkin Trans., No. 2, 649 (1998).
10. M. J. S. Dewar, E. G. Zoebisch, E. F. Healy, and J. J. P. Stewart, J. Am. Chem. Soc. **107**, 3902 (1985).
11. J. J. P. Stewart, J. Comput. Chem. **10**, 209 (1989).
12. M. J. S. Dewar, C. Jie, and J. Yu, Tetrahedron **49**, 5003 (1993).
13. W. J. Hehre, L. D. Burke, and A. J. Schusterman, *SPARTAN, Release 3.1.8* (Wavefunction Inc., Irvine, 1993).
14. *AMPAC 6.0* (Semichem, Shavnee, 1997).
15. M.-L. Sun, Z. Slanina, S.-L. Lee, *et al.*, Chem. Phys. Lett. **246**, 66 (1995).
16. B. W. Clare and D. L. Kepert, J. Mol. Struct.: THEOCHEM **315**, 71 (1994).
17. J. M. Rudziński, Z. Slanina, M. Togasi, *et al.*, Thermochim. Acta **125**, 155 (1988).
18. Z. Slanina, S.-L. Lee, and C.-H. Yu, Rev. Comput. Chem. **8**, 1 (1996).
19. Z. Slanina, X. Zhao, N. Kurita, *et al.*, J. Mol. Graph. Model. **19**, 216 (2001).
20. Z. Slanina, Int. Rev. Phys. Chem. **6**, 251 (1987).
21. Z. Slanina, X. Zhao, and E. Ōsawa, Adv. Strained Interest. Org. Mol. **7**, 185 (1999).

Physics of the Solid State, Vol. 44, No. 3, 2002, pp. 536–538. Translated from Fizika Tverdogo Tela, Vol. 44, No. 3, 2002, pp. 513–515.

PROCEEDINGS OF THE V INTERNATIONAL WORKSHOP "FULLERENES AND ATOMIC CLUSTERS"

(St. Petersburg, Russia, July 2–6, 2001)

A Study of $C_{60}F_{48}$ Solvates with Alkanes by Differential Scanning Calorimetry

Yu. A. Makeev, P. A. Troshin, O. V. Boltalina, M. A. Kirikova, and N. V. Chelovskaya

Moscow State University, Vorob'evy gory, Moscow, 119899 Russia
e-mail: yves@online.debryansk.ru

Abstract—The behavior of the $C_{60}F_{48}$ fluorofullerene—a compound with maximum fluorine content that can be synthesized in pure form through direct fluorination—is investigated in alkane solutions. The kinetics of formation of $C_{60}F_{48}$ crystal solvates at solid-phase equilibrium with a saturated solution is studied by differential scanning calorimetry (DSC) and thermogravimetry. The composition of the crystal solvates and the temperatures and enthalpies of their decomposition are determined. It is found that the $C_{60}F_{48}$ solvates formed upon crystallization from saturated solutions of pentane, hexane, and heptane are more stable than the hexagonal solvates (with octane, nonane, decane, and undecane). The latter solvates undergo decomposition into the initial fluorofullerene and liquid hydrocarbon at temperatures below the boiling points of the hydrocarbons. © *2002 MAIK "Nauka/Interperiodica".*

1. INTRODUCTION

Fluorofullerenes $C_{60}F_n$ (n = 12–48) were originally synthesized by Selig *et al.* [1] in 1990, shortly after Krätchmer *et al.* [2] had devised a procedure for synthesizing the C_{60} and C_{70} fullerenes in macroscopic amounts. Subsequent studies concerned with direct fluorination of [60]fullerenes under different conditions showed that, as a rule, this reaction results in the formation of a mixture of products. The first selective technique for producing fullerene fluoride was proposed by Gakh *et al.* [3]. Boltalina *et al.* [4] were the first to prepare a material with 68% $C_{60}F_{48}$ through two-stage synthesis involving the interaction of the C_{60} fullerene with fluorine in the presence of sodium fluoride at a temperature of 280°C. Recently, the $C_{60}F_{48}$ fluorofullerene was synthesized by direct fluorination of the [60]fullerene at 350°C.

It was found that the attachment of 48 fluorine atoms to the fullerene cage leads to a radical change in the properties of the fullerene compound [5, 6]. Fullerene fluorides possess pronounced electron-acceptor properties and, unlike alkyl fluorides, readily enter into nucleophilic substitution reactions. At the same time, [60]fullerene fluorides are highly soluble in a large number of organic solvents and, hence, can be used for producing numerous derivatives. Elucidation of the character of the interaction between fluorofullerene molecules and solvents is of importance in explaining S_N-type reactions.

Earlier [7], we synthesized solvates with *n*-alkanes and performed x-ray structure analysis of the new compounds. It was revealed that the $C_{60}F_{48}$ fluorofullerene forms orthorhombic isostructural solvates of 1 : 1 composition with pentane, hexane, and heptane. Moreover, the $C_{60}F_{48}$ fluorofullerene can form hexagonal crystal solvates with nonane, decane, and undecane.

In the present work, the kinetics of formation of $C_{60}F_{48}$ crystal solvates at solid-phase equilibrium with a saturated solution was investigated using differential scanning calorimetry (DSC) and thermogravimetry.

2. SAMPLE PREPARATION AND EXPERIMENTAL TECHNIQUE

2.1. We used a fluorofullerene sample of composition $C_{60}F_{48\pm1}$. This sample also contained $C_{60}F_{44}$, $C_{60}F_{46}$, and $C_{60}F_{48}O$ impurities in insignificant amounts. The content of the main compound in the sample was no less than 95%.

The $C_{60}F_{48}$ fluorofullerene is a white finely crystalline compound stable in air. No special caution should be exercised in handling this material.

The crystal solvates were prepared according to two procedures: (1) crystallization from saturated solutions and (2) treatment of crystalline fullerene fluoride in liquid alkanes. In the latter case, fullerene fluoride partially dissolved and the undissolved part gradually transformed into the corresponding solvate. The temperatures and enthalpies of decomposition of crystal solvates were determined by statistical methods.

The $C_{60}F_{48}$ complexes with octane, nonane, decane, and undecane undergo decomposition at temperatures below the boiling points of the hydrocarbons involved. This allowed us to use the DSC technique to examine their incongruent melting. The experiments were performed as follows. A weighed portion of $C_{60}F_{48}$ (7–

1063-7834/02/4403-0536$22.00 © 2002 MAIK "Nauka/Interperiodica"

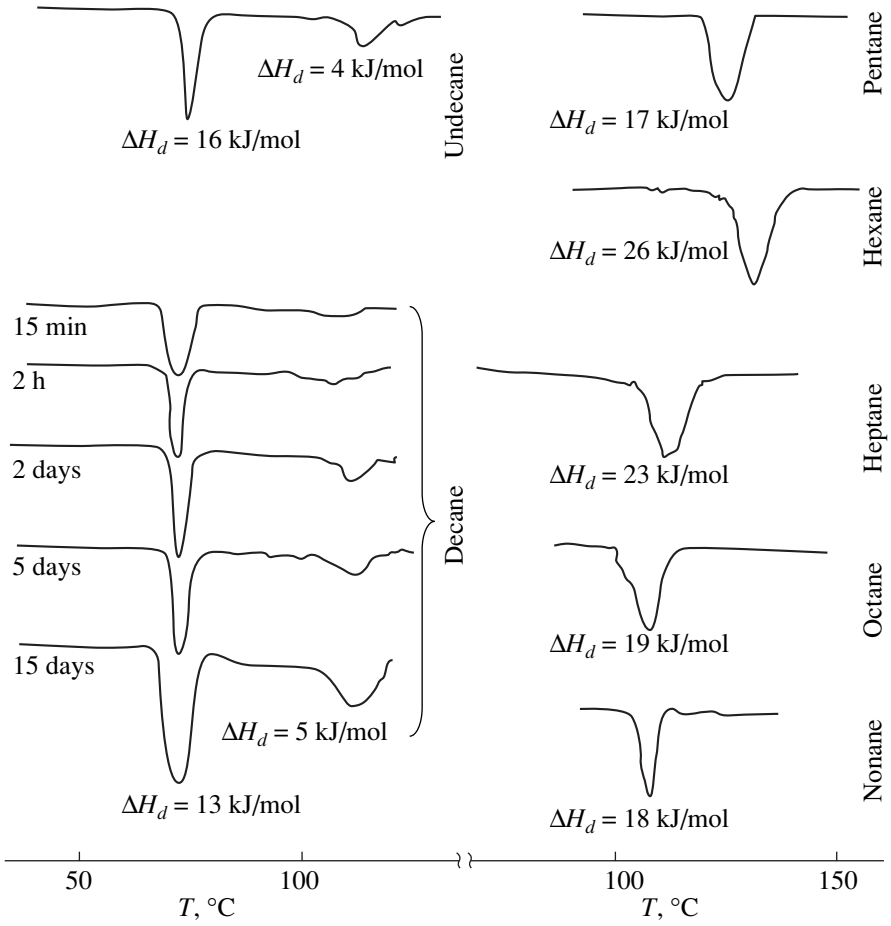

DSC curves for decomposition of $C_{60}F_{48}$ crystal solvates with alkanes upon heating.

12 mg) was placed in a DSC cell filled with a small amount of a solvent (5–8 mg). Then, the cell was covered and allowed to stand at room temperature. The calorimetric measurements were performed repeatedly for 20 days until the enthalpy ceased to change.

2.2. The crystal solvates under investigation were heated at a rate of 5 K/min in an argon atmosphere to the point of decomposition into $C_{60}F_{48}$ and hydrocarbon. The solvate composition was judged from the decrease in weight. The measurements were carried out on Mettler TA3000 and TG-50 instruments.

2.3. The decomposition of crystal solvates was examined using a Mettler TA3000 instrument with a DSC-20 attachment. The samples to be analyzed were placed in an aluminum cell, which was then nonhermetically sealed. The experiments were performed at a heating rate of 5 K/min in an argon atmosphere in the temperature range from 25 to 250°C.

The appearance of absorption peaks in the DSC curves was treated as an indication of the decomposition of crystal solvates into $C_{60}F_{48}$ and hydrocarbon. The same inferences regarding the decomposition of these solvates were made from the weight loss observed in thermogravimetric measurements.

3. RESULTS AND DISCUSSION

The molecular complexes studied in this work can be divided into three groups: (1) *n*-pentane, *n*-hexane, and *n*-heptane isostructural solvates crystallizing in an orthorhombic crystal system; (2) *n*-octane solvate crystallizing in a cubic crystal system; and (3) *n*-nonane, *n*-decane, and *n*-undecane solvates crystallizing in a hexagonal crystal system (see table).

Moreover, we analyzed the kinetics of solvation at equilibrium with saturated solutions. Using the above technique, we observed incongruent melting in the $C_{60}F_{48}$–octane and $C_{60}F_{48}$–nonane systems at temperatures of 109 and 106°C, respectively. On this basis, the inference was made that the $C_{60}F_{48}$ crystal solvate with octane should exhibit a hexagonal packing similar to that of the $C_{60}F_{48} \cdot 2$(nonane) crystal solvate. It is worth noting that, in this case, no additional effects are found at temperatures higher than the boiling points of the solvents used and the elimination of incorporated hydro-

Unit cell parameters and decomposition conditions for $C_{60}F_{48}$ solvates

Solvate	Packing	Unit cell parameters, nm	Scheme of decomposition	Decomposition temperature, °C
$C_{60}F_{48} \cdot C_5H_{12}$	Orthorhombic	a = 5.925(3), b = 1.215(1), c = 1.1987(4)	$C_{60}F_{48} \cdot C_5H_{12} \longrightarrow C_{60}F_{48(s)} + C_5H_{12(g)}$	127.6
$C_{60}F_{48} \cdot C_6H_{14}$	Orthorhombic	a = 3.876(4), b = 1.229(6), c = 1.198(1)	$C_{60}F_{48} \cdot C_6H_{14} \longrightarrow C_{60}F_{48(s)} + C_6H_{14(g)}$	131.4
$C_{60}F_{48} \cdot C_7H_{16}$	Orthorhombic	a = 3.895(3), b = 1.228(1), c = 1.197(4)	$C_{60}F_{48} \cdot C_7H_{16} \longrightarrow C_{60}F_{48(s)} + C_7H_{16(g)}$	111.3
$C_{60}F_{48} \cdot 2C_8H_{18}^*$	Hexagonal 1**	–	$C_{60}F_{48} \cdot nC_8H_{18} \longrightarrow C_{60}F_{48(s)} + nC_8H_{18(l)}$	109
$C_{60}F_{48} \cdot 2C_9H_{20}$	Hexagonal 1	a = 2.362(3), b = 2.129(3)	$C_{60}F_{48} \cdot 2C_9H_{20} \longrightarrow C_{60}F_{48(s)} + 2C_9H_{20(l)}$	106
$C_{60}F_{48} \cdot 2C_{10}H_{22}$	Hexagonal 2**	a = 2.0924(5), c = 1.1991(6)	$C_{60}F_{48} \cdot 2C_{10}H_{22} \longrightarrow C_{60}F_{48} \cdot C_{10}H_{22(s)} + C_{10}H_{22(l)}$	70.7
$C_{60}F_{48} \cdot C_{10}H_{22}$	Amorphous		$C_{60}F_{48} \cdot C_{10}H_{22} \longrightarrow C_{60}F_{48(s)} + C_{10}H_{22(l)}$	73.6
$C_{60}F_{48} \cdot 2C_{11}H_{24}$	Hexagonal 2	a = 2.0954(5), c = 1.2063(3)	$C_{60}F_{48} \cdot 2C_{11}H_{24} \longrightarrow C_{60}F_{48} \cdot C_{11}H_{24(s)} + C_{11}H_{24(l)}$	107
$C_{60}F_{48} \cdot C_{11}H_{24}$	Amorphous		$C_{60}F_{48} \cdot C_{11}H_{24} \longrightarrow C_{60}F_{48(s)} + C_{11}H_{24(l)}$	107

*The composition and structure of the crystal solvate with octane are assumed by analogy with the $C_{60}F_{48} \cdot 2C_9H_{20}$ solvate.

**Designations: hexagonal 1 is the packing in $C_{60}F_{48} \cdot 2C_9H_{20}$, and hexagonal 2 is the packing in $C_{60}F_{48} \cdot 2C_nH_{2n+2}$ (n = 10, 11).

carbon molecules proceeds in one stage. By contrast, the 1 : 2 crystal solvates with decane and undecane decompose in two stages. It can be concluded that the transformations observed in the crystal structure when changing over from $C_{60}F_{48} \cdot 2$(nonane) to $C_{60}F_{48} \cdot 2$(decane) and $C_{60}F_{48} \cdot 2$(undecane) lead to a regular decrease in the decomposition temperature of the crystal solvates under investigation (see figure).

4. CONCLUSION

The experimental results demonstrated that the orthorhombic solvates described earlier are formed upon crystallization from saturated solutions. These solvates are relatively stable in air and undergo decomposition at temperatures above the boiling points of the corresponding hydrocarbons. The hexagonal solvates are less stable and decompose at temperatures below the boiling points of the hydrocarbons involved. In this case, the structure is formed through the gradual incorporation of alkane molecules into the $C_{60}F_{48}$ lattice, thus changing the crystal lattice parameters.

No interrelation between the enthalpies of decomposition and the lattice parameters was revealed.

REFERENCES

1. H. Selig, C. Lifshitz, T. Peres, *et al.*, J. Am. Chem. Soc. **113**, 5475 (1991).
2. W. Krätchmer, L. D. Lamd, K. Fostiropoulos, and D. R. Huffman, Nature **347**, 354 (1990).
3. A. A. Gakh, A. A. Tuinman, J. L. Adcock, and R. N. Compton, Tetrahedron Lett. **34**, 7167 (1993).
4. O. V. Boltalina, L. N. Sidorov, V. F. Bagryantsev, *et al.*, J. Chem. Soc., Perkin Trans. 2, 2275 (1996).
5. O. V. Boltalina, V. Y. Markov, R. Taylor, and M. P. Waugh, Chem. Commun., No. 2, 2549 (1996).
6. O. V. Boltalina, J. M. Street, and R. Taylor, J. Chem. Soc., Perkin Trans. 2, 649 (1998).
7. P. A. Troshin, Y. A. Mackeyev, N. V. Chelovskaya, *et al.*, Fullerene Sci. Technol. **8**, 501 (2000).

Translated by O. Borovik-Romanova

Physics of the Solid State, Vol. 44, No. 3, 2002, pp. 539–541. Translated from Fizika Tverdogo Tela, Vol. 44, No. 3, 2002, pp. 516–518.

PROCEEDINGS OF THE V INTERNATIONAL WORKSHOP "FULLERENES AND ATOMIC CLUSTERS"

(St. Petersburg, Russia, July 2–6, 2001)

Investigation of Fluorination Reactions of the $C_{60}Br_{24}$ Bromofullerene with Xenon Difluoride

N. I. Denisenko, A. V. Streletskiĭ, and O. V. Boltalina

Moscow State University, Vorob'evy gory, Moscow, 119899 Russia
e-mail: Nadya00@ru.ru

Abstract—The products of the reaction between the $C_{60}Br_{24}$ bromofullerene and xenon difluoride are studied by IR spectroscopy, laser desorption mass spectrometry, ^{19}F NMR spectroscopy, and thermogravimetry. It is revealed that the degree of fluorination of the substrate is primarily determined by the duration of contact between the reactants. An attempt is made to perform nucleophilic substitution of fluorine for bromine in the $C_{60}Br_{24}$ bromofullerene in a solution with potassium fluoride. © *2002 MAIK "Nauka/Interperiodica"*.

1. INTRODUCTION

To date, different procedures have been developed for the selective synthesis of fluorofullerene compounds with a high fluorine content, for example, $C_{60}F_{18}$ [1], $C_{60}F_{36}$ [2], and $C_{60}F_{48}$ [3]. Of special interest are fluorofullerenes with a low fluorine content, because these compounds can be used as precursors for regioselective synthesis of fullerene derivatives.

In particular, fluorofullerenes with a low fluorine content can be synthesized by the fluorination of bromofullerenes or chlorofullerenes. It is known that halogen atoms can fulfill the function of blocking agents that prevent the formation of reaction products with a high fluorine content. Therefore, the fluorination reactions involving bromofullerenes or chlorofullerenes followed by heating should lead to the detachment of bromine or chlorine atoms with the formation of the ultimate fluorofullerene products characterized by a low fluorine content. Adamson *et al.* [4] were the first to use this approach. These authors examined the products of fluorination reactions between molecular fluorine and a number of bromofullerene and chlorofullerene derivatives, such as $C_{60}Br_6$, $C_{60}Br_8$, $C_{60}Br_{24}$, and $C_{60}Cl_{24}$. It was shown that the fluorination reaction of the $C_{60}Br_{24}$ bromofullerene with molecular fluorine at room temperature results in the formation of a mixture of $C_{60}F_n$ fluorofullerenes ($n \le 44$), which predominantly contains $C_{60}F_{36}$. Fluorination of the $C_{60}Br_6$ bromofullerene produces a mixture of $C_{60}F_n$ fluorides ($n < 36$). In this case, the mass spectrum of the reaction product exhibits peaks associated with ions of the $C_{60}F_{18}$ fluorofullerene and its monoxide and dioxide compounds.

According to Dementjev *et al.* [5], the $C_{60}Br_{24}$ bromofullerene reacts with xenon difluoride in anhydrous HF to form a product of the composition $C_{60}F_{24}$, as judged from the x-ray photoelectron spectroscopic data. The product of fluorination with the use of BrF_5 under the same conditions was identified as $C_{60}Br_4F_{20}$ [6].

In the present work, we investigated the solid-phase reactions of the $C_{60}Br_{24}$ bromofullerene with xenon difluoride over a wide range of temperatures. The reaction products were characterized using IR spectroscopy and laser desorption mass spectrometry.

2. SAMPLES AND EXPERIMENTAL TECHNIQUE

The $C_{60}Br_{24}$ bromofullerene was prepared according to the procedure described in [7]. The reaction of the $C_{60}Br_{24}$ bromofullerene with xenon difluoride was performed as follows. A weighed portion of the bromofullerene was mixed with a specified amount of xenon difluoride. The resulting mixture was placed in a copper cell cleaned from oxides, and the cell was sealed. Then, the cell was allowed to stand at a constant temperature (80–140°C) for a time (from one to three hours) and, after complete cooling, was opened. The color of the samples prepared varied from brown to light yellow.

The reaction temperature was chosen in such a way as to preclude thermal decomposition of bromofullerenes in the course of synthesis. The conditions for

Conditions for fluorination reactions of the $C_{60}Br_{24}$ bromofullerene with xenon difluoride

No.	T, °C	t, h	$C_{60}F_n$, n_{max}
a	220	1	22–24
b	80	1	30–32
c	80	3	36

1063-7834/02/4403-0539$22.00 © 2002 MAIK "Nauka/Interperiodica"

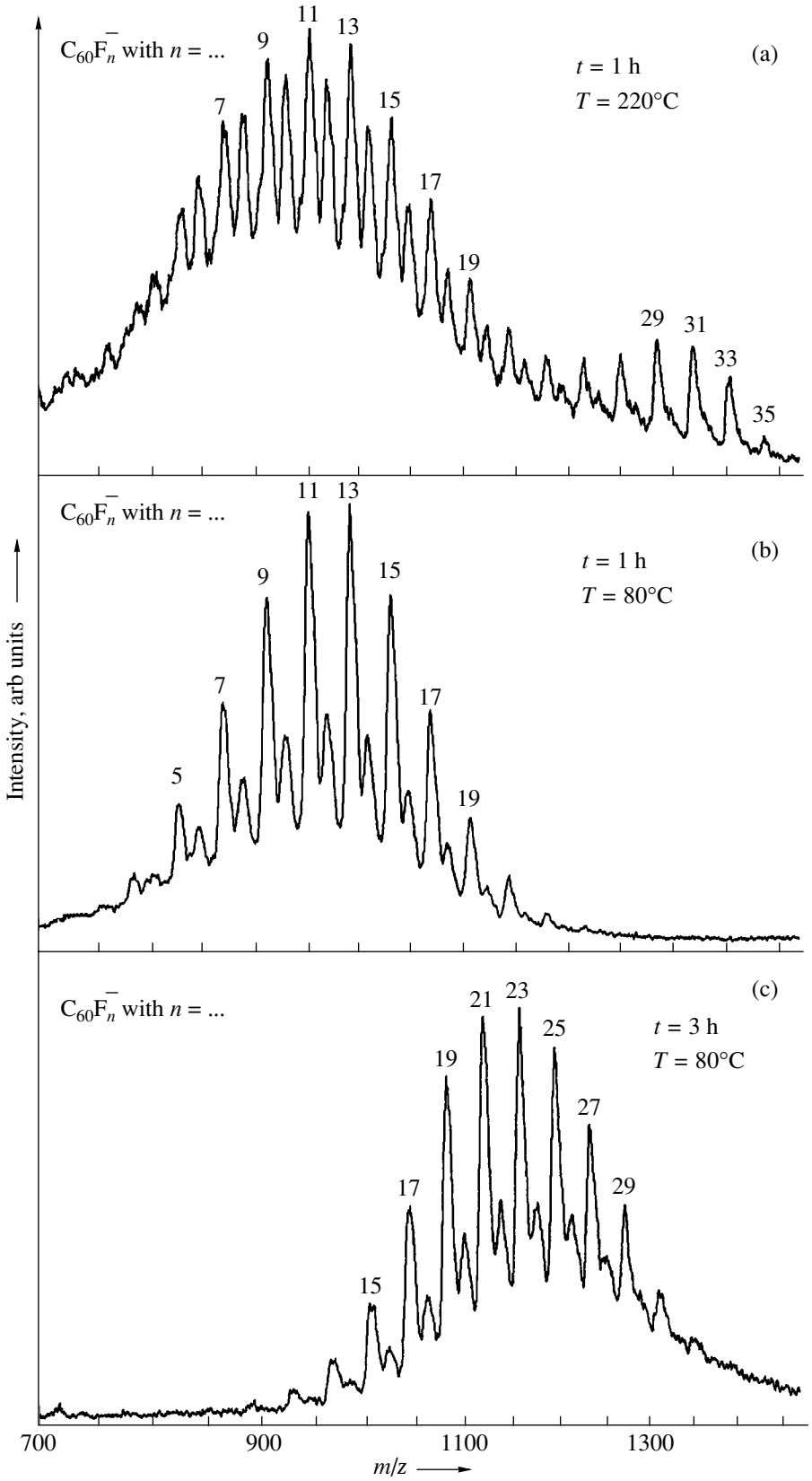

Fig. 1. Laser desorption–ionization mass spectra of the products of fluorination reactions of the $C_{60}Br_{24}$ bromofullerene with xenon difluoride.

fluorination reactions of the $C_{60}Br_{24}$ bromofullerene with xenon difluoride are given in the table.

The degree of fluorination was determined by laser desorption–ionization mass spectrometry. The mass spectra were recorded on a Vision 2000 time-of-flight mass spectrometer (Finnigan) with the use of a nitrogen laser (wavelength, 337 nm; pulse duration, 3 ns). The samples were dissolved in toluene so that their concentration ranged from 10 to 50 mM. A 0.2- to 0.4-μl drop of the solution was applied to a target. After evaporation of the solvent at room temperature, the target was inserted into the mass spectrometer. The mass spectra were measured in a reflectron mode. For the purpose of suppressing the possible fragmentation, the laser beam power was chosen so as to correspond to the threshold of ion formation.

3. RESULTS AND DISCUSSION

3.1. Fluorination of $C_{60}Br_{24}$. The fluorination of the $C_{60}Br_{24}$ bromofullerene was performed under two different temperature conditions. In the first series of experiments, the synthesis temperature was below the decomposition point of the bromofullerene (160–170°C). In the second series, the samples were prepared by fluorination for 1 h at a temperature slightly higher than the decomposition point of $C_{60}Br_{24}$ (220°C). As follows from the distribution of negative ions in the laser desorption–ionization mass spectrum of the sample from the second series (Fig. 1a), the sample contains two types of products involving up to 20 fluorine atoms (the mass falls in the range 815–1100 *m*/*z*) and a product involving up to 36 fluorine atoms (with a mass as large as 1404 *m*/*z*). The fluorination reaction performed at a lower temperature (80°C) for the same time leads to the formation of $C_{60}F_n$ fluorofullerenes with $n \leq 18$. In this case, the negative ion distribution indicates the predominance of the $C_{60}F_{18}$ stable fluorofullerene, which, as a rule, is produced in reactions with metal fluorides [1] (Fig. 1b). An increase in the synthesis time brings about a considerable change in the product composition: the reaction proceeding for three hours at a temperature of 80°C results in the formation of $C_{60}F_n$ fluorofullerenes with $n \leq 30$ in which the maximum fluorine content does not exceed 32 atoms (the mass falls in the range 967–1309 *m*/*z*) (Fig. 1c).

3.2. Thermal stability of the compounds synthesized. The thermogravimetric analysis of the products obtained in the fluorination reaction of the bromofullerene with xenon difluoride revealed that the maximum weight loss of the samples is observed in the temperature range 300–500°C. It is worth noting that the thermal decomposition is accompanied by the formation of the C_{60} fullerene. This suggests that the thermal stability of the fluorine derivatives synthesized is rather low. It should also be noted that, upon heating, the fullerene fluorides studied earlier in [2, 3] sublimate without noticeable decomposition.

3.3. ^{19}F NMR spectroscopy. All the lines revealed in the ^{19}F NMR spectra of the products synthesized are substantially broadened and poorly resolved. For this reason, we failed to draw any conclusions regarding the composition and structure of these products and could only infer the presence of a mixture of compounds in the studied sample from the analysis of these spectra.

3.4. Nucleophilic substitution for bromine in bromofullerene. We attempted to prepare fluorofullerenes through the substitution of fluorine for bromine in the $C_{60}Br_{24}$ bromofullerene. In the course of synthesis, a solution of $C_{60}Br_{24}$ in carbon tetrachloride with an excess of potassium fluoride and a catalytic amount of 18-crown-6 was boiled for a few hours. The laser desorption–ionization mass spectrum of the sample thus synthesized exhibits the most intense signal associated with the $C_{60}F_{35}^-$ fluorofullerene. The IR spectrum of the product obtained by the reaction of the $C_{60}Br_{24}$ bromofullerene with potassium fluoride shows a broad band at 1114 cm^{-1}, which is attributed to vibrations of the C–F bonds. Note that the IR spectrum described earlier in [2] for the $C_{60}F_{36}$ fluorofullerene essentially differs from the IR spectrum recorded in the present work. It is quite possible that the reaction under investigation leads to the formation of an unstable product ($C_{60}F_{24}$). Upon thermal heating prior to the ionization and recording of the mass spectra, this product can undergo disproportionation with the formation of more stable compounds, namely, the $C_{60}F_{36}$ fluorofullerene and the C_{60} fullerene.

ACKNOWLEDGMENTS

This work was supported by the Russian Foundation for Basic Research, project nos. 00-03-32964a and 00-03-32703a.

REFERENCES

1. O. V. Boltalina, L. N. Sidorov, V. F. Bagryantsev, *et al.*, J. Chem. Soc., Perkin Trans. 2, 2275 (1996).
2. O. V. Boltalina, A. Y. Borshevskii, L. N. Sidorov, *et al.*, J. Chem. Soc., Chem. Commun., No. 4, 529 (1996).
3. O. V. Boltalina, V. Yu. Markov, R. Taylor, and M. P. Waugh, Chem. Commun., No. 2, 2551 (1996).
4. A. J. Adamson, J. H. Holloway, E. G. Hope, and R. Taylor, Fullerene Sci. Technol. **5** (4), 629 (1997).
5. A. P. Dementjev, V. N. Bezmelnitsin, A. V. Ryjkov, and V. N. Sokolov, in *Proceedings of the 12th European Symposium on Fluorine Chemistry, Berlin, 1998*, Abstract P-II.
6. N. F. Yudanov, A. V. Ocotrub, L. G. Bulusheva, *et al.*, Mol. Mater. **43** (1), 122 (1998).
7. F. N. Tebbe, R. L. Harlow, D. B. Chase, *et al.*, Science **256**, 822 (1993).

Translated by O. Borovik-Romanova

Physics of the Solid State, Vol. 44, No. 3, 2002, pp. 542–544. From Fizika Tverdogo Tela, Vol. 44, No. 3, 2002, pp. 519–521.

PROCEEDINGS OF THE V INTERNATIONAL WORKSHOP "FULLERENES AND ATOMIC CLUSTERS"

(St. Petersburg, Russia, July 2–6, 2001)

Phase Transitions in Hydrofullerene $C_{60}H_{36}$ Studied by Luminescence and Raman Spectroscopy at Pressures up to 12 GPa[1]

K. P. Meletov*, **, S. Assimopoulos*, G. A. Kourouklis*, and I. O. Bashkin**

** Physics Division, School of Technology, Aristotle University of Thessaloniki, Thessaloniki, GR-54006 Greece*

e-mail: mele@issp.ac.ru

*** Institute of Solid State Physics, Russian Academy of Sciences, Chernogolovka, Moscow oblast, 142432 Russia*

Abstract—The effect of hydrostatic pressure on the photoluminescence and Raman spectra of hydrofullerene $C_{60}H_{36}$ was investigated for pressures up to 12 GPa at room temperature. The samples were synthesized by means of high-pressure hydrogenation. The pressure coefficients of the phonon modes were found to be positive and demonstrate singularities at ~0.7 and ~6 GPa. The pressure shift of the luminescence spectrum is unusually small and increases slightly at $P \geq 6$ GPa. All observed features are reversible with pressure, and $C_{60}H_{36}$ is stable in the pressure region investigated. © *2002 MAIK "Nauka/Interperiodica".*

Hydrofullerenes have been predicted theoretically [1] and synthesized using various methods [2, 3]. The stable hydrofullerene $C_{60}H_{36}$ has been studied extensively to identify its molecular structure and properties [4, 5]. It was found that the $C_{60}H_{36}$ molecule has a great number of isomers and that the most stable of them have T_h, D_{3d}, S_6, and T symmetry. The presence of various isomers in $C_{60}H_{36}$ samples depends mostly on the preparation method [4, 6, 7]. The condensed phase of $C_{60}H_{36}$ has a body-centered cubic (bcc) structure [lattice constant 11.78(5) Å] which is expected to transform into a body-centered tetragonal (bct) structure at low temperatures [5]. In the present paper, we report data on the pressure behavior of Raman and photoluminescence spectra of $C_{60}H_{36}$ prepared by high-pressure hydrogenation. Our goal was to study the effect of high pressure on the energy spectrum, phase transitions, and stability of the $C_{60}H_{36}$ molecule.

1. EXPERIMENTAL

For the preparation of hydrofullerene, pellets of C_{60} (99.99% purity) were placed into a copper capsule, covered with a disc of 0.01-mm thick Pd foil, and then annealed in vacuum at 620 K. The remaining space was filled with AlH_3, and the capsule was tightly plugged with a copper lid using gallium as a soldering agent. Since Cu and Ga are highly impermeable to hydrogen, the encapsulation described prevents hydrogen losses effectively during treatment. The assembled capsule was pressurized to 3 GPa in a toroid-shaped cell and maintained at 700 K for a time of up to 48 h. Above 400 K, AlH_3 decomposes and the evolved hydrogen reacts with C_{60}. The mass-spectroscopy data show that at least 95% of the final material is related to $C_{60}H_{36}$, while the x-ray study shows that the material has a bcc structure with a lattice parameter of 11.83 Å. For optical study at high pressure, colorless transparent specimens of $C_{60}H_{36}$ were placed into a diamond anvil cell. Photoluminescence and Raman spectra were recorded using a single (JOBIN YVON THR-1000) and a triple (DILOR XY-500) monochromator, both equipped with a CCD liquid-nitrogen cooled detector system. The 676.4 and 457.9 nm lines of Kr^+ and Ar^+ laser radiation, respectively, were used for excitation of the Raman and luminescence spectra. The laser power was varied from 2 to 10 mW when measured directly in front of the cell. A 4 : 1 methanol-ethanol mixture was used as the pressure-transmitting medium, and the ruby fluorescence technique was used for pressure calibration.

2. RESULTS AND DISCUSSION

The Raman spectrum of $C_{60}H_{36}$ under normal conditions is shown in Fig. 1. The spectrum is considerably richer than that of the pristine C_{60} and contains very sharp and intense peaks in the low-frequency region, while in the high-frequency region, its features are rather broad and faint. This rich spectrum is related to the hydrogenation of the C_{60} molecule, which results in the lowering of the molecular symmetry and the formation of new C–H bonds. In addition to the C–H stretch-

[1] This article was submitted by the authors in English.

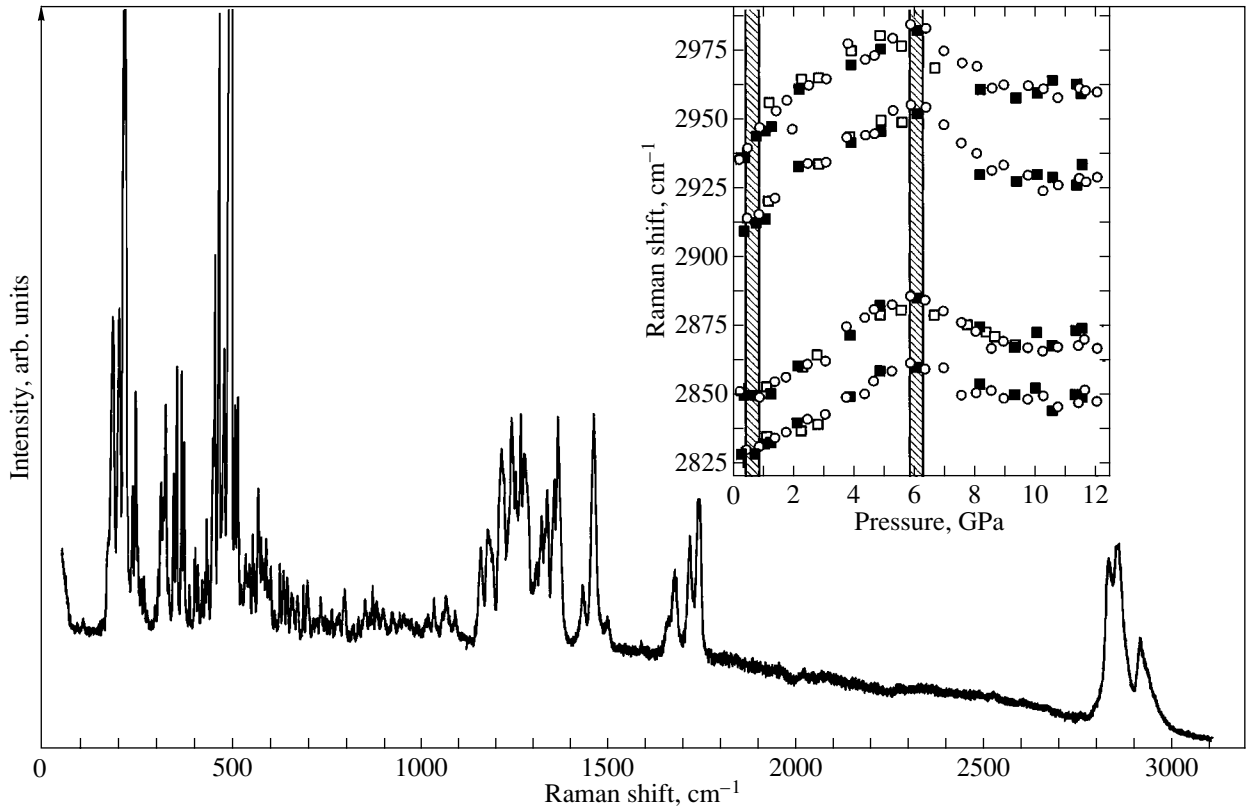

Fig. 1. Raman spectra of $C_{60}H_{36}$ recorded under normal conditions. Insert: the pressure behavior of the C–H stretching modes. The shaded areas near 0.7 and 6 GPa indicate possible phase transitions. Open and shaded symbols are related to an increase and decrease in pressure, respectively.

ing modes near ~2800 cm^{-1}, new modes related to C–H bending vibrations appear in the region 1150–1350 cm^{-1} [7]. The expected number of Raman active modes of the $C_{60}H_{36}$ molecule depends on the symmetry and is equal to 118, 60, 73, and 95 for the *T*, T_h, D_{3d}, and S_6 isomers, respectively. The number of recorded peaks in the Raman spectrum of $C_{60}H_{36}$ is at least 126, which means that the samples under investigation are a mixture of at least two basic isomers. A detailed study of the recorded Raman frequencies and a comparison with molecular dynamics calculations [4] indicate that the samples contain all five stable isomers, the most abundant among them being those with D_{3d} and S_6 symmetry [7]. The application of pressure strongly affects the Raman spectrum, resulting in a positive shift of the Raman peaks and a relative increase in their widths. The pressure dependence of almost all Raman modes shows two features (changes in the slope) near 0.7 and 6 GPa. However, the situation is essentially different for the C–H stretching vibration modes, whose behavior is shown in the inset to Fig. 1. These modes exhibit a positive shift up to ~6 GPa that changes into a negative one at higher pressures. The softening of the C–H stretching modes at high pressures may be associated with hydrogen bonding interaction between the hydrogen and carbon atoms of the adjacent molecules, resulting in a pressure-induced enlargement of the C–H bond length [8].

The photoluminescence spectrum of $C_{60}H_{36}$ under normal conditions is depicted in Fig. 2. The intensity of the luminescence and the threshold for the onset of the spectrum are higher than those for the pristine C_{60} [9]. The pressure behavior of the luminescence spectrum of $C_{60}H_{36}$ is shown in the inset to Fig. 2. The pressure coefficients for the main luminescence peaks, A and B, are negative and close to zero at pressures up to ~6.5 GPa; at higher pressures, they increase in absolute value to –7.5 and –9 meV/GPa, respectively. The pressure behavior of $C_{60}H_{36}$ is not typical of molecular crystals, whose electronic states usually exhibit a large negative pressure shift which rapidly decreases with pressure [10]. It is also known that the pressure-induced shift of electronic states in molecular crystals may be positive for molecules that have no center of symmetry [11]. Taking into account that our samples contain the (noncentrosymmetric) *T* isomer in abundance, the pressure behavior up to 6.5 GPa may be associated with mutual compensation of the opposite shifts of the luminescence spectra, originating from the electronic states of various isomers. At higher pressures, however, lumi-

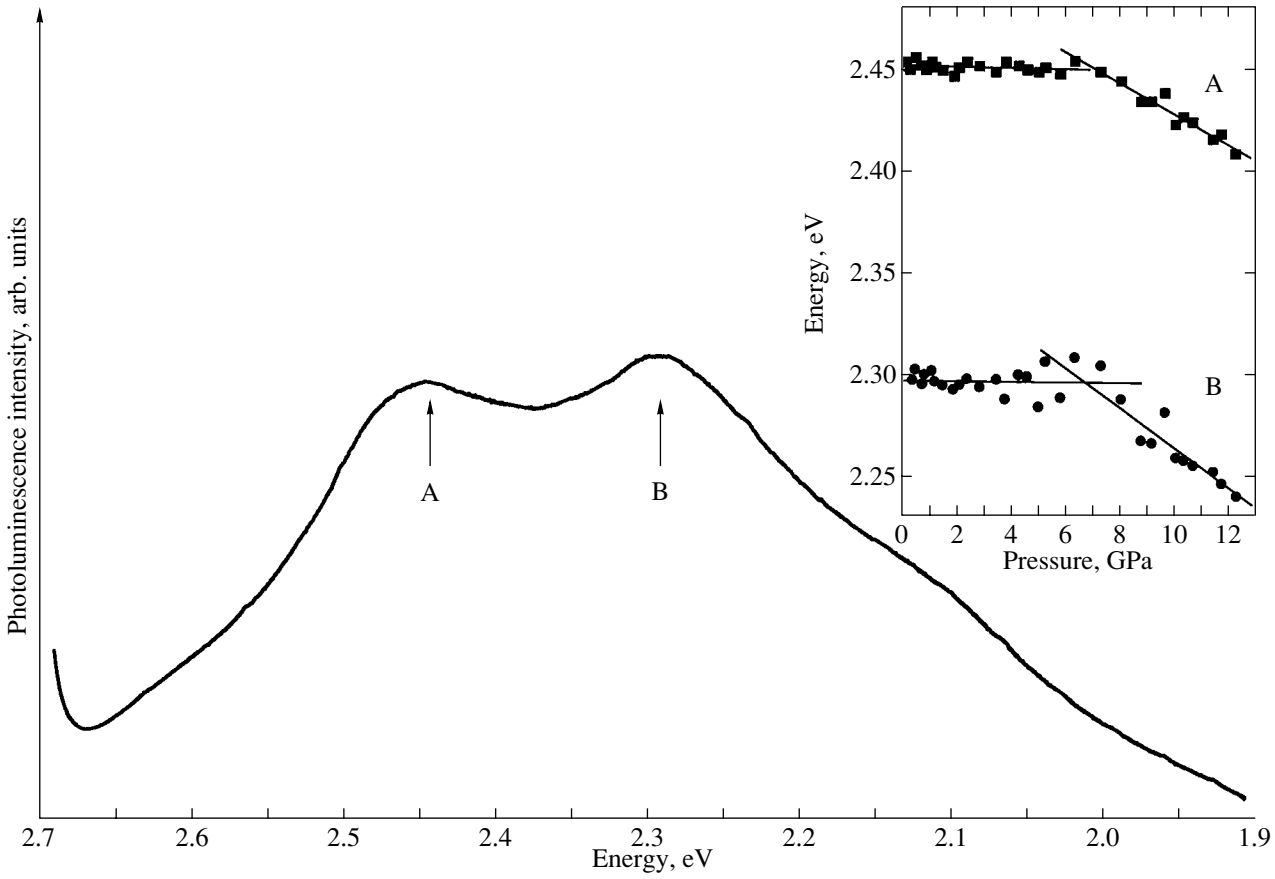

Fig. 2. Photoluminescence spectrum of $C_{60}H_{36}$ recorded under normal conditions. Insert: the pressure dependence of the positions of the main luminescence peaks.

nescence from other isomers (which have a center of symmetry) dominates; their electronic states are downshifted in energy, and, therefore, we have an overall negative pressure shift.

ACKNOWLEDGMENTS

The authors thank Dr. V. Kulakov and Mrs. I. Tsilika for their assistance.

This work was supported, in part, by the Russian Foundation for Basic Research (projects nos. 99-02-17555, 99-02-17299), the Russian Research and Development Program "Fullerenes and Atomic Clusters" (project no. 98079), and the General Secretariat for Research and Technology, Greece (grant no. ΠΕΝΕΔ99, 99EΔ/62).

REFERENCES

1. A. Ratna and J. Chandrasekhar, Chem. Phys. Lett. **203** (1–4), 217 (1993).
2. M. I. Attala, A. M. Vassalo, B. N. Tattam, and J. Hamma, J. Phys. Chem. **97** (24), 6329 (1993).
3. I. O. Bashkin, A. I. Kolesnikov, V. E. Antonov, *et al.*, Mol. Mater. **10**, 265 (1998).
4. R. Bini, J. Ebenhoch, M. Fanti, *et al.*, Chem. Phys. **232** (1–2), 75 (1998).
5. L. E. Hall, D. R. McKenzie, M. I. Attala, *et al.*, J. Phys. Chem. **97** (21), 5741 (1993).
6. R. V. Bensansson, T. J. Hill, E. J. Land, *et al.*, Chem. Phys. **215** (1), 111 (1997).
7. K. Meletov, S. Assimopoulos, I. Tsilika, *et al.*, Chem. Phys. **263** (2–3), 379 (2001).
8. E. Katoh, H. Yamawaki, H. Fujihisa, *et al.*, Phys. Rev. B **59** (17), 11244 (1999).
9. K. P. Meletov, D. Chirisofilos, S. Ves, and G. A. Kourouklis, Phys. Status Solidi B **198** (1), 553 (1996).
10. K. P. Meletov, V. K. Dolganov, O. V. Zharikov, *et al.*, J. Phys. I **2** (11), 2097 (1992).
11. A. S. Davydov, *Theory of Molecular Excitons* (Ukrain. Akad. Nauk, Kiev, 1951; Plenum, New York, 1971).

Physics of the Solid State, Vol. 44, No. 3, 2002, pp. 545–547. Translated from Fizika Tverdogo Tela, Vol. 44, No. 3, 2002, pp. 522–523.

PROCEEDINGS OF THE V INTERNATIONAL WORKSHOP "FULLERENES AND ATOMIC CLUSTERS"

(St. Petersburg, Russia, July 2–6, 2001)

On the Thermal Decomposition of the $C_{60}D_{19}$ Deuterium Fullerite

Yu. M. Shul'ga*, V. M. Martynenko*, B. P. Tarasov*, V. N. Fokin*, V. I. Rubtsov*, N. Yu. Shul'ga*, G. A. Krasochka*, N. V. Chapysheva*, V. V. Shevchenko*, and D. V. Schur**

** Institute of Problems of Chemical Physics, Russian Academy of Sciences, Chernogolovka, Moscow oblast, 142432 Russia*

*** Frantsevich Institute of Materials Science Problems, National Academy of Sciences of Ukraine, ul. Krzhizhanovskogo 3, Kiev, 03142 Ukraine*

e-mail: shulga@icp.ac.ru

Abstract—The gas-phase products of thermal decomposition of the $C_{60}D_{19}$ deuterium fullerite are studied by mass spectrometry. It is found that, in addition to D_2 molecules, the gas phase over the deuterium fullerite sample heated to a temperature of 773 K contains CD_4 methane and C_6D_6 benzene molecules. The deuterocarbon molecules are revealed in the gas phase even at 673 K. *© 2002 MAIK "Nauka/Interperiodica".*

1. INTRODUCTION

The problem of thermal decomposition of $C_{60}H_x$ fullerene hydroderivatives is of particular interest primarily from the standpoint of the possible use of fullerene-based materials as a medium for hydrogen accumulation. A thermal gravimetric analysis revealed that, during heating of $C_{60}H_x$ samples in an inert atmosphere, their weight begins to decrease at a temperature of 723 K [1–3]. It was shown that the reaction products of thermal decomposition of $C_{60}H_x$ fullerene hydroderivatives are hydrogen and fullerene. In particular, Nozu and Matsumoto [4] demonstrated that the formation of $C_{60}H_2$ upon the anodic oxidation of C_{60} films deposited onto a graphite electrode is a completely reversible reaction. Haufler *et al.* [5] made the inference that the hydrogenation of fullerenes is a reversible process. However, Shul'ga and Tarasov [6] established that, in addition to fullerene molecules, the products of thermal decomposition of $C_{60}D_{24}$ at 823 K contain impurity molecules. According to IR spectroscopy, this impurity was identified as a fullerene polymer. Moreover, Brosa *et al.* [3] revealed methane as a gas-phase product of thermal decomposition of $C_{60}H_{18.7}$ at temperatures above 823 K.

In the present work, the products of thermal decomposition of deuterium fullerite (solid deuterofullerene) were investigated by mass spectrometry. We chose deuterium fullerite as the object of our investigation in order to be able to distinguish between the products of thermal decomposition and hydrocarbon impurities, which, in some cases, can occur in the studied system due to desorption from cold walls, parts covered with a vacuum lubricant, and (or) residual vapors from high-pressure vacuum pumps.

2. EXPERIMENTAL TECHNIQUE

The deuterium fullerite samples were prepared according to the procedure described earlier in [7]. The deuterium fullerite polycrystals used in our experiments have the empirical formula $C_{60}D_{19}$, a face-centered cubic lattice, and the unit cell parameter a = 14.71 Å.

The mass spectra were recorded on an MI 1201V mass spectrometer. Ionization was accomplished with an electron impact. The electron energy was equal to 70 eV. Positively charged ions were analyzed in the m/z range from 4 to 90.

The gas phase was produced as follows. A weighed portion (16–40 mg) of deuterium fullerite was placed in a silica tube of the pyrolyzer. The silica tube was connected to an inflow system of the mass spectrometer through a finely adjusting valve. After the preliminary annealing of the sample at a temperature of 373 K for 1 h, the silica tube and inflow system were evacuated to approximately 1×10^{-6} Torr. In all the experiments performed in this work, the gas was allowed to bleed into the preliminarily evacuated tube beginning with a temperature of 373 K. For this reason, in the mass spectra presented, we specified only the temperature at which the sample heating was completed and the mass spectrometric analysis was started.

3. RESULTS AND DISCUSSION

It can be seen from the table that, apart from the peak attributed to the D_2^+ deuterium (m/z = 4), the mass spectrum of the gaseous products of thermal decomposition of the deuterium fullerite sample heated to a temperature of 773 K is characterized by an intense peak

Mass spectra (electron impact, 70 eV) of the gas phase over the deuterium fullerite sample heated to 673 and 773 K

m/*z*	*I*, rel. units		Assignment $[ion]^+$ (initial molecule)
	T = 673 K	*T* = 773 K	
4		300	$[D_2]^+$
12	2	95	
13		5	
14	11	357	
15	3	33	
16	24	910	
17	10	460	
18	139	9100	$[CD_3]^+$, (CD_4)
19	22	1170	
20	280	13500	$[CD_4]^+$, (CD_4)
21		142	
22		7	
24		25	
25		3	
26	10	187	$[C_2D]^+$, (C_2D_2, C_2D_4, C_2D_6)
27	5	59	
28	72	3826	$[C_2D_2]^+$, (C_2D_2, C_2D_4, C_2D_6, C_6D_6)
29	8	141	
30	84	3800	$[C_2D_3]^+$, (C_2D_4, C_2D_6)
31	20	580	
32	323	8700	$[C_2D_4]^+$, (C_2D_4, C_2D_6)
33	13	357	
34	67	1850	$[C_2D_5]^+$, (C_2D_6)
35	18	267	
36	75	3667	$[C_2D_6]^+$, (C_2D_6)
37		43	
38		23	
39	2	3	
40	3	40	
41	4	10	
42	7	153	
43	5	13	
44	15	718	
45		17	
46		143	
47		10	
48		77	
49		17	
50		150	
51		33	
52		250	$[C_2D_8]^+$, (C_3D_8); $[C_4D_2]^+$, (C_6D_6)
53		7	
54		27	$[C_4D_3]^+$, (C_6D_6)
80		6	
81		3	
82		18	
83		17	
84	5	138	$[C_6D_6]^+$, (C_6D_6)
85		9	

with the ratio $m/z = 20$. We assigned the latter peak to the CD_4^+ ion. It should be noted that residual gases contained in the mass spectrometer and silica tube used in measurements did not exhibit peaks with $m/z = 4$ and 20. These peaks were also not observed in the mass spectra of the products of preliminary degassing of the deuterium fullerite samples under investigation. However, in the case when the sample subjected to preliminary degassing at 373 K was then heated to a temperature of 673 K instead of 773 K, the mass spectrum exhibited a peak with $m/z = 20$. It is worth noting that the total amount of the gas released from the sample at 673 K is considerably less than that liberated at 773 K. According to the estimates, the pressure in the silica tube used at approximately the same weights of samples is equal to 10^{-2} Torr at 673 K and 2 to 5 Torr at 773 K. These values are in reasonable agreement with the intensities of the peaks observed in the mass spectra.

At 773 K, the gas phase over the $C_{60}D_{19}$ deuterium fullerite sample contains C_6D_6 molecules in addition to CD_4. This is indicated by the peak with $m/z = 84$, which is the most intense in the range $60 \le m/z \le 100$. Upon thermal decomposition of the $C_{60}H_x$ hydrofullerene, the most intense peak observed in this range of the mass spectrum is characterized by the ratio $m/z = 78$.

Thus, our results confirm the inferences made by Brosa *et al.* [3], according to which methane is liberated upon heating of the hydrofullerene to 773 K. Furthermore, our data indicate the possible formation of deuterocarbon molecules, including benzene-d^6 (C_6D_6), upon heating of the deuterium fullerite sample to 773 K (see table). It is quite possible that deuteromethane is formed not from deuterofullerene molecules but from a precursor formed at the stage of deuteration of the fullerite sample. It can be assumed that gas-phase deuteration (hydrogenation) of solid fullerenes leads not only to the formation of deutero(hydro)fullerenes but also to rupture of the closed carbon cages, if only in a small amount of deutero(hydro)fullerene molecules. This rupture is accompanied by the formation of both volatile and nonvolatile products, some of which remain in the lattice of the fullerite or deuterium fullerite. Most likely, it is these deuterated hydrocarbons that are responsible for the formation of the fullerite with an extended lattice upon dehydrogenation of crystalline hydrofullerenes [7]. It is clear that the ratio of the number of hydrofullerene molecules retaining their closed carbon cages to the number of hydrofullerene molecules stripped of their closed carbon cages is determined by the parameters of deuteration (hydrogenation), primarily by the temperature and pressure of gaseous D_2 (H_2).

ACKNOWLEDGMENTS

This work was supported by the Russian Foundation for Basic Research, project no. 00-03-32106.

REFERENCES

1. B. P. Tarasov, V. N. Fokin, A. P. Moravskiĭ, and Yu. M. Shul'ga, Izv. Akad. Nauk, Ser. Khim., No. 7, 1867 (1996).
2. B. P. Tarasov, V. N. Fokin, A. P. Moravskiĭ, and Yu. M. Shul'ga, Izv. Akad. Nauk, Ser. Khim., No. 4, 679 (1997).
3. E. L. Brosa, J. Davey, F. H. Garson, and S. Gooesfeld, J. Mater. Res. **14** (5), 2136 (1999).
4. R. Nozu and O. Matsumoto, J. Electrochem. Soc. **143** (6), 1919 (1996).
5. R. E. Haufler, J. Canciecao, Y. Chai, *et al.*, J. Phys. Chem. **94**, 8634 (1990).
6. Yu. M. Shul'ga and B. P. Tarasov, Pis'ma Zh. Éksp. Teor. Fiz. **68** (3), 239 (1998) [JETP Lett. **68**, 253 (1998)].
7. Yu. M. Shul'ga, B. P. Tarasov, V. N. Fokin, *et al.*, Fiz. Tverd. Tela (St. Petersburg) **41** (8), 1520 (1999) [Phys. Solid State **41**, 1391 (1999)].

Translated by O. Borovik-Romanova

Physics of the Solid State, Vol. 44, No. 3, 2002, pp. 548–550. From Fizika Tverdogo Tela, Vol. 44, No. 3, 2002, pp. 524–525.

PROCEEDINGS OF THE V INTERNATIONAL WORKSHOP "FULLERENES AND ATOMIC CLUSTERS"

(St. Petersburg, Russia, July 2–6, 2001)

A Computational Study of Entropy Rules for Charged Fullerenes[1]

Z. Slanina*, F. Uhlík, and O. V. Boltalina*****

** Institute of Chemistry, Academia Sinica, Nankang, Taipei, 11529 Taiwan-R.O.C.*
e-mail: zdenek@chem.sinica.edu.tw
*** Department of Physical and Macromolecular Chemistry, Charles University, Prague, 12843 Czech Republic*
**** Chemistry Department, Moscow State University, Vorob'evy gory, Moscow, 119899 Russia*

Abstract—Thermochemical data on fullerenes are relatively scarce. However, some thermochemical information can be derived from gas-phase experiments using the Knudsen cell mass spectrometry method. The third-law treatment can be carried out on the observed data, though one has to make the crucial presumption that the change in the thermodynamic potential $\Delta\Phi_T^o$ in the course of the reactions considered is negligible: $\Delta\Phi_T^o = 0$. It would be difficult to check the presumption directly in the experiment, but it can be checked computationally. Model reactions like $C_{60} + C_{70}^- = C_{60}^- + C_{70}$ are selected. The change in the thermodynamic potential $\Delta\Phi_T^o$ and the change in the standard entropy ΔS_T^o are computed. For example, at a temperature of $T = 1000$ K, the standard changes for the reaction evaluated using the SAM1 method are $\Delta\Phi_T^o = 1.513$ cal/(mol K) and $\Delta S_T^o = -0.054$ cal/(mol K). Overall, the computations support the critical thermodynamic presumption. *© 2002 MAIK "Nauka/Interperiodica".*

Charged fullerenes (in particular, charged C_{60}) have frequently been computed owing to their interesting Jahn–Teller distortions [1–10]. In this paper, charged fullerenes are computed with special attention given to their gas-phase thermodynamic functions. Thermochemical data on fullerenes remain scarce; only the heats of formation for C_{60}, C_{70}, and two C_{60} derivatives are available [11–17]. Some thermochemical information can, however, be derived from gas-phase experiments [18] using mass spectrometry. In this method, equilibrium constants for electron transfer reactions between fullerenes were measured [18] and the related standard Gibbs free-energy changes derived. A typical charging reaction under consideration is

$$C_{60} + C_{70}^- = C_{60}^- + C_{70}. \quad (1)$$

However, the second-law treatment of the data performed in [18] did not produce accurate enthalpy terms. The third-law treatment gives another option:

$$\Delta H_0^o = T\Delta\Phi_T^o - RT\ln K_p. \quad (2)$$

In Eq. (2), K_p denotes the measured equilibrium constant for electron transfer reactions of the type described by Eq. (1) and $\Delta\Phi_T^o$ refers to the change in the standard thermodynamic potential (also known as the Giauque function):

$$\Phi_T^o = -\frac{G_T^o - H_0^o}{T}. \quad (3)$$

A key presumption concerning the thermodynamic potentials was introduced in [18],

$$\Delta\Phi_T^o \approx 0. \quad (4)$$

From here, the standard enthalpy changes ΔH_0^o and electron affinities for higher fullerenes can be derived [18]. In this paper, presumption (4) and the related entropy conjecture

$$\Delta S_T^o \approx 0 \quad (5)$$

are studied for fullerene electron-exchange reactions (1).

1. COMPUTATIONS

The computations reported here are performed using the SAM1 (semi-*ab-initio* model 1) semiempirical quantum-chemical method [19], in particular, with its implementation in the AMPAC package [20]. The complete geometry optimizations are based on the analytical energy gradient in Cartesian coordinates. A harmonic vibrational analysis is carried out with the numerical second derivatives of energy. No scaling of the computed harmonic vibrational frequencies is used, as such scaling factors are not yet known for fullerenes.

[1] This article was submitted by the authors in English.

Table 1. SAM1 computed thermodynamic data for charged C_{60} and C_{70}

Species	S^o_{1000}, cal/(mol K)	$\Delta H^o_{f,298}$, kcal/mol	Point group of symmetry	$\frac{\sigma}{\chi}$	$H^o_{1000}-H^o_0$, cal/mol
C_{60}^0	382.37	775.26	I_h	60	173386
C_{60}^{1-}	404.19	694.77	C_2	1	178240
C_{60}^{1+}	402.06	934.14	C_2	1	177974
C_{60}^{2-}	392.14	744.16	D_{5d}	10	175079
C_{60}^{2+}	390.25	1220.77	D_{5d}	10	174908
C_{70}^0	442.90	829.65	D_{5h}	10	203024
C_{70}^{1-}	464.78	721.33	C_s	1	209445
C_{70}^{1+}	462.30	960.45	C_s	1	208478
C_{70}^{2-}	451.14	774.07	C_{2v}	2	204536
C_{70}^{2+}	447.55	1242.50	C_{2v}	2	203621

Note: Gas-phase species throughout; the standard state is the ideal-gas phase at a pressure of 1 atm = 101325 Pa; S^o_{1000} is the standard entropy at T = 1000 K; $\Delta H^o_{f,298}$ is the heat of formation at room temperature; σ/χ is the ratio of the symmetry number σ to the chirality factor χ; and $H^o_{1000}-H^o_0$ is the change in the standard enthalpy in going from 0 to 1000 K.

While the computations for closed shell species are relatively straightforward, open shell systems are numerically quite difficult. The results reported in this paper are based on the unrestricted Hartree–Fock treatment of open shell systems. Special attention is paid to evaluation [21] of the symmetries of the relaxed structures. From the computed rotational, vibrational, and symmetry parameters, the rigid-rotator and harmonic-oscillator partition functions are constructed and the thermodynamic functions of interest are derived.

2. RESULTS AND DISCUSSION

Charged high-symmetry fullerenes can frequently exhibit Jahn–Teller effects. A change in the point symmetry group can lead to a change in the symmetry number σ. Chirality is another issue pertinent to fullerene cages [22, 23], though only the C_n, D_n, T, O, and I groups allow for chirality. For an enantiomeric pair, its partition function has to be doubled. This can formally be done by means of the chirality partition function or chirality factor χ (assuming only two possible values, 1 or 2). Hence, in evaluations of thermodynamic terms, the ratio

$$\frac{\sigma}{\chi} \qquad (6)$$

is important. As seen from Table 1, this ratio can change dramatically upon charging.

Quotient (6) reflects only a part of the changes induced by charging. There are other changes in the structural and vibrational patterns and in the rotational–vibrational partition functions. Only after taking all the changes into account can one evaluate the changes in the thermodynamic functions upon charging.

Table 1 presents the SAM1 computed data for the neutral and charged fullerene cages under consideration. The presented heats of formation are not important for our purposes. In fact, the $\Delta H^o_{f,298}$ terms computed within SAM1 are overestimated compared to the observed values [11–15]. The standard entropy S^o_T and heat-content function $H^o_T - H^o_0$ are computed for a representative [18] temperature of 1000 K.

The standard reaction changes in the thermodynamic potential and entropy are given in Table 2. The presented values are very small in magnitude. Hence, the SAM1 results presented in Table 2 indeed support the conjectures formulated by Eqs. (4) and (5). In particular, the entropy conjecture for the reaction in Eq. (1) is written as

$$S^o_T(C_{60}^-) - S^o_T(C_{60}) \approx S^o_T(C_{70}^-) - S^o_T(C_{70}), \qquad (7)$$

Table 2. SAM1 standard thermodynamic-potential and entropy changes

Process	$\Delta\Phi^o_{1000}$, cal/(mol K)	ΔS^o_{1000}, cal/(mol K)
$C_{60}^0 + C_{70}^{1-} = C_{60}^{1-} + C_{70}^0$	1.513	−0.054
$C_{60}^0 + C_{70}^{1+} = C_{60}^{1+} + C_{70}^0$	1.152	0.286
$C_{60}^0 + C_{70}^{2-} = C_{60}^{2-} + C_{70}^0$	1.348	1.530
$C_{60}^0 + C_{70}^{2+} = C_{60}^{2+} + C_{70}^0$	2.308	3.232

Note: Gas-phase species throughout.

according to which the addition of one electron to a C_{60} or a C_{70} cage would bring about the same entropy change. With the large number of various factors involved, the results formulated by Eqs. (4), (5), or (7) are rather surprising. These results also suggest that the possible inaccuracy introduced by our presumption into the terms derived from the observed data is comparable to the primary experimental errors [18].

ACKNOWLEDGMENTS

The authors thank the National Center for High-Performance Computing in Hsinchu, Taiwan, Republic of China, for computer time.

This research was supported by the National Science Council, Taiwan, Republic of China.

REFERENCES

1. B. C. Wang and Y. N. Chiu, J. Chin. Chem. Soc. (Taipei) **39**, 111 (1992).
2. G. Endrédi and J. Ladik, Chem. Phys. Lett. **223**, 155 (1994).
3. Z. Slanina and S.-L. Lee, Chin. J. Phys. (Taipei) **34**, 633 (1996).
4. N. Koga and K. Morokuma, Chem. Phys. Lett. **196**, 191 (1992).
5. R. D. Bendale, J. F. Stanton, and M. C. Zerner, Chem. Phys. Lett. **194**, 467 (1992).
6. S. Suzuki, D. Inomata, N. Sashide, and K. Nakao, Phys. Rev. B **48**, 14615 (1993).
7. P. R. Surjan, L. Udvardi, and K. Nemeth, THEOCHEM **117**, 1438 (1994).
8. O. Gunnarsson, Phys. Rev. B **51**, 3493 (1995).
9. Z. Slanina, F. Uhlík, J.-P. François, and E. Ōsawa, Fullerene Sci. Technol. **8**, 403 (2000).
10. I. B. Bersuker, Chem. Rev. **101**, 1067 (2001).
11. H. D. Beckhaus, C. Ruchardt, M. Kao, *et al.*, Angew. Chem. Int. Ed. Eng. **31**, 63 (1992).
12. W. V. Steele, R. D. Chirico, N. K. Smith, *et al.*, J. Phys. Chem. **96**, 4731 (1992).
13. T. Kiyobayashi and M. Sakiyama, Fullerene Sci. Technol. **1**, 269 (1993).
14. H. P. Diogo, M. E. Minas da Pielade, T. J. S. Dennis, *et al.*, J. Chem. Soc., Faraday Trans. **89**, 3541 (1993).
15. H.-D. Bechhaus, S. Verevkin, C. Rüchardt, *et al.*, Angew. Chem. Int. Ed. Engl. **33**, 996 (1994).
16. T. S. Papina, V. P. Kolesov, V. A. Lukyanova, *et al.*, J. Chem. Thermodyn. **31**, 1321 (1999).
17. T. S. Papina, V. P. Kolesov, V. P. Lukyanova, *et al.*, J. Phys. Chem. B **104**, 5403 (2000).
18. O. V. Boltalina, E. V. Dashkova, and L. N. Sidorov, Chem. Phys. Lett. **256**, 253 (1996).
19. M. J. S. Dewar, C. Jie, and J. Yu, Tetrahedron **49**, 5003 (1993).
20. *AMPAC 6.0* (Semichem, Shavnee, 1997).
21. M.-L. Sun, Z. Slanina, S.-L. Lee, *et al.*, Chem. Phys. Lett. **246**, 66 (1995).
22. Z. Slanina and L. Adamowicz, Thermochim. Acta **205**, 299 (1992).
23. J. Cioslowski, *Electronic Structure Calculations on Fullerenes and Their Derivatives* (Oxford Univ. Press, Oxford, 1995).

Physics of the Solid State, Vol. 44, No. 3, 2002, pp. 551–553. Translated from Fizika Tverdogo Tela, Vol. 44, No. 3, 2002, pp. 526–528.

PROCEEDINGS OF THE V INTERNATIONAL WORKSHOP "FULLERENES AND ATOMIC CLUSTERS"

(St. Petersburg, Russia, July 2–6, 2001)

Negative Ions of Hydrogenated and Deuterated C_{60} Fullerenes

Sh. K. Nasibullaev*, Yu. V. Vasil'ev, R. R. Abzalimov*, A. S. Lobach***, I. O. Bashkin****, D. Wallis**, and T. Drewello****

** Institute of Physics of Molecules and Crystals, Russian Academy of Sciences, Ufa, 450075 Bashkortostan, Russia*
e-mail: nsk@anrb.ru

*** Department of Chemistry, University of Warwick, Coventry CV4 7AL, United Kingdom*

**** Institute of Problems of Chemical Physics, Russian Academy of Sciences, Chernogolovka, Moscow oblast, 142432 Russia*

***** Institute of Solid-State Physics, Russian Academy of Sciences, Chernogolovka, Moscow oblast, 142432 Russia*

Abstract—This paper reports on the results of mass spectrometric and theoretical investigations of hydrogenated and deuterated fullerene derivatives $C_{60}H(D)_x$. The formation and decay (through electron autodetachment) of negative molecular ions of the $C_{60}H_{18}$ and $C_{60}D_{18}$ hydrofullerenes are discussed. A comparative analysis of these processes is performed for different fullerene derivatives. © *2002 MAIK "Nauka/Interperiodica".*

1. INTRODUCTION

Over the last years, the hydrogenated fullerene derivatives $C_{60}H_x$ have been a subject of extensive experimental and theoretical studies [1]. Investigation of these compounds can provide important information on the nature of hydrogen bonding in molecules. Moreover, these compounds are very promising for practical applications. In the present work, the low-energy electron–molecular interactions in $C_{60}H_{18}$, $C_{60}H_{36}$, and $C_{60}D_{36}$ hydrogenated fullerene molecules and the formation of negative ions of these molecules under laser irradiation were investigated using resonant electron capture mass spectrometry in addition to the laser desorption mass spectrometric technique.

2. RESULTS AND DISCUSSION

The figure displays the negative ion resonant electron capture mass spectra of $C_{60}H_{36}$ and $C_{60}D_{36}$ hydrogenated fullerenes at an electron energy of ~0.3 eV. In addition, we recorded the effective yield curves for the $C_{60}H(D)_{18}^-$ negative ions and the $C_{60}H(D)_{18}^0$ neutral molecules as functions of the electron energy. (The $C_{60}H(D)_{18}^0$ neutral molecules are formed through electron autodetachment from the corresponding negative ions in the second field-free region of a single-focusing sector-type mass spectrometer.) The effective yield curves and curves for the mean lifetimes of negative ions with respect to the electron autodetachment are also depicted in the figure. All the curves were measured under almost identical conditions (the same operating mode of the ion source and the same temperatures of the molecular beams). It is found that, within the limits of the experimental error, the mass spectra of hydrogenated and deuterated derivatives of the C_{60} fullerene are similar to each other. However, both compounds are characterized by an interesting temperature effect associated with the mean lifetimes of the negative ions. An increase in the molecular beam temperature leads to an increase in the mean lifetime of the $C_{60}H(D)_{18}^-$ negative ions of both isotopomers in such a way that the high-temperature lifetimes are nearly twice as long as the low-temperature lifetimes. This occurrence was quite unexpected, because the reverse situation should be observed according to the general principles of the statistical theory of negative ions.

Here, it is pertinent to recall the data available in the literature on the $C_{60}H_{18}$ molecule and its fluorinated analog $C_{60}F_{18}$ [2]. It is believed that both molecules have only one stable isomer with C_{3v} symmetry and a specific arrangement of hydrogen (fluorine) atoms around one of the poles of the C_{60} cage, namely, $C_{60}H(F)_{18}$. The $C_{60}H(F)_{18}$ isomer has been thoroughly studied by nuclear magnetic resonance and crystallographic techniques, and the structure of this isomer is beyond question. Until presently, reliable data on the existence of any other stable $C_{60}H(F)_{18}$ isomers were unavailable. However, our preliminary mass spectrometric investigations of the $C_{60}F_{18}$ isomer produced by reactions of the C_{60} fullerene with different fluorine-containing compounds indicate that the $C_{60}F_{18}$ molecule has another thermodynamically stable isomer. We found that these isomers differ in ionization energy by 0.5 eV, exhibit dissimilar dependences of the negative ion formation cross section on the electron energy, and have different mean lifetimes of the $C_{60}F_{18}^-$ negative ions. So far, the possible structure of the new isomer remains unclear. Nonetheless, it is evident that our new data on the hydrogenated analogs of $C_{60}F_{18}$ cannot be explained without resorting to two $C_{60}H(D)_{18}$ isomers.

1063-7834/02/4403-0551$22.00

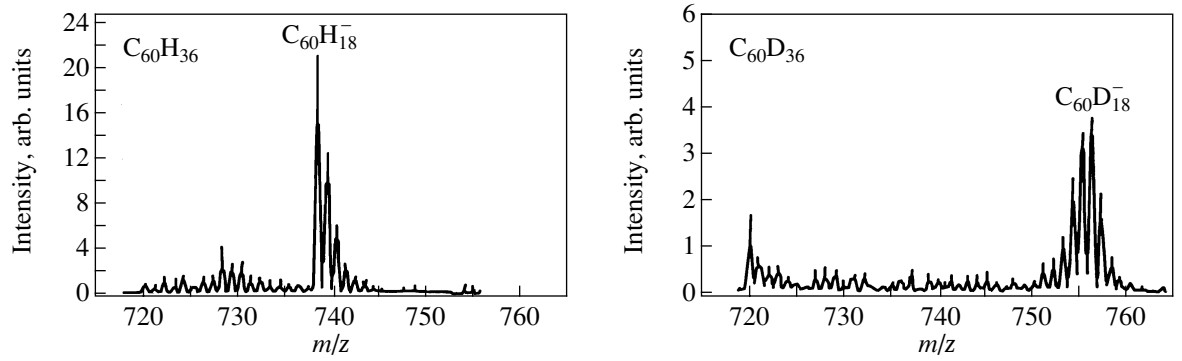

Negative ion mass spectra of $C_{60}H_{36}$ and $C_{60}D_{36}$ at an electron energy of 0.3 eV

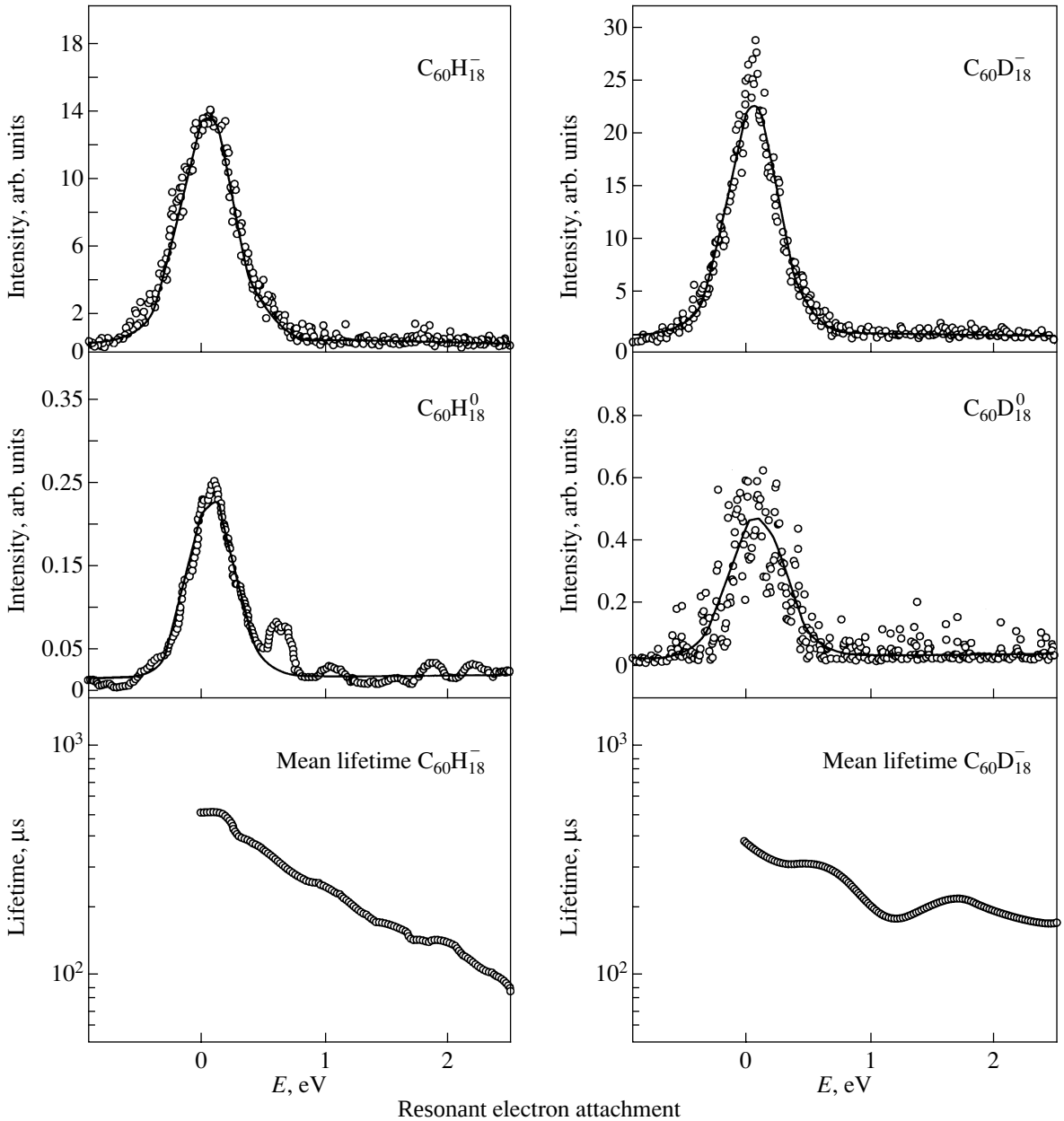

Resonant electron attachment

Negative molecular ion mass spectra and effective yield curves of $C_{60}H(D)_{18}^-$ ions for the compounds $C_{60}H_{36}$ (left column) and $C_{60}D_{36}$ (right column).

Indeed, the semiempirical calculations performed in the present work demonstrate that the ground state of the negative ion of the well-studied $C_{60}H_{18}$ isomer with the C_{3v} symmetry is doubly degenerate. In this case, according to the statistical theory, the electron autodetachment rate constant (the reciprocal of the negative ion lifetime) for this ion should be equal to twice the rate constant for the nondegenerate state (all other factors being the same, for example, approximately the same electron affinities). Consequently, the lifetime of the doubly degenerate state should be halved. Therefore, either an increase in the molecular beam temperature should lead to isomerization of the symmetric C_{3v} isomer with the formation of a nonsymmetric isomer or the initially existing nonsymmetric isomer should have a higher sublimation temperature and begin to manifest itself only at high molecular beam temperatures. According to our theoretical calculations, there exist a few $C_{60}H(D)_{18}$ isomers that are more thermodynamically stable than the aforementioned isomer with the C_{3v} symmetry. However, the formation of these isomers in nature can involve purely chemical difficulties, which were described by Darwish *et al.* [3]. It is more reasonable to assume that there exists a polar isomer that is similar to the C_{3v} isomer but has a lower symmetry.

An important problem arising in the study of the negative ions of the $C_{60}H_x$ hydrogenated fullerenes is associated with the possible formation of negative hydrofullerene ions at high hydrogen contents x. According to Hettich *et al.* [4], the maximum degree of hydrogen saturation at which negative hydrofullerene ions can be formed does not exceed 10. In our recent work [5], the existence of the long-lived negative ion $C_{60}H_{18}^-$ was proved using the laser desorption and resonant electron capture mass spectrometric techniques. In order to determine the maximum degree of hydrogenation x at which negative hydrofullerene ions can be formed, we calculated the electron affinities for the $C_{60}H_x$ molecules in the range $0 \le x \le 60$. The calculations were performed using the quantum-chemical semiempirical AM1 method. For each molecule, the geometry was optimized for both the neutral state and the negative molecular ion. The electron affinity was calculated from the formula $E_a(x) = E_x^{(0)} - E_x^{(-)}$, where $E_x^{(z)}$ is the total energy of the ion and z is the ion charge. The calculated electron affinities were reduced to the experimental electron affinity for the C_{60} fullerene (2.65 eV at $x = 0$). It should be noted that the electron affinity thus evaluated for $C_{60}H_{18}^-$ (1.18 eV) is in good agreement with the experimentally obtained estimate (1.4 eV). As follows from the calculated electron affinities, the maximum degree of hydrogenation x_{max} at which the hydrofullerene negative ions can be formed is approximately equal to 30.

ACKNOWLEDGMENTS

This work was supported by the Russian Foundation for Basic Research (project nos. 01-02-16561 and 99-02-17299) and the International Association of Assistance for the promotion of cooperation with scientists from the New Independent States of the former Soviet Union (project no. 97-30027).

REFERENCES

1. N. F. Gol'dshleger and A. P. Moravskiĭ, Usp. Khim. **66** (4), 353 (1997).
2. O. V. Boltalina, M. Bühl, A. Khong, *et al.*, J. Chem. Soc., Perkin Trans. 2, 1475 (1999).
3. A. D. Darwish, A. G. Avent, R. Taylor, and D. R. M. Walton, J. Chem. Soc., Perkin Trans. 2, 2051 (1996).
4. R. L. Hettich, C. Jin, P. F. Britt, *et al.*, Mater. Res. Soc. Symp. Proc. **349**, 133 (1994).
5. Y. V. Vasil'ev, R. R. Abzalimov, Sh. K. Nasibullaev, *et al.*, J. Phys. Chem. A **105** (4), 661 (2001).

Translated by O. Borovik-Romanova

Physics of the Solid State, Vol. 44, No. 3, 2002, pp. 554–556. Translated from Fizika Tverdogo Tela, Vol. 44, No. 3, 2002, pp. 529–531.

PROCEEDINGS OF THE V INTERNATIONAL WORKSHOP "FULLERENES AND ATOMIC CLUSTERS"

(St. Petersburg, Russia, July 2–6, 2001)

Negative Molecular Ions of Azafullerenes and Their Hydrogenated Derivatives

Yu. V. Vasil'ev, R. R. Abzalimov*, Sh. K. Nasibullaev*, R. F. Tuktarov*, F. Hauke***, U. Reuther***, A. Hirsch***, and T. Drewello****

** Institute of Physics of Molecules and Crystals, Russian Academy of Sciences, Ufa, 450075 Bashkortostan, Russia*
e-mail: nsk@anrb.ru
*** Department of Chemistry, University of Warwick, Coventry CV4 7AL, United Kingdom*
**** Universität Erlangen, Erlangen, D-91054 Germany*

Abstract—The formation and decay of negative molecular ions of azafullerenes and their hydrogenated derivatives are investigated by mass spectrometry. The mechanisms of resonant electron capture and the lifetimes of negative molecular ions with respect to the electron autodetachment in azafullerene molecules are discussed. A comparative analysis of the data obtained for azafullerenes and hydrogenated fullerene derivatives is carried out. © *2002 MAIK "Nauka/Interperiodica".*

1. INTRODUCTION

Nitrogen-based heterofullerenes, in particular, diazafullerene $(C_{59}N)_2$, have attracted considerable attention of many researchers. Investigation of these compounds allows one to elucidate how the modification of the fullerene cage can affect the physicochemical properties of fullerenes. In the present work, we applied different mass spectrometric techniques to the investigation of the $(C_{59}N)_2$ diazafullerene, its monomer analog $C_{59}N$ that exists only in a gas phase, and hydrogenated derivatives of the azafullerene monomer. The hydrogenated derivatives used in our experiments were obtained upon *in situ* thermal decomposition of the azafullerene dimer in a mass spectrometer and subsequent hydrogenation through the transfer of hydrogen atoms from different hydrogen-containing compounds.

2. RESULTS AND DISCUSSION

Before proceeding to measurements, the purity of the initial diazafullerene sample was checked by nanospray mass spectrometric analysis in the positive and negative ion modes. The mass spectra recorded in both modes demonstrated that, within the detection limits of the mass spectrometer used, the compound contained no impurities, except for diazafullerene oxides. These oxides either were formed in storage of the material in air prior to the insertion into the mass spectrometer or were the products of ion-molecular reactions proceeding in a solution prior to or in the course of spraying. It is interesting to note that the diazafullerene oxides were identified only in the negative ion nanospray mass spectra and virtually did not manifest themselves in the positive ion nanospraying mass spectra. The same effect was observed in the laser desorption–ionization mass spectra with a sole exception: we succeeded in revealing only the peaks associated with ions of the $C_{59}N$ monomer. This can be explained by the fact that laser desorption is a technique that operates in a relatively severe mode for the analysis of thermolabile azafullerenes. It should also be noted that electrospraying and nanospraying are the gentlest ionization mass spectrometric techniques used for azafullerenes and do not lead to their decomposition into monomers.

Moreover, the azafullerene dimer was examined using the resonant electron capture and electron impact mass spectrometric techniques. The positive and negative ion mass spectra contain peaks attributed to the $C_{59}N^{\pm}$, $C_{59}NH^{\pm}$, and $C_{59}NH_5^{\pm}$ ions. The origin of the last two ions is unambiguously explained by the attachment of hydrogen atoms to the $C_{59}N^{\bullet}$ radical monomer in an ionization chamber. Since the $C_{59}N^{\bullet}$ radical monomer is isoelectronic with the radical anion of the C_{60} fullerene [1], we can make the inference that the $C_{59}NH$ hydroazafullerene is the simplest azafullerene with a completely filled electron shell, whereas the $C_{59}NH_x^-$ hydroazafullerenes are isoelectronic with the $C_{60}H_{x+1}^-$ hydrofullerenes. Therefore, the comparative analysis of the behavior of hydrofullerene and hydroazafullerene molecules upon electron capture and electron ionization makes it possible to reveal the specific features in the formation of positive and negative ions of these molecules and to elucidate the mechanisms of their decomposition through different decay channels.

The negative ion effective yield curves for the azafullerene monomer and two hydrogenated deriva-

1063-7834/02/4403-0554$22.00 © 2002 MAIK "Nauka/Interperiodica"

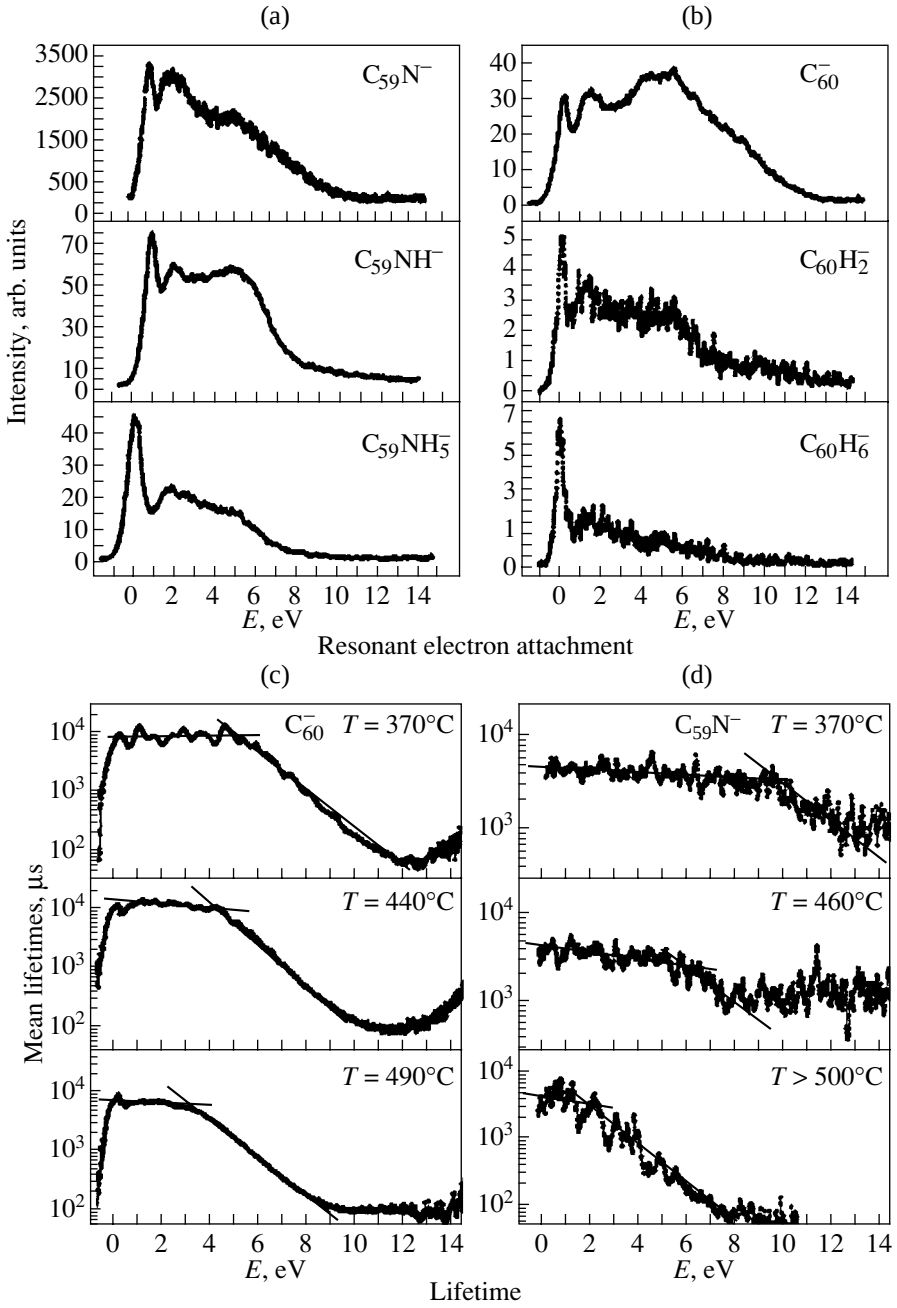

Fig. 1. Negative ion effective yield curves for (a) the $C_{59}N^-$ azafullerene monomer and two azafullerene hydrides and (b) the C_{60}^- fullerene and two fullerene hydrides and the mean lifetime curves for (c) C_{60}^- and (d) $C_{59}N^-$ negative molecular ions as functions of the incident electron energy at different molecular beam temperatures.

tives of this monomer as functions of the incident electron energy are depicted in Fig. 1a. For comparison, Fig. 1b displays the negative ion effective yield curves for the C_{60} fullerene and two fullerene hydrides, namely, $C_{60}H_2$ and $C_{60}H_6$. As can be seen from Fig. 1, an increase in the number of hydrogen atoms attached to the azafullerene and fullerene cages leads to a substantial decrease in the energy range of electron capture.

It is of interest to compare the mean lifetimes of the negative molecular ions of fullerene and azafullerene with respect to the electron autodetachment. Figures 1c and 1d depict the mean lifetime curves for these ions at different temperatures of the molecular beam. It is clearly seen that the mean lifetime curves have two characteristic portions. In the first portion (at low energies of incident electrons), the mean lifetime remains nearly constant and amounts to several milliseconds. In

the second portion (at high energies of incident electrons), the mean lifetime obeys a conventional exponential decay law due to fast electron autodetachment. Most likely, the plateaulike behavior of the mean lifetime curve at low electron energies is associated with the neutralization of the negative ions through their collision with molecules of the residual gas in the second field-free region of the mass spectrometer.

As is known, these processes are independent of the internal ion energy but depend on the pressure in the ion source of the mass spectrometer. The plateaulike behavior of the mean lifetime curve is observed in the case when, for some reason (for example, owing to the competition with one more monomolecular process of the negative ion decay, such as radiation cooling), the rate constant of negative ion decay due to electron autodetachment becomes less than the rate constant of collision-induced neutralization of the negative ions. In contrast with the plateaulike behavior, the energy range in which the negative ion lifetime obeys the exponential decay has found to be strongly dependent on the thermal excitation of the molecule. The lower the temperature, the wider the energy range. This pattern is qualitatively identical for both azafullerene and pure fullerene, even though the energy range for the negative azafullerene ion has found to be wider. By assuming identical experimental conditions, this finding can be explained by the lower internal energy of azafullerene, because some part of the internal energy is expended in forming the monomer from the dimer.

ACKNOWLEDGMENTS

This work was supported by the Russian Foundation for Basic Research (project no. 01-02-16561) and the International Association of Assistance for the promotion of cooperation with scientists from the New Independent States of the former Soviet Union (project no. 97-30027).

REFERENCE

1. M. Keshavarz-K, R. Gonzáles, R. G. Hicks, *et al.*, Nature **383**, 147 (1996).

Translated by O. Borovik-Romanova

Physics of the Solid State, Vol. 44, No. 3, 2002, pp. 557–559. Translated from Fizika Tverdogo Tela, Vol. 44, No. 3, 2002, pp. 532–533.

PROCEEDINGS OF THE V INTERNATIONAL WORKSHOP "FULLERENES AND ATOMIC CLUSTERS"

(St. Petersburg, Russia, July 2–6, 2001)

Determination of the Reaction Rate Constant and Activation Energy for Pressure-Induced 2 + 2 Cycloaddition of the C_{60} Fullerene

V. A. Davydov*, L. S. Kashevarova*, A. V. Rakhmanina*, V. M. Senyavin, N. N. Oleĭnikov**, and V. N. Agafonov*****

** Institute of High-Pressure Physics, Russian Academy of Sciences, Troitsk, Moscow oblast, 142190 Russia*

*** Moscow State University, Vorob'evy gory, Moscow, 119899 Russia*

**** Laboratoire de Chimie Physique, Faculte de Pharmacie de l'Universite de Tours, Tours, 37200 France*

Abstract—The kinetics of fullerene solid-phase dimerization proceeding through the 2 + 2 cycloaddition of C_{60} at a pressure of 1.5 GPa is investigated by vibrational spectroscopy in the temperature range 373–473 K. Kinetic curves for the formation of $(C_{60})_2$ dimers are obtained using the analytical band at 796 cm^{-1} in the IR spectra of the $(C_{60})_2$ dimer molecule. Under the assumption that the pressure-induced dimerization of C_{60} is an irreversible second-order reaction, the reaction rate constants are determined at different temperatures. The activation energy and the preexponential factor are found to be equal to 134 ± 6 kJ/mol and $(1.74 \pm 0.24) \times 10^{14}$ s^{-1}, respectively. © *2002 MAIK "Nauka/Interperiodica".*

1. INTRODUCTION

High-temperature treatment of carbon-containing systems under a high pressure with the use of the C_{60} fullerene as an initial compound offers strong possibilities of producing new types of carbon materials, for example, one-, two-, and three-dimensional polyfullerenes formed by the 2 + 2 cycloaddition of C_{60} molecules [1, 2]. The active interest expressed by researchers in comprehensive investigation of this reaction has stimulated attempts to construct a complete diagram of energy transitions. This requires knowledge of the activation energies E_a for both the direct and inverse reactions, i.e., in our case, the activation energies for polymerization and depolymerization. To date, many works have been performed to determine the activation energies E_a for the depolymerization of C_{60} polyfullerenes [3–8]. However, as far as we know, only two works have dealt with the determination of the activation barrier to polymerization. In particular, the activation energy (E_a = 38.6 kJ/mol) for pressure-induced polymerization of C_{60} was indirectly obtained by Soldatov *et al.* [9] from the experimental data on thermal conductivity. Ozaki *et al.* [10] used the molecular dynamics approach to determine the activation energy (E_a = 400.4 kJ/mol) for the dimerization of C_{60} molecules. Comparison shows that these (theoretical and experimental) activation energies differ drastically.

This work is the first attempt, directly from the experiment, to determine the activation energy for an elementary act of pressure-induced 2 + 2 cycloaddition of the C_{60} fullerene. For this purpose, the kinetics of formation of $(C_{60})_2$ dimer molecules under a pressure of 1.5 GPa was investigated by vibrational spectroscopy.

2. SAMPLES AND EXPERIMENTAL TECHNIQUE

The dimerized samples were synthesized by treating the initial fullerite in Maksim (piston–cylinder-type) and Toroid high-pressure chambers under a pressure of 1.5 GPa at temperatures of 373, 383, 393, 403, 413, 423, 433, 453, and 473 K for different times (from 1 to 50000 s). The samples synthesized were stabilized under normal conditions through quenching under pressure and were then analyzed using IR spectroscopy. The IR spectra of the samples prepared in the form of pellets with KBr were recorded on a Specord M80 spectrophotometer.

3. RESULTS AND DISCUSSION

The kinetic curves for dimerization were constructed using the 796-cm^{-1} band in the IR spectra as an analytical band of the dimer molecule (for more details, see [11]). The figure displays the time dependences of the optical density for the analytical band of the dimer

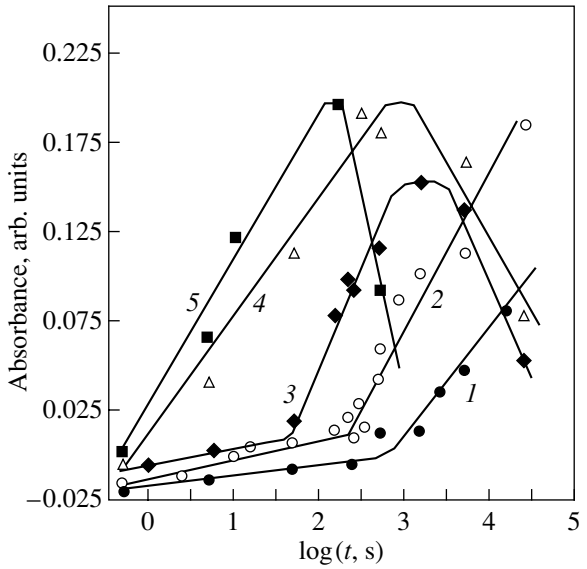

Dependences of the optical density for the analytical band of the $(C_{60})_2$ molecule on the logarithm of isothermal treatment time for C_{60} fullerite samples treated under a pressure of 1.5 GPa at different temperatures: (*1*) 373, (*2*) 393, (*3*) 413, (*4*) 423, and (*5*) 453 K.

molecule at different temperatures. These dependences characterize the changes in concentration of $(C_{60})_2$ dimers with variations in temperature. As is clearly seen from the curves shown in the figure, the dimerization of C_{60} molecules occurs through different mechanisms at temperatures above and below 423 K. In the temperature range below 423 K, which corresponds to the orientationally ordered phase of the fullerite [12, 13], the time dependences of the optical density are characterized by a pronounced induction period and represent *S*-shaped curves typical of autocatalytic reactions. At temperatures above 423 K, which correspond to the orientationally disordered phase of the fullerite, the induction period is absent and the formation of $(C_{60})_2$ dimers in appreciable amounts due to isothermal treatment occurs in a matter of seconds. It should also be noted that the kinetic curves exhibit maxima. This suggests that the dimers formed at the given parameters (pressure and temperature) are intermediate (rather than ultimate) products of the transformation of C_{60} linear polymers [11]. In view of the above features in the kinetic curves, their processing was performed only in portions corresponding to neither the induction periods nor the formation of C_{60} linear polymers. In order to determine the content of dimer molecules in the studied samples, we measured the optical density at a maximum of the analytical band. Then, this value was normalized to the optical density of the band for a pellet containing a specified amount of pure $(C_{60})_2$. This procedure made it possible to determine the degree of dimerization α. The reaction rate constants at different temperatures (see table) were determined under the assumption that the pressure-induced dimerization is an irreversible second-order reaction for which the integral kinetic equation can be represented in the form $kt = \alpha/(1 - \alpha)$, where k is the reaction rate constant and t is the treatment time.

Reaction rate constants for C_{60} dimerization at 1.5 GPa

T, K	*k*, s^{-1}
373	1.8×10^{-5}
383	1.0×10^{-4}
393	3.3×10^{-4}
403	4.4×10^{-4}
413	1.8×10^{-3}
423	5.8×10^{-3}
433	8.5×10^{-3}
453	5.2×10^{-2}

By using the data obtained and the Arrhenius equation $k = A\exp(-E_a/RT)$, we determined the preexponential factor $A = (1.74 \pm 0.24) \times 10^{14}$ s^{-1} and the activation energy $E_{a(\mathrm{dim})} = 134 \pm 6$ kJ/mol for dimerization of the C_{60} fullerene.

In conclusion, we should note that the activation energy $E_{a(\mathrm{dim})}$ for the dimerization of C_{60} molecules, which was directly determined in the present work, seems the most reliable among currently available data. In actual fact, unlike the activation energies obtained in [9, 10], the value of $E_{a(\mathrm{dim})} = 134 \pm 6$ kJ/mol is in good agreement with experimental and theoretical estimates of the activation energy E_a for the dissociation of $(C_{60})_2$ dimers [3–6].

ACKNOWLEDGMENTS

This work was supported by the Russian Foundation for Basic Research, project nos. 00-03-32600 and 97-03-71054.

REFERENCES

1. A. M. Rao, P. Zhou, K. A. Wang, *et al.*, Science **259**, 955 (1993).
2. B. Sundqvist, Adv. Phys. **48**, 1 (1999).
3. Y. Wang, J. M. Holden, X. Bi, and P. C. Eklund, Chem. Phys. Lett. **217**, 413 (1994).
4. P. Nagel, V. Pasler, S. Lebedkin, *et al.*, Phys. Rev. B **60**, 16920 (1999).
5. D. Porezag, M. R. Pederson, Th. Franenheim, and Th. Kohler, Phys. Rev. B **52**, 14963 (1995).

6. M. Menon, K. R. Subbaswany, and M. Sawtarie, Phys. Rev. B **49**, 13966 (1994).
7. G. B. Adams, J. B. Page, O. F. Sankey, and M. O. Keeffe, Phys. Rev. B **50**, 17471 (1994).
8. J. Fagerstrom and S. Stafstrom, Phys. Rev. B **53**, 13150 (1996).
9. A. Soldatov, K. Prassides, O. Andersson, and B. Sundqvist, in *Fullerenes: Proceedings of the Symposium on Recent Advances in the Chemistry and Physics of Fullerenes and Related Materials*, Ed. by K. M. Kadish and R. S. Ruoff (The Electrochemical Society, Pennington, 1998), Vol. 6.
10. T. Ozaki, Y. Iwasa, and T. Mitani, Chem. Phys. Lett. **285**, 289 (1998).
11. V. A. Davydov, L. S. Kashevarova, A. V. Rakhmanina, *et al.*, Phys. Rev. B **61**, 11936 (2000).
12. G. Kriza, J.-C. Ameline, D. Jerome, *et al.*, J. Phys. I **1**, 1361 (1991).
13. G. A. Samara, J. E. Schirber, B. Morosin, *et al.*, Phys. Rev. Lett. **67**, 3136 (1991).

Translated by O. Borovik-Romanova

Physics of the Solid State, Vol. 44, No. 3, 2002, pp. 560–562. Translated from Fizika Tverdogo Tela, Vol. 44, No. 3, 2002, pp. 534–536.

PROCEEDINGS OF THE V INTERNATIONAL WORKSHOP "FULLERENES AND ATOMIC CLUSTERS"

(St. Petersburg, Russia, July 2–6, 2001)

Synthesis and EPR Spectroscopy of Nitroxyl Derivatives of the C_{60} Fullerene

V. N. Ivanova, V. A. Nadolinnyĭ, I. A. Grigor'ev, and E. Rejerse

Institute of Inorganic Chemistry, Siberian Division, Russian Academy of Sciences, pr. Akademika Lavrent'eva 3, Novosibirsk, 630090 Russia

e-mail: iva@che.nsk.su

Abstract—The 2,2,5,5-tetramethyl-3-imidazoline-3-oxy-1-oxyl-4-(azidophenyl) derivatives of the C_{60} fullerene with one (compound **I**), two (compound **II**), and three (compound **III**) nitroxyl groups are synthesized and studied by EPR spectroscopy. It is demonstrated that successive addition of nitroxyl radicals to C_{60} leads to a decrease in the rotational mobility of molecules. Chromatographically inseparable isomers are found for compounds **II** and **III**. © *2002 MAIK "Nauka/Interperiodica".*

1. INTRODUCTION

Fullerenes and their derivatives have attracted considerable interest because they are promising materials for use in biology and medicine [1, 2]. A fullerene molecule has a size sufficiently large ($d \geq 7$ Å) for incorporation of several functional groups simultaneously, including bioactive groups [3] and radicals. The introduction of spin labels into fullerene molecules transforms them into objects convenient for EPR studies and substantially extends the range of problems solvable with their participation. For example, EPR oximetry [4] provides a means of monitoring the oxygen content in biological objects. This is one of the most important problems in molecular biology and modern medicine. The same is also true for controlled transport of bioactive groupings into specified regions of a particular cell or macromolecule [5, 6]. The use of spin labels offers a key to executing *in vivo* observations of the aforementioned processes. The labels most suitable for this purpose are 3-imidazoline nitroxyl radicals that possess unique properties and are traditionally used in molecular biology and biophysics [7].

The [3 + 2] cycloaddition reactions provide a convenient way of functionalizing the C_{60} molecule, which, in this case, manifests itself as a 1,3-subpolarophilic compound [8, 9]. These reactions, with the participation of the azomethine [10] and diazo [10, 11] compounds serving as 1,3-dipoles, were used to prepare fullerene derivatives with nitroxyl radicals in the 2,2,5,5-tetramethyl substituted piperidine ring. In the present work, we synthesized and performed an EPR study of the nitroxyl derivatives of C_{60} with 2,2,5,5-tetramethyl-3-imidazoline-3-oxy-1-oxyl-4-(azidophenyl) (RN_3 [12]):

$$C_{60} + RN_3 \xrightarrow{-N_2} \underset{\mathbf{I}}{C_{60}(RN)} + \underset{\mathbf{II}}{C_{60}(RN)_2} + \underset{\mathbf{III}}{C_{60}(RN)_3}.$$

2. SAMPLE PREPARATION AND EXPERIMENTAL TECHNIQUE

2.1. Instrumentation. The EPR measurements were performed using a Varian E-109 spectrometer operating in the *X* band. The UV spectra were recorded on a Specord UV–Vis spectrophotometer. The IR spectra were measured on a Specord M-80 spectrometer with the use of KBr pellets. The reaction products were separated by thin-layer chromatography on an $LSL_{254}5/40$ silica gel (Lachema–Chemapol). The progress of the reactions was monitored by thin-layer chromatography using Silufol UV 254 plates.

2.2. Materials. The C_{60} fullerene was prepared using a laboratory setup according to the modified procedure [13]. The product was isolated through extraction with benzene and (or) toluene followed by chromatography on a carbon sorbent with benzene used as an eluent. The fullerene purity was checked by high-performance liquid chromatography with spectrophotometric detection (λ = 330 nm) and by IR spectroscopy (KBr). Phenyl azide RN_3 was synthesized at the Novosibirsk Institute of Organic Chemistry, Siberian Division, Russian Academy of Sciences [12].

Nitroxyl derivatives **I**–**III** were prepared by the reaction of C_{60} (100 mg, 0.14 mmol) with the RN_3 azide (115 mg, 0.42 mmol) in a benzene solution (100 ml) at temperatures in the range from 75 to 80°C for four weeks. The reaction mixture was separated by chromatography on Silufol UV 254 plates with benzene and a benzene–ethanol mixture (10 : 1) used as eluents. The ultimate products isolated from the mixture were as follows: compound **I** (13 mg, 18 wt % with respect to the reacted C_{60} fullerene), compound **II** (3 mg, 3 wt %), compound **III** (1 mg, 0.9 wt %), and unreacted C_{60} fullerene (46 mg, 46 wt %). Compound **I**: UV (ethanol)

1063-7834/02/4403-0560$22.00 © 2002 MAIK "Nauka/Interperiodica"

(λ_{max}, nm) 258, 327, 480; IR (KBr) (ν, cm^{-1}) 1534, 1461, 1437, 1358, 1289, 1189, 585, 576, 545, 526.

For $C_{73}H_{16}O_2N_3 \cdot 2EtOH$, anal. calcd. (wt %): C, 87.32; H, 2.67; N, 3.97.

Found (wt %): C, 87.36; H, 2.62; N, 3.90.

3. RESULTS AND DISCUSSION

The reaction between C_{60} and RN_3 can result in one (compound **I**) or more (compounds **I**–**III**) products, depending on the reaction conditions (temperature, time, and reactant ratio). According to the chromatographic data, the polarity of the sequentially formed reaction products increases when changing over from **I** to **III**. As follows from the elemental analysis, compound **I** is the product of addition of an RN_3 molecule to the C_{60} molecule followed by the release of N_2.

The UV–Vis spectrum of compound **I** in ethanol exhibits bands at λ = 258 and 327 nm and a low-intensity broad absorption in the range of λ = 480 nm, which is typical of fullerene derivatives with an open annulene-like structure [14]. It has been demonstrated theoretically and experimentally that the [3 + 2] cycloaddition of azides to C_{60}, as a rule, leads to the formation of open 5,6-adducts of the annulene type [15]; however, there are exceptions [16].

The IR spectrum of compound **I** contains the vibrational bands assigned to its constituent molecules (C_{60} and RN_3), except for two intense bands associated with vibrations of the azide group at 2125 and 2094 cm^{-1}. The vibrational spectra of 3-imidazoline-3-oxide nitroxyl radicals are characterized by the bands attributed to the ν(C=N) and ν(N $\longrightarrow$ O) stretching vibrations of the nitro group [7]. In particular, the ν(C=N) band in the spectra of compounds **I** and RN_3 is observed at the same frequency (1534 cm^{-1}), even though this band for the former compound has a lower intensity. The vibrations of the N $\longrightarrow$ O bond, which is sensitive to vibrations of the imidazoline ring (1380–1350 cm^{-1} [7]), are most pronounced in the range of 1289 cm^{-1}. In the spectrum of RN_3, these vibrations are responsible for a strong band at 1289.5 cm^{-1}. The band associated with the stretching vibrations of the nitroxyl group is often masked by an intense band corresponding to the bending vibrations of the geminal methyl groups in the 2-position of the imidazoline ring. In the spectrum of compound **I**, the broadened intense band with a maximum at 1437 cm^{-1} can be attributed to the stretching vibrations of the N–O group and the geminal CH_3 groups in the 2-position of the imidazoline ring. The spectrum of the initial azide shows a relevant band at 1421 cm^{-1} and a doublet at 1448 and 1466 cm^{-1}. By analogy with ternary aromatic amines (1360–1310 cm^{-1} [17]), an intense band at 1358 cm^{-1} can be assigned to the C–N vibrations at the junction of the fullerene fragment and the phenyl ring. In the spectrum of RN_3, the relevant intense band is observed at 1354 cm^{-1}.

Correlation times of nitroxyl radicals

No.	Compound	$\tau \times 10^{10}$, s
1	RN_3	3
2	$C_{60}(RN)$, **I**	5.4
3	$C_{60}(RN)_2$, **II**	9.5
4	$C_{60}(RN)_3$, **III**	18.9

Of the four characteristic bands of the C_{60} fullerene (1428, 1182, 575, and 526 cm^{-1}), the spectrum of its derivative **I** contains only the narrow intense band attributed to the breathing vibrations of the C_{60} carbon cage at 526 cm^{-1}. The addition of RN_3 to the C_{60} fullerene brings about a lowering of the symmetry of the resulting compound and gives rise to a number of bands assigned to the bending vibrations (585, 576, and 545 cm^{-1}). The vibrations of C–C single bonds in the fullerene are observed in the range of 1189 cm^{-1} against the background of the carbon–carbon vibrations of the geminal CH_3 group (1195–1120 cm^{-1}). The vibrations of C=C double bonds in the C_{60} fragment (1428 cm^{-1}) contribute to the aforementioned broad band at 1437 cm^{-1}.

Compounds **I**–**III** were investigated by EPR spectroscopy in a benzene–ethanol (5 : 1) solution at room temperature. The mobility of these compounds was analyzed within the correlation time formalism [18]. The correlation times (table) were calculated from the formula $\tau = 6.65\Delta H^+(\sqrt{I^+/I^-} - 1) \times 10^{-10}$ s, where ΔH^+ is the width of the low-field component (in G) and I^+ and I^- are the intensities of the low-field and high-field components, respectively. A decrease in the mobility in the order $\tau(RN_3) < \tau(\mathbf{I}) < \tau(\mathbf{II}) < \tau(\mathbf{III})$ corresponds to successive additions of 3-imidazoline nitroxyl radicals to the bulk molecule of C_{60}.

The EPR spectra of compound **I** and the RN_3 azide exhibit a hyperfine structure due to the nitroxyl nitrogen splitting and are characterized by the hyperfine structure parameter $A_N(\mathbf{I}) = 14.61$ G. The EPR spectrum of adduct **II** is a superposition of two spectra, namely, the spectrum of a monoradical and a weaker spectrum of a biradical with the hyperfine structure parameter $A_N(\mathbf{II}) = A_N(\mathbf{I})/2 = 7.3$ G. Investigations into the isomerism of C_{60} fullerene bisadducts [19, 20] give grounds to believe that the second nitroxyl radical can be attached to compound **I** either in a polar position or in a mutually perpendicular equatorial position (more closely spaced) with respect to the already existing radical in the molecule. In the first two cases (the monoradical and the biradical with a polar arrangement), the distance between unpaired nitroxyl electrons is relatively large (>10 Å), the exchange interaction is absent, and

these electrons manifest themselves as single electrons in the EPR spectra. The weak spectrum of the biradical indicates the formation of small amounts of an isomeric $C_{60}(RN)_2$ compound with a close arrangement of radical fragments for which the exchange interaction is significant.

The EPR spectrum of adduct **III** is also a superposition of two spectra, namely, an intense spectrum of the monoradical and a weak spectrum whose hyperfine structure parameter is three times less than that for the monoradical [A_N(**III**) = A_N(**I**)/3 = 4.87 G]. This suggests that there are two trisadduct isomers with different spin states. The spectrum with a lower intensity corresponds to the energetically less favorable isomer with $S = 3/2$. This situation is observed when three nitroxyl radicals are closely spaced with respect to each other on the surface of the C_{60} fullerene. The isomer with $S = 1/2$ is formed in larger amounts. In this case, the radicals are arranged in such a way that the total spin S of two radicals is equal to zero and the third radical is free.

4. CONCLUSION

The above investigation demonstrated that spin labels can be introduced into fullerene molecules through the [3 + 2] cycloaddition of 3-imidazoline nitroxyl radicals. The synthesis of these compounds provides insight into the interaction between two and more paramagnetic centers in the same molecule. It was shown that EPR spectroscopy offers unique possibilities of revealing and examining microscopic amounts of inseparable isomers.

ACKNOWLEDGMENTS

We are grateful to M.A. Voĭnov and I.A. Kirilyuk for supplying the nitroxyl radical samples used in our investigations.

This work was supported by the NWO (Holland), grant no. 047-006-010.

REFERENCES

1. T. Da Ros and M. Prato, J. Chem. Soc., Chem. Commun., 663 (1999).
2. L. J. Wilson, Electrochem. Soc. Interface, 24 (1999).
3. C. Toniolo, A. Bianco, M. Maggini, *et al.*, J. Med. Chem. **37**, 4558 (1994).
4. V. K. Kol'tover, E. É. Laukhina, Ya. I. Éstrin, *et al.*, Dokl. Akad. Nauk **353** (1), 57 (1997).
5. S. H. Friedman, D. L. DeCamp, R. P. Sijbesma, *et al.*, J. Am. Chem. Soc. **115**, 6506 (1993).
6. R. P. Sijbesma, G. Srdanov, F. Wudl, *et al.*, J. Am. Chem. Soc. **115**, 6510 (1993).
7. L. B. Volodarskiĭ, I. A. Grigor'ev, S. A. Dikanov, V. A. Reznikov, and G. I. Shchukin, *Imidazoline Nitroxyl Radicals* (Nauka, Novosibirsk, 1988).
8. A. Hirsch, Synthesis **8**, 895 (1995).
9. O. G. Sinyashin, I. P. Romanova, G. G. Yusupova, *et al.*, Mendeleev Commun., 61 (2000).
10. F. Arena, F. Bullo, F. Conti, *et al.*, J. Am. Chem. Soc. **119**, 789 (1997).
11. T. Ishida, K. Shinozuka, T. Nogami, *et al.*, Tetrahedron **52** (14), 5103 (1996).
12. V. A. Reznikov, T. A. Berezina, I. A. Kirilyuk, and L. B. Volodarskiĭ, Izv. Akad. Nauk, Ser. Khim., No. 3, 465 (1994).
13. R. E. Haufler, J. Conceicao, L. P. F. Shibante, *et al.*, J. Phys. Chem. **94**, 8634 (1990).
14. A. B. Smith and H. Tokuyama, Tetrahedron **52** (14), 5257 (1996).
15. A. Hirsh, J. Phys. Chem. Solids **58** (11), 1729 (1997).
16. O. G. Sinyashin, I. P. Romanova, G. G. Yusupova, *et al.*, Mendeleev Commun., 96 (2000).
17. J. R. Dyer, *Applications of Absorption Spectroscopy of Organic Compounds* (Prentice-Hall, Englewood Cliffs, 1965; Khimiya, Moscow, 1970).
18. A. M. Vasserman and A. L. Kovarskiĭ, *Spin Labels and Probes in Physics and Chemistry of Polymers* (Nauka, Moscow, 1986).
19. B. Nuber, F. Hampel, and A. Hirsch, J. Chem. Soc., Chem. Commun., 1799 (1996).
20. L. Pasimeni, A. Hirsch, I. Lamparth, *et al.*, J. Am. Chem. Soc. **119**, 12896 (1997).

Translated by O. Borovik-Romanova

Physics of the Solid State, Vol. 44, No. 3, 2002, pp. 563–566. Translated from Fizika Tverdogo Tela, Vol. 44, No. 3, 2002, pp. 537–540.

PROCEEDINGS OF THE V INTERNATIONAL WORKSHOP "FULLERENES AND ATOMIC CLUSTERS"

(St. Petersburg, Russia, July 2–6, 2001)

Molecular Properties of C_{60} Fullerene Complexes with Cycle-Containing Polymers in Solutions

N. P. Yevlampieva*, P. N. Lavrenko, E. Yu. Melenevskaya**, L. V. Vinogradova**, E. I. Ryumtsev*, and V. N. Zgonnik****

** Institute of Physics, St. Petersburg State University, Ul'yanovskaya ul. 1, St. Petersburg, 198504 Russia*

*** Institute of Macromolecular Compounds, Russian Academy of Sciences, Bol'shoĭ pr. 31, St. Petersburg, 199004 Russia*

e-mail: yevlam@paloma.spbu.ru

Abstract—The donor–acceptor complexes of the C_{60} fullerene with cycle-containing polymers, namely, poly(2,6-dimethyl-1,4-phenylene oxide) (PPhO) and poly(*N*-vinylpyrrolidone) (PVP), are studied. A comparative analysis of the hydrodynamic and electrooptical properties of the initial polymers and their complexes with C_{60} in solutions demonstrates that the C_{60} fullerene has a restructuring effect on the polymer macromolecule, thus decreasing the degree of asymmetry of the macromolecular structure. © *2002 MAIK "Nauka/Interperiodica".*

1. INTRODUCTION

In recent years, increased interest has been expressed by researchers in the biological aspects of practical application of fullerene-containing compounds. This explains the considerable increase in the number of works dealing with the synthesis of donor–acceptor (especially, water-soluble) complexes of the C_{60} fullerene [1–3], among which are C_{60} complexes with polymers [4–6]. However, the majority of publications concerning polymer complexes of the C_{60} fullerene are reduced only to a description of the synthesis procedure and the determination or refinement of their composition. The available data on the molecular and physical properties of polymer complexes with fullerenes are very scarce, even though compounds of this class offer undeniable advantages over other fullerene-containing materials. First, compared to covalent bonds, coordination bonds involved in the structure of the new chemical compound are substantially more favorable to the retention of unique physical properties of the fullerene. Second, from the practical point of view, the polymer complex can serve as a matrix that is able to retain the fullerene during transfer in media that undissolve this fullerene and to release the fullerene in required small amounts under special actions that destroy the complex.

In the present work, we carried out a comparative investigation of the molecular properties of C_{60} complexes with two cycle-containing polymers, namely, poly(2,6-dimethyl-1,4-phenylene oxide) (PPhO) and poly(*N*-vinylpyrrolidone) (PVP), and the properties of the initial samples of PPhO and PVP. Moreover, we made an attempt to elucidate how the fullerene involved in the structure of the complexes affects the molecular characteristics of the initial polymers. For this purpose, we used traditional techniques of evaluating the hydrodynamic size, shape, and mobility of macromolecules in solutions, such as translational diffusion, velocity sedimentation, viscometry, and the electrooptical Kerr effect.

2. SAMPLES AND EXPERIMENTAL TECHNIQUE

The C_{60} complexes with PPhO and PVP at different molecular weights of the initial polymers were prepared by vacuum recondensation of a mixture of a C_{60} solution in toluene and a polymer solution in chloroform [6]. The formation of C_{60} complexes with these polymers was confirmed by spectral methods in our earlier works [4, 5]. The structural formulas of the initial polymers are depicted in Fig. 1. The degrees of polymerization *n* and the ratios of the number of fullerene molecules to the number of polymer mole-

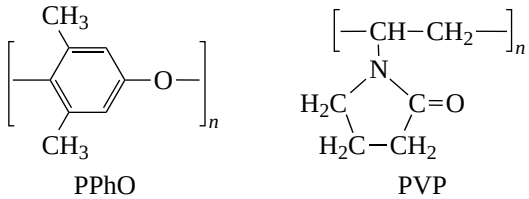

Fig. 1. Structural formulas of the initial polymers.

1063-7834/02/4403-0563$22.00 © 2002 MAIK "Nauka/Interperiodica"

Table 1. Degree of polymerization *n* of the initial PPhO and PVP samples and the fullerene-to-polymer molecule ratio *m* in the donor–acceptor complexes of C_{60} with PPhO and PVP

Sample	*n*	*m*
PPhO-1	530	1 : 1
PPhO-2	1500	1 : 1
PVP-1	90	1 : 6
PVP-2	110	1 : 6

cules in the composition of the complexes under investigation are listed in Table 1.

The electrooptical and hydrodynamic properties of PPhO polymers and their complexes with C_{60} were examined in benzene solutions. The PVP samples and their complexes with C_{60} were studied in two solvents: the translational diffusion and viscosity characteristics of PVP-1 and its complex with C_{60} were determined using aqueous solutions, and the electrooptical and viscosity characteristics of PVP-2 and its complex with C_{60} were obtained using chloroform.

The electrooptical Kerr effect in solutions of the initial polymers and their complexes was investigated in a rectangular-pulsed electric field. The compensation technique of measuring the Kerr effect was described in detail in [7]. The specific parameters of the setup used in our measurements are given in [8]. The equilibrium electrooptical properties of the studied polymers are characterized by the specific Kerr constant *K* defined as

$$K = \lim_{\substack{c \to 0 \\ E \to 0}} [(\Delta n - \Delta n_0)/E^2 c].$$

Here, $(\Delta n - \Delta n_0)$ is the difference between the birefringences induced by an electric field in a solution of the studied compound and in the solvent, respectively; *E* is the electric field strength; and *c* is the solute concentration.

The intrinsic viscosity [η] of the polymers and their complexes with C_{60} was determined using Ostwald capillary viscometers [9].

The translational diffusion was studied by the conventional method of forming the polymer solution–solvent interface in a Tsvetkov diffusiometer at a temperature of 25°C [9]. The diffusion coefficients *D* were calculated from the spreading of the diffusion boundary according to the standard algorithm [9]. Specifically, the diffusion coefficients were determined from the time change in the variance σ^2 of the diffusion curve: $D = (1/2)(d\sigma^2/dt)$. The diffusion coefficients $D_0 = \lim_{c \to 0} D$ were obtained by extrapolating the calculated coefficients *D* to zero concentration of the solution. The values of D_0 are presented in Table 2.

The velocity sedimentation was investigated using a MOM 3180 analytical ultracentrifuge (Hungary) with a two-section cell at a rotational speed $n = 5 \times 10^4$ min^{-1}. The technique of recording the sedimentation boundary and the method of measuring the translational diffusion were described in detail in [7, 9]. The sedimentation coefficients *S* were calculated from the shift in the concentration boundary with time. The sedimentation coefficients $S_0 = \lim_{c \to 0} S$ were determined by extrapolating the calculated coefficients *S* to zero concentration of the solute in the solution.

Table 2. Intrinsic viscosity [η], diffusion coefficient D_0, sedimentation coefficient S_0, molecular mass *M*, refractive index increment *dn*/*dc*, effective hydrodynamic volume *V*, and shape asymmetry function *f*(*p*) of an equivalent spheroid for molecules of the initial polymers and their complexes with the C_{60} fullerene in solutions at 25°C

Sample (solvent)	[η], cm^3/g	$D_0 \times 10^7$, cm^2/s	$S_0 \times 10^{13}$, s	$M \times 10^{-3}$	*dn*/*dc*, cm^3/g	$V \times 10^{20}$, cm^3	*f*(*p*)
PPhO-1 (benzene)	59 ± 1	6.1 ± 0.5	–	30 ± 5	0.1	88	3.3
C_{60}–PPhO-1 (benzene)	47 ± 2	6.0 ± 0.4	–	37 ± 5	0.09	93	3.1
PPhO-2 (benzene)	99 ± 2	3.0 ± 0.3	4.0 ± 0.1	140 ± 40	0.1	720	3.2
C_{60}–PPhO-2 (benzene)	86 ± 1	2.5 ± 0.5	3.8 ± 0.2	160 ± 20	0.09	1250	2.0
PVP-1 (H_2O)	12 ± 1	8.9 ± 0.5	–	12 ± 2	0.16	6.0	4.0
C_{60}–PVP-1 (H_2O)	9.5 ± 0.5	8.1 ± 0.5	–	12 ± 2	0.15	8.0	2.4
PVP-2 ($CHCl_3$)	15 ± 1	–	–	12	–	–	–
C_{60}–PVP-2 ($CHCl_3$)	12.5 ± 0.8	–	–	–	–	–	–

Note: The molecular masses *M* of the PPhO-2 and C_{60}–PPhO-2 samples are calculated from the Svedberg equation [9] $M_{SD} = [RT/(1 - \nu\rho_0)](S_0/D_0)$ at the buoyancy factor $(1 - \nu\rho_0) = 0.24$ [6]; the molecular masses *M* of the PPhO-1, C_{60}–PPhO-1, PVP-1, and C_{60}–PVP-1 samples are determined from the relationship [9] $M_{D\eta} = (A_0 T/\eta_0 D)^3/[\eta]$ at the hydrodynamic invariant $A_0 = 3.2 \times 10^{-10}$ g cm^2 K^{-1} mol$^{-1/3}$; and the molecular mass *M* of the PVP-2 sample is taken from the manufacturer (Serva) data.

3. RESULTS AND DISCUSSION

The electrooptical Kerr effect in polymer solutions is a very sensitive technique with respect to any changes in intramolecular interactions in the macromolecular chains [7]. The birefringence that arises in the polymer solution in an external electric field directly depends on the dipole moment and polarizability of the polymer macromolecules. Hence, it follows that the birefringence is determined by the conformation and flexibility of the macromolecular chains. In the case when the weight fraction of the polymer involved in the complex is predominant (as follows from Table 1, this is true for the studied complexes), the complex formation between polymer molecules and a small number of C_{60} molecules can also be treated as a factor affecting the character of intramolecular interactions in PPhO and PVP. For this reason, we could assume beforehand that the electrooptical properties of C_{60} complexes with PPhO and PVP should change compared to those of the initial polymers. However, the similarity observed in these changes for both polymers that strongly differ in structure and molecular parameters proved unexpected.

Figure 2 shows the concentration dependences of the Kerr constant K for C_{60} fullerene complexes with PPhO and PVP and for the initial polymer samples. As can be seen from this figure, the formation of the C_{60} coordination compounds with PPhO and PVP leads to a decrease in the magnitude of the electrooptical constant. Close values of K are observed for C_{60} fullerene complexes with the PPhO-1 and PPhO-2 polymers, which have different molecular weights but are characterized by the same ratio of the number of fullerene molecules to the number of polymer molecules in the corresponding complexes (Table 1). This can indicate that the C_{60} fullerene interacts with a specific number of PPhO monomer units, because the initial polymers PPhO-1 and PPhO-2 exhibit identical electrooptical properties. Observations of the translational diffusion demonstrate that the hydrodynamic size of diffusing particles increases upon formation of the C_{60} complexes with PPhO and PVP. The obtained data on changes in the volume V of equivalent spheres simulating the macromolecules are listed in Table 2. The volume $V = \pi a^3/6$ (where a is the diameter of a sphere) was calculated from the Stokes–Einstein relationship $a = kT/3\pi\eta_0 D_0$ with the use of the experimental diffusion coefficients D_0. In our previous work [6], we performed a comparative investigation of the diffusion and sedimentation processes in benzene solutions of the PPhO-2 polymer and the C_{60} complex with PPhO-2. It was found that the molecular mass M and translational mobility (the coefficients S_0 and D_0, respectively) of the PPhO complex with a single fullerene molecule virtually do not differ from those for the PPhO initial polymer [6]. However, for all the complex–initial polymer pairs considered in the present work, the hydrodynamic investigations clearly revealed small changes in the diffusion coefficients and electrooptical properties (see systematic changes in the refractive index increment dn/dc in Table 2) of the PPhO and PVP macromolecular complexes with C_{60} fullerene.

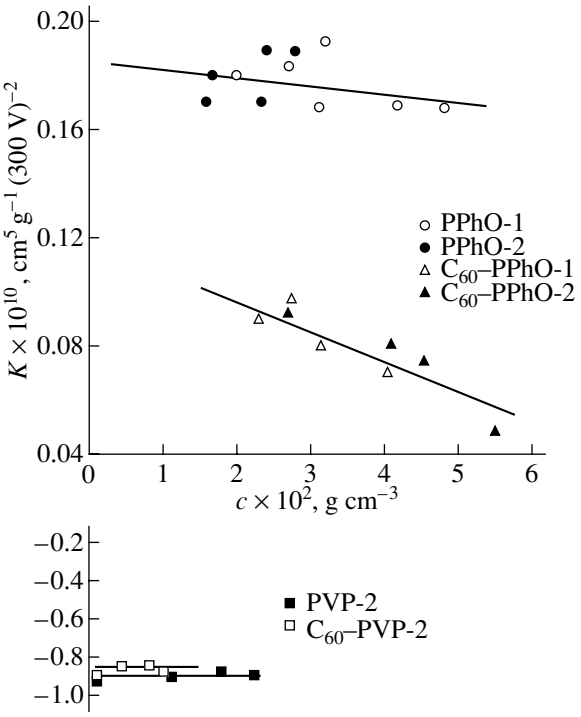

Fig. 2. Concentration dependences of the specific Kerr constant K for initial samples of PPhO-1 and PPhO-2 in benzene (circles), PVP-2 in chloroform (closed squares), and complexes of these polymers with C_{60} in the same solvents (triangles and open squares).

The viscometric measurements also indicate that the hydrodynamic behavior of the PPhO and PVP molecules differs from that of their fullerene complexes. It should be noted that, compared to the initial polymers, the effective hydrodynamic size V of the polymer complexes with the C_{60} fullerene increases, whereas the intrinsic viscosity $[\eta]$ of the complexes decreases (see the corresponding column in Table 2). This hydrodynamic characteristic of the macromolecule depends on the rotational mobility and shape of the particles involved. According to [9], the general relationship for the intrinsic viscosity of solid nondeformable spheroidal particles with a shape asymmetry p can be written as $[\eta] = N_A V f(p)/M$, where N_A is the Avogadro number and $f(p)$ is the shape asymmetry function of a spheroid. From this relationship and the above findings, we can conclude that the initial polymers and their complexes with the C_{60} fullerene differ in molecular shape asymmetry. It seems likely that the polymer complexes are more symmetric in shape, because the value of $f(p)$ for the C_{60} fullerene complexes with PPhO and PVP decreases compared to that for the initial polymers (see the last column in Table 2). This result of hydrody-

namic investigations qualitatively explains the experimentally observed decrease in the magnitude of the electrooptical effect in solutions of the polymer complexes, because a more symmetric distribution of chain units should lead to a decrease in the total optical anisotropy and polarity of the coiled macromolecule.

4. CONCLUSIONS

Thus, the basic results obtained in this work can be summarized as follows.

(1) It was shown that the PPhO and PVP polymers form stable complexes with the C_{60} fullerene. The hydrodynamic characteristics of the C_{60} fullerene complexes with PPhO (the initial fullerene-to-polymer molecule ratio is 1 : 1) and C_{60} complexes with PVP (the initial fullerene-to-polymer molecule ratio is 1 : 6) were determined in the concentration range 0.004–0.06 g cm^{-3}.

(2) No aggregates in solutions of the C_{60} complex with PPhO in benzene and the C_{60} complex with PVP in water and chloroform were revealed by the experimental techniques used in the present work.

(3) It was found that the effective hydrodynamic size of the C_{60} complexes with PPhO and PVP is slightly larger and the particle shape asymmetry for these complexes in solutions is smaller than those of the initial polymer molecules.

(4) A decrease in the magnitude of the electrooptical Kerr constant for polymer complexes with the C_{60} fullerene, as compared to that for the initial polymers, is in qualitative agreement with the hydrodynamic data, according to which the particles of the complexes in solutions exhibit a higher symmetry.

ACKNOWLEDGMENTS

This work was supported by the Russian Research Program “Fullerenes and Atomic Clusters” (project no. 98076) and the Federal Program “Integration” (project no. 326.38).

REFERENCES

1. D. V. Konarev and R. N. Lyubovskaya, Usp. Khim. **68** (1), 23 (1999).
2. M. Sundahl, T. Andersson, K. Nilsson, *et al.*, Synth. Met. **55–57**, 3252 (1993).
3. R. Bensasson, E. Bievenue, M. Dellinger, *et al.*, J. Phys. Chem. **98**, 3492 (1994).
4. L. V. Vinogradova, E. Yu. Melenevskaya, A. S. Khachaturov, *et al.*, Vysokomol. Soedin. **40** (11), 1854 (1998).
5. G. Torok, V. T. Lebedev, L. Scer, *et al.*, in *Proceedings of the 4th Biennial International Workshop “Fullerenes and Atomic Clusters,” St. Petersburg, 1999*, p. 59.
6. P. N. Lavrenko, N. P. Yevlampieva, D. M. Volokhova, *et al.*, Vysokomol. Soedin., Ser. A **44** (3), 289 (2002).
7. V. N. Tsvetkov, *Rigid-Chain Polymer Molecules* (Nauka, Leningrad, 1986; Plenum, New York, 1989).
8. Yu. F. Biryulin, N. P. Yevlampieva, E. Yu. Melenevskaya, *et al.*, Pis’ma Zh. Tekh. Fiz **26** (15), 39 (2000) [Tech. Phys. Lett. **26**, 662 (2000)].
9. V. N. Tsvetkov, V. E. Éskin, and S. Ya. Frenkel, *Structure of Macromolecules in Solutions* (Nauka, Moscow, 1964; Butterworths, London, 1970).

Translated by O. Borovik-Romanova

Physics of the Solid State, Vol. 44, No. 3, 2002, pp. 567–568. Translated from Fizika Tverdogo Tela, Vol. 44, No. 3, 2002, pp. 541–542.

PROCEEDINGS OF THE V INTERNATIONAL WORKSHOP "FULLERENES AND ATOMIC CLUSTERS"

(St. Petersburg, Russia, July 2–6, 2001)

Formation of Polymer Complexes of Transition Metals with Fullerene

A. P. Popov and I. V. Bazhin

Don State Technical University, Rostov-on-Don, 344010 Russia
e-mail: ib_rnd@mail.ru

Abstract—This paper reports on the results of *ab initio* unrestricted Hartree–Fock (UHF) calculations of the equilibrium geometry and binding energy for the transition-metal complexes $Me(C_5H_5)_2$ and $Me(C_6H_6)_2$ and the energetically stable metallofullerene complexes $Me(C_{60})_2$, where *Me* = Ti, V, Cr, Fe, and Ni. The calculation technique is worked out using the ferrocene molecule. The calculated geometry and binding energy agree satisfactorily with the experimental data. © *2002 MAIK "Nauka/Interperiodica".*

1. INTRODUCTION

In recent years, a large number of works have been devoted to the investigation of metal complexes with fullerenes. The considerable interest expressed in these compounds is motivated by their unique physicochemical properties and possible use in nanoelectronics. The majority of these works are concerned with description of the syntheses of metal complexes with fullerenes and the investigation of their properties [1–3]. So far, theoretical studies have been performed only with complexes of alkali metals with fullerenes. As far as we know, there are few works that deal with the calculations of the structure and electronic properties of iron complexes with fullerene [4]. However, by analogy with the properties of transition metal carbides, we can assume that fullerene complexes with other transition metals also exist.

In the present work, we carried out quantum-chemical calculations of the equilibrium geometry, total energy, and binding energy for fullerene complexes with Ti, V, Cr, Fe, and Ni. These compounds were chosen as the objects of investigation because they have been most frequently mentioned in published papers.

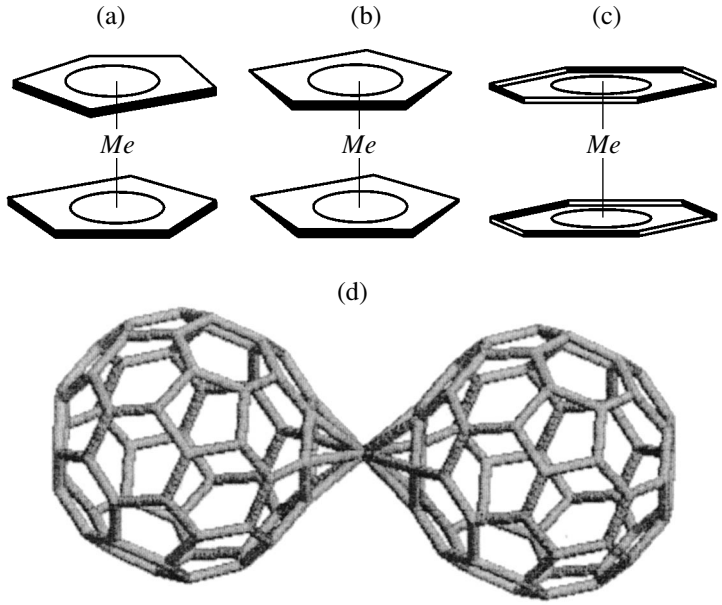

Fig. 1. Possible types of sandwich structures: (a) ferrocene type, (b) rutenocene type, (c) $Me(C_6H_6)_2$ type, and (d) metallofulerene complex.

1063-7834/02/4403-0567$22.00 © 2002 MAIK "Nauka/Interperiodica"

Table 1. Results of the calculation of $Me(C_5H_5)_2$ metallocenes in the configuration shown in Fig. 1a

Me	r_{5-5}, nm	E_{tot}, arb. units	ΔE_{bind}, kcal/mol
Ti	0.299	–1235.426	20.311
V	0.274	–1329.587	247.564
Cr	0.334	–1429.475	–25.675
Fe	0.326	–1647.586	160.343
Ni	0.329	–1891.043	–27.591

Table 2. Results of the calculation of $Me(C_5H_5)_2$ metallocenes in the configuration shown in Fig. 1b

Me	r_{5-5}, nm	E_{tot}, arb. units	ΔE_{bind}, kcal/mol
Ti	0.306	–1235.424	11.311
V	0.298	–1329.507	210.154
Cr	0.341	–1429.531	–8.901
Fe	0.299	–1647.177	135.875
Ni	0.345	–1890.543	102.624

Table 3. Results of the calculation of $Me(C_6H_6)_2$ complexes in the configuration shown in Fig. 1c

Me	r_{6-6}, nm	E_{tot}, arb. units	ΔE_{bind}, kcal/mol
Ti	0.277	–1304.508	307.896
V	0.298	–1398.687	–50.719
Cr	0.287	–1503.193	–16.793
Fe	0.283	–1716.775	105.864
Ni	0.368	–1959.384	2.775

Table 4. Results of the calculation of the most stable complexes $Me(C_{60})_2$

Me	Type of the complex	*r*, nm	E_{tot}, arb. units	ΔE_{bind}, kcal/mol
Ti	Fig. 1c	0.291	–5332.512	87.314
V	Fig. 1b	0.302	–5427.054	56.572
Cr	Fig. 1c	0.293	–5566.637	7.023
Fe	Fig. 1a	0.328	–5745.023	89.921
Ni	Fig. 1b	0.317	–5744.998	74.615

2. OBJECTS OF INVESTIGATION AND CALCULATION TECHNIQUE

At the initial stage of this work, we studied transition-metal complexes of the sandwich type with pentadienyl, $Me(C_5H_5)_2$ (Figs. 1a, 1b), and benzene, $Me(C_6H_6)_2$ (Fig. 1c). It is reasonable to assume that the chemical bond in these comparatively simple complexes is of the same nature as the chemical bond in $Me(C_{60})_2$ complexes. This is experimentally confirmed by the fact that the metal atoms in $Me(C_{60})_2$ complexes are located either between a pair of pentagons or between a pair of hexagons.

The calculations of the equilibrium configuration and electronic structure of the metal complexes under investigation were performed using the GAMESS software package [5]. The calculation technique, including justification of the choice of the *ab initio* unrestricted Hartree–Fock (UHF) method and procedures providing stable convergence of the self-consistency process, was worked out on a well-studied object, namely, the ferrocene molecule.

3. RESULTS AND DISCUSSION

Tables 1–3 represent the basic parameters of transition-metal complexes with pentadienyl, $Me(C_5H_5)_2$ (metallocenes), and benzene, $Me(C_6H_6)_2$, including the distance between the ligands, total energy, and binding energy. The calculations demonstrated that satisfactory agreement between our results and the available experimental data was achieved with mixed basis sets, namely, MINI (the minimal Huzinaga basis) for transition metals, STO-6G for carbon, and STO-3G for hydrogen. The calculated data presented in Tables 1–3 correspond to the mutual orientation of the ligands shown in Figs. 1a–1c. The binding energies listed in Tables 1 and 2 differ by 5–30 kcal/mol. This agrees with experimental data on the rotation potential barrier between two possible orientations of the pentadienyl rings. The results of calculations indicate that not all of the studied complexes are energetically stable.

The energy parameters of the metallofulerene complexes were calculated using available data on the mutual orientation and distances between the ligands in complexes with pentadienyl and benzene. Table 4 presents the geometric and energy characteristics of the most stable metallofulerene complexes. Figure 1d shows the typical arrangement of the metal and ligands in the complex.

REFERENCES

1. W. Zhao, Y. Li, L. Chen, *et al.*, Solid State Commun. **92**, 313 (1994).
2. J. Fye and M. Jarrold, Int. J. Mass Spectrom. Ion Processes **185**, 507 (1999).
3. L. Qian, L. Norin, J. Guo, *et al.*, Phys. Rev. B **59**, 12667 (1999).
4. E. G. Gal'pern, I. V. Stankevich, and A. L. Chistyakov, Fiz. Tverd. Tela (St. Petersburg) **43**, 951 (2001) [Phys. Solid State **43**, 989 (2001)].
5. M. W. Schmidt, K. K. Baldridge, and J. A. Boatz, J. Comput. Chem. **14**, 1347 (1993).

Translated by O. Moskalev

Physics of the Solid State, Vol. 44, No. 3, 2002, pp. 569–571. Translated from Fizika Tverdogo Tela, Vol. 44, No. 3, 2002, pp. 543–545.

PROCEEDINGS OF THE V INTERNATIONAL WORKSHOP "FULLERENES AND ATOMIC CLUSTERS"

(St. Petersburg, Russia, July 2–6, 2001)

A Neutron Spin-Echo Study of the Dynamics of Star-Shaped Polymers (with Polystyrene Arms Grafted to C_{60}) in Solutions and in the Bulk

V. T. Lebedev*, Gy. Török, L. Cser**, D. N. Orlova*, V. A. Bershteĭn***, V. N. Zgonnik****, E. Yu. Melenevskaya****, L. V. Vinogradova****, and V. P. Budtov*******

** St. Petersburg Institute of Nuclear Physics, Russian Academy of Sciences, Gatchina, Leningrad oblast, 188300 Russia*
e-mail: vlebedev@mail.pnpi.spb.ru
*** Institute of Solid-State Physics and Optics, Budapest, Hungary*
e-mail: torok@power.szfki.kfki.hu
**** Ioffe Physicotechnical Institute, Russian Academy of Sciences, Politekhnicheskaya ul. 26, St. Petersburg, 194021 Russia*
e-mail: vbersht@polmater.ioffe.rssi.ru
***** Institute of Macromolecular Compounds, Russian Academy of Sciences, Bol'shoĭ pr. 31, St. Petersburg, 199004 Russia*
e-mail: melen@hq.macro.ru
****** Center of Scientific Expert Examination, Elizarov prosp. 14, St. Petersburg, 193029 Russia*
e-mail: cnir@city.com.ru

Abstract—Methods of small-angle and inelastic neutron scattering were used to study star-shaped polymers obtained by grafting polystyrene to fullerene C_{60} (six arms with an elementary mass $M = 5 \times 10^3$). The behavior of stars in the solution and bulk was compared with the dynamics of free molecules of polystyrene with a mass equal to the mass of an arm. The slow dynamics of arms in the ranges of times $t = 0.01$–20 ns, momentum transfers $q = 0.2$–0.6 nm^{-1}, and temperatures $T = 20$–60°C does not obey the simple models of Rouse and Zimm. The interaction of the rays with the C_{60} fullerene under the conditions of the specific geometry of the macromolecule leads to unusual oscillations of time correlations in the arms of stars. © *2002 MAIK "Nauka/Interperiodica".*

INTRODUCTION

Fullerene derivatives can reveal extraordinary physical and chemical properties (such as superconductivity, ferromagnetism, and solubility anomalies) that are not observed in the initial substances [1, 2]. In particular, the bonding of polymer chains to a spherical surface of the fullerene C_{60} makes it possible to synthesize macromolecules in the form of stars with various numbers of arms [3]. These arms are not only covalently bonded to the fullerene through their end links but also can interact with the fullerene surface by the mechanism of charge transfer and van der Waals forces. This unusual combination of covalent bonds and possible donor–acceptor complexes in a single macromolecule can strongly change the polymer dynamics and its behavior in both solution and bulk. Thus, recently, when studying stars built of polyethylene oxide grafted to C_{60}, we revealed in D_2O an unusual dynamics of its arms, which is rather inherent of block polymers in the glass-transition range [4]. Based on the data on the solubility of fullerene C_{60} [5], it might be expected that an efficient interaction of the arms with fullerene would occur if the arms contain six-term cycles similar to hexagons present in C_{60}. Therefore, we synthesized and investigated just polystyrene stars.

1. STRUCTURE OF STARS FOUND FROM SMALL-ANGLE NEUTRON SCATTERING

The polystyrene (PS) molecules (six arms, each of mass $M = 5 \times 10^3$) were grafted to the fullerene core using the method of living chains [6] and then were studied using neutron diffraction in comparison with free PS molecules in deuterated benzene (C_6D_6) in the range of momentum transfers $q = (4\pi/\lambda)\sin(\theta/2) = 0.2$–$5$ nm^{-1} (θ is the scattering angle and $\lambda = 0.6$ nm is the neutron wavelength). In addition, we prepared deuterated stars, which were dissolved in an analogous ordinary (hydrogenated) polymer matrix in order to ensure maximum contrast in the scattering amplitudes in neutron diffraction experiments. To the first approximation, the scattering in solutions and in the bulk for labeled macromolecules of the stars and PS obeys the law $I(q) = I_0[1 + (r_C q)^2]^{-1}$, where I_0 is the scattering

1063-7834/02/4403-0569$22.00 © 2002 MAIK "Nauka/Interperiodica"

Correlation radii of stars and PS

Concentration of labeled molecules, wt %	r_C, nm	
	PS	stars
1.0 (protonated molecules in deuterated benzene C_6D_6)	1.35 ± 0.16	2.74 ± 0.14
1.0 (deuterated molecules in protonated matrix)	1.16 ± 0.20	2.69 ± 0.18
10.0 (deuterated molecules in protonated matrix)	1.00 ± 0.03	2.32 ± 0.09

intensity in the limit $q \longrightarrow 0$ and r_C is the correlation length of a molecule related to its radius of gyration $R_G = \sqrt{3}\, r_C$ (see table). At low concentrations of labeled molecules (C = 1 wt %), their experimentally measured dimensions in benzene and in the polymer matrix are virtually the same, which indicates the same virtually undisturbed conditions (θ conditions, under which no long-range interactions of chain units are observed). Indeed, both in the solution and in the bulk, the gyration radius of polystyrene R_{GPS} = 1.7–2.0 nm agrees with the estimate for a Gaussian chain R_{Gauss} = 2.0 nm. The experimentally measured radius of the star R_{GST} = 4.7 nm approaches the distance between the ends of the PS chain: $R_{GST} \approx h_{PS} = \sqrt{6}\, R_{GPS}$ = 4.9 nm. This means that the arms do not condense onto the surface of the fullerene but rather tend to move from it. At the same time, the measured ratio of the dimensions of the "star" and an arm in the bulk R_{GST}/R_{GPS} = 2.3 is larger by 40% than the calculated value for the Gaussian distribution of the elements of the chain [6]: $R_{GST}/R_{GPS} = [(3f - 2)/f]^{1/2}$ = 1.6, where f = 6 is the number of star arms. Thus, the star-shaped molecule is somewhat expanded as compared to the undisturbed conformation. Below, based on the above data, we studied the dynamics of these stars.

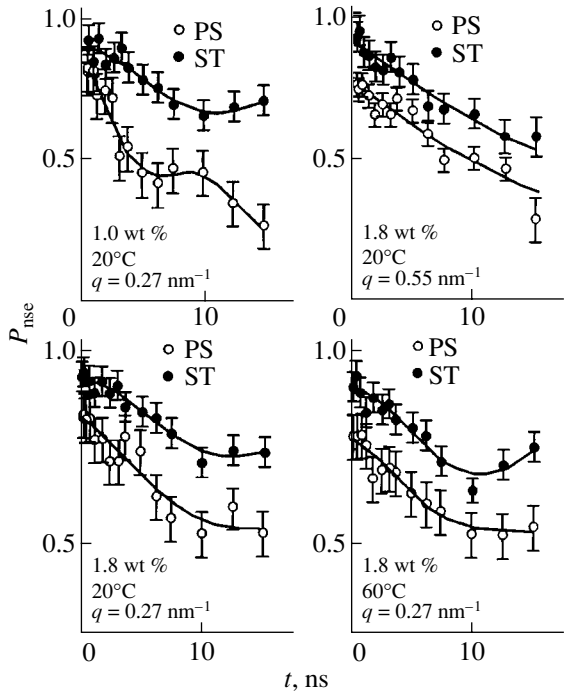

Dynamics of PS and stars in solution at various temperatures, polymer concentrations, and momentum transfers.

2. DYNAMICS OF STARS

Neutron spin-echo (NSE) experiments were performed in the L. Brillouin Laboratory, Saclay, using PS and stars in deuterated benzene (C_6D_6) at 20–60°C with characteristic momentum transfers q_1 = 0.27 and q_2 = 0.55 nm^{-1} in a range of times t = 0.1–20 ns. On the scale of $R \sim 1/q_1 \sim 3.7$ nm > $R_{GPS} \sim 2.3$ nm, which is greater than the dimensions of a PS arm but smaller than the "star" size, we can observe the dynamics of arms bonded to the fullerene core and interacting between themselves. On a smaller scale of $R \sim 1/q_2 \sim 1.8$ nm ≤ $L_S \sim 2$ nm, only segmental dynamics (L_S is the length of a PS segment) should mainly be observed. On the segmental level, the dynamics in stars is somewhat suppressed. In benzene at 20°C and a polymer concentration of C = 1.8 wt %, the coefficient of diffusion of arm segments $D_{ST} = (1.23 \pm 0.11) \times 10^{-6}$ cm^2/s is 20% smaller than the diffusion coefficient for free PS: $D_{PS} = (1.52 \pm 0.17) \times 10^{-6}$ cm^2/s (see figure). On the scale of an arm radius, the effect of the arm bonding to the fullerene surface is revealed more strongly (see figure). Even at a low concentration of the polymer in the solution (C = 1 wt %), the stars distinctly reveal a crossover to an oscillating dynamics (see figure). In the Gaussian approximation for the self-correlations of units, the spin-echo signal follows the function $P_{nse}(q, t) = S(q, t)/S(q, t = 0) = \exp[-q^2\Gamma(t)/2]$, where the root-mean square displacement of the scattering particle $\Gamma(t) = A^2[1 - \cos(\Omega t)]$ for the time t has the character of oscillations with an amplitude $A = 2.0 \pm 0.1$ nm and frequency $\Omega = (0.28 \pm 0.02) \times 10^9$ rad/s. Under the same conditions, the chains of free polystyrene take part in intense diffusive motion, when the displacement increases with time as $\Gamma(t) = D_{PS}t + a^2[1 - \cos(\omega t)]$. In the case of free chains, the dominating process is diffusion with a diffusion coefficient $D_{PS} = (8.1 \pm 1.1) \times 10^{-6}$ cm^2/s. The oscillations have the same amplitude $a = 2.0 \pm 0.2$ nm, but their frequency $\omega = (0.60 \pm 0.05) \times 10^9$ rad/s is twice as large as that characteristic of "stars." An increase in the polymer concentration leads to an increase in the molecular interaction, and the difference between the dynamics of PS and stars becomes less pronounced. At C = 1.8 wt %, no noticeable temperature variations in the dynamics are observed at T = 20–60°C in both solutions. The dynamics follows the same model. Under these conditions, PS has a smaller

diffusion coefficient $D_{PS}(q_1) = (3.1 \pm 0.7) \times 10^{-6}$ cm^2/s, showing oscillations with a smaller frequency $\omega = (0.37 \pm 0.05) \times 10^9$ rad/s and a smaller amplitude $a = 1.5 \pm 0.3$ nm. As was expected, an increase in the concentration by a factor of 1.8 produced a smaller effect on the internal dynamics of "stars," since the concentration of the polymer in their volume is already quite high (~30 wt %). At 20–60°C, the values of the corresponding parameters for the stars are smaller as compared to PS: $D_{ST}(q_1) = (1.9 \pm 0.7) \times 10^{-6}$ cm^2/s, $\Omega = (0.30 \pm 0.02) \times 10^9$ rad/s, and $A = 1.3 \pm 0.2$ nm.

Then, we studied stars and PS at a higher temperature $T = 90$°C near the glass temperature of the polymers ($T_G = 89$°C for PS and 94°C for stars). In the bulk, the diffusive mobility of the polymers is strongly suppressed. Thus, on the segmental scale, the diffusion coefficient in stars $D_{ST}(q_2) = (2.0 \pm 1.2) \times 10^{-7}$ cm^2/s is of an order of magnitude smaller than that in the solution. On a larger scale ($R \sim 1/q_1$), the oscillating dynamics is dominating, as in the solution. The PS chains have an amplitude of the oscillating motion $a = 2.52 \pm 0.12$ nm, which exceeds the segment length, and a frequency $\omega = (0.34 \pm 0.01) \times 10^9$ rad/s, which is close to that in the solution. Stars have smaller amplitudes and frequencies ($A = 1.66 \pm 0.09$ nm, $\Omega = (0.30 \pm 0.02) \times 10^9$ rad/s), which are close to the dynamical parameters obtained for these characteristics in the solution.

The dynamics of the polymers studied in this work, which strongly differ in their molecular structure from one another, reveals common regular features upon transition from the solution to the bulk state near the glass-transition temperature, when the diffusive motions are strongly slowed and the dynamic correlations between chain links oscillate with a period $T = 2\pi/\omega \sim 20$ ns. In the case of stars, the period is longer by 10–20%. Effectively, the complex dynamics of the polymer is described as an oscillation of a fragment of the chain with an amplitude of an order of the segment length. In a star, the amplitude is smaller by 10–30% as compared to free PS. The covalent bonding of an arm with the fullerene, as well as the van der Waals and donor–acceptor interactions with its surface, increase the energy of activation of molecular motion by a quantity of an order of $\Delta E \sim [\ln(\omega/\Omega)](kT) \sim 0.5$ kJ/mol.

ACKNOWLEDGMENTS

This work was supported in part by the Russian Foundation for Basic Research (project no. 00-15-96814), the Ministry of Industry and Science of the Russian Federation (project "Fullerene Stars"), and the program on the Neutron Studies of Condensed Matter. We are also grateful to Dr. A. Brûlet (L. Brillouin Laboratory) and I.N. Ivanova and S.M. Bogdanovich (St. Petersburg Institute of Nuclear Physics, Russian Academy of Sciences) for their assistance in the experiments and description of the results.

REFERENCES

1. E. N. Karaulova and E. I. Bagriĭ, Usp. Khim. **68** (1), 979 (1999).
2. S. V. Kozyrev and V. V. Rotkin, Fiz. Tekh. Poluprovodn. **27** (9), 1409 (1993).
3. D. Richter, O. Jucknischke, L. Willner, L. J. Fetters, M. Lin, J. S. Huang, J. Poovers, C. Toporovsky, and L. L. Zhou, J. Phys., Coll. C **8**, Suppl. 3, 4 (1993).
4. Gy. Török, V. T. Lebedev, L. Cser, D. N. Orlova, Gy. Kali, A. I. Sibilev, V. L. Alexeev, V. A. Bershteĭn, V. P. Budtov, V. N. Zgonnik, L. V. Vinogradova, and E. Yu. Melenevskaya, Physica B (Amsterdam) **297**, 45 (2001).
5. V. Zgonnik, E. Melenevskaya, L. Vinogradova, L. Litvinova, J. Kever, E. Bykova, A. Khachaturov, and S. Klenin, Mol. Mater. **8**, 45 (1996).
6. H. Benoit, J. Polym. Sci. **11**, 507 (1953).

Translated by S. Gorin

Physics of the Solid State, Vol. 44, No. 3, 2002, pp. 572–573. Translated from Fizika Tverdogo Tela, Vol. 44, No. 3, 2002, pp. 546–547.

PROCEEDINGS OF THE V INTERNATIONAL WORKSHOP "FULLERENES AND ATOMIC CLUSTERS"

(St. Petersburg, Russia, July 2–6, 2001)

Small-Angle Neutron-Scattering Study of Anomalous C_{60} Clusterization in Toluene

Gy. Török*, V. T. Lebedev, and L. Cser***

** Research Institute for Solid State Physics and Optics, POB 49, H-1525, Budapest, Hungary*
e-mail: torok@power.szfki.kfki.hu
*** St. Petersburg Nuclear Physics Institute, Russian Academy of Sciences, Gatchina, Leningrad oblast, 188300 Russia*
e-mail: vlebedev@mail.pnpi.spb.ru

Abstract—This paper reports on a small-angle neutron-scattering study (in the momentum transfer range q = 0.005–0.08 Å^{-1}) of the structure of C_{60} fullerene clusters in a saturated toluene solution at 20°C. Large-scale fractal structures formed by small clusters with radius $R_C \sim 30$ Å are shown to persist in the solution after prolonged storage (for one year) at 20°C. The results are discussed in terms of the well-known fullerene aggregation models. © *2002 MAIK "Nauka/Interperiodica".*

1. INTRODUCTION

The discovery by Ruoff [1] of the anomalous temperature dependence of solubility of the C_{60} fullerene in a number of solvents stimulated both experimental and theoretical studies of the unusual behavior of fullerenes in solutions, because this problem, besides being of fundamental significance, has considerable application potential in the technologies involved in the separation of fullerenes in mass in the course of their production. A good idea of the state of the art in this area of fullerene research can be gained from review [2]. This review presents a drop model of fullerene clusterization and puts forward a concept of long-lived structural relaxation of its solution, which gives rise to growth of large-scale fractal structures. The structural features of C_{60} solutions on the scale of tens of nanometers can be directly investigated using small-angle neutron diffraction. However, the low fullerene content in a solution (usually, at a level of a few tenths of 1 wt %) and the strict requirements on the solvent aimed at providing the maximum possible fullerene contrast make such experiments difficult. Another aspect of these experiments is that the solution has to reach the equilibrium state, which makes its prolonged storage in stationary conditions necessary (constant temperature, absence of perturbations due to vibrations). We succeeded in meeting these requirements in our experiment and in observing C_{60} fractal structures in toluene.

2. SMALL-ANGLE NEUTRON DIFFRACTION FROM A C_{60} SOLUTION IN TOLUENE

To obtain reliable information on fullerene clusterization in solution, we carried out small-angle diffraction measurements on a C_{60} sample dissolved in protonated toluene to saturation at 20°C (fullerene concentration $C \sim 2.8$ mg/ml). Next, the system was maintained for one year at the same temperature, after which it was studied again. The range of momentum transfers, $q = (4\pi/\lambda)\sin(\theta/2) = 0.005$–$0.08$ Å^{-1}, was chosen large enough to cover the scale region from $r \sim 1/q_{max} \sim 10$ Å, comparable to the fullerene diameter, to distances $R \sim 1/q_{min} \sim 200$ Å two orders of magnitude larger than the C_{60} radius within which molecular correlations inherent in fractal structures are observable. The neutron wavelength was varied from λ = 3 to 10 Å.

Figure 1 displays typical patterns of neutron scattering from clusters. It can be seen from the figure that the scattering intensity $I(q)$ is noticeably greater in the region of small momenta, $q < 0.02$ Å^{-1}, and that there is a broad local maximum of intensity within the interval q_m = 0.03–0.04 Å^{-1}. The first feature is indicative of the presence of large associates (not less than ~100 Å in size) in the solution. The second feature shows that the clusters do not scatter independently of one another; they are separated by a characteristic distance $L \sim 2\pi/q_m \sim 200$ Å. These two features are described by the scattering law

$$I(q) = I_0[1 + (R_C q)^2]^{-D/2} \times [1 + \Gamma \sin(q/L)/(qL)] + I_{inc}, \quad (1)$$

where I_{inc} is the intensity of incoherent scattering (primarily, from the solvent). The coherent part is determined by the form factor of a scattering particle (fullerene, cluster) and by the structural factor of the system. The parameter I_0 characterizes forward scattering, $I(q \longrightarrow 0) = I_0$, where there is no interference in scattering from single particles (Γ = 0). The length R_C is the correlation length of the particles, which may be

1063-7834/02/4403-0572$22.00 © 2002 MAIK "Nauka/Interperiodica"

Parameters of the scattering function in Eq. (1)

Experiment no.	q, Å^{-1}	R_C, Å	L, Å	Γ	D
1	0.01–0.08	33.3 ± 3.6	221 ± 8	3.2 ± 0.4	4
2	0.01–0.07	25.5 ± 3.6	200 ± 15	6.7 ± 4.1	4
3	0.005–0.04	1×10^3	201 ± 55	1.2 ± 1.0	2.95 ± 0.96

fractal clusters of dimension D spaced at a distance L. For the wavelengths λ = 3, 6, and 10 Å, the data are approximated by Eq. (1) with the fitting parameters given in the table.

Scattering in the region q = 0.01–0.08 Å^{-1} is dominated by small clusters of radius R_C = 25–30 Å, which form fractal structures such that there is interference from neutrons scattered from different structures. Judging from the magnitude of the parameter Γ = 3–7, this interference is fairly strong (for pairs of particles, we would have Γ = 1). The distance $L \sim 200$ Å, corresponding to the interference maximum, exceeds the size of a single cluster by an order of magnitude. An analysis made of the region of smaller momenta q = 0.005–0.04 Å^{-1} by the same model estimates the correlation length of fractal clusters as $R_C \sim 1 \times 10^3$ Å and their fractal dimension as $D_F \sim 2.9$, which supports the presence of interference in the scattering from clusters (see table). As seen from the parameters in the table, the structure reaches a close-to-equilibrium state practically during the first week of measurements (the first experiment) on an as-prepared sample. After this, small clusters change gradually during a year to become more compact, in the course of which their correlation and interference lengths decrease.

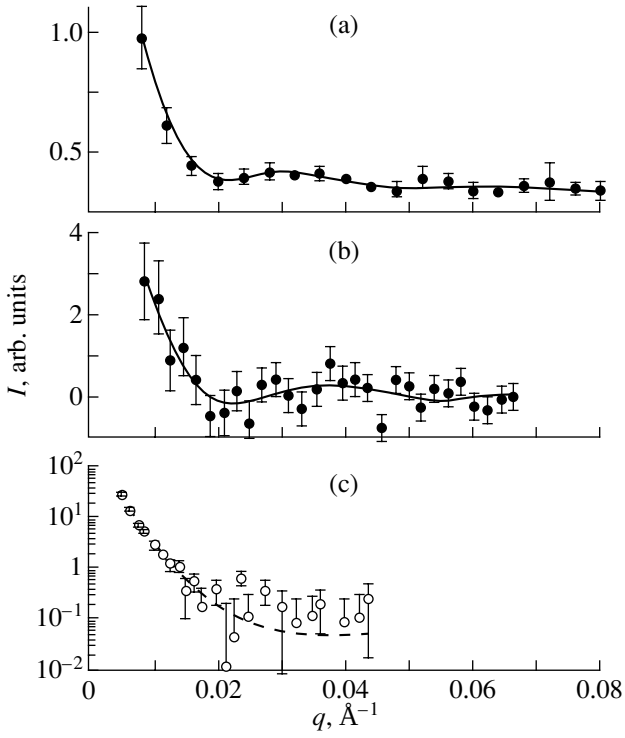

Fig. 1. Small-angle neutron scattering from C_{60} clusters in toluene. Measurements were made (a) over the period of a week on an as-prepared sample at 20°C (λ = 3 Å) and (b, c) on a sample stored for one year at 20°C (λ = 6 and 10 Å, respectively). The lines are fitting functions given by Eq. (1).

The results obtained lend support to the idea of the C_{60} fullerene being a unique cluster form of matter. Our experiments have established that, in solution, fullerene forms compact clusters with a characteristic radius $R_C \sim$ 25–30 Å which produce fractal structures. In Fig. 1a, the scattering from clusters is seen to be superposed on the background of incoherent scattering from the solvent protons. The intensity of the latter is I_{inc} = 0.35 arb. units. By crossing to absolute units, we obtained the cluster cross section and, knowing the scattering amplitude from one fullerene a_F, found the number of molecules per cluster $n = (I_0/I_{inc})N_P(\sigma_P/4\pi)(N_F a_F^2) \approx 50$, where N_P and N_F are the proton and fullerene concentrations in the sample, respectively, and σ_P is the total proton cross section. Assuming a cluster of radius $R \sim R_C \sim 30$ Å to contain 50 molecules, its volume $V = (4\pi/3)R_C^3$ will be filled only to ~30%. The results obtained agree qualitatively with the figures derived from the drop model of clusterization. A comprehensive comparison would require measurements with inclusion of an analysis of the cluster size distribution.

ACKNOWLEDGMENTS

The authors are indebted to A. Brûlet (Laboratoire Leon Brillouin, CEN-Saclay) and I.N. Ivanova and S.M. Bogdanovich of the PNPI for their assistance in the experiments and presentation of the results.

This study was supported by the Russian Foundation for Basic Research (project no. 00-15-96814), the Ministry of Industry and Science of the RF ("Fullerene Stars" project), and the program "Neutron Studies of Condensed Media."

REFERENCES

1. R. S. Ruoff, D. S. Tse, R. Malhotra, and D. C. Lorents, J. Phys. Chem. **97**, 3379 (1993).
2. V. N. Bezmel'nitsyn, A. V. Eletskiĭ, and M. V. Okun', Usp. Fiz. Nauk **168** (11), 1195 (1998) [Phys. Usp. **41**, 1091 (1998)].

Translated by G. Skrebtsov

Physics of the Solid State, Vol. 44, No. 3, 2002, pp. 574–575. From Fizika Tverdogo Tela, Vol. 44, No. 3, 2002, pp. 548–549.

PROCEEDINGS OF THE V INTERNATIONAL WORKSHOP "FULLERENES AND ATOMIC CLUSTERS"

(St. Petersburg, Russia, July 2–6, 2001)

Polyaniline Composites with Fullerene C_{60}[1]

I. Yu. Sapurina*, A. V. Gribanov*, M. V. Mokeev*, V. N. Zgonnik*, M. Trchová, and J. Stejskal*****

** Institute of Macromolecular Compounds, Russian Academy of Sciences, Bol'shoĭ pr. 31, St. Petersburg, 199004 Russia*

e-mail: sapurina@hq.macro.ru

*** Faculty of Mathematics and Physics, Charles University, Prague 8, 180 00 Czech Republic*

**** Institute of Macromolecular Chemistry, Academy of Sciences of the Czech Republic, Prague 6, 162 06 Czech Republic*

Abstract—Polyaniline–fullerene composites were prepared by the introduction of fullerene during polymerization of aniline. An investigation of the composites using FTIR and ^{13}C NMR spectroscopy indicated interaction between fullerene and the imine groups of polyaniline. The formation of a polyaniline–fullerene complex with a structure corresponding to a doped polyaniline was proved by wide-angle x-ray scattering analysis. The conductivity of composites is more than four orders of magnitude higher than that of undoped polyaniline and that of fullerene. Improvement in the thermal stability of composites was evaluated using TGA. © *2002 MAIK "Nauka/Interperiodica".*

Fullerene-C_{60}–conducting-polymer systems possess unique physical characteristics, including electronic conductivity and magnetic, optical, and photoinduced electron transfer properties. Ultrafast photoinduced electron transfer from polymeric donors, such as poly(*p*-phenylene vinylene) and polythiophene, to C_{60} enables the construction of plastic solar cells with energy conversion efficiencies of up to 3% [1–3]. Large-scale electro- and photodevices based on polyaniline (PANI) have been developed [4–6]. Combined with C_{60}, PANI is used in polymer grid triodes in which the current is controlled by the grid potential [7]. The efficiency of the devices is dramatically affected by the molecular morphology of C_{60} composites and, consequently, by the procedure of their preparation. The most commonly used method of blending solutions of both components is limited, because the solubility of these substances is very poor.

The procedure based on mixing *N*-methylpyrrolidone solutions of PANI and C_{60} reported in the literature [8–10] is complicated by the competitive reaction of C_{60} with the solvent. We developed a new method for preparing fullerene-containing PANI composites (PANI–C_{60}) that excludes the use of organic solvents.

1. PREPARATION OF PANI–C_{60} COMPOSITES AND BLENDS

The method for preparing PANI–C_{60} composites uses aniline polymerization for the introduction of C_{60} into growing polyaniline chains [11]. The oxidation of aniline with ammonium peroxydisulfate in an acidic aqueous medium can be summarized in the stoichiometric relation

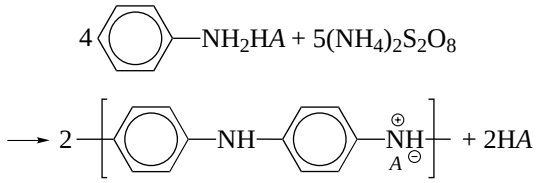

$$+ 5H_2SO_4 + 5(NH_4)_2SO_4.$$

Fullerene (2–10 wt % relative to aniline) was injected into an aqueous solution of aniline and sulfonic acid (H*A*, *A* denotes the corresponding anion). 4-Toluenesulfonic acid or dodecylbenzenesulfonic acid was used as the stabilizing and acidic agent. Polymerization was started through the addition of an aqueous solution of ammonium peroxydisulfate in an amount equimolar to that of aniline. The mixture was stirred or placed into an ultrasonic bath at room temperature for several hours. After polymerization, sulfonic acids were neutralized and repeatedly washed with an excess of aqueous (1 mol l^{-1}) ammonium hydroxide. This procedure excludes PANI doping with acids. The precipitates were separated by centrifugation, washed by acetone, and dried in vacuum at 25°C.

The PANI–C_{60} blends were prepared by mechanical mixing of both components with subsequent heat treatment at 85°C for 1 h.

[1] This article was submitted by the authors in English.

1063-7834/02/4403-0574$22.00 © 2002 MAIK "Nauka/Interperiodica"

2. CHARACTERIZATION OF PANI–C_{60} COMPOSITES

Properties of the composites are compared with those of corresponding blends and with two forms of neat PANI: emeraldine salt ($PANI_h$) and emeraldine base ($PANI_b$).

In the FTIR spectra of PANI–C_{60} composites, the peak corresponding to quinone-ring deformation shows a red shift to 1580 cm^{-1} in comparison with the spectrum of $PANI_b$ (1590 cm^{-1}), whereas the benzenoid-ring absorption peak remains virtually in the same position (at 1500 cm^{-1} in $PANI_b$). The 1240 cm^{-1} band characteristic of the conducting polaron structure C–N^+ and the characteristic vibration mode of the quinone ring at about 1165 cm^{-1} appear (both observed in the spectrum of $PANI_h$) and confirm the presence of an interaction between PANI and C_{60} [12]. Absorption at 1610 cm^{-1} observed in $PANI_h$ and corresponding to the N=ring stretching vibration mode is absent in the spectrum of PANI–C_{60} composites.

The ^{13}C NMR spectrum of C_{60} contains a single peak at 143 ppm. In the spectra of PANI–C_{60} composites, this signal shifts to 141 ppm. The main signal of neat $PANI_b$ at 121 ppm is assigned to the C–H groups of the quinoid rings. This peak shifts from 121 to 129 ppm as a result of acidic doping. Injection of C_{60} into polyaniline shifts the quinoid-ring carbon peak to 127 ppm.

The spectral investigation suggests the presence of an interaction between fullerene and the imine groups of PANI upon injection of C_{60} into PANI. Partial ground-state charge transfer, $PANI + C_{60} \longrightarrow PANI^{\delta+} - C_{60}^{\delta-}$, where $\delta \sim 0.05$, takes place in this system. However, there is no evidence of fullerene radical-anion formation.

The observed increase in the electrical conductivity caused by interaction of the components also reflects the charge transfer being associated with the doping of PANI. The conductivity of PANI–C_{60} composites (7×10^{-5} S cm^{-1}) increases by four orders of magnitude over the conductivities of the constituents (4×10^{-9} S cm^{-1} for $PANI_b$ and less than 10^{-9} S cm^{-1} for C_{60}) and by two orders of magnitude over the conductivity of the blend (1.5×10^{-7} S cm^{-1}).

Wide-angle x-ray diffractograms of a PANI–C_{60} composite are composed of the diffraction curve of C_{60} crystallites and a diffraction curve identical to that of the protonated form of PANI. This suggests that fullerene is a Lewis acid and acts as a dopant of PANI.

Photoluminescence spectra of $PANI_h$ and $PANI_b$ excited by 300-nm light exhibit a very similar shape in the range 350–510 nm. We observed PANI photoluminescence quenching upon addition of C_{60}. This fact points to photoinduced electron transfer in PANI–C_{60} blends and composites.

Thermogravimetric analysis shows an ordinary three-step decomposition pattern in the case of neat PANI forms and more complex degradation of composites. Blends and composites exhibit higher thermal stability than their parent polymers.

ACKNOWLEDGMENTS

This study was supported by the Russian Foundation for Basic Research (project no. 00-03-33083a), the Grant Agency of the Czech Republic (grant no. 202/02/0698), and the Academy of Sciences of the Czech Republic (grant no. K 4050111).

REFERENCES

1. C. J. Brabec, N. S. Sariciftci, and J. C. Hummelen, Adv. Funct. Mater. **11**, 15 (2001).
2. S. E. Shaheen, C. J. Brabec, N. S. Sariciftci, *et al.*, Appl. Phys. Lett. **78** (6), 841 (2001).
3. D. Gebeyehu, C. J. Brabec, F. Padinger, *et al.*, Synth. Met. **118**, 1 (2001).
4. P. Topart and P. Hourquebie, Thin Solid Films **352**, 243 (1999).
5. S.-A. Chen, K.-R. Chuang, C.-I. Chao, and H.-T. Lee, Synth. Met. **82**, 207 (1996).
6. G. Gustafsson, Y. Cao, G. M. Treacy, *et al.*, Nature **357**, 477 (1992).
7. J. McElvain, M. Keshavarz, H. Wang, *et al.*, J. Appl. Phys. **81** (9), 6468 (1997).
8. Y. Wei, J. Tian, A. G. MacDiarmid, *et al.*, J. Chem. Soc., Chem. Commun., 603 (1993).
9. M. Li and M. Wan, Solid State Commun. **93** (8), 681 (1995).
10. H. Y. Lim, S. K. Jeong, J. S. Suh, *et al.*, Synth. Met. **70**, 1463 (1995).
11. I. Sapurina, M. Mokeev, V. Lavrentev, *et al.*, Eur. Polym. J. **36**, 2321 (2000).
12. S. Quillard, G. Louarn, J. P. Buisson, *et al.*, Synth. Met. **84**, 805 (1997).

Physics of the Solid State, Vol. 44, No. 3, 2002, pp. 576–577. Translated from Fizika Tverdogo Tela, Vol. 44, No. 3, 2002, pp. 550–551.

PROCEEDINGS OF THE V INTERNATIONAL WORKSHOP "FULLERENES AND ATOMIC CLUSTERS"

(St. Petersburg, Russia, July 2–6, 2001)

Creation of a Donor–Acceptor Pair for Studying Intraprotein Electron Transfer with the Participation of Amino-Acid Derivatives of Fullerene C_{60}

R. A. Kotel'nikova*, G. N. Bogdanov*, G. V. Zotina*, V. S. Romanova, and Z. N. Parnes****

** Institute of Problems of Chemical Physics, Russian Academy of Sciences, Chernogolovka, Moscow oblast, 142432 Russia*

e-mail: kotel@icp.ac.ru

*** Nesmeyanov Institute of Organoelement Compounds, Russian Academy of Sciences, ul. Vavilova 28, Moscow, 117813 Russia*

Abstract—Efficient quenching of eosin phosphorescence by amino-acid derivatives of fullerene (AADFs) such as C_{60}–alanine and C_{60}–glycine in aqueous solutions indicates the possibility of transferring electrons from eosin to fullerene upon collisions or in the exciplex state. To investigate electron transfer in the protein structure, we studied the process of incorporation of C_{60}–alanine and C_{60}–glycine into the heme pocket of myoglobin by controlling Förster quenching. The dissociation constant for the protein–AADF complex was estimated. *© 2002 MAIK "Nauka/Interperiodica".*

Unique physical and chemical properties of fullerenes have attracted considerable interest from researchers. In recent years, special attention has been paid to the investigation of their effect on biological objects. Fullerenes were found to possess a cytotoxic activity [1], affect the selective cleavage of DNA [2], and exhibit antiviral activity, in particular, against the AIDS virus [3]. Many bioenergetic and biosynthesis processes include oxidation enzymatic reactions with stages of long-range electron transfer, in which an electron can tunnel distances of 5–20 Å from a donor to an acceptor along a protein molecule. Fullerenes, owing to their redox properties, can be used as efficient partners in such reactions. Recently, Kurz *et al.* [4] studied azurine with a covalently bound fullerene and revealed an efficient electron exchange between the copper-containing center of azurine and the fullerene. In some studies of electron transfer in proteins (in particular, in myoglobin), eosin was used as a photostimulated donor of electrons [5, 6]. Thus, eosin and fullerene can be used as an efficient donor–acceptor pair for the investigation of reactions of electron transfer in proteins and membranes. Such investigations can be performed using water-soluble amino-acid derivatives of fullerene (AADFs) [6, 7].

In this work, we studied photostimulated transfer of electrons between triplet-excited eosin and amino-acid derivatives of fullerene C_{60} in a solution and the interaction of these compounds with apomyoglobin to analyze reactions of long-range transfer of electrons in the protein.

To generate a donor–acceptor pair, we investigated the possibility of electron transfer between triplet-excited eosin (donor) and amino-acid derivatives of fullerene C_{60} (acceptors) in aqueous solutions by controlling the kinetics of the eosin-phosphorescence quenching using various concentrations of C_{60}–alanine and C_{60}–glycine. The samples were excited by pulse lasers with wavelengths λ_{ex} = 337 and 532 nm. The energy of a laser pulse was 70 mJ, which was sufficient for the complete excitation of the chromophores in the sample.

It was found that at λ_{ex} = 337 nm, the intensity and the lifetime of phosphorescence of the chromophore decreased with increasing concentration of the AADFs. In the case of eosin, the rate constant of quenching phosphorescence is $K_q = 0.4 \times 10^{-9}$ M^{-1} s^{-1}, which is close to that characteristic of the process of quenching the triplet-excited state of erythrosin by the mechanism described in [7]. At λ_{ex} = 532 nm, the intensity of the eosin phosphorescence decreased but the lifetime of the excited chromophore remained unaltered (see figure). This difference can be explained by the fact that at λ_{ex} = 377 nm, there occurs a simultaneous excitation of both eosin and the fullerene derivatives. The excited fullerene derivatives are efficient oxidation agents, and the quenching of the probe can occur by the mechanism of electron transfer upon diffusional collisions. When irradiating the sample with a laser with λ_{ex} = 532 nm, only eosin is excited, whereas the AADFs virtually do not absorb at 532 nm. In this case, the quenching of the

1063-7834/02/4403-0576$22.00 © 2002 MAIK "Nauka/Interperiodica"

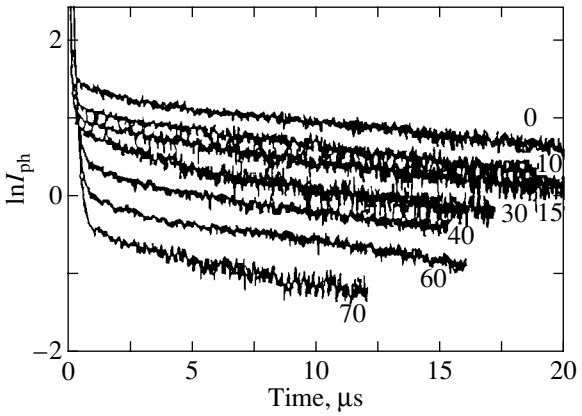

Effect of the concentration of C_{60}–alanine (in μM) on the kinetic of quenching of the eosin phosphorescence in a solution of tris-HCl (0.1 M, pH 7.2), λ_{ex} = 532 nm.

eosin phosphorescence appears to occur as a result of the formation of an exciplex.

The most important task in solving the problem of electron transfer in proteins is the production of a donor–acceptor pair in the protein structure. In this work, we studied the possibility of incorporating C_{60}–alanine and C_{60}–glycine into the heme pocket of myoglobin (instead of the removed heme) with the purpose of further realizing electron transfer from eosin bound to the terminal amino group of myoglobin. To solve this task, it was necessary to incorporate C_{60}–alanine and C_{60}–glycine into apomyoglobin. To this end, we removed the heme from the myoglobin by the technique described in [8]. Then, C_{60}–alanine and C_{60}–glycine were added to the solution of apomyoglobin. The process of incorporation of these compounds into apomyoglobin was controlled by changes in the intensity of fluorescence of the tryptophan residue of myoglobin. It is known that the tryptophan residue of myoglobin is located in the immediate proximity of the heme and that the spectrum of absorption of the C_{60} derivatives and the spectrum of fluorescence of the tryptophan residue overlap. This can result in the quenching of the fluorescence of the tryptophan residue by the mechanism of dipole–dipole resonance energy transfer at a distance not exceeding the Förster radius of quenching, which is 10 Å for the tryptophan–fullerene pair. When having been added to apomyoglobin in equimolar concentrations, the C_{60}–alanine and C_{60}–glycine were shown to quench the fluorescence of tryptophan by more than 50%. This permitted us to estimate the dissociation constant for the complexes of C_{60} derivatives with apomyoglobin to be $K \sim 10^{-5}$ M.

Thus, it is shown in this work that in aqueous solutions, there occurs a transfer of electrons from photoexcited eosin to C_{60}–alanine and C_{60}–glycine. The process of incorporation of amino-acid derivatives of the fullerene C_{60} into the heme pocket of apomyoglobin was effected, and the equilibrium constant for this complex was estimated.

ACKNOWLEDGMENTS

This work was supported in part by the Scientific and Technical Program “Fullerenes and Atomic Clusters” (project no. 3K-2001) and the Russian Foundation for Basic Research (project no. 00-04-48392).

REFERENCES

1. H. Tokuyama, S. Nakamura, and E. Nakamura, J. Am. Chem. Soc. **115**, 7918 (1993).
2. A. S. Boutorine, H. Tokuyama, M. Takasugi, H. Isobe, E. Nakamura, and C. Helene, Angew. Chem., Int. Ed. Engl. **33**, 2462 (1994).
3. S. H. Friedman, D. L. De Caamp, R. P. Sijbesma, G. Srdanov, F. Wudl, and G. L. Kenyon, J. Am. Chem. Soc. **115**, 6506 (1993).
4. A. Kurz, C. M. Halliwell, J. J. Davis, H. A. Hill, and G. Ganters, Chem. Commun. 433 (1998).
5. V. R. Vogel, A. V. Pastukhov, B. L. Psikha, and A. I. Kotelnikov, Biophysics **42**, 1019 (1997); E. Zagavy and I. Willner, J. Am. Chem. Soc. **118**, 12499 (1996).
6. R. A. Kotelnikova, A. I. Kotelnikov, G. N. Bogdanov, V. S. Romanova, E. F. Kuleshova, Z. N. Parnes, and M. E. Vol’pin, FEBS Lett. **389**, 111 (1996).
7. A. Bianco, T. Da Ros, M. Prato, and C. Toniolo, J. Peptide Sci. **7**, 208 (2001).
8. F. W. Teale, J. Biochim. Biophys. Acta **35**, 543 (1959).

Translated by S. Gorin

Physics of the Solid State, Vol. 44, No. 3, 2002, pp. 578–580. Translated from Fizika Tverdogo Tela, Vol. 44, No. 3, 2002, pp. 552–553.

PROCEEDINGS OF THE V INTERNATIONAL WORKSHOP "FULLERENES AND ATOMIC CLUSTERS"

(St. Petersburg, Russia, July 2–6, 2001)

Fullerene C_{60} Complexed with Poly(*N*-vinyl-pyrrolidone) Prevents the Disturbance of Long-Term Memory Consolidation

I. Ya. Podol'skiĭ, E. V. Kondrat'eva, I. V. Shcheglov, M. A. Dumpis, and L. B. Piotrovskiĭ

Institute of Theoretical and Experimental Biophysics, Russian Academy of Sciences, Pushchino, Moscow oblast, 142290 Russia

e-mail: podolski@venus.iteb.serpukhov.su

Abstract—A microinjection of C_{60}/poly-(*N*-vinyl-pyrrolidone) (C_{60}/PVP) adduct into the dorsal hippocampus is shown to prevent the disturbance of spatial memory consolidation induced by the administration of a high dose of cycloheximide, which inhibits protein synthesis in the central nervous system by more than 90%. It is supposed that microinjections of the C_{60}/PVP adduct into the hippocampus suppress the death of its neurons, which may be one of the essential factors that prevent the disturbance of long-term memory consolidation by protein-synthesis inhibition. Other mechanisms of the fullerene action are also possible; however, they remain as yet unknown. *© 2002 MAIK "Nauka/Interperiodica".*

1. INTRODUCTION

In the late 1990s, it was demonstrated on several experimental models, *in vitro* and *in vivo*, that fullerenes and their derivatives have a high antioxidant activity and protect neurons from genetically programmed cell death (apoptosis) [1, 2]. These findings suggest that these compounds may be efficient neuroprotectors useful in treating neurodegenerative human diseases such as amyotrophic lateral sclerosis and Parkinson's disease [1–3] and can prevent radiation damage [4].

Many diseases of the brain (Alzheimer's disease, atherosclerosis, and craniocerebral injuries) are accompanied by disturbances of long-term memory consolidation [5]. The suppression of protein synthesis in the brain by protein-synthesis inhibitors is one of the most thoroughly studied models of disturbances of long-term memory consolidation. Protein-synthesis inhibitors do not affect learning but strongly disturb information storage [6]. It was shown recently [7, 8] that high doses of protein-synthesis inhibitors lead to neuronal apoptosis [7, 8]. The hippocampus plays the key role in long-term memory consolidation; bilateral damage of the hippocampus disturbs this process in both humans and animals [5]. The aim of this work was to determine whether or not fullerenes and their derivatives injected into the hippocampus prevent the disturbance of long-term memory consolidation in rats induced by inhibitors of protein synthesis.

2. EXPERIMENTAL

Chronic experiments were performed on Wistar male rats (250–300 g). The spatial memory was tested using a modified Morris technique. In the Morris procedure, an animal is set to find an invisible platform in a circular tank filled with opaque water [9]. The time moment at which a rat was placed into the water maze and the time at which the rat found the platform were automatically registered with a recorder. The learning was carried out in one session consisting of six trials. In each trial, the rat was placed into the same sector of the maze. In the first trial, the animal, while trying to save itself from the water, finds the platform by chance. Using extramaze landmarks, the rats learned in six trials to find the invisible platform ten time more rapidly than in the first trial. After 24 h, the session was repeated. In the second session, the rats found the platform two to three times faster than in the first session. This indicated that the animals learned to find the target in space and retained information on its position in memory traces.

The memory disturbance was induced by a bilateral injection of a high dose (400 μg) of a protein-synthesis inhibitor (cycloheximide) 3 h before a learning session. This led to the suppression of protein synthesis in the brain and spinal cord by more than 90% during 4 h [10].

We used the adduct of the C_{60} fullerene with poly(*N*-vinyl-pyrrolidone) (C_{60}/PVP), which was synthesized

1063-7834/02/4403-0578$22.00 © 2002 MAIK "Nauka/Interperiodica"

in the Institute of Experimental Medicine, Russian Academy of Medical Sciences. The compound contained 0.8% C_{60}; the molecular weight of the PVP was about 10000. C_{60}/PVP and C_{60} were dissolved in 0.9% NaCl. Cannulae were stereotaxically implanted bilaterally into the lateral ventricles and dorsal hippocampus (field CA1). In the control experiments (n = 3D 10), a PVA solution (208 μg/1 μl/cannula) was administered into the hippocampus, and in the experiment (n = 3D 11), a fullerene preparation (1.7 μg C_{60}/206.3 μg PVP/1 μl/cannula) was injected 1 h before the cycloheximide administration (200 μg/10 μl/cannula). The teaching was performed three hours after the cycloheximide injection. The localization of the cannulae was determined by cutting a frozen brain on a freezing microtome. The statistical significance of the results was estimated by the Student t test.

3. RESULTS AND DISCUSSION

In the control, PVP was bilaterally administered into the hippocampus 1 h before the cycloheximide injection. The rats were taught to find the platform in six trials (the differences in the escape latencies between trials 1–3, 1–5, and 1–6 are statistically significant with $p < 0.05$). The second session of learning, which was carried out 24 h after the first session, showed no retention of the acquired information (graphs *1* and *2* in Fig. 1a are statistically indistinguishable).

By contrast, the rats that received a small dose of fullerene C_{60} (1.7 μg) injected into the hippocampus showed normal learning and retention of the memory traces (the differences between curves *1* and *2* are statistically significant with $p < 0.01$, see Fig. 1b). Thus, the preliminary bilateral microinjection of fullerene C_{60} into the dorsal hippocampus prevented the disturbance of spatial memory induced by cycloheximide administration.

How can we explain this result? According to modern concepts, long-term memory consolidation critically depends on the protein synthesis *de novo*, which contributes to the establishment of new connections between neurons [5]. It is generally accepted that long-term memory consolidation is disturbed by high doses of protein-synthesis inhibitors which suppress protein synthesis by no less than by 90% [6]. Cycloheximide in high doses possesses a toxic effect and causes apoptosis in various tissues, including nervous tissue [7, 8]. This permitted us to suggest that protein-synthesis inhibitors cause amnesia not only by the suppression of protein synthesis but also by apoptosis and/or necrosis of cells of the central nervous system. Fullerene derivatives prevent apoptosis in the culture of cells of the hippocampus, cerebellum, and substantia nigra, protecting them from the toxic effect of active forms of oxygen [2, 3, 11, 12].

We suggest that microinjections of fullerene C_{60} into the hippocampus prevent neuronal cell death, and this effect can be an important factor that prevents the disturbance of long-term memory consolidation caused by protein-synthesis inhibition. Other mechanisms of fullerene action are also possible; however, they remain unknown as yet.

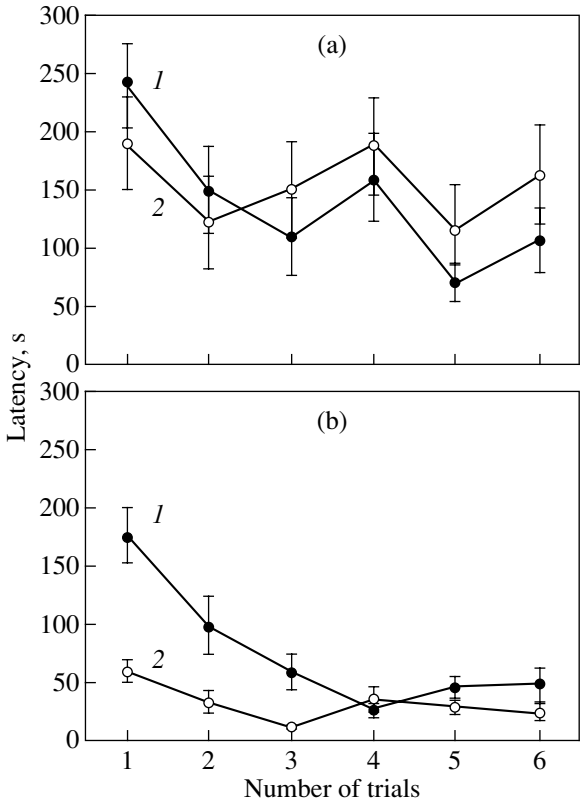

Fig. 1. Effect of bilateral injection into the dorsal hippocampus (field CA1) of (a) PVP and (b) C_{60}/PVP adduct on memory impairment in rats caused by intraventricular administration of cycloheximide (inhibitor of protein synthesis). The spatial memory was studied using a Morris water maze according to a modified Morris procedure. The abscissa axis corresponds to the order number of a trial in a learning session; the ordinate axis corresponds to the time of escape latency: (*1*) first learning session; (*2*) second learning session; PVP is poly(*N*-vinyl-pyrrolidone).

ACKNOWLEDGMENTS

This work was supported in part by the Russian Foundation for Basic Research (project no. 01-04-49826), Federal Program of Support for Prominent Scientists and Leading Research Schools (project no. 0015-07880), and Program of Support for Basic Research in Natural Sciences (project no. E00-6.0-284).

REFERENCES

1. L. L. Dugan, D. M. Turetsky, Ch. Du, *et al.*, Proc. Nat. Acad. Sci. USA **94** (17), 9434 (1997).

2. A. M. Lin, B. Y. Chyi, S. D. Wang, *et al*., J. Neurochem. **72** (4), 1634 (1999).
3. J. Lotharius, L. L. Dugan, and K. L. O'Malley, J. Neurosci. **15** (19), 4, 1284 (1999).
4. H. S. Lin, T. S. Lin, R. S. Lai, T. D'Rosario, and T. Y. Luh, Int. J. Radiat. Biol. **77** (2), 235 (2001).
5. B. Milner, E. R. Squire, and E. R. Kandel, Neuron **20** (2), 445 (1998).
6. H. P. Davis and L. R. Squire, Psychol. Bull. **96** (3), 518 (1984).
7. S. K. Rehen, M. H. Varella, F. G. Freitas, M. O. Moraes, and R. Linden, Development **122** (5), 1439 (1996).
8. W. M. Blom, H. J. de Bony, I. Meijerman, G. J. Mulder, and J. F. Nagelkerke, Biochem. Pharmacol. **15** (58), 1891 (1991).
9. R. Morris, J. Neurosci. Meth. **11** (1), 47 (1984).
10. I. V. Shcheglov, E. V. Kondrat'eva, and I. Ya. Podol'skiĭ, Neĭrokhimiya **3** (18), 200 (2001).
11. M. Bisaglia, B. Natalina, R. Pellicciari, E. Straface, W. Malorni, D. Monti, C. Franceschi, and G. Schettini, J. Neurochem. **74** (3), 1197 (2000).
12. M. C. Tsai, Y. H. Chen, and L. Y. Chiang, J. Pharm. Pharmacol. **49** (4), 438 (1997).

Translated by S. Gorin

Physics of the Solid State, Vol. 44, No. 3, 2002, pp. 581–584. From Fizika Tverdogo Tela, Vol. 44, No. 3, 2002, pp. 554–556.

PROCEEDINGS OF THE V INTERNATIONAL WORKSHOP "FULLERENES AND ATOMIC CLUSTERS"

(St. Petersburg, Russia, July 2–6, 2001)

New Approach to Nonlinear Dynamics of Fullerenes and Fullerites[1]

G. M. Chechin*, O. A. Lavrova*, V. P. Sakhnenko*, H. T. Stokes, and D. M. Hatch****

** Research Institute of Physics of Rostov State University, Rostov-on-Don, 344090 Russia*

e-mail: chechin@phys.rnd.runnet.ru

*** Brigham Young University, Provo, Utah, USA*

Abstract—A new type of nonlinear (anharmonic) excitations—bushes of vibrational modes—in physical systems with point or space symmetry is discussed. All infrared-active and Raman-active bushes for C_{60} fullerene are found by means of special group-theoretical methods. © *2002 MAIK "Nauka/Interperiodica".*

1. INTRODUCTION

Vibrations of many fullerenes and fullerites were investigated using different experimental and theoretical methods (see [1, 2] and references therein). Although the majority of such studies are based on the harmonic approximation only, some nonlinear (anharmonic) effects have also been discussed in a number of papers. For example, second-order combination modes brought about by the anharmonicity of interactions in the C_{60} fullerene are discussed and the corresponding lines in infrared transmission spectra are reported in [3]. The above effects do not exhaust the influence of anharmonicity on the fullerene and fullerite vibrational spectra, and we will consider these objects using the consistent group-theoretical approach developed in [4–7] for studying nonlinear vibrations in arbitrary physical systems with discrete (point or space) symmetry. This approach reveals the existence of new nonlinear dynamical objects (or a new type of anharmonic excitations) in systems with discrete symmetry, which we call bushes of normal modes. The concept of the bush of modes can be explained as follows.

In the harmonic approximation, a set of normal modes can be introduced which are classified in terms of irreducible representations of the symmetry group G of the physical system in equilibrium. In this harmonic approximation, normal modes are independent of each other, while interactions between them appear when some anharmonic terms in the Hamiltonian are taken into account. We note that a very specific pattern of atomic displacements corresponds to each normal mode. As a consequence, we can ascribe a definite symmetry group G_D to a given mode, which is a subgroup of the symmetry group G. The group G_D is a symmetry group of an instantaneous configuration of our system in its vibrational state.

Let us excite, at the initial instant t_0, only one, arbitrarily chosen mode, which will be called the root mode. We suppose that all other modes have zero amplitude at the initial moment. Let the symmetry group G_D and an irreducible representation Γ_0 correspond to this root mode. Then, we can pose the following question: to which other modes can this initial excitation spread from the root mode? We will refer to those initially sleeping modes, belonging to different irreducible representations Γ_j ($j \neq 0$), as secondary modes.

A very simple answer to the above question was found in [4, 5]. It turns out that initial excitation can spread from the root mode only to those modes whose symmetry is higher than or equal to the symmetry group G_D of the root mode. We will refer to the complete collection containing the root mode and all secondary modes that corresponded to it as a bush of modes. Since no other modes are excited, the energy is trapped in the given bush. As a consequence of the above idea, we can ascribe the symmetry group G_D (remember that this is a group of the root mode) to the whole bush; in this sense, we can consider the bush as a geometrical object.

It was proved in [4–6] that all modes belonging to a given bush B $[G_D]$ are coupled by force interactions. It is very important that the structure of a given bush is independent of the type of interactions between particles of our physical system.

A bush of normal modes can also be considered as a dynamical object. Indeed, the set of modes corresponding to a given bush B $[G_D]$ does not change in time, while the amplitudes of these modes do. We can write exact dynamical equations for the amplitudes of the modes contained in bush B $[G_D]$, if interactions between particles of our physical system are known. Thus, bush B $[G_D]$ represents a dynamical system whose dimension can be essentially less than that of the original physical system.

[1] This article was submitted by the authors in English.

1063-7834/02/4403-0581$22.00 © 2002 MAIK "Nauka/Interperiodica"

The above properties of bushes of normal modes can be summarized in the following manner. A normal mode represents a specific dynamical regime in a linear physical system, which, upon being excited at the initial instant t_0 continues to exist for any time $t > t_0$. Similarly, a bush of normal modes represents a specific dynamical regime in a nonlinear system, which can exist as a certain object for any time $t > t_0$.

2. SOME MATHEMATICAL ASPECTS OF BUSHES OF NORMAL MODES

Let us examine a nonlinear mechanical system of N mass points (atoms) whose Hamiltonian is described by a point or space group G. Let three-dimensional vectors $\mathbf{x}_i(t)$ ($i = 1, 2, \ldots, N$) determine the displacement of the ith atom from its equilibrium position at time t. The $3 \times N$-dimensional vector $\mathbf{X}(t) = \{\mathbf{x}_1(t), \mathbf{x}_2(t), \ldots, \mathbf{x}_N(t)\}$, describing the full set of atomic displacements, can be decomposed into the basis vectors (symmetry-adapted coordinates) of all irreducible representations Γ_j of the group G contained in the mechanical representation[2] Γ:

$$\mathbf{X}(t) = \sum_{ji} \mu_{ji}(t)\boldsymbol{\varphi}_i^{(j)} = \sum_j \boldsymbol{\Delta}_j. \quad (1)$$

Here, $\boldsymbol{\varphi}_i^{(j)}$ is the ith basis vector of the n_j-dimensional irreducible representation Γ_j. The $\mathbf{X}(t)$ depends on time only through the coefficients $\mu_{ji}(t)$, while the basis vectors are time-independent. Thus, a given nonlinear dynamical regime of the mechanical system described by the specific vector $\mathbf{X}(t)$ can be written as a sum of the contributions $\boldsymbol{\Delta}_j$ from the individual representations Γ_j of the group G.

Each vibrational regime $\mathbf{X}(t)$ can be associated with a definite subgroup G_D ($G_D \subseteq G$) describing the symmetry of the instantaneous configuration of the system. Now, the following essential idea is proposed. The subgroup G_D is invariant in time; its elements cannot disappear during time evolution, except for the case of spontaneous breaking of the symmetry, which we will not consider in the present paper. This is the direct consequence of the principle of determinism in classical mechanics.

We introduce operators $\hat{g} \in \hat{G}$ acting on the $3N$-dimensional vectors $\mathbf{X}(t)$, which correspond to the elements $g \in G$ acting on the three-dimensional vectors $\mathbf{x}_i(t)$, and write the above condition of invariance of G_D as a condition of invariance of the vector $\mathbf{X}(t)$ under the action of the elements of the group G_D:

$$\hat{g}\mathbf{X}(t) = \mathbf{X}(t), \quad g \in G_D. \quad (2)$$

[2] Considering vibrational regimes only, we can treat Γ as a $(3N - 6)$-dimensional vibrational representation of the group G.

Combining Eqs. (1) and (2), one obtains (for details, see [6]) the following invariance conditions for individual representations Γ_j:

$$(\Gamma_j \downarrow G_D)\mathbf{c}_j = \mathbf{c}_j. \quad (3)$$

Here, $\Gamma_j \downarrow G_D$ is the restriction of the representation Γ_j of the group G to the subgroup G_D, i.e., the set of matrices of Γ_j which correspond to the elements $g \in G_D$ only. The n_j-dimensional vector $\mathbf{c}_j$ in Eq. (3) is the invariant vector in the carrier space of the representation Γ_j corresponding to the given subgroup $G_D \subset G$. Note that each invariant vector of a given Γ_j belongs to a certain subspace of the carrier space of this representation and the total number of arbitrary constants upon which the vector depends is equal to the dimensionality of this subspace. If, in solving Eq. (3), we find that $\mathbf{c}_j \neq 0$, then the representation Γ_j will contribute to the dynamical regime $\mathbf{X}(t)$ with symmetry group G_D. Moreover, the invariant vector $\mathbf{c}_j$ determines the explicit form of the mode of the representation Γ_j belonging to the bush of modes associated with the given nonlinear dynamical regime.

We will illustrate the general statements of the bush theory using the C_{60} fullerene with a buckyball structure and the icosahedral symmetry group $G = I_h$. There are 10 irreducible representations of dimensions 1 (A_g, A_u), 3 (F_{1g}, F_{1u}, F_{2g}, F_{2u}), 4 (G_g, G_u), and 5 (H_g, H_u) associated with the group I_h. The infrared (IR) active modes belong to the representation F_{1u}, and the modes that are active in Raman (R) experiments belong to A_g or H_g. We found all bushes of modes for the C_{60} fullerene. There are 22 different bushes for this fullerene. Let us consider bush $B7$, corresponding to the symmetry group $G_D = C_{5v} \subset I_h$. Only four representations, namely, A_g, H_g, F_{1u}, and F_{2u}, contribute to this bush (the invariant vectors are zero for all other irreducible representations of the icosahedral group $G = I_h$)[3]

$B7$ [symmetry C_{5v}]:

$$A_g(a) - I_h,\ H_g(a, 0.577a, 0, 0.516a, -0.258a) - D_{5d},$$
$$F_{1u}(0, 0, a) - C_{5v},\ F_{2u}(a, 0.258a, 0.197a) - C_{5v}. \quad (4)$$

The arbitrary constants involved in the description of different invariant vectors are not connected with each other. As all invariant vectors listed in Eq. (4) are one-parametric (their arbitrary constants are denoted by the same symbol a only for clarity), it is clear that bush $B7$ depends on four arbitrary constants (one constant for each of the four representations). The structure of bush $B7$ [see Eq. (4)] shows that there are only four contributions $\boldsymbol{\Delta}_j$ to the corresponding dynamical regime $\mathbf{X}(t)$.

[3] Since some elements of the matrices of multidimensional irreducible representations of the group $G = I_h$ are irrational numbers, we keep only three digits after the decimal point when we write the invariant vectors.

We denote them[4] as $\mathbf{\Delta}[A_g]$, $\mathbf{\Delta}[H_g]$, $\mathbf{\Delta}[F_{1u}]$, and $\mathbf{\Delta}[F_{2u}]$. The invariant vectors listed in Eq. (4) permit us to write an explicit form of the dynamical regime $\mathbf{X}(t)$ corresponding to bush *B*7 by replacing the arbitrary constants with four functions of time $\mu(t)$, $\nu(t)$, $\gamma(t)$, and $\xi(t)$:

$$\begin{aligned}\mathbf{X}(t) &= \mathbf{\Delta}[A_g] + \mathbf{\Delta}[H_g] + \mathbf{\Delta}[F_{1u}] + \mathbf{\Delta}[F_{2u}]\\ &= \mu(t)\boldsymbol{\varphi}[A_g] + \nu(t)\{\boldsymbol{\varphi}_1[H_g] + 0.577\boldsymbol{\varphi}_2[H_g]\\ &+ 0.516\boldsymbol{\varphi}_4[H_g] - 0.258\boldsymbol{\varphi}_5[H_g]\} + \gamma(t)\boldsymbol{\varphi}_3[F_{1u}]\\ &+ \xi(t)\{\boldsymbol{\varphi}_1[F_{2u}] + 0.258\boldsymbol{\varphi}_2[F_{2u}] + 0.197\boldsymbol{\varphi}_3[F_{2u}]\}.\end{aligned} \tag{5}$$

Equation (5) is a consequence of the relation between the group *G* and its subgroup G_D only, and now we should take into account the specific structure of our physical system to find an explicit form of the basis vectors $\boldsymbol{\varphi}_i^{(j)}$ of the representations entering into Eq. (5). These basis vectors can be obtained using conventional group-theoretical methods, for example, using the projection operation method. The basis vectors of the irreducible representations determine the specific patterns of the displacements of all 60 atoms of the C_{60} fullerene structure.

It is important to note that each of the representations A_g, H_g, F_{1u}, and F_{2u} is contained several times in the vibrational representation of the C_{60} fullerene, namely, 2, 8, 4, and 5 times, respectively. (These numbers are equal to the numbers of fundamental frequencies of the normal modes associated with these representations.) As a consequence, we must treat the time-dependent coefficients in Eq. (5) as vectors of the appropriate dimensions. Because of this, we ascribe a new index (*k*) to the basis vectors, which indicates the number of times (m_j) the representation Γ_j enters into the vibrational representation. Each contribution $\mathbf{\Delta}_j$ splits into m_j copies $\mathbf{\Delta}_{jk}$, where $k = 1, 2, \ldots, m_j$ and, therefore,

$$\mathbf{X}(t) = \sum_j \mathbf{\Delta}_j = \sum_j \left(\sum_{k=1}^{m_j} \mathbf{\Delta}_{jk} \right). \tag{6}$$

For the case of bush *B*7, we have $\mathbf{\Delta}[A_g] = \mathbf{\Delta}_1[A_g] + \mathbf{\Delta}_2[A_g]$, $\mathbf{\Delta}[F_{1u}] = \mathbf{\Delta}_1[F_{1u}] + \mathbf{\Delta}_2[F_{1u}] + \mathbf{\Delta}_3[F_{1u}] + \mathbf{\Delta}_4[F_{1u}]$, etc.

Bush *B*7 in the C_{60} fullerene structure forms a 19-dimensional dynamical object; its evolution is described by the dynamical variables listed below as components of the four vectorial variables $\boldsymbol{\mu}(t)$, $\boldsymbol{\nu}(t)$, $\boldsymbol{\gamma}(t)$, and $\boldsymbol{\xi}(t)$: $\mu(t) = [\mu_1(t), \mu_2(t)]$, $\boldsymbol{\nu}(t) = [\nu_1(t), \ldots, \nu_8(t)]$, $\boldsymbol{\gamma}(t) = [\gamma_1(t), \ldots, \gamma_4(t)]$, $\boldsymbol{\xi}(t) = [\xi_1(t), \ldots, \xi_5(t)]$.

Thus, although only four of the ten representations contribute to bush *B*7, its dimension is equal to 19, because several copies of each of these four representations are contained in the full vibrational representation of the C_{60} fullerene. We cannot predict the specific evolution of the amplitudes of the bush modes without specific information on the nonlinear interactions in the physical system at hand, but we can assert that there is a nonlinear regime which involves only the modes belonging to a given bush.

3. OPTICAL BUSHES FOR THE C_{60} FULLERENE

As already noted, there are 22 bushes of vibrational modes for the C_{60} fullerene structure. Five of them are infrared active and six are Raman active. These bushes will be termed optical. The root modes of the optical bushes belong to the infrared-active representation F_{1u} or to the Raman-active representations A_g and H_g. We want to emphasize that some modes associated with representations that are not active in optics can be contained in a given optical bush.

All optical bushes with their symmetry groups (in square brackets), as well as the numbers of the irreducible representations contributing to them and their dimensions (in parentheses), are listed below.

Infrared active bushes:

$$B7[C_{5v}](4, 19); \quad B11[C_{3v}](6, 31); \quad B15[C_{2v}](7, 46);$$

$$B19[C_s](9, 89); \quad B22[C_1](10, 174).$$

Raman-active bushes:

$$B1[I_h](1, 2); \quad B4[D_{5d}](2, 10); \quad B5[D_{3d}](3, 16);$$

$$B10[D_{2h}](3, 24); \quad B16[C_{2h}](5, 45); \quad B20[C_i](5, 87).$$

Supposing the nonlinearity of the system at hand to be weak,[5] we can estimate the relative values of the contributions from different irreducible representations to a given bush. For example, for infrared-active bush *B*7, discussed above, we have

$$\mathbf{\Delta}[F_{1u}](root) = O(\varepsilon),$$

$$\mathbf{\Delta}[F_{1u}](secondary) = O(\varepsilon^3),$$

$$\mathbf{\Delta}[F_{2u}] = O(\varepsilon^3), \quad \mathbf{\Delta}[A_g] = O(\varepsilon^2), \quad \mathbf{\Delta}[H_g] = O(\varepsilon^2).$$

Here, ε is an appropriate small parameter characterizing the magnitude of the root mode.

Thus, in the case of weak nonlinearity, the contributions of different representations can be of essentially different values. This property seems to be important for interpretation of the vibrational spectra of bushes of modes.

[4] Hereafter, we write the symbol *j* of the irreducible representation Γ_j generating the contribution $\mathbf{\Delta}_j$ in square brackets next to symbol $\mathbf{\Delta}$.

[5] According to the results obtained in [3], this hypothesis is valid for C_{60} fullerene vibrations.

4. CONCLUSIONS

In the present paper, we considered a new type of possible nonlinear excitations—bushes of normal modes—in vibrational spectra of fullerenes and fullerites using, as an example, the C_{60} buckyball structure. We believe that special experiments for revealing the bushes of vibrational modes in their pure form will prove important for further elucidation of the role of these fundamental dynamical objects in various phenomena in fullerenes and fullerites. It seems that such experiments may be similar to those reported in [3]. However, unlike these experiments, monochromatic incident light with a frequency close to that of the root mode and with polarization along the symmetry axis of the bush chosen must be used.

First-principles calculations are desirable in obtaining the coefficients of the anharmonic terms in the C_{60} fullerene for a more detailed description of the bush dynamics to be made.

The concept of bushes of normal modes and the appropriate mathematical methods for their analysis are valid for both molecular and crystal structures. Such a possibility can simplify the assignment of the different optical lines in fullerites brought about by both internal and external vibrations in the C_{60} molecular clusters.

It will be of interest to study interactions between bushes of vibrational modes and electron subsystems in fullerenes and fullerites.

REFERENCES

1. C. H. Choi, M. Kertesz, and L. Mihaly, J. Phys. Chem. A **104**, 102 (2000).
2. H. Kuzmany, R. Winkler, and T. Pichler, J. Phys.: Condens. Matter. **7**, 6601 (1995).
3. M. C. Martin, X. Du, J. Kwon, and L. Mihaly, Phys. Rev. B **50** (1), 173 (1994).
4. V. P. Sakhnenko and G. M. Chechin, Dokl. Akad. Nauk **330**, 308 (1993) [Phys. Dokl. **38**, 219 (1993)].
5. V. P. Sakhnenko and G. M. Chechin, Dokl. Akad. Nauk **338**, 42 (1994) [Phys. Dokl. **39**, 625 (1994)].
6. G. M. Chechin and V. P. Sakhnenko, Physica B (Amsterdam) **117**, 43 (1998).
7. G. M. Chechin, V. P. Sakhnenko, H. T. Stokes, A. D. Smith, and D. M. Hatch, Int. J. Non-Linear Mech. **35**, 497 (2000).

Physics of the Solid State, Vol. 44, No. 3, 2002, pp. 585–587. Translated from Fizika Tverdogo Tela, Vol. 44, No. 3, 2002, pp. 557–559.

PROCEEDINGS OF THE V INTERNATIONAL WORKSHOP "FULLERENES AND ATOMIC CLUSTERS"

(St. Petersburg, Russia, July 2–6, 2001)

Cluster *ab initio* Calculations for the $C_{60}F_{24}$, $C_{60}Cl_{24}$, and $C_{60}Br_{24}$ Halofullerenes

O. E. Kvyatkovskiĭ*, M. G. Shelyapina, B. F. Shchegolev***, L. S. Vorotilova****, and I. B. Zakharova*******

** Ioffe Physicotechnical Institute, Russian Academy of Sciences, ul. Politekhnicheskaya 26, St. Petersburg, 194021 Russia*
e-mail: Kvyatkovskii@pop.ioffe.rssi.ru
*** St. Petersburg State University, ul. Pervogo maya 100, Petrodvorets, 198904 Russia*
**** Pavlov Institute of Physiology, Russian Academy of Sciences, nab. Makarova 6, St. Petersburg, 199034 Russia*
***** Grebenshchikov Institute of Silicate Chemistry, Russian Academy of Sciences, ul. Odoevskogo 24/2, St. Petersburg, 199155 Russia*
****** St. Petersburg State Technical University, ul. Politekhnicheskaya 29, St. Petersburg, 195251 Russia*

Abstract—This paper reports on *ab initio* cluster calculations of the equilibrium geometry, electronic structure, and vibrational properties of the C_{60}, $C_{60}F_{24}$, $C_{60}Cl_{24}$, $C_{60}Br_{24}$ molecules. *© 2002 MAIK "Nauka/Interperiodica".*

Recently, the properties of doped fullerenes have attracted considerable interest [1, 2]. Studies of the $C_{60}X_n$ halofullerenes (X = F, Cl, Br) have revealed that halogen atoms change the character of chemical bonding in the carbon cage and noticeably affect the optical spectra of these compounds [3–8]. This work used *ab initio* cluster calculations to study the equilibrium geometry, electronic structure, and the nature of the chemical bonding, as well as the vibrational spectra, of the C_{60}, $C_{60}F_{24}$, $C_{60}Cl_{24}$, and $C_{60}Br_{24}$ molecules. The geometry was optimized assuming that the halogen atoms occupied positions 1 and 4 on the fullerene surface [4]. This structure is realized for $C_{60}Br_{24}$ [4]; however, for $C_{60}F_{24}$ and $C_{60}Cl_{24}$, the structure with positions 1 and 2 occupied is apparently preferable [8]. Based on the results of [4, 9], we chose the T_h point group for all molecules. The calculations were carried out using the

Table 1. Mulliken atomic charges and distances from atoms to the fullerene center

Compound	Atom	Mulliken charge	R_0, Å
C_{60}	C_1	−0.000017	3.52 (Expt: 3.5)
	C_2	0.000016	
	C_3	0.000009	
$C_{60}F_{24}$	F	−0.329	5.145
	C_1	0.240	3.766
	C_2	0.082	3.574
	C_3	0.048	3.406
$C_{60}Cl_{24}$	Cl	0.160	5.597
	C_1	−0.555	3.740
	C_2	0.262	3.551
	C_3	0.265	3.435
$C_{60}Br_{24}$	Br	0.221	5.722
	C_1	−0.623	3.745
	C_2	0.263	3.537
	C_3	0.271	3.433

Note: Atoms C_1 occupy the $C1$ and $C4$ positions, atoms C_2 are in the C5 and C6 positions, and atoms C_3 are in the $C2$ and $C3$ positions following the notation in [4]. R_0 is the distance from the atom to the fullerene center.

1063-7834/02/4403-0585$22.00 © 2002 MAIK "Nauka/Interperiodica"

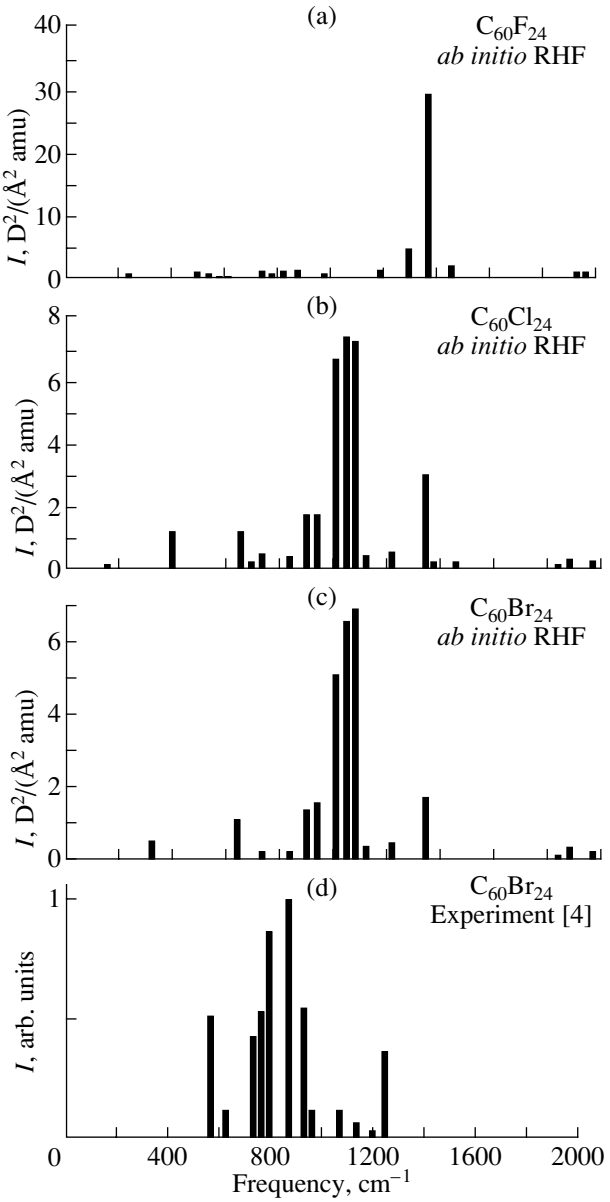

Fig. 1. Vibrational IR spectrum of the $C_{60}X_{24}$ molecules: (a–c) calculations (this work) and (d) experiment [4]. (a) $C_{60}F_{24}$, (b) $C_{60}Cl_{24}$, and (c, d) $C_{60}Br_{24}$.

PC GAMESS version [10] of the GAMESS (US) QC quantum-chemical code package [11], with a 3–21 G basis set employed in the restricted Hartree–Fock (RHF) formalism.

Tables 1 and 2 present the parameters of the equilibrium structure, as well as the Mulliken atomic charges and bond orders. The quantum-chemical determination of the bond order is given in [12]. As seen from Table 1, the fluorine atoms in $C_{60}F_{24}$ are negatively charged, in accordance with Pauling's electronegativity rule, whereas in $C_{60}Cl_{24}$ and $C_{60}Br_{24}$, the halogens are positive and the C_1 carbon atoms act as anions, in contrast to Pauling's rule. As follows from our calculations (Table 2), the pattern of chemical bonding in the carbon cage of the $C_{60}X_{24}$ molecules differs substantially from that for the pure fullerene molecule C_{60}; this is in full agreement with the experimental data [4] available for $C_{60}Br_{24}$. Moreover, it was found that the character of single and double bonds in the carbon cage changes strongly as one crosses over from the pure fullerene C_{60} to the halofullerenes $C_{60}X_{24}$; indeed, the bond order for single bonds decreases and that for double bonds grows simultaneously with the decrease in the double-bond length. This means that double bonds in $C_{60}X_{24}$ become considerably stronger and more localized than is the case with the pure fullerene. These results are in qualitative agreement with quantum-chemical calculations [13]. To test the validity of our method, we calculated the vibrational spectrum of the pure fullerene C_{60}. The frequencies and intensities of the four IR-active modes of symmetry T_{1u} (575, 610, 1242, 1549 cm^{-1} and 1.01, 0.14, 0.29, 0.36 $D^2/Å^2$ amu, respectively) obtained by us are in satisfactory agreement with the results of *ab initio* DFPT calculations [8] and experimental values [14]. Figure 1 displays IR spectra of $C_{60}F_{24}$, $C_{60}Cl_{24}$, and $C_{60}Br_{24}$. A comparison of Figs. 1c and 1d shows that the calculated IR spectrum of $C_{60}Br_{24}$ satisfactorily reproduces the structure of the corresponding experimental IR spectrum [4].

The most interesting features of the calculated spectra are the following:

(1) The spectra of $C_{60}Cl_{24}$ and $C_{60}Br_{24}$ are similar but differ from the $C_{60}F_{24}$ spectrum at frequencies below 1500 cm^{-1}.

(2) The spectra of all $C_{60}X_{24}$ molecules have a gap in the 1500- to 1800-cm^{-1} frequency interval.

(3) At high frequencies, 1800–2000 cm^{-1}, the spectra of all $C_{60}X_{24}$ molecules derive from double-bond vibrations (involving only the C_2 and C_3 atoms). There are eight vibrational modes in this region altogether (neglecting degeneracy), including three IR-active modes. This is in accord with a group-theoretical analysis and the experimental data available on $C_{60}Br_{24}$ [4].

(4) All vibrational modes of $C_{60}F_{24}$ above 1400 cm^{-1}, those of $C_{60}Cl_{24}$ above 700 cm^{-1}, and those of $C_{60}Br_{24}$ above 450 cm^{-1} involve, to a high accuracy, only carbon atoms (the halogens do not participate in these vibrations).

(5) All vibrational modes of $C_{60}Cl_{24}$ below 140 cm^{-1} and those of $C_{60}Br_{24}$ below 100 cm^{-1} involve only halogen atoms.

(6) All stretching and other mixed halogen–carbon modes lie in the frequency regions 140–700 cm^{-1} for $C_{60}Cl_{24}$ and 100–450 cm^{-1} for $C_{60}Br_{24}$.

Note that the calculated frequencies exceed the frequencies of the experimental spectrum by about 10%. One interesting result of our analysis consists in that the

Table 2. Bond lengths and bond orders in the fullerene and halofullerene molecules

Compound	Bond	Bond length, Å	Bond order
C_{60}	C_1–$C_{2,3}$	1.45 (Expt: 1.44 [2])	1.13
	C_3–C_3		
	C_2=C_2	1.37 (Expt: 1.39 [2])	1.48
	C_1=C_3		
$C_{60}F_{24}$	C_1–C_n	$1.53_{1–2}$, $1.52_{1–3}$, $1.50_{1–3}$	$0.85_{1–2}$, $0.82_{1–3}$, $0.81_{1–3}$
	C_n=C_n	$1.31_{2–2}$, $1.31_{3–3}$	$1.89_{2–2}$, $1.83_{3–3}$
	C_1–F	1.385	0.96
$C_{60}Cl_{24}$	C_1–C_n	$1.51_{1–2}$, $1.51_{1–3}$, $1.49_{1–3}$	$0.87_{1–2}$, $0.86_{1–3}$, $0.85_{1–3}$
	C_n=C_n	$1.31_{2–2}$, $1.32_{3–3}$	$1.92_{2–2}$, $1.84_{3–3}$
	C_1–Cl	1.86	1.05
$C_{60}Br_{24}$	C_1–C_n	$1.51_{1–2}$, $1.51_{1–3}$, $1.49_{1–3}$ (Expt: 1.50 [4])	$0.87_{1–2}$, $0.86_{1–3}$, $0.86_{1–3}$
	C_n=C_n	$1.31_{2–2}$, $1.32_{3–3}$ (Expt: 1.34 [4])	$1.92_{2–2}$, $1.84_{3–3}$
	C_1–Br	1.98 (Expt: 1.99 [4])	1.02

group of seven strongest IR-active modes observed in $C_{60}Br_{24}$ in the 550–1250 cm^{-1} region is associated with the carbon cage vibrations. Thus, the three IR-active T_{1u} modes, which, in terms of symmetry, originate from the bromine–carbon bond stretching vibration [4, 6], should lie in the 100- to 400-cm^{-1} region.

ACKNOWLEDGMENTS

The calculations were partially performed using the high-speed computer cluster of the St. Petersburg State University.

This study was supported by the Russian Foundation for Basic Research, project nos. 99-02-8170 and 00-02-6919.

REFERENCES

1. *The Fullerenes*, Ed. by H. W. Kroto, J. E. Fisher, and D. E. Cox (Pergamon, Oxford, 1993).
2. A. V. Eletskiĭ and B. M. Smirnov, Usp. Fiz. Nauk **165**, 977 (1995) [Sov. Phys. Usp. **38**, 935 (1995)].
3. P. L. Birkett, P. B. Hitchcock, H. W. Kroto, *et al.*, Nature **357**, 479 (1992).
4. F. N. Tebbe, R. L. Harlow, D. B. Chase, *et al.*, Science **256**, 822 (1992).
5. P. R. Birkett, H. W. Kroto, R. Taylor, *et al.*, Chem. Phys. Lett. **205**, 399 (1993).
6. M. R. Resmi, L. George, S. Singh, *et al.*, J. Mol. Struct. **435**, 11 (1997).
7. M. F. Limonov, Yu. E. Kitaev, A. V. Chugreev, *et al.*, Phys. Rev. B **57**, 7586 (1998).
8. P. J. Fagan, B. Chase, J. C. Calabrese, D. A. Dixon, R. Harlow, P. J. Krusic, N. Matsuzawa, F. N. Tebbe, D. L. Thorn, and E. Wasserman, in *The Fullerenes*, Ed. by H. W. Kroto, J. E. Fisher, and D. E. Cox (Pergamon, Oxford, 1993), p. 75.
9. P. Giannozzi and S. Baroni, J. Chem. Phys. **100**, 8537 (1994).
10. A. A. Granovsky, http://classic.chem.msu.su/gran/gamess/index.html.
11. M. W. Schmidt, K. K. Baldridge, J. A. Boatz, *et al.*, J. Comput. Chem. **14**, 1347 (1993).
12. I. Mayer, Theor. Chim. Acta **67**, 315 (1985); Int. J. Quantum Chem. **29**, 73 (1986); **29**, 477 (1986).
13. Yu. E. Kitaev, L. V. Laisheva, M. F. Limonov, *et al.*, Mol. Mater. **7**, 217 (1996).
14. P. C. Eklund, P. Zhou, K. Wang, G. Dresselhaus, and M. S. Dresselhaus, in *The Fullerenes*, Ed. by H. W. Kroto, J. E. Fisher, and D. E. Cox (Pergamon, Oxford, 1993), p. 221.

Translated by G. Skrebtsov

Physics of the Solid State, Vol. 44, No. 3, 2002, pp. 588–592. From Fizika Tverdogo Tela, Vol. 44, No. 3, 2002, pp. 560–564.

PROCEEDINGS OF THE V INTERNATIONAL WORKSHOP "FULLERENES AND ATOMIC CLUSTERS"

(St. Petersburg, Russia, July 2–6, 2001)

Ab initio Study of the Aromaticity of Hydrogenated Fullerenes[1]

G. van Lier, F. De Proft, and P. Geerlings

Vrije Universiteit Brussel, Department of General Chemistry, Brussel, B-1050 Belgium
e-mail: pgeerlin@vub.ac.be

Abstract—An analysis of the global and local aromaticity was made for a series of hydrogenated fullerenes of the type $C_{60}H_{2n}$ (n = 1–6) at the *ab initio* HF(Hartree–Fock)/3-21G level of theory, the isomers considered being obtained with an octahedral addition pattern. The relation between this addition pattern and the magnetic properties was established, showing low aromatic regions to be preferred for addition. These results show that local aromaticity, as shown in the nucleus-independent chemical shift, can be used to predict addition sites in these systems. © *2002 MAIK "Nauka/Interperiodica".*

In many chemical reactions, fullerenes behave as electron-deficient alkenes [1–3]. In terms of its chemical properties, no global aromaticity is expected for C_{60} and computed magnetic properties of closed-shell fullerenes show an overall diamagnetic behavior with significant variations in the local ring currents [4–10].

After computational studies of the chemical reactivity of hydrofullerenes and substituted hydrofullerenes of the type $C_{60}H_n$ [11], $C_{60}HR$ [12], and $C_{70}HR$ [13] were performed, the delocalization that occurred upon deprotonation of these systems was analyzed [13, 14]. With $C_{60}H_2$ and C_{60}Ht-Bu already being proven to belong to the most acidic hydrocarbons [15, 16], further modeling of the chemical behavior can be achieved upon modification of the functional group *R* and serve as a starting material for further synthesis [17].

Based on the expansion of C_{60} upon its three rotational axes, three distinct series of cylindrical fullerenes can be constructed. The C_5, C_3, and C_2 axes yield armchair, zigzag, and chiral cylinders ("capped nanotubes") of signatures (5,5), (9,0), and (8,2), respectively [18]. These series have provided useful test sets for exploration of the electronic structure [19–21] and elastic properties [22]. Global and local aromaticities were also recently described for these series [23]. The local aromaticity of a ring is described by its ability to support diamagnetic ring (i.e., diatropic) currents, which can be described by the nucleus-independent chemical shift (NICS) [24]. A more generally applicable model for local aromaticity, the so-called Pentagon-Proximity Model, could be derived, where the positioning of the pentagons in the system is seen to influence the whole pattern of local aromaticity for each system, as shown in *ab initio* NICS calculations. The overall magnetic structure can be understood in terms of a mechanical assembly of the counter-rotating rim and hub currents characteristic of circulene systems such as coronene and corannulene [25].

In this work, we analyze the global and local aromaticity upon multiple octahedral addition of hydrogen to C_{60} in the series $C_{60}H_{2n}$ (n = 1–6). The relation between the local aromaticity, as denoted by NICS, and the addition pattern is highlighted.

After describing the computational details in Section 2, the results are detailed in Section 3 for the global (Subsection 3.1) and local aromaticities (Subsection 3.2) and the relation with the addition pattern is discussed (Subsection 3.3). Conclusions are drawn and perspectives for further investigations are discussed in Section 4.

1. COMPUTATIONAL DETAILS

Structures were fully optimized at the AM1 (Austin Model 1) semiempirical level [26] using the MNDO (Modified Neglect of Differential Overlap) program [27] as a part of the graphical user interface UNICHEM [28].

Global aromaticities were analyzed by considering HOMO–LUMO gaps and molecular magnetizabilities. To investigate local aromaticities, NICS were calculated at all geometrical ring centers [24].

All property calculations were performed at the *ab initio* HF/3-21G level using GAUSSIAN98 [29]. The NICS values for all rings were computed at symmetry-distinct ring centers using the GIAO (gauge-independent atomic orbital) method (for a review of the different methods for analyzing magnetic properties, see [30] and the references therein), and magnetizabilities were evaluated at the same level using the CSGT (continuous set of gauge transformation) methodology [30].

[1] This article submitted by the authors in English.

1063-7834/02/4403-0588$22.00 © 2002 MAIK "Nauka/Interperiodica"

2. RESULTS AND DISCUSSION

2.1. Global Aromaticity

All the systems studied in this work are a part of the $C_{60}H_{2n}$ (n = 1–6) series that considers octahedral-addition patterns. They are listed in Table 1 together with their symmetries and numbering [31]. All systems are constructed from the addition of one or more of the six octahedrally positioned hexagon–hexagon edges, each being part of a distinct pyracyclenic unit. The calculated energies are also given in Table 1, with isomers listed in order of increasing energy, and found to be consistent with previous semiempirical calculations [32]. As different isomers can be formed from the previous series member, the following relations exist between isomers: starting from 1,2-$C_{60}H_2$, two distinct isomers for $C_{60}H_4$ (systems (3), (4)) can be formed.

Further addition to the former can yield all three $C_{60}H_6$ isomers, but the latter can only give (6) and (7). Finally, the first $C_{60}H_6$ isomer (5) can only form (8), whereas the others can each form both $C_{60}H_8$ isomers, which, in turn, yield unique isomers for $C_{60}H_{10}$ and $C_{60}H_{12}$ upon further hydrogenation.

The global aromaticity for these systems was described in terms of the HOMO–LUMO gap, the kinetic stability T [33], and molecular magnetizabilities, as given in Table 2. As the HOMO–LUMO gap Δ is an estimate of the chemical hardness [34] and the latter property has been proposed as a measure of the global aromaticity [34–38] (for recent reviews on the use of DFT (density function theory)-based reactivity and stability descriptors, see [39–41]), we can see from Table 2 that the trend shown in the energy (Table 1) coincides with that of the band gap. Indeed, the lower the energy, the higher the band gap, indicating a higher

Table 1. Symmetries and numbering [31] for all studied systems, together with their energies (in au), calculated at the *ab initio* 3-21G level

System	Symmetry	Numbering	Energy
C_{60} (1)	I_h		–2259.0405
$C_{60}H_2$ (2)	C_{2v}	1, 2	–2260.2050
$C_{60}H_4$ (3)	C_s	1, 2; 22, 23	–2261.3770
$C_{60}H_4$ (4)	D_{2h}	1, 2; 55, 60	–2261.3758
$C_{60}H_6$ (5)	C_3	1, 2; 16, 36; 22, 23	–2262.5491
$C_{60}H_6$ (6)	C_{2v}	1, 2; 22, 23; 31, 32	–2262.5474
$C_{60}H_6$ (7)	C_{2v}	1, 2; 22, 23; 55, 60	–2262.5466
$C_{60}H_8$ (8)	C_s	1, 2; 18, 36; 22, 23; 27, 45	–2263.7187
$C_{60}H_8$ (9)	D_{2h}	1, 2; 22, 23; 31, 32; 55, 60	–2263.7157
$C_{60}H_{10}$ (10)	C_{2v}	1, 2; 18, 36; 22, 23; 27, 45; 55, 60	–2264.8872
$C_{60}H_{12}$ (11)	T_h	1, 2; 18, 36; 22, 23; 27, 45; 31, 32; 55, 60	–2266.0552

Table 2. HOMO and LUMO energies, band gap Δ (au), number of conjugated atoms, T value in au, and magnetizabilities in ppm, calculated at the *ab initio* 3-21G level

System	ε_{HOMO}	ε_{LUMO}	Δ	# Conjugated atoms	T value	Magnetizability
C_{60} (1)	–0.3061	–0.0247	0.2814	60	16.9	–342
$C_{60}H_2$ (2)	–0.2863	–0.0240	0.2623	58	15.2	–360
$C_{60}H_4$ (3)	–0.2786	–0.0138	0.2648	56	14.8	–381
$C_{60}H_4$ (4)	–0.2761	–0.0206	0.2555	56	14.3	–362
$C_{60}H_6$ (5)	–0.2879	–0.0076	0.2803	54	15.1	–401
$C_{60}H_6$ (6)	–0.2680	–0.0020	0.2660	54	14.4	–380
$C_{60}H_6$ (7)	–0.2710	–0.0104	0.2606	54	14.1	–376
$C_{60}H_8$ (8)	–0.2808	–0.0137	0.2671	52	13.9	–396
$C_{60}H_8$ (9)	–0.2600	+0.0010	0.2609	52	13.6	–369
$C_{60}H_{10}$ (10)	–0.2760	–0.0242	0.2518	50	12.6	–385
$C_{60}H_{12}$ (11)	–0.2728	0.0424	0.2304	48	11.1	–369

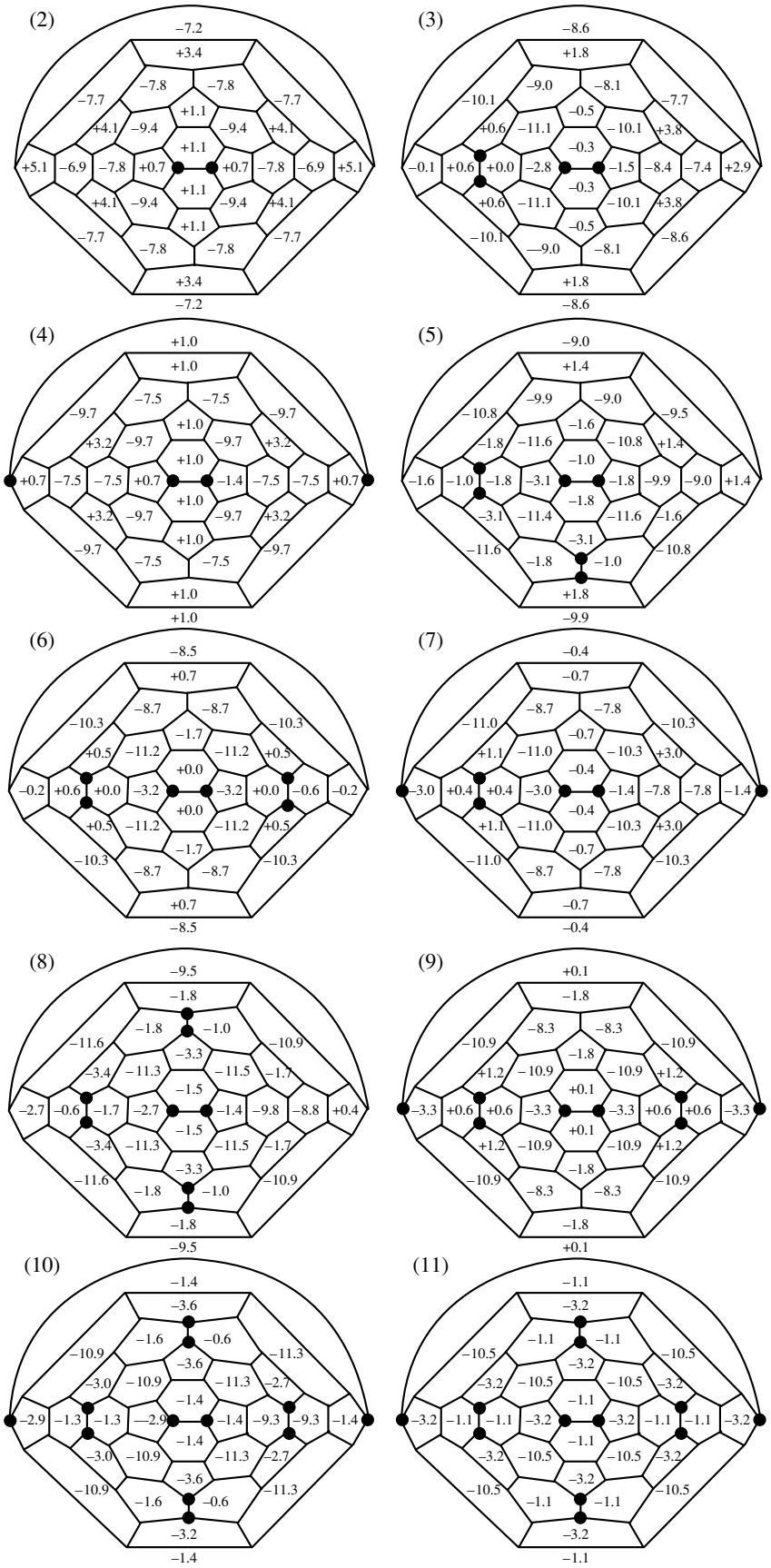

NICS values calculated for various fullerenes in the 3-21G basis in the AM1 geometries (ppm) (numbering, see Table 1).

global aromaticity. From these most stable isomers, we can see a clear increase in the band gap up to $C_{60}H_6$ (system (5)), followed by a decrease with increasing hydrogenation. The magnetizabilities show exactly the same trend and also show decreasing global aromaticity with increasing energy when comparing isomers.

The size dependence of the band gap can be removed by simple multiplication of Δ by the number of conjugated atoms to give the so-called "kinetic stability" *T* [33]. This quantity was recently found to correlate with the minimum bond resonance energy (min BRE) in a fullerene, and both *T* and min BRE have been proposed as useful measures for the chemical reactivity of fullerene systems [33]. The kinetic stability (given in Table 2 together with the number of conjugated atoms) shows a general decrease within series and isomers, but with (5) again as a more aromatic exception.

In the next subsection, local aromaticity is analyzed in order to gain insight into the possible addition patterns.

2.2. Local Aromaticity

In the figure, modified Schlegel forms are presented with the NICS calculated for all rings at the geometrical ring centers as an evaluation of the local aromaticity. In comparing these values with the respective values for C_{60}, significant differences can be seen in the addition region (the NICS of C_{60} are +5.1 ppm for the pentagons and –6.8 ppm for the hexagons). Starting from the picture of diamagnetic hexagons and paramagnetic pentagons, the addition of two hydrogens on a bond to form 1,2-$C_{60}H_2$ makes the four rings of the pyracyclenic unit become nonaromatic. On the other hand, four benzenoid rings adjacent to this pyracyclenic unit are created. The addition of another pair of hydrogens can now be expected to occur in such a way as to reinforce this local magnetic pattern rather than undo it. As seen from the NICS for $C_{60}H_4$, again four benzenoid rings are now created around the second added pair. Two of these are shared with the first addition in (3), indeed showing higher NICS compared to (4). The same applies to the possible isomers of $C_{60}H_6$ and $C_{60}H_8$, showing more negative NICS and thus higher local aromaticity for the isomers with higher global aromaticity (see Subsection 2.1). Furthermore, we can see three benzenoid rings, with the highest NICS value found (–11.6 ppm) being for isomer (5) of $C_{60}H_6$, which is consistent with the results found for the global aromaticity (see Table 1).

Upon increasing octahedral addition, a pattern appears where eight isolated benzenoid rings are created, surrounded by nonaromatic pentagons and hexagons at the hydrogenated pyracyclenic units. Such substructures have already been detected in analyzing the local aromaticity for cylindrical fullerenes [23] described in terms of recent results for coronene and corannulene [25].

2.3. Relation with the Addition Pattern

From a chemical point of view, addition to the C_{60} cage will occur at the most reactive bond, which is expected to be situated in the electronically most localized region of the system. In terms of its magnetic properties, such a region could be expected to show the lowest local aromaticity or antiaromaticity, which is marked by higher NICS values for the hexagons and lower NICS values for the pentagons involved in the corresponding addition site. From the results of the figure, it is seen that consecutive octahedral addition, indeed occurring at the pyracyclenic site with the pentagon with lowest NICS, will yield the isomer with the highest global aromaticity. Furthermore, in most cases, this addition site also involves the hexagon with lowest aromaticity (less negative NICS). In this way, the site with the lowest local delocalization is indeed found to yield, upon addition, the stablest isomer, being the addition product with the highest global aromaticity.

3. CONCLUSIONS

The global and local aromaticities were described for a number of hydrogenated fullerenes of the type $C_{60}H_{2n}$ (n = 1–6) obtained by octahedral addition. After an increase in the global aromatic character upon increasing hydrogenation, a decrease is noted from $C_{60}H_6$, considering the stablest isomer of each series member and its having the highest global aromaticity, as well as the lowest energy. From the results for the local aromaticity, as predicted by NICS, calculated at all geometrical ring centers, significant variations can be seen for the hydrogenated fullerenes as compared to C_{60}. Upon higher hydrogenation, a set of benzenoid rings can be detected, with higher local aromaticities occurring for the isomers with higher global aromaticity. Furthermore, the additions are seen to occur at the site with lowest local delocalization, as described by NICS. Indeed, consecutive octahedral additions occurring at the site comprising the less antiaromatic pentagon gives the stablest isomer of the next series member.

From these results, one can conclude that consideration of the local aromaticity, as monitored by NICS, can contribute to the prediction of multiple addition sites for substituted closed-shell fullerenes. As NICS describes the local aromaticity of the system, regions with smaller aromaticity and thus with smaller delocalization are mapped. Together with considerations of the aromaticity pattern of the addition product, a clear evaluation of the preferential isomer can be made. In our further investigations, this methodology will be applied to a broad range of functionalized fullerenes, including C_{70} and C_{76} derivatives, as well as charged fullerenes.

ACKNOWLEDGMENTS

The authors would like to thank Prof. P.W. Fowler (University of Exeter, UK) for many enlightening discussions.

REFERENCES

1. A. Hirsch, *The Chemistry of the Fullerenes* (Georg Thieme, Stuttgart, 1994).
2. R. Taylor, *The Chemistry of Fullerenes* (World Scientific, Singapore, 1996).
3. R. Taylor, *Lecture Notes on Fullerene Chemistry. A Handbook for Chemists* (Imperial College Press, 1999).
4. P. W. Fowler, P. Lazzeretti, and R. Zanasi, Chem. Phys. Lett. **165**, 79 (1990).
5. P. W. Fowler, P. Lazzaretti, M. Malagoli, and R. Zanasi, Chem. Phys. Lett. **179**, 174 (1991).
6. R. C. Haddon, Science **261**, 1545 (1993).
7. R. C. Haddon, L. F. Schneemeyer, J. V. Waszczak, *et al.*, Nature **350**, 46 (1993).
8. R. C. Haddon and A. Pasquarello, Phys. Rev. B **50**, 16459 (1994).
9. M. Bühl, Chem.-Eur. J. **4**, 734 (1998).
10. M. Bühl and A. Hirsch, Chem. Rev. **101**, 1153 (2001).
11. K. Choho, G. van Lier, G. van De Woude, and P. Geerlings, J. Chem. Soc., Perkin Trans. **2**, 1723 (1996).
12. G. van Lier, B. Safi, and P. Geerlings, Phys. Chem. Solids **58**, 1719 (1997).
13. G. van Lier and P. Geerlings, Chem. Phys. Lett. **289**, 591 (1998).
14. G. van Lier, B. Safi, and P. Geerlings, J. Chem. Soc., Perkin Trans. **2**, 349 (1998).
15. P. J. Fagan, P. J. Krisic, D. H. Evans, *et al.*, J. Am. Chem. Soc. **114**, 9697 (1992).
16. M. E. Nyazymbetov, D. H. Evans, S. A. Lerke, *et al.*, J. Phys. Chem. **98**, 13093 (1994).
17. T. Kitagawa and K. Takeuchi, Bull. Chem. Soc. Jpn. **74**, 785 (2001).
18. M. S. Dresselhaus, G. Dresselhaus, and P. C. Eklund, *Science of Fullerenes and Carbon Nanotubes* (Academic, San Diego, 1995).
19. P. W. Fowler, J. Chem. Soc., Faraday Trans. **86**, 2073 (1990).
20. P. W. Fowler, J. Phys. Chem. Solids **12**, 1825 (1993).
21. P. W. Fowler and D. E. Manolopoulos, *An Atlas of Fullerenes* (Oxford Univ. Press, Oxford, 1995), Vol. 30.
22. G. van Lier, C. van Alsenoy, V. van Doren, and P. Geerlings, Chem. Phys. Lett. **326**, 181 (2000).
23. G. van Lier, P. W. Fowler, F. De Proft, and P. Geerlings, J. Phys. Chem. (in press).
24. P. V. R. Schleyer, C. Maerker, A. Dransfeld, *et al.*, J. Am. Chem. Soc. **118**, 6317 (1996).
25. E. Steiner, P. W. Fowler, and L. W. Lenneskens, Angew. Chem. Int. Ed. Engl. **40**, 362 (2001).
26. J. P. P. Stewart, J. Comput.-Aided Mol. Des. **4**, 1 (1990).
27. M. J. S. Dewar and W. Thiel, J. Am. Chem. Soc. **99**, 4899 (1977).
28. C. R. I. UniChem (Eagon, 1994).
29. M. J. Frisch, G. W. Trucks, H. B. Schlegel, G. E. Scuseria, M. A. Robb, J. R. Cheeseman, V. G. Zakrzewski, J. A. Montgomery, Jr., R. E. Stratmann, J. C. Burant, S. Dapprich, J. M. Millam, A. D. Daniels, K. N. Kudin, M. C. Strain, O. Farkas, J. Tomasi, V. Barone, M. Cossi, R. Cammi, B. Mennucci, C. Pomelli, C. Adamo, S. Clifford, J. Ochterski, G. A. Petersson, P. Y. Ayala, Q. Cui, K. Morokuma, D. K. Malick, A. D. Rabuck, K. Raghavachari, J. B. Foresman, J. Cioslowski, J. V. Ortiz, A. G. Baboul, B. B. Stefanov, G. Liu, A. Liashenko, P. Piskorz, I. Komaromi, R. Gomperts, R. L. Martin, D. J. Fox, T. Keith, M. A. Al-Laham, C. Y. Peng, A. Nanyakkara, M. Challacombe, P. M. W. Gill, B. Johnson, W. Chen, M. W. Wong, J. L. Andres, C. González, M. Head-Gordon, E. S. Replogle, and J. A. Pople, *Gaussian 98, Revision A.9* (Gaussian Inc., Pittsburgh, 1998).
30. T. Helgaker, M. Jaszunski, and K. Ruud, Chem. Rev. **99**, 293 (1999).
31. R. Taylor, J. Chem. Soc., Perkin Trans. **2**, 813 (1993).
32. B. W. Clare and D. L. Kepert, J. Mol. Struct.: Theochem **281**, 45 (1993).
33. J. Aihara, Phys. Chem. Chem. Phys. **2**, 3121 (2000).
34. F. De Proft and P. Geerlings, Chem. Rev. **101**, 1451 (2001).
35. Z. X. Zhou, R. G. Parr, and J. F. Garst, Tetrahedron Lett. **29**, 4843 (1988).
36. Z. X. Zhou and R. G. Parr, J. Am. Chem. Soc. **111**, 7371 (1989).
37. Z. X. Zhou and R. G. Parr, J. Am. Chem. Soc. **112**, 5720 (1990).
38. R. Balawender, L. Komorowski, F. De Proft, and P. Geerlings, J. Phys. Chem. A **102**, 9912 (1998).
39. H. Chermette, J. Comput. Chem. **20**, 129 (1999).
40. P. Geerlings, F. De Proft, and W. Langenaeker, Adv. Quantum Chem. **33**, 303 (1999).
41. P. Geerlings and F. De Proft, Int. J. Quantum Chem. **80**, 227 (2000).

Physics of the Solid State, Vol. 44, No. 3, 2002, pp. 593–595. Translated from Fizika Tverdogo Tela, Vol. 44, No. 3, 2002, pp. 565–566.

PROCEEDINGS OF THE V INTERNATIONAL WORKSHOP "FULLERENES AND ATOMIC CLUSTERS"

(St. Petersburg, Russia, July 2–6, 2001)

On the Possible Existence of Exo- and Endohedral η^5–π Complexes of a C_{20} Fullerene with Transition Metals

A. L. Chistyakov and I. V. Stankevich

Nesmeyanov Institute of Organoelement Compounds, Russian Academy of Sciences, ul. Vavilova 28, Moscow, 119991 Russia
e-mail: stan@ineos.ac.ru

Abstract—The molecular and electronic structures of a number of C_{20} fullerene complexes (CpFe–C_{20}–FeCp, CpFe–$C_{20}H_{10}$–FeCp, H_5C_{20}–Fe–$C_{20}H_5$, $C_{20}H_5$–Fe–H_5C_{20}, C_{20}–Fe–C_{20}, Fe@C_{20}, and Cr@C_{20}, where $^{\cdot}$Cp is the $^{\cdot}C_5H_5$ cyclopentadienyl radical) are simulated using the density functional theory (DFT) method in the PBE/3z.bas approximation. © *2002 MAIK "Nauka/Interperiodica".*

1. INTRODUCTION

Fullerene C_{20} (molecule **1**) is the smallest polyhedral carbon cluster among the fullerenes consisting of five- and six-membered rings. Quantum-mechanical calculations demonstrate that fullerene C_{20} has the most strained structure. Moreover, according to some theoretical predictions [1–3], the C_{20} carbon cluster should be a chemically active particle with an unfilled electron shell. For this reason, it has been assumed that the dodecahedral C_{20} fullerene is unlikely to occur as an individual species. However, quite recently, this fullerene was chemically produced in a gas phase by Prinzbach *et al.* [4]. The initial product was the $C_{20}H_{20}$ dodecahedron (molecule **2**): it is a saturated hydrocarbon molecule that was synthesized well before the discovery of fullerenes [5]. Molecule **2** was subjected to bromination with the formation of the $C_{20}HBr_{13}$ bromide (compound **3**), which, in turn, was transformed into cluster **1**. Owing to the high reactivity, fullerene **1** should readily form compounds of different types, including exo- and endohedral η^n-type complexes with metals.

The present paper is concerned with the quantum-chemical design of the molecular and electronic structures of these hypothetical systems. We considered the possible existence of the following derivatives of the C_{20} fullerene: CpFe–C_{20}–FeCp (compound **4**), CpFe–$H_5C_{20}H_5$–FeCp (compound **5**), H_5C_{20}–Fe–$C_{20}H_5$ (compound **6**), $C_{20}H_5$–Fe–H_5C_{20} (compound **7**), C_{20}–Fe–C_{20} (compound **8**), Fe@C_{20} (compound **9**), and Cr@C_{20} (compound **10**), where Cp is the $^{\cdot}C_5H_5$ cyclopentadienyl radical. The calculations were performed in terms of the density functional theory (DFT) within the PBE/3z.bas approximation [6] using the PRIRODA program [7].

2. RESULTS AND DISCUSSION

2.1. Fullerene C_{20}. The calculations demonstrated that the ground state of the C_{20} fullerene (molecule **1**) is the singlet state of molecule **1a** with a structure of the D_{3d} symmetry. However, the lower-lying triplet state of molecule **1b** differs energetically from the singlet state by only 1.8 kcal/mol and, structurally, is also characterized by the D_{3d} symmetry. In the former state, the spin population is predominantly localized on six atoms (0.24 au per atom) adjacent to the atoms arranged along the threefold axis. The state with a multiplicity of five has a structure of the C_{2h} symmetry and exhibits a relatively high energy (48 kcal/mol higher than the ground-state energy). The calculated energy characteristics of states **1a** and **1b** for cluster **1** are listed in the table.

The calculations of the C_{20}^- radical anion and the C_{20}^+ radical cation made it possible to estimate the electron affinity (2.3 eV) and the ionization potential (10.0 eV) of molecule **1**.

2.2. Exohedral complexes of the η^5 type. For complexes **4**–**8**, the local energy minima on the potential energy surfaces were found from the optimization of the corresponding energies by the geometric parameters. The structures that correspond to these minima are shown in Figs. 1a and 1b. The total energies of complexes **4**–**8** and the energies of the relevant η^5 bonds are presented in the table. The Fe–C (C_{pent*}) distances in complexes **4**–**8** are approximately equal to 2.04 Å and almost coincide with those in $FeCp_2$ (complex **11**). For complex **11**, the calculated Fe–C distance (2.05 Å) coincides with the experimental value.

It was revealed that the energies of the η^5 Fe–C(C_{pent*}) bonds in complexes **4**–**7** are comparable to the energy of the η^5 Fe–Cp bond in the stable molecule **11**. The stabilization of the η^5 complexes through the introduction of additional hydrogen atoms into the α positions

1063-7834/02/4403-0593$22.00 © 2002 MAIK "Nauka/Interperiodica"

Energy characteristics of the C_{20} fullerene and its complexes (calculations according to the DFT–PBE/3z.bas method)

Molecule, complex	Designation	*m*	Symmetry	$-E_t$/au	ZPVE kcal/mol	E_a(Fe–*pent**), kcal/mol	E_d(Fe–*pent**), kcal/mol
C_{20}	*1a*	1	D_{3d}	760.8795	69.9	–	–
C_{20}	*1b*	3	D_{3d}	760.8761	68.8	–	–
η^5-CpFe–C_{20}–FeCp	*4*	1	D_{5d}	3574.7448	173.3	77.5	81.5
η^5-CpFe–$H_5C_{20}H_5$–FeCp	*5*	1	D_{5d}	3681.0935	247.0	101.3	102.7
η^5-H_5C_{20}–Fe–$C_{20}H_5$	*6*	1	D_{5h}	2791.6737	215.4	91.7	99.6
η^5-$C_{20}H_5$–Fe–H_5C_{20}	*7*	1	D_{5h}	2791.5836	213.8	63.5	87.6
η^2-C_{20}–Fe–C_{20}	*8*	3	C_i	2785.3782	138.5	37.0	52.8
η^5-Fe@C_{20}	*9a*	1	C_{5v}	2024.2673	68.2	32.5[a]	–
η^2-Fe@C_{20}	*9b*	3	C_{2v}	2024.2403	65.7	49.5[a]	–
η^5-Cr@C_{20}	*10a*	1	C_{5v}	1805.0804	67.9	14.7[a]	–
η^2-Cr@C_{20}	*10b*	3	C_{2v}	1805.0616	65.9	25.5[a]	–
$FeCp_2$	*11*	1	D_{5h}	1650.3022	103.1	97.9[b]	135.3

Designations: E_t is the total energy, ZPVE is the deviation from the total energy due to the inclusion of zero-point nuclear oscillations in the calculation, E_a(*M*–*pent**) is the mean energy of the *M*–*pent** bond, E_d(*M*–*pent**) is the energy of homolytic dissociation into two fragments, and *m* is the multiplicity.

[a] The energies used in the calculations: $E(^5\text{Fe}) = -1263.4397$ au and $E(^7\text{Cr}) = -1044.2243$ au.

[b] The experimental value is 76 kcal/mol.

with respect to the coordinated *pent** face, which was proposed earlier for the fullerenes C_{60}, C_{70}, and C_{40} (see [8] and references in [3]) and verified experimentally in [9], leads to a substantial increase in the length of certain bonds involved in the carbon skeleton and is thus less efficient in the case under consideration.

2.3. Endohedral complexes. For the Fe@C_{20} (**9**) and Cr@C_{20} (**10**) complexes, the local energy minima for singlet and triplet states were found from the optimization of the corresponding energies by the geometric parameters. In the case of singlet states, these minima correspond to the η^5-type structures in complexes

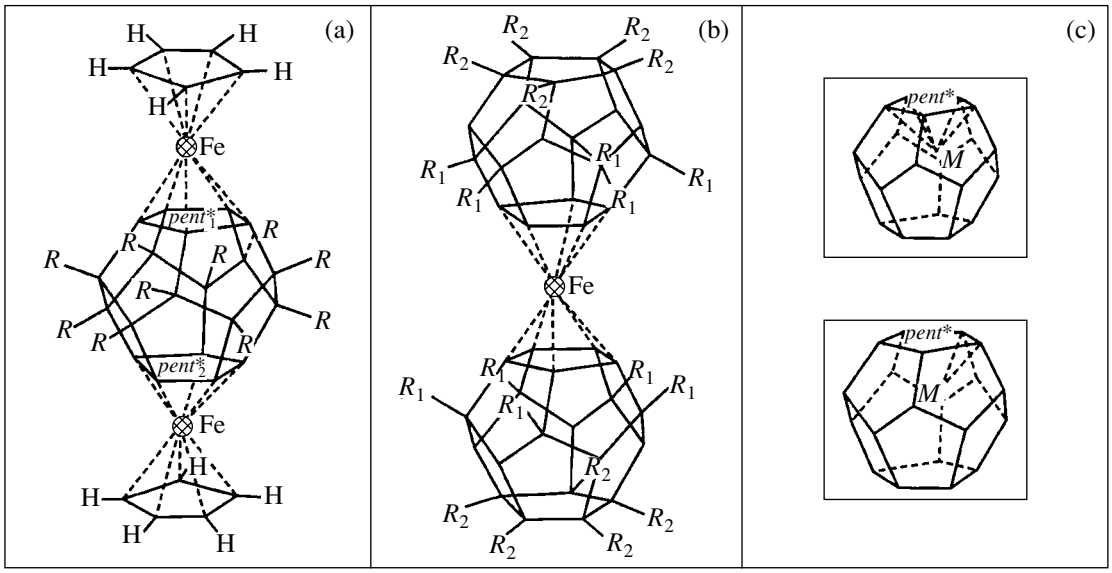

Fig. 1. Structures of complexes (a) **4** (*R* = –) and **5** (*R* = H); (b) **6** (R_1 = –, R_2 = H), **7** (R_1 = H, R_2 = –), and **8** ($R_1 = R_2$ = –); (c) C_{5v}—η^5-*M*@C_{20} (complex **9**) and C_{2v}—η^2-*M*@C_{20}(complex **10**). Designations of the complexes are given in the table.

9a and **10a** of the C_{5v} symmetry (Fig. 1c). For triplet states (with energies 12–15 kcal/mol higher than those for the singlet states), the local energy minima correspond to the η^2-type structures in complexes **9b** and **10b** of the C_{2v} symmetry. The M–C_{pent^*} distances are found to be considerably shorter than those in the complexes $FeCp_2$ (2.05 Å) and $CrCp_2$ (2.15 Å), namely, 1.80 (Fe–C_{pent^*}) and 1.91 Å (Cr–C_{pent^*}) for singlet states and shorter distances of 1.837 (Fe–C[η^5]) and 1.897 Å (Cr–C[η^2]) for triplet states. It should be noted that this coordination brings about a substantial increase (by ~0.2 Å) in the C–C bond lengths in the *pent** five-membered ring. The lengths of the remaining C–C bonds in the polyhedral carbon cage also increase. The energies of dissociation of the $M@C_{20}$ complexes into the C_{20} cluster and the M atom in the ground state are given in the table. These energies are found to be negative but small in magnitude.

ACKNOWLEDGMENTS

We are grateful to D.N. Laĭkov for placing the PRIRODA program at our disposal, which provided highly efficient calculations.

This work was supported by the Russian Foundation for Basic Research (project no. 01-03-33216) and the State Scientific and Technical Program "Fullerenes and Atomic Clusters," the Ministry of Science of the Russian Federation (project no. 9.4.06).

REFERENCES

1. D. A. Bochvar and E. G. Gal'pern, Dokl. Akad. Nauk SSSR **209**, 610 (1973).
2. G. Galli, F. Gygi, and J. C. Golaz, Phys. Rev. B **57**, 1860 (1998).
3. A. L. Chistyakov and I. V. Stankevich, Izv. Akad. Nauk, Ser. Khim., No. 2, 176 (2001).
4. H. Prinzbach, A. Weller, P. Landenberger, *et al.*, Nature **407**, 60 (2000).
5. L. A. Paquette, R. J. Ternansky, D. W. Balogh, and G. J. Kentgen, J. Am. Chem. Soc. **105**, 5446 (1983).
6. J. P. Perdew, K. Burke, and M. Ernzerhof, Phys. Rev. Lett. **77**, 3865 (1996).
7. D. N. Laikov, Chem. Phys. Lett. **281**, 151 (1997).
8. A. L. Chistyakov and I. V. Stankevich, Izv. Akad. Nauk, Ser. Khim., No. 10, 2422 (1996).
9. M. Sawamura, H. Iikura, and E. Nakamura, J. Am. Chem. Soc. **118**, 12850 (1996).

Translated by O. Borovik-Romanova

Physics of the Solid State, Vol. 44, No. 3, 2002, pp. 596–597. From Fizika Tverdogo Tela, Vol. 44, No. 3, 2002, pp. 567–568.

PROCEEDINGS OF THE V INTERNATIONAL WORKSHOP "FULLERENES AND ATOMIC CLUSTERS"

(St. Petersburg, Russia, July 2–6, 2001)

Correlation Effects in the (*e*, 2*e*) Process on C_{60}

O. Kidun and J. Berakdar [1]

Max-Planck Institut für Mikrostrukturphysik, Halle/Saale, Germany

e-mail: okidun@mpi-halle.mpg.de

Abstract—The effect of electronic correlations on the electron-impact induced ionization spectrum of free fullerene clusters is investigated. The unperturbed valence states of the clusters are described within the Hartree–Fock scheme based on a jellium shell model. To account for the many-body response of the cluster to an external perturbation, we utilize the random-phase approximation with exchange in order to describe the interaction of an incoming projectile with the metallic cluster, which leads to nonlocal screening of the interelectronic interaction. Within this model, we evaluate the ionization transition amplitudes numerically and compare the results with available experimental data for a C_{60} cluster. We point out that the neglect of the collective response of the cluster leads to results that are at variance with experimental findings. © *2002 MAIK "Nauka/Interperiodica".*

In this work, we study the single ionization of a fullerene cluster from its (single-particle) ground state $|\varphi_{2j}\rangle$ upon the impact of an electron with wave vector $\mathbf{k}_0$. In the final channel, two electrons recede from the residual cluster to emerge with asymptotic momenta $\mathbf{k}_1$ and $\mathbf{k}_2$. The transition amplitude for such a reaction is given by

$$T(\mathbf{k}_0, \mathbf{k}_1, \mathbf{k}_2, \varphi_v) = E_0 \langle \mathbf{k}_1 \mathbf{k}_2 | V_{12} \Pi | \varphi_{2j} \mathbf{k}_0 \rangle, \qquad (1)$$

where E_0 is the total kinetic energy of the two electrons and $\Pi = G_0 + G_0 V \Pi$ is the total Green operator of the projectile–cluster system with total potential V. The interaction between the projectile and the knocked-out electron is designated by V_{12}. Here, we report on a calculation of the first-order term of Eq. (1), as well as of the next terms due to the electron–hole excitations. In the presence of an external electron with momentum $\mathbf{k}_0$, the self-consistent cluster potential changes. Taking into account the polarization of the electronic cloud, we write the amplitude of the process as the sum of two terms. The direct term corresponds to the excitation of the cluster's electron, labeled by index 2, from the j^{th} bound state φ_{2j} to a continuum state with the asymptotic momentum $\mathbf{k}_2$.

The second correlation term describes a correction appearing from electron–hole excitations. Thus, in the random-phase approximation with exchange (RPAE), the matrix element reads

$$T \sim \langle \mathbf{k}_1 \mathbf{k}_2 | V_{\text{eff}} | \varphi_{2j} \mathbf{k}_0 \rangle = \langle \mathbf{k}_1 \mathbf{k}_2 | V_{12} | \varphi_{2j} \mathbf{k}_0 \rangle + \sum_{\varepsilon_\alpha \le \varepsilon_F < \varepsilon_\beta} \left(\frac{\langle \alpha \mathbf{k}_2 | V_{\text{eff}} | \varphi_{2j} \beta \rangle \langle \beta \mathbf{k}_1 | \dfrac{1}{r_{13}} | \mathbf{k}_0 \alpha \rangle}{\varepsilon_0 - (\varepsilon_\alpha - \varepsilon_\beta - i\delta)} - \frac{\langle \beta \mathbf{k}_2 | V_{\text{eff}} | \varphi_{2j} \alpha \rangle \langle \alpha \mathbf{k}_1 | \dfrac{1}{r_{13}} | \mathbf{k}_0 \beta \rangle}{\varepsilon_0 + (\varepsilon_\alpha - \varepsilon_\beta - i\delta)} \right), \qquad (2)$$

where V_{eff} is an effective interelectron interaction; $1/r_{13}$ is the bare Coulomb interaction between the impact electron and intermediate electrons; α, β are the intermediate electron and hole states with energies ε_α, ε_β; and ε_0 and ε_F are the initial energy of the projectile and the Fermi energy, respectively. The different terms in the sum describe electron–hole excitation and deexcitation.

The differential electron-impact ionization cross section is to be summed over ionization events from all initial bound states φ_{2j} accessible within the energy conservation; i.e.,

$$\frac{d^2\sigma}{d^3\mathbf{k}_1 d^3\mathbf{k}_2} = \frac{(2\pi)^4}{|k_0|} \times \sum_j |T(\mathbf{k}_0, \mathbf{k}_1, \mathbf{k}_2, \varphi_{2j})|^2 \delta(\varepsilon_0 - (\varepsilon_j^{\text{ion}} + k_1^2/2 + k_2^2/2)). \qquad (3)$$

The quantum states of the fullerene cluster are constructed within the Hartree–Fock approximation and within the spherical jellium model. The potential of

[1] This article was submitted by the authors in English.

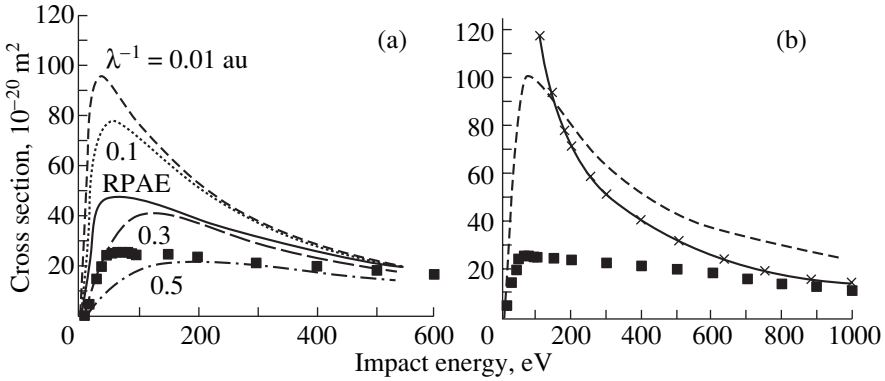

Fig. 1. Integrated electron impact ionization cross section of C_{60} as a function of the projectile energy: (a) present calculations in the Thomas–Fermi model (dashed curves) with different values of the inverse screening length and in the random-phase approximation with exchange (solid curve); dots are the experimental cross section for the production of C_{60}^+ ions [4]; (b) the solid line is a calculation in the plane-wave Born approximation for the jellium-shell model [5], the dashed line is the result of semiempirical model calculation [6], and dots are the experimental cross section for the production of C_{60}^+ ions [4].

C_{60}, which is a superposition of atomic potentials, is replaced by a potential of a fullerene shell. The latter is formed by delocalized valence electrons of carbon atoms and modeled by a potential well: $V(r) = V_0$ within the region $R - \Delta < r < R + \Delta$, and $V = 0$ elsewhere. Here, $R \approx 6.7a_0$ is the radius of the fullerene and the thickness of the shell is $2\Delta \approx 2a_0$, a_0 being the Bohr radius. The height of the well is chosen such that the experimental value of the electron affinity of C_{60} and the number of valence electrons are correctly reproduced.

Numerical calculation of the Hartree–Fock states is based on the nonlocal variable phase approach [1–3]. This method allows one to find the eigenfunctions and eigenvalues through the scattering phase (which is built for the set of cutoffs of the potentials at different distances) and through the poles of the scattering amplitude in the complex plane of the wavevector of the particle. Such a choice of numerical realization of the self-consistent procedure allows one to accelerate its convergence significantly.

To gain qualitative insight into the effect of screening on the ionization cross section, we compare our RPAE calculations with calculations in the following intuitively transparent approximation: due to the presence of there being a large number of mobile electrons on the surface of the fullerene, the interaction of an incident electron with the cluster electrons is screened. A simple model to account for this effect is the Thomas–Fermi approach, which yields a local screen electron–electron interaction described by the one-parameter Yukawa potential $V(r_{12}) = \exp(-\lambda r_{12}/r_{12})$, where λ is the inverse screening length. The results of our calculations are presented in Fig. 1a, where the total cross section of the process $\sigma(\varepsilon_0)$ is plotted as a function of the impact energy. Dashed curves correspond to different values of the inverse screening length, and the solid curve is the RPAE result.

Despite their conceptual simplicity, these models of electronic correlation yield encouraging results. We compare them with available experimental data [4] and with the theoretical calculations of [5, 6], where the bare Coulomb interaction was taken into account and the (*e*, 2*e*) total cross section was calculated in the plane-wave Born approximation (see Fig. 1b). Comparison with the calculations that neglect the screening effect shows that the screening results in a flattening of the total ionization cross section at lower energies. This effect can be traced back to the fact that, for the unscreened Coulomb interaction, the main contribution to the cross section originates from collisions with large impact parameters, whereas in the case of screening, there is a cutoff impact parameter beyond which the contribution of collisions to the cross section diminishes.

REFERENCES

1. F. Calogero, Nuovo Cimento **33**, 352 (1964).
2. V. Babikov, Preprint No. 2005, OIYaI (Joint Inst. for Nuclear Research, Dubna, 1964), pp. 28–32.
3. O. Kidun and J. Berakdar, in *Many-Particle Spectroscopy of Atoms, Molecules, Clusters and Surfaces*, Ed. by J. Berkdar and J. Kirschner (Plenum, New York, 2001), pp. 395–404.
4. V. Foltin, M. Foltin, S. Matt, *et al.*, Chem. Phys. Lett. **289** (1–2), 181 (1998).
5. S. Keller and E. Engel, Chem. Phys. Lett. **299** (2), 165 (1999).
6. H. Deutsch, K. Becker, J. Pittner, *et al.*, J. Phys. B **29**, 5175 (1996).

Physics of the Solid State, Vol. 44, No. 3, 2002, pp. 598–599. From Fizika Tverdogo Tela, Vol. 44, No. 3, 2002, pp. 569–570.

PROCEEDINGS OF THE V INTERNATIONAL WORKSHOP "FULLERENES AND ATOMIC CLUSTERS"

(St. Petersburg, Russia, July 2–6, 2001)

Fullerenes with Symmetrically Arranged Defects: Geometry and Electronic Structure[1]

A. Pérez-Garrido, J. D. Catalá, and F. Alhama

Dpto. Física Aplicada, Universidad Politécnica de Cartagena, Campus Muralla del Mar, Cartagena 30202 Murcia, Spain

Abstract—Recently, fullerene structures with symmetrically arranged pairs of pentagonal–heptagonal defects were proposed to explain the round shape of giant multilayer fullerene cages. Even though those proposed cages are defective, they belong to the icosahedral point group. Using the Tersoff–Brenner potential, we calculated the shape of the defective fullerenes. It is found that these fullerenes have a rounder shape than structures without defects. The electronic structure of the fullerenes with defects is also calculated within the Hückel approach. The electronic structures are closed and the energy gaps between bonding and antibonding orbitals are higher than those for fullerenes with no defects in almost all cases considered. © *2002 MAIK "Nauka/Interperiodica".*

Multilayer fullerene cages (MFC) have been obtained by intense electron-beam irradiation of carbon soot particles [1]. It was shown in [2] that these multilayer molecules are stabler than single-cage molecules above a certain critical number of atoms (about 6000 atoms). This stability is a consequence of van der Waals interactions between different shells. Transmission electron micrographs of MFC show that these molecules have an almost perfect round shape, while it is well known that large isolated fullerene cages have a polyhedral shape. Fullerene cages prefer a polyhedral shape, because planar arrangements of carbon atoms, such as those in graphite sheets, are stabler due to the fact that covalent bonds are less strained. This strain comes from the bending of sp^2 orbitals. The fullerene formation is possible due to the energy decrease produced when removing dangling bonds. It seems that, in order to keep round shapes, the strain of the lattice must be reduced.

Some authors have proposed that the addition of defects to fullerene structures could help in reducing the strain of covalent bonds [3–5]. In [5], defective fullerene structures were indicated to belong to the icosahedral point group, even though they were defective. Such fullerene structures are obtained after dualizing solutions to Thomson's problem (see [5] for details). Fullerenes with icosahedral symmetry have a number N of carbon atoms given by the expression $N = 60(k^2 + hk + h^2)$, where k and h are integers. When $h = k$ or $h > k = 0$, the structure belongs to the I_h point group. On the other hand, when $h > k > 0$, the structure has chirality and belongs to the pure rotational point group I. Molecules of this kind (whether they have chirality or not) have 12 five-membered rings, with the rest of the rings have six carbon atoms each. Henceforth, we name disclinations to each one of these 12 five-membered rings. We focus, in this work, on fullerenes with $h = k$; thus, the number N of carbon atoms is equal to $N = 60k^2$. These structures can be divided into 60 equivalent triangular patches of k^2 carbon atoms. Patches are formed by k zigzag lines. Disclinations are surrounded by five of these triangular patches. Each zigzag line has $2i - 1$ carbon atoms, where i is the ordinal number of the zigzag line.

1. DEFECTS IN FULLERENES

Basically, defects are bound pairs of seven- and five-membered rings. The defects can be symmetrically arranged around each disclination (one defect per triangular patch), with five defects being around each disclination and at the same distance. We say that we put defects on the ith line if this line is the first which does not have $2i - 1$ carbon atoms as in defect-free fullerenes. We study defects on the second and third lines. The structures obtained for the former case belong to the pure rotational point group I, while in the latter case, the structures belong to the point group I_h.

2. THE ELECTRONIC STRUCTURE

To calculate the electronic structure of fullerenes, we use the Hückel approximation with the improvement developed by Tang and Huang [6]. This method allows calculation of the electronic structure of giant fullerenes with I symmetry to be made at a low cost of

[1] This article was submitted by the authors in English.

computer time and resources. It consists of solving five secular equations, one for each irreducible representation of the I point group (A, T_1, T_2, G, H).

We found that fullerenes with defects either on the second line or on the third line have closed electronic shells, i.e., shells with an equal number of bonding and antibonding orbitals and without any nonbonding orbital. The difference between the highest occupied molecular orbital (HOMO) and the lowest unoccupied molecular orbital (LUMO) is larger for fullerenes with defects than for defect-free fullerenes for a sufficiently large number of carbon atoms. In Fig. 1a, this energy difference, HOMO–LUMO, is shown versus the number of carbon atoms for defect-free fullerenes (solid circles), for fullerenes with defects on the second line (solid squares), and for fullerenes with defects on the third line (empty diamonds). Some authors take this energy gap as a measure of chemical stability. Using this criteria, defective fullerenes seem to be stabler than defect-free fullerenes for a sufficiently large number of carbon atoms.

3. GEOMETRY OF FULLERENES WITH DEFECTS

To carry out a numerical study of the shapes of fullerene structures, we use the Tersoff–Brenner potential [7, 8]. This potential allows one to numerically calculate the energies of covalent bonds of carbon compounds. We minimize the Tersoff–Brenner energy using a conjugated gradient algorithm to obtain stable shapes for each structure. The energy landscape of this potential has many metastable minima. For this reason, we also use a simulated annealing-like method to improve the search for the lowest minimum for each case.

Pictures of the fullerene structures obtained after energy minimization show that defective fullerenes have a more spherical shape than defect-free fullerenes. The latter adopt a perfect polyhedral shape, as many other authors have already calculated. We found that the standard deviation (SD) of the radii is smaller for fullerenes with defects than for isolated defect-free fullerenes. Figure 1b shows the standard deviation of the radii as a function of the number of carbon atoms for defect-free fullerenes (solid circles), for fullerenes with defects on the second line (solid squares), and for fullerenes with defects on the third line (empty diamonds). In the figure, we can check that the type of defective fullerene with a rounder shape (lower SD) depends on the number N of carbon atoms; it is expected that as this number grows, new arrangements of defects could appear.

Thus, our numerical results indicate that the defectiveness of fullerenes could explain why multilayer fullerene cages exhibit an almost perfect spherical shape while isolated fullerenes have flat faces. We found that the electronic structures of defective fullerenes are closed for the cases considered and that the HOMO–LUMO gap is larger for defective fullerenes than for defect-free fullerenes for a sufficiently large number of carbon atoms. We also found that the standard deviation of the radii is lower for defective fullerenes, indicating that they are rounder than in the defect-free case.

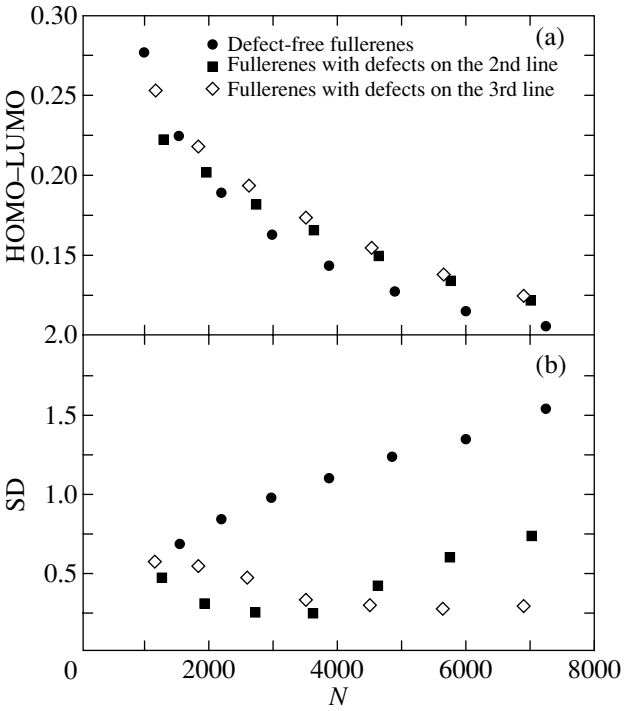

Fig. 1. (a) Energy gap, HOMO–LUMO, and (b) the standard deviation of the radii as a function of the number of carbon atoms. Solid circles correspond to defect-free fullerenes; solid squares, to fullerenes with defects on the second line; and empty diamonds, to fullerenes with defects on the third line.

REFERENCES

1. D. Ugarte, Nature **359**, 707 (1992).
2. A. Maiti, C. J. Brabec, and J. Bernholc, Phys. Rev. Lett. **70**, 3023 (1993).
3. K. R. Bates and G. E. Scuseria, Theor. Chem. Acc. **99**, 29 (1998).
4. C. J. Brabec, A. Maiti, and J. Bernholc, Chem. Phys. Lett. **219**, 473 (1994).
5. A. Pérez-Garrido, Phys. Rev. B **62**, 6979 (2000).
6. A. C. Tang and F. Q. Huang, Phys. Rev. B **51**, 13830 (1995).
7. J. Tersoff, Phys. Rev. Lett. **56**, 632 (1986).
8. D. Brenner, Phys. Rev. B **42**, 9458 (1990).